Bárbara Filipa Vasquez Vieira

**Engineering with Nature: An innovative
solution for coastal erosion protection**

setembro de 2022

Universidade do Minho
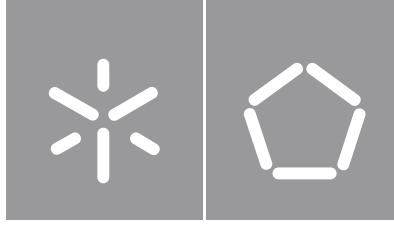Escola de Engenharia

Bárbara Filipa Vasquez Vieira

Engineering with Nature: An innovative solution for coastal erosion protection

Tese de Doutoramento
Programa Doutoral em Engenharia Civil

Trabalho realizado sob a orientação de
Professor Doutor José Luís da Silva Pinho
Professor Doutor Joaquim António Oliveira de Barros

setembro de 2022

To my parents, my two brothers and my grandmother

Cansamo-nos de tudo, excepto de compreender. O sentido da frase é por vezes difícil de atingir.

Cansamo-nos de pensar para chegar a uma conclusão, porque quanto mais se pensa, mais se analisa, mais se distingue, menos se chega a uma conclusão.

Caímos então naquele estado de inércia em que o mais que queremos é compreender bem o que é exposto – uma atitude estética, pois que queremos compreender sem nos interessar, sem que nos importe que o compreendido seja ou não verdadeiro, sem que vejamos mais no que compreendemos senão a forma exacta como foi exposto, a posição de beleza racional que tem para nós.

Fernando Pessoa *in* Livro do Desassossego

ACKNOWLEDGEMENTS

This thesis culminates the research work carried out within the framework of the doctoral program in Civil Engineering at the University of Minho. People and Institutions have contributed in a special way to make it possible to successfully complete this work and they deserve special thanks.

My first words of thanks are dedicated to my supervisors, Professor José Luis Pinho and Professor Joaquim Oliveira Barros to whom I would like to express my deepest gratitude for their exemplary guidance in the course of this research work. Much of the time for this work was spent during the COVID-19 pandemic which had a strong impact on our daily lives and the way of working never before experienced. Throughout this time, it was always possible to keep all essential processes running and obtain from them a word of encouragement and comfort to proceed with the work.

I would like to thank my supervisor Professor José Luis Pinho for having suggested that I develop this work in the fascinating field of nature-based engineering solutions applied in maritime hydraulics and for having accompanied me since the time of my Master's dissertation with his kindness, constant availability, and large scientific experience. I would also like to thank my co-supervisor Professor Joaquim Oliveira Barros for providing me the opportunity to deepen my studies in the area of structural design, and for his constant availability and scientific guidance in the course of this research.

I want to express my gratitude to Professor António Ventura Gouveia, Engineer Tiago Valente and my researcher colleague Luís Matos for their help and kindness sharing with me information and knowledge in subjects of concrete structures essential to the progress of this work.

I reserve a very special thanks to those I love very much, especially my parents, my two brothers and my grandmother for their constant and unfailing motivation and support in this new and important achievement in my life.

I want to express my gratitude to Hugo for the love, companionship and support in moments of distress, and to all my friends for the friendship and for never giving up on cheering me up.

I would also like to thank my host institutions at University of Minho, CTAC (Centre for Territory, Environment and Construction) and ISISE (Institute for Sustainability and Innovation in Structural Engineering), for providing the facilities and equipment needed for the development of this work.

STATEMENT OF INTEGRITY

I hereby declare having conducted this academic work with integrity. I confirm that I have not used plagiarism or any form of undue use of information or falsification of results along the process leading to its elaboration.

I further declare that I have fully acknowledged the Code of Ethical Conduct of the University of Minho.

ABSTRACT

Coastal zones are a much-appreciated environment by society, and support a large amount of economic and leisure activities. Growing demographic pressure on these very special territories that are associated to rapid economic growth and coastward migration has resulted in significant infrastructure and assets located in risk-prone areas, increasing exposure and vulnerability to natural disasters along the coast, including erosion, flooding and salt intrusion. In these areas, sediment transport and erosive processes are worldwide critical aspects for territory planning and management, especially in countries with long coastline like Portugal, since these phenomena often endanger human life and property protection. A research effort is still needed to find more robust and nature-based protection solutions adequate for high energetic coastal environments. The design, construction and maintenance of coastal protection structures incorporating principles of resilience to climate change impacts require a comprehensive multidisciplinary scientific approach for a deep understanding on coastal hydro-morphodynamics and on the behaviour of new eco-materials in marine environments. In this research work different methodologies were applied to describe: (i) wave climate regimes under uncertainty of climate changes scenarios off Iberian Peninsula coast; (ii) coastal hydro-morphology dynamics applying numeric modelling tools; and (iii) thermo-mechanical behaviour of an innovative eco-engineering solution for recycled steel fibre reinforced concrete armour unit. The main outcomes of this research are: (i) the determination of 10-, 50-, and 100-year return period of significant wave height and wave peak period values that can be used with confidence as design parameters for structural analyses in maritime works to be built in the western coast off Iberian Peninsula; (ii) results of a comparative study on coastal protection structures to promote wave energy dissipation and sediments retention; (iii) the proposal of an optimized geometry of maritime structures under longitudinal drift reversal conditions based on hydro- and morphodynamics modelling; (iv) a deep study on thermo-mechanical behaviour of a recycled steel fibre reinforced concrete armour unit; and (v) the proposal of an innovative eco-engineering solution for breakwater armour incorporating the new scientific achievements. Globally, this research work aims at the design and assessment of innovative nature-based coastal engineering solutions based on modelling and observation of natural accretion or sedimentary stable processes, and the application of high structural multifunctional eco-materials with high durability and ductility tested through numerical modelling.

Keywords: coastal erosion protection; hydro-morphodynamics modelling; innovative eco-engineering solutions; thermo-mechanical modelling; wave extreme values.

RESUMO

A crescente pressão demográfica sobre as zonas costeiras, associada ao rápido crescimento económico e à migração de pessoas para o litoral, tem tido como consequência a implantação de infraestruturas e ativos significativos em áreas propensas a riscos, aumentando a exposição e a vulnerabilidade a desastres naturais ao longo da costa, incluindo erosão, inundações e intrusão salina. O transporte de sedimentos e os processos erosivos nestas áreas constituem aspetos críticos para o ordenamento e gestão do território, especialmente em países de costa extensa como Portugal, uma vez que estes fenómenos colocam frequentemente em risco a vida humana e a proteção de bens. O projeto, construção e manutenção de estruturas de proteção costeira baseadas na natureza em ambientes altamente energéticos, incorporando princípios de resiliência aos impactos das alterações climáticas, requerem uma abrangente abordagem científica multidisciplinar para a compreensão da hidro-morfodinâmica costeira e do comportamento de novos eco-materiais em ambientes marinhos. Neste trabalho de investigação, foram aplicadas diferentes metodologias para descrever: (i) regimes de agitação marítima em cenários de incerteza provocados por alterações climáticas na costa da Península Ibérica; (ii) modelação da dinâmica da hidro-morfologia costeira; e (iii) comportamento termo-mecânico de uma solução inovadora de eco-engenharia para blocos de mantos de quebramar em betão reforçado com fibras de aço reciclado. Os principais resultados deste trabalho de investigação são: (i) a determinação do período de retorno de 10, 50 e 100 anos para a altura de onda significativa e para valores de período de pico de onda que podem ser aplicados com confiança como parâmetros de projeto para análises estruturais em obras marítimas a construir na costa ocidental da Península Ibérica; (ii) resultados de um estudo comparativo de estruturas de proteção costeira para promover a dissipação da energia das ondas e a retenção de sedimentos; (iii) a proposta de uma geometria otimizada para estruturas marítimas sob condições de inversão longitudinal da deriva com base em modelação hidro-morfodinâmica; (iv) um estudo aprofundado sobre o comportamento termo-mecânico de blocos de mantos de quebramar em betão reforçado com fibras de aço reciclado; e (v) a proposta de uma solução inovadora de eco-engenharia para mantos de quebramar, incorporando os novos resultados científicos obtidos. Em resumo, este trabalho de investigação visa o projeto e avaliação de soluções inovadoras de engenharia costeira baseadas na natureza, através de modelação e observação de processos estáveis de acreção natural ou sedimentar e a aplicação de eco-materiais multifuncionais de alta durabilidade e ductilidade testados através de modelação numérica.

Palavras-chave: modelação hidro-morfodinâmica; modelação termo-mecânica; proteção de erosão costeira; soluções inovadoras de eco-engenharia; valores extremos de onda.

TABLE OF CONTENTS

CHAPTER 7   CONCLUSIONS AND FUTURE RESEARCH

ACRONYMS AND ABBREVIATIONS

3D	Three Dimensional
BOUSS-2D	Boussinesq wave model for coastal regions and harbours
CAD	Computer Aided Design
CDF	Cumulative Distribution Function
CFD	Computational Fluid Dynamics
CI	Fibre Curvature Index
CMIP5	Coupled Model Intercomparison Project 5
CMIP6	Coupled Model Intercomparison Project 6
COBRAS-UC	Cornell Breaking Waves and Structures - University of Cantabria
COP13	United Nations Biodiversity Conference, Cancun 2016
COP21	United Nations Climate Change Conference, Paris 2015
COULWAVE	Cornell University Long and Intermediate WAVE Modelling
CTAC	Centre for Territory, Environment and Construction
DEFRA	Department for Environment, Food and Rural Affairs of United Kingdom
Delft3D	3D model to investigate hydrodynamics, sediment transport and morphology
EnCoRe	Environmentally-friendly solutions for Concrete with Recycled and natural components
FCT	Portuguese Foundation for Science and Technology
FEM	Finite Element Method
FEMIX	Finite Element Analysis of Structural Problems in Civil Engineering
FRC	Fibre Reinforced Concrete
FRPs	Fibre Reinforced Polymers
GEV	Generalized Extreme Value
GiD	Personal pre- and post- processor
GIS	Geographic Information System
HP	Historical Period
I-FORM	Inverse First-Order Reliability Method
IP	Integration Point
IPCC	United Nations Intergovernmental Panel on Climate Change
ISFRC	Industrial Steel Fibre Reinforced Concrete
ISFs	Industrial Steel Fibres
ISISE	Institute for Sustainability and Innovation in Structural Engineering
JONSWAP	Joint North Sea Wave Observation Project
LCA	Life Cycle Assessment
LST	Longshore Sediment Transport
MarRisk	R&D project financed under the programme INTERREGV (Spain-Portugal)
MFAR	Multifunctional Artificial Reef
MIROC5	Model for Interdisciplinary Research On Climate 5
ML	Mechanical Linear analysis
MNL1	Mechanical Nonlinear analysis with maximum of 1 crack allowed per IP
MNL2	Mechanical Nonlinear analysis with maximum of 2 cracks allowed per IP
Morfac	Morphological acceleration factor

MSL	Mean Sea Level
MSLR	Mean Sea Level Rise
N	North
NE	Northeast
NNW	North-Northwest
No.	Number
N-S	North - South
NSWE	Nonlinear Shallow Water Equations
NW	Northwest
Obs.	Observation
PE	Polyethylene
PET	Polyester
POOC	Plans for Spatial Planning of Coastal Zones
PP	Polypropylene
PVC	Polyvinylchloride
Q	Quadrant
RANS	Reynolds-averaged Navier Stokes
RB	Reference Bathymetry
RCP	Representative Concentration Pathway
RCP4.5_end	RCP with 4.5W/m^2 radiative forcing for the end of the 21st century (2081-2100)
RCP4.5_end	RCP with 4.5W/m^2 radiative forcing for the end of the 21st century (2081-2100)
RCP4.5_mid	RCP with 4.5W/m^2 radiative forcing for the mid of the 21st century (2026-2045)
RCP8.5_end	RCP with 8.5W/m^2 radiative forcing for the end of the 21st century (2081-2100)
RCP8.5_end	RCP with 8.5W/m^2 radiative forcing for the end of the 21st century (2081-2100)
RCP8.5_mid	RCP with 8.5W/m^2 radiative forcing for the mid of the 21st century (2026-2045)
RSFRC	Recycled Steel Fibre Reinforced Concrete
RSFs	Recycled Steel Fibres
S	South
SC	Scenario
	Shrinkage and Creep
SE	Southeast
SFRC	Steel Fibre Reinforced Concrete
SPM	Shore Protection Manual
SW	Southwest
SWAN	Simulation WAves Nearshore
UN	United Nations
UV	Ultraviolet radiation
W	West
WEC	Wave Energy Converter
WWIII	Wave Watch III model
XBeach	eXtreme Beach behaviour model

LIST OF FIGURES

LIST OF SYMBOLS

Latin uppercase letters

A_c	Concrete cross sectional area
A_T	Rate constant
D	Relative number of displaced armour units
D_{50}	Particle size distribution (e.g. 50% of the sample has a size of 200 µm or smaller)
D_{90}	Particle size distribution (e.g. 90% of the sample has a size of 300 µm or smaller)
D_i	Armour block height
D_m	Mean wave direction
D_n	Nominal diameter of the armour unit given by $(W/\rho_a)^{1/3}$
D_p	Peak wave direction
E	Wave energy per unit area
	Modulus of elasticity
E_a	Apparent activation energy
E_{After}	Wave energy after a structure
E_{Before}	Wave energy before a structure
E_c	Tangent modulus of concrete given by $1.05E_{cm}$
E_{cm}	Secant modulus of elasticity of concrete at 28 days
$F(X)$	Distribution function of a random variable, X
G	Gap width between structures
G_f^I	Mode I (in-plane) fracture energy
$G(P)$	Percent point function
H	Incident design wave height
H_0	Offshore wave height in deep water
H_b	Wave height at the break point (where the waves start to break)
H_{m0}	Significant wave height in front of the breakwater
H_{rms}	Root mean square wave height
H_s	Significant wave height
$H_{s,0,95}$	95th percentile of H_s
$H_{s\,After}$	Significant wave height after a structure
$H_{s\,Before}$	Significant wave height before a structure
$H_{s\,SWAN}$	Significant wave height computed by SWAN
$H_{s\,XBeach}$	Significant wave height computed by XBeach
H_{sb}	Significant wave height at breaking
K	Empirical coefficient
K_D	Stability coefficient of the armour unit
L_0	Deep-water wavelength
L_i	Thickness layer
L_m	Wave length
M	Armour block mass
N	Total number of samples

N_{od}	Armour units displaced out of the armour layer (hydraulic damage)
N_S	Structure stability number
N_z	Number of waves (between 1000 and 7000)
$P = S(X_i)$	Exceedance probability of a random variable, X
Q	Submerged total LST rate
$\dot{Q}$	Heat generation rate
$Q\,(t)$	Accumulated heat generated until a certain instant
Q_{total}	Final accumulated heat of the cement hydration
R	Universal gas constant
R^2	Coefficient of determination
S_a (m)	Distance between the apex of the protection structure and the undisturbed coastline
SZW (m)	Width of the natural surf zone
T	Wave period
	Temperature
T_m	Mean wave period
T_p	Peak wave period
T_r	Return period
W	Weight of an individual armour unit in the primary cover layer
X	Random variable
	Distance from the beach to the ledge of the structure

Latin lowercase letters

d_f	Fibre diameter
$f(\alpha_T)$	Normalized heat generation rate
f_{ct}	Concrete tensile strength
f_{cm}	Mean compressive strength of concrete at 28 days of age
$f_{ctk,min}$	Lower bound value of the characteristic tensile strength of concrete at 28 days of age
f_{ctm}	Mean tensile strength of concrete at 28 days of age
f_{Ftu}	Ultimate residual tensile strength (post-cracking strength for ultimate crack opening)
f_{Fts}	Serviceability residual tensile strength (post-cracking strength for serviceability crack opening)
f_{R1k}	Characteristic residual flexural tensile strength for serviceability conditions
f_{R3k}	Characteristic residual flexural tensile strength for ultimate conditions
g	Gravitational acceleration constant
h_0	Notional size of the cross section
h_b	Water depth at breaking
h_{cr}	Heat transfer coefficient
h_{eq}	Equivalent heat transfer coefficient
i	Number of sample values for which any variable value $x \leq X_i$
k	Fibre aspect ratio defined as the ratio between the l_d and d_f
k_i	Thermal conductivity

l_b	Crack bandwidth
l_d	Fibre developed length defined as the total length of the fibre along its axis
l_f	Fibre length defined as the distance between the outer ends of a fibre
r	Dolos waist ratio
s_m	Mean wave steepness given by $2\pi H / g T^2$
u	Perimeter of the part of the cross section exposed to drying
w	Crack width
w_{SLS}	Serviceability crack width
w_{ULS}	Ultimate crack width
x	Variable value

Greek uppercase letters

Δ	Relative density
$\Delta_{SWAN-XBeach}$	Comparison between SWAN and XBeach hydrodynamics results
ΔT	Temperature variation
$\phi(t, t_0)$	Creep coefficient

Greek lowercase letters

α	Numerical model H_s reduction for a specific location
	Coefficient of thermal expansion
α, θ	Angle of a structure slope measured from horizontal
α_G	Location parameter of the Gumbel distribution
α_i	Fracture parameter used to define the stress-strain softening diagram
α_T	Degree of heat development
α_{th}	Threshold angle
β	Numerical model E reduction for a specific location
β_F	Scale parameter of Fréchet distribution
β_G	Scale parameter of the Gumbel distribution
β_W	Scale parameter of Weibull distribution
γ	Specific weight of the armour unit in the cover layer
γ_b	Breaker index given by H_{sb}/h_b
γ_W	Seawater specific weight
$\varepsilon(t)$	Total strain
$\varepsilon^c(t)$	Creep strain at time $t > t_0$
$\varepsilon^{cr}_{n,u}$	Ultimate crack normal strain
$\varepsilon^{in}(t_0)$	Initial strain at loading
$\varepsilon^s(t)$	Shrinkage strain
$\varepsilon^T(t)$	Thermal strain
$\varepsilon_{ca}(t)$	Autogenous shrinkage strain at time t
$\varepsilon_{cd}(t, t_s)$	Drying shrinkage strain at time t
$\underline{\varepsilon}(t)$	Total strain vector

$\underline{\varepsilon}^c(t)$	Creep strain vectors
$\underline{\varepsilon}^{co}$	Strain vector of the uncracked concrete
$\underline{\varepsilon}^{cr}(t)$	Crack strain vector
$\underline{\varepsilon}^e(t_0)$	Elastic strain vectors
$\underline{\varepsilon}^s(t)$	Shrinkage strain vectors
$\underline{\varepsilon}^T(t)$	Thermal strain vectors
θ_b	Wave angle at breaking
λ_F	Shape parameter of Fréchet distribution
λ_W	Shape parameter of Weibull distribution
ν	Poisson's ratio
ξ	Breaker parameter or Iribarren number given by $(tan\theta/\sqrt{s_m})$
ξ_0	Iribarren number in deep water
ξ_b	Iribarren number at the break point (where the waves start to break)
ξ_i	Fracture parameter used to define the stress-strain softening diagram
ρ	Material volumetric mass density
ρ_a	Density of the (concrete) armour unit
ρ_w	Density of seawater
ρc	Specific heat capacity
σ_c	Constant stress applied at a concrete age t_0
$\varphi_{n=2}$	Packing density of 2 layers

LIST OF TABLES

CHAPTER 1

Introduction

"*Nothing in life is to be feared, it is only to be understood. Now is the time to understand more, so that we may fear less*"

Marie Curie. Polish and naturalized-French physicist and chemist. Nobel Prize in Physics in 1903, and Nobel Prize in Chemistry in 1911 (1867-1934)

(Page intentionally left blank)

CHAPTER 1   INTRODUCTION

1.1 Context and motivation of the research

1.1.1 The importance of coastal protection

Coastal areas are home to nearly half of the world's population and the preferred location for the majority of the world's largest cities. Those areas are a much-appreciated environment by society, supports a large amount of economic and leisure activities (Castelle *et al.*, 2018) and will continue to rapidly expand over the next century by population pressures with the increase of exploitation of coastal resources, contributing to their environmental degradation. Coastal low-lying, densely populated zones are highly vulnerable to natural and anthropogenic hazards, and coastal ecosystems are now facing a range of challenges, including coastal erosion, unsustainable beach and offshore sand mining practices, rapid urbanization, and unsustainable land use (Narra *et al.*, 2017; United Nations, 2015; Weinberg, 2015). Coastal zones require new strategies to deal with land subsidence, sea level rise and the increasing risk of storm-surge-induced floods due to frequent extreme weather events (IPCC, 2012).

Coastal erosion is a typical primary natural process that has shaped the surface of the Earth. It includes a broad range of processes such as rain and wind action, wind-induced waves breaking, coastal currents, amongst others that are acting at different temporal and spatial scales, and that are commonly self-related (van Rijn, 2011). It can be related to slow shoreline behaviours working for decades and that often affect long coastal stretches covering large areas. It can also be linked to rapid processes, sometimes comprising no more than movements during a time span of seconds, and usually involving the transport of small particles, less than a few millimetres or even micrometers in size (Larson and Kraus, 1995).

Projections presented by the Intergovernmental Panel on Climate Change (IPCC) indicate that global climate change may rise sea level as much as one meter over the next century (Figure 1.1) and, in some areas, increase the frequency and severity of storms (Gilbert and Vellinga, 1990) raising a significant hazard to ecosystems and human activities, generating a significant economic loss and ecological damage especially on extremely vulnerable regions with delicate physiographic equilibria such as the case of coastal zones. Other consequences of this can result in the thinning of beach width, constant loss of property and infrastructures, and the rupture of protective structures, which produce a high loss of valuable coastal habitats, resulting in difficult management issues (Rangel-Buitrago *et al.*, 2018). Flooding of hundreds of thousands of square kilometres of coastal wetlands and other lowlands would threaten lives, buildings, and infrastructures, as well as putting drinking water sources out of service due to salt intrusion in coastal aquifers. This way, functions and values of coastal zones are

degraded with the related social and economic impacts. Consequently, populated coastal areas are becoming more and more vulnerable to sea level rise and other impacts of climate change for which adequate responses are required.
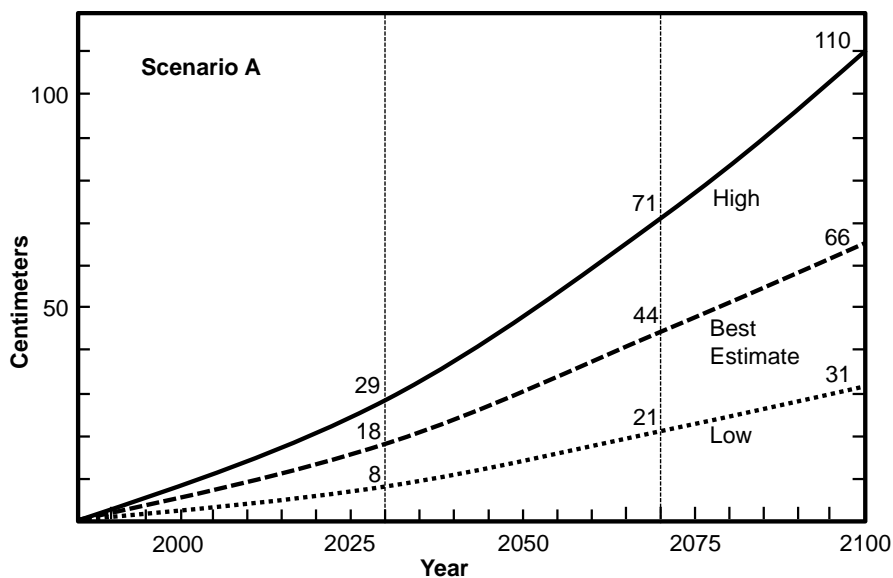
Figure 1.1: Global sea level rise, 1985-2100 for policy of no limitation of greenhouse gases (scenario A) (Adapted from Houghton *et al.*, 1990).

United Nations Sustainable Development Goal 13 (Climate Action) proposes that urgent measures should be taken to combat climate change and its impacts strengthening resilience and adaptive capacity to address damage of critical infrastructure. Special planning and management approaches with a paradigmatic shift from crisis management to risk management (hazard analysis and vulnerability analysis) in a changing environment are required.

Management strategies proposing pragmatic and feasible solutions must include the techniques, knowledge, equipment, and institutional instruments required to minimize and mitigate the consequences of coastal erosion related impacts (Adriana-Gracia *et al.*, 2018). One vital element of a plan to manage this phenomenon is to formulate and implement effective integrated coastal management programs. This was one of the recommendations of the IPCC and the 1992 Earth Summit in Rio de Janeiro. The implementation of such a plan implies the consideration of responses that fall broadly into four categories (Cardona, 2015; Granja and Pinho, 2012; Williams *et al.*, 2018):

- Retreat: involves no effort to protect the land from the sea. The coastal zone is abandoned and ecosystems shift landward (e.g., demolitions, relocations and compensations);
- Accommodation: implies that people continue to use the land at risk but do not attempt to prevent the land from being flooded, i.e., people adapt to the overall coastal marine dynamics

farming, or beach nourishment);

— Protection: involves hard structures (e.g., seawalls, groins, breakwaters, and dikes) as well as soft solutions like dunes and vegetation;

— Do nothing: allows the natural evolution of coastal marine dynamics.

Efficient strategies for these zones are required in order to protect society, economy and valuable natural environments. Traditional coastal protection engineering solutions like groins, breakwaters, storm surge barriers and defensive coastal maintenance strategies are often suboptimal with respect to other functions and are neither resilient nor sustainable in many cases (Airoldi *et al.*, 2005; Pilkey and Cooper, 2014). Thus, new coastal protection solutions that are able to follow climate changes and that are robust, sustainable, adaptable, multifunctional and yet economically feasible are needed (Antunes do Carmo, 2013; Hegde *et al.*, 2018; Misdorp and Salman, 2011; van Slobbe *et al.*, 2013; Waterman, 2010).

1.1.2 Management of coastal zones in Portugal

Portugal is one of the European countries most affected by coastal erosion with about one third of its coastline subject to erosion, where about 75% of the Portuguese population lives (Marinho, 2015; Schmidt and Mourato, 2015). The Atlantic coast of Portugal is exposed to rough wave climate conditions and frequently submitted to powerful storms (more frequent from October to March), endangering waterfronts, infrastructures and natural landscapes (Dias *et al.*, 2000; Narra *et al.*, 2015; Pereira *et al.*, 2013). Main wave crest orientation is from the Northwest (NW) (40%) (Rosa-Santos *et al.*, 2008), inducing a littoral sediments drift from North-South (N-S). However, this sediments transport pattern is, in some areas, reversed (Figure 1.2) due to the presence of some natural (bars, ebb tidal deltas, rocky outcrops) and artificial (breakwaters, jetties, groins) obstacles that promote local wave diffraction (capacity for a wave to contour an obstacle) and refraction (change of wave direction) (Granja and Pinho, 2012; USAEWES, 1992).
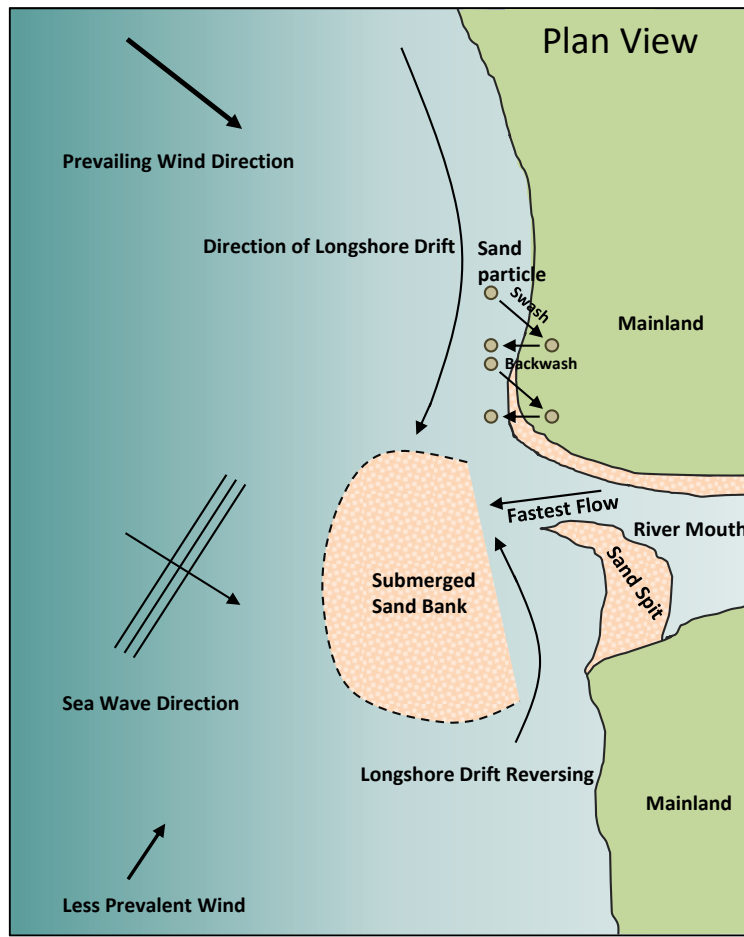
Figure 1.2: Scheme for longshore sediment transport and longshore drift reversing phenomena, and sand spit formation at a river mouth.

Coastal retreat is mainly influenced by two factors: sea level rise (10–20%) and sediment starving of the coasts (80–90%) (Dias *et al.*, 2000). The fall of cliffs and the sand reduction on beaches are some of the most evident symptoms of a process with deep social and economic implications, and despite heavy investments in coastal protection works, the Portuguese coastline is retreating at an accelerated rate. Cumulatively, public planning policies are insufficient to halt urban expansion along the Portuguese coastline, even in areas at risk (Schmidt and Mourato, 2015).

Some of the Portuguese coastal zones that suffer most from erosion are:

– From the Minho river mouth to Ofir: specially between the Cávado river mouth and Ofir where, during 1923 to 1950, the coastal erosion rates were of 0.2 m/year, and in the period between 1950 and 1980 the coastal erosion rate rose to about 1 m/year (Veloso-Gomes *et al.*, 2006);

– From Espinho to Mira: where between Maceda and Torrão do Lameiro (municipality of Ovar), during 1958 to 2010, the average coastal erosion rates were near 3 m/year (Silva, 2012);

- South of cape Mondego: where there is a coastal erosive process downdrift of Figueira da Foz (from Cova Gala to Leirosa), due to the north jetty installed at the Mondego river mouth (André and Cordeiro, 2013);

- Costa da Caparica: where, between 1958 and 2007, the coastline retreated 210 meters (Pinto *et al.*, 2012);

- From Olhos de Água to Formosa ria: where in Forte Novo, near Quarteira, between 1976 and 2001 the average coastal erosion rate was 2.9 m/year (Vargas *et al.*, 2012).

Sandy coastlines, without headlands or rocky foreshores are the most vulnerable Portuguese coastal areas to erosion (Veloso-Gomes and Taveira-Pinto, 1997). Figure 1.3 depicts some examples on the Portuguese coast of intense urban development on unstable and environmentally sensitive areas and the existent erosion problems (Veloso-Gomes and Taveira-Pinto, 1997).
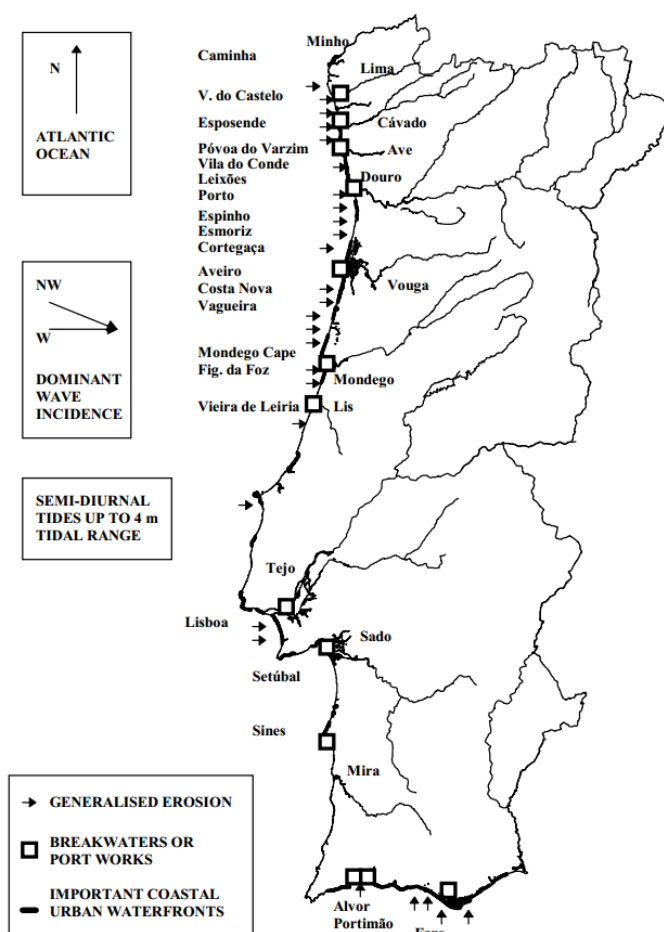
Figure 1.3: Portuguese coastal occupation and existent erosion problems. (Adapted from Veloso-Gomes and Taveira-Pinto, 1997).

The weaknesses of the coastal zone in Portugal are associated with several anthropogenic causes like urban and industrial occupation, river works, harbours and dams construction, and extraction of sediments. Other weaknesses are related with natural causes like wave climate characteristics, rise of mean sea level (MSL) and the frequency and intensity of storm events. These factors are responsible for reducing the amount of sediments that are transported to the coast, new coastal morphodynamic situations and major coastal landscape changes.

Dunes are the first natural protection barrier with an important contribution not only in terms of slowing down the ocean's advance, because they can act as sand reservoirs for beaches, but also in terms of protecting and recovering important coastal ecosystems. The continued destruction of dunes and vegetation by trampling and by building housing and improvised parking lots prevent the accumulation of sand, thus contributing greatly to the instability of natural protections (Veloso-Gomes and Taveira-Pinto, 2003). However, since the sediments that are accumulated in this natural deposits are wind selected, their size and density characteristics present a limited potential to reconstruct eroded beaches (Pinho and Granja, 2018).

The Portuguese winter of 2013/2014 was characterized by an intense sea storminess evidenced by more than a dozen storms, maximum wave heights of 15 m, significant wave heights (the average height of the highest one-third of all waves measured in a given period, $H_{1/3}$) of more than 9 m, storm surges over 1 m, wave periods of over 20 s and strong winds on beaches weakened by the progressive loss of sediments. These extreme meteorological phenomena are a sign that there is a natural climate variability that is "forgotten", but must be present in territorial planning instruments through prevention and adaptation measures (Veloso-Gomes, 2015).

As an example of these phenomena, Figures 1.4 and 1.5 depict some consequences of the storm of 2014 that occurred in the winter time in the Portuguese coastal zone (Ofir beach and Póvoa de Varzim). Most people claim for coastal protections from the responsible entities because they don't want to lose their homes due to erosion. Simões *et al.* (2013) explain that currently, there is already a concern to reset sediments on the beaches, both by feeding artificially and by building defence structures. In order to defend the urban areas and the land use, new solutions for coastal protection are needed. However, these works may induce or anticipate other erosion problems southwards. The planning, design and construction processes of coastal structures must be based on information and knowledge of maritime coastal dynamics and depend on the construction methods applied and on the characteristics of the available equipment, being numerical modelling an efficient tool for supporting planning and design innovative alternative engineering solutions.
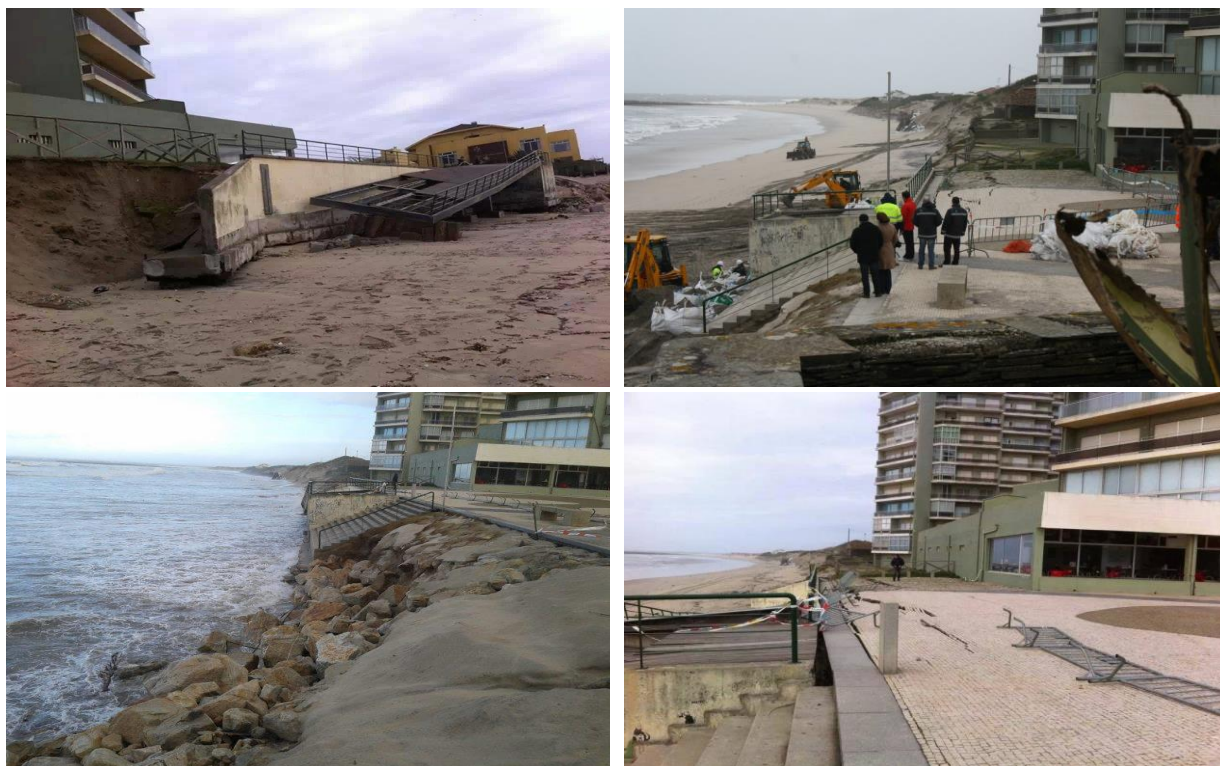
Figure 1.4: Erosion problems in Ofir beach – storm of 2014 (Vieira, 2014).

Figure 1.5: Flooding events in the city of Póvoa de Varzim – storm of 2014 (Vieira, 2014).

Although the consensus among stakeholders over adaptation strategies has been shown to be a complex process (Neves *et al.*, 2018), the implementation and assessment of plans for spatial planning

of coastal zones should be a key instrument for effective integrated management of coastal zones in Portugal and all over the world.

In the last decades, several different types of traditional coastal defence works have been built in Portugal in a tentative to achieve an "artificial stable" coastal zone. However, in most cases this methodology revealed inefficient in stabilizing the coastline. Thus, it is of paramount importance to understand the underlying causes for those results and create more efficient means to deal with the coastal erosion impacts (Granja and Pinho, 2012).

Recently, artificial beach nourishment has been applied in Portugal as an environmentally acceptable coastal defence and regeneration technique. This technique has been used in emergency situations as a local and short-term solution (e.g., mitigation of weather-induced erosion), or as a regional and long-term management strategy (e.g., mitigation of installed erosion tendency and vulnerability to rising mean sea level). However, this technical option has not been assessed and justified in terms of its efficiency and effectiveness (Pinto *et al.*, 2018).

Mitigate coastal erosion and recover beach areas must be considered strategic for environmental, social or economic reasons. Integrated management of coastal sediments can be achieved by studying and implementing adequate engineering solutions to prevent coastal retreat and thinning of beaches. This may lead to conclude on the great probability that it will be necessary to carry out protection works, which justifies this research work.

1.1.3 The Portuguese coastal protection situation

Many of the observed damages at the Portuguese coast are related to an inadequate occupation of coastal dynamic territories, which result in high protection costs. Although these bad planning practices began to be fought with the POOC (Plans for Spatial Planning of Coastal Zones), the built fronts remain and it is urgent to either defend or demolish them (Veloso-Gomes, 2015). Although technical protection solutions are known, its costs are high and challenges to find the perfect solution from an environmental or technical point of view will have to be faced.

Currently, around 15% of the Portuguese coast is protected by different types of artificial hard structures such as groins, jetties, breakwaters and longitudinal revetments. These structures are mainly concentrated in the NW coast due to the fact that this region is highly energetic with a wave regime typically from NW (40%), characterised by a mean significant wave height of 2 m and a mean period of 12 s. Storms, occurring especially in the winter, come predominantly from NW with offshore significant wave heights that may reach 8 m persisting for up to 5 days. The tide regime is semidiurnal (two high

and two low tides of approximately equal size every lunar day) with a tidal range between 2 m in neap tides and 4 m in spring tides. The potential longshore transport mainly due to the wave action is approximately 1-2 million m³/year (Oliveira, 1997). The longshore drift is the phenomenon that results from the action of sea waves incoming at an angle with the coastline that induce a net sediment transport alongshore.

The energetic Portuguese West coast wave climate requires a maintenance program that involves high investments throughout their life cycle. When these investments are not made, serious damage occurs to the structures, particularly during storm events. Artificial nourishment is not compatible with Portuguese West coast dynamics and nourished beach sediments are rapidly lost. Furthermore, some traditional coastal protection structures have contributed to the acceleration of erosion rates in several coastal stretches and their financial costs were very high (Granja and Pinho, 2012). For this reason, new coastal protection solutions are being tested, but their effectiveness is very dependent on local energy goals and levels (Neves *et al.*, 2015). When sea actions are very energetic (waves and tides), geosynthetic-based solutions confining sand may not be effective in protecting urban fronts, even though these solutions are being run and tested for dune protection (Veloso-Gomes, 2015).

1.2 Research objectives and methodology

The main objective of this research work is to design and assess an innovative coastal protection solution based on modelling and observation of natural accretion or sedimentary stable processes, applying high structural multifunctional eco-materials (tested through numerical modelling) with high durability and ductility. The purpose is to provide coastal infrastructure designers with nature-based solutions reproducing and manipulating natural processes, such as sediment transport involving longitudinal drift and drift reversal phenomena.

Several intermediate scientific contributions were coherently integrated in order to serve as a support to achieve this main objective, namely: (i) the study of wave regimes under uncertainty scenarios in the western coast off Iberian Peninsula computing return periods of significant wave height and wave peak period values to be used as design parameters for structural analyses in maritime works; (ii) comparative studies of coastal protection structures applied to promote wave energy dissipation and sediments retention; (iii) the proposal of an optimized geometry of maritime structures under longitudinal drift reversal conditions based on hydro- and morphodynamics modelling; and (iv) a deep study on strength of eco-materials focusing on the thermo-mechanical behaviour of a recycled steel fibre reinforced concrete armour unit.

The methodological approach to achieve the proposed objectives took into account the eminently multidisciplinary nature of this research where a combination of disciplines come together to devise an appropriate solution (Figure 1.6): i) statistical methods used to study extreme wave regimes under uncertainty of climate changes scenarios of Iberian Peninsula coast; ii) hydro-morphodynamics applying numerical modelling tools to determine optimized geometric solutions to promote wave energy dissipation and sediments retention mimicking and manipulating natural processes like longitudinal drift reversal; iii) strength of materials applying numerical tools for the study of the thermo-mechanical behaviour of a proposed eco-concrete armour unit.
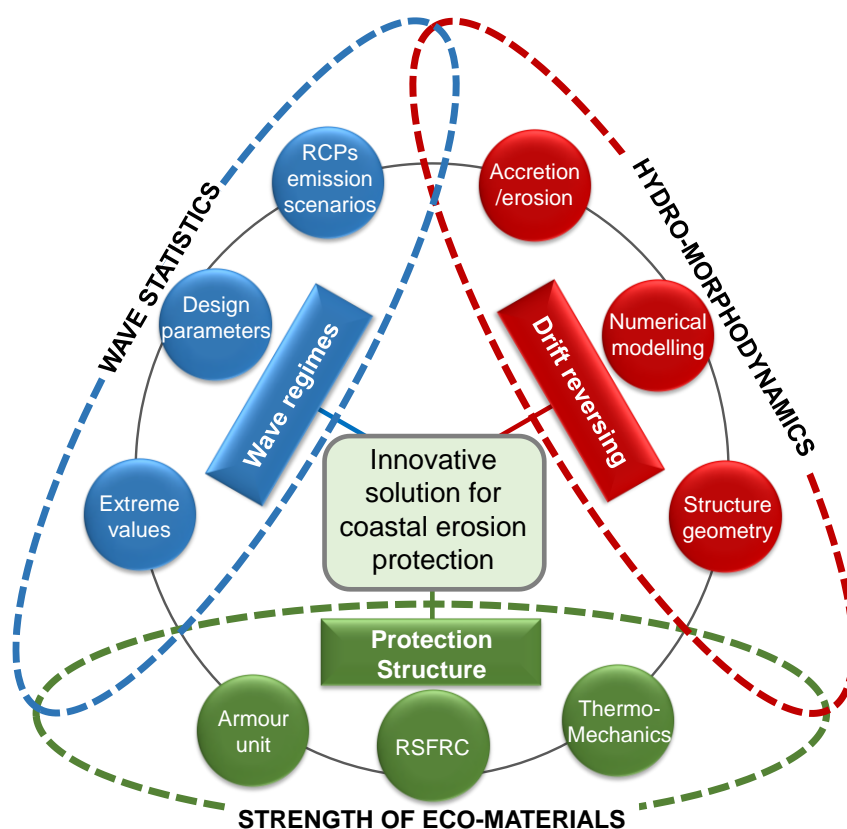
Figure 1.6: Multidisciplnary approach of the research.

The research methodology can be summarised as follows:

  – Use of wave datasets downscaled with the Wave Watch III model of Meteogalicia, for historical and future climates, to obtain wave climate data (significant wave height, peak period, and wave direction) off Iberian Peninsula coast;

  – Estimation of extreme values of design parameters for coastal engineering projects under uncertainty considering climate change scenarios;

– Study of different types of traditional and nature-based solutions, and sustainable eco-materials and innovative solutions for coastal protection and their impacts on coastal zones;

– Characterization of the processes responsible for morpho-sedimentary drivers that promote reversing of longshore drift, and consequently sediment accretion, based on full-scale observation data in the NW Portuguese coast;

– Analysis of different software solutions and implement numerical morphodynamics models capable of reproducing main sediment transport patterns involved in the drift phenomena and the occurrence of drift reversing, induced by wave deformation due to obstacle interposition;

– Design of innovative technical solutions for coastal protection through reversal of the dominant longshore drift, considering the results obtained from field data and numerical models, in order to mitigate installed erosive processes;

– Development of numerical modelling research in the application of high durable cement based materials, incorporating recycled constituents in coastal environments, promoting multifunctional structures that could preserve marine life;

– Definition of shape and dimensions, and study of thermo-mechanical stress cracking on concrete structures;

– Demonstration of the applicability of the methodology in the NW Portuguese coastal conditions and that this research work is contributing to at least three of the United Nations Sustainable Development Goals: determining the risk of coastal erosion and identifying adaptation interventions for reducing the vulnerability of coastal infrastructure and climate change impacts (Goal 13.1); and evaluating the most efficient options to protect the populations, the natural and cultural assets and the activities in selected zones (Goals 14.2 and 11.4).

1.3 Thesis layout

This thesis is organized into seven chapters and four appendices. The appendices provide supplementary information to the main chapters and are compiled in a separate volume.

Chapter 1. This chapter presents an overview of the context and motivation of the research. The main objectives, the research methodology and the organization of the present document are also detailed. A list of published research works is also presented.

Chapter 2. This chapter provides a broad literature review in the relevant domains of the research concerning coastal erosion protection structures based on existing projects and available publications, with a special focus on coastal hydrodynamics, morphodynamics and structural design. Fundamentals

on hydrodynamics and morphodynamics of coastal zones, as well as general aspects to be considered on coastal structures design are reviewed. A wide range of traditional and nature-based technical solutions for coastal protection is reviewed, including structural analysis of materials such as concrete and discrete fibres like recycled steel and sisal in order to understand their potential applicability. The main characteristics of different tools for hydro-morphodynamics and thermo-mechanical modelling, integrated in a so-called numerical laboratory, are also evaluated.

Chapter 3. An extreme wave value analysis under uncertainty scenarios due to climate change using comprehensive simulated wave datasets downscaled by Meteogalicia from CMIP5 models to 17 stations off the Iberian Peninsula coastal zone has been performed. For that purpose, descriptive statistical analysis using different distribution probabilities to determine wave climate regimes and predict intensity and duration of extreme events occurrences are presented. From this study, it is also proposed extreme values of waves for H_s and T_p, which are essential parameters for the maritime structural design in this coastal zone.

Chapter 4. In this chapter, a comparative study to assess the performance of a multifunctional artificial reef structure and three traditional coastal protection solutions in dissipating wave energy and protecting the beach using numerical models implemented with SWAN and XBeach software is described. Results obtained with both models on predicting significant wave heights, and the accretion and erosion patterns along the shoreline for the four structures scenarios are also presented.

Chapter 5. This chapter provides an in-depth assessment of hydro- and morphodynamics modelling for optimizing the geometry of maritime structures under longitudinal drift reversal conditions. For that, geometric jetty characteristics and sedimentary conditions near estuaries and numerical simulations on wave climate near Iberian Peninsula shoreline under different scenarios are presented. Obtained results for hydrodynamics and morphodynamics are discussed considering bathymetric changes characterized by their volumes, whereas the structures are considered detailing their dimensions, slopes, volumes and positions relatively to shoreline.

Chapter 6. This chapter describes the proposal design parameters for innovative recycled steel fibre reinforced concrete armour units based on good structural and hydraulic stabilities for coastal erosion protection. The results of a thermo-mechanical analysis performed to assess the structural behaviour of these units namely their composition, mechanical properties and the cracking mechanisms are discussed. This chapter also emphasises and discusses the eco-friendly design considering that the armour unit shape, with holes on its faces, increases the wave energy dissipation and allows the easy

attachment of colonies of marine organisms and at the same time allowing natural fibre rope confinement through the holes.

Chapter 7. This chapter provides a synthesis of the main achievements and original contributions of this research work, together with suggestions and perspectives for future research.

References. The references cited throughout the text are organized by chapter and appear listed by alphabetical order of the first author at the end of each of the respective chapters.

Appendix 1. Concrete mixes and mechanical properties of concrete structures.

Appendix 2. Wave statistics off Iberian Peninsula.

Appendix 3. Extreme wave data analysis off Iberian Peninsula under 5 wave climate regime scenarios.

Appendix 4. Thermo-mechanical analysis of the proposed concrete armour unit.

1.4 Publications

Several papers have been published in peer-reviewed ISI indexed journals or international conference proceedings in the course of the development of this research work. These publications are listed as follows:

(i) International Peer-Reviewed Journals

– **Vieira, B.F. V.**; Pinho, J.L.S.; and Barros, J.A.O. (2021). Extreme wave value analysis under uncertainty of climate change scenarios off Iberian Peninsula coast. Ocean Engineering, 229, 109018. https://doi.org/https://doi.org/10.1016/j.oceaneng.2021.109018.

– **Vieira, B.F.V.**; Pinho, J.L.S.; Barros, J.A.O.; and Antunes do Carmo, J.S. (2020). Hydrodynamics and Morphodynamics Performance Assessment of Three Coastal Protection Structures. Journal of Marine Science and Engineering, 8(3), 175. https://doi.org/doi.org/10.3390/jmse8030175.

(ii) International Conference proceedings

– **Vieira, B.F.V.**; Pinho, J.L.S.; and Barros, J.A.O. (2021). Assessment of different coastal defence structures to promote wave energy dissipation and sediments retention. In J. Sena-Cruz, L. Correia, & M. Azenha (Eds.), Proceedings of the 3rd RILEM Spring Convention and Conference (RSCC 2020). Volume 3: Service Life Extension of Existing Structures. Chapter 4 (p. 337). Springer International Publishing. https://doi.org/10.1007/978-3-030-76465-4.

– Vieira, J.M.P.; Pinho, J.L.S.; **Vieira, B.F.V.**; and Vieira, L.M.V. (2019). Flood forecast technological platforms: An adaptive response to extreme events. In World Engineers

Convention 2019, 20th to 22nd November 2019 (pp. 1966–1974). Melbourne, Australia. https://search.informit.com.au/documentSummary;dn=978870216429204;res=IELENG.

‒ **Vieira, B.**; Pinho, J.; Barros, J. (2019). Obras de Defesa Costeira: Potencialidades de Inovação. IX Congresso sobre Planeamento e Gestão das Zonas Costeiras dos Países de Expressão Portuguesa. Lisbon, 14th to 16th May, 2019.

‒ **Vieira, B.**; Pinho, J.; and Vieira, L. (2018). Comparison of 1DH and 2DH Mathematical Models for Modelling Wave Hydrodynamics in Ofir Beach. In G. La Loggia, G. Freni, V. Puleo, & M. De Marchis (Eds.), HIC 2018. 13th International Conference on Hydroinformatics (EPiC Series in Engineering), 1st to 5th July 2018 (Vol. 3, pp. 2196–2203). Palermo, Italy: EasyChair. https://doi.org/10.29007/gp4l.

1.5 References for Chapter 1

Adriana-Gracia, C.; Rangel-Buitrago, N.; Oakley, J.A.; and Williams, A. (2018). Use of ecosystems in coastal erosion management. *Ocean and Coastal Management*, *156*, 277–289. https://doi.org/10.1016/j.ocecoaman.2017.07.009.

Airoldi, L.; Abbiati, M.; Beck, M.W.; Hawkins, S.J.; Jonsson, P.R.; Martin, D.; Moschella, P.S.; Sundelöf, A.; Thompson, R.C.; and Åberg, P. (2005). An ecological perspective on the deployment and design of low-crested and other hard coastal defence structures. In *1st International Conference on Coastal Zone Management of River Deltas and Low Land Coastlines,* (Vol. 52, pp. 1073–1087). https://doi.org/10.1016/j.coastaleng.2005.09.007.

André, J.N.; and Cordeiro, M.F.N. (2013). Alteração da linha de costa entre a Figueira da Foz e S. Pedro de Moel após o prolongamento do molhe norte do Mondego. In *Actas do VI Congresso Nacional de Geomorfologia, 21 a 23 de Fevereiro 2013* (pp. 6–10). Coimbra, Portugal. Retrieved from http://www.uc.pt/fluc/depgeo/vicng/pdf/02.

Antunes do Carmo, J. (2013). Experiência de recuperação de um sistema dunar e proposta de instrumentos complementares de proteção, atração e valorização ambiental. *Revista de Gestão Costeira Integrada*, *13*(3), 317–328. https://doi.org/10.5894/rgci394.

Cardona, F.M.D.S. (2015). *Avaliação do risco de erosão, galgamento e inundação costeira em áreas artificiais de Portugal continental. Estratégias de adaptação face a diferentes cenários de risco (relocalização, acomodação e proteção).* MSc Thesis in Environmental Engineering, Faculty of Science and Technology of Nova University of Lisbon, Portugal. Retrieved from http://hdl.handle.net/10362/16198.

Castelle, B.; Guillot, B.; Marieu, V.; Chaumillon, E.; Hanquiez, V.; Bujan, S.; and Poppeschi, C. (2018). Spatial and temporal patterns of shoreline change of a 280-km high-energy disrupted sandy coast from 1950 to 2014: SW France. *Estuarine, Coastal and Shelf Science*, *200*, 212–223. https://doi.org/10.1016/j.ecss.2017.11.005.

Dias, J.M.A.; Boski, T.; Rodrigues, A.; and Magalhães, F. (2000). Coast line evolution in Portugal since the Last Glacial Maximum until present — a synthesis. *Marine Geology*, *170*(1–2), 177–186. https://doi.org/10.1016/S0025-3227(00)00073-6.

Gilbert, J.; and Vellinga, P. (1990). Climate Change: The IPCC Response Strategies - Chapter 5. In *Report prepared for Intergovernmental Panel on Climate Change by Working Groups III* (p. 330). Digitization and Microform Unit (2010), UNOG Library. Retrieved from https://www.ipcc.ch/ipccreports/far/wg_III/ipcc_far_wg_III_chapter_05.pdf.

Granja, H.; and Pinho, J.L. (2012). Coastal Defense in NW Portugal: The Improbable Victory. In J. A. G. Cooper & O. H. Pilkey (Eds.), *Pitfalls of Shoreline Stabilization: Selected Case Studies* (pp. 251–266). Dordrecht, The Netherlands: Springer. https://doi.org/10.1007/978-94-007-4123-2_15.

Hegde, A. V; Mohan, S.; Pinho, J.L.S.; and Sharhabeel, P.S. (2018). Physical model studies on the stability of emerged seaside perforated semicircular breakwaters. *Indian Journal of Geo-Marine Science*, *47*(3), 681–685.

Houghton, J.T.; Jenkins, G.J.; and Ephraums, J.J. (1990). *Climate change. The IPCC scientific assessment*. Cambridge, UK:

Cambridge University Press.

IPCC. (2012). *Managing the Risks of Extreme Events and Disasters to Advance Climate Change Adaptation. A Special Report of working groups I and II of the Intergovernmental Panel on Climate Change*. (C. B. Field, V. Barros, T. F. Stocker, D. Qin, D. J. Dokken, K. L. Ebi, M. D. Mastrandrea, K. J. Mach, G.-K. Plattner, S. K. Allen, M. Tignor, & P. M. Midgley, Eds.). Cambridge, UK: Cambridge University Press. https://doi.org/10.1017/CBO9781139177245.

Larson, M.; and Kraus, N.C. (1995). Prediction of cross-shore sediment transport at different spatial and temporal scales. *Marine Geology*, *126*(1–4), 111–127. https://doi.org/10.1016/0025-3227(95)00068-A.

Marinho, R.D.L. (2015). *Gestão de Zonas Costeiras: caso de estudo Caminha-Espinho*. MSc Thesis in Civil Engineering, School of Engineering of Polytechnic of Porto, Portugal. Retrieved from http://hdl.handle.net/10400.22/8233.

Misdorp, R.; and Salman, A. (2011). *Climate of Coastal Cooperation*. Leiden, The Netherlands: European Union of Coast Conservation (EUCC - Coastal & Marine Union). Retrieved from http://resolver.tudelft.nl/uuid:0eef9ca8-ab24-467b-962d-12296a2fb136.

Narra, P.; Coelho, C.; and Sancho, F. (2015). Evolução temporal da vulnerabilidade à erosão costeira no distrito de Aveiro. In *VIII Congresso sobre Planeamento e Gestão das Zonas Costeiras dos Países de Expressão Portuguesa, 14 a 16 de Outubro 2015* (pp. 1–15). Aveiro, Portugal: Associação Portuguesa dos Recursos Hídricos. Retrieved from https://www.researchgate.net/publication/316588576.

Narra, P.; Coelho, C.; Sancho, F.; and Palalane, J. (2017). CERA: An open-source tool for coastal erosion risk assessment. *Ocean and Coastal Management*, *142*, 1–14. https://doi.org/10.1016/j.ocecoaman.2017.03.013.

Neves, B.; Pires, I.M.; Fernandes, A.; Julião, R.P.; Rosendo, S.; Celliers, L.; and Craveiro, J.L. (2018). Desafios à adaptação em zonas costeiras: o papel dos stakeholders e a disponibilização de informação. In *25th APDR Congress: Circular Economy – Urban Metabolism and Regional Development, 5th to 6th July 2018* (pp. 29–34). Lisbon, Portugal.

Neves, L. das; Lopes, M. de L.; and Veloso-Gomes, F. (2015). Beach and Dune Reinforcement with Geotextile Encapsulated-sand Systems. The Portuguese Experience. In *The Proceedings of the Coastal Sediments, 11th to 15th May 2015*. San Diego, California, USA: World Scientific. https://doi.org/10.1142/9789814689977_0174.

Oliveira, I.B.M. (1997). Proteger ou não proteger ou sobre a viabilidade de diferentes opções face à erosão da costa oeste Portuguesa. In G. S. Carvalho (Ed.), *Colectânea de ideias sobre a zona costeira de Portugal* (pp. 205–227). Associação Eurocoast-Portugal.

Pereira, R.C.; Taveira-Pinto, F.; Silva, R.; and Neves, L. das. (2013). Avaliação experimental da influência de diferentes configurações da cabeça de quebramares destacados no comportamento morfológico da praia adjacente. *Revista de Gestão Costeira Integrada*, *13*(3), 301–316. https://doi.org/10.5894/rgci398.

Pilkey, O.H.; and Cooper, J.A.G. (2014). *The Last Beach*. USA: Duke University Press.

Pinho, J.L.S.; and Granja, H. (2018). Coastal erosion: results of a decade of monitoring at south of Mira beach, Portugal. In *IX Simpósio da Margem Ibérica Atlântica, 4 a 7 de Setembro 2018*. Coimbra, Portugal. Retrieved from http://ctac.uminho.pt/publication/coastal-erosion-results-decade-monitoring-south-mira-beach-portugal.

Pinto, C.A.; Silveira, T.; Taborda, R.; Andrade, C.; and Freitas, M.C. (2012). Morfodinâmica e evolução recente de praias alimentadas artificialmente. O exemplo da Costa da Caparica – Portugal. In *Actas do VII Simpósio da Margem Ibérica Atlântica, 16 a 20 Dezembro 2012*. Lisboa, Portugal: Faculdade de Ciências da Universidade de Lisboa. Retrieved from http://apambiente.pt/_zdata/DESTAQUES/2012/Caparica_MIA.pdf.

Pinto, C.; Silveira, T.; and Teixeira, S. (2018). *Alimentação artificial de praias na faixa costeira de Portugal continental: Enquadramento e retrospetiva das intervenções realizadas (1950-2017)*. https://doi.org/10.13140/RG.2.2.24446.48969.

Rangel-Buitrago, N.; Jonge, V. de; and Neal, W. (2018). How to make Integrated Coastal Erosion Management a reality. *Ocean and Coastal Management*, *156*, 290–299. https://doi.org/10.1016/j.ocecoaman.2018.01.027.

Rosa-Santos, P.J.; Veloso-Gomes, F.; Taveira-Pinto, F.; Brògueira-Dias, E.; and Guedes-Lopes, H. (2008). Improving Operational Conditions at Leixões Oil Terminal - Portugal. In *Proceedings of the 7th International Conference on Coastal and Port Engineering in Developing Countries, 24th to 28th February 2008*. Dubai, United Arab Emirates. Retrieved from http://hdl.handle.net/10216/91415.

Schmidt, L.; and Mourato, J.M. (2015). Políticas públicas costeiras e adaptação às alterações climáticas: que limites de implementação? In *VIII Congresso sobre Planeamento e Gestão das Zonas Costeiras dos Países de Expressão*

Portuguesa, 14 a 16 de Outubro 2015. Aveiro, Portugal: Associação Portuguesa dos Recursos Hídricos. Retrieved from http://hdl.handle.net/10451/20495.

Silva, P.M.C. (2012). *A tendência da linha de costa entre as praias de Maceda e S. Jacinto*. MSc Thesis in Ocean Sciences and Coastal Zones, University of Aveiro, Portugal. Retrieved from http://hdl.handle.net/10773/9652.

Simões, S.C.; Pereira, C.A.; Coelho, C.D.B.; and Antunes do Carmo, J.S. (2013). Quebramares destacados: Análises comparativas de eficiências de proteção na praia da Vagueira. *Recursos Hídricos*, *34*(2), 25–40. https://doi.org/10.5894/rh34n2-3.

United Nations. (2015). *Transforming Our World: The 2030 Agenda for Sustainable Development A/RES/70/1*. UN General Assembly: New York, NY, USA. Retrieved from https://sustainabledevelopment.un.org/content/documents/21252030 Agenda for Sustainable Development web.pdf.

USAEWES. (1992). *US Army Engineer Waterways Experiment Station - Coastal Engineering Technical Note: Using Morphology to Determine Net Littoral Drift Directions in Complex Coastal Systems*. Vicksburg, Mississippi, USA. Retrieved from http://www.dtic.mil/dtic/tr/fulltext/u2/a591263.pdf

van Rijn, L.C. (2011). Coastal erosion and control. *Ocean & Coastal Management*, *54*(12), 867–887. https://doi.org/10.1016/j.ocecoaman.2011.05.004.

van Slobbe, E.; de Vriend, H.J.; Aarninkhof, S.; Lulofs, K.; de Vries, M.; and Dircke, P. (2013). Building with Nature: In search of resilient storm surge protection strategies. *Natural Hazards*, *66*(1), 947–966. https://doi.org/10.1007/s11069-012-0342-y.

Vargas, C.I.C.; Santos, F.D.; Penha-Lopes, G.; Cardoso, P.; Lourenço, T.; Schmidt, L.; and Gomes, C. (2012). Avaliação e Comunicação de Suscetibilidade Costeira em Cenários de Alterações Climáticas: Dois Casos de Estudo na Costa Portuguesa. In J. M. Barragán Muñoz (Ed.), *Proceedings of I Congreso Iberoamericano de Gestión Integrada de Áreas Litorales, 25th to 27th January 2012* (pp. 898–911). Cádiz, Spain. Retrieved from https://www.researchgate.net/publication/303702471_Avaliacao_e_comunicacao_de_suscetibilidade_costeira_em _cenarios_de_alteracoes_climaticas_dois_casos_de_estudo_na_costa_portuguesa.

Veloso-Gomes, F. (2015). Consequências e Ensinamentos da Ocorrência de Extremos na Zona Costeira Portuguesa no Inverno de 2013/14. In *12º SILUSBA. Simpósio de Hidráulica e Recursos Hídricos dos Países de Expressão Portuguesa, 22 a 27 de Novembro 2015* (pp. 1–10). Brasília, Brazil. Retrieved from https://repositorio-aberto.up.pt/bitstream/10216/102544/2/179741.pdf.

Veloso-Gomes, F.; and Taveira-Pinto, F. (1997). Portuguese urban waterfronts expansion near coastal areas. In *Environmental Challenges in an Expanding Urban World and the Role of Emerging Information Technologies Conference*. Lisbon, Portugal.

Veloso-Gomes, F.; and Taveira-Pinto, F. (2003). Portuguese coastal zones and the new coastal management plans. *Journal of Coastal Conservation*, *9*(1), 25–34. https://doi.org/10.1652/1400-0350(2003)009[0025:pczatn]2.0.co;2.

Veloso-Gomes, F.; Taveira-Pinto, F.; Neves, L.; and Pais-Barbosa, J. (2006). *EUrosion – An European Initiative for Sustainable Coastal Erosion Management: Pilot Site of River Douro: Cape Mondego and Case Studies of Estela, Aveiro, Caparica, Vale do Lobo and Azores*. Porto, Portugal: Instituto de Hidráulica e Recursos Hídricos da Faculdade de Engenharia da Universidade do Porto.

Vieira, B.F.V. (2014). *Wave hydrodynamics in coastal stretches influenced by detached breakwaters*. MSc Thesis in Civil Engineering, University of Minho: Guimarães, Portugal. Retrieved from http://hdl.handle.net/1822/36113.

Waterman, R.E. (2010). *Integrated Coastal Policy via Building with Nature*. PhD Thesis in Hydraulic Engineering, Delft University of Technology, The Netherlands. Retrieved from http://resolver.tudelft.nl/uuid:fa9a36f9-7cf8-4893-b0fd-5e5f15492640.

Weinberg, J. (2015). The Big Squeeze: Coastal megacities face growing pressure from sea and land. *Stockholm Waterfront*, (1), 5–7. https://doi.org/10.1126/science.299.5615.1941a.

Williams, A.; Rangel-Buitrago, N.; Pranzini, E.; and Anfuso, G. (2018). The management of coastal erosion. *Ocean & Coastal Management*, *156*, 4–20. https://doi.org/10.1016/j.ocecoaman.2017.03.022.

CHAPTER 2

When Engineering meets Nature: A literature review on coastal erosion

protection structures

"*The whole of science is nothing more than a refinement of everyday thinking*"

Albert Einstein. German physicist. Nobel Prize in Physics in 1921 (1879-1955)

(Page intentionally left blank)

CHAPTER 2 WHEN ENGINEERING MEETS NATURE: A LITERATURE REVIEW ON COASTAL EROSION PROTECTION STRUCTURES

2.1 Introduction

This Chapter focuses on an extensive literature review on the scientific domains related to fundamental structuring aspects for establishing the objectives of this research work.

Up-to-date concepts, methodological approaches and scientific developments in research areas such as hydrodynamics and morphodynamics, and traditional and nature-based engineering solutions for coastal protection are addressed in a methodical and coherent way.

Cracking and failure mechanisms of concrete armour units as well as concrete steel fibre reinforcement with natural and man-made fibre rope were the subject of a scientific literature review.

A review was also carried out on a wide range of numerical models to simulate natural hydro-morphological phenomena and the impacts of protection structures on sediment removal and accretion in coastal areas. This review, integrated in a so-called numerical laboratory, focused on the study of the application of models mentioned in the literature in order to serve as a basis for the purposes of this work.

2.2 Fundamentals on coastal hydrodynamics and morphodynamics

2.2.1 Tidal parameters

The astronomical and gravitational forces of the Moon, Sun and the Earth are the mainly responsible for areas of high and low water levels on the Earth's surface. As the Earth rotates, the location of high and low tide changes. The Moon has the greatest effect on the ocean water levels compared with the Sun due to its proximity to the Earth and the configuration of the Sun and Moon, whether aligned or offset, has an effect on the tidal range. The tides of increased range occurring near the times of full Moon and new Moon are called spring tides. The gravitational forces of the Moon and the Sun act to reinforce each other. Since the combined tidal force is increased, the high tides are higher and the low tides are lower than average. The tides of decreased range occurring near the times of first and third quarter phases of the Moon are called neap tides. The gravitational forces of the Moon and the Sun counteract each other. Since the combined tidal force is decreased, the high tides are lower and the low tides are higher than average (PLA, 2019; Vieira, 2014).

According to Pita (1986), tides do not directly affect the stability of the structures, since its variations are not significant. However, tide currents can have very harmful effects in coastal structures

foundations, which can cause erosion next to the toe and lead to the potential failure of this type of structures (Lima, 2011).

2.2.2 Significant wave height and wave period

Wind-generated waves produce the most powerful loads on coastal structures (except for seismic sea waves). Coastal defence works should be designed to withstand the effect of the maximum predicted wave height at the site of work, making it necessary to define the design wave height (H). Its definition assumes special relevance, since an underestimation may result in a greater risk to the structure and an overvaluation results in an increase in the work cost (Taveira-Pinto and Neves, 2003). According to the same authors, for a better approximation of reality, in the definition of the design wave height, the irregular nature of the wave climate should be considered. Although studies suggest that the wave height with 10% probability of occurrence, $H_{1/10}$ (1.27H_s), should be adopted for the design wave height, it is usual to consider the significant wave height, H_s, (average of the highest third of the wave heights that were recorded during the observation period) of the most violent storm that is expected to reach the structure during its service life (Pita, 1986). The determination of wave heights extreme values, i.e., the regime of extremes, is a fundamental aspect in the design of coastal structures. From the distribution of the maximum annual significant wave heights, using Weibull or log-normal distributions it is possible to calculate by extrapolation the wave heights for a given return period (Taveira-Pinto and Neves, 2003).

Regardless of the depth considered, the wave period remains approximately constant and it is usual to admit between the mean value (the average of the periods observed during a given observation time that represents the typical wave period recorded during that time) and the peak value (period corresponding to the frequency with higher spectral density, which represents the more energetic waves), T_p. The relation between the two is indicated in Equation (2.1) (Basco and Hughes, 2006). The significant wave height in meters, H_s, and the mean period in seconds, T_m, are related to each other by Equation (2.2) (Coelho, 2005).

$$T_m = 0.82 T_p \qquad\qquad\qquad\qquad\qquad\qquad\qquad\qquad (2.1)$$

$$T_m = 1.03 H_s + 5.2 \qquad\qquad\qquad\qquad\qquad\qquad\qquad (2.2)$$

2.2.3 Longshore drift or Longshore Sediment Transport

Longshore sediment transport (LST) and interception of drifting sediment by natural or artificial barriers, including river mouths and inlets (the most dynamic with erosion and accretion), are, from a coastal

management point of view, very important as these processes are significant drivers of short to medium-term (days to years) shoreline change and contributing to sand spit formation (Castelle *et al.*, 2018; Sadio *et al.*, 2017; Sousa and Alves, 2002). Spits are common morphological features at tidal inlets and river mouths which in many cases, can act as a buffer zone and protect the mainland from natural calamities, i.e., storm surges, tsunami and coastal inundation (Pradhan *et al.*, 2015). Depending on magnitude and direction of the LST, the spit may form on one side or both sides of the inlet.

LST refers to the cumulative movement of nearshore sand parallel to the shore by the combined action of tides, wind, waves and the shore-parallel currents produced by them that usually result in an almost continuous movement of sand either in suspension or in bedload flows. This current is usually dominated by flows induced by waves approaching the shoreline at an angle, although this current can be enhanced or reduced by wind-driven or tidal currents. LST is also directly related to the incident wave energy since it mobilizes sand. The perception of the longshore motion is usually concealed due to a greater magnitude of the rapid shore-perpendicular motions of the individual sand particles.

Local values of LST are difficult to measure because it typically is a mixture of suspended and bedload transport. Largely based on inferences from the suspended sediment concentrations, it is generally believed that LST has its maximum in two zones: one that is under the breaking waves and the other that is in the swash zone on the beach face (Seymour, 2005). Variations in meteorological conditions from year to year during especially storms may result in changes in net drift. Therefore, one difficulty in determining the net drift direction (direction in which the majority of the sediment moves and is transported by longshore currents) is defining a pertinent time frame (Stauble and Morang, 1992). Estimations of the LST (Equation 2.3) can be carried out recurring to the well-known "CERC" formula that is based on the assumption that the total LST rate is proportional to longshore energy flux (CERC, 1984a; Smith *et al.*, 2003):

$$Q = \frac{K}{16\sqrt{\gamma_b}} \rho_w g^{\frac{3}{2}} H_{sb}^{\frac{5}{2}} \sin 2\theta_b \qquad (2.3)$$

where Q (m³/year) is the submerged total LST rate; K is an empirical coefficient; ρ_w (kg/m³) is the density of seawater; g (m/s²) is the acceleration of gravity; H_{sb} (m) is the significant wave height at breaking; γ_b is the breaker index (H_{sb}/h_b), where h_b is the water depth at breaking; and θ_b (degrees) is the wave angle at breaking. The Shore Protection Manuals recommend a value of 0.39 for K, which can be higher for measurements during storm events.

2.2.4 Ebb and flood deltas formation

Ebb and flood deltas are coastal landforms of emerged and submerged packages of fluvial-transported sediments deposited at a river mouth, where riverine sediment supplied to the coastline is not removed by tides or waves (Hayes, 2005; Penland and Kulp, 2005). Although sediments bypass from the updrift to the downdrift side, in general, sediments eroded from the tidal inlets and supplied by LST accumulate in tidal deltas at the seaward and at the landward side (the ebb- and flood-tidal delta, respectively). From a coastal management point of view, these processes are significant drivers of short-term to medium-term (days to years) shoreline change (Sadio *et al.*, 2017). The magnitude of the bypassing depends on how close the morphological units of the inlet are to their equilibrium states (Kraus, 1999; Kraus, 2000). Tidal inlets are openings in the shoreline through which water and sediments are exchanged between the open sea and the back-barrier basin, and are increasingly influenced by human interventions, such as maintenance dredging and jetty construction (Sadio *et al.*, 2017). The ratio between maximum depth of the inlet and depth of the active LST is also an important parameter. If the maximum depth of the channel is deeper than the depth of active LST it is expected that the entire LST falls into the channel. Otherwise, if the maximum depth of the channel is smaller than the depth of active LST, a fraction of the LST is directly transferred to the ebb-tidal shoal complex and then bypassed downdrift (or possibly lost into deep water, where depth is greater than half the wavelength). Weak hydrodynamic forces promote deposition of sediment, which may be the case for large cross-sectional areas at inlets or entrances.

Ebb deltas are dynamic features with varying morphologies resulting from the complex interplay between waves, tides, river discharge, sediment supply and sedimentation, wind velocity and also from anthropogenic changes (Boothroyd, 1985; FitzGerald *et al.*, 2002; Hayes, 1980). Wave-dominated ebb-tidal deltas are pushed close to the inlet throat, while tide-dominated ebb-tidal deltas extend offshore. The transport reversal interactions largely contribute in shaping delta shorelines, and together with the abundance of sediment supply and grain size, determine the resultant wave-formed shoreline barrier types, which include spits (Luo *et al.*, 2013). The stability of a spit depends on the balance between the LST rate coming into the channel and the tidal (and/or river) flow that scours the channel and also on dredging works to maintain channel navigation that modify the spit growth rate (Hoan *et al.*, 2011).

2.2.5 Sand spits formation

Sand spits are frequently found where the coast makes a sudden change in its orientation and can be defined as a type of barrier forming a narrow and elongated sand body, attached to a land mass at one

end and terminating in open water at the other due to significant amount of sediment transported due to LST. The sand spits morphology, growth and orientation are mainly influenced by the combination of interactions between natural factors (e.g., precipitation, wind, wave height changes, tidal variation, availability of sediment and river flow) and anthropic effects (e.g., resource exploitation, and the construction of dams and breakwaters) (Allard *et al.*, 2008; Castelle *et al.*, 2018; Coelho *et al.*, 2009; Dias *et al.*, 2002; Dinis *et al.*, 2016; Pradhan *et al.*, 2015). Petersen *et al.* (2008) affirm that the orientation of the dominant wave direction approach to the coast should be with an angle larger than 45° in order to a spit to be formed. Energetic waves seem to cause massive sand accumulation and spit elongation, whereas less energetic waves appear to be responsible for small sand accumulation and spit curvature (Dan *et al.*, 2011). This deposition may have a complex form, for example curved or hook-shaped if the waves forming it are coming from a wide range of directions and occur in a variety of sizes ranging from metres to kilometres. Dalrymple and Choi (2007) hypothesised that estuary width and curvature determine both the shape and the number of spits in cross-section. Sand spit height in estuaries is linearly related to local water depth, while spit length and width are strongly correlated to estuary width or with low velocity and tidal currents (Kraus, 1999; Leuven *et al.*, 2016; Schramkowski *et al.*, 2002; Seminara and Tubino, 2001).

Slope and shape may be of significance for the dynamics of a spit. The steepness of the profile and the incoming waves will be important for the significance of the swash zone for the sediment transport and the characteristics of a spit. The majority of wave directions generate LST which can modify the morphology of the spit dramatically if one of them is dominant. First, the sediment transport induced by the "updrift" wave directions is feeding the elongation of the spit by transferring the sediments towards the tip, contributing to the thinning of the spit. Second, the "middle" directions generate intense overwash being the main driving force for the lateral migration of the spit. Third, the "downdrift" directions do not generate significant sediment transport, being important only for their local contribution to the curvature of the spit tip (Dan *et al.*, 2011; Kraus, 1999). A study conducted by Thomas *et al.* (2014) suggests that conditions that focus wave energy through diffraction towards the spits lee with south (S) and southwest (SW) waves have a tendency to move sediments towards the spit (Figure 2.1a), while the southeasterly waves tend to reduce the size of the extremity of the structure (Figure 2.1b). Figure 2.1 conceptually shows the effects of inshore waves considering the S, SW, and southeast (SE) wave directions mentioned. Table 2.1 summarizes the different spit parameters responsible for spit properties and processes.
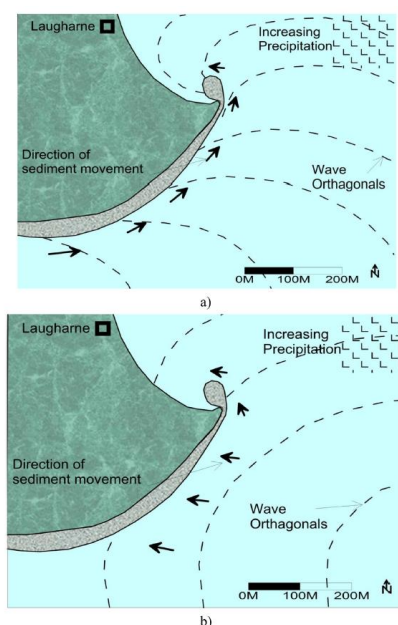
Figure 2.1: Conceptual wave vectors from a) S and SW; and b) SE offshore wave directions (Thomas *et al.*, 2014).

Table 2.1: Parameters controlling inlet spit geometry and evolution, and its processes (adapted from Kraus, 1999).

Spit Parameter	Processes
Length	LST rate; proximity to inlet channel; channel current strength; sediments supply; breaching
Elongation speed	LST rate; grain size; proximity to inlet channel; beach slope
Width	Run-up; tidal range
Overwash	Storm surge; frequency of storms
Elevation above MSL	Run-up; tidal range; aeolian transport; sea-level change; tsunami
Depth of closure	Wave height and period; tidal range; grain size; extreme storms
Tendency to curve	Proximity to channel; channel current strength; wave direction; extreme storms

2.2.6 Hydrodynamics influence on deltas and spits shapes

Most seabeds in coastal zones are composed of sediments, predominantly sands along the coast, and silts and clays in estuaries and lagoons. This material is often transported by currents and waves, causing morphological variations of the seabed. Most studies (e.g., Almeida *et al.*, 2015; Anthony, 2015; Luo *et al.*, 2013; Oertel, 1975) agree that dominant hydrodynamic processes that influence the morphology of the ebb-tidal delta is essentially determined by the importance of wave *versus* tidal energy. Winds and tide are the major sources of energy for carrying out these processes in an estuary. The wind acts mainly at the air-water interface, creating in addition a well-mixed and turbulent layer, surface currents, whereas the tide acts mainly in the internal region of the water column (Chang, 1997; FitzGerald *et al.*, 2002; FitzGerald, 1996; Garel *et al.*, 2014; Hayes, 1980; Oliveira, 2010). Parameters like tidal current, depth and Coriolis force have also an influence on ebb-tidal shoal (mouth bar) formation. The Coriolis force is the effect of the rotation of the Earth that causes the winds and ocean

currents to rotate as they move. Winds generally blow out from the subtropics towards the equator and subpolar regions; and from the polar regions to the subpolar latitudes, as shown in the theoretical map of Figure 2.2. As viewed by a stationary observer, the rotation of the Earth causes an object to deflect towards the right in the northern Hemisphere, which results in a clockwise motion, and to deflect towards the left in the southern Hemisphere, which results in a counter-clockwise motion. These rotations result in enormous surface winds that will influence wave currents (Bralower and Bice, 2018; Carbajal and Montaño, 2001). Waves approaching the delta shoreline can generate currents that redistribute fluvial and coastal sediments. Figure 2.3 illustrates the interactions between a river mouth and waves under different conditions of LST and river influence.
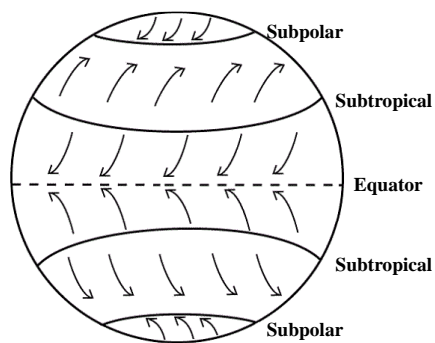
Figure 2.2: Earth major wind rotating zones caused by the Coriolis effect.
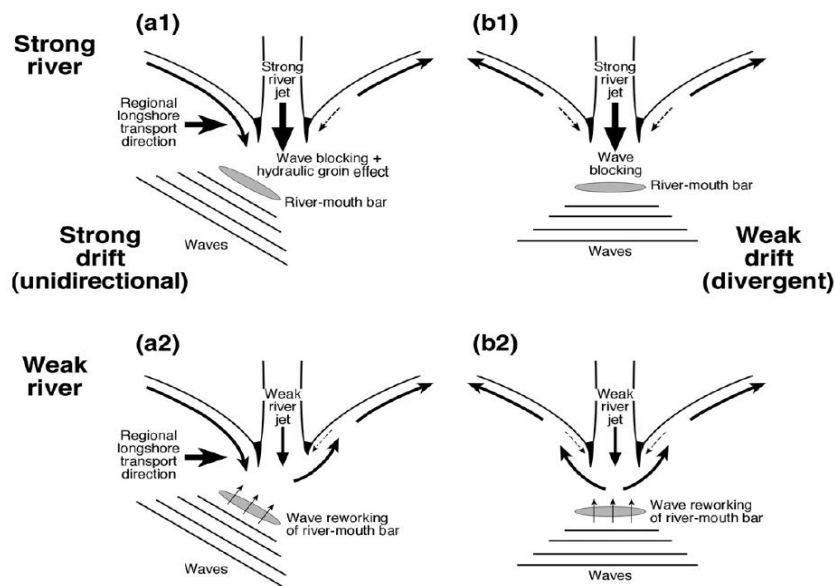
Figure 2.3: Simplified scheme interactions between a river mouth and waves under conditions of strong (a) and weak (b) longshore drift, and strong (1) and weak (2) river influence (Anthony, 2015).

Depending on the relationship between river strength and waves (more commonly as a function of changes in river strength rather than changes in wave climate), deltas can be symmetric, skewed,

deflected or straightened. The balancing of a weak river effect by strong LST can lead to strongly longshore-skewed deltas or even prevent delta development. Strong river influence can play an important role in delta shoreline and shape morphodynamic adjustments through both mouth bar deposits and the distance at which these form relative to the delta shoreline. Unidirectional drift is more likely to generate asymmetric deltas and highlights the significance of updrift bedload supply in the growth of some deltas in wave-influenced settings. Longshore drift reversing may locally prevail near the river mouth in all situations as a result of wave dissipation between the shoal zone and the adjacent coast (Anthony, 2015). The ebb-tidal shoal complex is composed of ebb-tidal shoal bypassing bars and attachment bars. Bar welding is a repetitive process with a frequency of 4 to 10 years (Fitzgerald *et al.*, 2000). These features are shown schematically in Figure 2.4a). Figure 2.4b) schematizes a sand spit breaching mechanism in the Guadiana river, Portugal. Firstly, updrift spit development is augmented as the ebb channel forms a hydrodynamic obstacle for the northward directed LST causing a preferential sedimentation at the updrift side of the channel (FitzGerald, 1988). This sediment accumulation causes a downdrift deflection of the main ebb channel due to the wave-driven flow and, as a result, the main channel and adjacent spits rotate and migrate in downdrift direction.
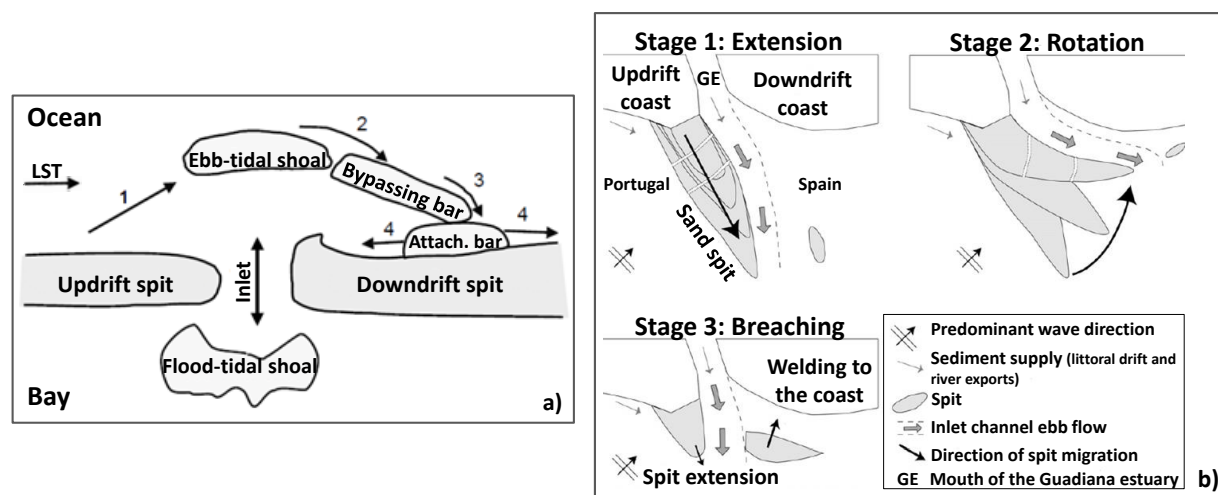
Figure 2.4: Sand spits: a) Ebb-tidal spit evolution and sand bypassing (adapted from Kraus, 2000); and b) Conceptual model of evolution of the Guadiana sand spit (adapted from Garel *et al.*, 2014).

Periodic spit breaching and downdrift channel relocation are the dominant mechanisms for sediment bypassing (Castilho, 2016; Elias and van der Spek, 2006) mainly responsible by storm currents. Once they are separated they are likely to gradually adjust to the offshore conditions (Figure 2.5a) and Figure 2.5b)) so that the sand bank height increases steadily in a seawards direction (Dyer and Huntley, 1999). The actual volume of sand bypassing that result in the formation, landward migration, and attachment of large bars to the downdrift shoreline is dependent on inlet geometry, ebb-tidal delta morphology,

sediment supply, tidal prism (volume of water leaving an estuary at ebb tide), wave and tidal energy, and engineering modifications.

Figure 2.6 depicts a model of formation of a spit in the Sfântu Gheorghe Danube delta (Romania), where it is showed (from left to right) the subaqueous platform growth and subsequent appearance of a shoal; the emergence of a spit (barrier island) followed by rapid elongation and shoreward migration; and the back-barrier infill by fluvial sediments and construction of secondary spits at a downdrift location.
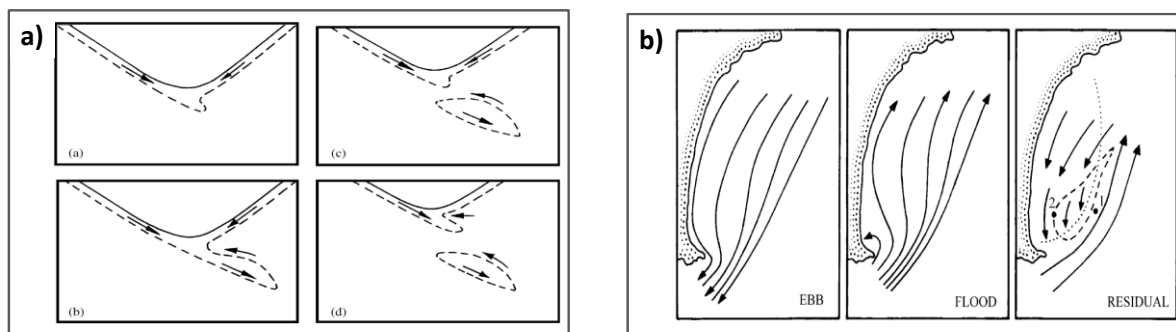
Figure 2.5: Diagrammatic representation of a spit breaching. a-d show stages in the process (a)); and Streamlines on flood and ebb tide, and of the tidal residual around a sandbank (b)) (Dyer and Huntley, 1999).
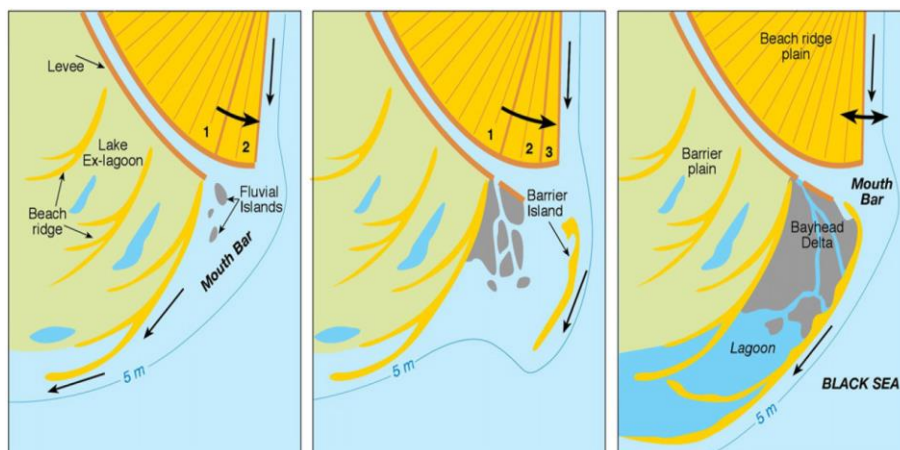
Figure 2.6: The Sfântu Gheorghe lobe of the Danube delta, Romania (Anthony, 2015).

In Portugal, the Douro estuary sand spit is an important natural defence against the impact of storm events. Aiming to improve navigation safety, between 2004 and 2008 a breakwater was built to stabilise the spit. Bastos *et al.* (2012) conducted a study to attempt quantifying the changes that occur in the Douro sand spit by relating spit dynamics to river discharge flows influenced by the Crestuma dam, ocean waves and wind actions. Before breakwater construction, erosion was significantly correlated with extreme river discharge and wind conditions; the spit often breached during severe flood, and accretion in the northeastern sector was significantly correlated with extreme wind conditions and

lower flow rates. After breakwater construction, while overall shape and volume stabilised with breakwater construction and most of the sand spit is less vulnerable to extreme conditions, its southeastern part has become less stable and more susceptible to extreme river discharge flows, wave and wind conditions, strongly affecting its shape and dynamics and threatening the local Nature Reserve (Bastos *et al.*, 2012). Although the concentration of suspended solids is directly proportional to the increase of the flow in Crestuma, it cannot be said that the sedimentation obeys the same order of magnitude. This is because the magnitude, turbulence and oscillation of the flow direction can keep them in suspension. In relation to the influence of the tide, the higher the tidal amplitude value, the higher the accumulation value. These results evidence the importance of these parameters on the erosion/accumulation patterns in the proximity of the river mouth (Almeida *et al.,* 2015). Figure 2.7 demonstrates the Douro river mouth sand spit evolution, where 1 is the Luís Gomes de Carvalho wall built in 1820; 2 is the São Paio Bay; 3 are the northern and southern jetties, 4 is the sand spit breakwater; and 5 is its access way. Contours for 1862 and 1950 were extracted from geo-referenced historical maps. Figure 2.8 depicts sand spit dynamics correlation with extreme river discharges, wave and wind power, before (Figure 2.8a)) and after (Figure 2.8b)) the breakwater.

Figure 2.7: Douro sand spit evolution. Aerial photography taken in November 2008 (Bastos *et al.*, 2012).
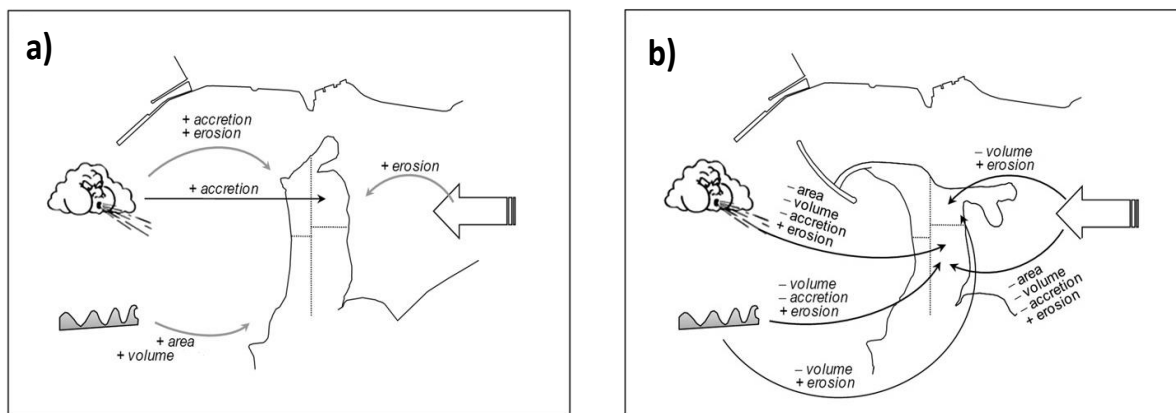
Figure 2.8: River discharge flow, wind and wave effects on the four sand spit sectors (black arrows) or the entire spit (grey arrows) for the period before (a)); and after (b)) breakwater construction (Bastos *et al.*, 2012).

2.2.7 Longshore drift reversing

As mentioned before, the interaction of large ebb-tidal deltas with wave energy plays a significant role in shaping the coastal configuration and morphology of adjacent sandbanks.

This can be achieved by accumulating and storing large quantities of sand-sized sediment or by inducing littoral current reversals driven by wave refraction. Wave refraction associated with large ebb-tidal deltas has been shown to cause reversals in the longshore transport system, resulting in changes in beach plan form (Hayes, 1979). Waves approaching the shoreline obliquely are refracted in such a way that a zone of sediment transport reversal occurs on the downdrift side of the inlet. This reversal produces a slowing down of sediment bypassing the inlet, allowing time for swash bars affiliated with the ebb tidal delta to weld onto the beach on the downdrift side of the inlet (Laïbi *et al.*, 2014; Stauble and Morang, 1992). This process is accentuated when the main ebb channel of the ebb tidal delta abandons a downdrift course for a more updrift one, which allows the large sand mass at the terminal lobe to be quickly driven onshore by wave action (Figure 2.9 and Figure 2.10).
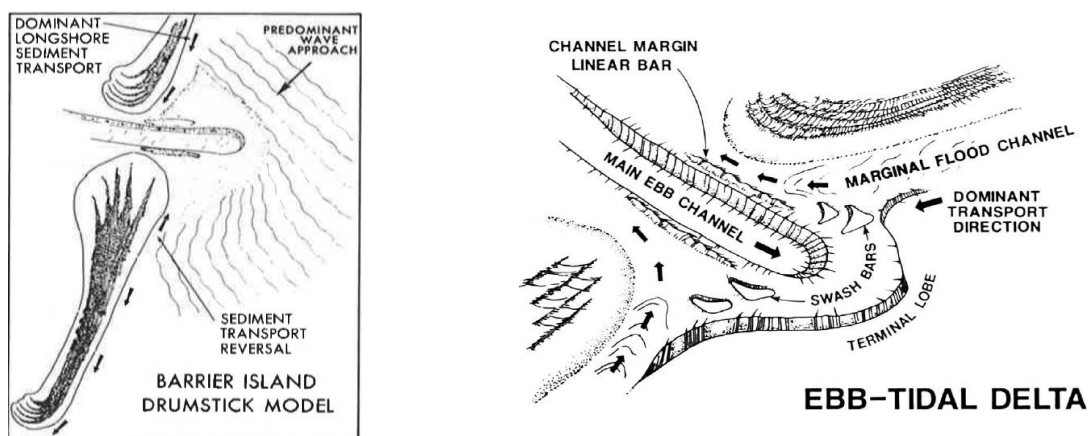
Figure 2.9: Reversal of longshore drift (Hayes, 1979).
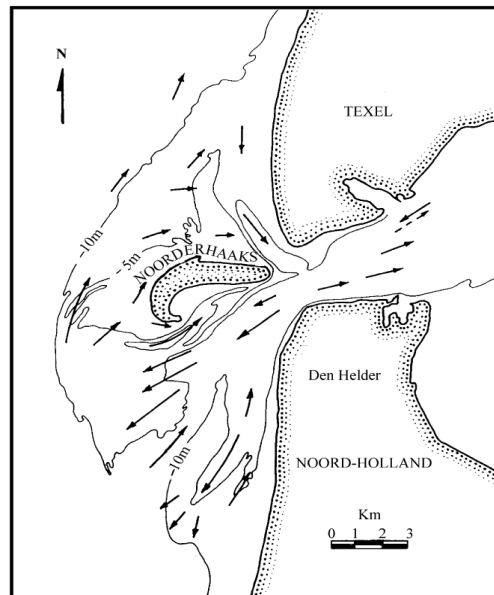
Figure 2.10: Longshore drift reversing at an ebb tidal delta at the mouth of the Texel Inlet, The Netherlands. The arrows show the dominant flow directions (Dyer and Huntley, 1999).

Accumulations on the downdrift side of jetties also suggest that occasional drift reversals may occur. Figure 2.11a) presents Portuguese examples of the longshore drift reversing without the presence of hard structures, while Figure 2.11b) and Figure 2.11c) depict this phenomenon in the presence of jetties. The aerial photography were retrieved from Google Earth.

Figure 2.11: Longshore drift reversing: a) in Mira river estuary, Portugal (2015); b) at a jetty in Guadiana river estuary, southern Portugal and Spain border (2017); and c) at the jetties in Ave river estuary, Portugal (2017).

2.3 Technical solutions for coastal protection

In a zone prone to shoreline retreat due to high tide/wave energy action without natural protection and a high sediment transport deficit, many different solutions can be used to reduce or to control coastal erosion, namely: adherent works, transversal works, beach nourishment, sand bypassing and dunes

rehabilitation, creating innovative and alternative breakwaters designs and, specially, environmental-friendly structures (Taveira-Pinto and Neves, 2004).

It is important to highlight that the existence or the possible construction of protection structures should not be used as an excuse to allow building in areas of risk. These structures may locally reduce risks of exposure to sea action, but do not eliminate them. Each of these approaches has economic, aesthetic, environmental and human advantages and disadvantages and the choice of the solution will vary widely according to local, regional and national priorities (Veloso-Gomes and Taveira-Pinto, 1997).

A typical coastal urban area evolution is represented in Figure 2.12.
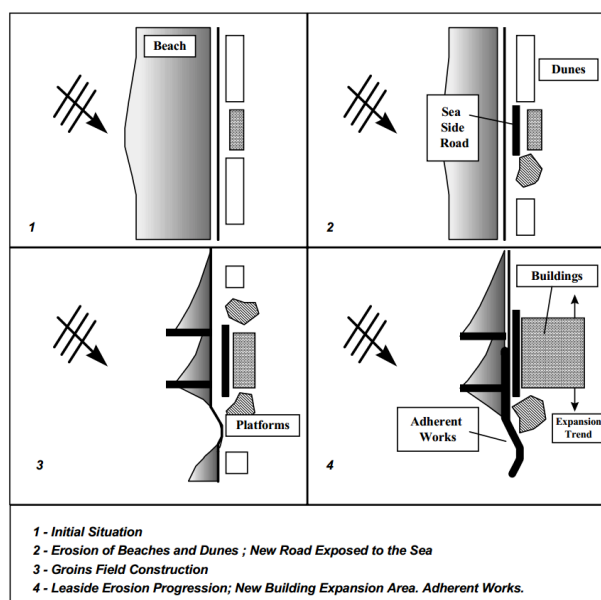
Figure 2.12: Coastal urban area: typical evolution (Veloso-Gomes and Taveira-Pinto, 1997).

Usually, the protection approach using hard structures is widely perceived as the best coastal erosion management strategy, and in many countries this method is the only alternative (Pranzini, 2017; Rangel-Buitrago *et al.*, 2017). However, hard and fragile structures are not necessarily the most adequate solution since they have not been very successful or failed in their purpose, and their negative influence has been seen as a critical problem along many coastlines around the world (Griggs, 2005; Charlier *et al.*, 2005; Pranzini and Williams, 2013; Pilkey and Cooper, 2014). This can give the opportunity to study flexible hard structures with capacity to cope with large deformations without fragile fracture.

Hard protection approaches can generate adverse effects, such as (Rangel-Buitrago *et al.*, 2018):

– Aggravation of erosion downdrift;

– Disturbance of sediment supply and beach reduction;

– Changes in LST;

- Restricted public access;

- Potential risks for people's lives;

- Adverse visual impacts.

Temmerman *et al.* (2013) argued that flood protection by ecosystem creation and restoration can provide a more sustainable, cost-effective and ecologically sound alternative to conventional coastal engineering and that, in suitable locations, it should be implemented globally and on a large scale. In their work, it is stated that hard structures are severely challenged in many locations, and are becoming unsustainable due to their costly and continual maintenance requirements, as well as any widening and height increase to keep in step with the increasing coastal erosion risk. Additionally, such structures significantly alter the natural adaptive capacity of any coastline. Negative experiences prevail over positive ones in the implementation of hard structures as protection measures against coastal erosion due to interfering processes operating at a wide spatial scale (>100 km) (Neal *et al.*, 2017; Pilkey and Young, 2009; Rangel-Buitrago *et al.*, 2017; Williams *et al.*, 2016).

In the following Sections, general characteristics of coastal protection technical solutions (traditional and nature-based) and suggestions on innovative protection strategies will be briefly described.

2.3.1 Traditional solutions

2.3.1.1 Breakwaters: Headland and Detached breakwaters

Breakwaters are constructed to provide a calm basin for ships and to protect harbour facilities. They are also sometimes used to protect the port area from the intrusion of longshore drift. In fact, for ports open to rough seas, breakwaters play a key role in port operations (Takahashi, 2002). General classification of breakwaters may be divided in two categories: rubble mound and composite breakwaters. Vieira (2014) presents summarized information regarding the characteristics of different structural types of breakwaters: sloping or mound type, vertical type, composite type, horizontally composite type, and special types.

The breakwaters can take many forms and can be permanently submerged (reefs), permanently exposed or visible between tides. These structures can be adherent (rooted and/or located against the coast), detached (built away from the coast), or may have a one end anchored to the ground (acquiring usually a curved or an L shape: headland breakwaters). In all cases, the depth of the structure, its size and its position relative to the shoreline determine the level of protection provided (Antunes do Carmo *et al.*, 2011).

Headland breakwaters are a series of breakwaters constructed in an "attached" fashion to the shoreline and angled in the direction of predominant wave approach such that the shoreline behind the features evolves into a log spiral embayment (USACE, 2014a). Figure 2.13 depicts some examples of these kinds of structures.

Figure 2.13: Examples of headland breakwaters (Vieira, 2014).

Detached breakwaters are another example of coastal protection structures that are built offshore inside/near the surf zone, having an approximate orientation parallel to the coast built in shallow nearshore environments (where depth is less than one-twentieth the wavelength) and that can be, according to their position relatively to the mean water level, emerged or submerged (Figure 2.14). Both constitute an obstacle to the normal wave propagation, allowing the dissipation of the incident wave energy and providing a "filter" shelter for the coast at their leeward side, reducing this way beach erosion. These structures also perform well in areas where the cross-shore current, or shore-perpendicular transport of materials, is stronger as the structures will provide greater protection of original beach material while capturing new sediments entering the system.

Taveira-Pinto and Neves (2004) focused their work on the basics of (submerged and emerged) detached breakwaters characteristics, their environmental impacts and on their possible practical application in the Portuguese coast. In their work, the authors analysed some case studies where detached breakwaters were used in Portugal and their role in beach protection (Leixões harbour,

protecting the head of the main breakwater; Caxinas-Vila do Conde beach, for beach improvement; near Neiva's river mouth and in Aguda beach, both for protecting a small fisherman community); and also stated the benefits of submerged structures and their possibility of application in high energetic coasts.

Figure 2.14: Examples of detached breakwaters (Vieira, 2014).

Emerged detached breakwaters are designed to attenuate the whole wave action and are submitted to the direct impact of breaking wave, resulting in larger structures that often eliminate water circulation at the leeward side (in the protected area). Consequently, degradation of water quality and of natural habitats in the leeward side is a frequent phenomenon (Taveira-Pinto and Neves, 2004). A disadvantage of emerged breakwaters, in terms of environment, is the necessity of gaps between the barriers that often give rise to rip currents, bed irregularities and tombolos. Figure 2.15 depicts the format of a tombolo near an emerged breakwater.

Figure 2.15: Formation of tombolo in the leeward side of an emerged breakwater due to diffraction currents (Vieira, 2014).

The submerged breakwater is also a particularly attractive solution for the creation and preservation of beaches, due to its low environmental and visual impact (Figure 2.16). Inherent to the improvement of water quality, maintenance of fish habitats due to its lower impact of coastal development on aquatic habitat and a better integration of the coastal protection structure in the shore zone, are examples of the advantages of submerged breakwaters over the conventional structures (Taveira-Pinto and Neves,

2004). Figure 2.17 demonstrates the main objective of a submerged breakwater: the capability for retaining or permitting sediment accumulation at its leeward side responsible for its important role in beach protection. This sediment accumulation is due to the attenuation of the wave height, caused by the energy dissipation and the formation of diffraction figures at the ends of the structure (Taveira-Pinto and Neves, 2004). Figure 2.18 illustrates the diffraction currents formed in the extremities of the submerged breakwater.

Figure 2.16: Examples of submerged breakwaters (Vieira, 2014).
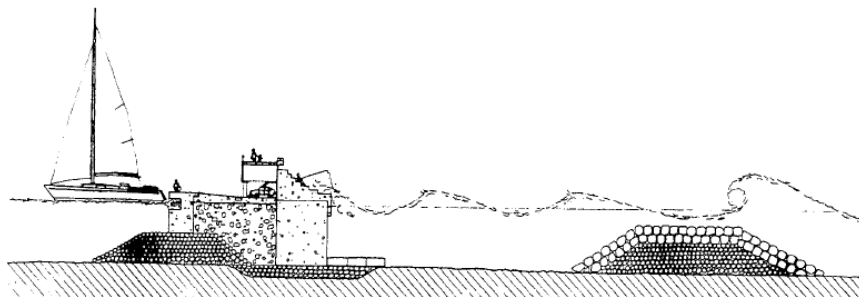
Figure 2.17: Schematic description of the effect of a submerged breakwater in the wave propagation, Olympic Port, Barcelona, Spain (Taveira-Pinto and Neves, 2004).
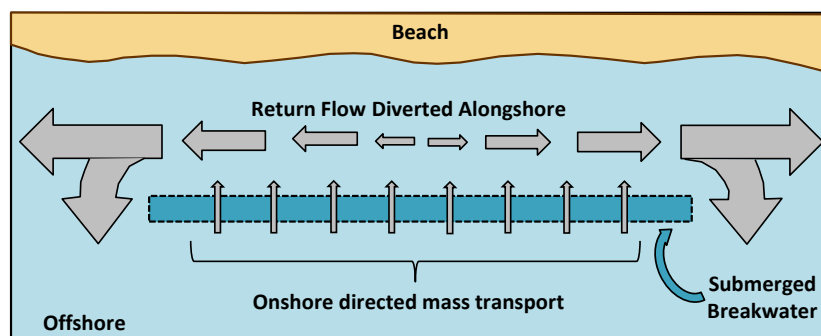
Figure 2.18: Schematics of rip currents generated in the leeward side of a submerged breakwater (Adapted from Browder *et al.*, 1996).

Submerged breakwaters are less subjected to wave action because of their lower height. Besides that, the required volume of material is smaller than in similar emerged structures. However, it is important to be aware that submerged breakwaters have, obviously, a lower level of protection, since its efficiency in the formation of tombolos is lower. According to Taveira-Pinto and Neves (2004), in high energetic coasts (e.g., the Portuguese coast) the construction of submerged breakwaters is not so recommended in some cases, since the structure could not protect the shoreline and attenuate efficiently the incident waves.

When constructing a detached breakwater or series of detached breakwaters, consideration must be given to the proper placement of the structure(s). A correctly designed breakwater system will result in the formation of a salient which allows longshore drift to flow downdrift between the breakwater and the sand beach. An incorrectly designed breakwater system will result in the formation of a tombolo. Schematic views of hydrodynamics and sand trapping near tombolo and salient generation are presented in Figure 2.19a), Figure 2.19b) and Figure 2.20.
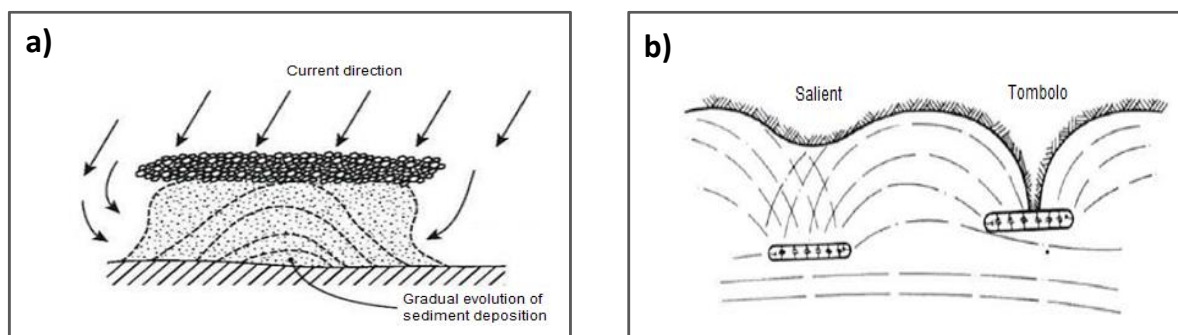
Figure 2.19: Scheme for: a) Formation of tombolo and action of refraction (French, 2001); and b) Salient and tombolo generation (Abbott and Price, 1993).
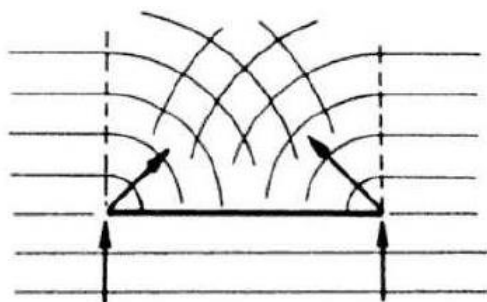
Figure 2.20: Scheme of diffraction caused by a detached breakwater (Silvester and Hsu, 1997).

Several studies on the ability to retain sediment by the breakwater are available in literature. In general these studies relate the efficiency of a breakwater with the distance of the structure to the shoreline (between 90 and 120 m), the increasing of wave steepness (wave height (H_s)/wave length (L_m)),

growth of the crest elevation above the mean water level, and the length of the breakwater (between 60 and 120 m) (Taveira-Pinto, 2007).

Cited by Herbich (2000), Toyoshima (1974) analysed several high breakwaters in Japan, a country with a significant number of structures of this type, and concluded that to obtain a tombolo, the distance of the structure to the original shoreline divided by the total length of the detached breakwater shall not be less than 0.74. The same author has also found a relation between the wavelength and the length of the detached breakwater, which should be two to six times the wavelength or should be between 61 and 198 meters, while the distance between breakwaters should be at least a wavelength, between 20 and 50 meters.

It is important to mention that the implementation of detached breakwaters cause impacts on currents that can be dangerous for bathing and can also cause impacts on wave conditions and affect wave phenomena like diffraction and refraction. Despite allowing maintenance of sediment placed through artificial feeding and accumulate sediments, a detached breakwater can also cause erosions in the longshore direction. However, this phenomenon is less shown than in the case of groins, which reduce more effectively the longitudinal sediment transport. The currents along the heads of detached breakwaters can create localized erosion and excavation at the seabed, which is most striking aspect in the case of a system of detached breakwaters, where the small gaps between them lead to higher speeds (Costa, 2009).

2.3.1.2 Groins

Groins are the oldest and most commonly beach stabilisation structure used on shore.

They are structures that extend, finger-like, perpendicularly to shoreline and are relatively short when compared to navigation jetties. Usually constructed in groups called groin fields, their primary purpose is to trap and retain sand, nourishing the beach compartments between them.

Groins work as physical barriers to the longshore transport of sand, which starts to accumulate updrift (Figure 2.21). They are most effective where longshore transport is predominantly in one direction, and where their action will not cause unacceptable erosion of the downdrift shore. When a well-designed groin field fills to capacity with sand, longshore transport continues at about the same rate as before the groins were built, and a stable beach is maintained. Modern coastal engineering practice is to combine beach nourishment with groin construction allowing sand to immediately begin to bypass the groin field system, reducing transient erosion downdrift (USACE, 2014b).
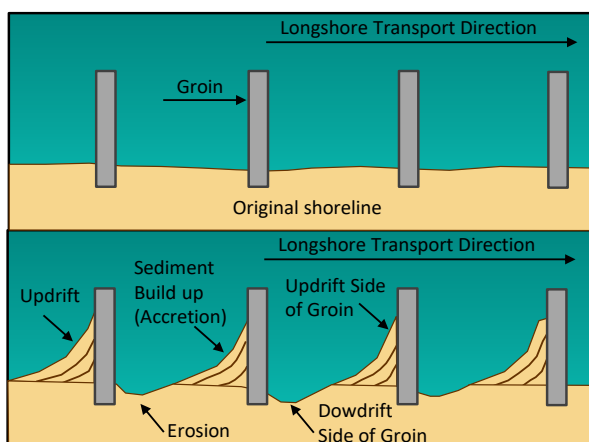
Figure 2.21: Schematic representation of the functioning of groins (Vieira, 2014).

The volume of sediments accumulated updrift from the groin is a function of its dimensions, wave conditions and sediment grain size, being indicative of the erosion contention. If the limiting retention capacity of the groin is reached it stops blocking sediments, letting them pass through. The time elapsed to fill a groin depends on several factors, like wave conditions at the groin location, beach morphology, tide regime and even current pattern in the surrounding area (Silva *et al.*, 2007). Therefore, the filling time would be given by the ratio between the accumulated volume and the longshore transport rate. It is important to be aware that although it may appear simple, both accumulated volume and longshore transport are difficult to evaluate.

A very negative impact that would result from these works, if they had the capacity of inducing rip currents, would be the irreversible loss of sediments dragged to offshore. Short groins cannot jet material far offshore and permeable groins reduce the rip current effect. However, long impermeable jetties might produce large rips and jet material beyond the average surf zone width. Affirming that groins erode the offshore profile is questionable and doubtful. Under this perspective, groins should be permeable, allowing water and sand to move alongshore, and reduce rip current formation (Silva *et al.*, 2007). Examples of existing groins in Portugal are presented in Figure 2.22.

Silva *et al.* (2007) concluded that combining beach nourishment with groin construction allowing sand to immediately begin to pass the groin and so reducing erosion downdrift, is a modern coastal engineering practice. The authors also recommend that groin design should be carefully done and success should be judged on two factors: to maintain a minimum dry beach width to guarantee protection beyond a reference baseline; and to minimise downdrift impacts.

Figure 2.22: Groins in Portugal: a) Ofir; b) Lagos; c) Madeira; and d) Espinho (Vieira, 2014).

Any obstacle introduced into the natural hydro- and morphodynamics coastal zone environment is prompt to create a reaction, which may sometimes be positive and other times negative. There is a controversy on the groins effect on coastal zones as a protective measure against erosion. It is common belief that groins act very negatively downdrift to where they are deployed.

The Deltares Aqua Monitor (Deltares, 2019b) is a platform for the planetary-scale scientific analysis of geospatial datasets that uses freely available satellite data and the Google Earth Engine. Although it is difficult to perceive tides with this platform, observations allow users to analyse profiles of the shoreline evolution, anywhere worldwide from 1985 to 2016. As an example, six locations where groins were constructed in NW Portuguese coast were analysed considering their updrift and dowdrift evolution during the last 30 years. Since the initial period may be doubtful due to the evident lack of information at those locations in some years, the analysis will be taken from 2000 forwards. From the observation of Figure 2.23, it can be stated that for all cases the erosion and accretion phenomena are present throughout the years, but in some cases the erosion visible in some year is somehow compensated with accretion in subsequent years, which, even though the shoreline position value is sometimes assumed negative by the platform, it can lead to an equilibrium state of the coast in areas where the groins were implemented (Updrift: Ofir north groin; Ofir south groin until 2014; Apúlia groin until 2015; Madalena groin until 2015; and Espinho north and south groins. Downdrift: Ofir north and south groins

until 2013; Apúlia groin; Madalena groin; Espinho north groing; and Espinho south groin until 2014). As previously mentioned, the NW Portuguese coast was affected by an intense storm in 2014, which had remarkable influence on the shoreline position as observed on Figure 2.23. In the Ofir south groin the noticeable erosion updrift the groin may be related to the influence of the north groin that interferes with the updrift sediments transport or by the reversing of the longitudinal drift that takes place at this location. It can be stated that even though in 2016 the shoreline values are lower than the registered in 2000, the evident tendency throughout the sixteen years showed scenarios of accretion in the forthcoming years, which may be repeated in the future if sediment condition allows it. It is important to mention that in some years sand nourishment may have had influence on these values.

Properties	
Profile	BOX_164_160_6
Country	Portugal
Continent	Europe
Sandy	True
Change rate	3.1 m/yr +- 0.6

Updrift

Properties	
Profile	BOX_164_160_8
Country	Portugal
Continent	Europe
Sandy	True
Change rate	-2.1 m/yr +- 0.3

Downdrift

a)

b)

c)

d)

e)
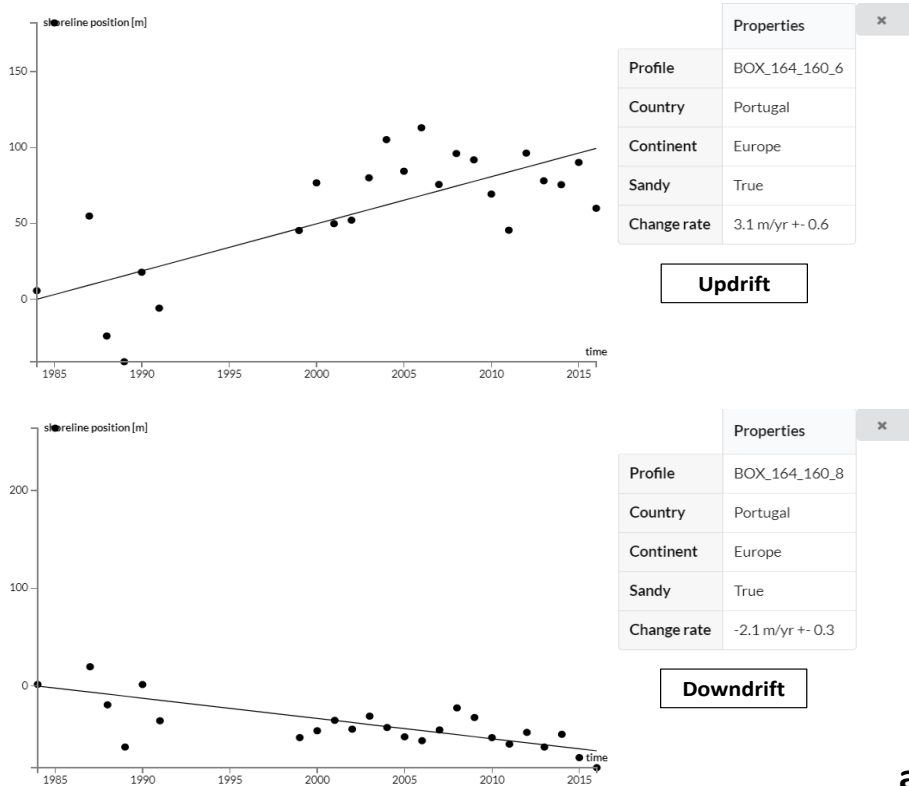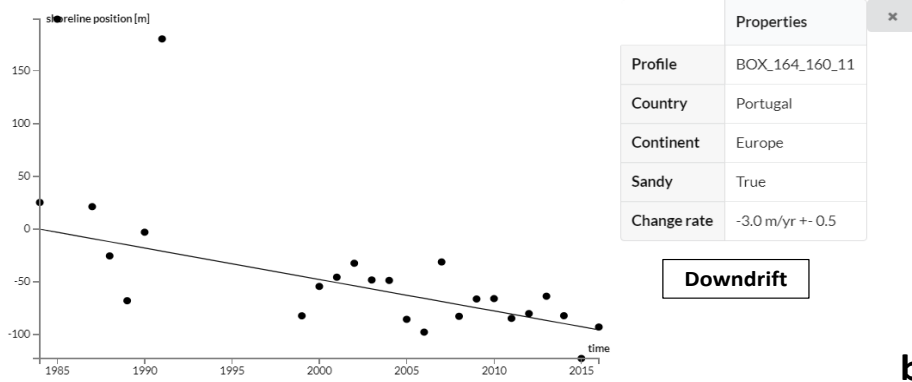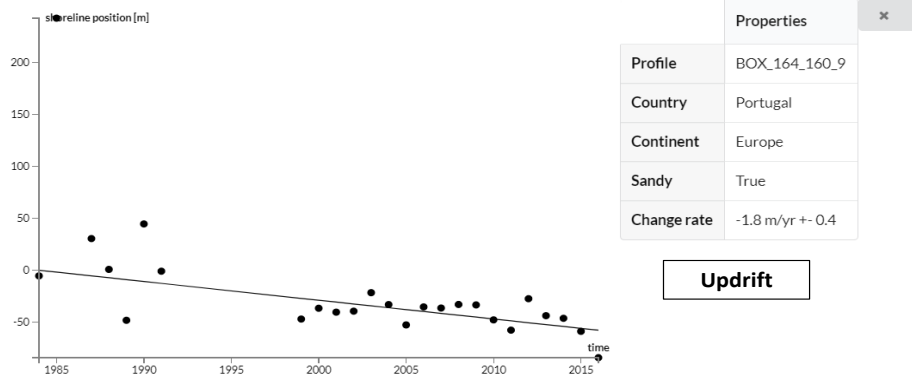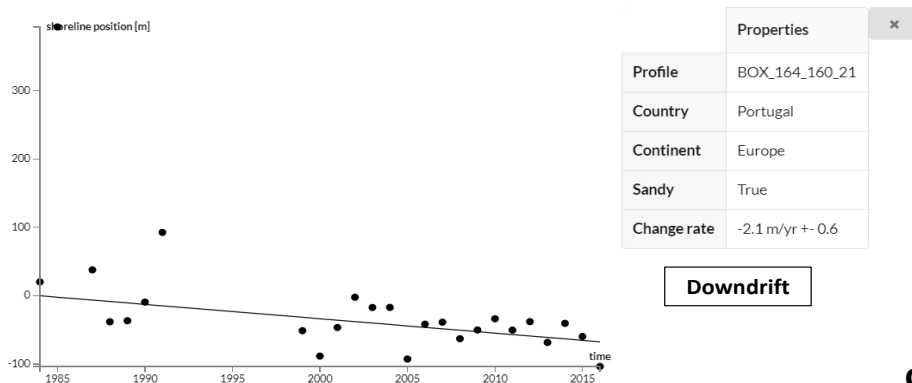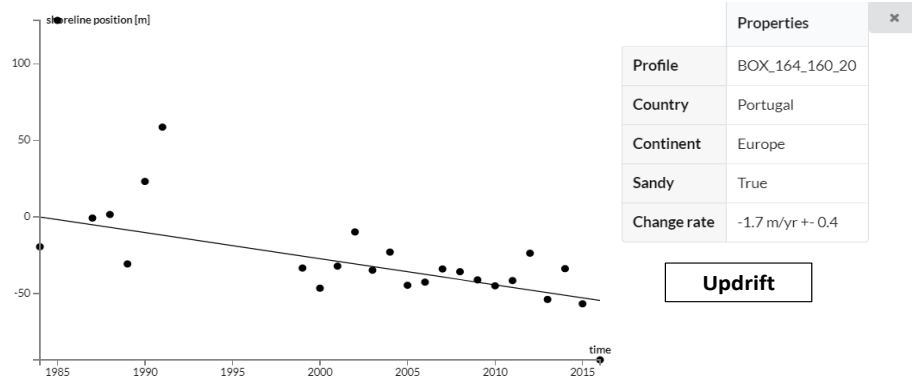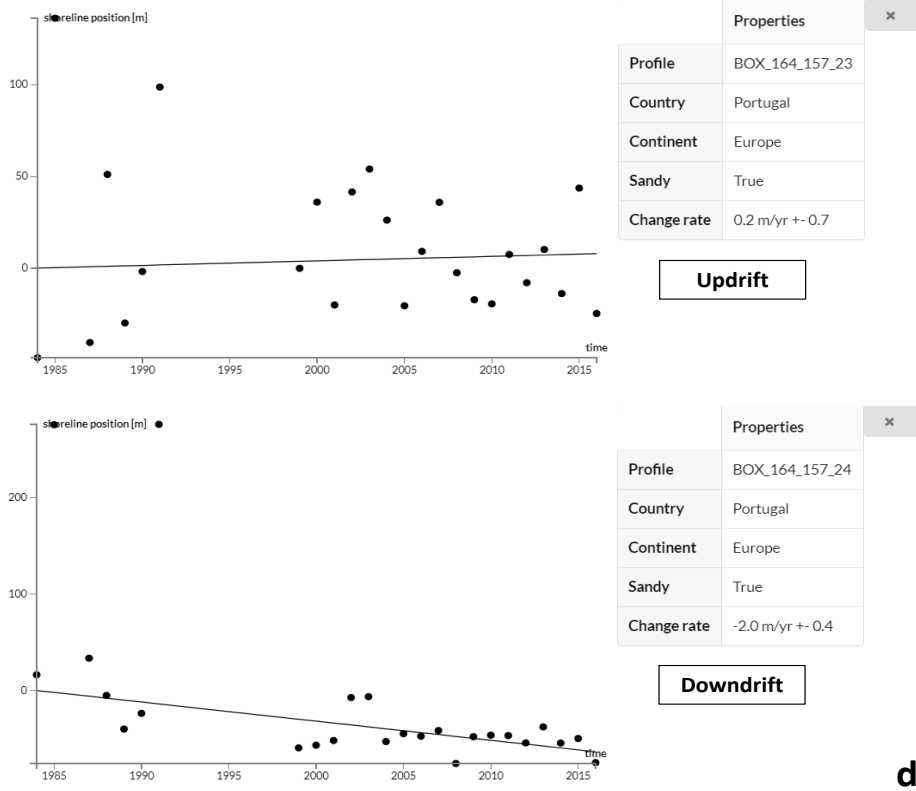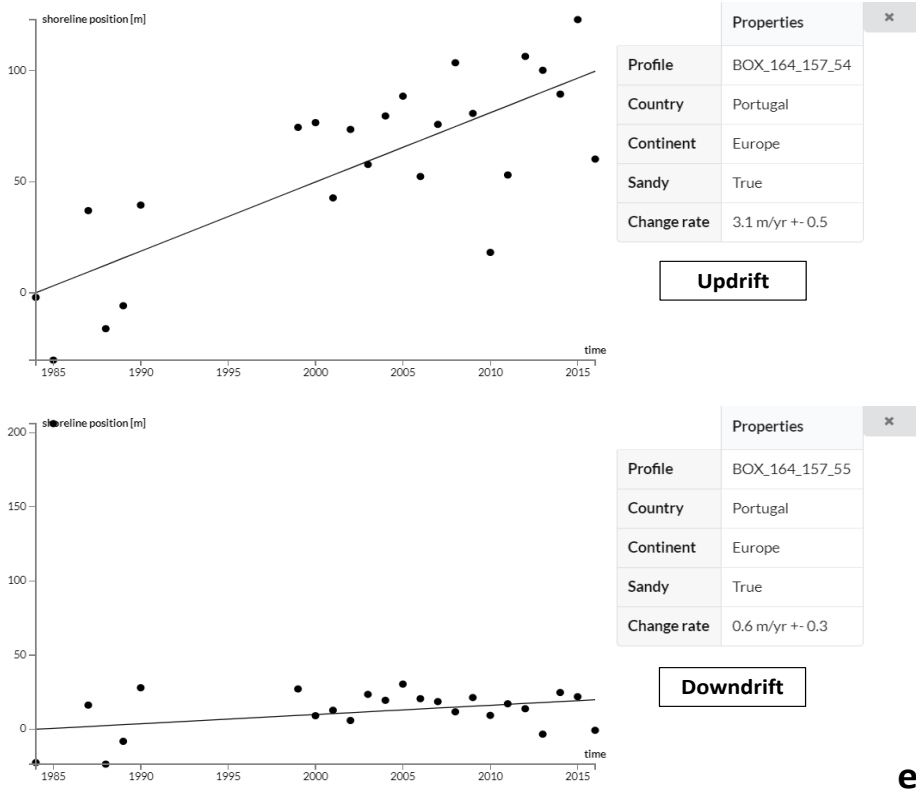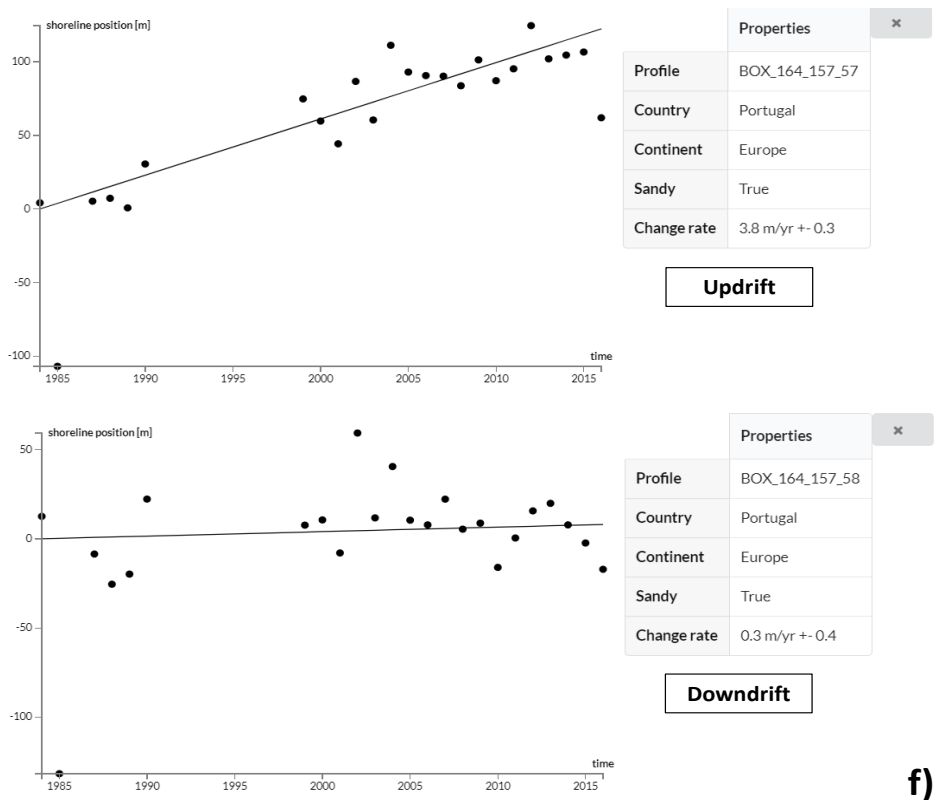
Figure 2.23: Updrift (upper panel) and downdrift (lower panel) shoreline evolution in: a) Ofir: north groin; b) Ofir: south groin; c) Apúlia; d) Madalena; e) Espinho: north groin; and f) Espinho: south groin.

2.3.1.3 Longitudinal revetments

Longitudinal revetments are artificial coastal protection structures built along the face of a dune strand or a beach slope. They are constituted by rubble, concrete blocks or geosynthetics and their main objective is the protection of the coastline from erosion (Burcharth and Hughes, 2012). They lead to a reduction and dissipation of wave energy through the direct impact of waves on the face of the blocks and the spaces between them (Coelho, 2005). These works are usually used in emergency situations in coastal areas of great vulnerability to maritime action where the risk of damage to the buildings and infrastructures located near the beach are high (Figure 2.24). They are often coupled with other types of coastal protection actions, such as groins or artificial sand nourishment (Burcharth and Hughes, 2012). In other cases they are also used to delimit marginal streets and/or landfills, assuming a complete soil retention function (Taveira-Pinto, 2001).

Figure 2.24: Longitudinal revetments at Ovar coast, Portugal: a) Cortegaça; and b) Furadouro.

2.3.2 Nature-based solutions

The need for ecosystem management is recognized worldwide as progressing from the local to the international level (Spalding *et al.*, 2014; UNFCCC, 2011). The United Nations Climate Change Conference, Paris 2015 (COP21) and the more recent United Nations Biodiversity Conference, Cancun 2016 (COP13) concluded that erosion is a real hazard for many coastal regions, and included ecosystem management in coastal erosion management strategies as a priority.

Eco-engineering solutions improve traditional structures using natural resources to increase the structure functionality, or the use of natural materials (flora and fauna) to create structures. Since, in some cases, traditional hard defence methods used so far have had more damaging than protective effects, there is a need for alternatives. In the last decade, management and development of wet nature values of dikes has been incorporated in Dutch policies, and several concepts for "green" dikes and submerged reefs have been developed. Bio-Builders organisms that naturally occur in the relatively shallow waters along the coast and in inland waters are capable of changing their environment in a way favourable to themselves. By means of their activity, they play a crucial role in the cycle of all kinds of substances in the water. Some of them filter water so it becomes clearer, others assimilate substances so that these form a food source for other organisms. In this natural way, the water quality can be improved with much lower costs than what would be possible with chemical or mechanical purification (Deltares, 2014).

The coastal ecosystems have some capacity for self-repair and recovery, and can provide significant advantages over traditional hard engineering approaches against coastal erosion. Recently, an ecosystem-based coastal erosion management strategy has been brought into practice as an approach that is more cost-effective, and sustainable than conventional hard protection approaches (ecosystem-based approach). Because ecosystems have the natural ability to reduce extreme wave effects (Shepard

et al., 2011), their growth can keep pace with sea-level rise by means of sediment accretion if available, allowing salt marshes to create stable ecosystems to deal with sea level rise (Kirwan *et al.*, 2010).

Adriana-Gracia *et al.* (2018) seek to undertake a general review of adaptation and protection measures against coastal erosion issues, based on incorporation of ecology and ecosystem services into coastal erosion management strategies. In order to achieve that, these authors analysed the influence of ecosystems for coral reefs, mangroves, seagrass, shellfish reefs and dune vegetation; their strengths and limitations; and methodologies to include ecosystems into coastal erosion management were also developed. As conclusion, the authors state that instead of hard engineering stabilization structures, an ecosystem-based approach with the creation and restoration of coastal ecosystems can offer optimal natural alternatives to help solve coastal erosion.

2.3.2.1 Artificial reefs

Across the world, certain types of artificial reefs generally built in mid to deep waters are seen as a management tool to sustain coastal fisheries to preserve marine life (Figure 2.25). By far, the most favoured reef material is concrete which has also been used in combination with other reef materials such as vessels, quarry rock, tyres and plastic, being natural stone and rock the next favoured material (Baine, 2001). The largest developmental, experimental, and deployment efforts have occurred in Italy, Spain, Portugal, and more recently, in France (Fabi *et al.*, 2011).

Figure 2.25: Artificial reefs (Vieira, 2014).

In Portugal, the same types of artificial reefs are more used in the region of Algarve (one of the largest in Europe with an area of about 43 km²) in order to avail the productive potential of surface currents because of their richness in nutrients and because it is a propitious area to natural coastal accidents (Whitmarsh *et al.*, 2008). Locations of these areas are shown in Figure 2.26.
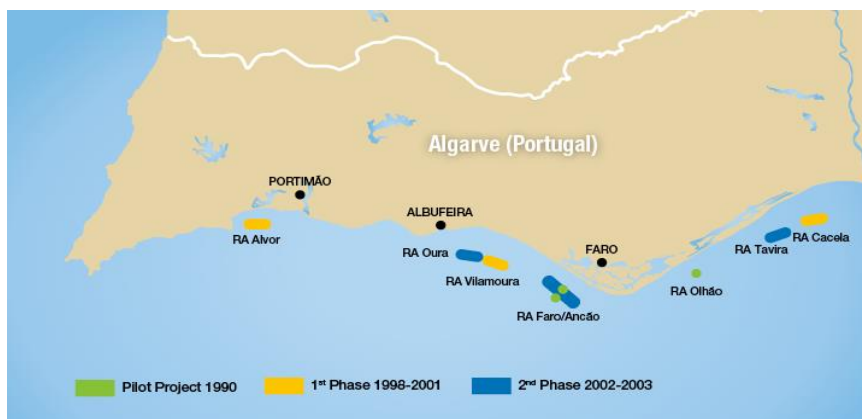
Figure 2.26: Artificial reefs in the Algarve (OR, 2014).

In California (United States) an artificial reef was built in 2001 at Dockweiler beach, which eventually was removed in 2008 for not complying with the intended goals. On the south coast of England, Boscombe area, in 2008, a reef was built in order to increase the number of visitors, to extend the tourist season and promote economic growth. However, after two years the construction of the reef has suffered significant damage, which derailed the effects of protection, particularly in terms of accumulation of sediments (Antunes do Carmo, 2013).

2.3.2.2 Multifunctional artificial reefs

The multifunctional artificial reefs (MFAR) are a particular case of artificial reefs and represent an innovative concept for coastal protection. Antunes do Carmo *et al.* (2011) state that in addition to have this function, these artificial reefs can be designed in order to also create favourable conditions for the surf practice, favouring other sporting activities such as diving and fishing, and enhance the environmental value of the area where they are located. To achieve this, in this work a step by step of a preliminary design of multifunctional artificial reefs was performed in order to use physical and numerical tests for the reef geometry as an initial design. The application of the numerical model COBRAS-UC (Cornell Breaking Waves and Structures - University of Cantabria) for several structure parameters was conducted to confirm the physical model results and gain a better insight into the influence of the breaker type and into the position of the breaking waves.

According to Antunes do Carmo *et al.* (2011), the construction of a MFAR may play an important role in different aspects of coastal protection, namely:

- Prevention of coastal erosion, and increase of beach stability;
- Increase of sand deposition in combination with artificial nourishment;
- Reduction of the wave load on the coast through a series of processes of wave transformation occurring on the structure (reflection, refraction and energy dissipation);
- Use for control waves propagation, creating good surfable waves, due to refraction and diffraction effects.

More recently, MFAR have been installed in shallow waters with coastal protection goals, particularly in protection of beaches and dunes, and in generating waves for surfing. In this context, arise as examples the MFAR in: a) Cable Station, Australia, built in 1999; b) Narrowneck Beach, Australia (Gold Coast), built in 2000; c) Maunganu Beach, New Zealand, built in 2008 using geotextile bags filled with sand; and d) Kovalam, India, built in 2010 which proved a case of great success to prevent coastal erosion and to generate great waves for surfing (Simioni and Esteves, 2010). In Portugal there are still no MFAR, although several studies for its implementation in some areas of the Atlantic coast have been conducted, particularly in locations that require urgent protection measures and that would be likely to benefit from good conditions for surfing. Examples are the coastal zones of São Pedro do Estoril (Mendonça *et al.*, 2010), Leirosa, South of Figueira da Foz (Antunes do Carmo *et al.*, 2011; Mendonça *et al.*, 2012; Ten Voorde *et al.*, 2009) and Vagueira beach (Di Bona, 2013; Mendonça *et al.*, 2021; Sancho *et al.*, 2020; Simões *et al.*, 2013).

2.3.2.3 Coral reefs

Corals are symbiotic organisms which has allowed them to become the main builders of reef structures in the tropics (Veron, 2000). They grow in warm, shallow, and nutrient depleted tropical or subtropical waters and these corals are slow growing. Corals have many functions in the coastal erosion management process, but the most important are related to energy dissipation and sediment retention (Figure 2.27). Perhaps the most evident are linked to their shape and structure that allows coral reefs to act as a barrier that dissipates wave energy, providing a natural submerged breakwater (Figure 2.28). The geometry (porosity, surface, tortuosity, roughness and the overall void matrix), water depth above the reef system (depth of flow) and length in the direction of wave propagation are key points in the wave energy dissipation process. Corals can also contribute to sedimentation by means of processes related to mucous secretions. Coral secretions trap suspended particles in the water column, forming

aggregates that sink rapidly to the seabed (Wild *et al.*, 2004) contributing to the sedimentation process. The importance of corals in coastal erosion management strategies is well documented. Wielgus *et al.* (2010) determined that ten years after the disappearance of some species of live corals in the Dominican Republic, erosion rates increased between 65 and 100%, due to substantial sedimentary deficits. Also, during extreme coastal erosion related to the Sumatra tsunami of 26th December 2004, waves were only 2-3 m high, due to energy dissipation benefits provided by the corals, with "damage caused" limited only to a distance of 50 m inland (Adriana-Gracia *et al.*, 2018).
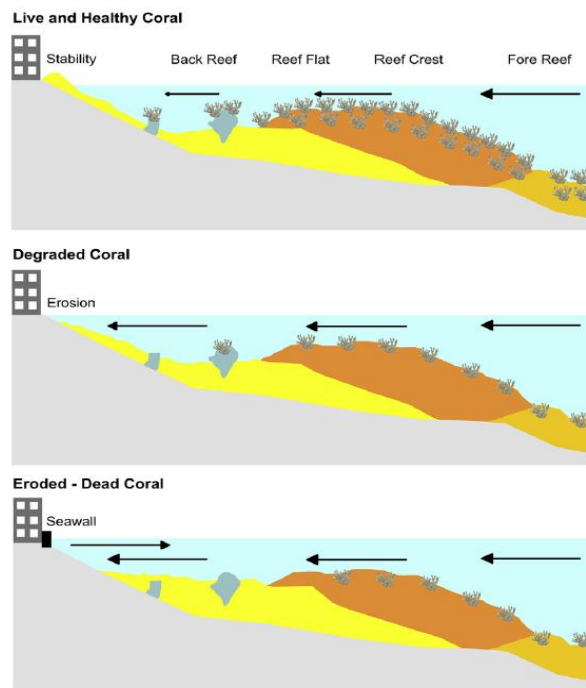
Figure 2.27: Wave attenuation and coastal erosion protection given by coral under different management scenarios (Adriana-Gracia *et al.*, 2018).

Figure 2.28: Coral reefs in Australia.

2.3.2.4 Salt marshes, mangroves and osier-beds

Vegetated areas, such as salt marshes, mangroves and osier-beds (Figure 2.29), trap sediment by reducing flow velocities, hydrodynamic forces on the seabed and by improving consolidation of muddy soils by means of evaporation. Furthermore, they attenuate waves in front of coastal protection constructions, meaning that these require less height, enforcement and repair (Deltares, 2014).
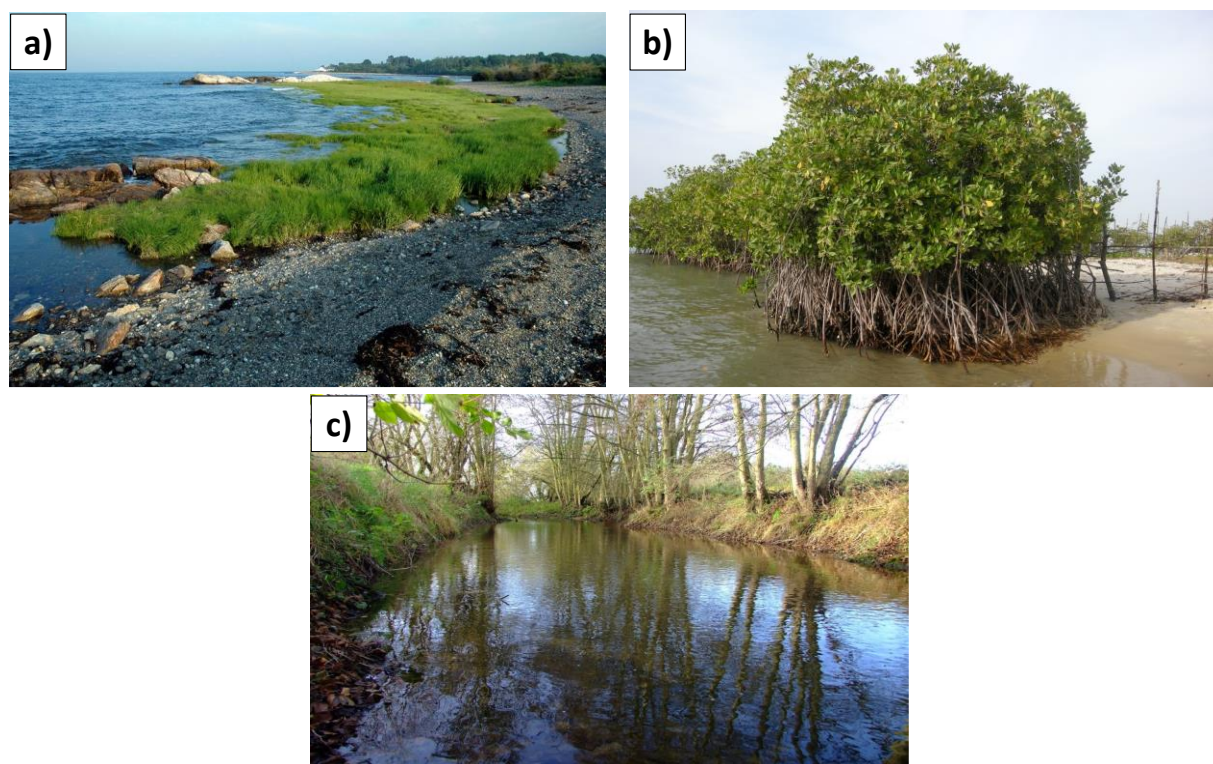
Figure 2.29: a) Salt marshes; b) Mangroves; and c) Osier-beds (Vieira, 2014).

Mangroves are assemblages of salt-tolerant trees and shrubs found in intertidal zones and estuarine margins, on shallow and muddy ground, with calm waters (estuaries, bays, coastal lagoons, etc.). The vegetation can be found in tropical and subtropical areas and has adapted to live in salt water, either continuously or during high tides. Mangroves grow in harsh environmental settings, such as high salinity, high temperature, high sedimentation, extreme tides, and anaerobic soils (Giri *et al.*, 2011). This ecosystem has the ability to significantly reduce the energy of any kind of fluid that is moving through them. The energy lost when wind and waves pass through mangrove roots and branches can range between 15 and 65%, minimizing seabed scour and further sediment movement (Spalding *et al.*, 2014). At the same time, their structure can reduce winds across the surface of the water, reducing the re-formation or propagation of waves. Mangrove roots help generate and bind new sediments and soils (Figure 2.30). The above-ground roots slow down the water-flow process, stimulate sediment deposition, and reduce erosion (Adriana-Gracia *et al.*, 2018). An example for this management strategy can be

stated along some coastal areas of Guyana (Figure 2.31), where mangroves forests have been destroyed to give way to aquaculture or agriculture, and as a consequence coastal erosion has increased significantly reaching rates of up to -3 m per year (Gratiot *et al.*, 2007). In addition, Hong (2019) developed a study at the water lab in Delft University of Technology that explored the influence of mangroves width on coastal stability. The results suggest that decreasing the vegetation width can significantly change the pattern of the water motions creating unfavourable conditions for deposition.
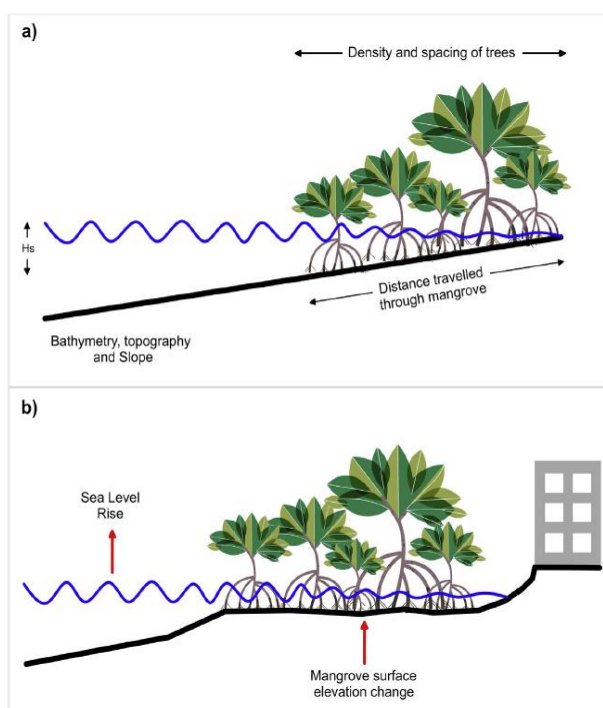
Figure 2.30: a) Factors affecting wave attenuation and coastal erosion in mangroves; and b) Example of how mangrove's soil surfaces rises and potentially allowed keep pace with sea-level rise (Adriana-Gracia *et al.*, 2018).

Figure 2.31: Mangroves in Guyana.

2.3.2.5 Seagrass

Seagrasses (Figure 2.32a)) are able to significantly influence the hydrodynamic environment by reducing current velocity, dissipating wave energy and stabilizing sediment, since they are permanently submerged and attached to the sediment (Adriana-Gracia *et al.*, 2018). When a wave reaches the ecosystem, a negligible energy reflection and weak wave attenuation by friction is produced (Figure 2.32b)). This situation is opposite to what happens to most hard structures, e.g., seawalls and breakwaters, where this same process gives rise to higher energy reflection and wave attenuation by breaking and friction with further loss of sediment (Ondiviela *et al.*, 2014). As an example, on the Albany coast, western Australia, the comparison between waves heights in dense and patchy seagrass with areas that had no vegetation, concluded that waves were 10-30% smaller in dense seagrass areas, compared to a bare seafloor (Adriana-Gracia *et al.*, 2018).
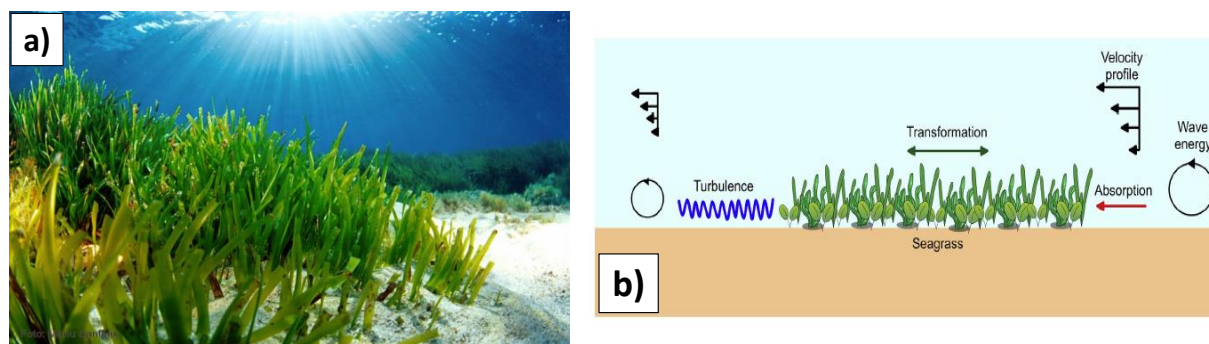
Figure 2.32: a)Seagrass; and b) Physical processes related to influence of seagrasses into wave attenuation and coastal erosion reduction (Adriana-Gracia *et al.*, 2018).

2.3.2.6 Oyster and mussel reefs

Reefs of bivalves can function as stabilising or protecting agents because they reduce wave and current intensity, and because of their ability to alter properties of the sediment. Figure 2.33 shows an oyster and a mussel reef (Deltares, 2014).
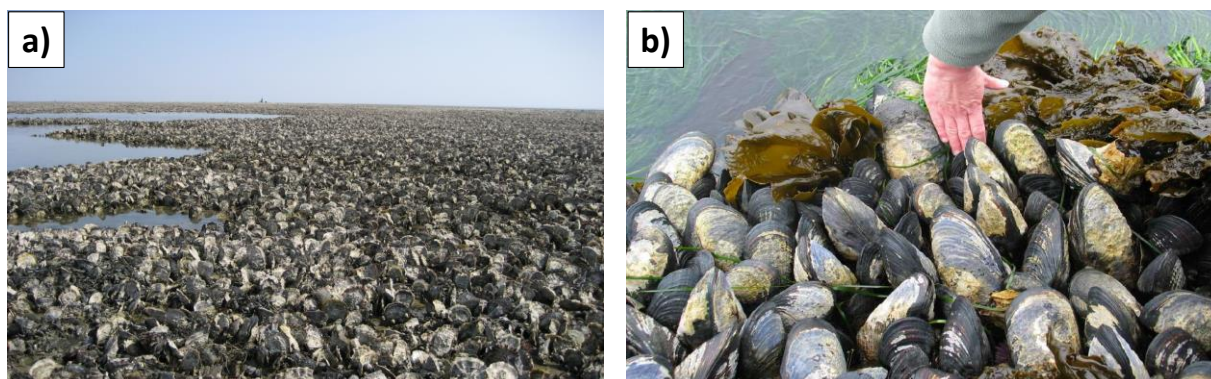
Figure 2.33: a) Oyster reef; and b) Mussel reef (Vieira, 2014).

Several hard-ground-building bivalve species occur in estuarine and temperate marine environments. These bivalves can build spatially and topographically complex habitats that foster unique assemblages of organisms. Oyster reefs can increase the biodiversity of the intertidal zone by forming a new hard substrate for other species in soft sediment environments, accumulate carbon in the calcium carbonate of their shells that help reduce the concentration of greenhouse gasses (Goldberg, 2013; Adriana Gracia *et al.*, 2017), and also have the capacity to filter the water and reduce turbidity by extracting phytoplankton and organic and inorganic particles from the water column (Vader, 2014). Individual mussels and the edges of small mussel patches reduce critical erosion velocity and this produces local scour (Figure 2.34). In Bangladesh, oyster farming is used as a management strategy to combat coastal erosion. It was tested the oyster potential as a way to increase sedimentation, thereby helping to protect vulnerable sectors of coastline against erosion, and it was also demonstrated that oyster reefs can induce accretion of sediment on the lee side of the reef (Adriana-Gracia *et al.*, 2018).
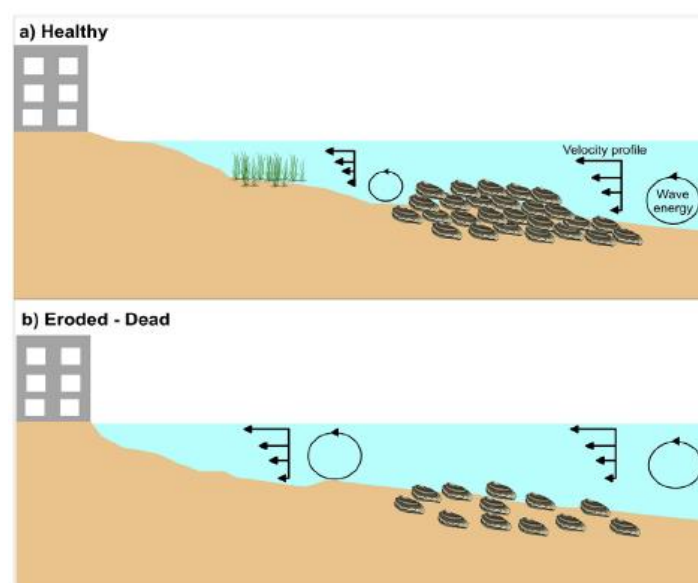
Figure 2.34: Wave attenuation and coastal erosion protection given by shellfish reefs under two different scenarios (Adriana-Gracia *et al.*, 2018).

2.3.2.7 Dune vegetation

Coastal vegetated dunes ecosystem has the capacity to dramatically modify and stabilize the physical environment (Gutiérrez *et al.*, 2011). Vegetation stimulates dune growth by trapping and stabilizing wind-moving sand. Small plants located on the face of eroded dunes can enhance the natural development above the limit of direct wind or wave attack. Additionally, grasses can be transplanted to encourage growth of new foredunes along the toe of existing dunes, as long as these species are

tolerant to occasional seawater inundation. Planting grasses from seed can be undertaken, but will not usually be successful along the dynamic foredune environment. Vegetation sowing and transplanting per se will not construct new dunes or completely prevent erosion. Plants encourage natural recovery creating a reservoir of sand within the dunes that better enables their ability to withstand erosion. Fencing is often necessary to help in sand accretion. Additionally, these works can provide extra protection from waves and will reduce damage due to trampling. Once vegetation is well established, dunes may become self-sustaining, although any erosion damage will need to be rapidly repaired (Adriana-Gracia *et al.*, 2018). In Papamoa, New Zealand (Figure 2.35) this management strategy has successfully reached a complete dune restoration, resulting in a seaward dune advance of 10-25 m, providing a much wider dune with a more gentle, vegetated and resilient front slope to help buffer current and future erosion (Adriana-Gracia *et al.*, 2018). Also, in Portugal, vegetation in seaward dune and wooden-made structures (palisade fencing) to retain sediments have been extensively built along coastal areas (e.g., Caminha, Gaia and Guincho beaches).

Figure 2.35: Dune vegetation in Papamoa, New Zealand.

2.3.2.8 Sand engine

If there is abundant sediment near the coast, artificial sand nourishment would be the preferable solution to the erosion problem. However, this solution has to be carefully assessed due to the high amounts of sediment in deficit and the costs involved. A solution may be achieved through the construction of coastal protection structures to protect urban sea fronts with the combination of beach nourishment allowing sand to immediately begin to pass the structure, reducing transient erosion downdrift (Silva *et al.*, 2007). Sand nourishment allows natural processes to maintain a sandy coast and "dynamically" keep it in place (Figure 2.36). The sand for nourishment is dredged either from rivers or from deep waters (below the 20 metre depth contours). Water and wind distribute this sand naturally along the beach and across the dunes (Deltares, 2013).

Figure 2.36: Sand engine (Deltares, 2013).

2.3.2.9 Reed floats and Tidal pools

In areas that are initially not suitable for seabed vegetation, for instance due to the lack of shallow shores or large variations in water levels, floating devices often are applicable (Deltares, 2013). Reeds do not affect the sediment stability directly, but do attenuate small waves and thereby protect nearby banks, prevent re-suspension of bed material and improve water clarity (Figure 2.37a)).

Solid constructions along the coast, such as dikes, harbour piers and dams, are the habitat of various marine species (Figure 2.37b)). Many of them live exclusively in places that are continuously underwater. By making simple and inexpensive adjustments to solid structures, water in higher parts of the intertidal zone will linger longer. This can be a huge boost to biodiversity and biomass and can be used as a mitigating measure for Natura 2000 objectives (Deltares, 2013).
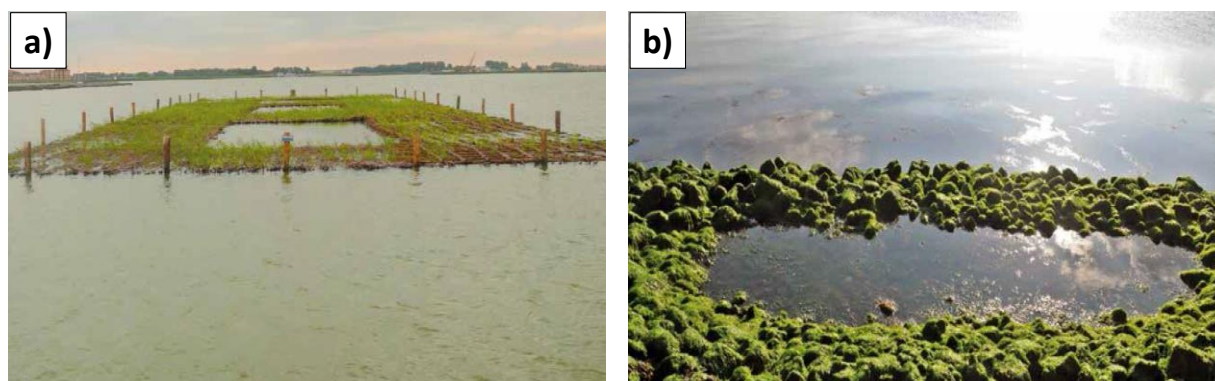
Figure 2.37: a) Reed floats (Deltares, 2013); and b) Tidal pools (Deltares, 2013).

2.3.2.10 Natural rocky outcrops

Rocky outcrops (Figure 2.38) are rock formations that appear at the surface of the sea, which can be seen as natural coastal protection solutions by contributing to the dissipation of wave energy before

reaching the beach and by being a barrier to the free movement of the sediments in situations of weak or moderate wave climate. Creating lower energetic zones will avoid direct wave action on beaches which will promote greater accumulation of sediments and consequently reduce beach retreat.

Similar to breakwaters and groins effect on coastal stretches, these natural formations retain sediments on sandy beaches, thus increasing beach width. Despite studies on this phenomenon not being conducted under the influence of rocky outcrops, several evidences of this positive effect can be found in several zones in the Portuguese coast (e.g., Viana do Castelo, Esposende, Póvoa de Varzim, Vila do Conde and Matosinhos).

Different rocky outcrops orientations, shapes, elevations and shoreline distance create different sediment deposition patterns. The influence of these rocky outputs can be evaluated in plan view by recurring to Google Earth. In Figure 2.39a), the presence of the upper rocks agglomerate promoted an accumulation of sediments that lead to the formation of a salient. In Figure 2.39b), both rocks agglomerate work as groins and the beach presents a parabolic shape between the two fixed points. Figure 2.39c) depicts a rocks agglomerate resembling a groin and a detached breakwater (upper and lower rocky outcrops, respectively) and its effects on sediments accretion. Figures 2.39d) to 2.39f) present sediment deposition due to rocky outcrops parallel to the shoreline (similar to the effect of breakwaters) and Figures 2.39g) and 2.39h) show groups of rocky outcrops parallel to the shoreline and their effect on sediments accretion and tombolo formations.

Thus, the presence of rocky outcrops has demonstrated a positive effect on coastal protection and on sediments accumulation. The observation of this natural way of protection is important to inspire new structures with shapes and volumes similar to these rocky outcrops that can encourage innovative solutions for coastal zones defence.

Figure 2.38: Natural rocky outcrops.
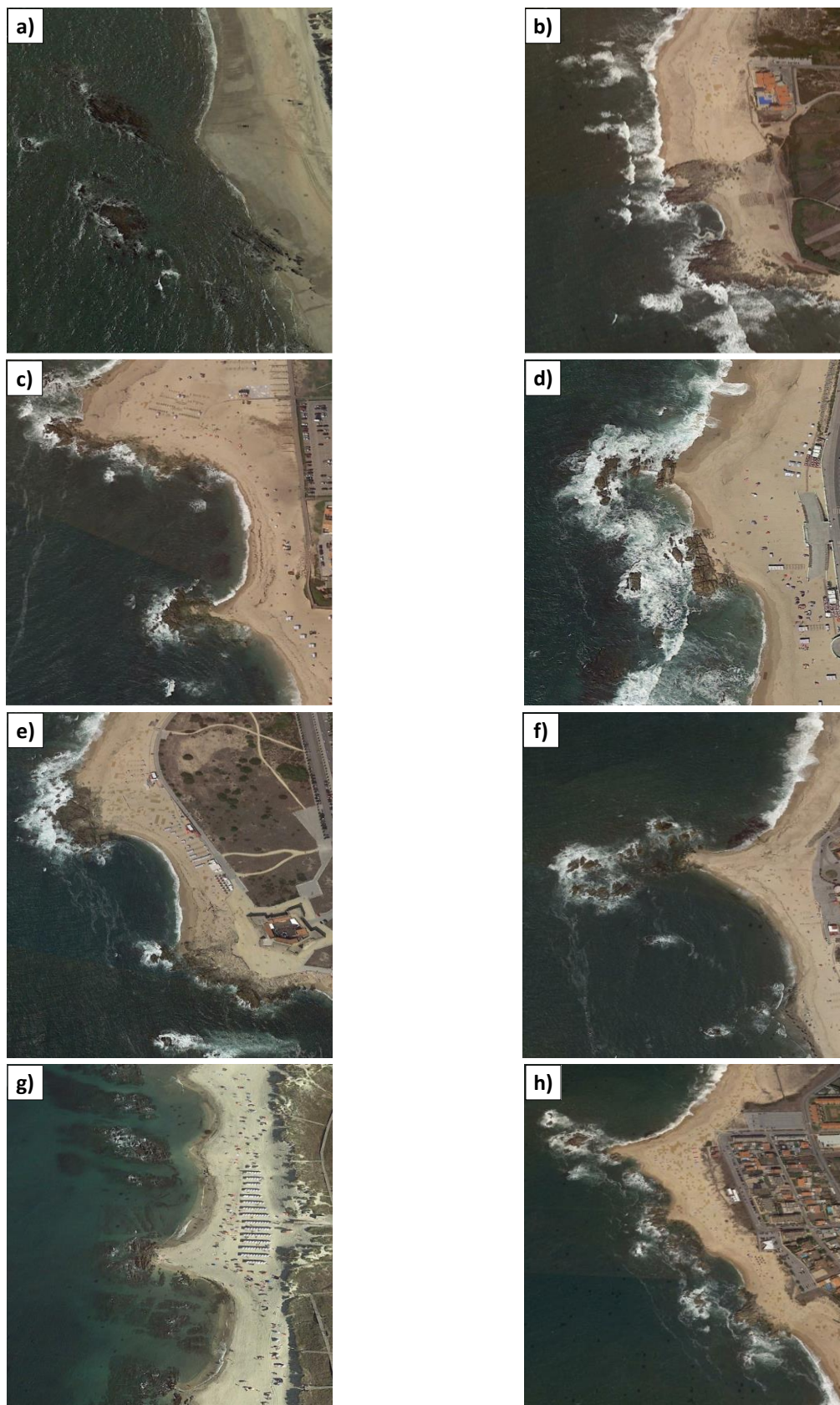
Figure 2.39: Sediment accretion by rocky outcrops in: a) Esposende, Portugal (2013); b) and c) Póvoa de Varzim, Portugal (2017); d) to f) Vila do Conde, Portugal (2017); g) Viana do Castelo, Portugal (2013); and h) Matosinhos, Portugal (2017).

2.3.2.11 Gravel beaches

Gravel beaches (Figure 2.40) are more frequent on many high-latitude, wave-dominated coasts across the world. Due to their natural efficient ability to dissipate large amounts of wave energy and their apparent resilience and stable behaviour, the use of coarse grained sediment to replenish eroding beaches is widely regarded as a cost-effective and sustainable form of coastal protection. The morphodynamic response of gravel barriers is related to the ratio between hydrodynamic forcing and the beach geometry and composition (Buscombe and Masselink, 2006; Gomes *et al.*, 2018; McCall *et al.*, 2015). The most important active agents in morphodynamic change processes on gravel beaches are tides, waves action and sea level rise, even under conditions of high accretion rates. The permanence of gravel systems is also influenced by storms, tectonic events and other factors that build and remodel highly dynamic coasts (Granja *et al.*, 2015; McCall *et al.*, 2015; Silva, 2014).

A study conducted by Loureiro (2006) concluded that the sedimentary deficit is much higher on sandy beaches than on gravel beaches and that regarding the value of cliffs retreat, gravel beaches present lower values compared to the ones verified in sandy beaches. This fact is based on the effect played by the presence of gravel ridges that creates relative beach stability, thus defending the sandy cliffs of direct waves attack.

The high permeability of these beaches, resulting from the dimensional characteristics of their sediments, causes a reduction in the waves backwash intensity, leading to a decrease in sedimentary transport from the beach face towards the sea. For that reason, these systems present a beach face slope quite elevated. The reflective behaviour is controlled by the high slope they present, with dissipative conditions occurring only in extreme situations of strong wave climate. On the other hand, in sandy beaches, the lower permeability and beach slope resulting from the sediments dimensions impels a more intense action of the incident waves and the backwash on the beach face, which will induce greater beach erosion (Buscombe and Masselink, 2006; Jennings and Shulmeister, 2002; Loureiro, 2006).

Figure 2.40: Belinho gravel beach in Esposende, Portugal.

2.3.2.12 Eco-concrete

Much marine life, such as mussels, barnacles and seaweed, need a hard surface to survive. Commonly, they find this surface on hydraulic engineering constructions, such as harbour piers and seawalls. But modern concrete is becoming increasingly plain and therefore less suitable for these organisms to establish themselves. The use of special "eco-concrete" during the construction or renovation of hydraulic engineering structures appears to significantly speed up the process by which these species establish themselves and their diversity. Eco-concrete is a concrete with a special texture and geometric shapes that enable organisms such as algae, seaweed and mussels to attach themselves more easily. These organisms, in turn, are a source of food for birds and fish. Mosquito larvae, which live among the algae, are also a source of food for protected bird species, such as the ruddy turnstone and the purple sandpiper (Deltares, 2013).

A pilot study was set-up to investigate the possibility to increase the settlement of algae and macro-fauna colonization by testing various textures and geometrical slabs shapes on the concrete blocks of one of the breakwaters at IJmuiden harbour (Netherlands). Slabs of eco-concrete of 75 cm x 50 cm with different shapes, such as horizontal and vertical ridges, hollows and holes, were used in the pilot project (Figure 2.41). The use of eco-concrete provides the same protection as "regular" concrete. The rough surface of the eco-concrete became overgrown with algae (Figure 2.42) much more quickly than plain concrete and within two and a half years, mussels established themselves on eco-concrete slabs, where water lingers longer during ebb tide. The production of concrete with special textures and geometric shapes is expected to cost 2% to 3% more than the production of traditional plain concrete. However, there are many benefits that outweigh these marginally higher costs, like water quality improvement since mussels filter water, making it cleaner (Deltares, 2013). Given the "scale-concept", these small scale adaptations can provide benefits for groins and revetments as sources of enhanced productivity and habitat diversity on the meso scale. For (possible future) large-scale production, it is recommended to apply the special textures and geometrical shapes directly on the concrete blocks instead of working with slabs.

Figure 2.41: Slabs of eco-concrete (Deltares, 2009).

Figure 2.42: Eco concrete (Deltares, 2013).

2.3.2.13 Geotextile tubes

Geotextiles for flexible coastal structures are intended to be versatile applications with environmental acceptance and long-term sustainability (Heerten *et al.*, 2001). They are not properly hard engineering solutions and are used as engineering structures for beach protection and nourishment. Sometimes, they are used as protective measurements to increase life time of the coastal hard engineering structures and they can take any form to suit specific types of applications. Sand is the best filling material, mostly thanks to its incompressibility; but other types of inert materials can also be used like gravel and mortar. The geotextiles are thin, flexible and porous continuous sheets very resistance to water forces and are normally made of polyethylene (PE), polypropylene (PP), polyvinylchloride (PVC) or polyester (PET) (Agrawal, 2011). Although their plastic derivative nature, they favour the attachment of marine life after few days because of its fibre structure. Their porosity is capable of retaining the injected materials and allowing, due to a great permeability, the flow out of water during the pumping phase. In addition, the geotextiles, as well as the seam, are highly strong, to resist the high tensions occurring during the hydraulic filling and maintain their geometrical shape. Geosynthetic systems have different forms: sheet like mattresses (geomattress), tubular long structure that can also be submerged (geotube) and bags of small volume (geobag) (Koffler *et al.*, 2008). Geomattresses are used for slope and bed protection works; geobags are suitable for the protection of beach slopes, cliffs and concrete walls; and geotubes (Figure 2.43a)) are mainly advised for the construction of groins and offshore breakwaters (Palmeira *et al.*, 2008; Sahu, 2014).

In Queensland, Australia (Figure 2.43b)) a submerged reef of 400 m × 200 m was constructed in 2001 with the aim to retain sand that is transported each year to the North along the shoreline. Nearly 400 mega sand containers varying from 3.0 m to 4.6 m in diameter were dropped and placed in depths of water ranging from 3 to 11 m, onto a sandy seabed. Monitoring has shown clear salient at

times, enhanced surfing conditions and within months, the containers were covered with a thick growth of seaweed. From this study it was concluded that geotextiles structures can be successfully used to solve conventional coastal problems and that sand-filled geotextile forms can create an excellent foundation for a broad diversity of marine species, since the porous nature of the geotextile made it an ideal platform for marine growth (Restall *et al.*, 2002).
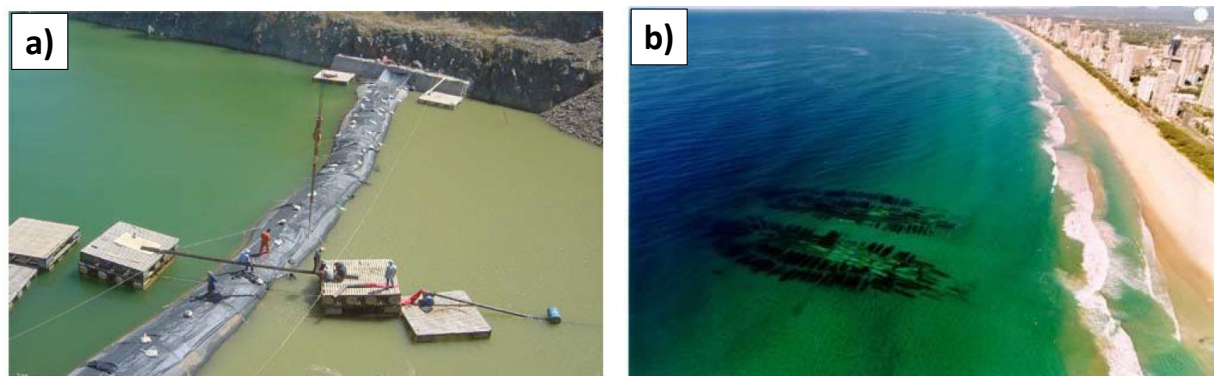
Figure 2.43: a) Geotubes filling (Koffler *et al.*, 2008); and b) Narrow Neck, Queensland, artificial reef aerial view (Restall *et al.*, 2002).

One of the most attractive advantages of geotextile tube technology is that *in situ* filling materials by hydraulic pumping can be used, which allows it to be implemented with lower costs and faster construction than other technology. The geotextile requirements and considerations include: UV-resistance and biological effects (the presence of marine growth enhances the geotextile durability); abrasion resistance (due to sands and gravel carried by currents and waves); fines retention and hydrodynamic stability (to ensure the container does not deflate and remains stable due to wave action and dynamic flow conditions); permeability (the faster the water is drained from the container the more stable the structure); interface friction (this angle is of importance when assessing the stability of the structure, particularly when containers are placed on top of each other); elongation (a high elongation geotextile allows the containers to mould itself in with the existing features and also allows a certain degree of self-healing of the structure, as presented in Figure 2.44a)) (Saathoff *et al.*, 2007).

These aspects and the accuracy of placement are important to prevent geotextile from sliding and overturning, especially during release and impact. In order to assess the stability of the filled geotextile tube structure, current wave forces have to be estimated (Figure 2.44b)) (Oh and Shin, 2006). Because of the lower price and easier installation, geotextile tube systems can be good alternatives for coastal structures (Pilarczyk, 2008).
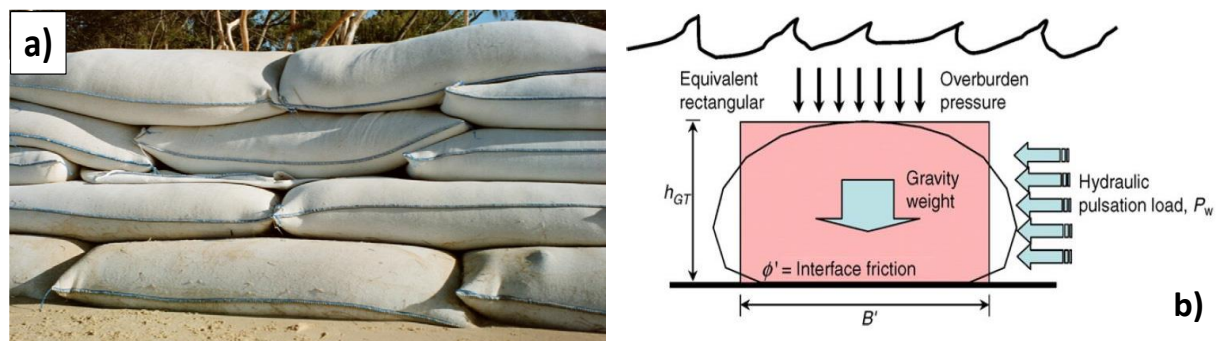
Figure 2.44: a) Self-healing characteristics of high elongation containers (Saathoff *et al.*, 2007); and b) : Schematic diagram of 2D hydraulic stability (Oh and Shin, 2006).

Studies conducted by Oh and Shin (2006), and Shin and Oh (2007) showed that a larger width and a higher crest height of the submerged structure have an important influence on wave energy reduction. Observations of the filling process show that settling and drainage occurred very fast and that the construction of one geotextile tube requires less than one hour and the desired final height was achieved after only four dredging and filling steps. After one year in use, seaweed had inhabited the surface of the submerged tube, which shows that the polymer material used is unlikely to have an adverse effect on marine life and that it can be environmentally sustainable to the adjacent ecology (Figure 2.45). Based on the results of stability analysis and hydraulic model tests, a double-lined geotextile tube installed with zero-water depth above crest was found to be the most stable and effective for wave reduction than other design plans. Corbett *et al.* (2010) have also shown that this type of material contributes to the increase of biodiversity of species implantation sites, as well as for the proliferation of the species. Manufacturing of these products leads to less carbon-dioxide emission than the construction of conventional types of retaining walls, which clearly demonstrates that geotextile containers can be seen as an important structural element in coastal engineering practice (Palmeira *et al.*, 2008; Saathoff *et al.*, 2007).

Figure 2.45: Type of organic growth associated with geotextiles (Shin and Oh, 2007; Vieira, 2014).

2.3.3 Synthesis

The main purpose of this study is to find an optimal alternative for costal protection that comprises a sustainable view inspired on existing solutions. Assessing the traditional solutions presented, the design of the proposed structure will somehow be based on the effects of detached breakwaters on coastal zones as it is going to be implemented offshore. Also, inspired by the presence of sand spits and sand banks effect near tidal inlets, the innovative structure should induce longitudinal drift reversal in order to promote sediments accretion on coastal stretches.

Although many of the nature-based solutions presented have great potential to combine coastal protection and marine life growth goals, the majority of them are limited by environmental conditions like low wave energy onsite. The Portuguese NW coast is known to be highly energetic especially during winter, which limits the choice for some of the nature-based solutions described in this study, since these conditions will induce more damage to the structure. Nature-based solutions like sand engine and eco-concrete have revealed good results and a potential inspiration for the main objectives of this study. Artificial sand nourishment (sand engine) is a nature-based solution that should be considered when combining with coastal protection structures. This way, with the effect of the coastal structure on the beach, sediments will be retained for longer periods, which will lead to sediments accretion and consequently to beach width growth. For this reason, in this study sand engine should be considered if availability of sediment sources are guaranteed.

Eco concrete is characterized as a concrete with a special texture and geometric shapes that enable organisms to attach themselves onto the concrete blocks more easily. Although with slighter higher costs, this solution provides the same protection as "regular" concrete with an increment on water quality and on promotion of marine life diversity. This way, by using rough textures like horizontal and vertical ridges, hollows and holes this solution should be studied for the proposed innovative solution.

Artificial reefs as a protection measure for coastal zones or MFAR to improve hydrodynamics for surfing and also to control beach erosion have been described as potential alternatives to reduce wave loads and thus to prevent coastal erosion. Both solutions have been deployed in several coastal zones worldwide but although results for artificial reefs have shown to be undesirable, MFAR proved to have great success to prevent coastal erosion and to generate great waves for surfing.

Coral reefs have an important role on energy dissipation and sediment retention by entrapping suspended particles with their mucous secretions which provides natural submerged detached breakwaters. Despite being a sustainable solution, they develop in tropical or subtropical waters, which limit their application on the NW Portuguese coast.

Vegetated areas, such as salt marshes, mangroves and osier-beds can survive on harsh environmental conditions, normally found in calm waters on shallow and muddy grounds on tropical and subtropical areas. Their role on controlling coastal erosion is achieved by reducing the energy through roots and branches and by reducing winds with their structure, thus decreasing the formation or propagation of waves and trapping sediment by significantly reducing flow velocities on the seabed. Because of their geographic conditions for survival, they cannot be deployed in the NW Portuguese coast.

The development of seagrass and oyster and mussel reefs could contribute to reduce current velocity and wave energy, and also contribute to the stabilization of sediment and to increase biodiversity by providing shelter and food to a diverse community of animals. Despite not being considered on this study, seagrass can ensure a negligible energy reflection contrary to what happens to breakwaters and other hard structures. The mentioned bivalves settle on hard submerged surfaces and develop in temperate and tropical zones, which although not considered in this study, their natural settlement can be possible and add benefits to existing structures if their rough geometry allow their settlement.

Dune vegetation can contribute to sediments retention. It is important to note that this natural solution for coastal protection will not construct new dunes or completely prevent erosion as they only encourage natural recovery creating a reservoir of sand. It is a solution that can provide protection from waves and prevent damage by trampling, and that also benefits from using fences. Although not considered in this study, it is a low cost solution to preserve dunes by retaining sediments on beaches.

Reed floats work as floating devices when seabed vegetation is not possible. This solution does not have any influence on sediments accretion, but only on wave attenuation for small waves and wave quality improvement. Tidal pools main concern is the possibility to create habitats of various marine species, not having great impact on coastal protection though. For these reasons, these two solutions mentioned will not be considered in this study.

Natural rocky outcrops are rock formations that appear at the surface of the sea and can reduce beach retreat since they create lower energetic zones that will promote great accumulation of sediments in weak to moderate wave climate situations. Although studies on this natural solution for coastal protection are scarce, observations in the Portuguese coast prove that structures with shapes and volumes similar to these rocky outcrops can encourage innovative solutions for coastal zones defence. For this reason, the described solution should be better assessed for this research work.

Resulting from the dimensional characteristics of their sediments, gravel beaches have high permeability that reduces the backwash intensity, leading to a decrease in sedimentary transport from the beach face towards the sea. The use of coarse grained sediment to replenish eroding beaches is

widely regarded as a cost-effective and sustainable form of coastal protection, since this resilient and stable solution provides dissipation of large amounts of wave energy. Although not being considered for this study, gravels can be used as an alternative solution to reduce sedimentary deficit that leads to beach erosion.

Geotextiles are highly strong flexible coastal structures that can take any form, normally used on beach protection and nourishment by wave reduction and are characterized as durable, eco-friendly, safe, pollution free, and space and cost saving. These structures are normally filled with sand due to its incompressibility and are able to maintain their geometrical shape. Although their plastic derivative nature, they increase biodiversity by favouring the attachment of marine life after few days because of its porous nature, and the manufacturing of these products leads to less carbon-dioxide emission than the construction of conventional structures. Because of the lower price and easier installation provided by *in situ* filling, geotextile tube systems can be good alternatives for coastal structures.

2.4 General aspects of coastal structures design

Cover layers of coastal structures must be designed to satisfy a number of sometimes conflicting criteria, including structural stability, functional performance, environmental impact, life-cycle cost, and other constraints which is challenging in terms of integrated design. Coastal protection structures are subject to extreme loading conditions associated to different phenomena of maritime hydrodynamics. These loads are mainly caused by physical factors like wave forces and current velocity forces. Other loads related with the structure use like impact forces from ships collisions and earth forces exerted by soil backfill should also be considered.

The study of wave loads on coastal structures can be classified in two ways: (a) by the type of structure on which the loads act; and (b) by the type of wave action against the structure. Fixed coastal structures can generally be classified as one of three types: (a) pile-supported structures such as piers and offshore platforms; (b) wall-type structures such as seawalls, bulkheads, revetments, and some breakwaters; and (c) rubble structures such as many groins, revetments, jetties and breakwaters. The types of waves that can act on these structures are nonbreaking, breaking, or broken waves, which will be determined by the depth in the vicinity of the structure (CERC, 1984a). In relation to the characterization of the actions, a generic description of the requests to which the coastal structures are subjected during their useful life is given.

According to Banyard and Mannion (2002) and Teixeira (2009), the maritime hydrodynamics phenomena caused by wave climate, tides, currents and winds translate practically all the actions that

structures are subjected during their useful life. For Taveira-Pinto and Neves (2003), the waves are the phenomenon that directly affects the structures, which can lead to the fall, displacement or rupture of the armour blocks in the cover layer and sometimes lead to the ruin of the structure. Thus, the design wave height is a fundamental parameter in the stability analysis of the structure resistant layer.

For the structure design it is recommended a correct characterization of the actions, a preliminary design and, if possible, the construction of reduced physical models with the purpose of testing the solutions obtained in the preliminary design phase due to its empirical formulations. This can be explained by the non-inclusion of some of the influential parameters considered in the stability of the structures, and with the wave climate (Pita, 1985; Taveira-Pinto and Neves, 2003). It should be noted that the methodologies used for preliminary design presented were developed mainly for breakwaters, but are often adapted and applied to other types of structures (Allen, 1998).

In the following Sections, important design parameters, and design aspects will be presented.

2.4.1 Types of structure and breaking wave type

The complexity of the wave climate on the armour blocks in the cover layer, coupled with the random-shaped and the random-placed in an orderly or random manner, makes it difficult to calculate the loads acting on the structure. The preliminary design of the structure cover layer is essentially characterized by the incident wave height, and consists on determining the minimum value for the armour blocks weight that is capable of resisting the requested actions, taking into account the permitted level of damage (Lima, 2011; Taveira-Pinto and Neves, 2003).

According to Fleming *et al.* (1998), the determination of the armour blocks weight to be placed in the cover layer depends on several parameters, which vary according to the type of structure required (non-overtopped, overtopped and submerged), and on the formulations used (usually, Hudson or van der Meer). Non-overtopped structures have sufficiently high crest elevations, where overtopping only occurs when subjected to severe weather conditions. This is the situation where the waves action on the structures slopes is more damaging, which implies the need for larger weights for the armour blocks in the cover layer. For this type of structure, three different formulations are commonly used: Hudson (generic), van der Meer (rubble) and van der Meer and Jong (tetrapods). With overtopping structures, the overtopping is admitted for a certain incident wave height, where the wave run-up can reach values higher than the structure crest. For the preliminary design of these structures, the van der Meer formulations for rubble are commonly used. Finally, submerged structures are those where the crest

elevation is below the MSL. The formulations for rubble used for these structures are the van der Meer's (Lima, 2011).
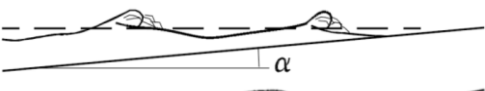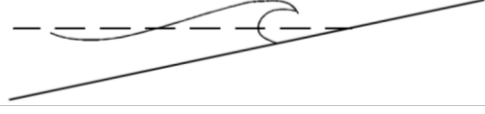
Due to the change and deformation phenomena of wave climate propagation towards the coast, the local wave height differs from point to point. When the waves propagate from higher to lower depths their length decreases while their height increases. When the depth reaches a certain value, the wave becomes unstable and breaks. Usually the breaking wave occurs when the ratio of wave height/wavelength exceeds 1/7, when the wave's crest peak is steep (less than 120°), or when the wave height is three-fourths of the water depth (Coelho, 2005). According to Veloso-Gomes (1981), in certain situations, the wave can reach the structure without having occurred breaking. There are different types of breaking wave, which depend essentially on the structure slope where the wave propagates and on the wave slope. The Iribarren number (ξ) is a dimensionless parameter that allows establishing the ranges of occurrence for the different types of breaking wave and it can be expressed by either Equation (2.4) or Equation (2.5). Table 2.2 presents the classification for different breaking wave types based on the Iribarren number (Burcharth and Hughes, 2001; Coelho, 2005; Lima, 2011).

$$\xi_0 = \frac{tan\,\alpha}{\sqrt{H_0/L_0}} \qquad \text{with} \qquad L_0 = \frac{g}{2\pi}T^2 \qquad\qquad (2.4)$$

$$\xi_b = \frac{tan\,\alpha}{\sqrt{H_b/L_0}} \qquad \text{with} \qquad L_0 = \frac{g}{2\pi}T^2 \qquad\qquad (2.5)$$

where ξ_0 is the Iribarren number in deep water; ξ_b is the Iribarren number at the break point (where the waves start to break); α (degrees) is the angle of the seaward slope of a structure; H_0 (m) is the offshore wave height in deep water; H_b (m) is the wave height at the break point; L_0 (m) is the deep-water wavelength; T (s) is the wave period; and g (m/s²) is the acceleration of gravity.

Table 2.2: Iribarren number range for different breaking wave types

Breaking Wave Type	ξ_0 Range	ξ_b Range	Schematization
Spilling	$\xi_0 < 0.5$	$\xi_b < 0.4$	
Plunging	$0.5 < \xi_0 < 3.3$	$0.4 < \xi_b < 2.0$	
Surging or Collapsing	$\xi_0 > 3.3$	$\xi_b > 2.0$	

2.4.2 Structure stability and velocity loads (currents)

The foundation of a coastal protection structure plays a very important role in its safety, mainly because strong currents that can cause the removal of adjacent materials are generated in these zones, creating

instabilities that can lead to the structure rupture (Figure 2.46). Currents are characterized by horizontal movements of the seawater and are generally defined by their direction and velocity (Souto, 1989). In the design of the armour blocks, current velocities should be considered for the structure to endure without being displaced. The armour blocks weight design is chosen by calculating the shear stress that a design stone weight can withstand. Since the local shear stress is a function of the revetment surface roughness, and the roughness is a function of the stone size, a range of stone sizes must be evaluated until a size is found that is stable under the shear it produces (CERC, 1984a). Thus, the foundation must be designed to: a) protect the structure against toe erosion; b) prevent sliding of the armour blocks slope; and c) be deep enough so that the surrounding sands do not compromise its stability due to seabed scour. Also, structure stability parameters like the crest height, the porosity factor (varying from 0.1 in case of armour blocks with an impermeable filter to 0.6 for armour blocks without any filter or core), the slope angle of the cover layers, and the evaluation of the seabed characteristics are relevant for the design of the coastal structure (Lima, 2011; Taveira-Pinto and Neves, 2003). It is important to mention that the surrounding environment of these works is very aggressive for the constituent materials. Its degradation will translate into a reduction of the resistance over time. The causes of material deterioration can be of two types: a) physical (abrasion, surface cracking and/or fracturing); and b) chemical (destruction of a block by chemical reactions starting at its surface). It is found that both rubble material and concrete blocks are subject to physical deterioration. However, the chemical effect on rubble materials is not very significant (Pita, 1986).
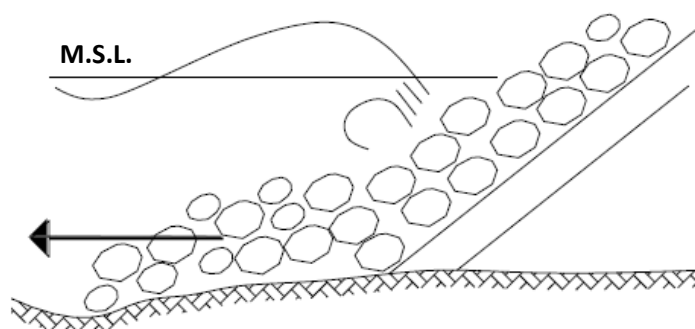
Figure 2.46: Typical rupture of a groin foundation after seabed erosion (Burcharth and Hughes, 2012).

2.5 Breakwater armour characteristics

General classification of breakwaters may be divided in two categories: rubble mound and composite breakwaters. Rubble mound breakwaters have a rubble mound and an armour layer that usually consists of shape-designed concrete blocks or rock material. Composite breakwaters consist of a rubble

foundation and vertical wall, and are therefore classified as vertical breakwaters (Takahashi, 2002; Vieira, 2014). Several structural types of breakwaters are used throughout the world; however, this research work will focus on the slopping rubble mound type detached breakwaters, which are the most frequent in coastal protection.

In general, the section of a rubble mound breakwater (Figure 2.47) contains a multi-layer system, since a homogenous structure of large armour units would make the structure too permeable and not efficient to dissipate waves. Thus, to prevent the structure from being too permeable, the following elements comprise a detached breakwater (Broere, 2015; Costa, 2009):

- **Armour layer:** exposed slope zone that receives the direct action of the wave climate; composed by one or two layers of artificial or natural blocks (armour units);

- **Under layer:** designed to prevent the fine sediments from the core from washing out through the voids; comprises rows of decreasing diameters towards the inside of the breakwater; geosynthetics like geotextile material type can also be used;

- **Core:** inner zone of the breakwater composed by small stones or quarry run;

- **Toe berm:** sturdy support for the lower armour layer composed by artificial or natural blocks; prevents infrastructure scour and the armour layer from sliding down.
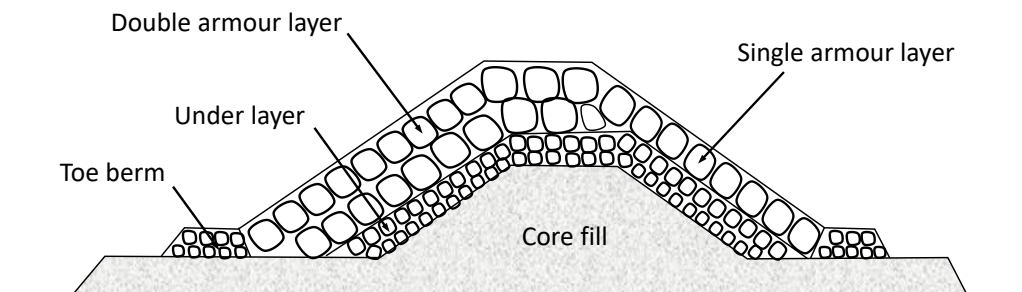
Figure 2.47: Sketch of a breakwater cross section.

The armour units are designed to withstand the impact of waves and to provide enough stability to prevent being washed away. Logically, the larger the waves, the larger the required blocks to maintain stability are going to be needed. However, when the size of the required armour units becomes too large due to higher waves, it becomes very difficult to find natural rocks that are heavy enough to provide sufficient stability.

Therefore, concrete armour units have been developed, as they can be made according to the design's needs (Goud, 2020). Table 2.3 provides some main differences on the use of both materials.

Table 2.3: Differences between rockfill and concrete armour blocks.

Rockfill	Concrete
More affordable when compared with concrete blocks	High stability coefficient value, which allows the use of steeper structure side slopes / lighter weight of armour units. Stability of the blocks depends on the units' shape
Good quality and resistance against wave climate	Several forms, varying the geometry, size and weight
Less history of breakage problems	More permeability when the blocks are arranged together (ability to dissipate energy)
In heavy climate conditions, required size and weight may not be available due to difficulty in finding adequate natural rocks	Ease on rearranging the blocks together to better dissipate energy

2.5.1 Concrete armour units timeline evolution

Regarding concrete armour units, three main types were developed since the 1930s (Hettiarachchi, 1987; Jensen, 2015; Salauddin, 2015): bulky and interlocking blocks, where voids are created between the armour; and hollow blocks, where voids are created within the armour. Tables 2.4 and 2.5 present those types and indicate how the placing can be held in relation to their shape. The blocks can be placed either in a single layer (Table 2.4) or double layers (Table 2.5), and displayed in uniform or random patterns, usually with rectangular or diamond-shape placing grids (Figure 2.48). The single layer system has the advantage of having less rocking, high interlocking, and cost efficiency than double layer system, while the double layer system has aggravated risk of breaking due to rocking (Broere, 2015). Rocking can be defined as the process of armour units colliding with each other under heavy wave attack, which may lead to high stresses in the concrete that would break them and jeopardize the breakwater stability (Goud, 2020).

Breakwater armour units are typically plain, unreinforced concrete without any steel reinforcement. As armour units are unreinforced, the tensile capacity of the concrete is an important functional requirement, as well as its good-quality casting. Any cracks or large surface defects can have a detrimental effect on the performance of the unit. Cracks cause a reduction in the cross-sectional area of the armour unit, and if it is located at a critical section, the armour unit can be significantly weakened. Large surface defects may also cause structural weakness or an underweight unit that would lead to loss of stability (Smith, 2016b; van Zwicht, 2009).

Table 2.4: Single layer armour units (adapted from Broere, 2015; and Reedijk and Muttray, 2009).

Single Layer Armour Systems					
Armour Unit Type	**Armour Unit**		**Placement Pattern**	**Main Stability Parameter**	**Year Developed**	**Country**
Bulky	Cube		Random Uniform	Own weight	–	–
Hollow block	Cob		Uniform	Friction	1969	UK
Hollow block	Seabee		Uniform	Friction	1978	Australia
Interlocking	Accropode™		Random	Interlocking	1980	France
Hollow block	Shed		Uniform	Friction	1982	UK
Interlocking	Core-loc®		Random	Interlocking	1996	USA
Hollow block	Diahitis		Uniform	Friction	1998	Ireland
Interlocking	A-Jack®		Random	Interlocking	1998	USA
Interlocking	Xbloc®		Random	Interlocking	2003	NL
Interlocking	Accropode II™		Random	Interlocking	2004	France
Interlocking	Cubipod®		Random Uniform	Own weight Interlocking	2005	Spain
Interlocking	Core-loc® II®		Random	Interlocking	2006	USA
Interlocking	Crablock™		Random/Uniform	Interlocking	2007	UAE

| Rectangular grid | Diamond-shaped grid | Random placement |

Figure 2.48: Examples of armour units placement patterns (Hendrikse and Heijboer, 2014; Salauddin, 2015).

Table 2.5: Double layer armour units (adapted from Broere, 2015; and Reedijk and Muttray, 2009).

Double Layer Armour Systems						
Armour Unit Type	Armour Unit		Placement Pattern	Main Stability Parameter	Year Developed	Country
Bulky	Cube		Random Uniform	Own weight	–	–
Interlocking	Tetrapod		Random Uniform	Own weight Interlocking	1950	France
Interlocking	Tribar		Random	Own weight Interlocking	1958	USA
Bulky	Modified cube		Random	Own weight	1959	USA
Interlocking	Stabit		Random	Interlocking	1961	UK
Interlocking	Akmon		Random	Own weight Interlocking	1962	NL
Interlocking	Tripod		Random	Own weight Interlocking	1962	NL
Interlocking	Dolos		Random	Interlocking	1963	Republic of South Africa
Bulky	Antifer cube		Random	Own weight	1973	France
Interlocking	Cubipod®		Random Uniform	Own weight Interlocking	2005	Spain
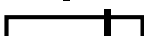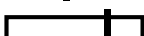
In the beginning of the development of precast armour unit blocks, the only concrete blocks used were the cubes, whose stability is derived from the weight of their blocks, which required that each block should be sufficiently heavy to withstand the wave impact pressure (Reedijk *et al.*, 2004).

Armour units with bulky shapes as Cube, Antifer Cube and Modified Cube are mainly stabilised by their own weight and only to a limited extend by interlocking (Reedijk and Muttray, 2009). After 1950, the armour unit stabilising development went from slightly interlocking armour units with relatively simple shape (as Tetrapod and Akmon) to more economical highly interlocking armour units with a more complex shape (as Dolos and Stabit) (Reedijk and Muttray, 2009). This interlocking stabilising mechanism led to a higher hydraulic stability of the units with more slender shapes, which not only use the weight of each individual element, but also of the surrounding elements. The increased porosity of the armour layer has contributed to wave energy absorption and reduction of wave run-up, as well as less concrete consumption. The first interlocking unit on the market was the Tetrapod (Bonfantini, 2014; Reedijk *et al.*, 2004).

Thus, during the period of 1950 to 1980, a number of different armour units were developed based on this combination of unit weight and interlocking mechanism (Bonfantini, 2014; Salauddin, 2015). Table

2.6 presents a qualitative relation between some armour units structural and hydraulic stabilities (Reedijk *et al.*, 2004). As previously mentioned, in this period, the increase in interlocking capacity has been achieved by an optimised block shape with increased slenderness, as is the case of Dolosse (Reedijk and Muttray, 2009). Due to the efficient interlocking properties of this type of blocks, the required unit weights reduced significantly compared to the Cubes, which eventually became vulnerable to premature failure. At this point, hydraulic stability (interlocking) was prioritised over the structural stability, which eventually led to the unfortunate occurrence of the Sines breakwater in Portugal collapse (1978), due to broken Dolosse. The applied Dolosse units were so slender (for optimal interlocking) that they broke into pieces due to the wave action, leaving the interlocking mechanism no longer efficient and eventually yielding to the failure of the entire armour layer (Gómez-Martín and Medina, 2008; Reedijk *et al.*, 2004). This situation raised awareness to the safety concept for breakwater armour units.

Table 2.6: Structural and hydraulic relation in some armour units (adapted from Reedijk *et al.*, 2004).

Armour Unit	Structural Stability	Hydraulic Stability	Layers
Cube			2
Tetrapod			2
Dolos			2
Accropode™			1
Core-loc®			1

The Sines breakwater was built with 42 tonnes unreinforced Dolosse armour units, with a very daring design to which nature proved to be unwise, since there was a limit to the slenderness of the Dolosse in the local harsh wave climate. The design wave condition was a significant wave height (H$_s$) of 11 m with a peak wave period (T$_p$) of 16 s, and a stability coefficient (K_D) of 23.6. The severe damage occurred in a storm with H$_s$ = 9 m and T$_p$=19 s (corresponding to K_D=13) (Jensen, 2015). The damage is defined by the ratio between the number of displaced armour units and the total number of structure units in a given reference area as indicated in Equation (2.6) (Frens, 2007). The design values suggested for K_D correspond to a "no damage" condition where up to 5% of the armour units may be displaced (van der Meer, 1998). The K_D increases with the units interlocking behaviour. Lower values for the stability coefficients are formulated to produce heavier armour units, which are stable against crack-causing movement, such as rocking under wave action (CERC, 1984b). In Sines, the substantial breaking and settlements of the armour layer that eventually resulted in total failure of the breakwater owed to the limited concrete strength of the large Dolosse and the loose packing density (placement distances

between armour units). It was concluded that for such high stability coefficients, the Dolosse were rocking under heavy wave attack (Jensen, 2015).

$$DamageRatio = \frac{number\ of\ displaced\ units}{total\ number\ of\ units\ within\ reference\ area} \qquad (2.6)$$

The most obvious method to define damage is based on the extraction of units from the armour layer. Next to displacements of units, settlement of the units may also lead to damage of the armour layer. When the movements become too big, the interlocking function between the units can be lost. In reality, rocking can harm the individual units and may lead to damage of the armour layer. The stability of a breakwater armour layer is provided by an interaction between gravity, interlocking and bottom friction with the under layer. The contribution of these three mechanisms depends on the shape of the unit, the placement method and packing density (Broere, 2015).

2.5.2 Single and double layers: advantages and fragilities

Ideally, the most efficient and economic type of armouring shall be selected with respect to (i) structural and hydraulic stability (including the risk of progressive damage), (ii) fabrication, storage, handling and placement of armour units, and (iii) maintenance and repair of armour layers (Dupray and Roberts, 2010; Reedijk and Muttray, 2009).

In the past, armour units have been placed in two layers in order to cover the uncertainties with respect to hydraulic and structural stability of the elements, since it confers better interlocking. However, since 1980, armour units have been placed in a single layer with higher safety margins for the hydraulic design and increased structural strength of individual units, due to the development of more interlocking shapes. The first randomly placed single layer armour unit was the Accropode™, which became the leading armour unit worldwide for the next 20 years, followed by Core-loc® and Xbloc® (Bonfantini, 2014; Reedijk and Muttray, 2009; Salauddin, 2015).

Usually, most double layer armour units as the Tetrapod, Dolos, Tribar, etc., are placed either on a randomly or uniform block orientation. The second layer does not provide any extra safety and it is only necessary to create interlocking, being an integral part of the armouring system. The armour units on the second layer tend to rock and have an aggravated risk of breaking, hence requiring a more frequent monitoring and regular replacing of broken armour units (Reedijk and Muttray, 2009). Possible reasons for breakage of armour units are related to the construction and breakages induced by movements. This solution is sensible for compact armour blocks as Cube, Antifer Cube, and Modified Cube, since they are stable mainly due to their own weight, and have high construction costs due to more robust elements. An improved design with more slender, interlocking double layer armour units will probably

reduce the construction cost but increase the costs for maintenance because slender blocks tend to rock and break more easily (Reedijk and Muttray, 2009). Armour units with slender shape as Dolos and Tribar, with a relatively slender central section and long legs face high stresses in central part of the armour block and have a relatively high risk of breaking in the central part, due to the cantilever nature of their components. Broken armour units have little residual hydraulic stability (Gómez-Martín and Medina, 2008; Reedijk and Muttray, 2009). Nevertheless, repairs are often relatively easy, as it can be done by adding more armour units for reinforcement and strengthening (Jensen, 2015).

Single layer armour units randomly placed are economically and technically advantageous due to lower susceptibility to rocking and lower total number of armour units. They are applicable for exposed breakwaters; can be placed in deep water; require less maintenance and are more cost efficient than double layer armour; and can withstand severe wave loads. For these reasons, it is considered the most advanced solution (Reedijk and Muttray, 2009; Salauddin, 2015; van der Meer, 1999). A relatively large safety margin is typically applied for the hydraulic stability of single layer armour units, and essential structural integrity of armour units is required, which can be guaranteed by either selecting compact armour blocks or by preventing rocking (Reedijk and Muttray, 2009). Also, due to high interlocking properties, single layer armour units can better sustain under higher wave heights compared to conventional double layer armour units (van der Meer, 1999). Packing density is an important parameter that governs the interlocking capacity of an armour layer and is defined as the number of units placed per square meter. A high packing density will result in good interlocking between the armour units, as well as higher hydraulic stability, which will prevent major failures in the armour layer (Bonfantini, 2014; Broere, 2015; Muttray and Costal, 2006; Salauddin, 2015; van der Meer, 1999).

A completely different type of armour units is formed by the uniformly placed elements hollow blocks. Examples of such elements are the simple hollow blocks Seabee and Diahitis, and the complex shape Cob and Shed. These revetment-like elements gain their stability mainly from the friction between the surrounding armour units, and partly on their own weight. Friction-type armour units are very stable and more homogeneous than interlocking armour units due to their less friction variability. However, this type of armour units is not recommended for exposed breakwaters. As placement of these elements is very difficult under water, they are only applied where construction can be done above low water (Reedijk *et al.*, 2004; Reedijk and Muttray, 2009; Salauddin, 2015).

2.5.3 Design aspects of armour layer blocks

Geometrical layout for coastal protection structures can be followed by the Department for Environment, Food and Rural Affairs of United Kingdom (DEFRA) methodology as guidance for an outline design. This methodology used for determining the most favourable distance from shore, structure length, structure crest level, and gap distance between structures is presented in Vieira (2014).

The determination of the size of armour units is usually based on empirical formulae. The most used for calculating the armour blocks unit weight are the Hudson formula, mentioned in the Shore Protection Manual (CERC, 1984b) presented by Equation (2.7), and the van der Meer formulae that are available for the most common types of armour units (Jensen, 2015; Reedijk and Muttray, 2009; Taveira-Pinto and Neves, 2003). Due to their inherent limitations, it is advisable to use them only in the preliminary design phase. The final design should be complemented with experimental model tests or based on the results of previous experiences, namely in large-scale works (Taveira-Pinto and Neves, 2003).

$$W = \frac{\gamma H^3}{K_D\left(\frac{\gamma-\gamma_w}{\gamma_w}\right)^3 \cot\alpha} = \frac{\gamma H^3}{K_D\Delta^3 \cot\alpha} \text{ or } M = \frac{\rho_a H^3}{K_D\Delta^3 \cot\alpha} \ (=)\frac{H}{\Delta D_n} = (K_D \times \cot\alpha)^{1/3} \tag{2.7}$$

where W (N) represents the weight of an individual armour unit in the primary cover layer; γ (N/m³) is the specific weight of the armour unit in the cover layer; H (m) is the incident design wave height; K_D is the stability coefficient that is empirically determined and depends on the shape of the armour units, roughness of the armour unit surface, sharpness of edges, degree of interlocking obtained in placement and the type of armour layer adopted (Freitas, 2013) (suggested K_D values for use in determining armour unit weight can be consulted in CERC (1984)); γ_W (N/m³) is the seawater specific weight; Δ is the relative density of armour unit; α (degrees) is the angle of structure slope measured from horizontal; M (kg) is the mass of an individual armour unit; ρ_a (kg/m³) is the density of the (concrete) armour unit; and D_n (m) is the nominal diameter of the armour unit.

It should be noted that the Hudson formula is based on experimental tests with regular waves only, and are valid for permeable non-overtopped structures with irregular placed armour units; therefore, they are not capable of reproducing the irregularity of the wave climate. Certain hydrodynamic parameters considered relevant to the cover layer stability, such as wave slope, relative depth, wave period, seabed slope, breaking wave type (spilling, plunging, surging) or storm duration (i.e., number of waves) are not considered in this method. Other aspects, more related to the cover layer characteristics, such as the crest height and crest width, the placement technique of the blocks, the core characteristics and the mechanical resistance of the blocks material (influential in the structure stability) are not also considered (Taveira-Pinto and Neves, 2003).

The main advantages of the Hudson formula are its simplicity, and the wide range of armour units and configurations for which K_D values have been derived (van der Meer, 1998). Nonetheless, the application of the Hudson formula should only be used as guidance for preliminary selection of armour units' sizes for hydraulic model testing (Frens, 2007).

The van der Meer method is based on the irregularity of the wave climate influence, since this type of waves was considered on the experimental tests. This method uses different semi-empirical design formulae depending on the type of structure (rubble, cubes, tetrapods, accropodes and dolosse). The design formulations can also be expressed by N_S which represents the structure stability number, in order to not exceed a certain damage level that could lead to structure instability. Thus, the modified Hudson formula can be expressed by Equation (2.8).

$$\frac{H_s}{\Delta D_n} < N_S \qquad \text{with} \qquad N_s = (K_D \, cotg \, \alpha)^{1/3} \qquad (2.8)$$

where H_s (m) is the incident design wave height; Δ is the relative density of armour unit; D_n (m) is a characterizing parameter of the blocks geometry that represents the nominal diameter of the unit blocks (equivalent size of the block) given by Equation (2.9); K_D is the stability coefficient; and α (degrees) is the angle of structure slope.

$$D_n = (M/\rho)^{1/3} \qquad (2.9)$$

where M (kg) represents the armour block mass in the cover layer and ρ (kg/m³) is the material density. For cube shaped blocks, the D_n value is equal to the length of the edges, for the tetrapod shape blocks is $0.65D_i$ and for the dolos is $0.54D_i$, with D_i being the blocks height.

The van der Meer method can be used in the design of structures with different core permeability, different breaking wave conditions and water depths, which was not considered in the previous method. Other parameters such as the percentage of allowed damage, the various structure rupture modes (such as rupture due to the direct action of wave climate on slopes, toe erosion, damage due to the structure overtopping, etc.), the crest height, the structure toe depth relatively to the MSL, the porosity factor and the angle of the material on the cover layer should also be considered (Taveira-Pinto and Neves, 2003). Taveira-Pinto and Neves (2003) present, in a systematic manner, the design expressions normally used, as well as its application field and applicability limits, as shown in Table 2.7.

Table 2.7: Design formulae for the most common types of armour units (adapted from Taveira-Pinto and Neves (2003)).

Armour Unit	Design Formula	Applicability Limitations	Reference
Cube	$$\frac{H_s}{\Delta D_n} = (6.7 N_{od}^{0.4} / N_z^{0.3} + 1.0) s_m^{-0.1}$$ Equation (2.10)	2 layers non-overtopping breakwaters $3 < \xi < 6$ or $0.01 < s_m < 0.05$ $cotg\theta = 1.5$ deep waters	van der Meer (1988)
Tetrapod	Surging breaker: $$\frac{H_s}{\Delta D_n} = (3.75\, N_{od}^{0.5} / N_z^{0.25} + 0.85) s_m^{-0.2}$$ Equation (2.11)	2 layers non-overtopping breakwaters $3.5 < \xi < 6$ $cotg\theta = 1.5$	van der Meer (1988)
	Plunging breaker: $$\frac{H_s}{\Delta D_n} = (8.6\, N_{od}^{0.5} / N_z^{0.25} + 3.94) s_m^{0.2}$$ Equation (2.12)	Not mentioned	Jong (1996)
Accropode	For $N_{od} = 0$: $$\frac{H_s}{\Delta D_n} = 3.7$$ Equation (2.13) For $N_{od} > 0.5$: $$\frac{H_s}{\Delta D_n} = 4.1$$ Equation (2.14)	1 layer $cotg\theta = 1.33$	van der Meer (1988)
Dolos	$$\frac{H_{m0}}{\Delta D_n} = (17 - 26r)\varphi_{n=2}^{2/3} N_{od}^{1/3} N_z^{-0.1}$$ Equation (2.15)	non-overtopping breakwaters $cotg\theta = 1.5$ $2.49 < \xi < 11.7$ $0.32 < r < 0.42$ $0.61 < \varphi < 1$ $1\% < D < 15\%$	Burcharth and Liu (1992)

Symbol	Designation
H_s	Significant wave height
Δ	Relative density $((\rho_a - \rho_w)/\rho_w)$
D_n	Nominal diameter given by the length of a cube with the same volume as the armour unit $(M/\rho_a)^{1/3}$
N_{od}	Armour units displaced out of the armour layer (hydraulic damage)
N_z	Number of waves (between 1000 and 7000)
s_m	Mean wave steepness $(2\pi H/gT^2)$; where H is the wave height, g is the gravitational acceleration, and T is the wave period
θ	Angle of structure slope measured from horizontal in degrees
ξ	Breaker parameter or Iribarren number $(tan\theta/\sqrt{s_m})$; where θ is the slope angle, and s_m is the mean wave steepness
H_{m0}	Significant wave height in front of the breakwater
$\varphi_{n=2}$	Packing density of 2 layers
r	Dolos waist ratio
D	Relative number of displaced armour units (e.g., for 2% displacement D=0.02)

The cross section parameters (crest width, cover layer thickness, and number of blocks per unit area) can be consulted in Lima (2011), where the author describes the recommended formulations for those parameters.

Thus, the van der Meer formulae considers irregular waves and are a function of the damage level given by the percentage of displaced armour units, the Iribarren parameter (type of wave breaking), storm duration (number of waves), the slope angle, and the permeability of the slope that depends on the size of filter layers and core. van der Meer (1998) assumes the wave period to be connected with the type of breaking waves and proposes the methodology for the determination of displaced armour units and permeability.

2.5.4 Main characteristics and comparisons of recent armour units

The Accropode™ was created to balance hydraulic stability and structural strength. This armour unit has many protruding elements for a good interlocking and compared to the Dolos, the Accropode™ is a robust and bulky unit, which is far less vulnerable to breakage. These armour units are usually placed in a single layer either in a uniform or random grid, and their orientation has to be varied to achieve optimum interlocking. For this reason, it is advised to use conservative stability coefficients for the design. The best interlocking of Accropode™ can be achieved on steep slopes, because it causes settlement of the units allowing each unit to contact several adjacent blocks and, therefore, rocking is less likely to occur. The Accropode™ was the first armour unit to be placed in a single layer (Bonfantini, 2014; Reedijk *et al.*, 2004; Reedijk and Muttray, 2009; Salauddin, 2015).

The Core-loc® is a mix of the Dolos and the Accropode™ shapes, where the legs configuration is similar to the Accropode™ and the shape of the legs to the Dolos. For this reason, the Core-loc® can be applied as repair units for Dolos armour layers. Relatively to the Accropode™, the hydraulic stability of Core-loc® armour units is slightly higher, which provides high stability with good interlocking; however, due to the slender nature of the Core-loc®, its structural integrity is more vulnerable to breakage. The recommended stability coefficients for design and the placement procedures are close to those for the Accropode™. The development of Core-loc® armour units shape proves that the balance between structural and hydraulic stability shifted towards the hydraulic stability (Bonfantini, 2014; Reedijk *et al.*, 2004; Reedijk and Muttray, 2009; Salauddin, 2015).

The Xbloc® is a compact armour unit with a hydraulic stability similar to that of the Core-loc® and slightly higher than that of the Accropode™. Regarding the structural strength, the Xbloc® has similar strength as the Accropode™, and is significantly stronger than the Core-loc®. Due to the simple shape

of the Xbloc®, production and handling is easier than that of the Accropode™ and Core-loc®. The important advantage over other units is the ease of placement, as Xbloc® are placed on a uniform grid and the orientation of the armour units varies randomly (Bonfantini, 2014; Reedijk and Muttray, 2009; Salauddin, 2015).

In 2009, a study on Cube armour units in single layer was developed and results showed that the use of a single top layer of Cubes was feasible and the armour layer became very stable (Bonfantini, 2014). The recent introduction of the Cubipod® presented advantages over the traditional Cube armour unit, especially on the improvement of the low hydraulic stability of Cubes, and on the enhancement of high structural strength and easier placement of the armour units (Bonfantini, 2014; Salauddin, 2015).

The Crablock™ is a symmetrical armour unit, which allows a regular placement in a single layer. The Crablock™ stability is ensured by its weight and interlocking, and has excellent structural porosity performance (the fraction of the total structure volume that is taken up by the open spaces among the blocks) that reduces wave overtopping. The Crablock™ presents some similarities in shape and in placement to the Xbloc®, since they are both symmetrical amour units and are designed to be placed in a single layer. However, while the Xbloc® is symmetrical in two directions, the Crablock™ is in three, which can result in a better performance, relatively to the Xbloc® (Bonfantini, 2014). Usually, a random placement of the armour units is relatively easier to be held under water when compared to a uniform placement. However, for symmetrical blocks like Crablock™, the uniform placement of armour units might be more stable in comparison to random placement, since this placement provides a more compact interlock between the armour units (Salauddin, 2015). Regarding stability, the Crablock™ has a high hydraulic stability, better than that of the Accropode™ or Xbloc®, and a good structural strength (Bonfantini, 2014; Broere, 2015; Salauddin *et al.*, 2015). This armour unit has less chance to rocking and settlements on the slope, and the packing density applied for Crablock™ is also higher than the Accropode™ or Xbloc®, which allows a safe design for the consideration of smaller units (less concrete) (Broere, 2015).

Table 2.8 summarises the main physical characteristics of the most common armour units.

Table 2.8: Summary of physical characteristics of most used concrete armour units.

Armour Unit	Physical Characteristics
Cube	High structural strength Lacks interlocking properties Mainly stabilised by their own weight
Tetrapod	First interlocking armour unit Slightly interlocking
Dolos	Highly interlocking Slender blocks that led to severe failure in Sines breakwater 1978
Accropode™	First single layer armour unit Leading armour unit worldwide for many years More robust than Dolos Good balance between hydraulic and structural stability
Core-loc®	Mix of Dolos and Accropode™ shapes Can be applied as repair units for Dolos armour layers High stability due to good interlocking More hydraulic stability than that of the Accropode™ Less structural stability than that of the Accropode™ because of a more slender nature
Xbloc®	Hydraulic stability similar to that of the Core-loc® and slightly higher than that of the Accropode™ Structural strength similar to that of the Accropode™ and significantly stronger than that of the Core-loc® Easier production, handling and placement than that of the Accropode™ and the Core-loc®
Cubipod®	Improved the low hydraulic stability associated to Cubes High structural strength Easy placement
Crablock™	Symmetrical unit Similarities in shape and in placement to the Xbloc® Stability ensured by its own unit weight and interlocking Requires a uniform placement of the armour units Higher hydraulic stability than the Accropode™ and the Xbloc® Good structural strength

2.5.5 Design recommendations for concrete armour units

Concrete is a material with excellent behaviour in compression, but it is susceptible to damage due to cracking; therefore, steel reinforcements are used to sustain the tensile stresses. However, in marine environment, concrete can suffer severe damage due to the susceptibility of steel reinforcements to corrosion, resulting spalling of concrete surrounding reinforcements, with continuous loss of their cross section and bond, and finally the strength capacity of the element can be detrimentally affected. Regarding plain concrete, although it is durable in the marine environment, precautions are still required in the design and construction to achieve the desired durability (Goud, 2020).

Concrete is a composition of cement and stony aggregates. During the production of concrete, the dry cement is mixed with the aggregates and water. The reaction between the cement and water hardens the mixture in a solid material named cement stone and binds all the components in a chemical process called hydration. The strength of the concrete depends on the water-cement mixture, the type of cement, the grading and strength of the aggregates (van Zwicht, 2009).

Depending on the abrasive or nonabrasive conditions of the site, Concrete Layer Innovations (2015) and Smith (2016a) recommend a low water/cement ratio (w/c); a minimum strength class of C35/45 (characteristic compressive strength of 35 MPa on cylinder and 45 MPa on cube); a XS2 or XS3 exposure class (EC2, 2004); and adequate combination of the concrete's constituents to create dense and low-penetrability concrete to chloride ion diffusion. This can be achieved with good grading of the aggregates such that the smaller elements fill the spaces between the larger elements, resulting in a very dense packing. Bad graded mixtures demand more water, which increases the chance of segregation, resulting in lower concrete strength (van Zwicht, 2009). In the Core-loc® technical specifications, Concrete Layer Innovations (2015) suggests a maximum size of 40 or 60 mm for the aggregates; a minimum equivalent binder content (cement + pozzolanic additions) of 350 kg/m³; a concrete workability of S2 to S4 (slump test class) (Instituto Português da Qualidade, 2009); a maximum w/c ratio of 0.45; and a minimum average splitting tensile strength of 3.5 MPa (EC2, 2004).

Concrete density is usually between 2300 and 2400 kg/m³, which can be changed by adding different aggregates to the concrete mixture. For instance, heavy concrete can be obtained by adding magnetite, barite or slag (by-product of smelting ores), which can result in a density up to 4000 kg/m³. However, heavy aggregates may interfere with getting a good mixture (van Zwicht, 2009). Smith (2016a) and van Zwicht (2009) suggest that a low-alkali cement should be used in marine concrete structures if the aggregate is reactive (containing silica, e.g., clay), as it may react with the cement making the concrete disintegrate or swell, resulting in crack formation. Binder components other than cement, like fly ash and granulated blast furnace slag assist in minimising the risk of alkali-silica reaction (ASR), since areas where cycles of wetting and drying occur might create the necessary conditions for this reaction.

Since plain concrete does not have reinforcements to resist the internal tensile stresses caused by early age shrinkage effects, it is important to understand the factors that cause shrinkage and how it can be minimized. Dupray and Roberts (2010) and Smith (2016a) point that the main contributor to shrinkage is the differential temperature between the core temperature due to the heat of hydration and the ambient temperature. For this reason, concrete with high cement content is not advisable, since higher cement content contributes to higher hydration temperatures. In order to reduce early age cracks and

improve the crack resistance of young concrete, fibres can be used in order to restrict the crack formation and propagation. Smith (2016a) also raises awareness on the fact that cracks can propagate and create weaknesses that may lead to the breakage and loss of a significant portion of the armour unit when it is loaded in service. However, the author does not recommend repairing the cracks and surface defects in armour units, as they may not be durable in service in the harsh coastal environment. In addition, Smith (2016a) suggests that marine concrete structures should ensure a minimum tensile flexural strength, in the order of 4.0 MPa at 28 days, and a compressive strength in the order of 40 MPa. Several experimental tests on the mechanical properties of unreinforced concrete for armour units have been conducted by Franco *et al.* (2000), Burcharth (1984), Hakenberg *et al.* (2004), Gómez-Martín and Medina (2008), and Azenha *et al.* (2011). Summary information regarding the concrete mixes used in each study, as well as the obtained results, can be found in Appendix 1A.

2.5.6 Cracking and failure mechanisms of concrete armour units

There are two main sets of limit states (Vidal, 2007): (i) ultimate, that produces the collapse (unrecoverable state) of the structure (e.g., loss of static equilibrium, breakage or deformation of the breakwater); and (ii) serviceability, that produces a loss of service and functionality in all or part of the structure due to a minor and repairable structural failure (e.g., deterioration of the building materials properties).

As previously mentioned, for a long time, breakwater design mainly focused on hydraulic stability problems, while the importance of structural strength was underestimated. The breakage of armour units due to their slender nature started being critical and raised the importance of developing elements that are more robust, while maintaining a good interlocking mechanism.

Breakage of armour units leads to reduced weight of the unit and reduced stability of the armour layer (van Zwicht, 2009). The stability of a rubble mound breakwater is ensured by an interaction between the hydraulic loads, the structural strength and the geotechnical capacity. When these interactions are unbalanced, the structure can fail on multiple mechanisms. Figure 2.49 presents possible failure mechanisms that would compromise the balance of the structure (Broere, 2015). CERC (1984) defends that any breakage exceeding random breakage of 15 % or 5 broken units in a cluster of units may lead to catastrophic failure of the armour layer. Failure of the structure may be related to (Broere, 2015; Vidal, 2007): (i) design failure, when either the whole structure or its individual components cannot withstand load conditions within the design criteria and/or when the structure does not perform as anticipated; (ii) load exceedance, when the design load conditions are exceeded; (iii) construction

failure, due to deficient construction or construction materials; and (iv) deterioration failure, due to structure deterioration and lack of structure's maintenance. Table 2.9 presents the types of loads that usually occur on the armour units.
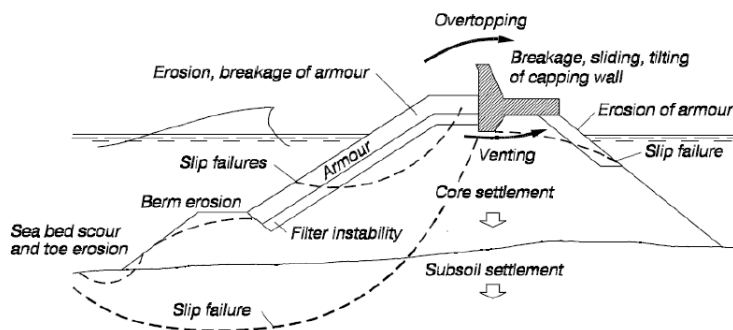
Figure 2.49: Failure modes for a rubble mound breakwater (Broere, 2015).
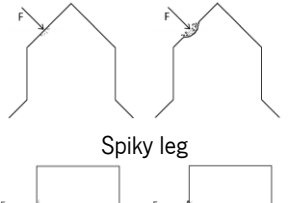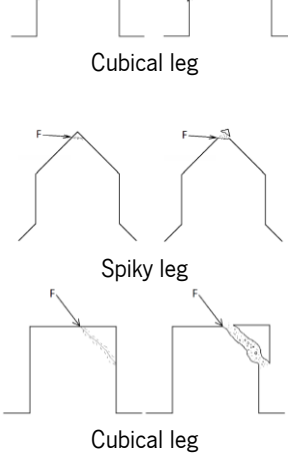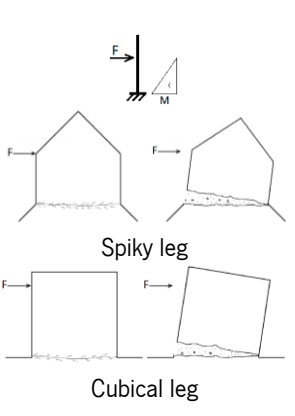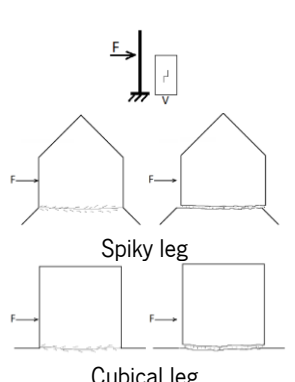
Table 2.9: Types of loads on armour units (Burcharth, 1984).

Types of Loads	Origins of Loads
Static	Weight of units Settlement of underlayers
Abrasion	Suspended material
Dynamic: Impact	Placing during construction Rocking/rolling units Missiles of broken units
Dynamic: Pulsating	Earthquake Gradually varying wave force
Thermal	Stresses due to temperature differences during hardening process Freeze-thaw (when water gets into cracks, freezes and expands, eventually breaking the material)
Chemical	Corrosion of reinforcement Sulphate reactions, etc.

Failure is a matter of strain/stress fields introduced by the loading *versus* the strength capacity that depends on the quality of the materials and geometry of the elements composition the structure, so those are important to determine (Goud, 2020). It is important to note that when the maximum tensile stress reaches the local material tensile strength, a crack is formed. In addition, armour units are submitted to repeated loadings during a storm, which will weaken the armour unit and eventually tear off some part of it (Goud, 2020). For this reason, studies on the reinforcement of armour units with fibres on some structures have already been conducted in order to improve the concrete post-cracking tensile capacity for avoiding brittle failure of that parts (Bottin and Appleton, 1997; Burcharth, 1984; CERC, 1984; Hoff, 1975; Melby and Turk, 1992).

Goud (2020) presented illustrations of several possible failure mechanisms for an Xbloc® armour unit, which can be assumed to occur on other blocks since most failure modes are similar for other types of armour units. Table 2.10 summarises the likelihood of occurrence and consequences of several failure mechanisms, as well as the representation of these failures.

Table 2.10: Likelihood of occurrence and consequences of several failure mechanisms (adapted from Goud, 2020).

Type of Failure	Consequences	Likelihood of Occurrence	Example
Local crushing	Very minor weight loss, although repeated loading weakens the armour unit	Likely. The forces can be huge, causing locally high compressive stresses.	Spiky leg / Cubical leg
Chipping off corners	Minor weight loss	Not very likely. It only happens in very specific cases.	Spiky leg / Cubical leg
Rupture due to bending	Severe weight loss	Quite likely to get bending failure for large waves, and sufficient bending moment arm. However, this is likely only for a few percent of the blocks.	Spiky leg / Cubical leg
Rupture due to shear	Severe weight loss	Unlikely. Rupture due to bending is governing in most cases.	Spiky leg / Cubical leg

The first step to determine the stresses is to identify the failure mechanism, in order to know which locations are critical on the overall state of the breakwater, since failure of the concrete does not necessarily lead to failure of the breakwater as a whole (Goud, 2020). One of the most important failure mechanisms of breakwaters is due to tensile bending stresses, which is usually located at the junctions, where the legs connect to the main body of the armour unit. Thus, the rupture of the legs is assumed to be the critical cross-sections due to rocking (Goud, 2020; Hoff, 1975). However, this type of failure is still barely incorporated in the standard design procedures, because there is not yet enough knowledge about predicting breakage due to rocking (Goud, 2020). Some other failure mechanisms may occur, such as local crushing or chipped off corners, but these generally do not have a severe effect on the overall state of the breakwater (Goud, 2020).

Local crushing occurs due to the high compressive stresses around the location of the impact, since the high concentrated loads of the enormous weight of the armour units will induce local stresses higher than the concrete strength that will result on the crushing of the concrete. Fibre reinforcement can have a very favourable effect offering resistance to the disintegration of the areas subjected to these impacts. In fact, the failure is not caused by excessive compressive strain, but always due to fracture because of the generation of tensile strains greater than the formation of cracks as a result of Poisson's ratio. However, this will only weaken the leg of the armour unit, since the loss of weight is negligible. The interlocking mechanism with the surrounding units will not be affected. Nevertheless, it is important to note that during a storm, multiple high waves will induce motion of the block in a similar way, thus it is probable that repeated crumbling will eventually break a larger piece of the leg, in which case the loss of weight could surely be significant (Goud, 2020; Hoff, 1975).

Chipping off corners occurs when the impact on one of the legs is near the corner under a specific angle. Since the effective area is smaller near the corner, this impact induces a shear force that will locally lead to high shear stresses. Although the chipped piece has more weight than the previous case, it is still a relatively small piece of the leg causing only a minor decrease of the weight of the armour unit. The interlocking mechanism will not be severely affected either. The probability of a corner being chipped off is rather large if the force comes in at the right location and under the right angle. However, these conditions are thus very specific, so overall, it will probably not happen as frequent as local crushing (Goud, 2020).

Rupture of the leg due to bending is the most severe failure mechanism. It occurs when the impact force induces a linear bending moment in the leg, which can lead to cracks at the base of the leg and to the eventual breakage of the whole leg due to the brittle behaviour of the concrete. This impact creates

a null bending moment at the location of the force, up until a maximum at the base of the leg, where it is attached to the body. This mechanism results in a significant loss of weight and a significant part of the interlocking capability (Goud, 2020).

Finally, rupture of the leg due to shear occurs when the impact force is applied near the connection of the leg and the core. This failure will induce the complete rupture of the piece of the leg.

2.6 Steel fibre reinforced concrete (SFRC)

The need to use artificial blocks in coastal protection structures requires that building materials should be as environmental friendly and multifunctional as possible. Cement based materials like paste, mortar or concrete are the most important and most frequent building materials used in the world. However, their production is associated with major environmental problems due to large energy consumption, solid waste generation and consumption of natural resources. One solution to minimize this negative impact is to use eco-materials characterized by the use of recycled materials, which consume little energy for production and transport. The constructive elements reinforced with short vegetable and/or tyre recycling fibres in conventional cement matrices, combined with mineral admixtures such as fly ash and metakaolin ensure an increase in mechanical strength, post-cracking tensile capacity and workability of the mixture. Fibre reinforcement can be tailored for limiting the crack width that do not compromise the strength and durability of innovative elements for costal protection, which can favour the fixation of compatible bio-diversity, with the derived favourable effects already pointed out in previous Sections. The potentialities of these composites for structural applications have been recently investigated (Barros *et al.*, 2017; Lima *et al.*, 2016; Soltanzadeh *et al.*, 2015).

Innovative concepts are emerging, motivated by the lack of sustainability and resilience of the traditional "hard" engineering approach, as well as by concerns for the environment (Pilkey and Cooper, 2014; Airoldi *et al.*, 2005). Under present and future environmental conditions, the world requires smarter coastal protection strategies that are adaptable, sustainable, multifunctional and economically viable to help solve immediate and predicted coastal erosion problems (Adriana-Gracia *et al.*, 2018). New coastal protection strategies around the world that are able to follow climate changes and other environmental conditions, while maintaining flood safety, ecological values and socio-economic functions have being reported in literature (McHarg, 1995; Mitsch and Jørgensen, 2004; Farber *et al.*, 2006; Waterman, 2010; Misdorp, 2011).

Unreinforced concrete is brittle, has relatively low tensile strength regarding its compressive strength, which is the reason why breakage is usually due to load induced tensile stresses. Moreover, repeated load reduces the tensile strength due to fatigue effects.

Slender armour units are known to be more vulnerable to breakage due to the relatively small structural strength capacity (flexural and shear) of their components (van Zwicht, 2009). Fibre reinforcement increases the post-cracking tensile capacity of cement-based materials, with a level that depends on the content and types of fibres, and the quality of the matrix. This attribute increases not only the static strength of the elements, but also their impact resistance, thus, prolonging the life of the armour units compared with unreinforced units (Caggiano *et al.*, 2017; Hoff, 1975).

Recently, substantial efforts have been focused on the sustainability and efficiency of using recycled materials as concrete constituents (Onuaguluchi and Banthia, 2018). For many years, the application of FRC was limited to cracking control and durability enhancements, however the incorporation of fibres as partial substitution of classical steel rebars has increased in the past years owing to the development of international design guidelines and codes for designing FRC, as the fib Model Code 2010 (Caggiano *et al.*, 2017). The employment of recycled steel fibres (RSFs) retrieved from waste tyres demonstrated that the geometrical characterization can be highly variable. These variations depend on the typology of the tyres and the recycling processes (Caggiano *et al.*, 2017; Frazão, 2019).

2.6.1 Tyres recycling processes

Nowadays, the need to find sustainable and efficient materials to build environmental-friendly structures has grown an interest to find "greener" products that could improve concrete properties. Thus, studies to develop cementitious composites internally reinforced with recycled steel fibres obtained from post-consumed pneumatic tyres have been conducted.

Recycling procedures for waste tyres requires separating their main components, which can be employed in various applications, among which the production of concrete. Waste tyres are fully recyclable and three main materials (rubber, metal and textiles) come out of this process. The importance of recycling waste tyres for producing new products arises, since tyres lifetime in landfill is considered to be between 80 and 100 years, which is considered to be an unsustainable solution.

Concrete reinforced with recycled steel fibres obtained from waste tyres is proved to improve the post-cracking behaviour of cement based materials as it enhances ductility, energy dissipation and impact resistance (Barros *et al.*, 2013). During the research project entitled "Environmentally-friendly solutions for Concrete with Recycled and natural components" (EnCoRe), Barros *et al.* (2017) empirically

investigate the physical and mechanical behaviour of these type of fibres and emphasize the great engineering potentials of this technology that has been accepted by several national and international design codes. In this study, the authors outline the theoretical models and the numerical procedures that can be formulated and implemented for simulating the behaviour of these materials. Moreover, a first attempt to propose a consistent conceptual formulation capable to make "predictable" their mechanical properties is also reported.

Annually, about 1.5 billion vehicle pneumatics are produced around the world and around 1 billion reach their end of life. The negative environmental impacts inherent to end of life waste tyres is therefore of great significance and the tyre recycling industry has developed various processes to extract the main tyre constituents: rubber, steel and polymer (Caggiano *et al.*, 2017; Hu *et al.*, 2018). The main processes to extract steel wire from tyres are mechanical treatment (ambient shredding and cryogenic process), and thermal degradation (conventional and microwave-induced pyrolysis), which produce steel fibres of irregular shapes, lengths and diameters (Barros *et al.*, 2017; Frazão, 2019; Hu *et al.*, 2018). The amount of extracted steel fibres depends on the type of tyre. Car tyres contain up to 15% steel, whereas truck tyres contain up to 25% steel. Therefore, RSFs derived from the tyre recycling industry can then be an effective solution for concrete applications with favourable economic and environmental impact (Frazão, 2019; Frazão *et al.*, 2019).

The ambient shredding process consists of removing the bead wires from tyres through mechanical action by pulling the wire and detaching it from the rubber, followed by shredding and chopping of the tyres, electromagnetic separation of the steel fibres from the rubber, and vacuum of the textile residues. Despite being quite costly due to constant maintenance of the cutting blades owed to the high rate of the blades deterioration, this process is the most environmentally friendly due to the low energy consumption when breaking down the tyres (Frazão, 2019).

The cryogenic process is a different mechanical process that involves the shredding and chopping of the tyres, followed by the cooling method in a freezing tunnel using gaseous nitrogen, and their subsequent brittle fracturing and reduction to rubber, steel and textile. It is important to note that this process may lead to loss of steel ductility if the cooling down process is set below its embrittling temperature (Frazão, 2019). Comparatively to the previous method, the cryogenic process is energy efficient because it requires less energy and fewer pieces of machinery to separate the rubber from the steel. However, the high cost of liquid nitrogen is the main shortcoming of this process (Barros *et al.*, 2017; Frazão, 2019).

The conventional pyrolysis process involves the shredding and decomposing of the tyres by applying heat in the absence of oxygen (anaerobic thermal degradation). Tyre pyrolysis leads to the release of gases (hydrogen, methane and other hydrocarbons), oils, solid carbon residues of steel and char, and steel. Because of their high calorific values, the gases and oils produced in this process can be used for power generation, which makes this thermochemical process the less aggressive in terms of environmental impact. This method also allows the possibility of using tyre by-products as raw materials, although some of them can be of low quality, especially the char (Frazão, 2019).

The microwave induced pyrolysis process begins with the tyre shredding and uses microwave power at relatively low temperatures at the molecular level to thermally decompose tyres to their constituents (Pilakoutas *et al.*, 2004). In this process, the derived steel cord and textile wire remain intact, while the rubber is converted to oil, gases and char. This process has the ability of heating in a short time comparing with traditional heating techniques (Frazão, 2019).

Hu *et al.* (2018) emphasizes the need to minimise rubber contamination and to avoid agglomeration before and during concrete mixing, since one of the major problems encountered during casting is the tendency for the steel fibres to "ball up" during concrete mixing. To counter this shortcoming, Frazão (2019) advises the use of a planetary vertical mixer, which is the best equipment to mix Recycled Steel Fibre Reinforced Concrete (RSFRC) with good workability.

2.6.2 Recycled Steel Fibres vs Industrial Steel Fibres

Based on results available in the scientific literature, Caggiano *et al.* (2017) states that RSFs and Industrial Steel Fibres (ISFs) exhibit similar mechanical response, both in terms of tensile strength and matrix-to-fibre bond. This finding supports the idea that industrial fibres can be replaced by an equal amount of recycled ones without a significant decay in the relevant mechanical properties. However, the resulting RSFRC post-cracking behaviour can be highly influenced by the intrinsic geometrical characteristics of the fibres.

The fibres can be geometrically characterized by their (Caggiano *et al.*, 2017): diameter (d_f) expressed in mm and measured by means of a micrometer; length (l_f) expressed in mm and defined as the distance between the outer ends of a fibre; developed length (l_d) expressed in mm and defined as the total length of the fibre along its axis; curvature index (CI), which represents a shape index aimed at evaluating the curvatures (a tortuosity index) of the fibre and is expressed through $(l_d - l_f)/l_d$; and aspect ratio (k) defined as the ratio between the l_d and d_f. The type of tyres defines the fibre diameter, while the processing procedures influence the fibre lengths (both nominal and developed), and

consequently the aspect ratio of the recycled fibres. The use of blended fibres with different aspect ratios and physical properties may provide better crack control over a broader range of crack widths (Hu *et al.*, 2018).

Many studies on the post-cracking load bearing capacity and energy absorption performance have demonstrated that RSFs improve concrete durability and are beneficial to limit crack width, since they restrain the crack opening by bridging the crack surface (Aiello *et al.*, 2009; Caggiano *et al.*, 2017; Centonze *et al.*, 2012; Lourenço *et al.*, 2018; Onuaguluchi and Banthia, 2018; Pilakoutas *et al.*, 2004; Zamanzadeh *et al.*, 2015). However, the RSFs ability to transfer stresses through a cracked section depends on the fibre properties, orientation and distribution. Therefore, these effects must be present when designing structures, since these fibre variations might affect the concrete mechanical properties (Caggiano *et al.*, 2017).

Results from a study conducted by Caggiano *et al.* (2017) demonstrated that the bending response is highly influenced by the RSFs contribution and that application of these fibres slightly increase the compressive strength, but this effect disappears for amount of fibres higher of a certain threshold. The authors also compared the performance of ISFs with RSFs and concluded that the consideration of RSFs with an aspect ratio of around 110 was important to explain the favourable results over the ISFs aspect ratio of around 60, since the RSFs were capable to replace ISFs in bridging the cracks opening within the concrete matrix. Frazão (2019) also confirmed that the RSF geometry heterogeneity provides a plurality of strengthening mechanisms to concrete that enhance its durability, and that RSFs showed higher carbon content and tensile strength when compared to ISFs. The performance of the RSFs with rubber content attached to the surface proved to have minor effects in the pull-out behaviour of RSF from the concrete. Moreover, the fibre shape of the embedded length had a significant influence in the fibre pull-out behaviour. During experimental tests, RSFRC and Industrial Steel Fibre Reinforced Concrete (ISFRC) presented similar tensile strength and post-cracking behaviour, and RSFRC showed higher flexural capacity and energy absorption performance than ISFRC, probably due to the higher aspect ratio and number of RSF per concrete volume (Frazão, 2019).

A Life Cycle Assessment (LCA) for quantifying the material and energy flows in the different life stages of tyres is commonly used to determine the most cost-effective waste option (Caggiano *et al.*, 2017). According to Frazão (2019), several studies on LCA have shown that RSFs production consumes only up to 5% of the energy required to produce ISFs.

2.6.3 Chloride attack on RSFRC

Steel reinforced structures exposed to coastal environments are vulnerable to chloride-induced reinforcement corrosion. The degradation of these structures due to chloride penetration into uncracked concrete depends of the Steel Fibre Reinforced Concrete (SFRC) pore structure, type and size of the steel fibres, and the mix design parameters, such as w/c ratio, type and proportion of mineral admixtures and cement, type and content of steel fibres, compaction, and curing. The concrete permeability may decrease significantly with the addition of fibres due to the reduction of shrinkage cracks and the breaking of pore continuity by the fibre reinforcement mechanisms. Despite the increased risk of corrosion near marine environments, studies have demonstrated that only steel fibres near the concrete surface are susceptible to corrosion, which has only an aesthetic detrimental impact (Balouch *et al.*, 2010; Frazão, 2019; Marcos-Meson *et al.*, 2018; Singh and Singhal, 2011).

An extensive study conducted by Frazão (2019) investigated the behaviour of RSFRC under chloride environment through experimental and analytical research. In this study, RSF and ISF were immersed in a 3.5 wt% NaCl solution in order to assess post-cracking performance of pre-cracked and non-pre-cracked RSFRC under long-term exposure to chloride environment. The main conclusions that resulted from this research work are:

− The RSF are slightly more susceptible to corrosion than ISF;

− Small rubber debris attached to RSF surface had a negligible influence in terms of fibre corrosion resistance;

− The corroded RSF from pre-cracked specimens submitted to chloride attack showed higher variability in terms of cross section loss, probably due to irregular chloride attack at the exposed irregular geometry of RSF in the crack and, consequently, variable susceptibility to fibre corrosion. Fibre failure occurred for most pull-out tests of RSF embedded in cracked specimens after subjected to 10 days of immersion in 3.5 wt% NaCl solution;

− For pre-cracked RSFRC panels with crack widths up to 1 mm, the cracked surfaces were completely penetrated by chlorides during the 10-days of immersion period, and corrosion products were visible in the RSF located in the cracked surfaces, mainly near the exposure faces of the panels;

− Surface corrosion has occurred on the RSFRC panels after 10 days of immersion and 3 months of dry-wet cycles in chloride solution;

− The RSF subjected to continuous immersion in chloride solution showed uniform mass loss, while the RSF submitted to more aggressive dry-wet cycles in chloride solution showed uneven

mass loss due to a localized corrosion action. The loss of tensile strength of RSF has increased with the exposure time in chloride solution;

— After 10 days, and 3 and 6 months of chloride immersion in 3.5 wt% NaCl solution, no significant signs of RSF corrosion on uncracked RSFRC were observed, which can be concluded that uncracked RSFRC was not significantly affected by chloride attack. However, corrosion spots were observed at exposed surfaces of all specimens;

— The predicted critical chloride penetration depth into a RSFRC structural element was only about 11 mm after exposed to dry-wet cycles in a 3.5 wt.% NaCl solution for 100 years.

2.6.4 Reinforced armour units

Although reinforced armour units are not commonly considered in coastal protection structures, some studies developed by different authors demonstrated promising results on the application of steel fibres to the concrete mix.

Results from the Bottin and Appleton (1997) research work on Humboldt Bay jetties rehabilitation to evaluate reinforced and unreinforced Dolosse showed that the durability of the metal fibre reinforced Dolosse was greater than those without reinforcement. Knowledge obtained from the testing of Dolosse on this location was later applied to the Dolosse rehabilitation project on a breakwater at Crescent City, California (Appleton *et al.*, 1996; Melby and Turk, 1992). Myrick and Melby (2005) conducted monitoring tests on these fibre reinforced Dolosse and results shown that the concrete strength in these units was very high, as they were more than double the typical concrete armour units specifications. The flexural tensile strength in all tested Dolosse showed strengths of an average of 10.1 MPa. The increase ranges from 9 % to 76 %, with the lowest increase being in the most heavily loaded units near the low water level. In addition, a review on the use of fibre reinforced concrete of Dolosse conducted by Hoff (1975) states that after two winter seasons, a visual inspection of the armour units revealed no damage to the fibre reinforced Dolosse, while some of the unreinforced Dolosse had failed after the first season.

Studies developed by Appleton *et al.* (1996), Melby and Turk (1992), Myrick and Melby (2005), Burcharth (1984) and Hoff (1975) on the analysis of the concrete mix and mechanical properties of industrial steel fibre reinforced concrete armour units can be found in Appendix 1B. Concrete mix compositions and mechanical properties results from physical experiments on recycled steel fibre reinforced concrete considering fibre lengths of at least 41 mm developed by Aghaee *et al.* (2015), Sengul (2016), Köroğlu (2019) and Sengul (2018) are presented in Appendix 1C.

2.7 Confinement of concrete elements

Armour units subjected to rocking under heavy wave attack might break and compromise the breakwater stability. To help reduce the vulnerability against rocking, some modification to the concrete surface might be conducted. Some examples are (Goud, 2020): shape modifications without changing the actual shape of the concrete armour unit, such as adding "saw tooth" ridges to the surface; or adding a different material on the concrete surface (layer of an asphalt-like product, or adding wooden or plastic strips). The first ensures that the ridges have a neutralizing effect giving a significant reduction in the percentage of broken units, while the latter would dampen the rocking and reduce the contact stiffness, therefore a relatively large amount of energy will be dissipated during rocking.

A different solution to enhance the concrete strength is the new method of strengthening or retrofitting called "rope jacketing" that has been developed by some researchers. External steel jacketing for retrofitting and strengthening concrete members has been tested in previous researches, but the use of this solution can have unwanted outcomes as increasing dead weight and volume, as well as corrosion problems, depending on the selected materials (Daftardar *et al.*, 2016; Hussain *et al.*, 2017).

2.7.1 FRP confinement

The use of Fibre Reinforced Polymers (FRPs) materials for strengthening and rehabilitation of concrete structures is a solution that presents several advantages and has been recently investigated all over the world (Hussain *et al.*, 2020; Jirawattanasomkul *et al.*, 2019; Padanattil *et al.*, 2017, 2019; Sen and Paul, 2015; Sen and Reddy, 2014; Suwattanakorn *et al.*, 2016). The main advantages of FRP materials are related to their lightweight, high strength and stiffness, resistance to corrosion, flexibility, and ease of application (Janwaen *et al.*, 2019; Rousakis, 2012).

Externally bonded FRP composite jacketing is one of the most common applications that can provide significant confinement to the concrete, since it allows the increase of axial load and deformation capacity, as well as its energy absorption performance (Barros and Ferreira, 2008; Janwaen *et al.*, 2019; Nisticò *et al.*, 2014; Shayanfar *et al.*, 2020). The confinement effectiveness depends on the lateral confining pressure applied to the concrete core, and studies confirm that the confinement of FRP on circular sections is more efficient than in columns with non-circular sections, due to an uniform confining pressure assured by the circular cross-section (Colajanni *et al.*, 2014; Faustino *et al.*, 2014; Harajli, 2006; Janwaen *et al.*, 2019; Mirmiran *et al.*, 1998). The confinement effectiveness also depends on several parameters, such as concrete strength, type of fibres and resins, fibre volume and fibre orientation in the jacket, jacket thickness, slenderness ratio of the column, and the interface bond

between the core and the jacket (Janwaen *et al.*, 2019; Mirmiran *et al.*, 1998). In addition, the size and aspect ratio of the cross-section (largest edge to smallest edge ratio) can also compromise the effective confinement provided by FRP systems. When this aspect ratio increases, the confinement effectiveness of the columns significantly decreases (Janwaen *et al.*, 2019; Wu and Wei, 2010).

Recent studies conducted by Janwaen *et al.* (2019) and Shayanfar *et al.* (2020) present different developments on the confinement of concrete elements for increasing the axial load carrying capacity and deformation prediction, and performance of reinforced concrete. Janwaen *et al.* (2019) proposed an innovative strengthening technique denominated strip constriction that consists of the application of a mechanical device to induce a certain prestress level on the FRP (Figure 2.50), while Shayanfar *et al.* (2020) developed a new model to predict the dilation behaviour of fully and partially FRP confined concrete elements of circular cross sections.

Figure 2.50: Representation of the prestress application on the FRP strips (Janwaen *et al.*, 2019).

2.7.2 Natural and man-made fibre rope confinement

Sisal fibre, obtained from the leaves of the plant *Agave Sisalana*, is very easily cultivated and it is one of the most extensively cultivated hard fibres, which makes them easily available. Nearly 4.5 million tonnes of sisal fibres are produced every year throughout the world, being Tanzania and Brazil the two main producing countries (Chand *et al.*, 1988). The harvest period is not fixed, which means the farmers can cut the leaves at their convenience, but an interval between cuttings of approximately one year is recommended (Yu, 2005). Sisal fibre is usually obtained by machine decortications in which the leaf is crushed between rollers and then mechanically scraped. The fibres are then dried and brushed off to remove the remaining dirt, resulting in a clean fibre. From Ancient times, sisal has been the leading material for agricultural ropes and was mainly used in naval vessels because of its excellent resistance to deterioration in seawater and better resistance to some chemical agents than other natural fibres. Sisal fibre is also characterised by high strength, sturdiness, durability (as long as treated appropriately (Yu, 2005)), deformability, and good resistance to cold and to abrasion. It is also

lightweight, does not cause any harm to the environment and does not present the problem of toxicity and waste disposal (Olusegun *et al.*, 2012; Sapuan *et al.*, 2006; Wambua *et al.*, 2003; Yu, 2005).

The resistance of sisal fibre to seawater is higher than that to fresh water, because when immersed in seawater, the salt delays the growth of microorganisms that weaken the inter-fibre cohesion (Yu, 2005). Properties of sisal fibres (Table 2.11) can be improved or changed by chemical treatment modification, mainly with the use of sodium hydroxide, which "purifies" the fibres and improves their performance. However, careful control is required since complete removal would reduce the fibres bundles to single cells.

Table 2.11: Physical properties of sisal fibres (adapted from Di Bella *et al.* (2014)).

Property	Sisal Fibres
Length (mm)	5
Diameter (µm)	120-140
Density (g/cm³)	1.45

An alternative method to FRPs for concrete confinement can be held by using ropes (Figure 2.51). The ropes for confining concrete elements are easily available all around the world with different nominal diameter and strength properties (Hussain *et al.*, 2017). At the present time, different kinds of ropes are manufactured, such as steel wire ropes, polypropylene, nylon, vinylon and natural fibres as sisal, hemp and basalt (Hussain *et al.*, 2017; Rousakis, 2017; Rousakis, 2014; Rousakis and Tourtouras, 2014; Rousakis, 2012; Rousakis and Tourtouras, 2015; Shabana *et al.*, 2015). One of the most studied natural fibres on the rope confinement is the sisal. Table 2.12 presents ranges of mechanical properties of some natural and man-made reinforcing fibres mentioned.

Although natural fibres are lightweight, with low environmental impact both in production and in biodegradability, these type of fibres presents restrictions that require awareness for their use. Natural fibres have variability in properties; less durability than common inorganic fibres due to chemical absorption; and weakening in alkaline environment (Parveen *et al.*, 2012; Rousakis, 2017).

The failure strength and the modulus of elasticity of sisal fibres depend on the orientation of microfibers and on the amount of cellulose, which is a basic component of plant tissues that gives firmness to plants. The sisal cordage are found commercially in several formats: fabric, cords, strips, wire, rolls, etc. (Daftardar *et al.*, 2016; Rousakis, 2017). Sisal ropes are made of twisted twines characterised by high strength, good anti-slippage properties, and better resistance to some chemical agents than other natural fibres. The main kinds of sisal ropes are 3- and 4-twines. Rope diameters usually range from 3-60 mm (Yu, 2005).

Recent studies conducted by Rousakis (2012), Shabana *et al.* (2015), Daftardar *et al.* (2016), Rousakis (2017) and Hussain *et al.* (2017) using man-made and natural organic and inorganic fibres show that the application of the confining technique using ropes as external strengthening reinforcement on concrete elements are an effective method to enhance: i) compressive strain ductility; ii) ultimate load carrying capacity; and iii) ultimate strain.

Figure 2.51: Wrapping process of dry rope to the concrete specimen (Suparp *et al.*, 2017).

Table 2.12: Ranges of mechanical properties of some natural and man-made reinforcing fibres (Rousakis, 2017).

Type of Fibre	Fibres	Modulus of Elasticity (GPa)	Tensile Strength (MPa)	Ultimate Strain (%)
Natural organic	Hemp	30-70	310-900	1.6-6
	Sisal	9-38	80-840	2-25
Natural inorganic	Basalt	89-95	3000-4900	3-5
Man-made	Vinylon	16	735	4.6
	Polypropylene	2	400	20

2.8 Numerical laboratory

The use of hydro- and morphodynamics modelling tools is of crucial importance to better understand the erosion/accretion processes at coastal areas. Detailed environmental conditions, including morpho-sedimentary dynamics, currents and wave propagation, where the reversal of longshore drift takes place should be better understood providing the basis for new sustainable engineering solutions that will be proposed using both field observations data and numerical simulations.

Given the importance of coastal areas, it becomes increasingly important to provide the decision-making entities of tools that allow, through certain scenarios, evaluating the evolution and the impact of measures on the coast. The sustainable management of coastal areas also involves predictive power of morphological evolution at medium and long term. This prediction is difficult and often times accompanied by a great uncertainty, due to the high number and complexity of the processes involved and their interaction. In this context, numerical modelling plays a paramount role in simulating the evolution of coastal morphology.

The purpose of a model is to address and define the necessary detail for various scalar and temporal components of a model structure, its boundary conditions and key operational parameters. An important component of most coastal and ocean engineering projects is an accurate evaluation of the wave climate at the project site. Typical applications include design of structures and the evaluation of the impact of coastal structures on adjacent shorelines. In the last decades, a number of powerful models have been developed to simulate currents and the propagation of waves in coastal regions and harbours with many different capabilities/limitations and data requirements that limit the types of problems to which they can be applied (Pinho *et al.*, 2004). In general, despite being based on different assumptions, all of them are of hard calibration and validation due to the large amount of parameters included in those models (Nwogu and Demirbilek, 2001). A numerical model is considered to be ready to produce reliable results only if the questions and problems to be addressed by the model are properly defined, all of the key input data have been thoroughly checked, and if model sensitivity, calibration and verification analyses have been carefully completed (NHC, 2012).

Thus, these tools can be used to analyse the performance of traditional and innovative coastal protection engineering solutions to mitigate present erosion that will need, in a second phase, technical, economic and environmental characterization (Anfuso *et al.*, 2011; Ferreira *et al.*, 2006; Firth *et al.*, 2014; Granja *et al.*, 2014; Schmidt *et al.*, 2013; van Wesenbeeck *et al.*, 2014).

A collection of available software solutions for hydrodynamics, morphodynamics and structural design was analysed in terms of overall functionalities. The models considered in this overview were the following: BOUSS-2D; COULWAVE; Delft3D-FLOW; Delft3D-WAVE (SWAN); XBeach; TELEMAC-2D; TELEMAC-3D; TOMAWAC; SISYPHE; SAP2000; FEMIX; and ABAQUS. Despite all being valid for coastal regions and their similarities in terms of formulations or input data and output results, some are more adequate than others by offering more options for the purpose of this study.

The next Sections present a brief assessment of the main characteristics of numerical models adopted in this study.

2.8.1 Delft3D

Delft3D is an integrated modelling suite based on the finite difference method (Delft3D 4 Suite) that includes Delft3D-FLOW, Delft3D-MOR, Delft3D-WAVE (SWAN), Delft3D-WAQ, Delft3D-ECO and Delft3D-PART modules.

Delft3D simulates two-dimensional (in either the horizontal or a vertical plane) and three-dimensional flow, sediment transport and morphology, waves, water quality and ecology and is capable of handling

the interactions between these processes, thus comprising natural environments such as coastal areas, rivers, reservoirs and estuaries (Deltares, 2019c).

Delft3D has been used in two- and three-dimensional applications for simulating coastal morphodynamics induced by currents and waves, and is a model that reproduces measured water levels, velocities and nearshore waves. It is a high complexity numerical model and it is applicable on analysing flows of tides, currents due to wind, river runoff simulations and lakes, propagation of tsunamis, hydraulic rebounds, coastal and fluvial morphodynamics and pollutant transportation analysis as well as water temperature changing panorama and salinity gradients.

One major application of this model was to successfully hindcast the initial response of a sand engine mega-nourishment in The Netherlands. This sand nourishment allows natural processes to maintain a sandy coast and "dynamically" keep it in place as a result of morphological modelling application (Luijendijk *et al.*, 2017).

The FLOW module is the heart of Delft3D and is a multi-dimensional (2D or 3D) hydrodynamic (and transport) simulation programme which calculates non-steady flow and transport phenomena resulting from tidal and meteorological forcing on a curvilinear, boundary fitted grid or spherical coordinates. The MOR module computes sediment transport (both suspended and bed total load) and morphological changes for an arbitrary number of cohesive and non-cohesive fractions. Both currents and waves act as driving forces, and a wide variety of transport formulae have been incorporated. For the suspended load, this module connects to the 2D or 3D advection-diffusion solver of the FLOW module; density effects may be taken into account. An essential feature of the MOR module is the dynamic feedback with the FLOW and WAVE modules, which allow the flows and waves to adjust themselves to the local bathymetry and allows for simulations on any time scale from days (storm impact) to centuries (system dynamics). It can keep track of the bed composition to build up a stratigraphic record. The MOR module may be extended to include extensive features to simulate dredging and dumping scenarios (Deltares, 2019a).

Delft3D is a robust model which has been applied in a range of alluvial and marine environments. The model has successfully been applied in the coastal environment to study processes related to shoreface nourishments (Grunnet *et al.*, 2004, 2005; van Duin *et al.*, 2004), hydrodynamics, sediment transport and morphological changes in different environments, including for geomorphologic features similar to spits (Almeida *et al.*, 2015; Capitão *et al.*, 2009; Carvalho *et al.*, 2017; Dan *et al.*, 2011; Ferreira *et al.*, 2017; Hartog *et al.*, 2008; Ruggiero *et al.*, 2009; Silva *et al.*, 2009; Silva *et al.*, 2015; Tung *et al.*,

2009). In several tidal inlet studies (der Wegen *et al.*, 2010), the model showed good agreement with well-known empirical relations of Jarrett (1976).

2.8.1.1 Delft 3D-FLOW for Hydro-Morphodynamics

The primary purpose of Delft3D-FLOW is to solve various one, two and three-dimensional, time-dependent, nonlinear differential equations related to hydrostatic and non-hydrostatic free-surface flow problems on a structured orthogonal grid to cover problems with complicated geometry. The equations are formulated in orthogonal curvilinear coordinates on a plane or in spherical coordinates on the globe. In Delft3D-FLOW, models with a rectangular or spherical grid (Cartesian frame of reference) are considered as a special form of a curvilinear grid (Kernkamp *et al.*, 2005; Willemse *et al.*, 1986).

The equations solved are mathematical descriptions of physical conservation laws for water volume (continuity equation), momentum (Reynolds-averaged Navier-Stokes (RANS) equations), and tracer mass (transport equation) and suspended sediments or passive pollutants. Furthermore, bed level changes are computed, which depend on the quantity of bottom sediments. In case of hydrostatic modelling, the so-called shallow water equations are solved, whereas in non-hydrostatic mode the Navier-Stokes equations are taken into account by adding non-hydrostatic terms to the shallow water equations. A fine horizontal grid is needed to resolve non-hydrostatic flow phenomena.

Delft3D-FLOW can be used for an accurate prediction of the: a) tidal dynamics (water elevation, currents) in estuaries or coastal seas; b) density (salinity and/or temperature) driven flow; c) wind driven flow and storm surges; d) horizontal transport of matter, both on large and small scales; e) waste water dispersion from coastal outfalls; and f) thermal stratification in seas, lakes and reservoirs. Flows resulting from dam breaks can also be accurate predicted as well as small scale current patterns near harbour entrances, sediment concentrations can be taken into account with respect to density values. Other use of this software is the ability to investigate the hydrodynamic impact of engineering works, such as land reclamation, breakwaters, dikes; the impact of hydraulic structures such as gates, weirs and barriers.

2.8.1.2 Delft 3D-WAVE (SWAN)

SWAN (Simulation WAves Nearshore) can be used as stand-alone application, but it is also included in the Delft3D 4 Suite. SWAN (SWAN, 2018) is a wave model for obtaining realistic estimates of wave parameters in coastal areas, lakes and estuaries from given wind, bottom and current conditions.

However, SWAN can be used on any scale relevant for wind-generated surface gravity waves. The model is based on the wave action balance equation with sources and sinks.

This model spreads the wave propagation from deep waters to the transition zone considering the physical processes of refraction, diffraction and shoaling due to background variations and the presence of currents, wave growth by action of wind, wave breaking under the influence of background and excess slope, power dissipation due to friction from the bottom, blocking and reflection by opposing currents and transmission through obstacles.

The wave field in the area is characterized by two-dimensional spectrum of the density of sea wave action. With this representation, it is possible to apply the model in areas where growth of waves by wind is remarkable or where sea states, or even waving, are present. The spread of wave propagation in stationary or non-stationary modes, in the geographical and spectral spaces is performed using implicit numerical schemes. The area under study can be described in spherical coordinates or Cartesian coordinates using a "rectangular" mesh.

An important question addressed is how to choose various grids in SWAN (resolution, orientation, etc.). In general, it is considered two types of grids: structured and unstructured. Structured grids may be rectilinear and uniform or curvilinear. They always consist of quadrilaterals in which the number of grid cells that meet each other in an internal grid point is 4. In unstructured grids, this number can be arbitrarily (usually between 4 and 10). For this reason, the level of flexibility with respect to the grid point distribution of unstructured grids is far more optimal compared to structured grids. Unstructured grids may contain triangles or a combination of triangles and quadrilaterals (so-called hybrid grids). This type of flexible meshes is particularly useful in coastal regions where the water depth varies greatly offering modest effort needed to generate grids about complicated geometries, e.g., islands and irregular shorelines. As a result, this variable spatial meshing gives the highest resolution where it is most needed. The use of unstructured grids facilitates to resolve the model area with a relative high accuracy but with a much fewer grid points than with regular grids (SWAN, 2018).

The data required for the implementation of SWAN are bathymetric mesh modelling area and wave conditions on the border of the input field, plus a host of other calculation parameters. Among the several results obtained by SWAN, these are the ones that stand out: significant wave height, peak and average time periods, peak and average directions, directional dispersion, and level of water anywhere in the computational domain (Capitão and Fortes, 2011).

The most relevant limitations of SWAN can be listed as:

- The calibration of many of the parameters involved in the description of different physical phenomena in SWAN was based on data from the JONSWAP (Joint North Sea Wave Project) campaign undertaken in the North Sea (Hasselmann *et al.*, 1973). Such parameters may not be correct for areas with different climate characteristics of waves or with different characteristics of the seabed;

- The diffraction in SWAN is modelled simply as a directional dispersion, which may constitute the main limitation;

- The inclusion in numerical computations of diffraction implies that the computational mesh spacing relative to the wavelength is such that ensures the convergence of the computations. This sometimes implies that the meshes are of such size that can derail the implementation of the calculations;

- It must be pointed out that the application of SWAN on ocean scales is not recommended from an efficiency point of view. The WAVEWATCH III model, which has been designed specifically for ocean applications, is probably one order of magnitude more efficient than SWAN. SWAN can be run on large scales (much larger than coastal scales), but this option is mainly intended for the transition from ocean scales to coastal scales;

- SWAN does not calculate wave-induced currents. If relevant, such currents should be provided as input to SWAN, e.g., from a circulation model, which can be driven by waves from SWAN in an iteration procedure;

- SWAN is not applicable to shallow waters (it is valid to deep waters and transition zones).

2.8.2 XBeach

XBeach (Deltares, 2019d) model is used for the computation of 2D-horizontal nearshore hydrodynamics of wave propagation, including surf-beat (long period waves), mean flow, and wave-induced currents in combination with non-cohesive sediment transports, overwash (wave uprush over a natural or artificial coastal barrier), scour around buildings, and morphological changes of the nearshore beaches and dunes during storm events. An example of this application is the assessment of dune safety in complex situation along the Dutch coast and in hindcasting hurricane impacts in the United States of America. XBeach has also been applied to coasts along every European regional sea under a variety of conditions, and has been extended so that it can be applied to (coral) reef-lined coasts, gravel coasts and vegetated coasts. It is even possible to compute ship-induced waves. The XBeach model has a large and

expanding community of users, and has been independently validated in more than 60 peer-reviewed articles.

XBeach concurrently solves the time-dependent short wave action balance, the roller energy equations, the nonlinear shallow water equations (NSWE) of mass and momentum, sediment transport formulations and bed variations. The model has been extensively validated for sandy coastlines with series of analytical, laboratory and field test cases, and offers the study on storm impacts of up to a few days of duration, and on coastal regions of longshore and cross-shore lengths of up to 12 km and 3 km, respectively (de Alegria-Arzaburu *et al.*, 2010). This limited extent implies boundary conditions of tidal- and wind/pressure-driven water levels, deeper-water (outside the surf zone) wave boundary conditions and bathymetry (Bolle *et al.*, 2010). The wave boundary conditions can be applied as time series of the instantaneous wave height including wave grouping, or alternatively, the time-steady wave (Roelvink *et al.*, 2009). The model accounts for feedback between the evolving bathymetry and the hydrodynamics at each time step.

Although the XBeach model has been successfully applied across a large number of sandy coasts (De Vet *et al.*, 2015; Nederhoff *et al.*, 2015; Smallegan *et al.*, 2017; Splinter *et al.*, 2014; Splinter and Palmsten, 2012), the model assumes that the surf zone is fully saturated during energetic conditions. While the assumption of a saturated surf zone allows a simplification of the incident waves into an energy balance, it also limits the application of the XBeach model on steeper coasts. This limitation led to the development of a new branch of a XBeach model for steep gravel coasts, called XBeach-G, which allows a phase-resolving approach for infragravity and incident waves using a non-hydrostatic pressure correction term for the NSWE (Roelvink *et al.*, 2018).

XBeach allows users to choose which mode options to implement: a) Stationary wave mode (efficiently solving wave-averaged equations but neglecting infragravity waves); b) Surf-beat mode (instationary), where the short wave variations on the wave group scale and the long waves associated with them are resolved; and c) Non-hydrostatic mode (wave-resolving), where a combination of the NSWE with a pressure correction term is applied, allowing to model the propagation and decay of individual waves.

Stationary mode is useful for conditions where the incident waves are relatively small and/or short (wave height), and infragravity motions would be small anyway. Processes that are resolved are wave propagation, directional spreading, shoaling, refraction, bottom dissipation and wave breaking, and a roller model (Roelvink *et al.*, 2018).

Using the surf-beat mode is necessary when the focus is on swash zone processes rather than time-averaged currents and setup (increase in mean water level due to the presence of breaking waves).

Thus, wave-driven currents (longshore current, rip currents), long (infragravity) waves, and run-up and run-down of long waves (swash and backwash) are included (Roelvink *et al.*, 2018).

The main advantages of the non-hydrostatic mode are that the short wave run-up and overtopping are included, which is especially important on steep slopes such as gravel beaches. Another advantage is that the wave asymmetry and skewness are resolved by the model and no approximate local model is required for these terms. Finally, in cases where diffraction is a dominant process, wave-resolving modelling is needed as it is neglected in the short wave averaged mode. Despite the advantages mentioned, the wave-resolving mode is generally computationally more expensive than the surf-beat mode, because it requires higher spatial resolution and associated smaller time steps. An application of the non-hydrostatic mode is XBeach-G, which is specifically developed to simulate storm impacts on gravel beaches. The formulations for gravel beaches were developed and extensively tested for the non-hydrostatic mode, and the model showed great skill at predicting extreme wave run-up and barrier overtopping and overwash events. Sandy morphology can be simulated using the wave-resolving mode but has not yet been validated as extensively, though promising results are presented in literature (Roelvink *et al.*, 2018).

2.8.3 FEMIX

The finite element method (FEM) is a useful tool in the interpretation and understanding of several engineering phenomena. The existing codes have proved to be too complex and monolithic, making it difficult to test new ideas as well as to modify some of their components. These difficulties motivated the development of software based on modules that include all the code necessary to the processing of the corresponding block of information. This architecture makes the introduction of new finite elements and new models of nonlinear analysis of structures simple and flexible (Azevedo *et al.*, 2003).

FEMIX is a generic finite element structural analysis program developed by Álvaro Azevedo (University of Porto) and Joaquim Barros (University of Minho). It presents a simple data generation module and a graphical visualization module of data and results. FEMIX is structured in the following modules (Azevedo *et al.*, 2003; Ribas, 2016):

- Pre-FEMIX: reading of a "_gl.dat" extension data file containing all the data, validation of the information contained in it, and writing of the data to a non-formatted file with an "_gl.bin" extension (binary file);

‒ FEMIX: reading of the binary file mentioned, calculation of results based on the finite element method and saving of binary files containing all the results of this phase, which can be linear or nonlinear;

‒ Post-FEMIX: generation of different types of results based on information from previous modules. It is possible to generate several types of information for graphic visualization. This information is stored in files compatible with the DRAWMESH program, which consists of a generic viewer of three-dimensional models.

FEMIX is based on the displacement method; it has a large number of types of finite elements inside, such as 3D frames and trusses, plane stress elements, flat or curved elements for shells, and 3D solid elements. Embedded line elements can be included in the analysis with the availability of static or dynamic tests using both linear and nonlinear material configurations (Almassri *et al.*, 2016).

Several studies on the behaviour of composite materials for structural strengthening and fibre reinforced concrete have been conducted using FEMIX (Almassri *et al.*, 2015, 2016; Barros, 2010, 2012; Dalfré and Barros, 2011; Dias *et al.*, 2008; Gonçalves *et al.*, 2008; Lourenço *et al.*, 2006; Sena-Cruz *et al.*, 2004).

2.8.3.1 GID/FEMIX

FEMIX code can be integrated with GiD (personal pre and post-processor) interface software (GiD-FEMIX, 2017) which provides pre- and post-processing for numerical simulations analysis. GiD is an adaptive and user friendly graphical interface for computer analysis in science and engineering, together with a solver module, which in this case is the FEMIX 4.0 software.

As schematically depicted in the Figure 2.52, the definition, preparation and visualization of all the data related to a numerical simulation can be conducted in GiD, which will run FEMIX separately for numerical calculation of the model without having to leave its graphical interface: GiD will automatically recognize FEMIX's output files, and therefore all post-processing related to a given model can also be conducted in the GiD interface. For the development of a finite element model, the geometry and mesh creation can be done exclusively in the GiD software, using the original tools that are explained in the GiD user manuals and tutorials, which can be accessed in the official GiD website. After the mesh creation, the user should load the GiD-FEMIX Problem Type in order to proceed to the additional steps of the finite element model: (i) definition of material properties, load and supports conditions (pre-processing); (ii) calculation (GiD will run FEMIX separately); and (iii) analysis of results (post-processing). "Problem Type" is what GiD defines as the collection of files used to configure GiD for a particular type

of analysis/solver. Basically, it works as a translator between GiD and FEMIX languages. For the users of GiD-FEMIX, the Problem Type will be a directory with the name of the problem type (FEMIX) and the extension ".gid": FEMIX.gid. This directory should be located in the main GiD executable directory. The FEMIX Problem Type will hence be added to the problem types already included in the system, and will automatically appear in the GiD menu (Data>Problem type) (GiD-FEMIX, 2017).
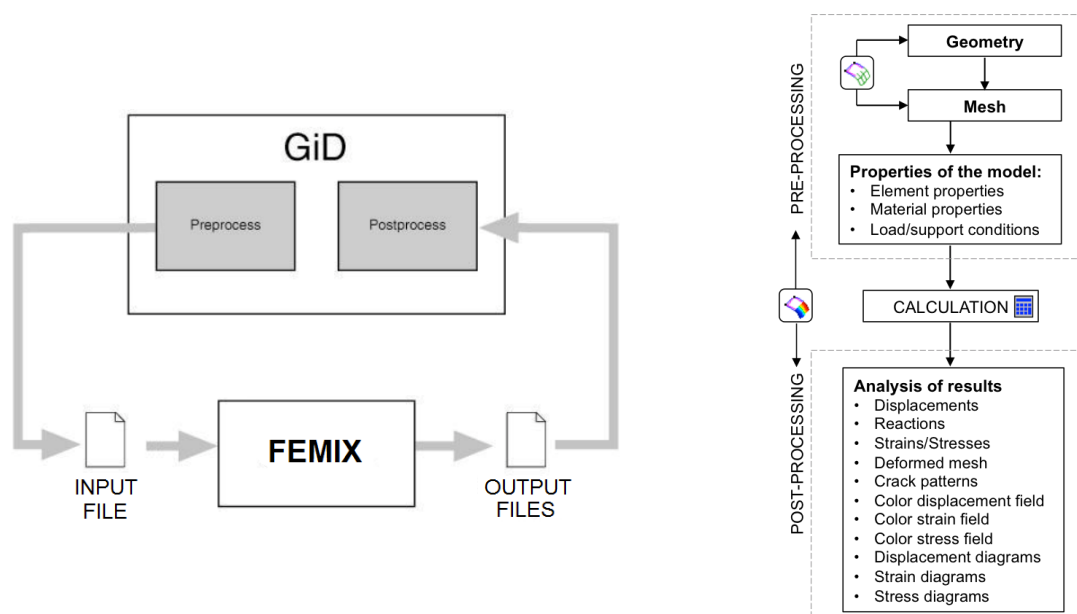
Figure 2.52: Interrelation between GiD and FEMIX (GiD-FEMIX, 2017).

2.9 References for Chapter 2

Abbott, M.B.; and Price, W.A. (1993). *Coastal, Estuarial, and Harbour Engineers' Reference Book*. (M. Fleming & B. Tysoe, Eds.) (1st Ed.). London, UK: CRC Press. https://doi.org/10.1201/9781482267020.

Adriana-Gracia, C.; Rangel-Buitrago, N.; Oakley, J.A.; and Williams, A. (2018). Use of ecosystems in coastal erosion management. *Ocean and Coastal Management*, *156*, 277–289. https://doi.org/10.1016/j.ocecoaman.2017.07.009.

Aghaee, K.; Yazdi, M.A.; and Tsavdaridis, K. (2015). Investigation into the mechanical properties of structural lightweight concrete reinforced with waste steel wires. *Magazine of Concrete Research*, *67*(4), 197–205. https://doi.org/http://dx.doi.org/10.1680/macr.14.00232.

Agrawal, B.J. (2011). Geotextile: It's Application to Civil Engineeering - Overview. In *National Conference on Recent Trends in Engineering & Technology, 13th to 14th May 2011* (pp. 1–6). Anand, Gujarat, India. Retrieved from http://www.bvmengineering.ac.in/misc/docs/published-20papers/civilstruct/struct/101052.pdf.

Aiello, M.A.; Leuzzi, F.; Centonze, G.; and Maffezzoli, A. (2009). Use of steel fibres recovered from waste tyres as reinforcement in concrete: Pull-out behaviour, compressive and flexural strength. *Waste Management*, *29*(6), 1960–1970. https://doi.org/https://doi.org/10.1016/j.wasman.2008.12.002.

Airoldi, L.; Abbiati, M.; Beck, M.W.; Hawkins, S.J.; Jonsson, P.R.; Martin, D.; Moschella, P.S.; Sundelöf, A.; Thompson, R.C.; and Åberg, P. (2005). An ecological perspective on the deployment and design of low-crested and other hard coastal defence structures. In *1st International Conference on Coastal Zone Management of River Deltas and Low Land Coastlines,* (Vol. 52, pp. 1073–1087). https://doi.org/10.1016/j.coastaleng.2005.09.007.

Allard, J.; Bertin, X.; Chaumillon, E.; and Pouget, F. (2008). Sand spit rhythmic development: A potential record of wave climate variations? Arçay Spit, western coast of France. *Marine Geology*, *253*(3–4), 107–131. https://doi.org/10.1016/j.margeo.2008.05.009.

Allen, R.T.L. (1998). *Concrete in Coastal Structures*. (R. Allen, Ed.). London, UK: Thomas Telford.

Almassri, B.; Al Mahmoud, F.; and Francois, R. (2016). Behaviour of corroded reinforced concrete beams repaired with NSM CFRP rods, experimental and finite element study. *Composites Part B: Engineering*, *92*, 477–488. https://doi.org/10.1016/j.compositesb.2015.01.022.

Almassri, B.; Barros, J.A.O.; Al Mahmoud, F.; and Francois, R. (2015). A FEM-based model to study the behaviour of corroded RC beams shear-repaired by NSM CFRP rods technique. *Composite Structures*, *131*, 731–741. https://doi.org/10.1016/j.compstruct.2015.06.030.

Almeida, J.; Pinho, J.L.; Venâncio, S.S.; and Vieira, J.M. (2015). Avaliação do transporte sedimentar no estuário do rio Douro em diferentes cenários hidrodinâmicos. In *VIII Congresso sobre Planeamento e Gestão das Zonas Costeiras dos Países de Expressão Portuguesa, 14 a 16 de Outubro 2015* (pp. 1–14). Aveiro, Portugal: Associação Portuguesa dos Recursos Hídricos. Retrieved from https://repositorium.sdum.uminho.pt/handle/1822/43262.

Anfuso, G.; Pranzini, E.; and Vitale, G. (2011). An integrated approach to coastal erosion problems in northern Tuscany (Italy): Littoral morphological evolution and cell distribution. *Geomorphology*, *129*(3–4), 204–214. https://doi.org/10.1016/j.geomorph.2011.01.023.

Anthony, E.J. (2015). Wave influence in the construction, shaping and destruction of river deltas: A review. *Marine Geology*, *361*, 53–78. https://doi.org/10.1016/j.margeo.2014.12.004.

Antunes do Carmo, J. (2013). Experiência de recuperação de um sistema dunar e proposta de instrumentos complementares de proteção, atração e valorização ambiental. *Revista de Gestão Costeira Integrada*, *13*(3), 317–328. https://doi.org/10.5894/rgci394.

Antunes do Carmo, J.S.; Neves, M.G.; and ten Voorde, M. (2011). Designing a multifunctional artificial reef: studies on the influence of parameters with most influence in the vertical plane. *Journal of Coastal Conservation*, *15*(1), 99–112. https://doi.org/10.1007/s11852-010-0124-1.

Appleton, W.S.; Kendall, T.; and Melby, J.A. (1996). A Ten-Year History of Dolos Monitoring at Crescent City. In *Coastal Engineering Proceedings 1(25)* (pp. 4664–4675). https://doi.org/https://doi.org/10.9753/icce.v25.%25p.

Azenha, M.; Sena-Cruz, J.; Camões, A.; and Ferreira, R.M. (2011). Numerical simulation of the structural behaviour of concrete tetrapods subject to imposed deformations and applied loads. In *Congress on Numerical Methods in Engineering, 14th to 17th June 2011*. Coimbra, Portugal. Retrieved from http://hdl.handle.net/1822/12989.

Azevedo, Á.F.M.; Barros, J.A.O.; Sena-Cruz, J.; and Ventura-Gouveia, A. (2003). Software no ensino e no projecto de estruturas. In *III Congresso Luso Moçambicano de Engenharia, 19 a 22 de Agosto 2003* (pp. 81–92). Maputo, Moçambique. Retrieved from https://repositorium.sdum.uminho.pt/handle/1822/13106.

Baine, M. (2001). Artificial reefs: a review of their design, application, management and performance. *Ocean & Coastal Management*, *44*(3–4), 241–259. https://doi.org/10.1016/S0964-5691(01)00048-5.

Balouch, S.; Forth, J.; and Granju, J.-L. (2010). Surface corrosion of steel fibre reinforced concrete. *Cement and Concrete Research*, *40*, 410–414. https://doi.org/10.1016/j.cemconres.2009.10.001.

Banyard, L.S.; and Mannion, M.B. (2002). Design of rock groynes and sand beach replenishment under strong tidal flows. In *Breakwaters, coastal structures and coastlines* (pp. 191–202). London, UK: Thomas Telford. https://doi.org/10.1680/bcsac.30428.0016.

Barros, Joaquim, A.; and Ferreira, D.R. (2008). Assessing the Efficiency of CFRP Discrete Confinement Systems for Concrete Cylinders. *Journal of Composites for Construction*, *12*(2), 134–148. https://doi.org/10.1061/(ASCE)1090-0268(2008)12:2(134).

Barros, J.A.O. (2010). Modelação da interação solo estrutura na simulação do comportamento de box-culvert em betão reforçado com fibras. In *12º Congresso Nacional de Geotecnia, 26 a 29 de Abril 2010*. Guimarães, Portugal. Retrieved from http://repositorium.sdum.uminho.pt/handle/1822/13036.

Barros, J.A.O. (2012). Betões auto-compactáveis reforçados com fibras: propriedades e aplicações. In *5º Simpósio Internacional sobre concretos especiais, 29 a 31 de Março 2012* (pp. 1–37). Fortaleza, Brasil: Universidade Estadual Vale do Acaraú (UVA). Retrieved from https://repositorium.sdum.uminho.pt/handle/1822/21527.

Barros, J.A.O.; Baghi, H.; Dias, S.J.E.; and Ventura-Gouveia, A. (2013). A FEM-based model to predict the behaviour of RC beams shear strengthened according to the NSM technique. *Engineering Structures*, *56*, 1192–1206. https://doi.org/10.1016/J.ENGSTRUCT.2013.06.034.

Barros, J.A.O.; Ferrara, L.; and Martinelli, E. (Eds.). (2017). *Recent Advances on Green Concrete for Structural Purposes*. Cham: Springer International Publishing. https://doi.org/10.1007/978-3-319-56797-6.

Barros, J.A.O.; Frazão, C.; Caggiano, A.; Folino, P.; Martinelli, E.; Xargay, H.; and Zamanzadeh, Z. Lourenço, L. (2017). Cementitious Composites Reinforced with Recycled Fibres - Chapter 8. In J. A. . Barros, L. Ferrara, & E. Martinelli (Eds.), *Recent Advances on Green Concrete for Structural Purposes – The Contribution of the EU-FP7 Project EnCoRe* (pp. 141–195). Springer. https://doi.org/10.1007/978-3-319-56797-6.

Basco, D.R.; and Hughes, S. (2006). Example Problems - Chapter 7. In *Coastal Engineering Manual Part VI: Design of Coastal Project Elements* (p. 31). Washington, DC, USA: U.S. Army Corps of Engineers. Retrieved from https://pt.scribd.com/document/365474397/Coastal-Engineering-Manual-U-S-Army-Corps-of-Engineers-2002-2006.

Bastos, L.; Bio, A.; Pinho, J.L.S.; Granja, H.; and Jorge da Silva, A. (2012). Dynamics of the Douro estuary sand spit before and after breakwater construction. *Estuarine, Coastal and Shelf Science*, *109*, 53–69. https://doi.org/10.1016/j.ecss.2012.05.017.

Bolle, A.; Mercelis, P.; Roelvink, D.; Haerens, P.; and Trouw, K. (2010). Application and Validation of Xbeach for Three Different Field Sites. In *Proceedings of 32nd Conference on Coastal Engineering, 30th to 5th July 2010* (pp. 1–14). Shanghai, China. https://doi.org/10.9753/icce.v32.sediment.40.

Bonfantini, F. (2014). *Set-up to design guidance for the Crablock armour unit*. Retrieved from http://resolver.tudelft.nl/uuid:312e6c4b-aac5-4720-98b7-d45e4df56752.

Boothroyd, J.C. (1985). Tidal Inlets and Tidal Deltas - Chapter 7. In R. J. Davis (Ed.), *Coastal Sedimentary Environments* (pp. 445–532). New York, NY, USA: Springer New York. https://doi.org/10.1007/978-1-4612-5078-4_7.

Bottin, R.R.; and Appleton, W.S. (1997). *Periodic Inspection of Humboldt Bay Jetties, Eureka, California: Base Conditions. Report 1*. US Army Engineer Waterways Experiment Station. Retrieved from https://citeseerx.ist.psu.edu/viewdoc/download?doi=10.1.1.371.1567&rep=rep1&type=pdf.

Bralower, T.; and Bice, D. (2018). Earth in the Future: The Coriolis Effect. Penn State's College of Earth and Mineral Sciences. OER Initiative. Retrieved December 7, 2018, from https://www.e-education.psu.edu/earth103/node/840.

Broere, A. (2015). *Physical model tests on stability and interlocking of new breakwater armour block Crablock*. MSc Thesis in Hydraulic Engineering, Faculty of Civil Engineering and Geosciences of the Delft University of Technology, The Netherlands. https://doi.org/https://doi.org/10.4121/uuid:4251048f-f408-42cc-b1cf-83522430e420.

Browder, A.E.; Dean, R.G.; and Chen, R. (1996). Performance of a submerged breakwater for shore protection, ASCE, Vol. 2. In *Proceedings of the 25th International Conference on Coastal Engineering, 2nd to 6th September 1996* (pp. 2312–2323). Orlando, Florida, USA. https://doi.org/10.1061/9780784402429.179.

Burcharth, H.; and Liu, Z. (1992). Design of Dolos armour Units. In *Proceedings of the 23rd International Coastal Engineering Conference, 4th to 9th October 1992* (pp. 1053–1066). Venice, Italy.

Burcharth, H.F. (1984). Fatigue in Breakwater Concrete Armour Units. In *19th International Conference on Coastal Engineering, 3rd to 7th September 1984* (pp. 2592–2607). Houston, Texas, United States. https://doi.org/doi:10.1061/9780872624382.175.

Burcharth, H.F.; and Hughes, S.A. (2012). Fundamentals of Design. In *Coastal Engineering Manual, Part VI: Design of Coastal Project Elements* (p. 312). Washington, DC, USA: U.S. Army Corps of Engineers.

Burcharth, H.F.; and Hughes, S.A. (2012). Types and Functions of Coastal Structures. In *Coastal Engineering Manual, Part VI: Design of Coastal Project Elements* (p. 48). Washington, DC, USA: U.S. Army Corps of Engineers.

Buscombe, D.; and Masselink, G. (2006). Concepts in gravel beach dynamics. *Earth-Science Reviews*, *79*(1), 33–52. https://doi.org/10.1016/j.earscirev.2006.06.003.

Caggiano, A.; Folino, P.; Lima, C.; Martinelli, E.; and Pepe, M. (2017). On the mechanical response of Hybrid Fiber Reinforced Concrete with Recycled and Industrial Steel Fibers. *Construction and Building Materials*, *147*, 286–295. https://doi.org/https://doi.org/10.1016/j.conbuildmat.2017.04.160.

Capitão, R.; and Fortes, C. (2011). Análise comparativa entre estimativas do modelo SWAN e medições de agitação marítima efectuadas na Praia da Amoreira, Portugal. *Revista Da Gestão Costeira Integrada*, *11*(3), 283–296. https://doi.org/10.5894/rgci269.

Capitão, R.; Fortes, C.J.; Santos, J.A.; and Pinheiro, L. (2009). In-situ and Model Wave Characterization at the Alfeite Beach. *Journal of Coastal Research*, (56), 168–172. Retrieved from http://www.jstor.org/stable/25737559.

Carbajal, N.; and Montaño, Y. (2001). Comparison between Predicted and Observed Physical Features of Sandbanks. *Estuarine, Coastal and Shelf Science*, *52*(4), 435–443. https://doi.org/10.1006/ecss.2000.0760.

Castelle, B.; Guillot, B.; Marieu, V.; Chaumillon, E.; Hanquiez, V.; Bujan, S.; and Poppeschi, C. (2018). Spatial and temporal patterns of shoreline change of a 280-km high-energy disrupted sandy coast from 1950 to 2014: SW France. *Estuarine, Coastal and Shelf Science*, *200*, 212–223. https://doi.org/10.1016/j.ecss.2017.11.005.

Castilho, L.M. (2016). *Caraterização da evolução volumétrica do delta vazante do estuário do Guadiana para a otimização das estratégias de dragagem*. MSc Thesis in Coastal and Marine Systems, Faculty of Science and Technology of University of Algarve, Portugal. Retrieved from http://hdl.handle.net/10400.1/9872.

Centonze, G.; Leone, M.; and Aiello, M.A. (2012). Steel fibers from waste tires as reinforcement in concrete: A mechanical characterization. *Construction and Building Materials*, *36*, 46–57. https://doi.org/https://doi.org/10.1016/j.conbuildmat.2012.04.088.

CERC. (1984a). *Coastal Engineering Research Center. US Army Corps of Engineers - Shore Protection Manual Volume 2-1* (4th Ed.). Washington, DC, USA: U.S. Government Printing Office. Retrieved from http://ft-sipil.unila.ac.id/dbooks/S P M 1984 volume 2-1.pdf.

CERC. (1984b). *Coastal Engineering Research Center. US Army Corps of Engineers - Shore Protection Manual Volume 2-2* (4th Ed.). Washington, DC, USA: U.S. Government Printing Office. Retrieved from https://ft-sipil.unila.ac.id/dbooks/S P M 1984 volume 2-2.pdf.

Chand, N.; Tiwary, R.K.; and Rohatgi, P.K. (1988). Bibliography Resource structure properties of natural cellulosic fibres - an annotated bibliography. *Journal of Materials Science*, *23*(2), 381–387. https://doi.org/10.1007/BF01174659.

Chang, H.H. (1997). Modeling Fluvial Processes in Tidal Inlet. *Journal of Hydraulic Engineering*, *123*(12), 1161–1165. https://doi.org/10.1061/(ASCE)0733-9429(1997)123:12(1161).

Charlier, R.H.; Chaineux, M.C.P.; and Morcos, S. (2005). Panorama of the History of Coastal Protection. *Journal of Coastal Research*, *21*(1), 79–111. https://doi.org/10.2112/03561.1.

Coelho, C. (2005). *Riscos de exposição de frentes urbanas para diferentes intervenções de defesa costeira.* PhD Thesis in Civil Engineering, University of Aveiro. Retrieved from https://core.ac.uk/download/pdf/15562624.pdf.

Coelho, C.; Silva, R.; Veloso-Gomes, F.; and Taveira-Pinto, F. (2009). Potential effects of climate change on northwest Portuguese coastal zones. *ICES Journal of Marine Science*, *66*(7), 1497–1507. https://doi.org/10.1093/icesjms/fsp132.

Colajanni, P.; Fossetti, M.; and Macaluso, G. (2014). Effects of confinement level, cross-section shape and corner radius on the cyclic behavior of CFRCM confined concrete columns. *Construction and Building Materials*, *55*, 379–389. https://doi.org/https://doi.org/10.1016/j.conbuildmat.2014.01.035.

Concrete Layer Innovations. (2015). *CORE-LOC™ TID Abstract Version D 03-02-2015*. Retrieved from https://www.concretelayer.com/sites/default/files/2019-05/CORE-LOC™_Basic Specifications_Version D_0.pdf.

Corbett, B.; Jackson, L.A.; Evans, T.; and Restall, S. (2010). Comparison of geosynthetic materials as substrates on coastal structures – Gold Coast (Australia) and Arabian Gulf. In *Proceedings of 32nd Conference on Coastal Engineering, 30th June to 5th July 2010* (pp. 1–7). Shanghai, China. https://doi.org/10.9753/icce.v32.structures.69.

Costa, N.; Venancio, S.; Pinho, J.; and Vieira, J. (2017). Análise hidrodinâmica do estuário do rio Lima, Portugal, a partir de simulação numérica. *Ambiente & Agua - An Interdisciplinary Journal of Applied Science*, *12*(3), 476–488. https://doi.org/10.4136/ambi-agua.1925.

Costa, G.M.S. da. (2009). *Modelação de Quebramares Destacados*. MSc Thesis in Civil Engineering, Faculty of Engineering of University of Porto, Portugal. Retrieved from https://repositorio-aberto.up.pt/browse?type=author&value=Costa%2C+Gustavo+Manuel+Santos+da.

Daftardar, A.; Vashi, J.; and Vichare, S. (2016). Deflection in RCC Beam Covered with Sisal Cordage. *Advances in Engineering & Scientific Research*, *2*(1), 7. Retrieved from http://manuscript.advancejournals.org/uploads/70d59d920203d655e93c12da45e30dab1b0f5038d99126c3d323724282eef3dc/Manuscript/8675.pdf.

Dalfré, G.; and Barros, J.A.O. (2011). Experimental and numerical analysis of RC two-span slabs strengthened with NSM CFRP laminates. In *American Concrete Institute, ACI Special Publication: 10th International Symposium on Fiber Reinforced Polymer Reinforcement for Reinforced Concrete Structures, 2nd to 4th April 2010* (Vol. 2, pp. 1241–

1260). Tampa, Florida, USA. Retrieved from http://hdl.handle.net/1822/13153.

Dalrymple, R.W.; and Choi, K. (2007). Morphologic and facies trends through the fluvial–marine transition in tide-dominated depositional systems: A schematic framework for environmental and sequence-stratigraphic interpretation. *Earth-Science Reviews*, *81*(3–4), 135–174. https://doi.org/10.1016/j.earscirev.2006.10.002.

Dan, S.; Walstra, D.-J.R.; Stive, M.J.F.; and Panin, N. (2011). Processes controlling the development of a river mouth spit. *Marine Geology*, *280*(1–4), 116–129. https://doi.org/10.1016/j.margeo.2010.12.005.

de Alegria-Arzaburu, A.R.; Williams, J.J.; and Masselink, G. (2010). Application of XBeach to model storm response on a macrotidal gravel barrier. In *Proceedings of 32nd Conference on Coastal Engineering, 30th June to 5th July 2010* (pp. 1–15). Shanghai, China. https://doi.org/10.9753/icce.v32.sediment.39.

De Vet, P.L.M.; Mccall, R.T.; Den Bieman, J.P.; Stive, M.J.F.; and Van Ormondt, M. (2015). Modelling Dune Erosion, Overwash and Breaching at Fire Island (NY) During Hurricane Sandy. In *The Proceedings of the Coastal Sediments, 11th to 15th May 2015*. San Diego, California, USA: World Scientific. https://doi.org/doi:10.1142/9789814689977_0006.

Deltares. (2009). Building with Nature Guideline: Eco-concrete breakwater structures. IJmuiden, The Netherlands. Retrieved November 15, 2018, from https://publicwiki.deltares.nl/display/BTG/Eco-concrete+Structures+-+IJmuiden+-+NL.

Deltares. (2013). *Eco-engineering in the Netherlands. Soft interventions with a solid impact*. The Nertherlands. Retrieved from http://publications.deltares.nl/Deltares058.pdf.

Deltares. (2014). Eco-engineering. Retrieved February 25, 2014, from http://www.innoverenmetwater.nl/upload/documents/Eco engineering (brochure).pdf.

Deltares. (2019a). About Delft3D. Retrieved February 7, 2019, from https://oss.deltares.nl/web/delft3d/about.

Deltares. (2019b). Aqua Monitor. Retrieved March 16, 2019, from http://aqua-monitor.appspot.com.

Deltares. (2019c). Delft3D 4 Suite (structured). Retrieved February 7, 2019, from https://www.deltares.nl/en/software/delft3d-4-suite.

Deltares. (2019d). XBeach. Retrieved February 12, 2019, from https://www.deltares.nl/en/software/xbeach.

der Wegen, M. van; Dastgheib, A.; and Roelvink, J.A. (2010). Morphodynamic modeling of tidal channel evolution in comparison to empirical PA relationship. *Coastal Engineering*, *57*(9), 827–837. https://doi.org/10.1016/j.coastaleng.2010.04.003.

Di Bella, G.; Fiore, V.; Galtieri, G.; Borsellino, C.; and Valenza, A. (2014). Effects of natural fibres reinforcement in lime plasters (kenaf and sisal vs. Polypropylene). *Construction and Building Materials*, *58*, 159–165. https://doi.org/10.1016/j.conbuildmat.2014.02.026.

Di Bona, S. (2013). *Modelling of Coastline Evolution: Long-term Simulation in the Vagueira region (Portugal)*. University of Padova. Retrieved from http://tesi.cab.unipd.it/43715/1/Silvia_Di_Bona_626470IA.pdf.

Dias, J.M..; Jouanneau, J..; Gonzalez, R.; Araújo, M..; Drago, T.; Garcia, C.; Oliveira, A.; Rodrigues, A.; Vitorino, J.; and Weber, O. (2002). Present day sedimentary processes on the northern Iberian shelf. *Progress in Oceanography*, *52*(2–4), 249–259. https://doi.org/10.1016/S0079-6611(02)00009-5.

Dias, J.P.; Lourenço, L.; Barros, J.A.O.; and Oliveira, F. (2008). Aplicação de novos materiais e de modelos de análise não linear material no desenvolvimento de sistemas estruturais pré-fabricados para edifícios industriais. In *2º Congresso Nacional da Préfabricação em Betão, 6 a 7 de Março 2008*. Lisboa, Portugal: Associação Nacional dos Industriais da Prefabricação em Betão (ANIPB). Retrieved from http://hdl.handle.net/1822/12957.

Dinis, P.A.; Huvi, J.; Cascalho, J.; Garzanti, E.; Vermeesch, P.; and Callapez, P. (2016). Sand-spits systems from Benguela region (SW Angola). An analysis of sediment sources and dispersal from textural and compositional data. *Journal of African Earth Sciences*, *117*, 171–182. https://doi.org/10.1016/j.jafrearsci.2016.01.020.

Dupray, S.; and Roberts, J. (2010). Review of the use of concrete in the manufacture of concrete armour units. *Coasts, Marine Structures and Breakwaters: Adapting to Change*, *1*, 245–259. https://doi.org/10.1680/cmsb.41301.0021.

Dyer, K.R.; and Huntley, D.A. (1999). The origin, classification and modelling of sand banks and ridges. *Continental Shelf Research*, *19*(10), 1285–1330. https://doi.org/10.1016/S0278-4343(99)00028-X.

EC2. (2004). Eurocode 2 - Design of Concrete Structures—Part 1-1: General rules and rules for buildings, CEN, EN 1992-1-1. Brussels, Belgium.

Elias, E.P.L.; and van der Spek, A.J.F. (2006). Long-term morphodynamic evolution of Texel Inlet and its ebb-tidal delta (The Netherlands). *Marine Geology*, *225*(1–4), 5–21. https://doi.org/10.1016/j.margeo.2005.09.008.

Fabi, G.; Spagnolo, A.; Bellan-Santini, D.; Charbonnel, E.; Çiçek, B.A.; García, Juan J. Goutayer, Jensen, A.C.; Kallianiotis, A.; and Santos, M.N. dos. (2011). Overview on artificial reefs in Europe. *Brazilian Journal of Oceanography*, *59*, 155–166. Retrieved from http://www.scielo.br/scielo.php?pid=S1679-87592011000500017&script=sci_arttext&tlng=es.

Farber, S.; Costanza, R.; Childers, D.L.; Erickson, J.; Gross, K.; Grove, M.; Hopkinson, C.S.; Kahn, J.; Pincetl, S.; Troy, A.; Warren, P.; and Wilson, M. (2006). Linking Ecology and Economics for Ecosystem Management. *BioScience*, *56*(2), 121–133. https://doi.org/10.1641/0006-3568(2006)056[0121:LEAEFE]2.0.CO;2.

Faustino, P.; Chastre, C.; and Paula, R. (2014). Design model for square RC columns under compression confined with CFRP. *Composites Part B: Engineering*, *57*, 187–198. https://doi.org/https://doi.org/10.1016/j.compositesb.2013.09.052.

Ferreira, C.; Silva, P.; Fernández-Fernández, S.; Baptista, P.; Abreu, T.; Romão, S.; Fontán Bouzas, A.; and Bertin, X. (2017). Modelação da agitação marítima na região da Figueira da Foz. In *Livro de resumos da 4ª Conferência sobre Morfodinâmica Estuarina e Costeira, 18 a 19 de Maio 2017*. Porto, Portugal. Retrieved from https://www.researchgate.net/profile/Paulo_Silva32/publication/317041595_Modelacao_da_agitacao_maritima_n a_regiao_da_Figueira_da_Foz/links/59d8e6c0458515a5bc2623eb/Modelacao-da-agitacao-maritima-na-regiao-da-Figueira-da-Foz.pdf.

Ferreira, Ó.; Garcia, T.; Matias, A.; Taborda, R.; and Dias, J.A. (2006). An integrated method for the determination of set-back lines for coastal erosion hazards on sandy shores. *Continental Shelf Research*, *26*(9), 1030–1044. https://doi.org/10.1016/j.csr.2005.12.016.

Firth, L.B.; Thompson, R.C.; Bohn, K.; Abbiati, M.; Airoldi, L.; Bouma, T.J.; Bozzeda, F.; Ceccherelli, V.U.; Colangelo, M.A.; Evans, A.; Ferrario, F.; Hanley, M.E.; Hinz, H.; Hoggart, S.P.G.; Jackson, J.E.; Moore, P.; Morgan, E.H.; Perkol-Finkel, S.; Skov, M.W.; Strain, E.M.; van Belzen, J.; and Hawkins, S.J. (2014). Between a rock and a hard place: Environmental and engineering considerations when designing coastal defence structures. *Coastal Engineering*, *87*, 122–135. https://doi.org/10.1016/j.coastaleng.2013.10.015.

FitzGerald, D..; Buynevich, I..; Davis, R..; and Fenster, M.. (2002). New England tidal inlets with special reference to riverine-associated inlet systems. *Geomorphology*, *48*(1–3), 179–208. https://doi.org/10.1016/S0169-555X(02)00181-2.

FitzGerald, D.M. (1988). *Shoreline Erosional-Depositional Processes Associated with Tidal Inlets*. (D. Aubrey & L. Weishar, Eds.), *Hydrodynamics and Sediment Dynamics of Tidal Inlets*. New York, NY: Springer Science+Business Media, LLC. https://doi.org/10.1007/978-1-4757-4057-8_11.

FitzGerald, D.M. (1996). Geomorphic Variability and Morphologic and Sedimentologic Controls on Tidal Inlets. *Journal of Coastal Research*, (23), 47–71. https://doi.org/10.2307/25736068.

Fitzgerald, D.M.; Kraus, N.C.; and Hands, E.B. (2000). *Natural Mechanisms of Sediment Bypassing at Tidal Inlets*. ERDC/CHL CHETN-IV-30 (Engineer Research and Development Center Vicksburg MS Coastal and Hydraulics Lab.). Vicksburg, Mississipi, USA. Retrieved from https://apps.dtic.mil/dtic/tr/fulltext/u2/a588774.pdf.

Franco, L.; Noli, A.; De Girolamo, P.; and Ercolani, M. (2000). Concrete strength and durability of prototype tetrapods and dolosse: results of field and laboratory tests. *Coastal Engineering*, *40*(3), 207–219. https://doi.org/https://doi.org/10.1016/S0378-3839(00)00011-9.

Frazão, C.M.V. (2019). *Recycled Steel Fiber Reinforced Concrete for Structural elements subjected to chloride attack: Mechanical and Durability performance*. PhD Thesis in Civil Engineering, University of Minho, Portugal. Retrieved from http://hdl.handle.net/1822/66884.

Frazão, C.M.V; Barros, J.A.O.; and Bogas, J.A. (2019). Durability of Recycled Steel Fiber Reinforced Concrete in Chloride Environment. *Fibers*, *7*(12). https://doi.org/10.3390/fib7120111.

Freitas, P. (2013). Hydraulic stability of antifer block armour layers. Physical model study. Retrieved from https://fenix.tecnico.ulisboa.pt/downloadFile/395145277327/Resumo alargado_Paulo_Freitas.pdf.

French, P.W. (2001). *Coastal Defences* (1st Ed.). London, UK: Routledge. https://doi.org/10.4324/9780203187630.

Frens, A.B. (2007). *The impact of placement method on Antifer-block stability*. MSc Thesis in Coastal Engineering, Faculty of Civil Engineering and Geosciences of the Delft University of Technology, The Netherlands. https://doi.org/https://doi.org/10.4233/uuid:0528aadb-3415-43d0-876e-b0f399395030.

Garel, E.; Sousa, C.; Ferreira, Ó.; and Morales, J.A. (2014). Decadal morphological response of an ebb-tidal delta and down-drift beach to artificial breaching and inlet stabilisation. *Geomorphology*, *216*, 13–25. https://doi.org/10.1016/j.geomorph.2014.03.031.

GiD-FEMIX. (2017). Overview. Retrieved February 11, 2019, from http://gidfemix.civil.uminho.pt.

Giri, C.; Ochieng, E.; Tieszen, L.L.; Zhu, Z.; Singh, A.; Loveland, T.; Masek, J.; and Duke, N. (2011). Status and distribution of mangrove forests of the world using earth observation satellite data. *Global Ecology and Biogeography*, *20*(1), 154–159. https://doi.org/10.1111/j.1466-8238.2010.00584.x.

Goldberg, W.M. (2013). *The Biology of Reefs and Reef Organisms*. Chicago, USA: University of Chicago Press.

Gomes, A.; Pinho, J.; and Granja, H. (2018). Morphodynamic modelling of a gravel beach at the NW Portuguese coast. In *IX Simpósio da Margem Ibérica Atlântica, 4 a 7 de Setembro 2018*. Coimbra, Portugal.

Gómez-Martín, M.E.; and Medina, J.R. (2008). Erosion of cube and cubipod armor layers under wave attack. In *Proceedings of the 31st International Conference, 31st August to 5th September 2008* (pp. 3461–3473). Hamburg, Germany: World Scientific Publishing Company. https://doi.org/doi:10.1142/9789814277426_0287.

Gonçalves, D.; Dias, J.P.; Lourenço, L.; Barros, J.A.O.; and Sampaio, C. (2008). Painéis pré-fabricados em betão autocompactável reforçado com fibras de aço para fachadas de edifícios. In *2º Congresso Nacional da Préfabricação em betão – ANIPB, 6 a 7 de Março 2008*. Lisboa, Portugal. Retrieved from http://hdl.handle.net/1822/13018.

Goud, T. (2020). *Rocking revisited 4: Analysis of rocking-induced stresses for concrete breakwater armour units*. MSc Thesis in Hydraulic Engineering, Delft University of Technology, The Netherlands. Retrieved from http://resolver.tudelft.nl/uuid:f2613769-08af-404a-b1a0-1d076318edcd.

Granja, H.; Pinho, J.; and Mendes, J. (2014). A Multi-criteria Approach for Erosion Risk Assessment Using a New Concept of Spatial Unit Analysis, Wave Model and High Resolution DEMs. In C. Finkl & C. Makowski (Eds.), *Remote Sensing and Modeling* (pp. 481–494). Cham, Switzerland: Springer. https://doi.org/10.1007/978-3-319-06326-3_20.

Granja, H.; Pinho, J.; and Silva, A. (2015). Praias de Seixos na Costa NW Portuguesa: Génese e Morfodinâmica de Curto Termo. In *VII Congresso Nacional de Geomorfologia, 8 a 9 de Outubro 2015*. Lisboa, Portugal. Retrieved from https://www.researchgate.net/publication/296701549.

Gratiot, N.; Gardel, A.; and Anthony, E.J. (2007). Trade-wind waves and mud dynamics on the French Guiana coast, South America: Input from ERA-40 wave data and field investigations. *Marine Geology*, *236*(1–2), 15–26. https://doi.org/10.1016/j.margeo.2006.09.013.

Griggs, G.B. (2005). The impacts of coastal armoring. *Shore and Beach*, *73*(1), 13–22. Retrieved from https://www.researchgate.net/publication/285969581_The_impacts_of_coastal_armoring.

Grunnet, N.M.; Ruessink, B.G.; and Walstra, D.-J.R. (2005). The influence of tides, wind and waves on the redistribution of nourished sediment at Terschelling, The Netherlands. *Coastal Engineering*, *52*(7), 617–631. https://doi.org/10.1016/j.coastaleng.2005.04.001.

Grunnet, N.M.; Walstra, D.-J.R.; and Ruessink, B.G. (2004). Process-based modelling of a shoreface nourishment. *Coastal Engineering*, *51*(7), 581–607. https://doi.org/10.1016/j.coastaleng.2004.07.016.

Gutiérrez, M.H.; Pantoja, S.; Tejos, E.; and Quiñones, R.A. (2011). The role of fungi in processing marine organic matter in the upwelling ecosystem off Chile. *Marine Biology*, *158*(1), 205–219. https://doi.org/10.1007/s00227-010-1552-z.

Hakenberg, R.; Vos-Rovers, I.; Reedijk, B.; and Muttray, M. (2004). Structural integrity of Xbloc® breakwater armour units prototype and numerical drop tests. In *International Conference on Coastal Engineering, 19th to 24th September 2004*. Lisbon, Portugal. https://doi.org/10.1142/9789812701916_0363.

Harajli, M.H. (2006). Axial stress–strain relationship for FRP confined circular and rectangular concrete columns. *Cement and Concrete Composites*, *28*(10), 938–948. https://doi.org/https://doi.org/10.1016/j.cemconcomp.2006.07.005.

Hartog, W.M.; Benedet, L.; Walstra, D.-J.R.; van Koningsveld, M.; Stive, M.J.F.; and Finkl, C.W. (2008). Mechanisms that Influence the Performance of Beach Nourishment: A Case Study in Delray Beach, Florida, U.S.A. *Journal of Coastal Research*, *24*(5), 1304–1319. https://doi.org/10.2112/06-0749.1.

Hasselmann, K.; Barnett, T.P.; Bouws, E.; Carlson, H.; Cartwright, D.E.; Enke, K.; Ewing, J.A.; Gienapp, H.; Hasselmann, D.E.; Kruseman, P.; Meerburg, A.; Müller, P.; Olbers, D.J.; Richter, K.; Sell, W.; and Walden, H. (1973). *Measurements of wind-wave growth and swell decay during the Joint North Sea Wave Project (JONSWAP)*. *Ergänzungsheft 8-12*. Deutches Hydrographisches Institut. Retrieved from http://resolver.tudelft.nl/uuid:f204e188-

13b9-49d8-a6dc-4fb7c20562fc.

Hayes, M. (1979). Barrier Island Morphology as a Function of Tidal and Wave Regime. In S. Leatherman (Ed.), *Barrier islands: from the Gulf of St. Lawrence to the Gulf of Mexico* (pp. 1–27).

Hayes, M. (1980). General morphology and sediment patterns in tidal inlets. *Sedimentary Geology*, *26*(1–3), 139–156. https://doi.org/10.1016/0037-0738(80)90009-3.

Hayes, M.O. (2005). Barrier Islands. In M. Schwartz (Ed.), *Encyclopedia of Coastal Science* (pp. 117–119). Dordrecht, the Netherlands: Springer. Retrieved from https://www.academia.edu/1157484/Encyclopedia_of_Coastal_Science.

Heerten, G.; Jackson, A.; Restall, S.; and Saathoff, F. (2001). New Geotextile Developments with Mechanically-Bonded Nonwoven Sand Containers as Soft Coastal Structures. In B. L. Edge (Ed.), *27th International Conference on Coastal Engineering (ICCE), 16th to 21st July 2000* (pp. 2342–2355). Sydney, Australia: American Society of Civil Engineers. https://doi.org/10.1061/40549(276)183.

Hendrikse, C.; and Heijboer, D. (2014). Hydraulic design conditions and marine structures design philosophy: The UAE Case. In *The 7th Annual Arabian World Construction Summit, 12th to 14th May 2014*. Dubai, UAE.

Herbich, J.B. (2000). *Handbook of coastal engineering*. New York, USA: McGraw-Hill. Retrieved from https://trove.nla.gov.au/work/5447084?q&versionId=6737024.

Hettiarachchi, S.S.L. (1987). *The influence of geometry on the performance of breakwater armour units*. PhD Thesis in Civil Engineering, Imperial College of Science and Technology of the University of London, UK. Retrieved from https://spiral.imperial.ac.uk/bitstream/10044/1/47170/2/Hettiarachchi-SSL-1987-PhD-Thesis.pdf.

Hoan, L.X.; Hanson, H.; Larson, M.; and Kato, S. (2011). A mathematical model of spit growth and barrier elongation: Application to Fire Island Inlet (USA) and Badreveln Spit (Sweden). *Estuarine, Coastal and Shelf Science*, *93*(4), 468–477. https://doi.org/10.1016/j.ecss.2011.05.033.

Hoff, G.C. (1975). *Use of Fiber-Reinforced Concrete in Hydraulic Structures and Marine Environments*. Vicksburg, Mississippi, USA. Retrieved from https://usace.contentdm.oclc.org/digital/api/collection/p266001coll1/id/5840/download.

Hong, S.T. (2019). Physical implications of "mangrove squeeze" for coastal stability. *TU Delft DeltaLinks*, 1–8. Retrieved from http://flowsplatform.nl/documents/Physical implications of mangrove squeeze for coastal stability_Son Truong Hong_DeltaLinks.pdf.

Hu, H.; Papastergiou, P.; Angelakopoulos, H.; Guadagnini, M.; and Pilakoutas, K. (2018). Mechanical properties of SFRC using blended manufactured and recycled tyre steel fibres. *Construction and Building Materials*, *163*, 376–389. https://doi.org/https://doi.org/10.1016/j.conbuildmat.2017.12.116.

Hussain, Q.; Ruangrassamee, A.; Tangtermsirikul, S.; and Joyklad, P. (2020). Behavior of concrete confined with epoxy bonded fiber ropes under axial load. *Construction and Building Materials*, *263*, 120093. https://doi.org/https://doi.org/10.1016/j.conbuildmat.2020.120093.

Hussain, Q.; Shoaib, S.; and Joyklad, P. (2017). Confinement of Concrete by Rope. In *Proceedings of the 2nd International Symposium on Mechanical Engineering and Material Science, 17th to 19th November 2017* (pp. 86–89). Suzhou, China: Atlantis Press. https://doi.org/https://doi.org/10.2991/ismems-17.2018.20.

Instituto Português da Qualidade. (2009). NP EN 12350-2 - Ensaios do betão fresco. Parte 2: Ensaio de abaixamento.

Janwaen, W.; Barros, J.A.; and Costa, I.G. (2019). A new strengthening technique for increasing the load carrying capacity of rectangular reinforced concrete columns subjected to axial compressive loading. *Composites Part B: Engineering*, *158*, 67–81. https://doi.org/https://doi.org/10.1016/j.compositesb.2018.09.045.

Jarrett, J.T. (1976). *Tidal prism-inlet area relationships*. Vicksburg, Mississipi, USA: Army Engineer Waterways Experiment Station.

Jennings, R.; and Shulmeister, J. (2002). A field based classification scheme for gravel beaches. *Marine Geology*, *186*(3–4), 211–228. https://doi.org/10.1016/S0025-3227(02)00314-6.

Jensen, O.J. (2015). Safety of Breakwater Armour Layers with Special Focus on Monolayer Armour Units. In *From Sea to Shore – Meeting the Challenges of the Sea* (pp. 33–44). https://doi.org/10.1680/fsts.59757.005.

Jirawattanasomkul, T.; Ueda, T.; Likitlersuang, S.; Zhang, D.; Hanwiboonwat, N.; Wuttiwannasak, N.; and Horsangchai, K. (2019). Effect of natural fibre reinforced polymers on confined compressive strength of concrete. *Construction and*

Building Materials, *223*, 156–164. https://doi.org/https://doi.org/10.1016/j.conbuildmat.2019.06.217.

Jong, T. (1996). *Stability of Tetrapods at Front Crest and Rear of a Low-Crested Breakwater. Delft Hydraulics Publication No. 453, Delft Hydraulics Laboratory, The Netherlands*.

Kernkamp, H.W.J.; Petit, H.A.H.; Gerritsen, H.; and de Goede, E.D. (2005). A unified formulation for the three-dimensional shallow water equations using orthogonal co-ordinates: theory and application. *Ocean Dynamics*, *55*(3–4), 351–369. https://doi.org/10.1007/s10236-005-0017-2.

Kirwan, M.L.; Guntenspergen, G.R.; D'Alpaos, A.; Morris, J.T.; Mudd, S.M.; and Temmerman, S. (2010). Limits on the adaptability of coastal marshes to rising sea level. *Geophysical Research Letters*, *37*(23). https://doi.org/10.1029/2010GL045489.

Koffler, A.; Choura, M.; Bendriss, A.; and Zengerink, E. (2008). Geosynthetics in protection against erosion for river and coastal banks and marine and hydraulic construction. *Journal of Coastal Conservation*, *12*(1), 11–17. https://doi.org/10.1007/s11852-008-0023-x.

Köroğlu, M. (2019). Behavior of composite self-compacting concrete (SCC) reinforced with steel wires from waste tires. *Revista de La Construcción*, *17*, 484–498. https://doi.org/10.7764/RDLC.17.3.484

Kraus, N.C. (1999). Analytical model of spit evolution at inlets. In *Coastal Sediments '99: Proceedings of the 4th International Symposium on Coastal Engineering and Science of Coastal Sediment Processes: Confrence Theme: Scales of Coastal, 21st to 23rd June 1999* (pp. 1739–1754). Hauppauge, New York, USA.

Kraus, N.C. (2000). Reservoir Model of Ebb-Tidal Shoal Evolution and Sand Bypassing. *Journal of Waterway, Port, Coastal, and Ocean Engineering*, *126*(6), 305–313. https://doi.org/10.1061/(ASCE)0733-950X(2000)126:6(305).

Laïbi, R.A.; Anthony, E.J.; Almar, R.; Castelle, B.; Senechal, N.; and Kestenare, E. (2014). Longshore drift cell development on the human-impacted Bight of Benin sand barrier coast, West Africa. *Journal of Coastal Research*, (70), 78–83. https://doi.org/10.2112/SI70-014.1.

Leuven, J.R.F.W.; Kleinhans, M.G.; Weisscher, S.A.H.; and van der Vegt, M. (2016). Tidal sand bar dimensions and shapes in estuaries. *Earth-Science Reviews*, *161*, 204–223. https://doi.org/10.1016/j.earscirev.2016.08.004.

Lima, M. (2011). *Programação de métodos de pré-dimensionamento de obras costeiras*. MSc Thesis in Civil Engineering, University of Aveiro, Portugal. https://doi.org/10.13140/RG.2.1.2650.9681.

Lima, P.R.L.; Santos, D.O.J.; Fontes, C.M.A.; Barros, J.A.O.; and Toledo Filho, R.D. (2016). Deflection hardening of sustainable fiber–cement composites. *Green Materials*, *4*(1), 18–30. https://doi.org/10.1680/jgrma.15.00018.

Loureiro, E. (2006). *Indicadores Geomorfológicos e Sedimentalógicos na Avaliação da Tendência Evolutiva da Zona Costeira: Aplicação ao concelho de Esposende*. Tese de Doutoramento em Geologia, Universidade do Minho. Retrieved from http://hdl.handle.net/1822/7096.

Lourenço, L.; Barros, J.A.O.; Santos, S.P.F.; and Mesquita, A. (2006). Análise estrutural de aduela prefabricada em betão reforçado com fibras para o revestimento de túneis. In *4.s Jornadas Portuguesas de Engenharia de Estruturas, 13 a 16 de Dezembro 2006*. Lisboa, Portugal. Retrieved from http://hdl.handle.net/1822/5991.

Lourenço, L.; Zamanzadeh, Z.; Barros, J.A.O.; and Rezazadeh, M. (2018). Shear strengthening of RC beams with thin panels of mortar reinforced with recycled steel fibres. *Journal of Cleaner Production*, *194*, 112–126. https://doi.org/https://doi.org/10.1016/j.jclepro.2018.05.096.

Luijendijk, A.P.; Ranasinghe, R.; de Schipper, M.A.; Huisman, B.A.; Swinkels, C.M.; Walstra, D.J.R.; and Stive, M.J.F. (2017). The initial morphological response of the Sand Engine: A process-based modelling study. *Coastal Engineering*, *119*, 1–14. https://doi.org/10.1016/j.coastaleng.2016.09.005.

Luo, J.; Li, M.; Sun, Z.; and O'Connor, B.A. (2013). Numerical modelling of hydrodynamics and sand transport in the tide-dominated coastal-to-estuarine region. *Marine Geology*, *342*, 14–27. https://doi.org/10.1016/j.margeo.2013.06.004.

Marcos-Meson, V.; Michel, A.; Solgaard, A.; Fischer, G.; Edvardsen, C.; and Skovhus, T.L. (2018). Corrosion resistance of steel fibre reinforced concrete - A literature review. *Cement and Concrete Research*, *103*, 1–20. https://doi.org/https://doi.org/10.1016/j.cemconres.2017.05.016.

McCall, R.T.; Masselink, G.; Poate, T.G.; Roelvink, J.A.; and Almeida, L.P. (2015). Modelling the morphodynamics of gravel beaches during storms with XBeach-G. *Coastal Engineering*, *103*, 52–66. https://doi.org/10.1016/j.coastaleng.2015.06.002.

McHarg, I.L. (1995). *Design with nature*. New York, USA: Turtleback Books.

Melby, J.A.; and Turk, G.F. (1992). Dolos design using reliability methods. *Coastal Engineering Proceedings*, *1*(23 SE-Conference Proceedings). https://doi.org/10.9753/icce.v23.%p.

Mendonça, A.; Fortes, C.J.; Capitão, R.; Neves, M. da G.; Moura, T.; and Antunes do Carmo, J.S. (2012). Wave hydrodynamics around a multi-functional artificial reef at Leirosa. *Journal of Coastal Conservation*, *16*(4), 543–553. https://doi.org/10.1007/s11852-012-0196-1.

Mendonça, A.; Fortes, C.J.E.M.; and Oliveira, F.S.B.F. (2021). Modelação numérica: Análise dos parâmetros de surfabilidade de um quebra-mar destacado multinfuncional em frente à praia da Vagueira. In *15º Congresso da Água, 22 a 26 de Março 2021*. Lisboa, Portugal. Retrieved from https://www.aprh.pt/congressoagua2021/docs/15ca_145.pdf.

Mendonça, A.; Proença, B.; Fortes, C.; and Neves, A. (2010). Estudo da hidrodinâmica em torno do recife artificial para a prática do surf a construir em São Pedro do Estoril, Cascais. Aplicação dos Modelos de Boussinesq: COULWAVE e FUNWAVE. *Revista Da Gestão Costeira Integrada*, *10*(1), 95–125. https://doi.org/10.5894/rgci169.

Mirmiran, A.; Shahawy, M.; Samaan, M.; Echary, H. El; Mastrapa, J.C.; and Pico, O. (1998). Effect of Column Parameters on FRP-Confined Concrete. *Journal of Composites for Construction*, *2*(4), 175–185. https://doi.org/10.1061/(ASCE)1090-0268(1998)2:4(175).

Misdorp, R.; and Salman, A. (2011). *Climate of Coastal Cooperation*. Leiden, The Netherlands: European Union of Coast Conservation (EUCC - Coastal & Marine Union). Retrieved from http://resolver.tudelft.nl/uuid:0eef9ca8-ab24-467b-962d-12296a2fb136.

Mitsch, W.J.; and Jørgensen, S.E. (2004). *Ecological engineering and ecosystem restoration*. Hoboken, New Jersey: John Wiley & Sons, Inc.

Muttray, M.; and Costal, S. (2006). Placement and Structural Strength of Xbloc and Other Single Layer Armour Units. Retrieved from https://www.researchgate.net/publication/266049105_Placement_and_Structural_Strength_of_Xbloc_and_Other_Single_Layer_Armour_Units.

Myrick, G.; and Melby, J. (2005). *Monitoring of Dolos Armor Units at Crescent City, California*. Retrieved from https://www.researchgate.net/publication/235203900_Monitoring_of_Dolos_Armor_Units_at_Crescent_City_California.

Neal, W.J.; Pilkey, O.H.; Cooper, J.A.G.; and Longo, N.J. (2018). Why coastal regulations fail. *Ocean & Coastal Management*, *156*, 21–34. https://doi.org/10.1016/j.ocecoaman.2017.05.003.

Nederhoff, C.M.; Lodder, Q.J.; Boers, M.; Den Bieman, J.P.; and Miller, J.K. (2015). Modeling the effects of hard structures on dune erosion and overwash: A case study of the impact of Hurricane Sandy on the New Jersey coast. In *The Proceedings of the Coastal Sediments, 11th to 15th May 2015*. San Diego, California, USA: World Scientific. https://doi.org/10.1142/9789814689977_0219.

NHC. (2012). *Northwest Hydraulic Consultants. Yolo Bypass MIKE-21 Model Review: Strengths, Limitations and Recommendations for Refinement*. Retrieved from http://baydeltaconservationplan.com/Libraries/Dynamic_Document_Library/YBFE_Planning_Team_-_Revised_Yolo_Bypass_MIKE_21_Model_Review_Report_9-21-12.sflb.ashx.

Nisticò, N.; Pallini, F.; Rousakis, T.; Wu, Y.-F.; and Karabinis, A. (2014). Peak strength and ultimate strain prediction for FRP confined square and circular concrete sections. *Composites Part B: Engineering*, *67*, 543–554. https://doi.org/https://doi.org/10.1016/j.compositesb.2014.07.026.

Nwogu, O.G.; and Demirbilek, Z. (2001). *BOUSS-2D: A Boussinesq wave model for coastal regions and harbors. Theoretical Background and User's Manual, U.S. Army Corps of Engineers*. Washington, DC, USA. Retrieved from https://apps.dtic.mil/dtic/tr/fulltext/u2/a400294.pdf.

Oertel, G.F. (1975). Ebb-tidal Deltas of Georgia Estuaries. *Geology and Engineering*, 267–276. https://doi.org/10.1016/B978-0-12-197502-9.50021-6.

Oh, Y.I.; and Shin, E.C. (2006). Using submerged geotextile tubes in the protection of the E. Korean shore. *Coastal Engineering*, *53*(11), 879–895. https://doi.org/10.1016/j.coastaleng.2006.06.005.

Oliveira, K. (2010). *Comportamento da Maré e das Correntes de Maré em um Sistema Estuarino utilizando o modelo*

Regional Ocean Modeling System (ROMS). Bacharelato em Oceanografia, Universidade Federal do Espírito Santo. Retrieved from http://www.oceanografia.ufes.br/sites/oceanografia.ufes.br/files/field/anexo/KYSSYANNE SAMIHRA SANTOS OLIVEIRA.pdf.

Olusegun, D.S.; Stephen, A.; and Adekanye, T.A. (2012). Assessing Mechanical Properties of Natural Fibre Reinforced Composites for Engineering Applications. *Journal of Minerals and Materials Characterization and Engineering*, *11*(1), 780–784. https://doi.org/10.4236/jmmce.2012.118066.

Ondiviela, B.; Losada, I.J.; Lara, J.L.; Maza, M.; Galván, C.; Bouma, T.J.; and van Belzen, J. (2014). The role of seagrasses in coastal protection in a changing climate. *Coastal Engineering*, *87*, 158–168. https://doi.org/10.1016/j.coastaleng.2013.11.005.

Onuaguluchi, O.; and Banthia, N. (2018). Scrap tire steel fiber as a substitute for commercial steel fiber in cement mortar: Engineering properties and cost-benefit analyses. *Resources, Conservation and Recycling*, *134*, 248–256. https://doi.org/https://doi.org/10.1016/j.resconrec.2018.03.014.

OR. (2014). Ocean Revival. Artificial reefs. Retrieved February 25, 2014, from http://www.oceanrevival.pt/en/projecto/recifes-artificias.html.

Padanattil, A.; Karingamanna, J.; and K.M., M. (2017). Novel hybrid composites based on glass and sisal fiber for retrofitting of reinforced concrete structures. *Construction and Building Materials*, *133*, 146–153. https://doi.org/https://doi.org/10.1016/j.conbuildmat.2016.12.045.

Padanattil, A.; Lakshmanan, M.; Jayanarayanan, K.; and Mini, K.M. (2019). Strengthening of Plain Concrete Cylinders with Natural FRP Composite Systems. *Iranian Journal of Science and Technology, Transactions of Civil Engineering*, *43*(3), 381–389. https://doi.org/10.1007/s40996-018-0197-x.

Palmeira, E.M.; Tatsuoka, F.; Bathurst, R.J.; Stevenson, P.E.; and Zornberg, J.G. (2008). Advances in Geosynthetics Materials and Applications for Soil Reinforcement and Environmental Protection Works. *Electronic Journal of Geotechnical Engineering*, *13*, 1–38. Retrieved from https://www.researchgate.net/publication/228631055_Advances_in_Geosynthetics_Materials_and_Applications_for_Soil_Reinforcement_and_Environmental_Protection_Works.

Parveen, S.; Rana, S.; and Fangueiro, R. (2012). Natural fiber composites for structural applications. In A. J. M. Ferreira & E. Carrera (Eds.), *International Conference on Mechanics of Nano, Micro and Macro Composite Structures, 18th to 20th June 2012*. Turin, Italy. Retrieved from http://paginas.fe.up.pt/%0Awicnmmcs/.

Penland, S.; and Kulp, M.A. (2005). Deltas. In M. L. Schwartz (Ed.), *Encyclopedia of Coastal Science* (pp. 362–368). Dordrecht, the Netherlands: Springer. Retrieved from https://www.academia.edu/1157484/Encyclopedia_of_Coastal_Science.

Petersen, D.; Deigaard, R.; and Fredsøe, J. (2008). Modelling the morphology of sandy spits. *Coastal Engineering*, *55*(7–8), 671–684. https://doi.org/10.1016/j.coastaleng.2007.11.009.

Pilakoutas, K.; Neocleous, K.; and Tlemat, H. (2004). Reuse of tyre steel fibres as concrete reinforcement. In *Proceedings of the Institution of Civil Engineers - Engineering Sustainability* (Vol. 157, pp. 131–138). https://doi.org/10.1680/ensu.2004.157.3.131.

Pilarczyk, K. (2008). Alternatives for coastal protection. *Journal of Water Resources and Environmental Engineering*, *23*. Retrieved from http://citeseerx.ist.psu.edu/viewdoc/download?doi=10.1.1.452.8219&rep=rep1&type=pdf.

Pilkey, O.H.; and Cooper, J.A.G. (2014). *The Last Beach*. USA: Duke University Press.

Pilkey, O.H.; and Young, R. (2009). *The Rising Sea*. USA: Island Press.

Pinho, J.L.S.; Vieira, J.M.P.; and Antunes do Carmo, J.S. (2004). Hydroinformatic environment for coastal waters hydrodynamics and water quality modelling. *Advances in Engineering Software*, *35*(3–4), 205–222. https://doi.org/10.1016/J.ADVENGSOFT.2004.01.001.

Pita, C. (1985). *Considerações sobre a observação de quebra-mares de talude. Memória Nº 647*. Lisboa, Portugal.

Pita, C. (1986). *Dimensionamento hidráulico do manto resistente de quebra-mares de talude*. Lisboa, Portugal.

PLA. (2019). Port of London Authority. Tides - Definitions and Notes. Retrieved January 27, 2019, from http://www.pla.co.uk/Safety/Tides-Definitions-and-Notes.

Pradhan, U.; Mishra, P.; Mohanty, P.K.; and Behera, B. (2015). Formation, Growth and Variability of Sand Spit at Rushikulya

River Mouth, South Odisha Coast, India. In *Procedia Engineering, 7th to 10th September 2015* (Vol. 116, pp. 963–970). Chennai, India: Elsevier B.V. https://doi.org/10.1016/j.proeng.2015.08.387.

Pranzini, E. (2018). Shore protection in Italy: From hard to soft engineering ... and back. *Ocean & Coastal Management*, *156*, 43–57. https://doi.org/10.1016/j.ocecoaman.2017.04.018.

Pranzini, E.; and Williams, A.T. (2013). *Coastal Erosion and Protection in Europe* (1st Ed.). London, UK: Routledge. https://doi.org/10.4324/9780203128558.

Rangel-Buitrago, N.; Williams, A.; and Anfuso, G. (2018). Hard protection structures as a principal coastal erosion management strategy along the Caribbean coast of Colombia. A chronicle of pitfalls. *Ocean & Coastal Management*, *156*, 58–75. https://doi.org/https://doi.org/10.1016/j.ocecoaman.2017.04.006.

Reedijk, B.; Bakker, P.; and Klabbers, M. (2004). Introduction of the Xbloc Breakwater Armour Unit. *Terra et Aqua*, *94*. Retrieved   from https://www.researchgate.net/publication/275960538_Introduction_of_the_Xbloc_Breakwater_Armour_Unit.

Reedijk, B.; and Muttray, M. (2009). Design of Concrete Armour Layers. *Hansa International Maritime Journal*, *6*, 111–118. Retrieved from https://www.researchgate.net/publication/275960407_Design_of_Concrete_Armour_Layers.

Restall, S.; Jackson, L..; Heerten, G.; and Hornsey, W.. (2002). Case studies showing the growth and development of geotextile sand containers: an Australian perspective. *Geotextiles and Geomembranes*, *20*(5), 321–342. https://doi.org/10.1016/S0266-1144(02)00030-4.

Ribas, R.L. (2016). *Modelação de vigas de betão armado reforçadas à flexão com laminados de CFRP inseridos*. MSc Thesis in Civil Engineering, University of Minho, Portugal. Retrieved from http://hdl.handle.net/1822/49928.

Roelvink, D.; McCall, R.; Mehvar, S.; Nederhoff, K.; and Dastgheib, A. (2018). Improving predictions of swash dynamics in XBeach: The role of groupiness and incident-band runup. *Coastal Engineering*, *134*, 103–123. https://doi.org/https://doi.org/10.1016/j.coastaleng.2017.07.004.

Roelvink, D.; Reniers, A.; van Dongeren, A.; de Vries, J. van T.; McCall, R.; and Lescinski, J. (2009). Modelling storm impacts on beaches, dunes and barrier islands. *Coastal Engineering*, *56*(11–12), 1133–1152. https://doi.org/10.1016/j.coastaleng.2009.08.006.

Rousakis, T. (2012). Confinement of Concrete Columns by Fiber Rope Reinforcements. In *Proceedings of the 6th International Conference on FRP Composites in Civil Engineering, 13th to 15th June 2012*. Rome, Italy.

Rousakis, T. (2017). Natural fibre rebar cementitious composites - Chapter 9. In M. Fan & F. B. T.-A. H. S. N. F. C. in C. Fu (Eds.), *Advanced High Strength Natural Fibre Composites in Construction* (pp. 215–234). Woodhead Publishing. https://doi.org/https://doi.org/10.1016/B978-0-08-100411-1.00009-1.

Rousakis, T.; and Tourtouras, I. (2015). Modeling of passive and active external confinement of RC columns with elastic materia. *ZAMM Journal of Applied Mathematics and Mechanics: Zeitschrift Für Angewandte Mathematik Und Mechanik*, *95*(10), 1046–1057. https://doi.org/10.1002/zamm.201500014.

Rousakis, T.C. (2014). Elastic Fiber Ropes of Ultrahigh-Extension Capacity in Strengthening of Concrete through Confinement. *Journal of Materials in Civil Engineering*, *26*(1), 34–44. https://doi.org/10.1061/(ASCE)MT.1943-5533.0000796.

Rousakis, T.C.; and Tourtouras, I.S. (2014). RC columns of square section – Passive and active confinement with composite ropes. *Composites Part B: Engineering*, *58*, 573–581. https://doi.org/https://doi.org/10.1016/j.compositesb.2013.11.011.

Ruggiero, P.; Walstra, D.J.R.; Gelfenbaum, G.; and van Ormondt, M. (2009). Seasonal-scale nearshore morphological evolution: Field observations and numerical modeling. *Coastal Engineering*, *56*(11–12), 1153–1172. https://doi.org/https://doi.org/10.1016/j.coastaleng.2009.08.003.

Saathoff, F.; Oumeraci, H.; and Restall, S. (2007). Australian and German experiences on the use of geotextile containers. *Geotextiles and Geomembranes*, *25*(4–5), 251–263. https://doi.org/10.1016/j.geotexmem.2007.02.009.

Sadio, M.; Anthony, E.J.; Diaw, A.T.; Dussouillez, P.; Fleury, J.T.; Kane, A.; Almar, R.; and Kestenare, E. (2017). Shoreline Changes on the Wave-Influenced Senegal River Delta, West Africa: The Roles of Natural Processes and Human Interventions. *Water*, *9*(5), 357. https://doi.org/10.3390/w9050357.

Sahu, A.S. (2014). Coastal Geosynthetics Protection— an environmental appraisal. *Indian Journal of Spatial Science*, *5*(2), 55–61. Retrieved from https://www.researchgate.net/publication/277479070_Coastal_Geosynthetics_Protection-

_an_environmental_appraisal_Indian_Journal_of_Spatial_Science.

Salauddin, M. (2015). *Physical model tests on new armour block Crablock for breakwaters to come to preliminary design guidance*. MSc Thesis in Hydraulic Engineering, Delft University of Technology, The Netherlands. Retrieved from http://resolver.tudelft.nl/uuid:0d4daf90-d8fc-460f-8b42-fc1e33861b1a.

Salauddin, M.; Broere, A.; van der Meer, J.; Verhagen, H.; and Bijl, E. (2015). A New Symmetrical Unit for Breakwater Armour: First Tests. In *Proceedings of the 7th Coastal Structures conference, 9th to 11th September 2015 (authors version)*. Boston, USA. https://doi.org/10.13140/RG.2.1.3134.7289.

Sancho, F.; Oliveira, F.S.B.F.; Fortes, C.J.E.M.; Baptista, P.; and Roebeling, P. (2020). Estudo de caracterização e viabilidade de um quebra-mar destacado multifuncional em frente à Praia da Vagueira. In *6ᵃˢ Jornadas de Engenharia Hidrográfica / 1ᵃˢ Jornadas Luso-Espanholas de Hidrografia, 3 a 5 de Novembro 2020*. Lisboa, Portugal. Retrieved from http://repositorio.lnec.pt:8080/jspui/bitstream/123456789/1013285/2/6JEH_-_1JLEH_paper_110_alt.pdf.

Sapuan, S.M.; Leenie, A.; Harimi, M.; and Beng, Y.K. (2006). Mechanical properties of woven banana fibre reinforced epoxy composites. *Materials & Design*, *27*(8), 689–693. https://doi.org/10.1016/j.matdes.2004.12.016.

Schmidt, L.; Prista, P.; Saraiva, T.; Riordan, T.O.; and Gomes, C. (2013). Adapting governance for coastal change in Portugal. *Land Use Policy*, *31*, 314–325. https://doi.org/10.1016/j.landusepol.2012.07.012.

Schramkowski, G.P.; Schuttelaars, H.M.; and de Swart, H.E. (2002). The effect of geometry and bottom friction on local bed forms in a tidal embayment. *Continental Shelf Research*, *22*(11–13), 1821–1833. https://doi.org/10.1016/S0278-4343(02)00040-7.

Seminara, G.; and Tubino, M. (2001). Sand bars in tidal channels. Part 1. Free bars. *Journal of Fluid Mechanics*, *440*, 49–74. https://doi.org/10.1017/S0022112001004748.

Sen, T.; and Paul, A. (2015). Confining concrete with sisal and jute FRP as alternatives for CFRP and GFRP. *International Journal of Sustainable Built Environment*, *4*(2), 248–264. https://doi.org/https://doi.org/10.1016/j.ijsbe.2015.04.001.

Sen, T.; and Reddy, H.N.J. (2014). Flexural strengthening of RC beams using natural sisal and artificial carbon and glass fabric reinforced composite system. *Sustainable Cities and Society*, *10*, 195–206. https://doi.org/https://doi.org/10.1016/j.scs.2013.09.003.

Sena-Cruz, J.; Barros, J.A.O.; and Azevedo, Á.F.M. (2004). Modelação de vigas reforçadas com laminados de CFRP inseridos no betão de recobrimento. In *Encontro Nacional Betão Estrutural* (pp. 1–8). Porto, Portugal: Universidade do Porto. Faculdade de Engenharia (FEUP). Retrieved from http://hdl.handle.net/1822/3147.

Sengul, O. (2016). Mechanical behavior of concretes containing waste steel fibers recovered from scrap tires. *Construction and Building Materials*, *122*, 649–658. https://doi.org/https://doi.org/10.1016/j.conbuildmat.2016.06.113.

Sengul, O. (2018). Mechanical properties of slurry infiltrated fiber concrete produced with waste steel fibers. *Construction and Building Materials*, *186*, 1082–1091. https://doi.org/https://doi.org/10.1016/j.conbuildmat.2018.08.042.

Seymour, R.J. (2005). Longshore Sediment Transport. In M. L. Schwartz (Ed.), *Encyclopedia of Coastal Science* (pp. 600–600). Dordrecht, the Netherlands: Springer. Retrieved from https://www.academia.edu/1157484/Encyclopedia_of_Coastal_Science.

Shabana, S.K.; Athira, M.M.; Lalna, S.S.; Prasun, C.; Rafeekha, K.K.; Rajimol, K.R.; and Safna, A.M. (2015). Effect of Coir Rope Wrapping on the Compressive Strength of Short Axially Loaded Concrete Members. In *International Conference on Technological Advancements in Structures and Construction, 10th to 11th June 2015* (pp. 20–25). Retrieved from https://1library.net/document/q73r71ny-effect-wrapping-compressive-strength-axially-loaded-concrete-members.html.

Shayanfar, J.; Rezazadeh, M.; and Barros, J. (2020). Analytical Model to Predict Dilation Behavior of FRP Confined Circular Concrete Columns Subjected to Axial Compressive Loading. *Journal of Composites for Construction*, *24*(6). https://doi.org/10.1061/(ASCE)CC.1943-5614.0001087.

Shepard, C.C.; Crain, C.M.; and Beck, M.W. (2011). The Protective Role of Coastal Marshes: A Systematic Review and Meta-analysis. *PLOS ONE*, *6*(11), 1–11. https://doi.org/10.1371/journal.pone.0027374.

Shin, E.C.; and Oh, Y.I. (2007). Coastal erosion prevention by geotextile tube technology. *Geotextiles and Geomembranes*, *25*(4–5), 264–277. https://doi.org/10.1016/j.geotexmem.2007.02.003.

Silva, F.S.; Pinto, J.P.; and Almeida, S. (2009). Operational Wave Forecasting System for the Portuguese Coast. *Journal of Coastal Research*, (56), 1055–1059. Retrieved from http://www.jstor.org/stable/25737948.

Silva, P.; Coelho, C.; Abreu, T.; Baptista, P.; Bernardes, C.; Bouzas, Á.; Dias, J.; Pinheiro, L.; Ferreira, C.; Garrido, C.; Pereira, C.; Pinto, A.; Rua, J.; Lima, L.; and Vaz, N. (2015). Contribuição para o Estudo da Dinâmica Sedimentar na Embocadura do Porto da Figueira da Foz, Portugal. In *VIII Congresso sobre Planeamento e Gestão das Zonas Costeiras dos Países de Expressão Portuguesa, 14 a 16 de Outubro 2015*. Aveiro, Portugal: Associação Portuguesa dos Recursos Hídricos. Retrieved from http://www.aprh.pt/ZonasCosteiras2015/pdf/1A6_Artigo_053.pdf.

Silva, R.; Coelho, C.; Veloso-Gomes, F.; and Taveira-Pinto, F. (2007). Dynamic Numerical Simulation of Medium-term Coastal Evolution of the West Coast of Portugal. *Journal of Coastal Research*, (50), 263–267. Retrieved from https://www.jstor.org/stable/26481595.

Silva, A.P. da. (2014). *Estudo da morfodinâmica da praia de seixos de Belinho sob a influência de diferentes estados de agitação e tipos de maré*. Dissertação de Mestrado Integrado em Engenharia Civil, Universidade do Minho. Retrieved from http://hdl.handle.net/1822/36108.

Silvester, R.; and Hsu, J.R.C. (1997). *Coastal stabilization*. Singapore: World Scientific. Retrieved from https://trove.nla.gov.au/work/22832809?q&versionId=46592091.

Simioni, B.I.; and Esteves, L.S. (2010). Avaliação Qualitativa do Desempenho dos Recifes Artificiais Multifuncionais (RAM). *Revista Da Gestão Costeira Integrada*, *10*(1), 127–145. Retrieved from http://www.redalyc.org/html/3883/388340128008.

Simões, S.C.; Pereira, C.A.; Coelho, C.D.B.; and Antunes do Carmo, J.S. (2013). Quebramares destacados: Análises comparativas de eficiências de proteção na praia da Vagueira. *Recursos Hídricos*, *34*(2), 25–40. https://doi.org/10.5894/rh34n2-3.

Singh, A.P.; and Singhal, D. (2011). Permeability of Steel Fibre Reinforced Concrete Influence of Fibre Parameters. *Procedia Engineering*, *14*, 2823–2829. https://doi.org/https://doi.org/10.1016/j.proeng.2011.07.355.

Smallegan, S.M.; Irish, J.L.; and van Dongeren, A.R. (2017). Developed barrier island adaptation strategies to hurricane forcing under rising sea levels. *Climatic Change*, *143*(1–2), 173–184. https://doi.org/10.1007/s10584-017-1988-y.

Smith, E.; Wang, P.; and Zhang, J. (2003). Evaluation of the CERC Formula Using Large-Scale Model Data. In *Coastal and Hydraulics Laboratory - Engineer Research and Development Center Waterways Experiment Station* (p. 14). Vicksburg, Mississippi, USA. Retrieved from https://www.researchgate.net/publication/235130344_Evaluation_of_the_CERC_Formula_Using_Large-Scale_Model_Data.

Smith, P.E. (2016a). Design and specification of marine concrete structures - Chapter 3. In *Marine Concrete Structures* (pp. 65–114). https://doi.org/10.1016/B978-0-08-100081-6.00003-9.

Smith, P.E. (2016b). Types of marine concrete structures - Chapter 2. In *Marine Concrete Structures* (pp. 17–64). https://doi.org/10.1016/B978-0-08-100081-6.00002-7.

Soltanzadeh, F.; Barros, J.A.O.; and Santos, R.F.C. (2015). High performance fiber reinforced concrete for the shear reinforcement: Experimental and numerical research. *Construction and Building Materials*, *77*, 94–109. https://doi.org/10.1016/j.conbuildmat.2014.12.003.

Sousa, F.; and Alves, J.F. (2002). *Leixões: uma história portuária*. Porto, Portugal: APDL.

Souto, C.D. (1989). *Recolha de Elementos de Base no Instituto Hidrográfico. Obras de Defesa Costeira. Seminário* (Vol. 210).

Spalding, M.D.; Ruffo, S.; Lacambra, C.; Meliane, I.; Hale, L.Z.; Shepard, C.C.; and Beck, M.W. (2014). The role of ecosystems in coastal protection: Adapting to climate change and coastal hazards. *Ocean & Coastal Management*, *90*, 50–57. https://doi.org/10.1016/j.ocecoaman.2013.09.007.

Splinter, K.D.; Carley, J.T.; Golshani, A.; and Tomlinson, R. (2014). A relationship to describe the cumulative impact of storm clusters on beach erosion. *Coastal Engineering*, *83*, 49–55. https://doi.org/10.1016/j.coastaleng.2013.10.001.

Splinter, K.D.; and Palmsten, M.L. (2012). Modeling dune response to an East Coast Low. *Marine Geology*, *329–331*, 46–57. https://doi.org/10.1016/j.margeo.2012.09.005.

Stauble, D.K.; and Morang, A. (1992). *Using Morphology to Determine Net Littoral Drift Directions in Complex Coastal Systems. Coastal and Hydraulics Engineering Technical Note* (CETN II-30). Vicksburg, Mississipi, USA: US Army Engineer Research and Development Center. Retrieved from https://apps.dtic.mil/dtic/tr/fulltext/u2/a591263.pdf.

Suparp, S.; Hussain, Q.; and Joyklad, P. (2017). Axial Compressive Behavior of Rope Fiber Reinforced Polymer Composite Concrete. In *Proceedings of the 2nd International Symposium on Mechanical Engineering and Material Science, 17th to 19th November 2017* (pp. 90–93). Atlantis Press. https://doi.org/https://doi.org/10.2991/ismems-17.2018.21.

Suwattanakorn, A.; Hussain, Q.; Rattanapitikon, W.; and Pimanmas, A. (2016). Behavior of Rectangular Concrete Column Confined with Sisal Fiber Reinforced Polymers (Sisal FRP). *Materials Science Forum*, *860*, 140–143. https://doi.org/10.4028/www.scientific.net/MSF.860.140.

SWAN. (2018). SWAN manual. Retrieved February 8, 2019, from http://swanmodel.sourceforge.net/online_doc/swanuse/node3.html.

Takahashi, S. (2002). *Design of Vertical Breakwaters. Version 2.1. Port and Airport Research Institute*. Japan. Retrieved from https://repository.tudelft.nl/islandora/object/uuid%3A7fd92ccc-74d7-469d-b648-a456d96a18a4.

Taveira-Pinto, F. (2001). *Análise das oscilações e dos campos de velocidades nas proximidades de quebramares submersos sob a acção da agitação marítima*. PhD Thesis in Civil Engineering, Faculty of Engineering of University of Porto, Portugal. Retrieved from https://hdl.handle.net/10216/11852.

Taveira-Pinto, F. (2007). *Análise da concepção e dimensionamento hidráulico-estrutural de quebramares destacados. Lição de Síntese*. Porto, Portugal: Faculdade de Engenharia da Universidade do Porto.

Taveira-Pinto, F.; and Neves, A.C. (2003). A Importância da Consideração do Carácter Irregular da Agitação Marítima no Dimensionamento de Quebramares de Taludes. *Revista Engenharia Civil Universidade Do Minho*, (16), 95–111. Retrieved from http://www.civil.uminho.pt/revista/artigos/Num16/Pag 95-111.pdf.

Taveira-Pinto, F.; and Neves, A.C. (2004). Environmental aspects of using detached breakwaters for coastal protection purposes. *Management of Environmental Quality: An International Journal*, *15*(1), 62–71. https://doi.org/10.1108/14777830410513621.

Teixeira, S.B. (2009). *Demarcação do leito e da margem das águas do mar no litoral sul do Algarve. Administração da Região Hidrográfica do Algarve*. Faro, Portugal. Retrieved from https://www.researchgate.net/publication/304114589_Demarcacao_do_leito_e_da_margem_das_aguas_do_mar_no_litoral_sul_do_Algarve.

Temmerman, S.; Meire, P.; Bouma, T.J.; Herman, P.M.J.; Ysebaert, T.; and De Vriend, H.J. (2013). Ecosystem-based coastal defence in the face of global change. *Nature*, *504*, 79–83. https://doi.org/10.1038/nature12859.

Ten Voorde, M.; Antunes do Carmo, J.A.; and Neves, M.G. (2009). Designing a Preliminary Multifunctional Artificial Reef to Protect the Portuguese Coast. *Journal of Coastal Research*, *25*(1), 69–79. https://doi.org/10.2112/07-0827.1.

Thomas, T.; Lynch, S.K.; Phillips, M.R.; and Williams, A.T. (2014). Long-term evolution of a sand spit, physical forcing and links to coastal flooding. *Applied Geography*, *53*, 187–201. https://doi.org/10.1016/j.apgeog.2014.06.020.

Toyoshima, O. (1974). Design of a Detached Breakwater System. In *Proceedings of 14th Conference on Coastal Engineering, 24th to 28th June 1974* (pp. 1419–1431). Copenhagen, Denmark: American Society of Civil Engineers. https://doi.org/10.1061/9780872621138.086.

Tung, T.T.; Walstra, D.-J.R.; van de Graaff, J.; and Stive, M.J.F. (2009). Morphological Modeling of Tidal Inlet Migration and Closure. *Journal of Coastal Research*, *2*(56), 1080–1084. Retrieved from https://www.jstor.org/stable/25737953.

UNFCCC. (2011). *United Nations Framework Convention on Climate Change. Report of the conference of the Parties on its sixteenth session, held in Cancun from 29 november to 10 december 2010. In: Part Two: Action Taken by the Conference of the Parties at its Sixteenth Sess*. Cancun, Mexico. Retrieved from https://unfccc.int/sites/default/files/resource/docs/2010/cop16/eng/07a01.pdf.

USACE. (2014a). Coastal & Hydraulics Laboratory. US Army Corps of Engineers. Breakwaters. Retrieved February 25, 2014, from http://chl.erdc.usace.army.mil/chl.aspx?p=s&a=Articles;187&g=41.

USACE. (2014b). Coastal & Hydraulics Laboratory. US Army Corps of Engineers. Groins. Retrieved February 25, 2014, from http://chl.erdc.usace.army.mil/chl.aspx?p=s&a=Articles;188&g=41.

Vader, P. (2014). *Oyster reefs and coastal protection. A literature review*. The Hague, The Netherlands. Retrieved from https://www.deltaexpertise.nl/images/f/ff/Vader_(2014)_-_Oyster_reefs_and_coastal_protection.pdf.

van der Meer, J.W. (1988). Stability of Cubes, Tetrapodes and Accropodes. In *Proceedings of the Breakwaters '88 Conference, London, UK* (pp. 71–80).

van der Meer, J.W. (1998). Application and stability criteria for rock and artificial units - Chapter 11. In *Dikes And Revetments* (pp. 191–216). Routledge. Retrieved from http://www.vandermeerconsulting.nl/downloads/stability_b/1998_vandermeer_ch11.pdf.

van der Meer, J.W. (1999). Design of Concrete Armour layers. In *Proceedings of the International Conference on Coastal Structures '99, 7th to 10th June 1999* (pp. 213–221). Santander, Spain. Retrieved from http://www.vandermeerconsulting.nl/downloads/stability_c/1999_vandermeer.pdf.

van Duin, M.J.P.; Wiersma, N.R.; Walstra, D.J.R.; van Rijn, L.C.; and Stive, M.J.F. (2004). Nourishing the shoreface: observations and hindcasting of the Egmond case, The Netherlands. *Coastal Engineering*, *51*(8–9), 813–837. https://doi.org/10.1016/j.coastaleng.2004.07.011.

van Wesenbeeck, B.K.; Mulder, J.P.M.; Marchand, M.; Reed, D.J.; De Vries, M.B.; De Vriend, H.J.; and Herman, P.M.J. (2014). Damming deltas: A practice of the past? Towards nature-based flood defenses. *Estuarine, Coastal and Shelf Science*, *140*, 1–6. https://doi.org/10.1016/j.ecss.2013.12.031.

van Zwicht, B.N.M. (2009). *Effect of the concrete density on the stability of Xbloc armour units*. MSc Thesis in Coastal Engineering, Faculty of Civil Engineering and Geosciences, Delft University of Technology, The Netherlands. Retrieved from http://resolver.tudelft.nl/uuid:8866d0ca-1ecf-4ea0-bb91-f0623a14de94.

Veloso-Gomes, F.; and Taveira-Pinto, F. (1997). Portuguese urban waterfronts expansion near coastal areas. In *Environmental Challenges in an Expanding Urban World and the Role of Emerging Information Technologies Conference*. Lisbon, Portugal.

Veloso Gomes, F. (1981). *Espraiamento de Ondas Regulares sobre Taludes de Obras Marítimas*. PhD Thesis in Civil Engineering, Faculty of Engineering of University of Porto, Portugal. Retrieved from https://sigarra.up.pt/flup/pt/pub_geral.pub_view?pi_pub_base_id=27494&pi_pub_r1_id=.

Veron, J.E.N. (2000). *Corals of the World*. (M. Stafford-Smith, Ed.). Townsville, Australia: Australian Institute of Marine Science.

Vidal, C. (2007). Design tools related to engineering - Chapter 13. In H. F. Burcharth, S. J. Hawkins, B. Zanuttigh, A. Lamberti, M. Kramer, & P. Moschella (Eds.), *Environmental Design Guidelines for Low Crested Coastal Structures*. Retrieved from http://103.159.250.162:81/fdScript/RootOfEBooks/CED/CIVIL/Hawkins, Stephen J.& Lamberti, Alberto/Environmental Deastal Structures/Environmenins & H. F. Burcharth & Barbara Zanuttigh & Alberto Lamberti.pdf.

Vieira, B.F.V. (2014). *Wave hydrodynamics in coastal stretches influenced by detached breakwaters*. MSc Thesis in Civil Engineering, University of Minho: Guimarães, Portugal. Retrieved from http://hdl.handle.net/1822/36113.

Wambua, P.; Ivens, J.; and Verpoest, I. (2003). Natural fibres: can they replace glass in fibre reinforced plastics? *Composites Science and Technology*, *63*(9), 1259–1264. https://doi.org/10.1016/S0266-3538(03)00096-4.

Waterman, R.E. (2010). *Integrated Coastal Policy via Building with Nature*. PhD Thesis in Hydraulic Engineering, Delft University of Technology, The Netherlands. Retrieved from http://resolver.tudelft.nl/uuid:fa9a36f9-7cf8-4893-b0fd-5e5f15492640.

Whitmarsh, D.; Santos, M.N.; Ramos, J.; and Monteiro, C.C. (2008). Marine habitat modification through artificial reefs off the Algarve (southern Portugal): An economic analysis of the fisheries and the prospects for management. *Ocean & Coastal Management*, *51*(6), 463–468. https://doi.org/10.1016/j.ocecoaman.2008.04.004.

Wielgus, J.; Balmford, A.; Lewis, T.B.; Mora, C.; and Gerber, L.R. (2010). Coral reef quality and recreation fees in marine protected areas. *Conservation Letters*, *3*(1), 38–44. https://doi.org/10.1111/j.1755-263X.2009.00084.x.

Wild, C.; Rasheed, M.; Werner, U.; Franke, U.; Johnstone, R.; and Huettel, M. (2004). Degradation and mineralization of coral mucus in reef environments. *Marine Ecology Progress Series*, *267*, 159–171. https://doi.org/10.3354/meps267159.

Willemse, J.B.T.M.; Stelling, G.S.; and Verboom, G.K. (1986). Solving the Shallow Water Equations with an Orthogonal Coordinate Transformation. In *International Symposium on Computational Fluid Dynamics, 9th to 12th September 1985*. Tokyo, Japan: Waterloopkundig Laboratorium.

Williams, A.T.; Giardino, A.; and Pranzini, E. (2016). Canons of Coastal Engineering in the United Kingdom: Seawalls/Groynes, a Century of Change? *Journal of Coastal Research*, *32*(5), 1196–1211. https://doi.org/10.2112/JCOASTRES-D-15-00213.1.

Wu, Y.-F.; and Wei, Y.-Y. (2010). Effect of cross-sectional aspect ratio on the strength of CFRP-confined rectangular concrete columns. *Engineering Structures*, *32*(1), 32–45. https://doi.org/https://doi.org/10.1016/j.engstruct.2009.08.012.

Yu, C. (2005). Sisal - Chapter 6. In R. Franck (Ed.), *Bast and other plant fibres* (1st Ed., pp. 228–273). USA: Woodhead Publishing. https://doi.org/https://doi.org/10.1533/9781845690618.228.

Zamanzadeh, Z.; Lourenço, L.; and Barros, J. (2015). Recycled Steel Fibre Reinforced Concrete failing in bending and in shear. *Construction and Building Materials*, *85*, 195–207. https://doi.org/10.1016/J.CONBUILDMAT.2015.03.070.

(Page intentionally left blank)

CHAPTER 3

Extreme wave value analysis under uncertainty scenarios

"If a man will begin with certainties, he shall end in doubts; but if he will be content to begin with doubts, he shall end in certainties"

Francis Bacon. British philosopher (1561-1626)

(Page intentionally left blank)

CHAPTER 3   EXTREME WAVE VALUE ANALYSIS UNDER UNCERTAINTY SCENARIOS

3.1 Introduction

The special characteristics of coastal zones including their high population density has greatly increased during the recent decades, which is associated to rapid economic growth and coastward migration (Merkens *et al.*, 2016; Neumann *et al.*, 2015). Demographic pressure on coastal areas has resulted in significant infrastructure and assets being located at risk-prone areas, increasing exposure and vulnerability to natural hazards along the coast.

Coastal zones are extremely vulnerable regions with delicate physiographic equilibria, whose ecosystems are highly influenced by mean sea level rise (MSLR) and related hazards (including erosion, flooding and salt intrusion) that are expected to significantly increase by the end of this century in the absence of major additional adaptation efforts (Callaghan *et al.*, 2020; Cheng and Chen, 2017; Chini *et al.*, 2010; Ding *et al.*, 2013; Feng *et al.*, 2019; Mori *et al.*, 2013; SROCC, 2019; Warner and Tissot, 2012; Xie *et al.*, 2019). The evolution over the past two centuries suggests that the tendency for sea levels rising and consequent coastal erosion will aggravate in the 21ˢᵗ century independently of the considered global warming scenarios (Mase *et al.*, 2013; Mori *et al.*, 2013; Zhang *et al.*, 2004).

Climate change and its undesirable consequences, such as an expected increasing frequency and magnitude of extreme events, generate additional risks to water-related infrastructure, requiring an ever-increasing need for adaptation measures (SROCC, 2019).

A diversity of adaptation responses to coastal impacts and risks have been implemented around the world, but mostly as a reaction to current coastal risk or experienced disasters: hard coastal protection measures (dikes, embankments, sea walls, surge barriers); ecosystem-based adaptation; advance, which refers to the creation of new land by building into the sea (e.g., land reclamation); accommodation measures, such as early warning systems for extreme sea level events; and retreat.

Risk management approaches require actual and future projections of wave climates, including storm wave data. For this purpose, application of probability distributions for extreme wave climate data is a usual applied methodology to estimate extreme wave data for the design, operation and maintenance of coastal structural and non-structural infrastructures, under uncertainty caused by climate change.

The special characteristics of coastal zones require special planning and management approaches with a paradigmatic shift from crisis management to risk management (hazard analysis and vulnerability analysis) in a changing environment. Extreme events demand sustainable and effective technical solutions for climate change adaptation and disaster risk reduction for increased societal resilience. To

this end, statistical type predictions to describe the frequency of occurrence of extreme wave data are necessary.

The United Nations Intergovernmental Panel on Climate Change (IPCC) adopted different greenhouse gas concentration trajectories (Representative Concentration Pathway – RCP), to describe different future climates based on the volume of greenhouse gases emitted in the future years. The RCPs, originally RCP2.6, RCP4.5, RCP6, and RCP8.5, are labelled after a possible range of radiative forcing values in the year 2100 (net change in the energy balance of the Earth system due to some imposed perturbation averaged over a particular period of time: 2.6, 4.5, 6, and 8.5 W/m^2, respectively). These RCPs are commonly used to assess scientific, technical and socio-economic information concerning climate change, its potential effects and options for adaptation and mitigation (IPCC, 2020).

Predicted change in global mean surface temperature and global MSLR for the mid and end 21st century (2046–2065 and 2081–2100 averages, respectively), relative to the 1986–2005 period, is strongly dependent on which RCP emission scenario is followed.

MSLR is projected to rise between 0.47 m (0.32–0.63 m, likely range) (RCP4.5) and 0.63 m (0.45–0.82 m, likely range) (RCP8.5) by 2100 (likely range) relative to 1986–2005 (IPCC, 2014). These sea levels rise (Table 3.1) will imply the dissipation of wave energy at higher levels in the nearshore that could be exacerbated by eventual aggravation of the extreme wave climates (IPCC, 2014).

Table 3.1: Projections of global MSLR (m) based on the RCPs (adapted from IPCC, 2014).

Scenario	2046 – 2065		2081 – 2100	
	Mean	Likely Range	Mean	Likely Range
RCP2.6	0.24	0.17 to 0.32	0.40	0.26 to 0.55
RCP4.5	0.26	0.19 to 0.33	0.47	0.32 to 0.63
RCP6.0	0.25	0.18 to 0.32	0.48	0.33 to 0.63
RCP8.5	0.30	0.22 to 0.38	0.63	0.45 to 0.82

The need for reliable data on wave climate regimes is of relevant matter when implementing coastal infrastructure projects, risk analysis under climate change scenarios, and wave modelling. The most used descriptor of the wave field is the energy-density spectrum in both frequency and direction of propagation. From this spectrum, most of the parameters commonly used for describing wave climate regimes can be derived, namely: the significant wave height, H_s (m), the peak wave period, T_p (s), the mean wave direction, D_m (°), and the peak wave direction, D_p (°). Three main types of wave data are available: from observation, measurement or simulations. The observation or measurement of waves require personnel and measuring equipment *in situ* at the time of observation, whereas the simulated

wave data are produced and operated by many major meteorological services by making use of numerical wave modelling (WMO, 1998).

The most widely used variables to design offshore and onshore structures are H_s, T_p and D_m (Capitão and Fortes, 2011; Carvalho and Capitão, 1995; Park *et al.*, 2020; WMO, 1998). Much of the effort given to wave climate studies in recent years has concentrated upon statistical methods for estimating extreme values of these parameters, which require representativeness, consistency, and validity of the collected data to avoid incorrect extrapolation. Gumbel, Fréchet, Weibull, and log-normal value distributions are mostly applied to derive extreme wave data (Capitão and Fortes, 2011; Martucci *et al.*, 2010; Mathiesen *et al.*, 1994; Park *et al.*, 2020; Silva *et al.*, 2008; Wang *et al.*, 2013).

In this study, downscaled wave data of MeteoGalicia (Bio *et al.*, 2020; Pinho *et al.*, 2020) has been used for describing three different wave climates recurring to statistical analysis of H_s, T_p, D_m, and D_p and in estimating extreme wave data values at 17 selected stations in the Atlantic Ocean off the Iberian Peninsula. This dataset consists of 46 years of historical data (1960–2005) and two twenty-year time periods of RCPs projected data (2026–2045 and 2081–2100).

Although extreme H_s values computed by wave models could underestimate real values (Dentale *et al.*, 2018; Reale *et al.*, 2020), an extreme value analysis is applied to the datasets defined from the calculation of the 95th percentile of H_s, in order to identify storm waves (Castelle *et al.*, 2015; Goda, 2000; Harley, 2017; Masselink *et al.*, 2014). The 10-, 50-, 100-year return period (T_r) of H_s and T_p are estimated using the Gumbel, Fréchet, and Weibull distributions. Performance studies applying these three methods concluded that Fréchet and Weibull distributions fit better in estimating extreme values of H_s (Capitão and Fortes, 2011; Carvalho and Capitão, 1995; Guedes-Soares and Carvalho, 2001; Mathiesen *et al.*, 1994; Piccinini, 2006; Vanem, 2015). Projections from RCP4.5 and RCP8.5 datasets also allow to introduce uncertainty in the results obtained, since the effects of plausible climate change scenarios are considered.

Previous studies in the western coast of Portugal were based on limited time series periods and considered single locations over the region (e.g., Capitão and Fortes, 2011, and Silva *et al.*, 2008 using a time series of 14 years collected at a buoy located at Leixões; and Guedes-Soares and Carvalho, 2001 using a time series of 1 year, collected at a buoy located off port of Sines).

Following those studies, more updated research on extreme value analysis and descriptive statistics on the variability of wave parameters off the Iberian Peninsula, especially at the Portuguese coast, is needed to better understand the wave climate at this region. Based on this recognized gap, this

research work intends to address a comprehensive analysis on the wave extremes variability off the Iberian Peninsula under climate change scenarios.

The comprehensiveness of the wave climate regime database including historical data and projected data for two different greenhouse gases emission RCP4.5 and RCP8.5 scenarios, as well as the statistical methods used, allowed a descriptive statistics and an extreme value analysis of the local wave climate regimes.

Outcomes of this research work include the estimation of extreme values of H_s and T_p. This information can be a valuable contribution for the establishment of design parameters for coastal engineering projects in the study area and for coastal vulnerability analysis of the Atlantic Iberian coast to climate change.

3.2 Study area and data sources

The southwestern European Atlantic Ocean near the coast of the Iberian Peninsula is shared by two countries (Portugal and Spain) and has an extensive coastline for more than 1.300 km. This energetic coast has been subject to intensive urbanisation and coastward migration associated mainly to tourism, fishing, aquaculture, industry, and port activities. In the last decades, this region has being subject to an erosional process, coastal floods and aquifers salinization as showed in different studies (Álvarez *et al.*, 2020; Baptista *et al.*, 2014; Cherneva *et al.*, 2005; Guedes-Soares and Carvalho, 2001; Pereira and Coelho, 2013; Pinho *et al.*, 2020).

Winter storms are of common occurrence in this region (Gomes *et al.*, 2018; Santos *et al.*, 2018). Due to scarcity of monitoring data, hydrodynamics modelling works have been performed to assess the effect of three categories of storms on water levels at this coast. Ensemble simulations performed by Gomes *et al.* (2018) estimated a maximum sea level of 2.3 m for tropical storms, and a maximum sea level of 1.2 m for tropical depressions (values above mean spring-tide level of 3.75 m). The effects of these phenomena combined with storm waves can be associated with wave-overtopping and coastal flooding events with harmful consequences for coastal environments.

The costs involved in implementing a monitoring programme, especially on a regional basis, and the time spent waiting for a reasonable amount of data to be collected, are increasingly unaffordable. In this study, the wave climate data (significant wave height, peak period, and wave direction) were obtained from wave datasets downscaled with the Wave Watch III model (WWIII) of Meteogalicia, both for historical and future climates. This model was forced with results of the Model for Interdisciplinary Research On Climate 5 (MIROC5), which is included in the Coupled Model Intercomparison Project 5

(CMIP5) atmospheric/ocean global simulations (Qu *et al.*, 2020; Sperna-Weiland *et al.*, 2016; Vanem, 2017). Historical Period (HP) original CMIP5 (MIROC5) results were obtained by properly assimilate ocean and atmospheric observed data as reproduced in Tatebe *et al.* (2012).

Within the scope of the MarRisk project (Bio *et al.*, 2020; Ferreira *et al.*, 2021; Pinho *et al.*, 2020), the Meteogalicia WWIII model was forced with CMIP5 data, allowing this way to downscale model results for 17 stations off the western coast of Iberian Peninsula. Figure 3.1 presents the study area and the location of those stations.
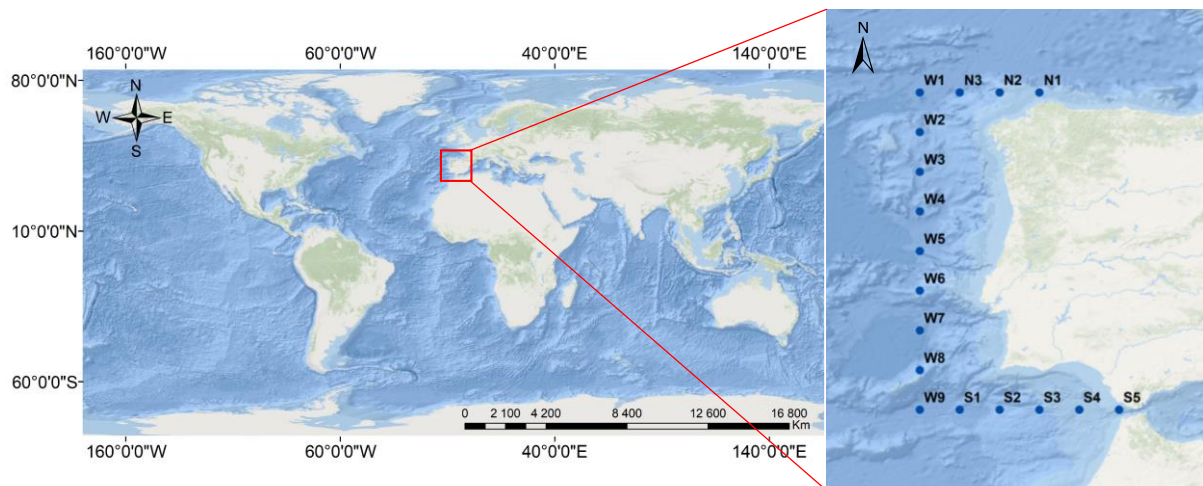
Figure 3.1: Study area with location of the 17 stations around the Iberian Peninsula.

The spectral data resulting from the WWIII model runs was provided for the 17 selected stations, which are properly numbered and aggregated according to their location (North, West, and South) in relation to the Iberian Peninsula (Table 3.2).

WWIII spectral data results comprises historical wave climate data, as well as wave climate projections based on the RCP climate change scenarios. The CMIP5 selected model used to simulate climate change scenarios was possible, since it have yielded reasonable calibration results using a sound 46 years wave climate data.

Results obtained from the application of recently developed phase 6 of CMIP (CMIP6) demonstrated similar outcomes as those obtained with CMIP5 (McKenna *et al.*, 2020; Plecha and Soares, 2020; Zhu *et al.*, 2020). While there was a significant improvement from CMIP3 to CMIP5 in simulating mean sea level, the same was not verified from CMIP5 to CMIP6. Major differences are mainly found in middle-to-high latitudes in the Southern Hemisphere. Moreover, regarding ocean dynamic sea level projections, a similarity of results was also verified between CMIP5 and CMIP6 (Lyu *et al.*, 2020).

Table 3.2: Coordinates of the study selected stations.

Station	Longitude	Latitude	Depth Related to Mean Sea Level (m)
N1	-8.00	44.00	-206.60
N2	-9.00	44.00	-1199.45
N3	-10.00	44.00	-4971.26
W1	-11.00	44.00	-4998.02
W2	-11.00	43.00	-2490.85
W3	-11.00	42.00	-2734.10
W4	-11.00	41.00	-3890.95
W5	-11.00	40.00	-4723.50
W6	-11.00	39.00	-3333.70
W7	-11.00	38.00	-5018.40
W8	-11.00	37.00	-2533.70
W9	-11.00	36.00	-4870.75
S1	-10.00	36.00	-4542.95
S2	-9.00	36.00	-3700.45
S3	-8.00	36.00	-1522.45
S4	-7.00	36.00	-809.55
S5	-6.00	36.00	-161.93

The used data includes five different wave climate scenarios: one for the historical period, HP, (1960–2005), and four projections under the climate change scenarios RCP4.5_mid (2026–2045), RCP4.5_end (2081-2100), RCP8.5_mid (2026–2045), and RCP8.5_end (2081-2100). The historical period includes 46 years of data, while the projection periods comprise two twenty-year time periods (for the mid and end periods of 21st century), which give a reasonably extensive datasets enabling reliable extrapolations for wave climate regimes analysis (Capitão and Fortes, 2011; Park *et al.*, 2020; Wang *et al.*, 2016; Wang and Swail, 2001).

The WWIII spectral information files, in NetCDF format, are divided into 1512 files making up 12.9 GB of disk space. Each NetCDF file contains spectral information for one month and the temporal resolution of the data is 3 hours. Table 3.3 shows the structure of the information used in each of the NetCDF files.

Table 3.3: List of variables used in each WWIII NetCDF file.

Variable	Description	Type	Unit
direction	Sea surface wave direction	1D	degree
Dpt	Depth	2D	m
Efth	Sea surface wave directional variance spectral density	2D	$m^2 s\ rad^{-1}$
frequency	Frequency of centre band	1D	s^{-1}
frequency1	Frequency of lower band	1D	s^{-1}
frequency2	Frequency of upper band	1D	s^{-1}
latitude	Latitude	2D	Degree North
longitude	Longitude	2D	Degree East
station	Station id	1D	-
station_name	Station name	-	-
time	Julian day	1D	day

3.3 Methodology

3.3.1 Methods for extreme wave data analysis under uncertainty

Waves extremes eventually exacerbated by climate change increase the magnitude of hazards to coastal infrastructure, either expressed in terms of frequency or severity (IPCC, 2014; Marone *et al.*, 2017; Pinho *et al.*, 2020). The use of probability models is of paramount importance for determining wave climate regimes and predicting intensity and duration of extreme events occurrences. Climate projections for the 21ˢᵗ century are inherently uncertain since there is low confidence in projections of many aspects of climate phenomena that influence regional climate change (Sun *et al.*, 2017). The rate of future global warming effects depends on unpredictable natural influences on climate like volcanic eruptions, as well as on greenhouse gas concentrations due to anthropogenic activities (IPCC, 2020).

Uncertainties arising from climate change scenarios may question the validity of future projections based on data collected in the past. Some authors claim that "stationarity is dead" stating that climate change undermines basic assumption that historically has facilitated management of water resources and risks (Milly *et al.*, 2008). However, this philosophical approach has been contradicted by many authors who consider that the process of climate change is accepted as a "certainty" and value the need for hydrological predictions based on assumptions that should include stationarity (Montanari and Koutsoyiannis, 2014). In line with these authors, this research work follows a pragmatic approach in predicting extreme wave climate regimes based on the exploitation of simulated datasets generated by numerical models applied to historical and to RCP scenarios.

An extensive temporal and spatial wave database is used to effectively deal with climate change uncertainty. The usual parameter chosen to estimate the severest conditions likely to be experienced by coastal infrastructures is either the 50- or the 100-year return period of wave height (H_s), where the N-

year return period is defined as that which is exceeded on average once every N years (WMO, 1998). This parameter is very important in coastal vulnerabilities analysis and coastal defence solutions design. However, for a complete description of extreme conditions, information on wave peak period (T_p) and direction of propagation is also required. This research work has concentrated upon methods for estimating extreme values of H_s, and the correspondent T_p.

Techniques for extreme value analysis consist of adjusting a theoretical probability distribution function to the function of the estimated distribution of a sample, in order to describe a certain random variable behaviour (Silva *et al.*, 2008). Several methods for estimating extreme wave data and to define the local wave climates are available elsewhere (Karian and Dudewicz, 2000; Naghettini and Pinto, 2007; Nascimento, 2009; Park *et al.*, 2020; Sansigolo, 2008; Thevasiyani and Perera, 2014; Urošev *et al.*, 2016).

For this purpose, different probability distributions have been applied: Gumbel (Cotta *et al.*, 2016; Silva *et al.*, 2008); Gumbel and Weibull (Mathiesen *et al.*, 1994; Park *et al.*, 2020); Gumbel, Fréchet and Weibull (Capitão and Fortes, 2011; Carvalho and Capitão, 1995; Goda, 2000; Sansigolo, 2008).

In order to assess the relative performance of different methods, this research applies three generalized extreme value (GEV) probability distributions (Gumbel, Fréchet, and Weibull) to estimate the extreme values of the H_s and the associated T_p for the 10-, 50-, 100-year return period. The application of these probability distributions required a previous selection of annual maxima H_s values for all 17 stations. Usually, two different methods (annual maxima and peaks-over-threshold) are widely used in extreme value analysis. According to Goda (2000), the annual maxima approach should be used for databases covering more than 20 years, while for shorter records of extreme data the peaks-over-threshold seems to be a more reliable method. For methodological coherence reasons, in this study the annual maxima method is selected for the 46-year span HP data and for the two 20-year span RCP scenarios data. These GEV probability distribution methods consider that the distribution of maxima of *n* values are asymptotic with increasing the number *n*, and this is the reason for their usual application on extreme meteorological events with good results.

Extreme value analysis is conducted after transforming the extreme value distributions from the probability distribution function form to the cumulative distribution function (CDF) form for the convenience of computation. Equations (3.1) to (3.3) show the CDF of Gumbel, Fréchet and Weibull distributions (Vivekanandan, 2012):

$$F(X) = e^{-e^{-\left(\frac{X-\alpha_G}{\beta_G}\right)}}, \beta_G > 0 \text{ and } -\infty < X < \infty \text{ (for Gumbel)} \tag{3.1}$$

$$F(X) = e^{-\left(\frac{X}{\beta_F}\right)^{(-\lambda_F)}}, \beta_F > 0 \text{ and } -\infty < X < \infty \text{ (for Fréchet)} \tag{3.2}$$

$$F(X) = e^{-\left(\frac{X}{\beta_W}\right)^{\lambda_W}}, \beta_W > 0 \text{ and } -\infty < X < \infty \text{ (for Weibull)} \tag{3.3}$$

where X is the random variable under consideration (H_s, T_p); α_G and β_G are the location and scale parameters of the Gumbel distribution; β_F, λ_F and β_W, λ_W are the scale and shape parameters of Fréchet and Weibull distributions, respectively.

The inverse first-order reliability method (I-FORM), as proposed by Winterstein *et al.* (1993), is applied to calculate the exceedance probability according to the Equation (3.4):

$$P = S(X_i) = i/(N + 1), \ P \in]0,1[\tag{3.4}$$

where P is the exceedance probability of X; N is the total number of samples; $i(i = 1, ..., N)$ is the number of sample values for which any variable value $x \leq X_i$.

The method of fitting the chosen distribution is based on the application of the probability plot correlation coefficient technique (Filliben, 1975). The use of this graphical technique requires the computation of the percent point function, which is the inverse of the cumulative distribution function. The formulae for the percent point function $G(P)$ expressing graphical coordinates that fit the Gumbel, Fréchet, and Weibull distributions are presented in Table 3.4.

Table 3.4: Wave conditions for the Iberian Peninsula simulations.

Probability Distribution	Percent Point Function Plotting	
	x-axis coordinate	y-axis coordinate
Gumbel	X_i	$G_g(P) = -\ln[\ln(1/P)]$
Fréchet	$\ln(X_i)$	$G_f(P) = -\ln[-\ln(P)]$
Weibull	$\ln(X_i)$	$G_w(P) = \ln[ln[1/(1-P)]]$

Equation (3.5) is employed to estimate the 10-, 50-, 100-year return period of extreme wave data, which gives the correspondence between the exceedance probability, P, and the return period, T_r (Silva *et al.*, 2008).

$$T_r = \frac{1}{1-P} \tag{3.5}$$

The chosen distribution function is then fitted by approximating a linear function through the plotted values by the least squares method. The parameters are obtained using the slopes and y-intercept values when the coefficient of determination (R^2) value is the highest.

3.3.2 Descriptive statistics of the local wave regimes

A comprehensive statistical analysis is performed to determine the characteristics of wave regimes for each of the stations located off the Iberian Peninsula coastal zone. The downscaled CMIP5 results are used in the construction of the following five wave climate regimes datasets: (i) HP; (ii) RCP4.5_mid and RCP4.5_end; and RCP8.5_mid and RCP8.5_end.

A statistical analysis is performed for two datasets established from the wave climate regimes and future predicted wave climates: (i) wave dataset, with all the information contained in the data source; and (ii) for a storm sub-dataset, obtained from the application of a criterion based on H_s values exceeding the 95th percentile as storm definition (a peaks-over-threshold method where a set of values above a certain threshold level are selected). This methodology is applied to obtain characteristics of wave climate evolution with special focus on storms due to the relevance of extreme phenomena.

Wave dataset serves as the basis for determining the mean values for H_s, T_p, D_m, and D_p (independent variables); the maximum values for H_s; and the 95th percentile of H_s ($H_{s,0.95}$). For the purpose of this study, a storm event is considered when the significant wave height exceeds $H_{s,0.95}$ (Castelle *et al.*, 2015; Harley, 2017, Masselink *et al.*, 2014). From the calculation of $H_{s,0.95}$, a sub-dataset is obtained with mean storm values. Based on this sub-dataset, descriptive statistics are obtained for mean peak H_s, mean T_p, D_m, and D_p. Moreover, for the storm event data, a frequency analysis is also conducted to analyse which D_m and D_p direction quadrants are more frequent at each station. An analysis of the maximum, and mean storms duration, as well as the number of storms registered and the mean storms per year at each station is also performed.

A diagrammatic scheme that shows the followed descriptive statistics analysis is presented in Figure 3.2.
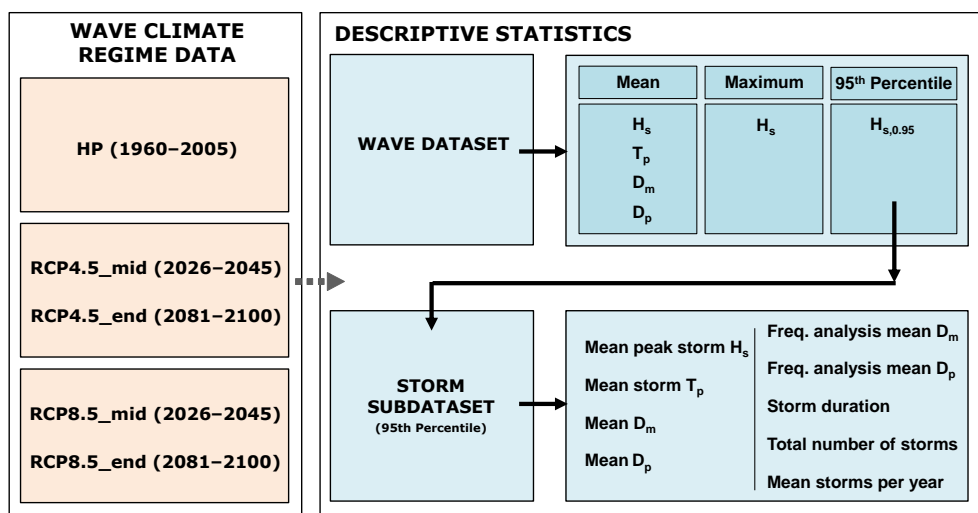
Figure 3.2: Methodological scheme applied for descriptive statistics.

3.3.3 Extreme value analysis of wave climate regimes

The extreme value analysis of storm sub-dataset is performed to estimate the 10-, 50-, 100-year return period of H_s and T_p for all stations off the Iberian Peninsula coastal zone, covering the five wave climates regimes. The method employed follows two sequential steps: (i) the wave regime historical data for the period of 1960–2005 is selected and the Gumbel, Fréchet, and Weibull GEV probability distributions are used comparing which of them give better fitting of extreme wave regime values, by calculating the respective coefficient of determination (R^2); (ii) selected GEV probability distributions (Fréchet for H_s, and Weibull for T_p, based on the best fitting method) are applied to estimate the extreme values for two time periods (2026–2045 and 2081–2100) under the RCP4.5 and RCP8.5 climate change scenarios. Figure 3.3 depicts the scheme adopted in estimating the extreme values for wave regimes.
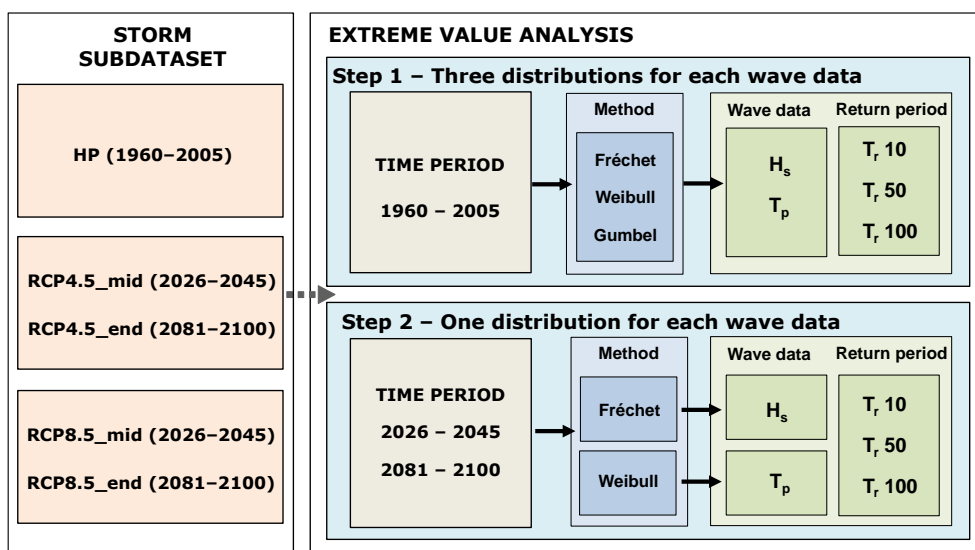
Figure 3.3: Methodological scheme applied for extreme value analysis.

3.4 Results and discussion

At southwestern coast of Iberian Peninsula variable wave climatic regimes are notorious depending on the different climate scenarios and on the geographical location. Descriptive statistics for complete wave dataset and storm sub-dataset under 5 wave climate regime scenarios (HP data, RCP4.5_mid and RCP4.5_end data, and RCP8.5_mid and RCP8.5_end data), as well as extreme value analysis of H_s and T_p (for historical and projected data) have been performed for all analysed stations. Obtained results are presented in a graphical form supported by tables that include wave climate data numerical values. Comparison with existing studies and proposal of extreme values for coastal engineering design are also discussed.

The stations are clustered into four groups as presented in Table 3.5. Geo-location of the stations and the homogeneity of the obtained results served as criteria to define the station groups: N for North stations; WN and WS for West stations; and S for South stations.

Table 3.5: Station groups.

Station Group	Stations
N	N1; N2; N3
WN	W1; W2; W3; W4
WS	W5; W6; W7; W8; W9
S	S1; S2; S3; S4; S5

3.4.1 Descriptive statistics: complete wave dataset

In Figure 3.4 main descriptive statistical results for mean H_s, $H_{s,0.95}$, maximum H_s, mean T_p, mean D_m and mean D_p values for wave dataset are presented in a graphical and tabulated forms, while mean D_m and mean D_p are only presented in tabulated form. A complete set of results on parameters per wave climate regime scenario and individual parameters under 5 wave climate regime scenarios for wave dataset descriptive statistics can be found in Appendices 2A and 2B, respectively.

Wave data: Historical data

	N1	N2	N3	W1	W2	W3	W4	W5	W6	W7	W8	W9	S1	S2	S3	S4	S5
Mean Hs (m)	2,52	2,73	2,87	2,97	2,92	2,88	2,84	2,81	2,78	2,75	2,73	2,68	2,58	2,41	2,02	1,59	1,25
Hs, 95% (m)	5,20	5,55	5,78	5,91	5,78	5,63	5,48	5,38	5,26	5,05	4,92	4,82	4,64	4,08	3,44	2,82	
Max Hs (m)	13,98	14,78	15,17	15,41	14,70	14,94	14,80	14,22	15,11	15,59	15,11	13,82	12,58	11,60	10,81	10,04	8,54
Mean Tp (s)	10,89	10,73	10,61	10,57	10,60	10,64	10,67	10,69	10,69	10,70	10,71	10,73	10,80	10,90	10,92	10,66	10,05
Mean Dm (°)	290	284	278	273	278	288	299	305	309	312	313	314	313	308	299	288	274
Mean Dp (°)	285	279	269	253	252	252	258	267	272	275	275	275	302	311	301	290	277

Wave data: RCP4.5 2026-2045

	N1	N2	N3	W1	W2	W3	W4	W5	W6	W7	W8	W9	S1	S2	S3	S4	S5
Mean Hs (m)	2,45	2,65	2,80	2,91	2,86	2,82	2,79	2,77	2,75	2,73	2,71	2,66	2,56	2,37	1,97	1,55	1,23
Hs, 95% (m)	5,07	5,42	5,62	5,73	5,61	5,44	5,30	5,20	5,08	4,99	4,90	4,78	4,66	4,45	3,90	3,33	2,73
Max Hs (m)	15,70	16,27	16,77	16,79	15,83	15,01	13,99	13,37	12,40	11,84	11,08	10,66	10,51	10,34	9,81	9,42	8,32
Mean Tp (s)	10,73	10,57	10,45	10,40	10,44	10,47	10,50	10,53	10,53	10,53	10,55	10,58	10,65	10,75	10,78	10,52	9,88
Mean Dm (°)	289	282	275	271	275	284	298	307	311	314	315	316	314	309	298	287	272
Mean Dp (°)	283	277	265	248	246	245	252	262	269	272	272	270	302	311	301	289	274

Wave data: RCP4.5 2081-2100

	N1	N2	N3	W1	W2	W3	W4	W5	W6	W7	W8	W9	S1	S2	S3	S4	S5
Mean Hs (m)	2,33	2,54	2,69	2,80	2,76	2,72	2,69	2,67	2,64	2,63	2,61	2,56	2,45	2,27	1,88	1,49	1,19
Hs, 95% (m)	4,84	5,21	5,42	5,55	5,40	5,22	5,07	4,94	4,83	4,73	4,65	4,54	4,40	4,18	3,68	3,11	2,58
Max Hs (m)	12,66	14,88	14,58	14,63	15,54	16,17	16,03	15,63	14,73	12,95	12,04	10,91	10,77	10,60	10,14	9,33	7,97
Mean Tp (s)	10,47	10,28	10,14	10,10	10,14	10,19	10,23	10,27	10,28	10,29	10,31	10,35	10,41	10,52	10,58	10,31	9,67
Mean Dm (°)	286	278	269	264	268	279	297	308	312	314	316	317	314	309	299	287	271
Mean Dp (°)	279	272	259	243	239	239	247	261	268	270	270	269	301	312	301	289	274

Wave data: RCP8.5 2026-2045

	N1	N2	N3	W1	W2	W3	W4	W5	W6	W7	W8	W9	S1	S2	S3	S4	S5
Mean Hs (m)	2,40	2,60	2,75	2,85	2,81	2,78	2,76	2,74	2,72	2,70	2,68	2,63	2,52	2,34	1,94	1,54	1,22
Hs, 95% (m)	5,00	5,39	5,63	5,72	5,62	5,47	5,34	5,22	5,10	5,01	4,92	4,78	4,67	4,47	3,92	3,30	2,69
Max Hs (m)	13,19	14,37	14,86	14,90	13,50	12,83	11,36	10,95	10,42	10,89	11,28	10,77	10,33	10,03	9,28	8,81	7,87
Mean Tp (s)	10,65	10,48	10,37	10,32	10,35	10,38	10,41	10,44	10,46	10,47	10,50	10,53	10,60	10,71	10,76	10,51	9,89
Mean Dm (°)	289	282	276	271	275	286	300	308	313	315	316	317	314	309	299	288	274
Mean Dp (°)	281	274	263	247	245	245	253	263	269	271	271	270	301	312	301	290	276

Wave data: RCP8.5 2081-2100

	N1	N2	N3	W1	W2	W3	W4	W5	W6	W7	W8	W9	S1	S2	S3	S4	S5
Mean Hs (m)	2,27	2,48	2,63	2,73	2,70	2,67	2,65	2,63	2,62	2,60	2,59	2,54	2,43	2,25	1,88	1,49	1,18
Hs, 95% (m)	4,91	5,30	5,52	5,62	5,53	5,39	5,27	5,17	5,05	4,93	4,81	4,68	4,56	4,36	3,90	3,33	2,69
Max Hs (m)	15,79	19,17	20,35	20,78	19,04	17,48	15,81	13,95	13,03	12,35	12,22	12,54	12,32	12,28	11,57	10,65	9,22
Mean Tp (s)	10,39	10,21	10,07	10,00	10,01	10,04	10,08	10,11	10,12	10,14	10,17	10,20	10,28	10,39	10,44	10,22	9,57
Mean Dm (°)	289	281	274	269	272	282	297	307	312	314	315	316	314	308	299	287	271
Mean Dp (°)	282	274	264	251	247	247	256	270	275	277	276	273	302	312	301	289	274

Figure 3.4: Mean H_s, $H_{s,0.95}$, maximum H_s, mean T_p, mean D_m and mean D_p values for wave dataset under five wave climate regime scenarios.

Results for wave dataset are organized in Table 3.6, where minimum and maximum values for each station group for the five wave climate regimes are presented.

Significant wave height values (mean H_s, $H_{s,0.95}$, and maximum H_s) decrease, in general, from the northern to southern station groups in the sequence WN>N>WS>S, where values found for S are considerably lower than those of the remaining station groups. Comparing the HP results for mean H_s,

$H_{s,0.95}$, and maximum H_s among the station groups, it was found that $H_{s,0.95}$ values are twice the mean H_s values, and the maximum H_s is thrice the $H_{s,0.95}$ values (ranges from 1.25–2.97 m for mean H_s; 2.82–5.91 m for $H_{s,0.95}$; and 8.54–15.59 m for maximum H_s).

Table 3.6: Descriptive statistics results for the local wave regime using wave dataset from CMIP5.

Wave data	Station Group	Wave Climate Regime Scenario				
		HP	RCP4.5_mid	RCP4.5_end	RCP8.5_mid	RCP8.5_end
Mean H_s (m)	N	2.52–2.87	2.45–2.80	2.33–2.69	2.40–2.75	2.27–2.63
	WN	2.84–2.97	2.79–2.91	2.69–2.80	2.76–2.85	2.65–2.73
	WS	2.68–2.81	2.66–2.77	2.56–2.67	2.63–2.74	2.54–2.63
	S	1.25–2.58	1.23–2.56	1.19–2.45	1.22–2.52	1.18–2.43
$H_{s,0.95}$ (m)	N	5.20–5.78	5.07–5.62	4.84–5.42	5.00–5.63	4.91–5.52
	WN	5.48–5.91	5.30–5.73	5.07–5.55	5.34–5.72	5.27–5.62
	WS	4.92–5.38	4.78–5.20	4.54–4.94	4.78–5.22	4.68–5.17
	S	2.82–4.82	2.73–4.66	2.58–4.40	2.69–4.67	2.69–4.56
Max. H_s (m)	N	13.98–15.17	15.70–16.77	12.66–14.88	13.19–14.86	15.79–20.35
	WN	14.70–15.41	13.99–16.79	14.63–16.17	11.36–14.90	15.81–20.74
	WS	13.82–15.59	10.66–13.37	10.91–15.63	10.42–11.28	12.22–13.95
	S	8.54–12.58	8.32–10.51	7.97–10.77	7.87–10.33	9.22–12.32
Mean T_p (s)	N	10.61–10.89	10.45–10.73	10.14–10.47	10.37–10.65	10.07–10.39
	WN	10.57–10.67	10.40–10.50	10.10–10.23	10.32–10.41	10.00–10.08
	WS	10.69–10.73	10.53–10.58	10.27–10.35	10.44–10.53	10.11–10.20
	S	10.05–10.92	9.88–10.78	9.67–10.58	9.89–10.76	9.57–10.44
Mean D_m (°)	N	278–290	275–289	269–286	276–289	274–289
	WN	273–299	271–298	264–297	271–300	269–297
	WS	305–314	307–316	308–317	308–317	307–316
	S	274–313	272–314	271–314	274–314	271–314
Mean D_p (°)	N	269–285	265–283	259–279	263–281	264–282
	WN	252–258	245–252	239–247	245–253	247–256
	WS	267–275	262–272	261–270	263–271	270–277
	S	277–311	274–311	274–312	276–312	274–312

For each station group, when historical values are compared with the projected results of the RCP scenarios for mean H_s and $H_{s,0.95}$, tendencies show that HP results are higher than those calculated in any of the RCP scenarios. For example, differences in percentage between RCP8.5_mid scenario and HP for the most energetic station group (WN) show H_s minimum and maximum values of: -2.82 % and -4.04 % for mean H_s; -2.55 % and -3.21 % for $H_{s,0.95}$; and -22.72 % and -3.31 % for max H_s. Regarding the differences between RCP8.5_end scenario and HP, the corresponding percentages are: -6.69 % and -8.08 % for mean H_s; -3.83 % and -4.91 % for $H_{s,0.95}$; and +7.55 % and +34.59 % for max H_s. Similar results for the Iberian coast can also be found in the assessment of CMIP5 wave projections conducted by Morim *et al.* (2019). These results are very important as they contradict results obtained by other

authors when the effects of climate change on H_s are simulated. Wang and Swail (2001) showed significant linear increasing trends on wave height in both the North Atlantic and North Pacific, when the global model hindcast results were analysed for the time period of 1958–1997. In a more recent study, Wang *et al.* (2016) presented results showing H_s increases in the tropics (especially in the eastern tropical Pacific) and in southern hemisphere high-latitudes, which are based on the CMIP5 historical (2005), RCP4.5 (2050) and RCP8.5 (2099) forcing scenario simulations. Moreover, tendencies show that projected values obtained for RCP4.5 and RCP8.5 scenarios have slight differences apparently without major influence on these wave statistical results.

Maximum H_s values show contradictory tendencies when HP data are compared to projected data. The maximum values obtained for RCP4.5_mid and RCP8.5_end scenarios are higher (10−35 %) than those of the HP data for the northern station groups N and WN (ranging from 16.79 m to 20.74 m, respectively) and lower for the southern station groups WS (13.37 m to 13.95 m) and S (10.51 m to 12.32 m). For RCP4.5_end and RCP8.5_mid scenarios, the results obtained follow the same tendency as verified with mean H_s, and $H_{s,0.95}$, with lower values than those of the HP data. This can be justified by the fact that the use of model data often originates undervaluation of the H_s in projected scenarios, and by the application of a single model (MIROC5) without assembly with other CMIP5 models.

Mean T_p appears to maintain constant values around 10.50 s in all station groups, independently the scenario considered.

Wave direction defined by D_m and D_p values show slight differences both in station group location and in wave climate regime scenarios. However, it can be noted that for D_m the values for N and WN station groups have analogous behaviour with maximum values around 300°, and in WS and S station groups maximum values around 315°. D_p maximum values around 280°, 250°, 275°, and 312° can be found in station groups N, WN, WS, S, respectively.

3.4.2 Descriptive statistics: storm sub-dataset

Storm sub-dataset for the five wave climate regime scenarios are used to calculate mean peak storm H_s, mean storm T_p, mean D_m, mean D_p, frequency analysis of mean D_m and D_p, storm durations, total number of storms and mean storms per year. Figure 3.5 presents the results obtained for these wave data in the HP data scenario. Figure 3.6 depicts some of the statistical results obtained under RCP4.5 and RCP8.5 scenarios (storm durations, total number of storms and mean storms per year).
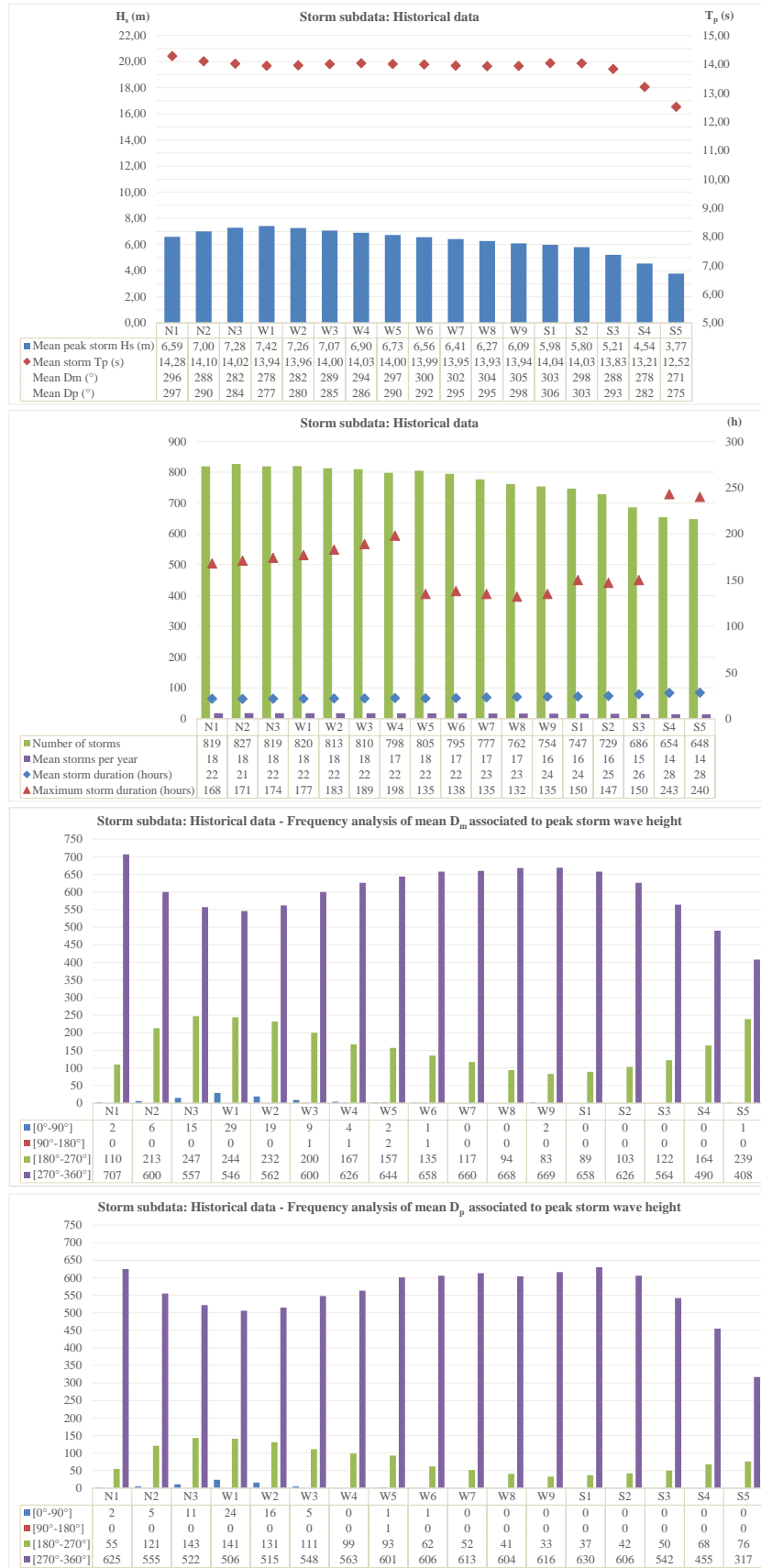
Figure 3.5: Mean peak storm H$_s$, mean storm T$_p$, mean D$_m$, mean D$_p$, frequency analysis of mean D$_m$ and D$_p$, storm durations, total number of storms and mean storms per year results for HP data.

Storm subdata: RCP4.5 2026-2045

	N1	N2	N3	W1	W2	W3	W4	W5	W6	W7	W8	W9	S1	S2	S3	S4	S5
Number of storms	314	324	320	301	301	287	281	285	282	288	284	278	284	273	268	261	256
Mean storms per year	16	16	16	15	15	14	14	14	14	14	14	14	14	14	13	13	13
Mean storm duration (hours)	22	21	22	22	23	23	24	23	23	23	24	25	24	23	24	27	28
Maximum storm duration (hours)	135	132	135	132	132	135	135	132	108	111	135	135	135	135	144	198	201

Storm subdata: RCP4.5 2081-2100

	N1	N2	N3	W1	W2	W3	W4	W5	W6	W7	W8	W9	S1	S2	S3	S4	S5
Number of storms	292	291	296	289	284	253	258	248	240	246	228	234	226	218	206	212	219
Mean storms per year	15	15	15	14	14	13	13	12	12	12	11	12	11	11	10	11	11
Mean storm duration (hours)	19	19	19	19	20	22	21	22	21	22	23	22	22	23	25	27	26
Maximum storm duration (hours)	93	123	123	123	129	132	135	138	138	135	138	162	165	162	198	204	204

Storm subdata: RCP8.5 2026-2045

	N1	N2	N3	W1	W2	W3	W4	W5	W6	W7	W8	W9	S1	S2	S3	S4	S5
Number of storms	301	310	327	311	316	313	327	300	301	303	296	283	281	280	283	266	258
Mean storms per year	15	16	16	16	16	16	16	15	15	15	15	14	14	14	14	13	13
Mean storm duration (hours)	22	22	21	22	22	22	21	22	23	22	23	24	24	23	23	25	26
Maximum storm duration (hours)	171	165	117	114	117	108	117	99	93	87	90	93	102	105	153	156	156

Storm subdata: RCP8.5 2081-2100

	N1	N2	N3	W1	W2	W3	W4	W5	W6	W7	W8	W9	S1	S2	S3	S4	S5
Number of storms	282	281	281	278	272	282	281	266	267	269	253	244	241	237	234	230	222
Mean storms per year	14	14	14	14	14	14	14	13	13	13	13	12	12	12	12	12	11
Mean storm duration (hours)	21	23	23	22	23	23	23	25	24	24	25	26	26	26	29	31	31
Maximum storm duration (hours)	117	126	126	126	123	141	126	228	138	138	141	141	144	144	150	228	228

Figure 3.6: Results for storm durations, total number of storms and mean storms per year for RCP4.5 and RCP8.5 scenarios.

A complete set of results on parameters per wave climate regime scenario and individual parameters under 5 wave climate regime scenarios for storm subdataset descriptive statistics can be found in Appendices 2C and 2D, respectively.

Table 3.7 shows minimum and maximum values obtained for storm wave data in each station group for the five wave climate regime scenarios. Mean peak storm H_s mean storm T_p, total number of storms, mean storms per year, mean storm duration, and maximum storm duration are presented.

For mean peak storm H_s, differences in percentage between RCP8.5_mid scenario and HP for the most energetic station group (WN) show H_s minimum and maximum values of +1.01 % and -1.21 %, while between RCP8.5_end scenario and HP the corresponding percentages are +4.49 % and +3.23 %.

Table 3.7: Descriptive statistics results for the local wave regime using storm sub-dataset (1).

Wave data	Station Group	Wave Climate Regime Scenario				
		HP	RCP4.5_mid	RCP4.5_end	RCP8.5_mid	RCP8.5_end
Mean peak storm H_s (m)	N	6.59–7.28	6.60–7.26	6.53–7.24	6.57–7.14	6.71–7.50
	WN	6.90–7.42	6.96–7.49	6.98–7.43	6.97–7.33	7.21–7.66
	WS	6.09–6.73	6.13–6.77	6.09–6.85	6.11–6.77	6.29–6.88
	S	3.77–5.98	3.78–5.97	3.74–5.98	3.71–5.99	3.91–6.17
Mean storm T_p (s)	N	14.02–14.28	13.83–14.15	13.54–13.95	13.66–14.15	13.83–14.14
	WN	13.94–14.03	13.81–14.11	13.44–13.75	13.54–13.66	13.72–13.83
	WS	13.93–14.00	13.75–14.03	13.66–13.83	13.57–13.77	13.88–14.05
	S	12.52–14.04	12.56–13.80	12.29–13.89	12.38–13.80	13.04–14.06
Total number of storms	N	819–827	314–324	291–296	301–327	281–282
	WN	798–820	281–301	253–289	311–327	272–282
	WS	754–805	278–288	228–248	283–303	244–269
	S	648–747	256–284	206–226	258–283	222–241
Mean storms per year	N	18–18	16–16	15–15	15–16	14–14
	WN	17–18	14–15	13–14	16–16	14–14
	WS	16–18	14–14	11–12	14–15	12–13
	S	14–16	13–14	10–11	13–14	11–12
Mean storm duration (h)	N	21–22	21–22	19–19	21–22	21–23
	WN	22–22	22–24	19–22	21–22	22–23
	WS	22–24	23–25	21–23	22–24	24–26
	S	24–28	23–28	22–27	23–26	26–31
Max. storm duration (h)	N	168–174	132–135	93–123	117–171	117–126
	WN	177–198	132–135	123–135	108–117	123–141
	WS	132–138	108–135	135–162	87–99	138–228
	S	147–243	135–201	162–204	102–156	144–228

Mean peak storm H_s decrease, in general, from the northern to southern groups of stations in the sequence WN>N>WS>S, where values found for S are considerably lower (approximately, one-half in minimum values) than those of the remaining station groups. The results obtained for RCP scenarios

are similar to the historical ones, notwithstanding there is a slight increase in these values for the climate scenario RCP8.5_end. The results obtained for mean storm T_p show similar values in the range [13–14 s], independently the station groups and the scenario considered.

Total number of storms values decrease in the sequence of N>WN>WS>S, as well as from the historical (maximum values ranging from 747–827 in 46 years) to the RCP scenarios (maximum values ranging from 226–327 in 40 years). Mean storms per year have the same behaviour as total number of storms, with values ranging from 10 to 18 events per year.

Results for mean storm duration values show a slight increase in the sequence of N>WN>WS>S (with maxima in the range of 22–28 h), while small variations for the different scenarios are verified. Maximum storm duration values have a decreasing behaviour in the sequence of N>WN>WS>S for HP data, and an increase behaviour for RCP4.5_end and RCP8.5_end in the same sequence. Maximum storm duration projected values for RCPs in S are higher than in N, WN, and WS with maximum values ranging from 156 h to 228 h.

Table 3.8 shows minimum and maximum values obtained for mean D_m and D_p, in each station group for the five wave climate regime scenarios. In addition, for these two wave data, the range of percentages of their occurrence in the Q4 [270°–360°] related to the other three quadrants are also presented.

Table 3.8: Descriptive statistics results for the local wave regime using storm sub-dataset (2).

Wave data	Station Group	Wave Climate Regime Scenario				
		HP	RCP4.5_mid	RCP4.5_end	RCP8.5_mid	RCP8.5_end
Mean D_m (°)	N	282–296	283–298	281–294	282–296	281–291
	WN	278–294	279–296	278–292	280–289	276–281
	WS	297–305	297–309	294–306	297–309	290–299
	S	271–303	272–305	271–303	272–306	273–298
Mean D_p (°)	N	284–297	287–300	285–296	285–298	282–290
	WN	277–286	276–281	275–284	283–286	279–282
	WS	290–298	277–282	288–296	287–294	286–297
	S	275–306	275–306	275–302	276–310	277–302
Q4 Freq. Mean D_m (%)	N	68–86	67–85	68–86	67–88	65–81
	WN	67–78	65–79	66–72	67–73	61–65
	WS	80–89	78–91	73–89	80–91	73–87
	S	63–88	65–90	59–87	64–90	68–86
Q4 Freq. Mean D_p (%)	N	77–92	78–91	73–89	78–95	71–86
	WN	75–85	75–86	70–80	76–83	68–75
	WS	86–95	86–94	86–93	88–95	83–94
	S	81–94	82–94	79–93	82–96	85–95

The results obtained for either mean D_m or mean D_p show similar values in the range [271°–310°], independently the station groups and the scenario considered. For HP data, the occurrence of the wave

directions falling in the Q4 have a frequency ranging from 63 % to 89 % for mean D_m and from 75 % to 95 % for mean D_p. It is also relevant to mention that the second most frequent wave direction falls in the third quadrant (Q3: 180°–270°).

3.4.3 Extreme values analysis

3.4.3.1 Historical data

Storm data is used as the basis for extreme wave climate regime analysis. Since the probability distribution methods (Gumbel, Fréchet and Weibull) applied in this study are built on specific assumptions, a comparison of the estimates obtained by each of these methods has been performed. The three methods used the HP dataset for estimating H_s and T_p of three return periods: 10-, 50-, 100-year. As a representative example, Figure 3.7 shows the results obtained for determining extreme values for H_s and T_p in one of the stations, applying the percent point function plotting technique. A complete set of results on calculated values in 17 stations under 5 wave climate regime scenarios for extreme wave data analysis off Iberian Peninsula can be found in Appendix 3.
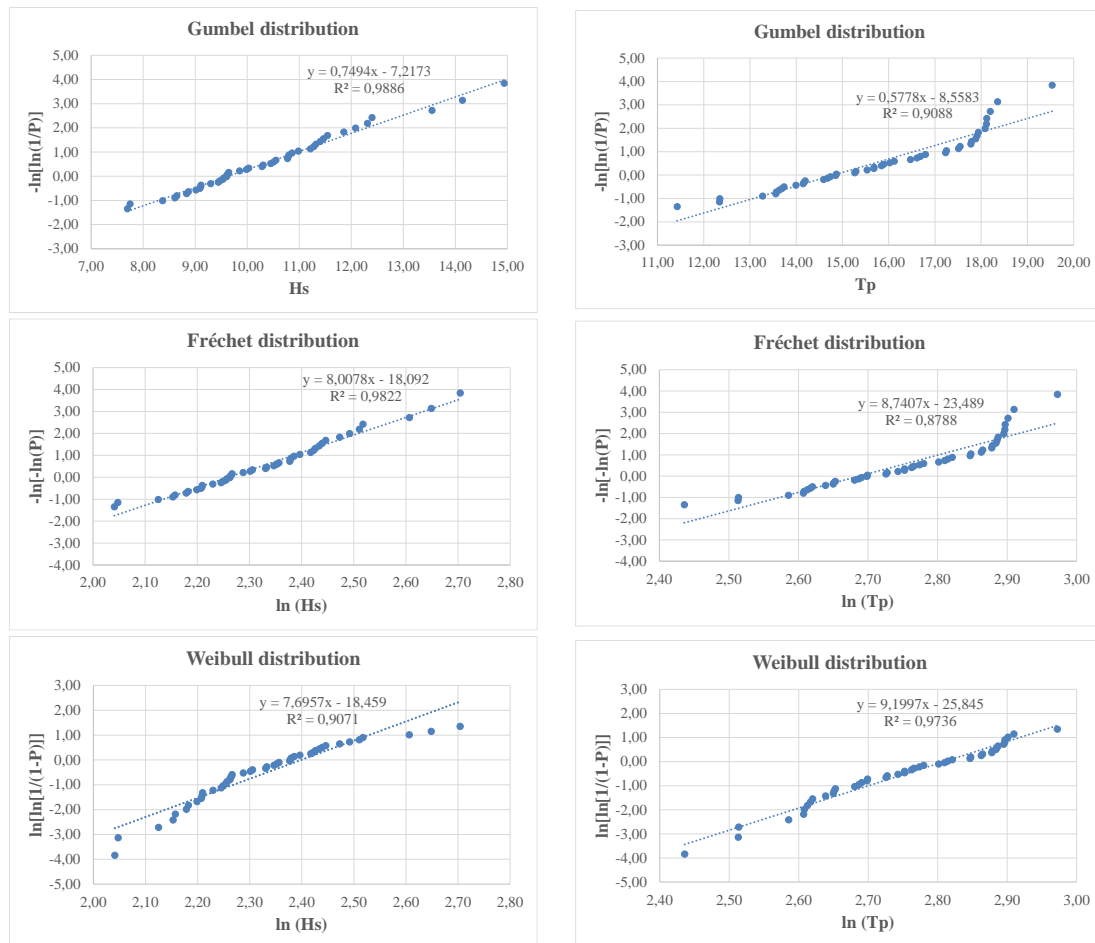
Figure 3.7: Parameter estimation of extreme value distribution using the least squares method for H_s and T_p in station W3.

Table 3.9 summarises the estimates for wave data (H_s and T_p) applying the three probability distribution methods in all stations for the considered return periods. The obtained coefficient of determination (R^2) value, which served as selection factor of the most appropriate method to apply in the RCP4.5 and RCP8.5 scenarios is presented in Table 3.10. From the calculated results, it can be noted that Fréchet distribution overestimates wave heights for longer return periods. However, this distribution provided higher R^2 values in estimating H_s results, whereas Weibull distribution has demonstrated to give the best fit (higher R^2 values) for the T_p (Table 3.11).

Table 3.9: Extreme wave climate analysis for the historical scenario in all stations. Comparison of H_s and T_p values for 10-, 50-, and 100-year return periods obtained with Gumbel, Fréchet and Weibull probability distributions.

Station	T_r (years)	H_s (m)			T_p (s)		
		Gumbel	Fréchet	Weibull	Gumbel	Fréchet	Weibull
N1	10	12.00	12.19	11.64	18.56	18.72	18.13
	50	14.07	15.12	12.46	21.04	21.91	19.05
	100	14.95	16.57	12.72	22.08	23.41	19.35
N2	10	12.72	12.85	12.35	18.24	18.40	17.82
	50	14.90	15.83	13.21	20.64	21.49	18.72
	100	15.82	17.28	13.49	21.66	22.94	19.00
N3	10	13.01	13.12	12.63	18.17	18.29	17.73
	50	15.23	16.12	13.51	20.67	21.51	18.68
	100	16.16	17.58	13.79	21.73	23.03	18.99
W1	10	13.23	13.38	12.85	17.96	18.12	17.53
	50	15.52	16.53	13.76	20.44	21.34	18.47
	100	16.49	18.08	14.05	21.49	22.86	18.77
W2	10	12.93	13.04	12.56	18.18	18.41	17.72
	50	15.18	16.08	13.45	20.80	21.91	18.71
	100	16.13	17.57	13.74	21.91	23.58	19.03
W3	10	12.63	12.68	12.27	18.71	19.01	18.17
	50	14.84	15.59	13.14	21.56	22.96	19.25
	100	15.77	17.01	13.42	22.77	24.87	19.60
W4	10	12.34	12.36	11.98	18.69	19.02	18.18
	50	14.56	15.28	12.88	21.44	22.83	19.20
	100	15.50	16.71	13.16	22.60	24.66	19.53
W5	10	12.14	12.10	11.78	18.62	18.93	18.12
	50	14.36	14.94	12.68	21.36	22.71	19.15
	100	15.31	16.34	12.97	22.52	24.53	19.48
W6	10	11.86	11.73	11.47	18.25	18.44	17.80
	50	14.08	14.45	12.36	20.78	21.76	18.76
	100	15.02	15.79	12.64	21.86	23.34	19.06
W7	10	11.62	11.43	11.21	18.04	18.22	17.60
	50	13.86	14.10	12.09	20.46	21.38	18.51
	100	14.81	15.41	12.38	21.48	22.87	18.80

Table 3.9: Extreme wave climate analysis for the historical scenario in all stations. Comparison of H_s and T_p values for 10-, 50-, and 100-year return periods obtained with Gumbel, Fréchet and Weibull probability distributions (cont.).

Station	T_r (years)	H_s (m)			T_p (s)		
		Gumbel	Fréchet	Weibull	Gumbel	Fréchet	Weibull
	10	11.30	11.10	10.92	18.40	18.66	17.92
W8	50	13.46	13.66	11.78	21.26	22.59	19.03
	100	14.38	14.91	12.06	22.47	24.50	19.39
	10	10.88	10.79	10.55	18.25	18.59	17.75
W9	50	12.88	13.27	11.35	21.20	22.79	18.90
	100	13.73	14.48	11.61	22.44	24.83	19.27
	10	10.47	10.40	10.20	18.59	18.98	18.06
S1	50	12.28	12.64	10.93	21.61	23.33	19.24
	100	13.05	13.73	11.17	22.89	25.46	19.61
	10	10.11	10.06	9.85	18.73	19.10	18.20
S2	50	11.86	12.24	10.56	21.69	23.32	19.33
	100	12.60	13.30	10.78	22.94	25.38	19.70
	10	9.43	9.42	9.15	18.28	18.69	17.73
S3	50	11.14	11.63	9.84	21.48	23.39	18.98
	100	11.86	12.72	10.06	22.83	25.72	19.39
	10	8.69	8.70	8.40	17.54	17.92	16.99
S4	50	10.45	11.08	9.12	20.67	22.51	18.22
	100	11.19	12.28	9.35	21.99	24.79	18.61
	10	7.50	7.56	7.22	17.09	17.41	16.56
S5	50	9.13	9.93	7.91	20.41	22.30	17.92
	100	9.82	11.14	8.13	21.81	24.75	18.36

Table 3.10: Extreme wave climate analysis for the historical scenario in all stations. Comparison of R^2 values obtained with the application of Gumbel, Fréchet and Weibull probability distributions.

Station	H_s			T_p		
	Gumbel	Fréchet	Weibull	Gumbel	Fréchet	Weibull
N1	0.954	0.922	0.961	0.958	0.936	0.957
N2	0.960	0.941	0.931	0.959	0.934	0.960
N3	0.970	0.953	0.929	0.968	0.951	0.942
W1	0.979	0.955	0.943	0.963	0.939	0.954
W2	0.977	0.961	0.921	0.949	0.918	0.968
W3	0.989	0.982	0.907	0.909	0.879	0.974
W4	0.993	0.993	0.886	0.908	0.870	0.990
W5	0.973	0.986	0.842	0.928	0.889	0.989
W6	0.940	0.973	0.796	0.961	0.935	0.969
W7	0.906	0.955	0.758	0.961	0.932	0.975
W8	0.901	0.952	0.733	0.937	0.908	0.943
W9	0.958	0.984	0.808	0.943	0.900	0.976
S1	0.963	0.983	0.797	0.921	0.878	0.976
S2	0.961	0.977	0.804	0.915	0.873	0.980
S3	0.969	0.976	0.856	0.926	0.887	0.979
S4	0.962	0.964	0.859	0.920	0.888	0.974
S5	0.973	0.963	0.905	0.936	0.913	0.928

Table 3.11: Most fitting probability distributions for the historical scenario in all stations

Station	Best Probability Distribution	
	H_s	T_p
N1	Weibull	Gumbel
N2	Gumbel	Weibull
N3	Gumbel	Gumbel
W1	Gumbel	Gumbel
W2	Gumbel	Weibull
W3	Gumbel	Weibull
W4	Gumbel	Weibull
W5	Fréchet	Weibull
W6	Fréchet	Weibull
W7	Fréchet	Weibull
W8	Fréchet	Weibull
W9	Fréchet	Weibull
S1	Fréchet	Weibull
S2	Fréchet	Weibull
S3	Fréchet	Weibull
S4	Fréchet	Weibull
S5	Gumbel	Gumbel

3.4.3.2 Projected data

Extreme wave climate regime projections for RCP4.5 and RCP8.5 scenarios are performed using the Fréchet and the Weibull methods in estimating H_s and T_p, respectively. Wave data values are calculated for 10-, 50-, 100-year return periods.

Table 3.12 summarises the estimation of wave data under the RCP scenarios for 10-, 50-, and 100-year return periods at all stations. Table 3.13 presents the obtained R^2 values for the RCP4.5 and RCP8.5 scenarios.

Table 3.12: Extreme wave climate values estimated by using the Fréchet and Weibull probability distributions under the RCP scenarios for 10-, 50-, and 100-year return periods at all stations.

Station	T_r (years)	RCP4.5_mid		RCP4.5_end		RCP8.5_mid		RCP8.5_end	
		H_s (m)	T_p (s)	H_s (m)	T_p (s)	H_s (m)	T_p (s)	H_s (m)	T_p (s)
	10	13.36	17.91	11.80	17.04	12.12	18.01	13.23	17.62
N1	50	18.28	18.97	14.44	17.87	15.71	18.91	17.63	18.61
	100	20.87	19.31	15.73	18.13	17.53	19.20	19.90	18.93
	10	14.17	17.79	13.10	16.90	12.87	18.02	15.37	17.29
N2	50	18.96	18.97	16.62	17.81	16.76	19.18	21.70	18.07
	100	21.44	19.35	18.38	18.11	18.74	19.56	25.11	18.32
	10	14.62	18.01	13.66	17.38	13.18	17.62	15.96	17.23
N3	50	19.42	19.20	17.47	18.50	17.05	18.77	22.64	17.95
	100	21.90	19.58	19.39	18.86	19.01	19.14	26.25	18.18

Table 3.12: Extreme wave climate values estimated by using the Fréchet and Weibull probability distributions under the RCP scenarios for 10-, 50-, and 100-year return periods at all stations (cont.).

Station	T_r (years)	RCP4.5_mid		RCP4.5_end		RCP8.5_mid		RCP8.5_end	
		H_s (m)	T_p (s)	H_s (m)	T_p (s)	H_s (m)	T_p (s)	H_s (m)	T_p (s)
W1	10	14.67	18.20	13.93	16.65	13.32	17.77	16.32	17.19
	50	19.47	19.36	17.74	17.41	17.26	18.94	23.14	17.87
	100	21.94	19.73	19.66	17.66	19.26	19.32	26.81	18.09
W2	10	13.87	17.90	14.15	16.99	12.94	17.49	15.80	17.63
	50	18.05	19.16	18.71	17.77	16.39	18.62	22.12	18.49
	100	20.17	19.56	21.05	18.02	18.11	18.98	25.50	18.76
W3	10	13.00	18.06	13.98	17.18	12.27	17.39	15.10	17.33
	50	16.55	19.39	18.80	18.00	15.12	18.45	20.76	18.13
	100	18.33	19.82	21.31	18.26	16.51	18.79	23.75	18.39
W4	10	12.42	18.01	13.49	17.11	13.18	17.62	15.96	17.23
	50	15.76	19.22	18.04	17.90	17.05	18.77	22.64	17.95
	100	17.44	19.61	20.40	18.15	19.01	19.14	26.25	18.18
W5	10	12.19	18.76	13.12	17.16	10.80	17.13	13.68	17.20
	50	15.69	20.30	17.69	18.01	12.34	18.15	18.19	17.89
	100	17.46	20.80	20.07	18.28	13.06	18.48	20.53	18.11
W6	10	11.70	18.55	12.62	17.02	10.58	16.74	13.22	17.20
	50	14.89	20.02	17.11	17.79	11.98	17.60	17.69	17.93
	100	16.49	20.50	19.45	18.03	12.63	17.87	20.01	18.16
W7	10	11.43	18.61	11.87	17.26	10.58	16.70	12.63	16.97
	50	14.60	20.21	15.80	18.20	12.13	17.56	16.64	17.74
	100	16.18	20.73	17.83	18.49	12.85	17.83	18.70	17.98
W8	10	11.20	17.36	11.31	17.24	10.41	16.76	12.46	17.39
	50	14.10	18.72	14.94	18.24	12.13	17.74	16.76	18.19
	100	15.54	19.15	16.81	18.55	12.93	18.05	19.00	18.45
W9	10	11.18	17.83	10.75	17.12	9.92	16.74	12.13	17.10
	50	14.35	19.28	14.05	18.22	11.51	17.72	16.20	17.86
	100	15.94	19.75	15.73	18.57	12.25	18.03	18.31	18.10
S1	10	11.09	17.94	10.46	17.64	9.73	16.82	11.80	17.22
	50	14.47	19.54	13.63	18.94	11.28	17.79	15.64	18.16
	100	16.20	20.06	15.24	19.36	12.00	18.10	17.62	18.46
S2	10	10.96	18.13	10.13	17.96	9.56	16.85	11.52	17.57
	50	14.58	19.68	13.14	19.21	11.29	17.79	15.36	18.53
	100	16.45	20.18	14.67	19.61	12.12	18.09	17.34	18.83
S3	10	10.21	15.77	9.54	17.52	8.69	17.14	10.78	17.17
	50	13.72	16.47	12.58	18.94	10.31	18.17	14.58	18.12
	100	15.55	16.69	14.14	19.40	11.09	18.50	16.57	18.42
S4	10	9.03	15.57	8.87	17.17	7.83	16.93	9.74	17.33
	50	12.19	16.37	12.06	18.51	9.50	18.07	13.46	18.50
	100	13.84	16.62	13.73	18.95	10.31	18.43	15.44	18.88
S5	10	7.64	15.29	7.89	17.35	6.85	17.00	8.45	17.27
	50	10.40	16.01	11.27	19.22	8.66	18.70	12.06	18.59
	100	11.85	16.24	13.11	19.84	9.56	19.25	14.02	19.01

Table 3.13: Extreme wave climate analysis for the RCP scenarios in all stations. Comparison of R^2 values obtained with the application of Fréchet and Weibull probability distributions.

Station	RCP4.5_mid				RCP4.5_end				RCP8.5_mid				RCP8.5_end			
	H_s		T_p		H_s		T_p		H_s		T_p		H_s		T_p	
	Fréchet	Weibull	Fréchet	Weibull	Fréchet	Weibull	Fréchet	Weibull	Fréchet	Weibull	Fréchet	Weibull	Fréchet	Weibull	Fréchet	Weibull
N1	0.925	0.921			0.952	0.946			0.982	0.968			0.929	0.967		
N2	0.949	0.928			0.966	0.944			0.974	0.969			0.924	0.991		
N3	0.950	0.945			0.946	0.940			0.972	0.956			0.921	0.960		
W1	0.947	0.930			0.953	0.870			0.955	0.977			0.910	0.969		
W2	0.953	0.944			0.979	0.934			0.975	0.920			0.959	0.962		
W3	0.952	0.933			0.982	0.954			0.960	0.913			0.973	0.977		
W4	0.984	0.866			0.966	0.919			0.972	0.956			0.921	0.960		
W5	0.981	0.880			0.949	0.909			0.950	0.891			0.958	0.964		
W6	0.961	0.900			0.932	0.948			0.922	0.845			0.936	0.971		
W7	0.943	0.902			0.899	0.978			0.962	0.844			0.939	0.972		
W8	0.900	0.854			0.897	0.970			0.981	0.872			0.937	0.946		
W9	0.861	0.872			0.880	0.959			0.979	0.885			0.965	0.956		
S1	0.849	0.911			0.901	0.954			0.979	0.875			0.965	0.963		
S2	0.837	0.932			0.930	0.934			0.962	0.902			0.973	0.938		
S3	0.833	0.964			0.959	0.971			0.966	0.841			0.973	0.975		
S4	0.919	0.970			0.921	0.961			0.968	0.835			0.963	0.958		
S5	0.954	0.964			0.889	0.962			0.933	0.958			0.935	0.963		

3.4.3.3 Significant wave height

Results obtained for different H_s return periods (Table 3.14) show increasing values from 10- to 100-year, as expected. In general, the values of H_s decrease from the northern to southern station groups in the sequence WN>N>WS>S, where values found for S are considerably lower (average from 67 % to 77 %) than those of the remaining station groups.

For each station group, when HP data values are compared with the projected results from the RCP scenarios for H_s, tendencies show that: (i) HP data values are slightly analogous to those calculated in the RCPs_mid; (ii) projected values obtained from RCPs_end have higher values when compared to HP data values, with special incidence of the results obtained from RCP8.5.

H_s return values obtained from RCP4.5_mid and RCP4.5_end are apparently contradictory, since results are mostly lower for RCP4.5_end than for RCP4.5_mid. However, similar results can also be found in Copernicus Climate Change Service (2019) for the Iberian Peninsula. This is not the case with the RCP8.5 scenarios, where the return values from RCP8.5_end are consistently higher than those from RCP8.5_mid.

Table 3.14: Return values for H_s (m).

Return period (years)	Station Group	Wave Climate Regime Scenario				
		HP	RCP4.5_mid	RCP4.5_end	RCP8.5_mid	RCP8.5_end
10	N	12.19–13.12	13.36–14.62	11.80–13.66	12.12–13.18	13.23–15.96
	WN	12.36–13.38	12.42–14.67	13.49–14.15	12.27–13.32	15.10–16.32
	WS	10.79–12.10	11.18–12.19	10.75–13.12	9.92–10.80	12.13–13.68
	S	7.56–10.40	7.64–11.09	7.89–10.46	6.85–9.73	8.45–11.80
50	N	15.12–16.12	18.28–19.42	14.44–17.47	15.71–17.05	17.63–22.64
	WN	15.28–16.53	15.76–19.47	17.74–18.80	15.12–17.26	20.76–23.14
	WS	13.27–14.94	14.10–15.69	14.05–17.69	11.51–12.34	16.20–18.19
	S	9.93–12.64	10.40–14.58	11.27–13.63	8.66–11.29	12.06–15.64
100	N	16.57–17.58	20.87–21.90	15.73–19.39	17.53–19.01	19.90–26.25
	WN	16.71–18.08	17.44–21.94	19.66–21.31	16.51–19.26	23.75–26.81
	WS	14.48–16.34	15.54–17.46	15.73–20.07	12.25–13.06	18.31–20.53
	S	11.14–13.73	11.85–16.45	13.11–15.24	9.56–12.12	14.02–17.62

3.4.3.4 Wave peak period

For each return period, wave peak period T_p (Table 3.15) appears to maintain constant values in all station groups, independently the scenario considered. Approximate values of 17.50 s, 18.00 s, and 19.00 s have been obtained for 10-, 50-, 100-year return period, respectively.

Table 3.15: Return values for T_p (s).

Return period (years)	Station Group	Wave Climate Regime Scenario				
		HP	RCP4.5_mid	RCP4.5_end	RCP8.5_mid	RCP8.5_end
10	N	17.73–18.13	17.79–18.01	16.90–17.38	17.62–18.02	17.23–17.62
	WN	17.53–18.18	17.90–18.20	16.65–17.18	17.39–17.77	17.19–17.63
	WS	17.60–18.12	17.36–18.76	17.02–17.26	16.70–17.13	16.97–17.39
	S	16.56–18.20	15.29–18.13	17.17–17.96	16.82–17.14	17.17–17.57
50	N	18.68–19.05	18.97–19.20	17.81–18.50	18.77–19.18	17.95–18.61
	WN	18.47–19.25	19.16–19.39	17.41–18.00	18.45–18.94	17.87–18.49
	WS	18.51–19.15	18.72–20.30	17.79–18.24	17.56–18.15	17.74–18.19
	S	17.92–19.33	16.01–19.68	18.51–19.22	17.79–18.70	18.12–18.59
100	N	18.99–19.35	19.31–19.58	18.11–18.86	19.14–19.56	18.18–18.93
	WN	18.77–19.60	19.56–19.82	17.66–18.26	18.79–19.32	18.09–18.76
	WS	18.80–19.48	19.15–20.80	18.03–18.57	17.83–18.48	17.98–18.45
	S	18.36–19.70	16.24–20.18	18.95–19.84	18.09–19.25	18.42–19.01

3.4.4 Comparison with existing studies

Two studies (Carvalho and Capitão, 1995 and Capitão and Fortes, 2011) were carried out to estimate 10-, 50-, 100-year return period of H_s at three sites on the western coast of Portugal (Leixões, Figueira

da Foz and Sines). These studies differ partly in their research approach and scope from the present one, but are anyway useful benchmark to test the validity of the obtained results.

The main important difference is that the present study uses an extensive modelled dataset consisting of 46 years of historical data and two twenty-year time periods of RCPs projected data applied at 17 locations far from the coast, whereas in the other studies the wave data have been recorded for 13 years in the harbours of Figueira da Foz and Sines (Carvalho and Capitão, 1995) and 14 years in Leixões (Capitão and Fortes, 2011).

Table 3.16 compares the H_s extremes values predictions of this study for the HP scenario against those obtained in the other two studies. Stations W3, W5 and W7 are considered geographically near to Leixões, Figueira da Foz and Sines, respectively. The comparison between the results obtained in the present study and in Carvalho and Capitão (1995) shows small differences. However, large discrepancies are found when the comparison is made with Capitão and Fortes (2011). The discrepancies found can be justified for three main reasons: (i) the temporal and spatial dimensions of data sources; (ii) the fact that a storm sub-dataset extracted from the wave dataset was used in the calculation of extreme values in the present study; and (iii) the wave climate data near the coast (as used by those authors) is influenced by wave refraction due to local bathymetric characteristics.

Table 3.16: Estimate values of H_s on the western coast of Portugal obtained in different studies.

Location	T_r (years)	Extreme Values of H_s (m)		
		Present Study (HP data)	**(Carvalho and Capitão, 1995)**	**(Capitão and Fortes, 2011)**
W3 Leixões	10	12.69	–	7.25
	50	15.59	–	9.62
	100	17.01	–	10.84
W5 Figueira da Foz	10	12.14	10.60	–
	50	14.36	12.80	–
	100	15.31	13.80	–
W7 Sines	10	11.43	10.70	–
	50	14.10	15.80	–
	100	15.41	18.20	–

3.4.5 Extreme values for coastal engineering design

The results obtained in this study for 100-year return values of H_s and T_p derived for HP data and RCP8.5_end in four station groups are summarised in Table 3.17. The methodology followed for extreme value analysis based on a storm sub-dataset obtained from the H_s 95th percentile of original wave datasets justifies the higher estimated values for 100-year H_s from the RCP8.5_end scenario when compared to the one estimated for HP data. The obtained results are aligned with other similar

works (e.g., Copernicus Climate Change Service (2019)) that project more intense extreme H_s for the end of the century.

Awareness on the prediction of 100-year return values from RCP scenarios should be taken, since these scenarios are based on uncertainty and a 20-year span data. However, the obtained results are robust and can be of valuable interest in engineering practice.

These values can be used as design parameters in maritime structures projects to be applied in the Iberian Peninsula coastal zone, once propagated to the local of interest by appropriate methodologies.

Table 3.17: 100-year return period values for H_s and T_p as parameters for structural engineering design.

Wave data		Station Group			
		N	WN	WS	S
HP data	H_s (m)	16.57–17.58	16.71–18.08	14.48–16.34	11.14–13.73
	T_p (s)	18.99–19.35	18.77–19.60	18.80–19.48	18.36–19.70
RCP8.5_end	H_s (m)	19.90–26.25	23.75–26.81	18.31–20.53	14.02–17.62
	T_p (s)	18.18–18.93	18.09–18.76	17.98–18.45	18.42–19.01

3.5 Summary and conclusions

The present study developed an extreme wave value analysis under uncertainty scenarios using comprehensive simulated wave datasets downscaled by Meteogalicia from CMIP5 models to 17 stations off the Iberian Peninsula coastal zone.

The extreme wave data values for H_s and T_p were calculated through the Gumbel, Fréchet and Weibull distributions for the 10-, 50-, and 100-year return period. Five wave climate scenarios using HP data and projected data of RCP4.5_mid, RCP4.5_end, RCP8.5_mid and RCP8.5_end were considered.

Descriptive statistical analysis of the obtained wave results demonstrated that: (i) H_s has different values at different locations in the coastal zone with decreasing values from North to South; (ii) HP data values are higher than those calculated in any of the RCP scenarios; (iii) projected H_s values obtained from RCP4.5 and RCP8.5 have slight differences (approximately 4 %) between these considered scenarios; (iv) maximum H_s values show contradictory tendencies when HP data are compared to projected data; (v) maximum values of H_s obtained for RCP4.5_mid and RCP8.5_end scenarios are higher than those of the HP data for the northern stations and lower for the southern stations; (vi) mean T_p appears to maintain constant values in all stations, independently the wave climate regime scenario considered; (vii) results for mean D_m and mean D_p show higher frequency of occurrence in Q4 (270°–360°) followed by a smaller frequency in Q3 (180°–270°).

Extreme H_s values for all return periods have different values in different locations in the coastal zone with decreasing values from North to South, being considerably lower on the most southern stations. In each station, HP data values are similar to those calculated in the RCPs_mid, and projected values obtained from the RCPs_end have higher values when compared to HP data values. For each return period, wave peak period, T_p, results show constant values in all stations, independently the scenario considered.

Wave extreme value analysis for the H_s and T_p is an essential element for marine structural design. The high-quality of the database applied and the assumptions taken in this research work allowed the determination of 100-year return period of H_s and T_p values that can be used with confidence as design values for structural analyses in maritime works to be built in the western coast off Iberian Peninsula.

3.6 References for Chapter 3

Álvarez, F.; Pan, S.; Coelho, C.; and Baptista, P. (2020). Modeling Shoreline Changes in Northwest Portugal Using a Process-Based Numerical Model: COAST2D. *Journal of Waterway, Port, Coastal, and Ocean Engineering*, *146*(4). https://doi.org/10.1061/(ASCE)WW.1943-5460.0000563.

Baptista, P.; Coelho, C.; Pereira, C.; Bernardes, C.; and Veloso-Gomes, F. (2014). Beach morphology and shoreline evolution: Monitoring and modelling medium-term responses (Portuguese NW coast study site). *Coastal Engineering*, *84*, 23–37. https://doi.org/https://doi.org/10.1016/j.coastaleng.2013.11.002.

Bio, A.; Gonçalves, J.A.; Pinho, J.; Vieira, L.; Vieira, J.; Smirnov, G.; and Bastos, L. (2020). Indicadores de vulnerabilidade de erosão costeira: Um estudo de caso no Norte de Portugal. *Revista de Gestão Costeira Integrada - Journal of Integrated Coastal Zone Management*, *20*(3), 197–209. https://doi.org/10.5894/rgci-n337.

Callaghan, D.P.; Wainwright, D.J.; and Hanslow, D.J. (2020). Consideration of uncertainty in sea level rise in Australia's most exposed estuary: A discussion on allowances under different epistemic uncertainties. *Coastal Engineering*, *159*, 103718. https://doi.org/https://doi.org/10.1016/j.coastaleng.2020.103718.

Capitão, R.; and Fortes, C. (2011). A variabilidade das extrapolações do regime de extremos com a natureza das amostras: o caso de estudo do porto de vila do conde. In *7as Jornadas Portuguesas de Engenharia Costeira e Portuária, 6 e 7 de Outubro de 2011* (p. 16). Porto, Portugal. Retrieved from https://www.researchgate.net/publication/285163986_A_variabilidade_das_extrapolacoes_do_regime_de_extremos_com_a_natureza_das_amostras_o_caso_de_estudo_do_porto_de_vila_do_conde.

Carvalho, M.; and Capitão, R. (1995). Extreme wave heights off the western coast of Portugal. In *Proceedings of the 14th International Conference on Offshore Mechanics and Arctic Engineering, 18th to 22th June 1995*. Copenhagen, Denmark.

Castelle, B.; Marieu, V.; Bujan, S.; Splinter, K.D.; Robinet, A.; Sénéchal, N.; and Ferreira, S. (2015). Impact of the winter 2013–2014 series of severe Western Europe storms on a double-barred sandy coast: Beach and dune erosion and megacusp embayments. *Geomorphology*, *238*, 135–148. https://doi.org/https://doi.org/10.1016/j.geomorph.2015.03.006.

Cheng, H.-Q.; and Chen, J.-Y. (2017). Adapting cities to sea level rise: A perspective from Chinese deltas. *Advances in Climate Change Research*, *8*(2), 130–136. https://doi.org/https://doi.org/10.1016/j.accre.2017.05.006.

Cherneva, Z.; Petrova, P.; Andreeva, N.; and Guedes-Soares, C. (2005). Probability distributions of peaks, troughs and heights of wind waves measured in the black sea coastal zone. *Coastal Engineering*, *52*(7), 599–615. https://doi.org/https://doi.org/10.1016/j.coastaleng.2005.02.006.

Chini, N.; Stansby, P.; Leake, J.; Wolf, J.; Roberts-Jones, J.; and Lowe, J. (2010). The impact of sea level rise and climate change on inshore wave climate: A case study for East Anglia (UK). *Coastal Engineering*, *57*(11), 973–984.

https://doi.org/https://doi.org/10.1016/j.coastaleng.2010.05.009.

Cotta, H.; Correa, W.; and Albuquerque, T. (2016). Aplicação da distribuição de Gumbel para valores extremos de precipitação no município de Vitória-ES.

Dentale, F.; Furcolo, P.; Carratelli, E.P.; Reale, F.; Contestabile, P.; and Tomasicchio, G.R. (2018). Extreme Wave Analysis by Integrating Model and Wave Buoy Data. *Water (Switzerland)*, *10*(4). https://doi.org/10.3390/w10040373.

Ding, Y.; Nath Kuiry, S.; Elgohry, M.; Jia, Y.; Altinakar, M.S.; and Yeh, K.-C. (2013). Impact assessment of sea-level rise and hazardous storms on coasts and estuaries using integrated processes model. *Ocean Engineering*, *71*, 74–95. https://doi.org/https://doi.org/10.1016/j.oceaneng.2013.01.015.

Feng, J.; Wen-Shan, L.; Hui, W.; Jian-Li, Z.; and Jun-Xing, D. (2019). Evaluation of sea level rise and associated responses in Hangzhou Bay from 1978 to 2017. *Advances in Climate Change Research*, *9*. https://doi.org/10.1016/j.accre.2019.01.002.

Ferreira, M.; Fernández-Fernández, S.; Coelho, C.; and Silva, P.A. (2021). Caracterização de tempestades e da deriva litoral no litoral de Aveiro, em cenários de alterações climáticas. In *15º Congresso da Água, 22 a 26 de Março 2021*. Lisboa, Portugal. Retrieved from https://www.aprh.pt/congressoagua2021/docs/15ca_17.pdf.

Filliben, J.J. (1975). The Probability Plot Correlation Coefficient Test for Normality. *Technometrics*, *17*(1), 111–117. https://doi.org/10.1080/00401706.1975.10489279.

Goda, Y. (2000). Statistical Analysis of Extreme Waves. In P. L.-F. Liu (Ed.), *Random Seas and Design of Maritime Structures, Volume 15* (2nd ed., pp. 377–425). Singapore: World Scientific Publishing Co. Pte. Ltd.

Gomes, M.; Santos, L.; Pinho, J.; and Antunes do Carmo, J. (2018). Hazard Assessment of Storm Events for the Portuguese Northern Coast. *Geosciences*, *8*(5), 178. https://doi.org/10.3390/geosciences8050178.

Guedes-Soares, C.; and Carvalho, A. (2001). Probability Distributions of Wave Heights and Periods in Measured Two-Peaked Spectra from the Portuguese Coast. In *Proceedings of the 20th International Conference on Offshore Mechanics and Arctic Engineering, 3rd to 8th June 2001* (Vol. 2). Rio de Janeiro, Brazil.

Harley, M. (2017). Coastal Storm Definition. In G. Coco & P. Ciavola (Eds.), *Coastal Storms: Processes and Impacts* (First Edit, pp. 1–22). Wiley-Blackwell. https://doi.org/10.1002/9781118937099.ch1.

IPCC. (2014). *Climate Change 2014: Synthesis Report. Contribution of Working Groups I, II and III to the Fifth Assessment Report of the Intergovernmental Panel on Climate Change [Core Writing Team]*. (R. k. Pachauri & L. A. Meyer, Eds.). Geneva, Switzerland. Retrieved from https://www.ipcc.ch/site/assets/uploads/2018/05/SYR_AR5_FINAL_full_wcover.pdf.

IPCC. (2020). Scenario Process for AR5 - Representative Concentration Pathways (RCPs). Retrieved May 12, 2020, from https://sedac.ciesin.columbia.edu/ddc/ar5_scenario_process/RCPs.html.

Karian, Z.A.; and Dudewicz, E.J. (2000). *Fitting statistical distributions: The generalized lambda distribution and generalized bootstrap methods. Fitting Statistical Distributions: The Generalized Lambda Distribution and Generalized Bootstrap Methods*.

Lyu, K.; Zhang, X.; and Church, J.A. (2020). Regional Dynamic Sea Level Simulated in the CMIP5 and CMIP6 Models: Mean Biases, Future Projections, and Their Linkages. *Journal of Climate*, *33*(15), 6377–6398. https://doi.org/10.1175/JCLI-D-19-1029.1.

Marone, E.; Camargo, R. de; and Castro, J.S. (2017). Coastal Hazards, Risks, and Marine Extreme Events. *Oxford Handbooks Online Coastal*, (May), 1–19. https://doi.org/10.1093/oxfordhb/9780190699420.013.34.

Martucci, G.; Carniel, S.; Chiggiato, J.; Sclavo, M.; Lionello, P.; and Galati, M.B. (2010). Statistical trend analysis and extreme distribution of significant wave height from 1958 to 1999 – an application to the Italian Seas. *Ocean Science*, *6*(2), 525–538. https://doi.org/10.5194/os-6-525-2010.

Mase, H.; Tsujio, D.; Yasuda, T.; and Mori, N. (2013). Stability analysis of composite breakwater with wave-dissipating blocks considering increase in sea levels, surges and waves due to climate change. *Ocean Engineering*, *71*, 58–65. https://doi.org/https://doi.org/10.1016/j.oceaneng.2012.12.037.

Masselink, G.; Austin, M.; Scott, T.; Poate, T.; and Russell, P. (2014). Role of wave forcing, storms and NAO in outer bar dynamics on a high-energy, macro-tidal beach. *Geomorphology*, *226*, 76–93. https://doi.org/https://doi.org/10.1016/j.geomorph.2014.07.025.

Mathiesen, M.; Goda, Y.; Hawkes, P.J.; Mansard, E.; Martín, M.J.; Peltier, E.; Thompson, E.F.; and Van Vledder, G. (1994). Recommended practice for extreme wave analysis. *Journal of Hydraulic Research*, *32*(6), 803–814. https://doi.org/10.1080/00221689409498691.

McKenna, S.; Santoso, A.; Gupta, A. Sen; Taschetto, A.S.; and Cai, W. (2020). Indian Ocean Dipole in CMIP5 and CMIP6: characteristics, biases, and links to ENSO. *Scientific Reports*, *10*(1), 11500. https://doi.org/10.1038/s41598-020-68268-9.

Merkens, J.-L.; Reimann, L.; Hinkel, J.; and Vafeidis, A.T. (2016). Gridded population projections for the coastal zone under the Shared Socioeconomic Pathways. *Global and Planetary Change*, *145*, 57–66. https://doi.org/https://doi.org/10.1016/j.gloplacha.2016.08.009.

Milly, P.C.D.; Betancourt, J.; Falkenmark, M.; Hirsch, R.M.; Kundzewicz, Z.W.; Lettenmaier, D.P.; and Stouffer, R.J. (2008). Stationarity Is Dead: Whither Water Management? *Science*, *319*(5863), 573 LP-574. https://doi.org/10.1126/science.1151915.

Montanari, A.; and Koutsoyiannis, D. (2014). Modeling and mitigating natural hazards: Stationarity is immortal! *Water Resources Research*, *50*(12), 9748–9756. https://doi.org/10.1002/2014WR016092.

Mori, N.; Shimura, T.; Yasuda, T.; and Mase, H. (2013). Multi-model climate projections of ocean surface variables under different climate scenarios—Future change of waves, sea level and wind. *Ocean Engineering*, *71*, 122–129. https://doi.org/https://doi.org/10.1016/j.oceaneng.2013.02.016.

Morim, J.; Hemer, M.; Wang, X.L.; Cartwright, N.; Trenham, C.; Semedo, A.; Young, I.; Bricheno, L.; Camus, P.; Casas-Prat, M.; Erikson, L.; Mentaschi, L.; Mori, N.; Shimura, T.; Timmermans, B.; Aarnes, O.; Breivik, Ø.; Behrens, A.; Dobrynin, M.; Menendez, M.; Staneva, J.; Wehner, M.; Wolf, J.; Kamranzad, B.; Webb, A.; Stopa, J.; and Andutta, F. (2019). Robustness and uncertainties in global multivariate wind-wave climate projections. *Nature Climate Change*, *9*(9), 711–718. https://doi.org/10.1038/s41558-019-0542-5.

Naghettini, M.; and Pinto, É.J. de A. (2007). Análise local de frequência de variáveis hidrológicas. In *Hidrologia estatística*. CPRM. Retrieved from http://www.cprm.gov.br/publique/media/hidrologia/mapas_publicacoes/livro_hidrologia_estatistica/cap10-anal_reg.pdf.

Nascimento, L. (2009). *Análise de Valores Extremos de Parâmetros de Resposta Dinâmica de Plataformas Auto-Elevatórias*. MSc Thesis in Civil Engineering, Federal University of Rio de Janeiro, Brazil. https://doi.org/10.13140/RG.2.2.28024.85764.

Neumann, B.; Vafeidis, A.T.; Zimmermann, J.; and Nicholls, R.J. (2015). Future coastal population growth and exposure to sea-level rise and coastal flooding-a global assessment. *PloS One*, *10*(3), e0118571.

Park, S.B.; Shin, S.Y.; Shin, D.G.; Jung, K.H.; Choi, Y.H.; Lee, J.; and Lee, S.J. (2020). Extreme Value Analysis of Metocean Data for Barents Sea. *J. Ocean Eng. Technol.*, *34*(1), 26–36. https://doi.org/10.26748/KSOE.2019.094.

Pereira, C.; and Coelho, C. (2013). Mapping erosion risk under different scenarios of climate change for Aveiro coast, Portugal. *Natural Hazards*, *69*(1), 1033–1050. https://doi.org/10.1007/s11069-013-0748-1.

Piccinini, F. (2006). A onda de projeto por meio de análise estatística de extremos a partir de dados medidos por satélite. *Revista Pesquisa Naval*, (19), 84–90. Retrieved from http://gtimotheo.com/Arquivos/estatistica.pdf.

Pinho, J.; Vieira, L.; Vieira, J.; Smirnov, G.; Gomes, A.; Bio, A.; Gonçalves, J.A.; and Bastos, L. (2020). Modelação da hidrodinâmica e da morfodinâmica na costa Noroeste de Portugal em cenários de alterações climáticas. *Journal of Integrated Coastal Zone Management / Revista de Gestão Costeira Integrada*, *20*(2), 89–102. https://doi.org/10.5894/rgci-n297.

Plecha, S.M.; and Soares, P.M.M. (2020). Global Marine Heatwave events using the new CMIP6 multi-model ensemble: from shortcomings in present climate to future projections. *Environmental Research Letters*, *15*(12). https://doi.org/https://doi.org/10.1088/1748-9326/abc847.

Qu, Y.; Liu, Y.; Jevrejeva, S.; and Jackson, L.P. (2020). Future sea level rise along the coast of China and adjacent region under 1.5 °C and 2.0 °C global warming. *Advances in Climate Change Research*. https://doi.org/https://doi.org/10.1016/j.accre.2020.09.001.

Reale, F.; Dentale, F.; Furcolo, P.; Di Leo, A.; and Carratelli, E.P. (2020). An Experimental Assessment of Extreme Wave Evaluation by Integrating Model and Wave Buoy Data. *Water (Switzerland)*, *12*(4). https://doi.org/10.3390/w12041201.

Sansigolo, C.A. (2008). Distribuições de extremos de precipitação diária, temperatura máxima e mínima e velocidade do vento em Piracicaba, SP (1917-2006). *Revista Brasileira de Meteorologia*, *23*, 341–346. https://doi.org/doi.org/10.1590/S0102-77862008000300009.

Santos, L.; Gomes, M.; Vieira, L.; Pinho, J.; and Antunes do Carmo, J. (2018). Storm surge assessment methodology based on numerical modelling. In G. La Loggia, G. Freni, V. Puleo, & M. De Marchis (Eds.), *HIC 2018 EPiC Series in Engineering, Volume 3* (pp. 1876–1884). https://doi.org/10.29007/hrlw.

Silva, R.; Coelho, C.; Veloso-Gomes, F.; and Taveira-Pinto, F. (2008). A importância de alguns parâmetros hidromorfológicos em estudos de modelação na zona costeira (The importance of some hydro-morphological parameters in coastal zones modeling studies). In *Jornadas de Hidráulica, Recursos Hídricos e Ambiente. Faculdade de Engenharia da Universidade do Porto* (pp. 25–35).

Sperna-Weiland, F.C.; Hegnauer, M.; Boogaard, H. Van den; Buiteveld, H.; Lammersen, R.; and Beersma, J. (2016). Implications of CMIP5 derived climate scenarios for discharge extremes of the Rhine. In S. Erpicum, B. Dewals, P. Archambeau, & M. Pirotton (Eds.), *Proceedings of the 4th IAHR Europe Congress (Liege, Belgium, 27-29 July 2016). Sustainable Hydraulics in the Era of Global Change: Hydrometeorological extremes, uncertainties and global change* (pp. 790–795). London, UK: CRC Press. https://doi.org/doi.org/10.1201/b21902.

SROCC. (2019). IPCC SR Ocean and Cryosphere Sea Level Rise and Implications for Low Lying Islands, Coasts and Communities - Chapter 4, Final Draft (p. 31). Retrieved from https://report.ipcc.ch/srocc/pdf/SROCC_FinalDraft_Chapter4_SM.pdf.

Sun, Q.-H.; Xia, J.; Miao, C.-Y.; and Duan, Q.-Y. (2017). Bayesian multi-model projections of extreme hydroclimatic events under RCPs scenarios. *Advances in Climate Change Research*, *8*(2), 80–92. https://doi.org/https://doi.org/10.1016/j.accre.2017.06.001.

Tatebe, H.; Ishii, M.; Mochizuki, T.; Chikamoto, Y.; Sakamoto, T.T.; Komuro, Y.; Mori, M.; Yasunaka, S.; Watanabe, M.; Ogochi, K.; Suzuki, T.; Nishimura, T.; and Kimoto, M. (2012). The Initialization of the MIROC Climate Models with Hydrographic Data Assimilation for Decadal Prediction. *Journal of the Meteorological Society of Japan. Ser. II*, *90A*, 275–294. https://doi.org/10.2151/jmsj.2012-A14.

Thevasiyani, T.; and Perera, K. (2014). Statistical analysis of extreme ocean waves in Galle, Sri Lanka. *Weather and Climate Extremes*, *5–6*, 40–47. https://doi.org/https://doi.org/10.1016/j.wace.2014.07.003.

Urošev, M.; Lešˇcešen, I.; Štrbac, D.; and Dolinaj, D. (2016). Extreme hydrological situations on Danube River – Case study Bezdan hydrological station (Serbia). In S. Erpicum, B. Dewals, P. Archambeau, & M. Pirotton (Eds.), *Proceedings of the 4th IAHR Europe Congress (Liege, Belgium, 27-29 July 2016). Sustainable Hydraulics in the Era of Global Change: Hydrometeorological extremes, uncertainties and global change* (pp. 771–778). London, UK: CRC Press. https://doi.org/doi.org/10.1201/b21902.

Vanem, E. (2015). Uncertainties in extreme value modelling of wave data in a climate change perspective. *Journal of Ocean Engineering and Marine Energy*, *1*, 339–359. https://doi.org/10.1007/s40722-015-0025-3.

Vanem, E. (2017). A regional extreme value analysis of ocean waves in a changing climate. *Ocean Engineering*, *144*, 277–295. https://doi.org/https://doi.org/10.1016/j.oceaneng.2017.08.027.

Vivekanandan, N. (2012). Comparison of Estimators of Extreme Value Distributions for Wind Data Analysis. *Bonfring International Journal of Data Mining*, *2*, 16–20. https://doi.org/10.9756/BIJDM.1503.

Wang, L.; Chen, B.; Zhang, J.; and Chen, Z. (2013). A new model for calculating the design wave height in typhoon-affected sea areas. *Natural Hazards*, *67*(2), 129–143. https://doi.org/10.1007/s11069-012-0266-6.

Wang, X.; Feng, Y.; and Swail, V.R. (2016). Projected changes, climate change signal, and uncertainties in the CMIP5-based projections of ocean surface wave heights. In *EGU General Assembly 2016, 17th to 22nd April 2016* (Vol. 18). Vienna, Austria. Retrieved from https://ui.adsabs.harvard.edu/abs/2016EGUGA..18.2006W/abstract.

Wang, X.; and Swail, V.R. (2001). Changes of Extreme Wave Heights in Northern Hemisphere Oceans and Related Atmospheric Circulation Regimes. *Journal of Climate*, *14*(10), 2204–2221. https://doi.org/10.1175/1520-0442(2001)014<2204:COEWHI>2.0.CO;2.

Warner, N.N.; and Tissot, P.E. (2012). Storm flooding sensitivity to sea level rise for Galveston Bay, Texas. *Ocean Engineering*, *44*, 23–32. https://doi.org/https://doi.org/10.1016/j.oceaneng.2012.01.011.

Winterstein, S.R.; Ude, T.C.; Cornell, C.A.; Bjerager, P.; and Haver, S. (1993). Environmental parameters for extreme response: Inverse FORM with omission factors. In *Proceedings of the 6th International Conference on Structural*

Safety and Reliability (ICOSSAR-93), 9th to 13th August 1993. Innsbruck, Austria.

WMO. (1998). *Guide to wave analysis and forecasting - 2nd edition, WMO-No. 702*. Geneva, Switzerland. Retrieved from https://library.wmo.int/doc_num.php?explnum_id=3110.

Xie, D.; Zou, Q.-P.; Mignone, A.; and MacRae, J.D. (2019). Coastal flooding from wave overtopping and sea level rise adaptation in the northeastern USA. *Coastal Engineering*, *150*, 39–58. https://doi.org/https://doi.org/10.1016/j.coastaleng.2019.02.001.

Zhang, K.; Douglas, B.C.; and Leatherman, S.P. (2004). Global Warming and Coastal Erosion. *Climatic Change*, *64*(1), 41. https://doi.org/10.1023/B:CLIM.0000024690.32682.48.

Zhu, H.; Jiang, Z.; Li, J.; Li, W.; Sun, C.; and Li, L. (2020). Does CMIP6 Inspire More Confidence in Simulating Climate Extremes over China? *Advances in Atmospheric Sciences*, *37*(10), 1119–1132. https://doi.org/10.1007/s00376-020-9289-1.

(Page intentionally left blank)

CHAPTER 4

Coastal protection structures to promote wave energy dissipation and sediments retention. A comparative study

"The scientist is not a person who gives the right answers, he's one who asks the right questions"

Claude Levi-Strauss. French anthropologist and ethnologist (1908-2009)

(Page intentionally left blank)

CHAPTER 4   COASTAL PROTECTION STRUCTURES TO PROMOTE WAVE ENERGY DISSIPATION AND SEDIMENTS RETENTION. A COMPARATIVE STUDY

4.1 Introduction

In the past, coastal engineering was essentially based on empirical approaches and physical concepts of the hydrodynamics and morphodynamic processes involved. In general, coastal interventions were based on structural projects without public consultation, and without a sound assessment of their environmental impact (Antunes do Carmo, 2019a, b).

The need and urgency of such projects were a consequence of the large sedimentary deficits that occurred mainly as a result of activities in the river systems, notably, the increase in dam construction after World War II. This has led to a large reduction of beaches in coastal areas and the destruction of many natural protections such as dunes (Bergillos *et al.*, 2016). With the ongoing climate change, the vulnerability coastal zones has increased and, according to most forecasts, will tend to worsen further from the middle of the current century (Antunes do Carmo, 2019a). By preventing the normal course of sediment along the coast, these projects have also caused erosion and land loss at considerable distances from the installation site (Schreck-Reis *et al.*, 2008). Additionally, by allowing urban expansions in marginal areas, often over dune fields, they contributed to negative consequences locally (Antunes do Carmo, 2019b; Granja and Pinho, 2012).

Indeed, demand for coastal areas has been increasing, which is reflected in more population, more construction, more services, more pollution, more natural and marine resource needs, and greater pressure on ecosystems (Castelle *et al.*, 2018; Narra *et al.*, 2017; United Nations, 2015; Weinberg, 2015). All this hinders the sustainability of coastal zones. This population growth is evident on some coasts of the Mediterranean, as noted by the European Environment Agency for the coastal zones of Spain, France, and Italy (EEA, 2006).

In fact, predictions provided by the Intergovernmental Panel on Climate Change (IPCC) point out that global climate change might contribute to sea level rise, and, in some regions, to the increase in the frequency and magnitude of storms (Gilbert and Vellinga, 1990). Addressing the outcomes of sea level rise will involve appropriate reactions for minimizing impacts (Adriana-Gracia *et al.*, 2018; IPCC, 2012). Facing this threat and reversing the increasing degradation and vulnerability of coastal zones can only be achieved through the involvement of local communities and regular and properly planned interventions in accordance with the best-integrated coastal management rules.

Aiming to preserve coastal dunes and properly stabilize the coastal foundation in an environmentally friendly and aesthetically pleasing manner, a strategy based on the use of artificial nourishments, possibly supplemented with other (usually soft) protection measures to prevent sand loss, is strongly recommended (Antunes do Carmo, 2019b).

The negative impacts of traditional hard structures have been a serious problem observable on shorelines around the world. Indeed, the potential advantages of these structures locally are often reduced in the face of the negative effects felt on many coasts around the world (Charlier *et al.*, 2005; Griggs, 2005; Pilkey and Cooper, 2014; Pranzini and Williams, 2013). Among the main adverse effects of hard protections are aggravation of erosion downdrift, disturbance of sediment supply and beach reduction, and adverse visual impacts (Rangel-Buitrago *et al.*, 2018; Williams *et al.*, 2018). These effects urge the need to consider more adequate and successful solutions to control coastal erosion problems.

Protection of coastal zones predisposed to coastline recession due to the action of high tides, high sediment transport deficit, and high wave energy, might involve various coastal structures to reduce or at least to mitigate coastal erosion problems. Hard emerging protections such as breakwaters, groins, and seawalls provide direct protection, whereas hard submerged structures, such as artificial reefs, provide indirect protection by reducing the hydrodynamic loads and maintaining the dynamic shore balance. However, it is important to highlight that the implementation of coastal protection structures do not eliminate sea action hazards, and can only locally decrease them. For this reason, these approaches should not be imprudently considered for construction in dangerous areas.

Wave transmission can be controlled, considering the following factors: structure slope, crest height and width, wave height and period, tidal level, core, and armour material (permeability and roughness). The higher the wave transmission, the less intense the diffraction phenomenon and the accretion by the transmitted waves into the shadow zone. For this reason, for submerged detached structure design, the consideration of a transmission coefficient is of paramount importance (Pilarczyk, 2009).

A type of submerged structure that can prevent coastal erosion and increase beach stability, whether or not combined with sand nourishment, is a multifunctional artificial reef (MFAR). The main objective of the MFAR is to contribute simultaneously to the protection of a sand dune system and the practice of water sports, as well as to ensure good environmental bathing characteristics.

Another developing new concept of coastal protection that has been recently demonstrated to protect coastal areas against erosion and flooding are the wave energy farms. This strategy consists of arrays of wave energy converters (WECs) with a dual function of carbon-free energy generation and coastal

erosion protection. This approach has been tested on the Playa Granada (Spain) using numerical modelling (SWAN and XBeach-G), and has demonstrated that wave farms can reduce significant wave heights and wave run-up on the coast down to 18% and 11%, respectively, which resulted in a beach erosion reduction of 45% (Bergillos *et al.*, 2018).

According to Ranasinghe *et al.* (2006), about 70% of submerged structures built for beach protection to date have resulted in net shoreline erosion. Recognizing that the existing knowledge on the shoreline response to MFAR is not sufficient, the study carried out by Ranasinghe *et al.* (2006) also analysed the influence of several characteristic parameters.

In an attempt to address the knowledge gap of shoreline response to submerged structures, the study in Black and Andrews (2001) quantified the shape and dimensions of some features of natural reefs by visual inspection of aerial photographs. The study concluded that if all parameters (structure dimensions, distance from the shoreline to structure, wave climate, etc.) were the same, a larger salient would develop in the lee of a submerged structure than in the lee of an emerged structure.

However, a subsequent review conducted by Ranasinghe and Turner (2006) showed that the approach used by Black and Andrews (2001) incorporated several shortcomings. According to Ranasinghe *et al.* (2006), the main mode of shoreline response to submerged structures can range from erosive to accretive, depending on the distance from the structure to the shoreline. This same conclusion was obtained by Mendonça *et al.* (2012a, b), using COULWAVE numerical model as shown in Figure 4.1a (case of accretion—convergent vectors), using the currents (the structure-induced circulation pattern) as an indication of the shoreline response on Leirosa beach.

It was also identified that the incidence angle of the predominant wave and the crest level of the structure have implications for the magnitude of the shoreline response. The analyses carried out also provided a useful empirical relationship to evaluate the shoreline response to submerged structures. Such relationship can suggest shoreline accretion if $S_a/SZW > 1.5$, where SZW is the width of the natural surf zone and S_a is the distance between the apex of the structure and the undisturbed coastline (Ranasinghe *et al.*, 2006), as shown in Figure 4.1b.

The hydrodynamic processes that govern the development of nearshore circulation patterns around relatively simple delta-form of MFARs are explained in Ranasinghe *et al.* (2006), using appropriate modules from the MIKE 21 model suite, and are also shown in Mendonça *et al.* (2012a, b) using the Boussinesq-type COULWAVE model (Lynett and Liu, 2008).
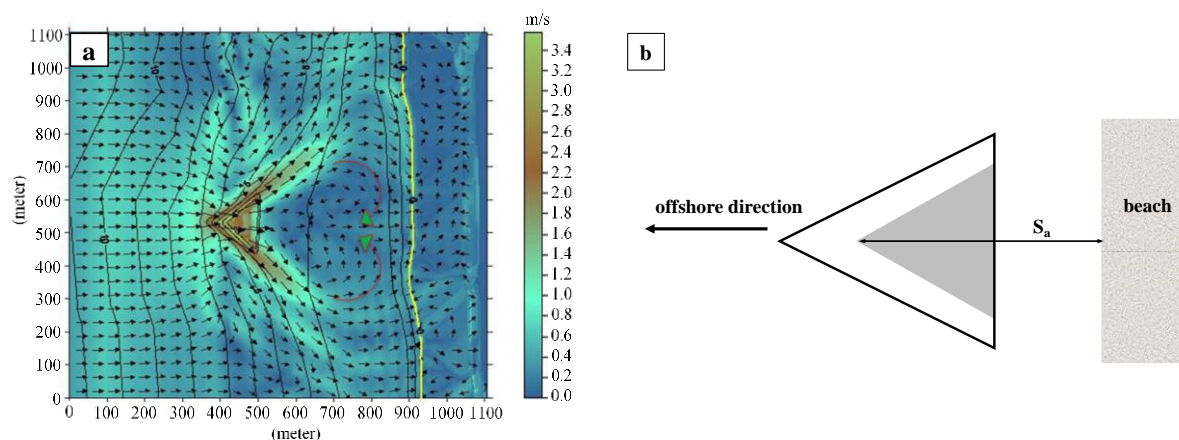
Figure 4.1: a) Velocity pattern around the reef structure (adapted from Mendonça *et al.* (2012a)); b) Reef shape and location: definition of S_a.

Behind the search for more effective and sustainable strategies to deal with coastal retreat, this study focuses on an innovative approach through a comparison between the performance of three traditional coastal protection solutions (submerged and emerged detached breakwaters) and an MFAR on a particular coastal stretch. This innovative approach includes a comparative study on the behaviour and effectiveness of the four protection structures tested using two different numerical models. In order to analyse the hydro- (wave height and wave energy dissipation) and morphodynamics (accretion and erosion areas) of the structures and beach interactions, the two numerical models used are: SWAN (Simulation WAves Nearshore) (SWAN, 2018) for hydrodynamics and XBeach (Deltares, 2019b) for hydrodynamics and morphodynamics. These programs are included in a hydroinformatic environment that facilitated model implementation (Pinho *et al.*, 2004). In addition, a comparison between SWAN and XBeach hydrodynamics results for the protection structures is also performed.

4.2 Characterization of the study area

The application of SWAN and XBeach models to study the influence of four different structures on a specific coastal stretch regarding hydrodynamics and morphodynamics analyses was driven using Leirosa's beach bathymetry. Leirosa (40.0561° N, 8.8874° W) is a village located south of the city of Figueira da Foz, on the west coast of Portugal (Figure 4.2).

Figure 4.2: Leirosa aerial view and location in Portugal.

The selected area is justified by the fact that, according to Schreck-Reis *et al.* (2008), Leirosa's beach is affected by notable erosion due to sediment retention at the North as a consequence of the Figueira da Foz port, and also due to the decreasing sediment deposition caused by Mondego river interventions. Schreck-Reis *et al.* (2008) stated that, during the 1970s, the construction of the jetties in the Mondego estuary triggered major erosion problems that were later mitigated by the construction of groins along the coast, southwards Figueira da Foz, and by sand nourishment dredged from the Figueira da Foz port, in order to protect urban population and the Leirosa beach.

Several technologies on Leirosa beach have been locally used over the past two decades (namely, the reconstruction/rehabilitation of the dune system with local sand and adequate vegetation), and the installation of geotubes for dune strengthening and protection (Antunes do Carmo, 2019a, b; Schreck-Reis *et al.*, 2008). After the occurrence of several storms, it was concluded that the methodology followed was not sufficiently resistant to protect an existing industrial plant in the vicinity of Leirosa (Antunes do Carmo, 2019b; Mendonça *et al.*, 2012a, b). Thus, a complementary reinforcement methodology was developed, which consisted of inducing the waves to break in an area sufficiently far from the dune system, and consequently preventing the waves from breaking on the emerged beach or even at the base of the dune system (Antunes do Carmo, 2019a, b; Mendonça *et al.*, 2012a, b).

The Leirosa coastal area is geologically defined by dune systems of about 1800 m in length, extensive emerged and submerged beaches with slopes of about 1%, and essentially consisting of medium-fine white grain sands (Paredes *et al.*, 2006; Rocha and Bernardes, 1997). Thus, Leirosa beach counts with soft protection from dunes stabilized with *Ammophila arenaria* vegetation, which is characterized by being the most appropriate and most used species in revegetation due to its complex roots (Schreck-

Reis *et al.*, 2008). Regarding the wave climate conditions, Mendonça *et al.* (2012b) indicates that: (a) wave angles vary from 275° to 325°; (b) significant wave heights at the Leirosa beach vary from 0 m to 8.5 m; and (c) average wave periods vary from 4 s to 12 s. Most occurrences for: (a) wave angles were found between 295° to 310°; (b) significant wave heights occurred in the (1.0–1.5) m and (1.5–2.0) m classes; and (c) average wave periods were found between 5 to 10 s, as presented in Figure 4.3.
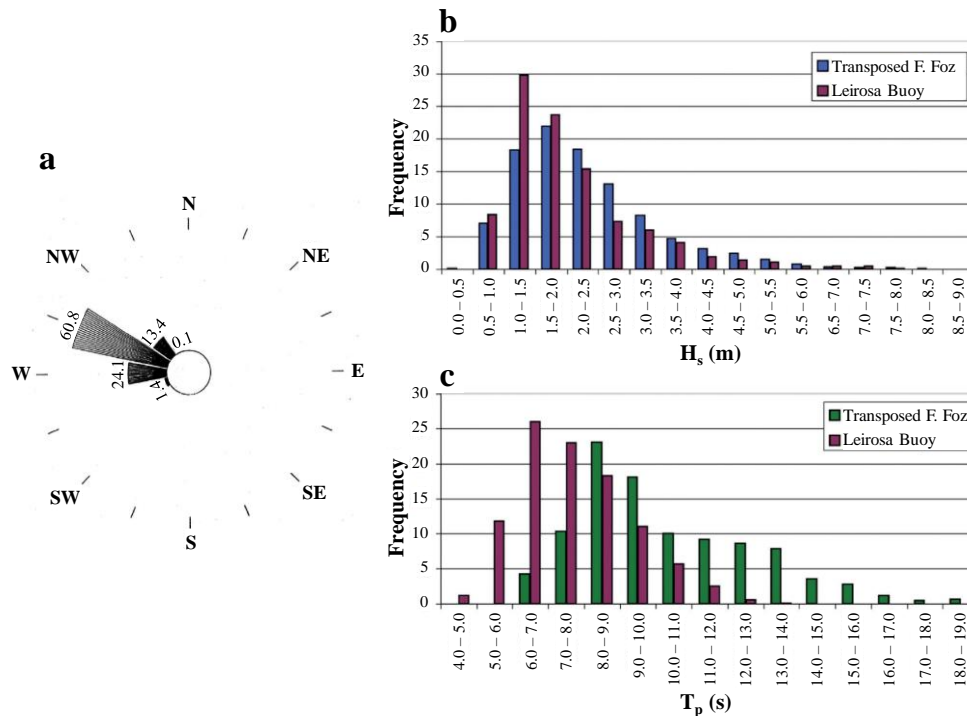
Figure 4.3: a) Wave rose: wave direction relative frequency distribution (%) in Cabo Mondego, near Leirosa beach (adapted from Schreck-Reis *et al.* (2008)); and b) and c) frequency histogram for significant wave heights and peak periods, respectively, in Leirosa (red bar) (adapted from Antunes do Carmo (2019a, b)).

In order to understand the effectiveness of traditional and innovative structures, an analysis for several numerical studies were carried out considering four protection structural options. The local bathymetry was adapted from Mendonça *et al.* (2012a).

4.3 Materials and methods

4.3.1 SWAN and XBeach numerical models

SWAN (SWAN, 2018) is a spectral wave model that follows the wave action balance equation and that can be used to compute wave propagation from deep waters to the transition zone of coastal areas. SWAN can be used as a stand-alone application, but it is also included in the Delft3D 4 Suite (Deltares, 2019a). Although the SWAN model does not calculate wave-induced currents, the model considers a great variety of physical phenomena, such as diffraction, refraction, shoaling, current interaction, wave

breaking due to excess slope, wind waves, and wave transmission through obstacles. The implementation of the SWAN numerical model requires bathymetry of the study area and wave conditions at the boundaries. Amongst other results, SWAN provides results for significant wave heights (H_s), peak and mean periods (T_p and T_m), peak and mean directions (D_p and D_m), and level of water anywhere in the computational domain (Capitão and Fortes, 2011). From an effectiveness point of view, SWAN should not be used on ocean scales nor in shallow waters, as it should be limited to deep and transitional waters.

XBeach (Deltares, 2019b) numerical model is used for the computation of 2D horizontal nearshore hydrodynamics due to wave propagation by simultaneously solving several equations: the roller energy equations, the nonlinear shallow water equations (NSWE) of mass and momentum, the short wave action balance, and the sediment transport and bed change equations. The required XBeach boundary conditions are bathymetry, wave conditions, and tidal levels (Bolle *et al.*, 2010).

Moreover, processes such as the short wave run-up and overtopping are incorporated, which is an important phenomenon on steep slopes. The wave-resolving mode is adequate when diffraction is a relevant process. Simulations on the wave-resolving mode are computationally more demanding than the surf-beat mode, as it requires a more substantial spatial resolution and smaller time steps (Roelvink *et al.*, 2018). At each time step, the XBeach model considers feedback between the bathymetry and the hydrodynamics.

4.3.2 Coastal protection structures geometry

For a comparative study focused on coastal protection purposes, four different geometries are analysed: three submerged detached breakwaters (regular breakwater, group of two breakwaters, and MFAR) and an emerged detached breakwater. Summarised information regarding the geometry of the protection structures considered in this study are detailed in Table 4.1.

Table 4.1: Information regarding structure geometry.

Geometric characteristics of protection structures	Submerged Detached Breakwater			Emerged Detached Breakwater
	Regular Breakwater	Group of 2 Breakwaters	MFAR	
Length (m)	250	2 x 83	250	250
Crest level (m)	−1.5	−1.5	−1.5	1.0
Crest width (m)	10	10	75	10
Side slope	1:2	1:2	1:10	1:2
Opening angle (°)	–	–	45	–
Distance to shoreline (m)	440	440	440	440

4.3.3 Wave characteristics for hydrodynamics and morphodynamics modelling

In this study, different wave characteristics are applied in hydrodynamics and morphodynamics modelling for determining the influence of the protection structure on significant wave height attenuation and sediment transport. These characteristics are presented in Table 4.2.

Table 4.2: Wave characteristics for hydrodynamics and morphodynamics modelling.

Wave condition	Wave Direction	Significant Wave Height H_s (m)	Peak Wave Period T_p (s)
Frequent wave	West + Northwest	1.5	9.0
Storm wave	West	4.0	15.0

4.3.4 Scenarios for modelling simulations

The hydrodynamics and morphodynamics modelling process is developed in two phases of comparative studies. Phase I considers for hydrodynamics and morphodynamics: submerged (regular breakwater and MFAR), and emerged structures under frequent wave conditions with W and NW directions, and storm wave conditions with W direction for MFAR; and Phase II considers: submerged structures (regular breakwater, group of two breakwaters, and MFAR) under conditions of frequent and storm waves with W direction. Tables 4.3 and 4.4 summarize the modelling scenarios studied for each phase.

Table 4.3: Hydrodynamics and morphodynamics modelling scenarios (Phase I).

Item	Hydrodynamics Modelling		Morphodynamics Modelling	
	Frequent Wave Conditions	Storm Wave Conditions	Frequent Wave Conditions	Storm Wave Conditions
Wave Direction	W + NW	W	W + NW	W
Models	SWAN XBeach Models Comparison	XBeach	XBeach	XBeach
Protection Structures	Submerged Emerged MFAR	MFAR	Submerged Emerged MFAR	MFAR

Table 4.4: Hydrodynamics and morphodynamics modelling scenarios (Phase II).

Item	Hydrodynamics Modelling		Morphodynamics Modelling
	Frequent Wave Conditions	Storm Wave Conditions	Frequent Wave Conditions
Wave Direction	W	W	W
Models	SWAN XBeach Models Comparison	SWAN XBeach Models Comparison	XBeach
Protection Structures	Submerged Submerged x 2 MFAR	Submerged Submerged x 2 MFAR	Submerged Submerged x 2 MFAR

4.4 Modelling Phase I

4.4.1 Simulated Scenarios

In this modelling Phase I, three different geometries for coastal protection structures are analysed. For a deeper understanding on the performance of an MFAR, the impact of this structure on a coastal zone is compared with a submerged detached breakwater (Figure 4.4a) and an emerged detached breakwater (Figure 4.4b). The case study developed by Mendonça *et al.* (2012a; b) was taken as reference for the MFAR modelling that resembles a triangular prism (Figure 4.4c), where the structure performance was conducted, considering "surfability" and coastal protection. The scenarios often considered in projects of this type are identified as frequent and typical storm conditions. The studies in Mendonça *et al.* (2012a, b) analysed the performance of two MFAR differing in their opening angles (45° and 66°) for two different incident wave conditions (frequent wave: H_s = 1.5 m, T_p = 9 s; and storm wave: H_s = 4 m, T_p = 15 s) and concluded that both geometries contribute to sedimentation by convergent velocity vectors observation near the shoreline.

For the current study, the analysis focuses on coastal protection purposes, and it considers the structure geometry of 45° opening angle due to its wider shadow zone benefits for coastal protection. As geometrical considerations, all structures share the same length (250 m). The detached breakwater design considers a crest width of 10 m and side-slopes of 1:2, which are representative of regular structures of this type as presented in Vieira (2014). The MFAR follows the design proposed by Mendonça *et al.* (2012a, b), which considers a crest width of 75 m and side slopes of 1:10. The submerged detached breakwater and the MFAR have their crests submerged at -1.5 m, and the emerged detached breakwater has its crest emerged at 1.0 m relative to mean sea level (MSL). All three structures are located at the same distance from the shoreline (440 m).
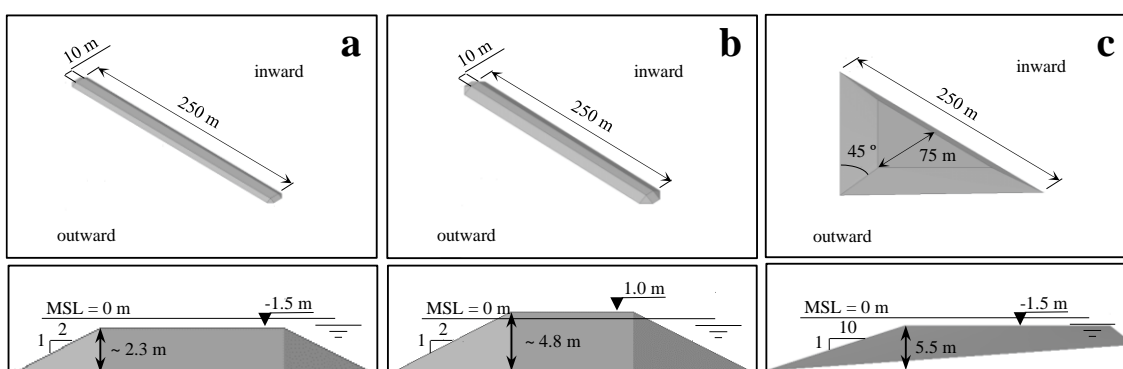
Figure 4.4: Geometrical shapes considered in the modelling Phase I (upper panel: plan view; lower panel: cross-section): a) submerged detached breakwater; b) emerged detached breakwater; and c) multifunctional artificial reefs (MFAR).

In order to study the influence of the structure on significant wave height attenuation and sediments accumulation, a realistic bathymetry is used for the model simulations, which was based on Mendonça *et al.* (2012a, b). Regarding model conditions, the computational domain is 1670 m × 1870 m (crosshore×longshore) with a node spacing of dx=dy=5.0 m for both hydro-and morphodynamics analyses. Simulations considering other grid cell sizes were tested, as in the followed reference study. The selected grid cell size of 5 m was adequate considering the simulated area, the structure dimensions, and the confirmation that the obtained results were independent of the grid cell size. The total simulation time is 2 hours for the hydrodynamics analysis (using SWAN and XBeach) and 75 days for morphodynamics (XBeach) with a morphological acceleration factor (morfac) of 100 for a 20-year forecast. Some of the XBeach model parameters considered, such as model simulation time, Chézy parameter (surface roughness), directional energy distribution (dtheta), and morfac value, were implemented based on a study conducted by Razak and Nor (2018) that focused on the analysis of salient and tombolo formations for different detached breakwater conditions.

For hydrodynamics (using SWAN and XBeach), the frequent wave scenario is analysed for all structures in order to give insights on the response to a mean wave climate with waves incoming from the west (270°) and northwest (315°) directions, whereas the tidal level considered is 0 m relatively to the MSL (tidal influence not considered in the simulations). For morphodynamics analysis (using XBeach), the frequent wave scenario is also analysed for incoming waves from the west (270°) and northwest (315°) directions. An extra analysis is also developed with SWAN and XBeach models for a storm wave condition with the west direction (only for MFAR due to its innovative shape). Regarding seabed composition, the sediment dimensions considered are 200 μm for D_{50} and 300 μm for D_{90}. D_{50} and D_{90} are common metrics used to describe particle size distributions. In this case, D_{50} means that 50% of the sample has a size of 200 μm or smaller, and D_{90} means that 90% has a size of 300 μm or smaller. Boundary conditions for SWAN model (hydrodynamics) are defined for north, west, and south boundaries; for frequent wave condition in all scenarios; and storm wave condition for one scenario. Boundary conditions for XBeach model (hydrodynamics and morphodynamics) are defined as absorbing–generating (weakly-reflective) boundary in 2D (abs_2d) for front and back boundaries, and wall boundary condition (simple no flux boundary condition) for left and right boundaries are defined. In XBeach model, the left and right designations correspond to North and South, whereas front and back correspond to West and East.

For hydrodynamics (SWAN and XBeach), the wave type considered is a JONSWAP spectrum, whereas the stationary mode is selected for morphodynamics (XBeach). The consideration of stationary mode is

justified by the need to reduce model calculation time for morphodynamics. A morfac to hasten the morphological period in relation to the hydrodynamics is also considered. The numerical model results obtained by the SWAN model are the significant wave heights and their mean directions, whereas XBeach model computed root mean square wave heights (H_{rms}), and estimated the accretion and erosion near shoreline. In addition, bed level results are presented for the MFAR under the storm wave condition. In order to compare SWAN hydrodynamics results with XBeach model results, a H_{rms} to H_s conversion of the XBeach numerical results is required, according to Equation (4.1) (Hanson, 2019):

$$H_s = \sqrt{2} \times H_{rms}$$

(4.1)

In addition, the wave energy dissipation also requires separate calculations using the following equation (Equation (4.2)) (MetED, 2012; Vieira, 2014):

$$E = \frac{1}{8}(\rho_w g H^2)$$

(4.2)

where E is the wave energy per unit area (J/m²), ρ_w is the seawater density (kg/m³), g is the gravitational acceleration constant (m/s²), and H is the wave height (m). The wave energy is computed for all scenarios, considering ρ_w = 1025 kg/m³ and g = 9.81 m/s².

Extensive information concerning the input conditions for both SWAN and XBeach models are detailed in Table 4.5.

Table 4.5: Input conditions for SWAN and XBeach models.

Numerical Model Conditions			
Model Input	**SWAN (hydrodynamics)**	**XBeach (hydrodynamics)**	**XBeach (morphodynamics)**
Tidal level (m)	0	0	0
Wave condition	Frequent	Frequent	Frequent
Wave directions	West and northwest	West and northwest	West and northwest
Wave condition (extra scenario for MFAR)	–	Storm	Storm
Wave direction (extra scenario for MFAR)	–	West	West
Boundary conditions for frequent wave scenario (west)	North, west, and south: H_s = 1.5 m, T_p = 9 s, Direction = 270°	Front and back: abs_2d Left and right: wall	Front and back: abs_2d Left and right: wall
Boundary conditions for frequent wave scenario (northwest)	North, west, and south: H_s = 1.5 m, T_p = 9 s, Direction = 315°	Front and back: abs_2d Left and right: wall	Front and back: abs_2d Left and right: wall
Boundary conditions for storm wave scenario	–	Front and back: abs_2d Left and right: wall	Front and back: abs_2d Left and right: wall
Sediments dimensions (µm)	–	–	D_{50} = 200 D_{90} = 300

Table 4.5: Input conditions for SWAN and XBeach models (cont.).

Numerical Model Conditions			
Model Input	**SWAN (hydrodynamics)**	**XBeach (hydrodynamics)**	**XBeach (morphodynamics)**
Morphological acceleration factor (morfac)	–	–	100
Chèzy	–	–	60
Directional energy distribution (dtheta)	–	–	10
Wave type process	JONSWAP spectrum	JONSWAP spectrum	Stationary mode
Simulation time (hours)	2	2	1800
Computational domain (m)	1670 × 1870 (crosshore × longshore)	1670 × 1870 (crosshore × longshore)	1670 × 1870 (crosshore × longshore)
Grid spatial resolution (m)	dx=dy=5	dx=dy=5	dx=dy=5

4.4.2 Results and discussion

The following sections present the key results of hydrodynamics and morphodynamics using SWAN and XBeach numerical models.

4.4.2.1 Hydrodynamics with SWAN model

Numerical simulations for the analysis of significant wave heights dissipation and their mean directions for a frequent wave condition is performed for each structure for the west wave direction: submerged detached breakwater (Figure 4.5a1), emerged detached breakwater (Figure 4.5b1), and MFAR (Figure 4.5c1); and for the northwest wave direction: submerged detached breakwater (Figure 4.5a2), emerged detached breakwater (Figure 4.5b2), and MFAR (Figure 4.5c2). For a more legible analysis, the SWAN results are centred in a limited window around the structures. The contour lines are also depicted in all results shown. The indicated numbers in Figure 4.5 relate to: 1—wave shoaling in the structure outward zone; 2—wave shoaling at the structure apex; 3—wave shoaling in the structure inward zone; 4—negligible overtopping; 5—pronounced shadow zone; 6—significant wave height increase due to diffraction.
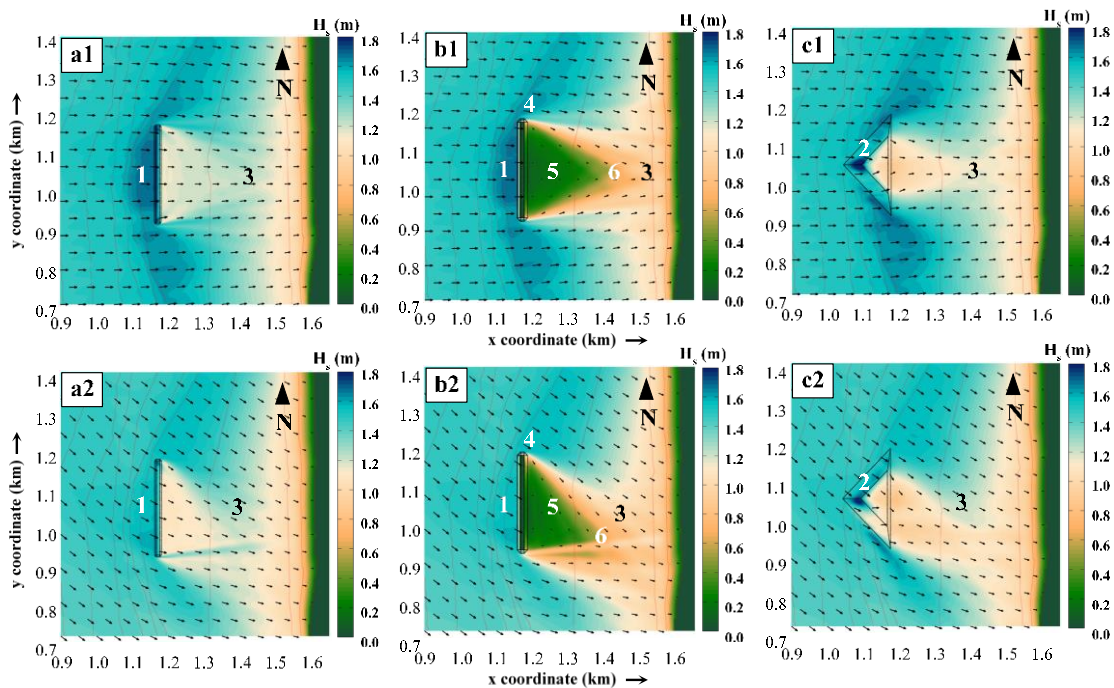
Figure 4.5: Significant wave height dissipation (arrows represent their mean direction) for frequent wave condition (SWAN model) for the west wave direction (upper panel): submerged detached breakwater (a1), emerged detached breakwater (b1), and MFAR (c1); and for the northwest wave direction (lower panel): submerged detached breakwater (a2), emerged detached breakwater (b2), and MFAR (c2).

From the results presented in Figure 4.5, for both west and northwest wave directions, wave shoaling (increase of the wave height) in every structure is evident due to a decrease of the depth. This phenomenon is visible at the outward extremity along the submerged detached breakwater (represented by number 1 in Figure 4.5a1 (H_s = 1.7 m) and Figure 4.5a2 (H_s = 1.6 m) for the west and northwest wave directions, respectively), along the emerged detached breakwaters (also represented by number 1 in Figure 4.5b1 (H_s = 1.7 m) and Figure 4.5b2 (H_s = 1.6 m) for the west and northwest wave directions, respectively), and at the apex of the MFAR (represented by number 2 in Figures 4.5c1 (H_s = 1.8 m) and 4.5c2 (also H_s = 1.8 m) for the west and northwest wave directions, respectively). For the northwest wave direction scenarios, the wave shoaling mentioned is less intense.

At the inward side of all structures, wave shoaling is also visible for both wave directions. For the submerged detached breakwater, a progressive increase in significant wave heights is also visible from the structure inward (protected) extremity to position 1.4 km (represented by number 3 in Figures 4.5a1 (H_s = 1.1 m to H_s = 1.3 m) and 4.5a2 (also H_s = 1.1 m to H_s = 1.3 m) for the west and northwest wave directions, respectively). For the emerged detached breakwater, this phenomenon is more noticeable for waves incoming from the northwest direction (represented by number 3 in Figure 4.5b2 (H_s = 0.0 m to H_s = 1.1 m)), although wave shoaling is also visible for the west wave (represented by

number 3 in Figure 4.5b1 ($H_s = 0.0$ m to $H_s = 0.9$ m)). For the MFAR, this phenomenon is also present where an increase in significant wave heights is perceptible from the structure inward extremity to position 1.4 km (represented by number 3 in Figures 4.5c1 ($H_s = 0.8$ m to $H_s = 1.3$ m) and 4.5c2 (also $H_s = 0.8$ m to $H_s = 1.3$ m) for the west and northwest wave directions, respectively). These phenomena are explained by the shoaling and breaking due to depth decrease. After these positions, the significant wave heights progressively decrease towards the shoreline.

Relative to the influence of a structure on significant wave heights, it is clear that all structures contribute to a significant wave heights reduction for both wave directions. The most substantial decrease is for the emerged detached breakwater, where there is a negligible overtopping on the structure of approximately 0.2 m (represented by number 4 in Figures 4.5b1 ($H_s = 1.2$ m) and 4.5b2 (also $H_s = 1.2$ m) for the west and northwest wave directions, respectively), which contribute to a very calm area immediately after the structure (represented by number 5 in Figures 4.5b1 ($H_s = 0.2$ m) and 4.5b2 (also $H_s = 0.2$ m) for the west and northwest wave directions, respectively). Increase in significant wave heights after position 1.4 km is explained by the diffraction phenomena (represented by number 6 in Figures 4.5b1 ($H_s = 0.2$ m to $H_s = 0.8$ m) and 4.5b2 (also $H_s = 0.2$ m to $H_s = 0.8$ m) for the west and northwest wave directions, respectively) observed by the mean wave direction vectors convergence.

For all northwest wave direction scenarios, the shadow zone triggered by the structures presence take a southeast direction, relative to the structures, as expected. This effect lessens the protection purpose at the structures alignment relative to the shoreline. Near the shoreline, it can be concluded that the emerged detached breakwater and the MFAR have a more substantial and larger shadow zone than the submerged detached breakwater.

4.4.2.2 Hydrodynamics with XBeach model

The XBeach model for the analysis of significant wave height dissipation for a frequent wave condition is also used for each structure in the west wave direction: submerged detached breakwater (Figure 4.6a1), emerged detached breakwater (Figure 4.6b1), and MFAR (Figure 4.6c1); and for the northwest wave direction: submerged detached breakwater (Figure 4.6a2), emerged detached breakwater (Figure 4.6b2), and MFAR (Figure 4.6c2). XBeach post-processing does not allow for representation of wave mean direction with vectors. The presented XBeach results are cropped around the structures for a more legible analysis. The contour lines are also depicted in all results shown. The indicated numbers in Figure 4.6 relate to: 1—wave shoaling in the structure outward zone; 2—wave shoaling at the structure apex; 3—wave shoaling in the structure inward zone; 4—significant wave height decrease

(suggesting accretion); 5—negligible overtopping; 6—pronounced shadow zone; 7—waves progression towards shoreline (indicating erosion problems).
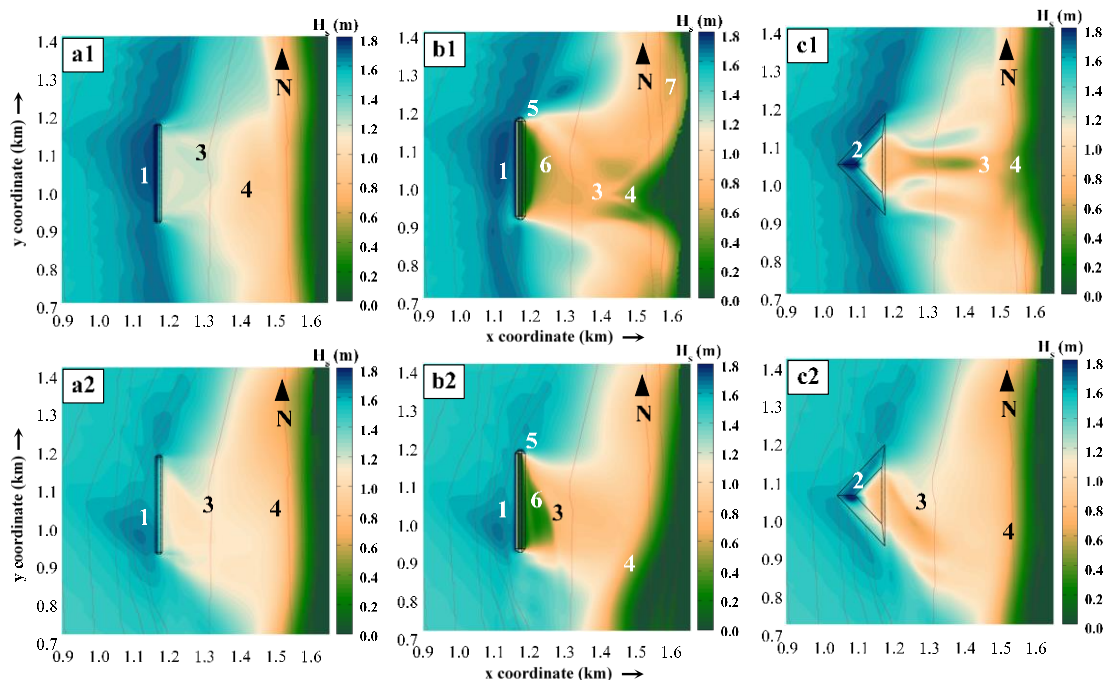
Figure 4.6: Significant wave height dissipation for frequent wave condition (XBeach model) for the west wave direction (upper panel): submerged detached breakwater (a1), emerged detached breakwater (b1), and MFAR (c1); and for the northwest wave direction (lower panel): submerged detached breakwater (a2), emerged detached breakwater (b2), and MFAR (c2).

Similar to SWAN results, for both west and northwest wave directions, wave shoaling in every structure is evident due to a decrease in the depth along the outward extremity of the submerged detached breakwater (represented by number 1 in Figures 4.6a1 (H_s = 1.7 m) and 4.6a2 (H_s = 1.6 m) for the west and northwest wave directions, respectively), along the outward extremity of the emerged detached breakwaters (also represented by number 1 in Figures 4.6b1 (H_s = 1.7 m) and 4.6b2 (H_s = 1.6 m) for the west and northwest wave directions, respectively), and at the apex of the MFAR (represented by number 2 in Figures 4.6c1 (H_s = 1.8 m) and 4.6c2 (also H_s = 1.8 m) for the west and northwest wave directions, respectively). As in the SWAN numerical model, the wave shoaling is less intense for the northwest wave direction scenarios.

At the inward side of all structures, wave shoaling is also visible for both wave directions. For the submerged detached breakwater, a progressive increase in significant wave heights is visible from the structure inward extremity to position 1.3 km (represented by number 3 in Figures 4.6a1 (H_s = 1.1 m to H_s = 1.5 m) and 4.6a2 (H_s = 1.0 m to H_s = 1.2 m) for the west and northwest wave directions, respectively). For the emerged detached breakwater, this phenomenon is also noticeable for waves

incoming from the west direction (represented by number 3 in Figure 4.6b1 (H_s = 0.3 m to H_s = 0.8 m)), and the northwest wave (represented by number 3 in Figure 4.6b2 (H_s = 0.2 m to H_s = 0.8 m)) for different positions. For the MFAR, this phenomenon is very noticeable for both waves incoming from the west direction (represented by number 3 in Figure 4.6c1 (H_s = 0.4 m to H_s = 0.8 m)), and for the northwest direction (represented by number 3 in Figure 4.6c2 (H_s = 0.9 m to H_s = 1.1 m)) also for different positions. After these locations, the significant wave heights gradually decrease towards the shoreline.

Concerning the influence of a structure on significant wave heights, it is clear that all structures contribute to a substantial decrease in wave heights for both wave directions. Comparatively to SWAN, XBeach presents smaller significant wave heights in the inward zones (from structures to the coast). This phenomenon is represented by number 4 in all six scenarios in Figure 4.6, and can be detected by the wide areas of small values for significant wave heights. The most substantial decrease in significant wave heights is, as presented in SWAN numerical model results, for the emerged detached breakwater. A negligible wave overtopping on this structure (approximately 0.1 m) is also simulated by XBeach (represented by number 5 in Figures 4.6b1 (H_s = 1.1 m) and 4.6b2 (H_s = 1.1 m) for the west and northwest wave directions, respectively). The shadow zone, spawned immediately after the structure, presents a narrower width when compared to SWAN results (represented by number 6 in Figures 4.6b1 (H_s = 0.3 m) and 4.6b2 (H_s = 0.2 m) for the west and northwest wave directions, respectively). The increase in significant wave heights in position number 6 is explained by the diffraction phenomena. The MFAR presents the second most substantial reduction in significant wave heights. For the northwest wave direction condition (Figure 4.6c2), results are similar to those obtained with SWAN. Regarding the submerged detached breakwater (Figures 4.6a1, 6a2), results are also close to the ones presented in SWAN. In all emerged detached breakwater and MFAR scenarios in Figure 4.6, shoreline width is noticeably affected by the structure with apparent accretion areas (represented by number 4 in Figures 4.6b1, 4.6c1 for the west wave direction, and Figures 4.6b2, 4.6c2 for the northwest wave direction) and erosion areas (represented by number 7 in Figure 4.6b1 for the west wave direction). For the submerged detached breakwater, this effect is not substantial. As expected, the shadow zones generated by the incoming northwestern waves have a southeast direction relative to the structures.

4.4.2.3 Hydrodynamics comparison SWAN versus XBeach models

SWAN and XBeach are two powerful tools able to simulate hydrodynamics environments: SWAN for deep to transitional waters and XBeach for transitional and shallow waters. Because all actual coastal

hydrodynamics models present limitations and simplified assumptions, it was decided that both numerical models would be used to increase the confidence in the obtained results. In order to understand their performance in this particular case, the plots depicted in Figure 4.7 show the similarities and differences between the significant wave height results for SWAN and XBeach for a cross-section in each structure.
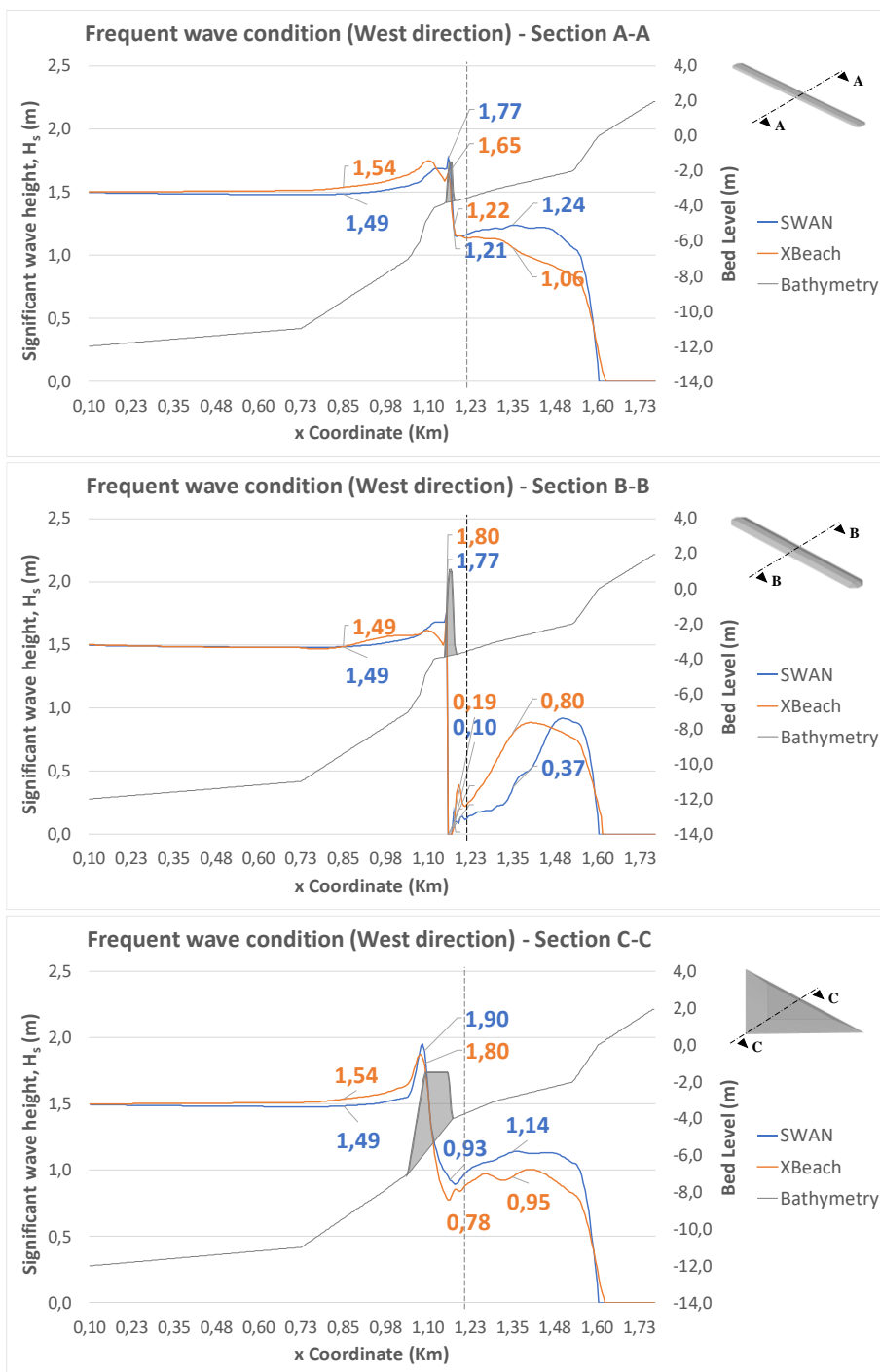
Figure 4.7: Comparison of SWAN and XBeach significant wave height results for frequent wave condition (west direction): submerged detached breakwater (section A-A), emerged detached breakwater (section B-B), and MFAR (Section C-C).

As the results of significant wave heights for the west and northwest wave direction were not substantially different in magnitude, only the west wave direction is analysed. The values shown in the plots are selected for four positions: before, immediately before, immediately after, and after the structures. The plotted vertical line represents a relevant seabed slope change.

As mentioned before, the wave shoaling due to a sudden depth change immediately before the structure is visible for all cases. From the analysis of Figure 4.7, it is clear that both SWAN and XBeach simulate this phenomenon for all structures, and that SWAN simulates a wave shoaling due to the slope change starting at position 1.23 km. The XBeach model also represents a substantial wave shoaling at the same position for all structures, except for the submerged detached breakwater in this cross-section. Immediately after the emerged detached breakwater, both models show slight turbulence due to wave overtopping.

Table 4.6 presents an overall comparison between SWAN and XBeach hydrodynamics results taken from Figure 4.7, and an overall percentage of significant wave height result reduction before and after the structures for the west wave direction.

From the results presented in Table 4.6, it is evident that the significant wave height results computed by SWAN before the structures are lower than those calculated by the XBeach model for the submerged detached breakwater and the MFAR (−0.05 m and −0.05 m, respectively), and are higher after the mentioned structures (0.18 m and 0.19 m, respectively). For the emerged detached breakwater, the SWAN and XBeach results for significant wave heights are the same before the structure (0.00 m); after the structure, the SWAN computed results are smaller than those obtained with XBeach (−0.43 m).

Regarding the difference between significant wave heights before and after the structures, XBeach presents greater reduction values than the SWAN model for the submerged detached breakwater and MFAR, and a smaller reduction for the emerged detached breakwater. Regarding structure performance, the emerged detached breakwater has the best performance (for both numerical models) due to higher reduction values, whereas the submerged detached breakwater is the least effective. Because wave energy is proportional to wave heights, the same conclusion can be drawn for wave energy.

Table 4.6: Comparison of model results before and after each structure for the west wave direction condition.

	Structure: Submerged Detached Breakwater			
Model	$H_s = 1.5$ m, $T_p = 9$ s | West Wave Direction			
	Before (m)	**After (m)**	**Reduction (%)**	**Energy Reduction (%)**
SWAN	1.49	1.24	16.77	30.72
XBeach	1.54	1.06	31.00	52.38
SWAN - XBeach	−0.05	0.18	–	–

Table 4.6: Comparison of model results before and after each structure for the west wave direction condition (cont.).

Structure: Emerged Detached Breakwater				
Model	H_s = 1.5 m, T_p = 9 s | West Wave Direction			
	Before (m)	**After (m)**	**Reduction (%)**	**Energy Reduction (%)**
SWAN	1.49	0.37	75.4	93.9
XBeach	1.49	0.80	46.1	71.0
SWAN - XBeach	0.00	-0.43	–	–
Structure: MFAR				
Model	H_s = 1.5 m, T_p = 9 s | West Wave Direction			
	Before (m)	**After (m)**	**Reduction (%)**	**Energy Reduction (%)**
SWAN	1.49	1.14	23.30	41.17
XBeach	1.54	0.95	38.21	61.82
SWAN - XBeach	−0.05	0.19	–	–

4.4.2.4 Morphodynamics with XBeach model

One of the suggestions proposed by Mendonça *et al.* (2012a, b) was to study morphodynamics around the structure to enable a deeper understanding on sedimentation and erosion areas near the coast under the influence of an MFAR. In order to develop that study, the XBeach morphodynamics model is applied to each one of the structures.

Numerical simulations for the analysis of cumulative sedimentation and erosion are conducted for each shape: submerged detached breakwater (Figure 4.8a1, 4.8a2 for the west and northwest wave directions, respectively), emerged detached breakwater (Figures 4.8b1, 4.8b2 for the west and northwest wave directions, respectively), and MFAR (Figures 4.8c1, 4.8c2 for the west and northwest wave directions, respectively). In Figure 4.8, more intense wave velocities indicate erosion areas, whereas less intense wave velocities indicate sediments accumulation. The study is performed for 75 days with a morfac of 100, which insights results for 20 years. The simulations are taken for a frequent wave condition and the presented results are cropped for a more legible analysis. The indicated numbers in Figure 4.8 relate to: 1—substantial erosion; 2—erosion in the structure outward zone due to wave reflection; 3—erosion due to increase of wave velocity; 4 and 5—erosion due to vortexes local scouring near shoreline; 6—accretion in the structure inward zone; 7—noticeable accretion near shoreline; 8—accretion southwards the structure.
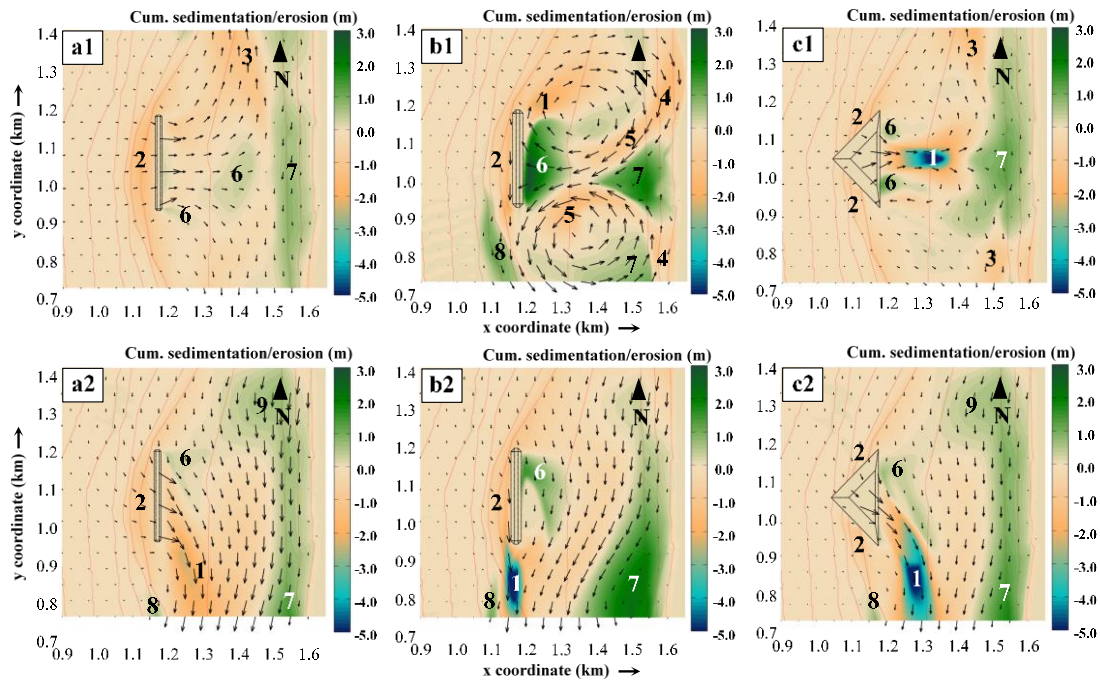
Figure 4.8: Cumulative sedimentation and erosion (arrows represent wave velocity vectors) for frequent wave condition (XBeach model) for the west direction (upper panel): submerged detached breakwater (a1), emerged detached breakwater (b1), and MFAR (c1); and the northwest direction (lower panel): submerged detached breakwater (a2), emerged detached breakwater (b2), and MFAR (c2).

From the results depicted in Figure 4.8, it is evident that the most substantial erosion areas are at the inward area of the MFAR for the west wave direction, 120 m away from the structure, and at the south extremity, 110 m away from the structure, for the northwest wave direction (represented by number 1 in Figures 4.8c1 (−5 m) and 4.8c2 (also −5 m), respectively); at the north extremity for the emerged detached breakwater, 70 m away from the structure, (represented by number 1 in Figure 4.8b1 (−1.5 m)); and at the south extremities for the submerged and emerged detached breakwaters, 110 m and 50 m away from the structure, respectively, for the northwest wave direction (represented by number 1 in Figures 4.8a2 (−2.0 m) and 4.8b2 (−5.0 m), respectively). For the MFAR (Figure 4.8c1 for the west wave direction) the local scouring might be explained by the increase in wave velocities and a small wave refraction due to wave propagation at different depths, whereas for the northwest wave direction (Figure 4.8c2), erosion might have been induced by the combination of the waves diffracted due to the structure presence and the incoming waves from the North that created fields with more intense velocities at this area. For the submerged and emerged detached breakwaters (Figure 4.8a2 and 4.8b2 for the northwest wave direction), the erosion is induced by the combination of waves incoming from the north direction and the increased waves velocities incoming from along the structure. Regarding the emerged detached breakwater for the west wave direction, local scouring is induced by the vortexes

formed near the inward area of the structure. Erosion in the structures outward areas due to wave reflection are presented in all scenarios (represented by number 2), with more intense values for the west wave direction condition. Observations on the increase of wave velocities, in the submerged and the MFAR (represented by number 3 in Figures 4.8a1 (−1.5 m) and 4.8c1 (−1.0 m) for the west wave direction), and on the vortexes presented in the emerged detached breakwater (represented by numbers 4 and 5 in Figure 4.8b1 (−1.5 m and −1.0 m, respectively) for the west wave direction) suggest that local scouring is present at these positions.

By the observation of the convergence of both vortexes presented in the emerged detached breakwater results (Figure 4.8b1 for the west wave direction), it is clear that accretion areas are created due to the intensity of currents in the structure inward zone (represented by number 6 (+3.0 m)). On the shoreline, accretion at the structure alignment with a formation of a noticeable salient (represented by number 7 (+2.0 m)) is created due to the decreasing of wave velocities. For the submerged detached breakwater and the MFAR (Figures 4.8a1 and 4.8c1 for the west wave direction), a slight sediments accretion is created in the structure inward zone (represented by number 6 (+0.5 m and +1.0 m, respectively)). Along the shoreline, great sediments accretion is visible (represented by number 7), particularly for the MFAR (Figure 4.8c1 (+1.5 m) for the west wave direction) where, similar to the emerged detached breakwater, a formation of a salient is evident. This salient is developed immediately after the erosion area represented by number 1, which might suggest that part of the sediments on the eroded area settle further ahead. For the emerged detached breakwater, a noticeable sediments accretion south of the structure is developed due to decrease in wave velocity from the outer contour of the south vortex (represented by number 8 in Figure 4.8b1 (+2.0 m) for the west wave direction). Regarding results for the northwest direction, similar sediments accretion patterns are visible for the submerged detached breakwater and the MFAR (represented by numbers 6 (+0.5 m), 7 (+2.0 m), 8 (+1.0 m), and 9 (+1.0 m)), although with greater areas of sediments accumulation for the MFAR (Figure 4.8c2). For the emerged detached breakwater, great sediments accretion is visible at three different locations: in the structure inward zone, southeast of the structure, and south of the structure (represented by numbers 6 (+1.5 m), 7 (+2.5 m), and 8 (+1.5 m) in Figure 4.8b2 for the northwest wave direction, respectively). All the protection patterns reported in the observation of the attenuation of significant wave heights by the structures are corroborated by the presented morphodynamics results.

Overall, by observation of the west wave condition results, it is clear that a pronounced variation on wave velocities induce more accumulation and erosion areas. This asymmetrical layout might have been related to the incidence of incoming waves on the non-symmetric bathymetry. The vortexes

presented in the emerged detached breakwater by observation of the wave velocity vectors indicate sediments accretion and erosion at different locations, with formation of a substantial salient (as previously mentioned), similar to the study in Razak and Nor (2018) where patterns of salient formations were created for similar conditions. A salient formation inwards the MFAR is also observed. Sediments accretion patterns presented for the MFAR corroborate the studies developed by Mendonça *et al.* (2012a, b), where the authors expected sediments to accumulate at the structure alignment through the observation of wave velocity vectors. This way, it can be concluded that the studies of Mendonça *et al.* (2012a, b) were consistent, and that, similar to the study of Ranasinghe *et al.* (2006), slight cell circulation systems can be found for this scenario. The coherence between the previous and the presented results confirm the quality of results in this research work. It is important to note that despite these salients being formed, erosion areas along the shoreline are present for the west wave direction.

4.4.2.5 Storm scenario: Hydrodynamics and Morphodynamics

In order to analyse the MFAR performance on a storm wave condition (H_s = 4.0 m, T_p = 15 s) with a west wave direction, numerical simulations for hydrodynamics and morphodynamics using XBeach (Figure 4.9) are conducted. Because these conditions create a shallow water environment (significant wave height/wavelength < 0.05), SWAN is not considered for this scenario (wavelength is above 100 m). Output for hydrodynamics consists of significant wave height results for a 2-hour simulation and, for morphodynamics, an evaluation of cumulative sedimentation/erosion and bed level after 20 years. The indicated numbers in Figure 4.9a and Figure 4.9b relate to: 1—substantial significant wave heights in the structure outward zone; 2—wave shoaling at the structure apex; 3—wave shoaling in the structure inward zone due to depth decrease; 4—wave progression towards shoreline (indicating erosion problems); 5a—substantial erosion due to local scouring from the increase in waves velocity and small wave refraction (due to wave propagation at different depths); 5b—substantial erosion due to local scouring from the combination of incoming waves from the North and the vortex (increased waves velocity); 5c—substantial erosion due to local scouring from the intersection of both vortexes in the same direction; 6—noticeable erosion near shoreline; 7a—substantial accretion in the structure outward zone; 7b—substantial accretion southeast of the structure, near shoreline; 7c—accretion near shoreline and southwards the structure. The indicated numbers in Figure 4.9c relate to 1—erosion phenomenon; 2—sedimentation phenomenon.
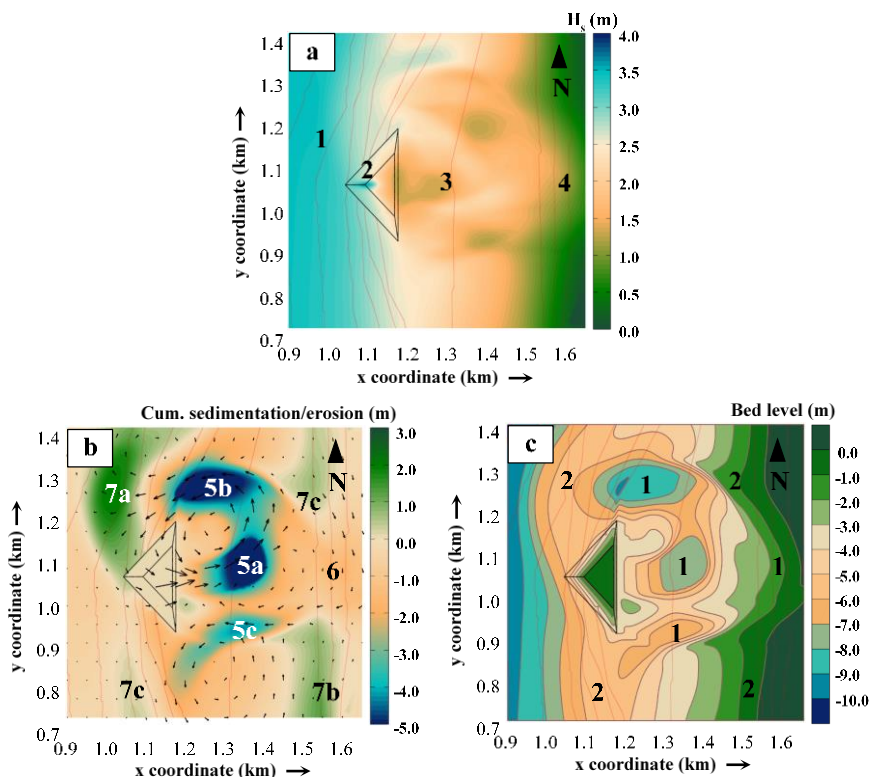
Figure 4.9: Effect of storm wave condition with west wave direction on an MFAR for a) significant wave heights dissipation for XBeach model; b) cumulative sedimentation and erosion (arrows represent wave velocity vectors) for XBeach; and c) configuration of bed level.

Regarding the performance of the MFAR in reducing wave energy, it is clear that the XBeach model indicates a positive and substantial wave height reduction from the observed outward and inward extreme results (represented by numbers 1 (H_s = 3.5 m) and 4 (H_s = 1.0 m) in Figure 4.9a).

Similar to the previous results for frequent wave condition, for this scenario, XBeach computes the wave shoaling at the apex of the structure (represented by number 2 in Figure 4.9a) and a slight wave shoaling due to depth decrease (represented by number 3 in Figure 4.9a) from the inward extremity to position 1.3 km. Near the shoreline, the XBeach model presents a vulnerable area at the structure alignment (represented by number 4 in Figure 4.9a). This noticeable disturbance in shoreline width indicates apparent erosion at that particular stretch. The increase in significant wave heights in position number 4, when compared with areas located North and South, might have resulted from the erosion that occurs in the back of the MFAR, as presented in Figure 4.9c.

Similar to the results presented for the emerged detached breakwater for the west wave direction, two vortexes are presented in the MFAR inward area by observing the wave velocity vectors (Figure 4.9b). The local scouring represented by number 5a in Figure 4.9b (−5.0 m) might be explained by the increase in the wave velocities and a small wave refraction due to wave propagation at different depths,

whereas the erosion represented by number 5b (also −5.0 m) might be explained by the combination of incoming waves from the North with the vortex, which created more intense velocity fields at this area. The erosion represented by number 5c in Figure 4.9b (−4.0 m) is induced by the fact that both vortexes have the same direction, which aggravates local scouring on the area where they both meet. Wave velocity vectors in the storm wave scenario indicate a more turbulent state than the condition for frequent waves. Near the shoreline, the wave velocity vectors that indicate the waves incoming from the North (represented by number 6 in Figure 4.9b (−2.0 m)), due to turbulence induced by the north vortex, contribute to local scouring at the structure alignment. This phenomenon is mentioned by observations of significant wave height results.

Regarding sediments accretion, it is clear that the areas with smaller wave velocity vectors indicate calmer zones, which contribute to accretion (represented by numbers 7a, 7b, and 7c in Figure 4.9b (+2.0 m, +1.0 m, and +0.5 m, respectively)). The less turbulent areas that are located away from the vortexes are induced by the decreased magnitude of this phenomenon, and are located away from the structure; they also appear in the MFAR outward zone. Substantial sediments accretion is observed in the structure outward zone (7a) and at the southeast (7b) of the structure (along the shoreline), whereas smaller areas of sediments accretion are presented northeast of the structure, near the shoreline (7c) and south of the structure (7c). This scenario does not create any salient at the structure alignment.

From the results presented in Figure 4.9c, it can be concluded that there are substantial changes in morphology for this scenario where the erosion (1) and sedimentation (2) phenomena altered the bed level.

4.4.3 Summary and conclusions for Phase I modelling

Coastal zones are a much-appreciated environment that attract people, as they are supportive of a large amount of activities and leisure. Despite the fact these environments are highly vulnerable to natural and anthropogenic hazards, it has been noted by the European Environment Agency that coastal population growth is evident on some coasts of the Mediterranean (Spain, France, and Italy). This growth requires special attention when dealing with climate change consequences, and new strategies to deal with sea level rise are crucial.

This study aimed to evaluate the performance of an MFAR and two traditional coastal protection solutions (submerged and emerged detached breakwaters) in dissipating wave energy and protecting the beach (through significant wave heights and sediments accumulation) using numerical models

implemented with SWAN and XBeach. In addition, a comparison between SWAN and XBeach hydrodynamics results was also performed. In previous studies, the wave climate at Leirosa beach was evaluated for frequent and typical storm conditions, and a possible option consisting of a submerged structure of triangular shape (plan view) with multi-functions (MFAR) was also analysed. The results obtained in those studies were compared with the numerical results obtained in the present work for a structure with identical characteristics (MFAR). The proximity (qualitative and quantitative) of the results of those studies with the results of the numerical models used in the present work was reliable proof of good behaviour of the SWAN and XBeach numerical models to analyse and compare the efficiencies of the three possible options of structures to be installed. Moreover, the wave dissipation was quantitatively compared, and similar results were obtained. Thus, the MFAR characteristics were based on previous research works, and all structures analysed were simulated for frequent wave conditions with waves incoming from the west and northwest directions. A storm wave condition scenario was also addressed to the MFAR for the west wave direction.

Regarding significant wave height results for both SWAN and XBeach models, a substantial decrease between before and after every structure shape was clear for both wave directions, which indicates that all structures have a great influence on reducing significant wave heights and wave energy. Amongst all structures, the emerged detached breakwater was the most efficient in reducing significant wave heights at a larger scale compared to the submerged detached breakwater and the MFAR. This is corroborated by the fact that the emerged detached breakwater presented a more substantial and larger shadow zone than the other two solutions, which was expected because it constituted a higher obstacle to the incoming waves. Regarding both submerged structures (detached breakwater and the MFAR), the MFAR presented a more substantial shadow zone. Overall, for the west wave direction scenarios, all structures provided protection at the structures alignment, whereas for the northwest wave direction scenarios, protection was observed in the southeast of all structures.

Comparing both models, it can be concluded that at the inward zones of the submerged detached breakwater and the MFAR, the SWAN numerical model presented greater significant wave height results than the XBeach model, and that XBeach presented greater percentages of substantial reduction of wave heights for frequent wave conditions. For the emerged detached breakwater, SWAN presented lower significant wave height results compared with the XBeach model, as well as greater percentages of substantial reduction of wave heights. Despite the differences, both numerical models indicate that, regarding structure performance, the emerged detached breakwater had the best performance due to higher reduction values, whereas the submerged detached breakwater was the least effective. The

same conclusions can be drawn for wave energy results. Near the shoreline, although the three cases did not present any substantial differences for the SWAN model, the same cannot be stated for the XBeach. From the analysis of XBeach results, the emerged detached breakwater and the MFAR insight changes in the shoreline for both wave directions. For the submerged detached breakwater, there were no substantial changes. For the northwest wave direction, XBeach results for the submerged detached breakwater and the MFAR were similar to those of SWAN. For the emerged detached breakwater results, the SWAN numerical model presented a wider shadow zone than the XBeach model.

Regarding morphodynamics, the obtained results presented favourable tendencies to sediments accretion near the shoreline, as well as at the inward areas for the three structures, as the greatest values for accretion were located in these sites. The most substantial sediments accretion at the shoreline was noticeable for the emerged detached breakwater for both wave directions. Comparing the three structures for the western incoming waves, it was observable that for the emerged detached breakwater and the MFAR, the shoreline sediments accumulated at the structures alignment, forming a substantial salient, whereas for the submerged detached breakwater, the sediments accumulated continuously along the shoreline. For the northwest incoming waves, sediments accretion for the submerged detached breakwater and the MFAR were developed continuously along the shoreline and had similar patterns. The emerged detached breakwater had substantial sediments accumulation in the southeast and inwards of the structure. All protection patterns reported in the attenuation of significant wave heights by the structures were corroborated by the morphodynamics results presented.

Erosion areas were, however, also evident along the shoreline and near all structures. Contribution to overall coastal erosion protection would only be ensured if accretion rates are higher than the erosion rates. Lower accretion rates compromise shoreline stability, and substantial erosion near the structures might also put structures stability at risk due to local scouring. Substantial erosion areas were visible inwards the MFAR for the west incoming waves and at the south extremity for the northwest wave direction, as well as at the north extremity for the emerged detached breakwater, and at the south extremities for the submerged and emerged detached breakwaters for the northwest wave direction. Along the shoreline, substantial erosion was depicted for the emerged detached breakwater and for the MFAR for the west wave direction, with more noticeable values for the emerged detached breakwater. For the submerged detached breakwater, no noticeable erosion areas along the shoreline were visible for either wave directions. For all the northwest wave direction scenarios, no noticeable erosion areas were visible along the shoreline. Although further analysis is required, for the west incoming waves, the sedimentation immediately after the erosion area in the MFAR suggests that part of the sediments on

the eroded area might have settled further ahead. Erosions outwards the structures due to wave reflection appeared in all scenarios, with more intense values for the west wave direction condition.

Regarding structures overall benefits, it can be concluded that for the west and northwest wave predominance, the submerged detached breakwater and the MFAR presented overall better solutions for morphodynamics, considering the balance of erosion and accretion rates.

Regarding the storm wave condition on the performance of the MFAR, the XBeach numerical model indicated positive and substantial significant wave height reduction. Near the shoreline, the XBeach model for hydrodynamics presented a vulnerable area at the structure alignment with noticeable disturbance in shoreline width that indicated apparent erosion at that particular stretch. These observations were corroborated with the morphodynamics results. Wave velocity vectors in the storm wave scenario indicated a more turbulent state than the condition for frequent waves, as expected. Substantial sediments accretion was observed outwards of the structure and on the shoreline. This scenario did not create any salient at the structure alignment. Similar to results presented for the emerged detached breakwater for the west wave direction (frequent wave condition), two vortexes were created inwards the MFAR by wave velocity vector observation. This phenomenon contributed to substantial erosion areas located around the structure, which added substantial changes in the bed level.

4.5 Modelling Phase II

4.5.1 Simulated Scenarios

In this modelling Phase II, the impact of the MFAR (Figure 4.10a) on a coastal zone is compared with a typical submerged detached breakwater (Figure 4.10b) and a group of submerged detached breakwaters (Figure 4.10c).

The case study developed by Mendonça *et al.* (2012a) is again taken as a reference for the modelling of the MFAR and the incident wave conditions for frequent and storm waves are practically the same as presented for Phase I. As geometrical considerations, all structures share the same length (250 m), except the two detached breakwaters in Figure 4.10c that presents a third of the length considered in the other structures (83 m). The detached breakwaters were designed to have a crest width of 10 m and side-slopes of 1:2, which are representative of regular structures of this type as presented in Vieira (2014). The MFAR presents a crest width of 75 m and side slopes of 1:10. All structures have their crests submerged at -1.5 m relatively to mean sea level and are located at the same distance from the shoreline (440 m).

Regarding model conditions, the computational domain is 1670 m x 1870 m (crosshore × longshore) with a node spacing of dx=dy=5.0 m for both hydro- and morphodynamics analysis. The total simulation time is two hours for the hydrodynamics analysis (using SWAN and XBeach) and one day for morphodynamics (XBeach) with a morphological acceleration factor to speed up the morphological time scale relative to the hydrodynamics timescale (morfac) of 50, which insights results for fifty days. Although the simulation time for the morphodynamics is shorter than that of the Phase I, which is justified by the need to reduce calculation time, the selection of morfac 50 is adequate to study the sediments transport tendency to erosion or accretion. The bathymetry used for the numerical simulations is the same as that in the Phase I.
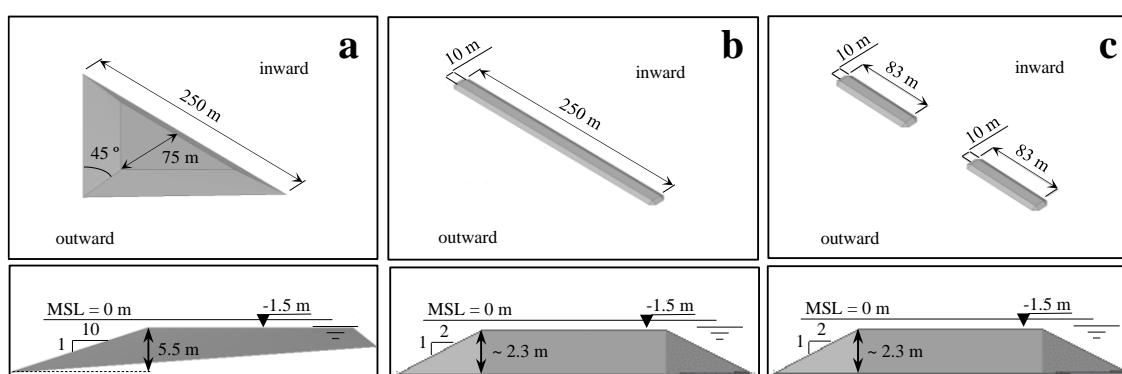
Figure 4.10: Geometrical shapes considered in the modelling Phase II (upper panel: plan view; lower panel: cross-section): a) MFAR; b) regular detached breakwater; and c) group of detached breakwaters.

For hydrodynamics (using SWAN and XBeach), the frequent wave and the storm wave conditions considered in Mendonça *et al.* (2012a) are adopted in this study, with waves incoming from west (270°), while the tidal level considered was 0 m (mean sea level). For morphodynamics analysis (using XBeach), only the frequent wave scenario was analysed, in order to give insights on the response to a mean wave climate. Regarding seabed composition, the sediments dimensions considered are 200 μm for D_{50} and 300 μm for D_{90}. Boundary conditions for SWAN model (hydrodynamics) are defined for north, west and south boundaries (frequent and storm wave conditions), while for XBeach model (hydrodynamics and morphodynamics) absorbing-generating (weakly-reflective) boundary in 2D (abs_2d) for front and back boundaries, and wall boundary condition (simple no flux boundary condition) for left and right boundaries are defined. In XBeach model the left and right designations correspond to North and South, while front and back to West and East, respectively.

For hydrodynamics (SWAN and XBeach), the wave type considered is a JONSWAP spectrum, whereas for morphodynamics (XBeach) the stationary mode is selected. The consideration of stationary mode is justified by the need to reduce model calculation time for morphodynamics. The numerical model

results obtained by the SWAN model are the significant wave heights, while XBeach model estimates the sediments accumulation and erosion near shoreline as well as the bed level. XBeach presents H_{rms} values, which require a conversion to H_s, in order to be compared to SWAN hydrodynamics results. The wave energy dissipation also requires separate calculation.

4.5.2 Results and discussion

4.5.2.1 Hydrodynamics with SWAN and XBeach models

Numerical simulations for the analysis of significant wave heights dissipation for two different scenarios (frequent wave and storm wave conditions) are performed for each structure: MFAR (Figures 4.11a1 and 4.11a2), detached breakwater (Figures 4.11b1 and 4.11b2) and group of detached breakwaters (Figures 4.11c1 and 4.11c2). Comparatively to a situation without structure, an analysis of the influence of each structure on the significant wave heights on a storm wave condition is also performed (Figures 4.11a3, 4.11b3 and 4.11c3). For a more legible analysis, the presented results are centred in a limited window around the structures. The contour lines are also depicted in all presented results.
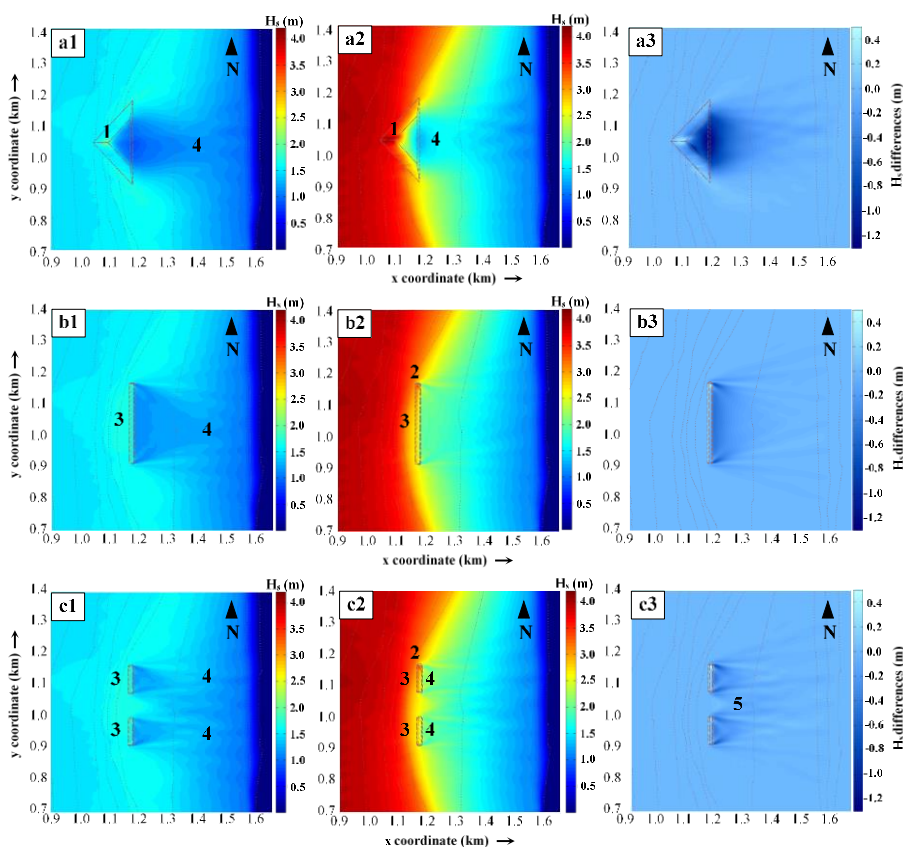
Figure 4.11: Significant wave heights dissipation for frequent wave condition using XBeach: MFAR (a1); detached breakwater (b1), and group of detached breakwaters (c1); and storm wave condition: MFAR (a2), detached breakwater (b2), and group of detached breakwaters (c2). Significant wave heights difference with and without any structure on a storm wave condition: MFAR (a3), detached breakwater (b3), and group of detached breakwaters (c3).

From the results presented in Figure 4.11, wave shoaling (increase of the wave height) in every structure shape is evident due to a decrease of the depth. This phenomenon is visible at the apex of the MFAR for both wave conditions (represented with number 1 in Figures 4.11a1 and 4.11a2); at the north extremity of the detached breakwater and group of detached breakwaters for the storm wave condition (represented with number 2 in Figures 4.11b2 and 4.11c2); a small wave shoaling along the detached breakwater for both wave conditions (represented with number 3 in Figures 4.11b1 and 4.11b2), and also a small wave shoaling along the group of detached breakwaters for both wave conditions (also represented with number 3 in Figures 4.11c1 and 4.11c2). A more intense variation of bottom elevation due to the presence of the detached breakwaters near the north extremities, relatively to the south extremities, might explain the wave shoaling at this particular area (2). The most evident wave shoaling is at the apex of the MFAR (1), while on the other mentioned cases (2 and 3) the differences are more subtle. Regarding significant wave heights decrease, it is clear the effect for every structure shape under both wave conditions. This dissipation is more significant for the storm wave condition. For the MFAR, a progressive increase on significant wave heights is visible from the structure inward (protected) extremity to position 1.45 km for frequent wave condition (represented with number 4 in Figure 4.11a1) and 1.28 km for storm wave condition (also represented with number 4 in Figure 4.11a2). After the position 1.28 km for storm wave condition, the significant wave heights progressively decrease towards shoreline. These phenomena are explained by the shoaling and breaking due to depth decrease. For the detached breakwater this phenomenon is not visible for the storm wave condition, but it is present for the frequent wave where an increase of significant wave height is perceptible from the structure inward extremity to position 1.42 km (also represented with number 4 in Figure 4.11b1). From this position towards shoreline, the significant wave heights decrease gradually.

Finally, for the group of detached breakwaters a small increase on the significant wave height is visible from the structure inward extremity to position 1.21 km for the storm wave condition (also represented with number 4 in Figure 4.11c2), and also an increase of significant wave height from the structure inward extremity to position 1.42 km for the frequent wave condition (also represented with number 4 in Figure 4.11c1). After those positions, the significant wave heights decrease towards shoreline. Results for the north and south detached breakwater from the group of detached breakwaters are similar.

Relatively to the influence of a structure on significant wave heights, it is clear that all structures contribute to a decrease and that the MFAR reduces significant wave heights at a larger scale (Figure 4.11a3) than the detached breakwater and group of detached breakwaters. On the group of detached

breakwaters, even though there is a gap between the structures, a small significant wave height reduction at the inward side is observable in Figure 4.11c3 (represented with number 5). Near the shoreline, although the three cases (Figures 4.11a3, 4.b3 and 4.11c3) do not present any significant differences, it can be concluded that the MFAR presents a more significant and larger shadow zone than the other two solutions. This effect can bring protection benefits if the structure is positioned closer to shoreline.

The XBeach numerical results for root mean square wave heights (H_{rms}) are converted to significant wave heights (H_s) using Equation (4.1).

The plots depicted in Figure 4.12 present the similarities and differences between the significant wave heights results for SWAN and XBeach. The plots show the results for a cross-section at each structure.
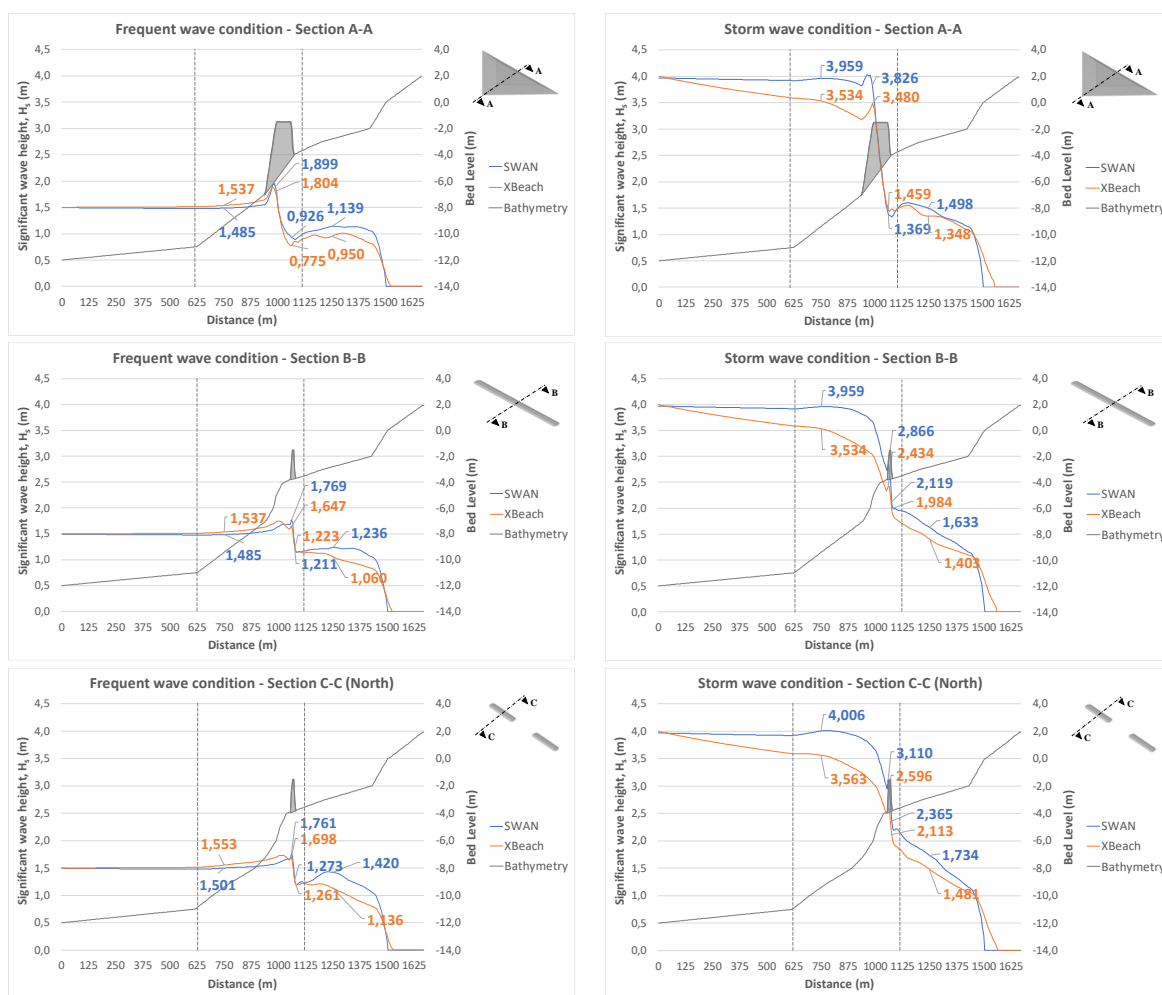
Figure 4.12: Comparison of SWAN and XBeach significant wave height results for frequent (H_s = 1.5 m, T_p = 9 s) and storm (H_s = 4 m, T_p = 15 s) conditions for: MFAR (Section A-A), detached breakwater (Section B-B), and North detached breakwater from the group of detached breakwaters (Section C-C).

Results for the south detached breakwater from the group of detached breakwaters are not presented in this study due to results similarity to the north structure. The indicated values in the plots are selected

for four positions: before, immediately before, immediately after and after the structures. The vertical lines plotted represent relevant seabed slope changes.

As mentioned before, the wave shoaling due to a sudden depth change immediately before the structure is visible for all cases with both numerical models. From the analysis of Figure 4.12, it is clear that both SWAN and XBeach simulate this phenomenon for all structures and that for the all storm wave conditions, SWAN simulates a small wave shoaling due to the slope change at positions 625 m and 1125 m, and a wave shoaling for all frequent wave condition at position 1125 m. The XBeach model only represents a significant wave shoaling for the frequent and storm wave condition for the MFAR at position 1125 m.

Equation (4.2) is used for calculating the wave energy (E) per unit area (J/m²). Equations (4.3), (4.4) and (4.5) are, respectively, applied in order to proceed to: an overall comparison between SWAN and XBeach hydrodynamics results (Δ); an overall percentage of significant wave height results reduction before and after the structures for both wave conditions (α); and their wave energy reduction results (β).

$$\Delta_{SWAN-XBeach} = H_{s\,SWAN} - H_{s\,XBeach} \tag{4.3}$$

$$\alpha = \left(H_{s\,Before} - H_{s\,After}\right)/H_{s\,Before} \times 100 \tag{4.4}$$

$$\beta = \left(E_{Before} - E_{After}\right)/E_{Before} \times 100 \tag{4.5}$$

where $\Delta_{SWAN-XBeach}$ is the comparison between significant wave height results between both models for a specific location (m); $H_{s\,SWAN}$ and $H_{s\,XBeach}$ are the significant wave height computed by, respectively, SWAN and XBeach model for a specific location (m); α is the numerical model H_s reduction for a specific location (%); $H_{s\,Before}$ and $H_{s\,After}$ are the significant wave height, respectively, before and after, a structure (m); β is the numerical model E reduction for a specific location (%); E_{Before} and E_{After} are the wave energy, respectively, before and after, a structure (J/m²); Considering ρ_w= 1025 kg/m³ and g = 9.81 m/s² the wave energy was computed for all scenarios.

From Figure 4.12 and using Equation (4.3), it is clear that for the frequent wave condition, the SWAN results before the structures (MFAR; detached breakwater; and group of detached breakwaters) present smaller significant wave heights than the XBeach model (-0.05; -0.05; -0.05), and greater significant wave heights after the structures (0.19, 0.18, 0.28). For the storm wave condition, SWAN model computes greater significant wave heights than the XBeach model before (0.43; 0.43; 0.44) and after (0.15; 0.23; 0.25) the structures.

Regarding the difference between significant wave heights before and after the structures, using Equation (4.4), overall, XBeach presents greater reduction values than the SWAN model. Similar

reduction values for significant wave height (SWAN, XBeach) can be seen for the storm wave conditions [(62.16%, 61.86%); (58.75%, 60.30%); (56.71, 58.43%)], while for the frequent wave condition significant differences are evident [(23.30%, 38.19%); (16.77%, 31.03%); (5.40%, 26.85%)] (MFAR; detached breakwater; and group of detached breakwaters). For both scenarios, the MFAR has the best performance, due to higher reduction values, whereas the group of detached breakwater is the least effective.

Overall, for extreme wave conditions, results for significant wave height reductions for both SWAN and XBeach models are similar, which indicate that, even though the significant wave heights calculated are different, the performance for each structure is comparable. Since wave energy is proportional to wave heights (Equation 4.2), the same conclusion for wave energy can be taken (Equation 4.5).

4.5.2.2 Morphodynamics with XBeach model

One of the suggestions proposed by Mendonça *et al.* (2012a) was to study morphodynamics around the structure to enable a deeper understanding on sedimentation and erosion areas. In order to develop that study, XBeach morphodynamics models for each one of the structures are performed.

Numerical simulations for the analysis of cumulative sedimentation and erosion for the frequent wave condition are conducted for each shape: MFAR (Figure 4.13a1), detached breakwater (Figure 4.13b1) and group of detached breakwaters (Figure 4.13c1). Figures 4.13a2, 4.13b2 and 4.13c2 show the bed level evolution at the end of the XBeach simulation for each structure shape. The study was performed for one day with a morfac of 50, which insights results for fifty days. The simulations are taken for a frequent wave condition and the results presented are cropped for a more legible analysis.

From the results depicted in Figures 4.13a1, 4.13b1, and 4.13c1, it is evident the most significant erosion areas are immediately after the MFAR (1) (over -0.9 m); outwards the detached breakwater and group of detached breakwaters (2) due to waves reflection (-0.1 m); at the north and south extremities of the detached breakwater and group of detached breakwaters (3) due to waves diffraction (-0.1 m); and downdrift near the shoreline of all the three structures (4) (-0.3 m). Along the shoreline, a very small erosion with the same magnitude (-0.1 m) for the three scenarios is also evident. Outwards the MFAR (5), it is also noticeable a slight erosion due to waves reflection (-0.1 m). Regarding the erosion on the detached breakwater and group of detached breakwaters (marked with numbers 2 and 3), it is noticeable a more intense phenomenon on the detached breakwater scenario. These erosion areas

near the structures might put at risk the structures stability due to scouring. Near the shoreline, the downdrift erosion on the detached breakwater and group of detached breakwaters scenarios (4) is slightly more intense than the erosion in the MFAR scenario (4). In the group of detached breakwaters there is no erosion at the gap between the structures.
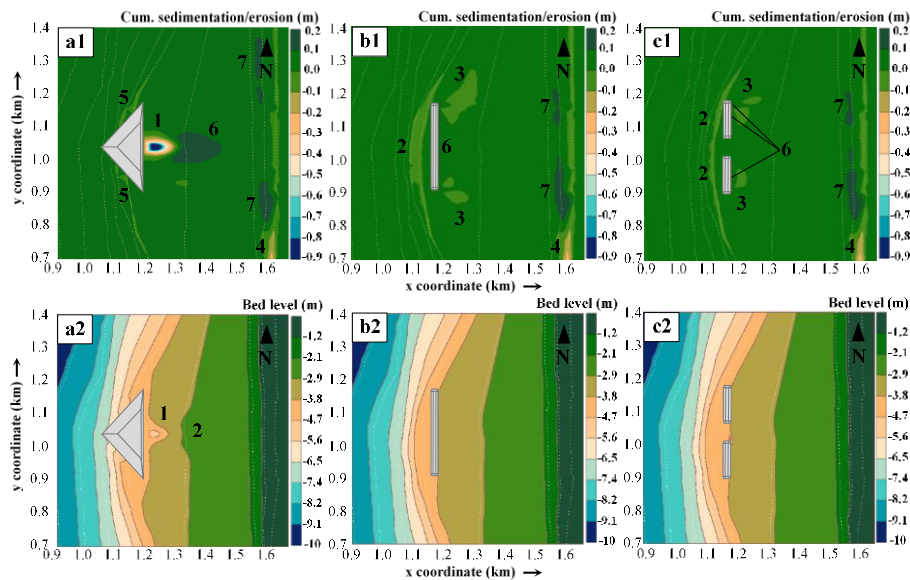
Figure 4.13: Cumulative sedimentation and erosion for frequent wave condition: MFAR (a1); detached breakwater (b1); and group of detached breakwaters (c1). Bed level for frequent wave condition: MFAR (a2); detached breakwater (b2); and group of detached breakwaters (c2).

Regarding sedimentation areas, it is visible a significant sediments accretion of 0.2 m inwards the MFAR (6) immediately after the erosion area, which might suggest that part of the sediments on the eroded area settle further ahead. Along the shoreline, in the MFAR there is a significant sedimentation updrift and downdrift the structure (7) (0.2 m), while on the detached breakwater and group of detached breakwaters the corresponding sedimentation (7) is located at the structures protected region. Immediately after the detached breakwater and group of detached breakwaters (6) there is also a slight sediments accretion (0.2 m). From the results presented in Figures 4.13a2, 4.13b2, and 4.13c2, it can be concluded that there are no significant changes in morphology in all scenarios, except for immediately after the MFAR (Figure 4.13a2) where the erosion (1) and sedimentation (2) phenomena altered the bed level.

4.5.3 Summary and conclusions for Phase II modelling

This study aimed to assess the performance of a MFAR and two traditional coastal protection solutions in dissipating wave energy and protecting the beach using numerical models implemented with SWAN

and XBeach. In addition, a comparison between SWAN and XBeach hydrodynamics results was also performed. The MFAR characteristics were based on a previous (Mendonça *et al.*, 2012a) research work, and all structures analysed were simulated for storm and frequent wave conditions. Regarding significant wave heights results, a substantial decrease between before and after every structure shape was clear for both wave scenarios (especially during storm wave conditions), which indicates that all structures have great influence on reducing significant wave heights and wave energy. Amongst all structures, for both scenarios, the MFAR was the best for reducing significant wave heights at a larger scale and a larger shadow zone compared to the submerged detached breakwater and group of submerged detached breakwaters, which can bring protection benefits if the structure is positioned closer to shoreline. The least effective structure was the group of detached breakwaters.

Comparing both models, it can be concluded that, overall, SWAN numerical model tends to present greater significant wave heights results; and that XBeach presents greater percentages of significant wave heights reduction for frequent wave conditions, and similar values for storm wave conditions. This similarity indicates that, even though the significant wave heights calculated are different, the performance for each structure is comparable. The same conclusions can be taken for wave energy results.

Regarding morphodynamics, the obtained results presented a favourable tendency to sediments accretion near the shoreline, and at the inward areas for the three structures, since the greatest values for sediments accumulation are located at these sites. The most significant sediments accretion at the shoreline was noticeable for the group of detached breakwaters, while the largest overall sediments accumulation was visible for the MFAR. The accretion and erosion patterns along the shoreline for the three structures scenarios were similar for the fifty days insights. It is important to note that erosion areas near all structures jeopardise their stability due to local scouring. In the simulated numerical models, the widely known erosion effects near the detached breakwaters (simple and group) were evident due to waves reflection and diffraction phenomena. The obtained results suggest that the longer the detached breakwater, the more intense the erosion is near the structure. The largest overall erosion was located inwards the MFAR.

In this study, patterns of salient formations were not created for these conditions, since there were no evidences of significant changes in bed level results. For further studies, emerged structures and/or structures placed closer to shoreline should be better analysed. In addition, the consideration of a JONSWAP spectrum for the XBeach morphodynamics analysis might present more realistic morphodynamics results.

4.6 References for Chapter 4

Adriana-Gracia, C.; Rangel-Buitrago, N.; Oakley, J.A.; and Williams, A. (2018). Use of ecosystems in coastal erosion management. *Ocean and Coastal Management*, *156*, 277–289. https://doi.org/10.1016/j.ocecoaman.2017.07.009.

Antunes do Carmo, J.S. (2019a). Coastal Adaptation: Past Behaviors, Contemporary Management, and Future Options. In *Coastal and Marine Environments - Physical Processes and Numerical Modelling* (p. 20). IntechOpen, London, UK. https://doi.org/10.5772/intechopen.88123.

Antunes do Carmo, J.S. (2019b). The changing paradigm of coastal management: The Portuguese case. *Science of The Total Environment*, *695*, 133807. https://doi.org/https://doi.org/10.1016/j.scitotenv.2019.133807.

Bergillos, R.J.; López-Ruiz, A.; Medina-López, E.; Moñino, A.; and Ortega-Sánchez, M. (2018). The role of wave energy converter farms on coastal protection in eroding deltas, Guadalfeo, southern Spain. *Journal of Cleaner Production*, *171*, 356–367. https://doi.org/https://doi.org/10.1016/j.jclepro.2017.10.018.

Bergillos, R.J.; Rodríguez-Delgado, C.; Millares, A.; Ortega-Sánchez, M.; and Losada, M.A. (2016). Impact of river regulation on a Mediterranean delta: Assessment of managed versus unmanaged scenarios. *Water Resources Research*, *52*(7), 5132–5148. https://doi.org/10.1002/2015WR018395.

Black, K.P.; and Andrews, C.J. (2001). Sandy Shoreline Response to Offshore Obstacles Part 1: Salient and Tombolo Geometry and Shape. *Journal of Coastal Research*, *Winter2001*(SI 29), 82–93. Retrieved from http://www.jstor.org/stable/25736207.

Bolle, A.; Mercelis, P.; Roelvink, D.; Haerens, P.; and Trouw, K. (2010). Application and Validation of Xbeach for Three Different Field Sites. In *Proceedings of 32nd Conference on Coastal Engineering, 30th to 5th July 2010* (pp. 1–14). Shanghai, China. https://doi.org/10.9753/icce.v32.sediment.40.

Capitão, R.; and Fortes, C. (2011). Análise comparativa entre estimativas do modelo SWAN e medições de agitação marítima efectuadas na Praia da Amoreira, Portugal. *Revista Da Gestão Costeira Integrada*, *11*(3), 283–296. https://doi.org/10.5894/rgci269.

Castelle, B.; Guillot, B.; Marieu, V.; Chaumillon, E.; Hanquiez, V.; Bujan, S.; and Poppeschi, C. (2018). Spatial and temporal patterns of shoreline change of a 280-km high-energy disrupted sandy coast from 1950 to 2014: SW France. *Estuarine, Coastal and Shelf Science*, *200*, 212–223. https://doi.org/10.1016/j.ecss.2017.11.005.

Charlier, R.H.; Chaineux, M.C.P.; and Morcos, S. (2005). Panorama of the History of Coastal Protection. *Journal of Coastal Research*, *21*(1), 79–111. https://doi.org/10.2112/03561.1.

Deltares. (2019a). Delft3D 4 Suite (structured). Retrieved February 7, 2019, from https://www.deltares.nl/en/software/delft3d-4-suite.

Deltares. (2019b). XBeach. Retrieved February 12, 2019, from https://www.deltares.nl/en/software/xbeach.

EEA. (2006). *European Environment Agency - The Changing Faces of Europe's Coastal Areas*. Copenhagen: Office for Official Publications of the European Communities.

Gilbert, J.; and Vellinga, P. (1990). Climate Change: The IPCC Response Strategies - Chapter 5. In *Report prepared for Intergovernmental Panel on Climate Change by Working Groups III* (p. 330). Digitization and Microform Unit (2010), UNOG Library. Retrieved from https://www.ipcc.ch/ipccreports/far/wg_III/ipcc_far_wg_III_chapter_05.pdf.

Granja, H.; and Pinho, J.L. (2012). Coastal Defense in NW Portugal: The Improbable Victory. In J. A. G. Cooper & O. H. Pilkey (Eds.), *Pitfalls of Shoreline Stabilization: Selected Case Studies* (pp. 251–266). Dordrecht, The Netherlands: Springer. https://doi.org/10.1007/978-94-007-4123-2_15.

Griggs, G.B. (2005). The impacts of coastal armoring. *Shore and Beach*, *73*(1), 13–22. Retrieved from https://www.researchgate.net/publication/285969581_The_impacts_of_coastal_armoring.

Hanson, H. (2019). Wave transformation. Retrieved October 28, 2019, from http://www.tvrl.lth.se/fileadmin/tvrl/files/vvr040/3_Wave_transformation_3pp.pdf.

IPCC. (2012). *Managing the Risks of Extreme Events and Disasters to Advance Climate Change Adaptation. A Special Report of working groups I and II of the Intergovernamental Panel on Climate Change*. (C. B. Field, V. Barros, T. F. Stocker, D. Qin, D. J. Dokken, K. L. Ebi, M. D. Mastrandrea, K. J. Mach, G.-K. Plattner, S. K. Allen, M. Tignor, & P. M. Midgley, Eds.). Cambridge, UK: Cambridge University Press. https://doi.org/10.1017/CBO9781139177245.

Lynett, P.J.; and Liu, P.L.-F. (2008). Modeling Wave Generation, Evolution, and Interaction with Depth-Integrated, Dispersive

Wave Equations. COULWAVE Code Manual. Long and Intermediate Wave Modeling Package, v. 2.0. Cornell University, NY, USA, 90. Retrieved from https://pdfs.semanticscholar.org/f07d/a390c4590b880607037be8d900538f42c992.pdf.

Mendonça, A.; Fortes, C.J.; Capitão, R.; Neves, M. da G.; Moura, T.; and Antunes do Carmo, J.S. (2012a). Wave hydrodynamics around a multi-functional artificial reef at Leirosa. *Journal of Coastal Conservation*, *16*(4), 543–553. https://doi.org/10.1007/s11852-012-0196-1.

Mendonça, A.; Fortes, C.J.; Capitão, R.; Neves, M.G.; Antunes do Carmo, J.S.; and Moura, T. (2012b). Hydrodynamics around an Artificial Surfing Reef at Leirosa, Portugal. *Journal of Waterway, Port, Coastal, and Ocean Engineering*, *138*(3), 226–235. https://doi.org/10.1061/(ASCE)WW.1943-5460.0000128.

MetED. (2012). Wave Energy Equation. Retrieved November 5, 2019, from https://www.meted.ucar.edu/marine/mod1_wv_type_char/print.htm#page_4.5.4.

Narra, P.; Coelho, C.; Sancho, F.; and Palalane, J. (2017). CERA: An open-source tool for coastal erosion risk assessment. *Ocean and Coastal Management*, *142*, 1–14. https://doi.org/10.1016/j.ocecoaman.2017.03.013.

Paredes, R.; Callapez, P.M.; Danielsen, R.; Dinis, P.; Carvalho, M.; and Soares, A.F. (2006). Paleoecologia da malacofauna salobra e biofácies da laguna holocénica de Leirosa (Figueira da Foz). In *Proceedings of VII Congresso Nacional de Geologia, 5 de Julho a 7 de Julho 2006* (pp. 737–740). Estremoz, Portugal. Retrieved from https://www.socgeol.org/documents/type_5/VIICNGVolIII099.pdf.

Pilarczyk, K. (2009). Remarks on Coastal Stabilization and Alternative Solutions. In *Handbook of Coastal and Ocean Engineering* (pp. 521–551). Singapore: WORLD SCIENTIFIC. https://doi.org/doi:10.1142/9789812819307_0020.

Pilkey, O.H.; and Cooper, J.A.G. (2014). *The Last Beach*. USA: Duke University Press.

Pinho, J.L.S.; Vieira, J.M.P.; and Antunes do Carmo, J.S. (2004). Hydroinformatic environment for coastal waters hydrodynamics and water quality modelling. *Advances in Engineering Software*, *35*(3–4), 205–222. https://doi.org/10.1016/J.ADVENGSOFT.2004.01.001.

Pranzini, E.; and Williams, A.T. (2013). *Coastal Erosion and Protection in Europe* (1st Ed.). London, UK: Routledge. https://doi.org/10.4324/9780203128558.

Ranasinghe, R.; and Turner, I.L. (2006). Shoreline response to submerged structures: A review. *Coastal Engineering*, *53*(1), 65–79. https://doi.org/https://doi.org/10.1016/j.coastaleng.2005.08.003.

Ranasinghe, R.; Turner, I.L.; and Symonds, G. (2006). Shoreline response to multi-functional artificial surfing reefs: A numerical and physical modelling study. *Coastal Engineering*, *53*(7), 589–611. https://doi.org/https://doi.org/10.1016/j.coastaleng.2005.12.004.

Rangel-Buitrago, N.; Williams, A.; and Anfuso, G. (2018). Hard protection structures as a principal coastal erosion management strategy along the Caribbean coast of Colombia. A chronicle of pitfalls. *Ocean & Coastal Management*, *156*, 58–75. https://doi.org/https://doi.org/10.1016/j.ocecoaman.2017.04.006.

Razak, M.S.A.; and Nor, N.A.Z.M. (2018). XBeach Process-Based Modelling of Coastal Morphological Features Near Breakwater. *MATEC Web Conferences*, *203*(1007). https://doi.org/10.1051/matecconf/201820301007.

Rocha, F.; and Bernardes, C. (1997). Caracterização mineralógica dos níveis lodosos no sistema de dunas costeiras a sul do Cabo Mondego (Leirosa, Portugal). *Estudos Do Quaternário*, (1), 67–72. https://doi.org/10.30893/eq.v0i1.10.

Roelvink, D.; McCall, R.; Mehvar, S.; Nederhoff, K.; and Dastgheib, A. (2018). Improving predictions of swash dynamics in XBeach: The role of groupiness and incident-band runup. *Coastal Engineering*, *134*, 103–123. https://doi.org/https://doi.org/10.1016/j.coastaleng.2017.07.004.

Schreck-Reis, C.; Antunes do Carmo, J.; and Freitas, H. (2008). Learning with Nature: A Sand Dune System Case Study (Portugal). *Journal of Coastal Research*, 1506–1515. https://doi.org/10.2112/07-0858.1.

SWAN. (2018). SWAN manual. Retrieved February 8, 2019, from http://swanmodel.sourceforge.net/online_doc/swanuse/node3.html.

United Nations. (2015). *Transforming Our World: The 2030 Agenda for Sustainable Development A/RES/70/1*. UN General Assembly: New York, NY, USA. Retrieved from https://sustainabledevelopment.un.org/content/documents/21252030 Agenda for Sustainable Development web.pdf.

Vieira, B.F.V. (2014). *Wave hydrodynamics in coastal stretches influenced by detached breakwaters*. MSc Thesis in Civil Engineering, University of Minho: Guimarães, Portugal. Retrieved from http://hdl.handle.net/1822/36113.

Weinberg, J. (2015). The Big Squeeze: Coastal megacities face growing pressure from sea and land. *Stockholm Waterfront*, (1), 5–7. https://doi.org/10.1126/science.299.5615.1941a.

Williams, A.; Rangel-Buitrago, N.; Pranzini, E.; and Anfuso, G. (2018). The management of coastal erosion. *Ocean & Coastal Management*, *156*, 4–20. https://doi.org/10.1016/j.ocecoaman.2017.03.022.

CHAPTER 5

Investigation of an adequate geometry to induce longitudinal drift reversal

using hydro- and morphodynamics modelling

"Every man takes the limits of his own field of vision for the limits of the world"

Arthur Schopenhauer. German philosopher (1788-1860)

(Page intentionally left blank)

CHAPTER 5   INVESTIGATION OF AN ADEQUATE GEOMETRY TO INDUCE LONGITUDINAL DRIFT REVERSAL USING HYDRO- AND MORPHODYNAMICS MODELLING

5.1 Introduction

The search for an innovative coastal protection structure intends to minimize the common fragilities associated to the traditional structures as seawalls, groins and detached breakwaters by promoting a reversal of longshore drift, increasing the protection of the coast and avoiding local erosions that normally result from the abrupt interruption of sediment transport when traditional structures are implemented. This reversal of the longitudinal drift is observed at different coastal segments and is induced by natural or anthropic coastal features, like ebb river deltas, rocky outcrops or harbour jetties. In general, these features induce a wave direction modification of the prevailing wave propagation direction that favour the formation of coastal accretion areas.

The main used design criterion considered for the assessment of the new structures performance is the observation of wave energy dissipation (based on the significant wave height) and modification of wave propagation directions. This analysis is based on numerical models implemented with SWAN/XBeach models to understand the new structural shapes contribution to the formation of a beneficial shadow zone and the reversal of longshore drift. Since in previous numerical models analysis (Chapter 4), the simulated hydrodynamics based on XBeach presented similar results to the SWAN's, only SWAN model is henceforth used to understand the influence of each structure on the wave energy dissipation and on wave directions propagation.

For this analysis, the Delft3D-FLOW model is coupled with SWAN to simulate the hydrodynamic fields around the structures and the sediment transport is assessed recurring to XBeach model. Initially, a routine to generate simplified bathymetries for large domains and simple shaped coastal structures was adapted and developed in order to initiate the numerical simulations. This pre-processing task is semi-automatic allowing to readily generate different models geometries. However, despite the grid generation routine being functional, restrictions for complex or rounded shapes for coastal structures requires the design of generic bathymetries and complex structures to be complemented with AutoCAD. The nature-based observation located in the Portuguese coast (Mira, Guadiana and Ave estuaries) described in Chapter 2 complemented with selected hotspots in this Chapter inspired the development of different innovative coastal protection structures (new shapes that are considered in the modelling framework as bathymetric changes) that promote the reversal of longshore drift. The observation of

these sites will lead to the preliminary characterization of the adequate dimensions to promote the reversal of the sediment drift along a coastal stretch.

Several structure shapes with different performances favouring the longshore drift reversal are proposed and tested under storm wave conditions that characterize the NW Portuguese coastal wave climate previously studied in Chapter 3. The structure shape with the best hydrodynamics outcomes is identified and presented in detail as the final proposal. For this new structure shape it is conducted: (i) a sound analysis focusing the morphodynamics of the defended coastal stretch; (ii) and a comparison of results obtained for a traditional structure (groin) and the proposed innovative structure. Also, scenarios without the presence of any structure are developed as reference bathymetries to understand the natural hydro- and morphodynamics without the influencing effect of any hindrance.

Delft3D-FLOW, SWAN and XBeach are the selected software to implement the numerical laboratory to analyse the influence of the maritime structures on wave energy dissipation, wave propagation patterns modifications and accretion/erosion phenomena at different time and spatial scales. The obtained results provide the possibility of evaluating wave shoaling and diffraction that are of paramount importance to understand the reversal of longshore drift.

The first step to define the simulation conditions for those models requires the consideration of a domain with significant dimensions to replicate a real situation and a grid generation in RGFGRID (Delft3D module), which allows the definition of the bathymetry to be created. One of the main objectives of this study is the applicability of a coastal protection solution to a generalized bathymetry. Therefore, rather than considering a characteristic bathymetry of a specific location, the analysis is performed using a general simplified bathymetry with a constant slope of 1:50 (2%) and a large domain as reference bathymetries. The large domain avoids computational boundary instabilities that might interfere with the bed level modifications where the structures are being placed. Based on another work (Vieira, 2014), the 2% slope has been considered adequate for a beach slope. In order to induce the reversal of longshore drift, the new shapes are considered in the numerical models as changes to the bed level of the reference bathymetry and the implantation of defined geometries for structures.

The models integration methodology considered the following sequence of simulations: 1 – Delft3D-FLOW; 2 – SWAN; and 3 – Delft3D-FLOW + SWAN; 4 – XBeach (restricted to the structures that revealed the best hydrodynamic performances). Results for all numerical models are processed in QUICKPLOT (post-processing module of Delft3D). Coupling Delft3D-FLOW with SWAN is conducted after the two models have been individually running without limitations. For the sake of simplicity, this combination is subsequently referred to as SWAN. The XBeach implemented considerations assume a

null sediment layer thickness (non-erodible, corresponding to the use of artificial armour blocks) or a non-null sediment layer thickness composed by sediments. The grid and depth files are generated using the RGFGRID and QUICKIN Delft3D modules.

5.2 Geometric jetty characteristics and sedimentary conditions near estuaries

As previously mentioned in Chapter 2, when waves encounter the presence of an obstacle, a change of waves' direction occur. This is the diffraction phenomenon that can occur either in shallow or deep waters, which is key to induce the reversal of longshore drift, and in this Section is analysed by selecting several hotspots (the majority being in Portugal) where wave crests rotation is observable.

The analysis of longshore drift reversing phenomenon is developed using GIS (Google Earth Pro) on the characterization of the geometric and sedimentary conditions influence on selected sites, which allows a more in-depth study of the wave diffraction where the reversal of longshore drift takes place (usually at estuaries mouths – ebb tidal deltas). The analysis is performed based on the nature response to the impact of existing engineering structures on: Cabedelo beach near the Viana do Castelo jetty (Figure 5.1); Matosinhos beach near the Leixões harbour (Figure 5.2); Douro estuary near the jetties and the detached breakwater (before and after interventions depicted in Figures 5.3 and 5.4, respectively); Vouga estuary near the jetty (Figure 5.5); and Corona del Mar (California) near the jetties (Figure 5.6). In addition, observations on the Cávado estuary morphodynamics (Figure 5.7) and on the influence of the natural surrounding outcrops in Laguna beach (California) (Figure 5.8) are analysed.

For the sake of replicating the reversal of longshore drift through bathymetric changes or innovative coastal structures, geometrical characteristics of the obstacles are necessary to understand the impact on sediments transport along the coast. Thus, information regarding the geometric conditions (jetties and rocky outcrops dimensions in plan view: length, orientation and distance in relation to the coast, and crest width) and/or the sedimentary conditions (up- and downdrift width beach comparison: beach width resulting from the longshore drift reversal) are presented in the right panel of each Figure.

In all Figures, the waves' diffraction can be observed by the wave crests rotation from NW to SW (except in Figure 5.3) as the waves encounter the obstacles. Figure 5.4 enlightens the influence of the prolongation of the Douro estuary south jetty on the waves diffraction (combined with the detached breakwater construction southwards) as in comparison of Figure 5.3 before the interventions, where this diffraction is not noticeable. Figure 5.3 shows waves incoming from NW without any rotation near the south jetty, while Figure 5.4 clearly depicts the reversal of the main wave direction propagation as

waves get oriented to SW due to the south jetty. The natural protection provided by rocky outcrops presented in Figure 5.8 also noticeably depicts the rotation on waves' direction.

Lima estuary: Viana do Castelo north jetty	
Length (red line):	886 m
Orientation (approximate):	NNW
Distance (yellow line):	1169 m
Crest width:	21.5 m

Figure 5.1: Lima estuary: Viana do Castelo north jetty (Cabedelo beach) characteristics (2006).

Leixões harbour	
Length (red line):	2027 m
Orientation (approximate):	NNW
Distance (yellow line):	1257 m
Crest width:	17.9 m
north beach (purple line)	221 m
south beach (purple line)	263 m
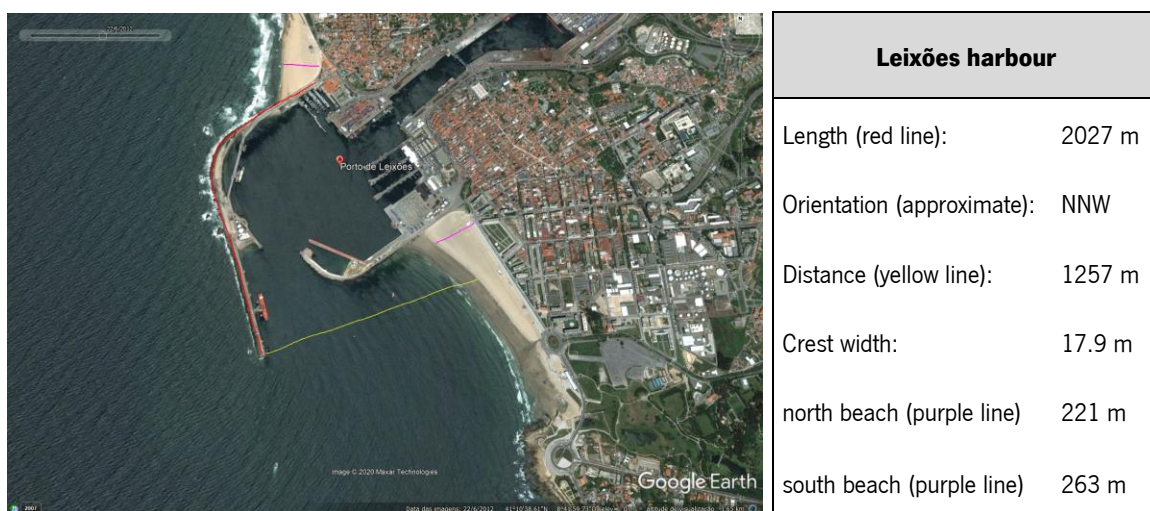
Figure 5.2: Leixões harbour (Matosinhos beach) jetty characteristics (2012).

Douro estuary: north jetty	
Length (red line):	239 m
Orientation (approximate):	NE
Crest width:	6.3 m
Douro estuary: south jetty (before interventions)	
Length (red line):	286 m
Orientation (approximate):	NW
Crest width:	16.4 m
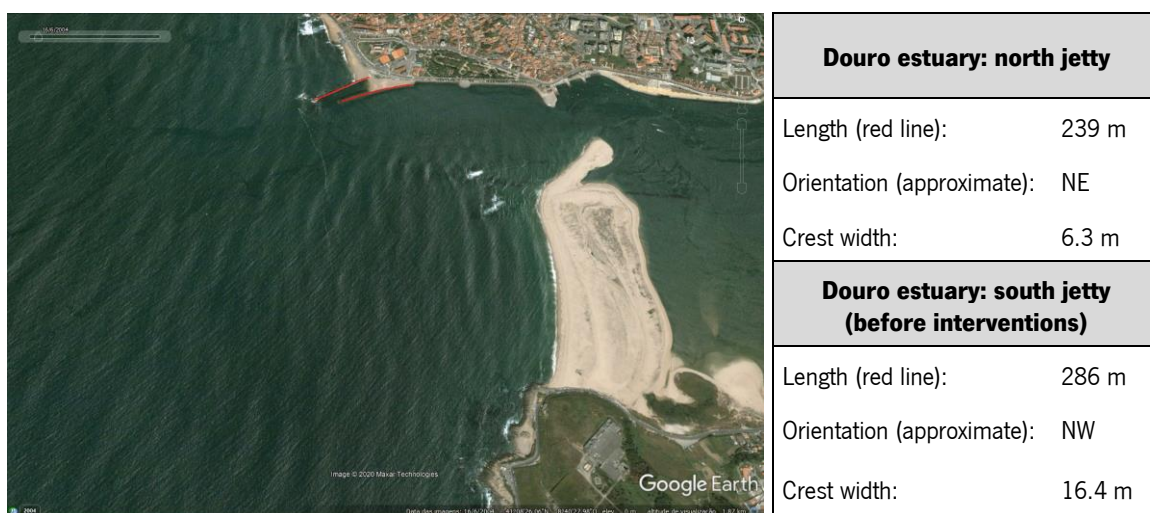
Figure 5.3: Douro estuary: characteristics before south jetty extension and detached breakwater construction (2004).

Douro estuary: south jetty (after interventions)	
Length (red line):	609 m
Orientation (approximate):	NE
Crest width:	22.8 m
Douro estuary: Detached breakwater	
Length (red line):	471 m
Orientation (approximate):	NW
Crest width:	17.5 m

Figure 5.4: Douro estuary: characteristics after south jetty extension and detached breakwater construction (2013).

Vouga estuary: Aveiro north jetty	
Length (red line):	752 m
Orientation (approximate):	NE
Distance (yellow line):	1268 m
Crest width:	32.7 m

Figure 5.5: Vouga estuary: Aveiro north jetty characteristics (2018).

Newport bay: Corona del Mar west jetty	
Length (red line):	868 m
Orientation (approximate):	N
Crest width:	11.4 m
Newport bay: Corona del Mar east jetty	
Length (red line):	514 m
Orientation (approximate):	N
Crest width:	12.0 m
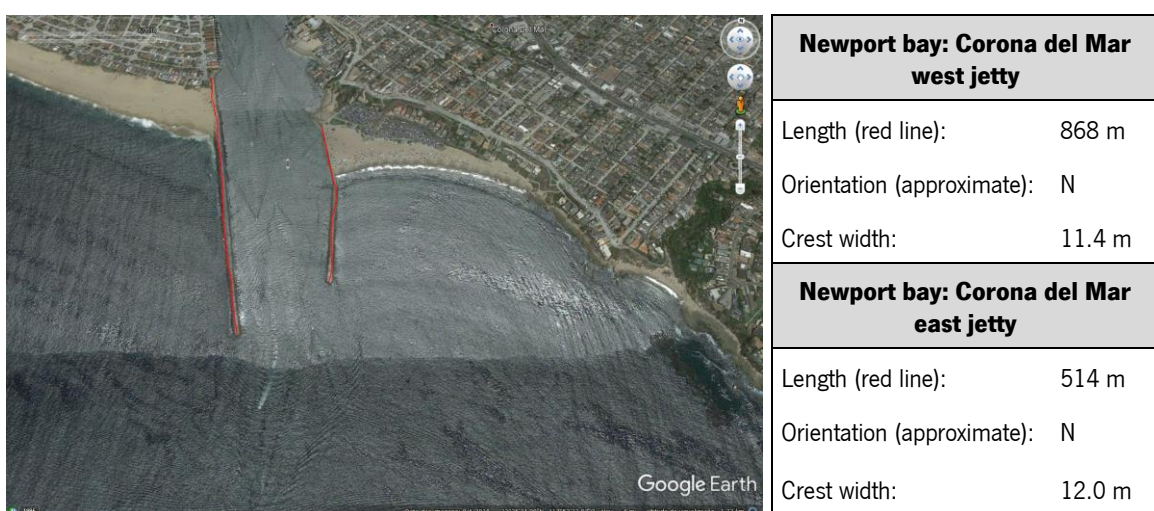
Figure 5.6: Newport bay (California): Corona del Mar jetties characteristics (2018).

Cávado estuary: north beach	
Mean beach width:	96.4 m
Cávado estuary: south beach	
Mean beach width:	115 m
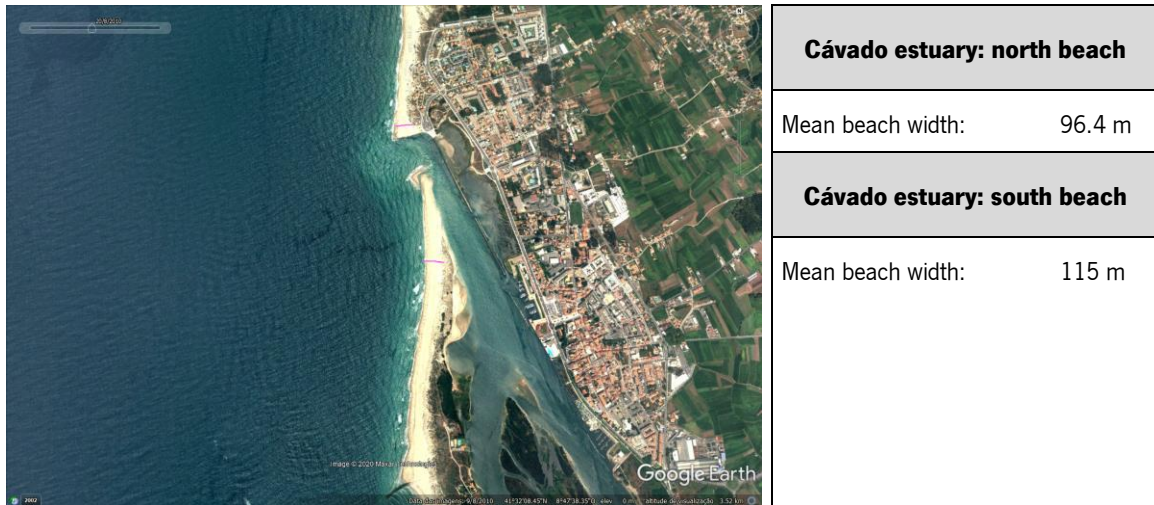
Figure 5.7: Cávado sand spit and beach characteristics (2010).

Laguna beach: rocky outcrops	
Length (blue line)	189 m
Orientation (approximate):	N
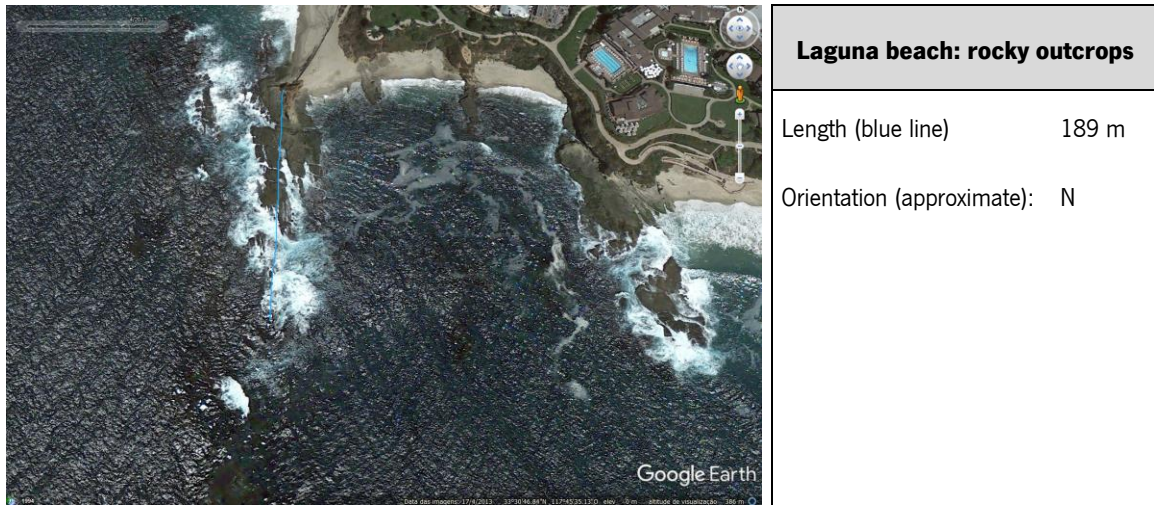
Figure 5.8: Laguna beach (California) rocky outcrops characteristics.

5.3 Wave climate near Iberian Peninsula shoreline: numerical simulations

The uncertainty analysis developed in Chapter 3 allowed the characterization of the western coast of the Iberian Peninsula wave climate regimes considering the HP and the RCPs scenarios. Since the collected data is related to offshore locations in deep waters, necessary numerical simulations to understand the waves' propagation from deep waters to beach locations is required to determine wave conditions for the hydro- and morphodynamics models. In spite of Delft Dashboard allowing collecting GEBCO bathymetries (van Ormondt *et al.*, 2020) for any location worldwide, detailed bathymetry near shoreline is restricted. For this reason, it was required to nest a specific local grid to the Iberian Peninsula Coast model grid. The region selection for the local grid and bathymetry was based on previous studies within the scope of the MarRisk project (Bio *et al.*, 2020; Ferreira *et al.*, 2021; Pinho *et*

al., 2020) with detailed data near the Lima estuary (Minho region in Portugal). Thus, the Iberian Peninsula grid and bathymetry were automatically generated in Delft Dashboard with a coarser cell grid of 0.05 degrees of latitude (5.55 km), while the local grid and bathymetry were defined using information from MarRisk project with a more refined cell grid for the Lima estuary with 0.0005 degrees of latitude (0.0555 km).

The wave propagation was analysed for three scenarios: HP (Iberian_HP), RCP4.5_end (Iberian_4.5) and RCP8.5_end (Iberian_8.5) using SWAN hydrodynamics. The input H_s and T_p conditions for the numerical simulations were based on the return values estimates for WN Station Group (due to Lima's estuary location) by determining their mean values for a 100-year return period. For the simulations, JONSWAP spectra were considered with incoming waves from Northwest (315°) without tidal influence (tidal level = 0 m relatively to the MSL). Tables 5.1 and 5.2 summarise the wave conditions and present the main numerical model conditions for the Iberian Peninsula simulations, respectively.

Table 5.1: Wave conditions for the Iberian Peninsula Coast simulations.

Mean Values for WN Station Group for a 100-year Return Period					
HP		RCP4.5_end		RCP8.5_end	
H_s (m)	T_p (m)	H_s (m)	T_p (m)	H_s (m)	T_p (m)
17.4	19.2	20.5	18.0	25.3	18.4

Table 5.2: SWAN numerical model conditions for the Iberian Peninsula Coast simulations.

SWAN Numerical Model Conditions			
Parameters	HP	RCP4.5_end	RCP8.5_end
Tidal level (m)	0	0	0
Wave condition	Storm	Storm	Storm
Wave direction	Northwest	Northwest	Northwest
Boundary conditions	North, West and South: H_s = 17.4 m, T_p = 19.2 s, Direction = 315°	North, West and South: H_s = 20.5 m, T_p = 18.0 s, Direction = 315°	North, West and South: H_s = 25.3 m, T_p = 18.4 s, Direction = 315°
Wave type conditions	JONSWAP spectrum	JONSWAP spectrum	JONSWAP spectrum
Simulation time (hours)	2	2	2
Computational domain for the Iberian Peninsula (degrees)	$\approx 5 \times 8$ (cross-shore × longshore)	$\approx 5 \times 8$ (cross-shore × longshore)	$\approx 5 \times 8$ (cross-shore × longshore)
Computational domain for the Lima estuary (degrees)	$\approx 0.1816 \times 0.0504$ (cross-shore × longshore)	$\approx 0.1816 \times 0.0504$ (cross-shore × longshore)	$\approx 0.1816 \times 0.0504$ (cross-shore × longshore)
Grid spatial resolution for the Iberian Peninsula (degrees)	dx=dy=0.05	dx=dy=0.05	dx=dy=0.05
Grid spatial resolution for the Lima estuary (degrees)	dx=dy=0.0005	dx=dy=0.0005	dx=dy=0.0005

Results for significant wave heights along the western coast of the Iberian Peninsula and the Lima estuary adjacent coastal domain are presented for the Iberian_HP, Iberian_4.5 and Iberian_8.5

scenarios in Figures 5.9, 5.10 and 5.11, respectively. The bathymetry influence on significant wave heights decrease was also analysed for each scenario by drawing a profile (represented by a dash-dotted line) along the Lima estuary adjacent coastal domain. Figure 5.12 presents the combination of bed level profile with significant wave height results from deep to shallow water at the selected site.
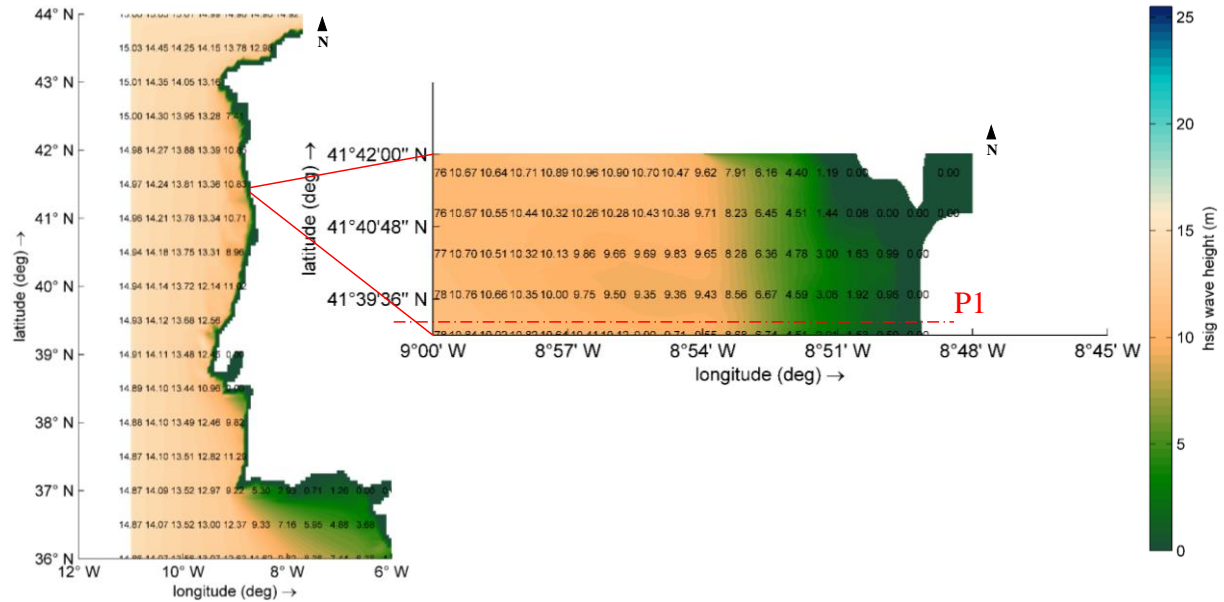
Figure 5.9: Significant wave height results for the Iberian_HP scenario (Iberian Peninsula + Lima estuary).
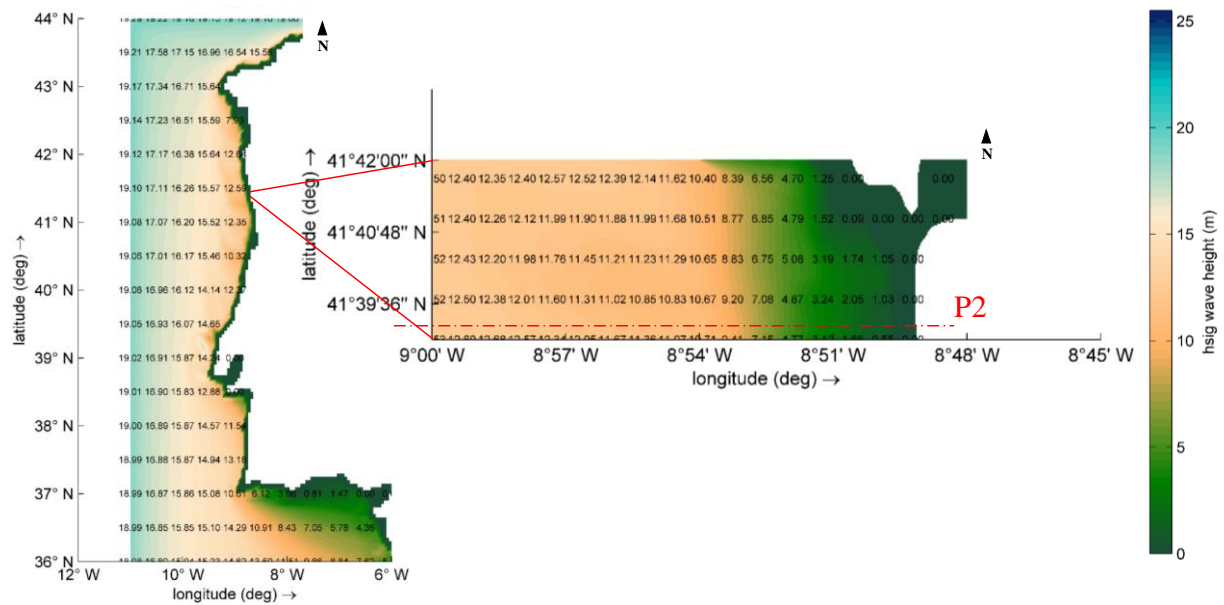
Figure 5.10: Significant wave height results for the Iberian_4.5 scenario (Iberian Peninsula + Lima estuary).
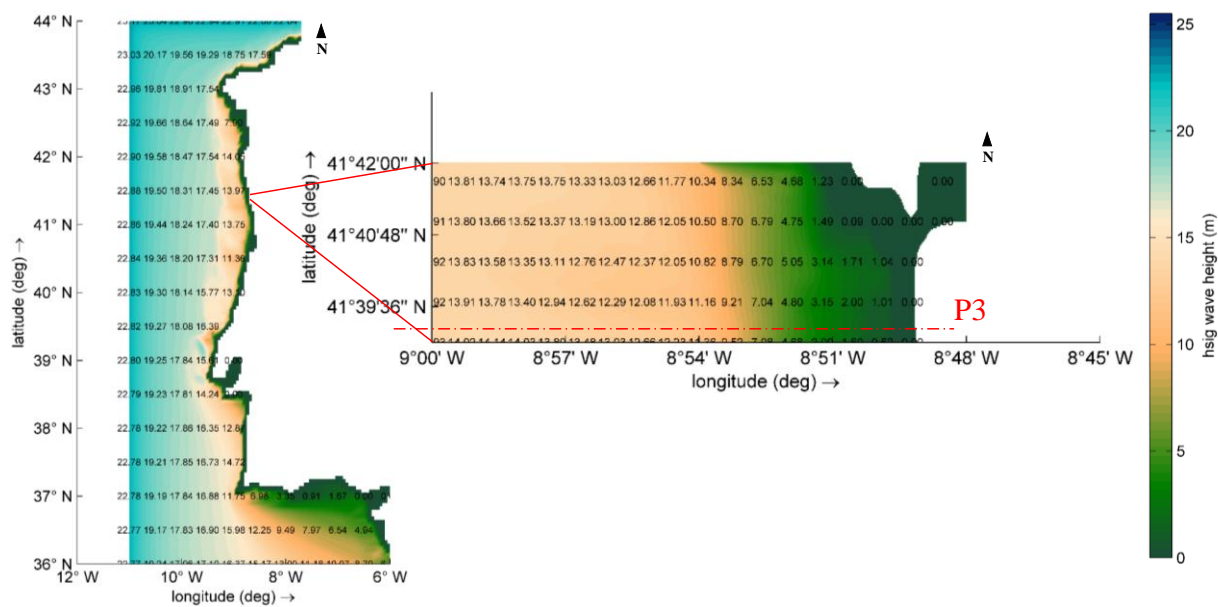
Figure 5.11: Significant wave height results for the Iberian_8.5 scenario (Iberian Peninsula + Lima estuary).
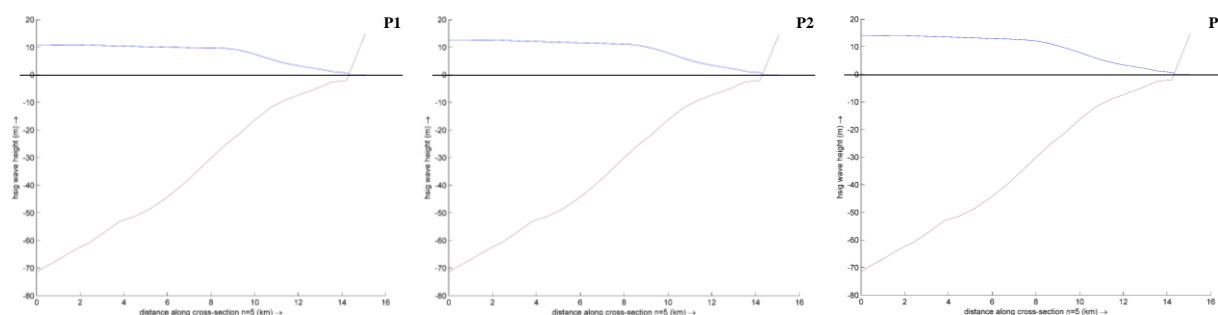
Figure 5.12: Significant wave height variation along the selected profiles (P) for scenarios Iberian_HP (P1); Iberian_4.5 (P2); and Iberian_8.5 (P3).

For the three scenarios presented in Figures 5.9, 5.10 and 5.11, significant wave height results corroborate previous results presented in Chapter 3 as the distribution along the Iberian Peninsula demonstrate that the wave climate tends to be less energetic as the latitude decreases. The significant wave heights decrease is also perceptible as waves reach the coast (smaller depths). Regarding the profile results (Figure 5.12), the significant wave heights have similar behaviours along the cross-section. The significant wave height corresponding to each scenario remains constant until a more abrupt variation of the bed slope (approximately 5 km from the coast for P1 and P2 and 6 km for P3) where the waves tend to break. Also, despite the input values being different for the HP and RCPs scenarios (H_s=17.4 m; H_s=20.5 m; H_s=25.3 m), wave propagation results at 14 km from the coast show that there are no significant discrepancies between them (P1: H_s=10.7 m; P2: H_s=12.4 m; P3: H_s=13.8 m). Near the coast, for the three scenarios results are also very similar (approximately H_s=1.0 m). This

demonstrates that the wave energy dissipation leads to similar significant wave heights near shoreline and for this reason, for future simulations the Iberian_HP scenario results will be used.

5.4 Scenarios for assessment of innovative structures geometry under alongshore drift reversal conditions

As previously mentioned, SWAN and XBeach are the selected software to implement the numerical laboratory to analyse the reversal of alongshore drift. To conduct this analysis, the first step consisted in defining a computational domain with adequate dimensions that could guarantee an extensive useful area without interference from eventual boundary instabilities. Depending on the size of the analysed interventions, the reassessment of the computational domain dimensions is necessary in order to ensure a coastal stretch with considerable dimensions to study the interventions' influence downdrift. These interventions are implemented in form of bed level changes (bathymetric changes without structure) or the implantation of a structure in a specific location in order to attain the reversal of longshore drift, which is achieved based on the general bathymetry, henceforth referred as reference bathymetry (RB). The initial approach of changing the bathymetry is a necessary mean to understand the reversal phenomenon in order to replicate its effect in a form of a structure.

The first computational domain to be tested (RB1) considers the reference bathymetry with the same dimensions as the numerical simulations conducted in Chapter 4 (1670 m × 1870 m). Two other computational domains with 1670 m × 2370 m (RB2) and 1670 m × 3120 m (RB3) are tested according to the dimensions of the interventions tested throughout the scenarios, which are presented in Tables 5.3 to 5.5. The grid spatial resolution is 5 m for all cases, which means the grid sizes are: i) 334 × 374 for RB1; ii) 334 × 474 for RB2; iii) and 334 × 624 for RB3. The selected grid cell size has already been confirmed as adequate for the numerical simulations as aforementioned in Chapter 4.

Recurring to the pre-processing tools and the numerical models environment, new shapes implemented with bathymetric changes and structures are proposed and assessed based on these RBs. In order to obtain an efficient solution at an acceptable cost, the selection criteria for this analysis is a combination of acceptable total volume of the structure with the ability to induce the reversal of longshore drift. The bathymetric changes are characterized by their volumes, whereas the structures are represented detailing their dimensions, slopes, volumes and positions relatively to shoreline. The volumes are calculated using AutoCAD and this allows estimating the necessary volume of armour units and other materials to be included in the structure.

Table 5.3: RB1 scenarios: bathymetric changes and structures.

RB1 (334 × 374)	
Bathymetric Changes (without structure)	**Structures on RB1**
RB1_1	RB1_S1
RB1_2	RB1_S2
RB1_3	RB1_S3
RB1_4	RB1_S4
RB1_5	RB1_S5
RB1_6	RB1_S6
	RB1_S7
	RB1_S8
	RB1_S9
	RB1_S10
	RB1_S11
	RB1_S12
	RB1_S13
	RB1_S14

Table 5.4: RB2 scenario: bathymetric changes.

RB2 (334 × 474)
Bathymetric Changes (without structure)
RB2_1

Table 5.5: RB3 scenarios: bathymetric changes and structures.

RB3 (334 × 624)	
Bathymetric Changes (without structure)	**Structures on RB3**
RB3_1	RB3_S1
RB3_2	RB3_S2
RB3_3	RB3_S3
RB3_4	RB3_S4
RB3_5	RB3_S5
	RB3_S6
	RB3_S7
	RB3_S8
	RB3_S9
	RB3_S10
	RB3_S11
	RB3_S12
	RB3_S13
	RB3_S14

The RBs are characterized by a constant slope of 1:50 (2%) with a maximum offshore depth of -31.4 m and a maximum coastal elevation of +2 m. The elevation +2 m allows a sound analysis of the hydro- and morphodynamics' influence on the beach, since the tidal level is set to 0 m.

In view of the fact that simulations will start the wave propagation 1670 m off the coast ($\approx$ 1.7 km) at a depth of -31.4 m, the Iberian_HP scenario results have to be obtained in order to determine the most adequate input wave conditions at that location. Figure 5.13 shows the two possible approaches for choosing the H_s input values for the models: i) H_s = 3.5 m if the decision is to select the distance criterion (1.7 km) to the beach (red dotted line); ii) H_s = 10.0 m if the choice is the depth criterion (-31.4 m) (black dotted line).

Since the previous numerical simulations presented in Chapter 4 for a storm condition considered a significant wave height of 4 m, for the following simulations it has been decided to select the first approach and to approximate the H_s value to 4 m (instead of 3.5 m) to match the storm simulation conditions already tested. For the sake of keeping the same wave conditions for T_p presented in Chapter 4, the adopted T_p value is also 15 s. Therefore, the storm wave scenario defined by the JONSWAP spectrum with H_s = 4 m and T_p = 15 s is applied to all structures with incoming waves from Northwest (315°) without any tidal influence (tidal level = 0 m relatively to the MSL). The total simulation time is two hours for the hydrodynamic analysis and the numerical model outputs obtained by the SWAN model are the initial bed level, significant wave heights and their mean directions. As for boundary conditions, the storm waves are defined for north, west and south boundaries for all scenarios. Table 5.6 summarises the SWAN model conditions selected for the reference bathymetry and all scenarios derived from them.

Regarding XBeach morphodynamics, the simulations are conducted for proposals with the best hydrodynamic performances. Numerical conditions are detailed in Section 5.4.8.
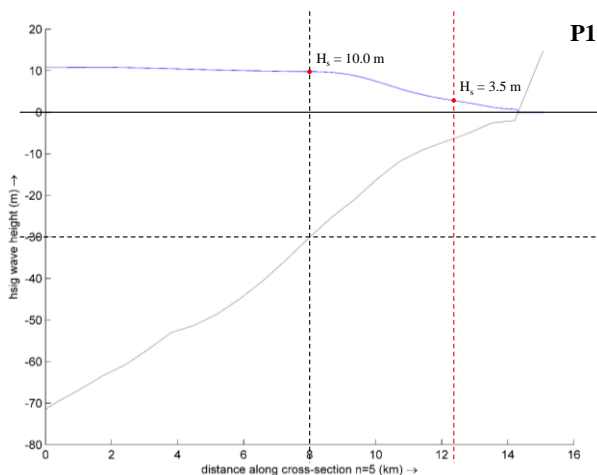
Figure 5.13: Approaches for selecting H_s storm values for the numerical simulations (Iberian_HP scenario).

Table 5.6: SWAN numerical model conditions for the RB1, RB2 and RB3 scenarios.

SWAN Numerical Model Conditions			
Parameters	**RB1 (all scenarios)**	**RB2 (all scenarios)**	**RB3 (all scenarios)**
Tidal level (m)	0	0	0
Wave condition	Storm	Storm	Storm
Wave direction	Northwest	Northwest	Northwest
Boundary conditions	North, West and South: H_s = 4.0 m, T_p = 15.0 s, Direction = 315°	North, West and South: H_s = 4.0 m, T_p = 15.0 s, Direction = 315°	North, West and South: H_s = 4.0 m, T_p = 15.0 s, Direction = 315°
Wave type conditions	JONSWAP spectrum	JONSWAP spectrum	JONSWAP spectrum
Simulation time (hours)	2	2	2
Computational domain (m)	1670 × 1870 (cross-shore × longshore)	1670 × 2370 (cross-shore × longshore)	1670 × 3120 (cross-shore × longshore)
Grid spatial resolution (m)	dx=dy=5	dx=dy=5	dx=dy=5
Computational grid	334 × 374	334 × 474	334 × 624

The following Sections present the different tested scenarios. Firstly, an introduction for each scenario is presented with domain/geometry details, and secondly, the hydrodynamics results are analysed based on the effect of the bathymetric changes/structure on significant wave heights and on the reversal of longitudinal drift. In order to facilitate the results analysis, some scenarios are grouped based on bathymetric changes/structure similarities. The contour lines are depicted in all results.

5.4.1 Reference bathymetry: RB1, RB2 and RB3

The reference bathymetries presented in Figure 5.14 indicate the maximum offshore depth of -31.4 m and maximum coastal elevation of +2 m for RB1 (Figure 5.14a), RB2 (Figure 5.14b), and RB3 (Figure 5.14c). As aforementioned, the domain dimensions are variable but all bathymetries have a constant slope of 2%. Each RB serves as basis to the bathymetric changes (scenarios without structure) and the implantation of structures with different geometries and dimensions. In addition, these domains are a reference for the volumes estimation, since bed level variations are calculated based on the RBs by subtracting the bed level of each scenario from the reference domain.
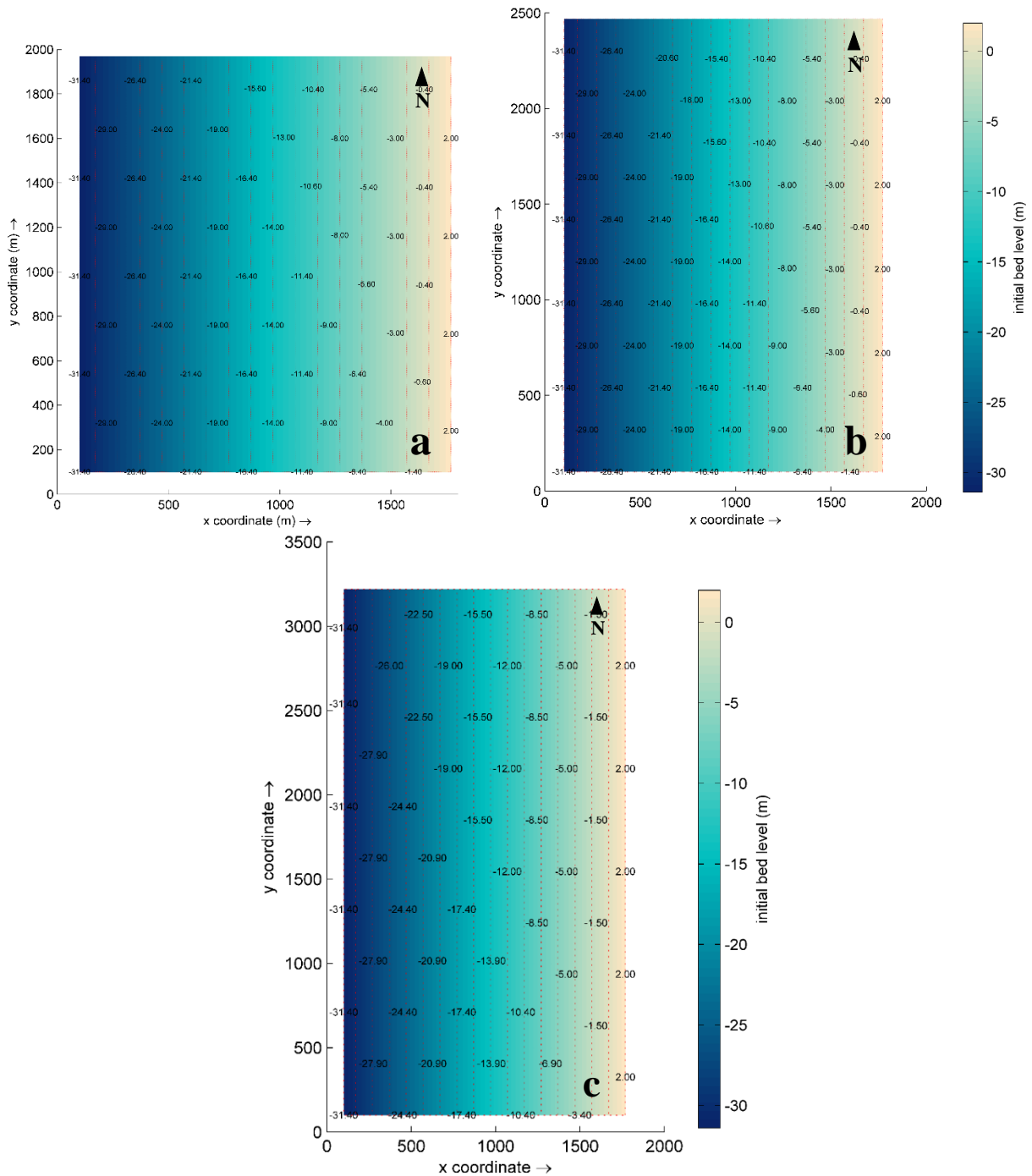
Figure 5.14: Bed level values for scenarios: a) RB1; b) RB2; and c) RB3.

5.4.1.1 Hydrodynamics. Results and discussion

Results for significant wave height and their mean directions (represented by vectors) in Figure 5.15 for each RB demonstrate an extended wave shoaling (H_s = 4.5 m) near the north boundary that scatters as the domain is longer due to the consideration of waves entering through this boundary with the same height. It is important to note that this might compromise hydrodynamics results for subsequent

scenarios with bathymetric changes and/or structures. Despite this, SWAN is selected to evaluate the significant wave height mean direction vectors, which is crucial for the analysis of longshore drift reversal. RB1 (Figure 5.15a), RB2 (Figure 5.15b) and RB3 (Figure 5.15c) significant wave heights tend to decrease gradually from position 1400 m onwards until reaching a significant wave height of 0 m, due to wave breaking.
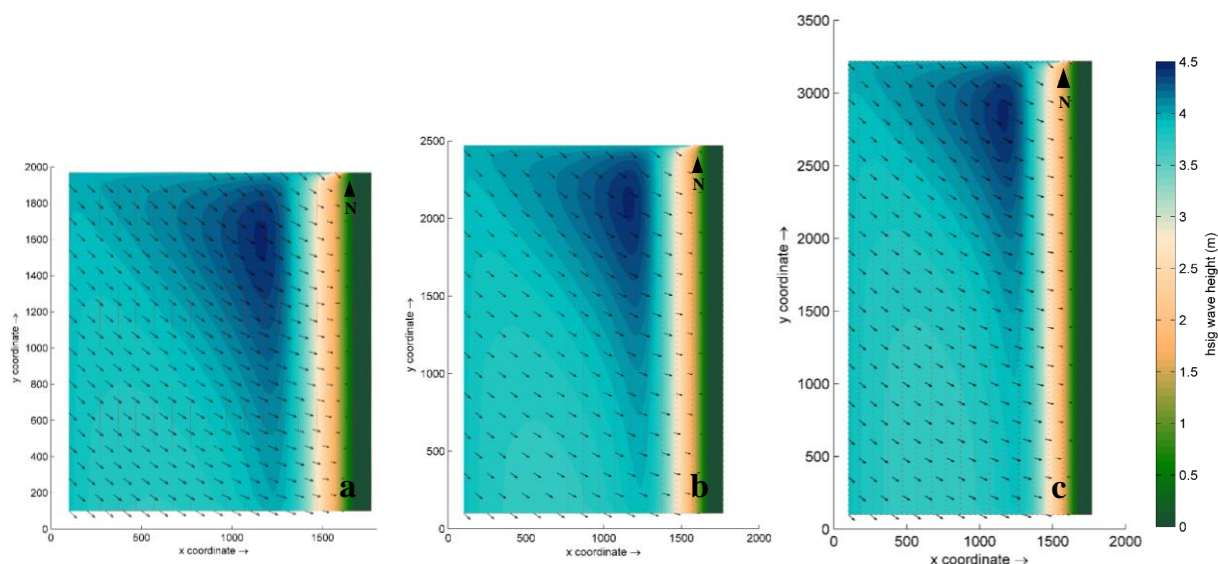
Figure 5.15: Hs for scenarios: a) RB1; b) RB2; and c) RB3.

5.4.2 RB1 bathymetric changes

The left column presented in Table 5.3 corresponds to the scenarios of bathymetric changes without structure. In the following Sections, several scenarios are presented with the purpose of assessing the influence of bathymetry on the reversal of longitudinal drift in order to understand the phenomenon and to serve as basis to define a favourable structure geometry. This reversal is presented in the results section through the vectors of significant wave height and the analysis is conducted in three groups based on bathymetric changes similarities: i) RB1_1, RB1_2 and RB1_3; ii) RB1_4 and RB1_5; and iii) RB1_6. The first two groups consider seabed changes bellow MSL (submerged) while the third group considers seabed changes above MSL (emerged).

5.4.2.1 RB1_1, RB1_2 and RB1_3

The first group intends to characterize the study of significant wave height directions rotation in order to create a shape with the configuration of curved contour lines. RB1_1 and RB1_2 (left panel in Figures 5.16a and 5.16b) indicate the slopes were not altered and that the contour lines have constant curvatures of 48° and 75°, respectively. In Figure 5.16c (left panel), the RB1_3 curvatures are variable

(varying from 25° to 75° from middle to extremities) with a steep slope in the middle (6%) of the domain, and a more subtle slope in the adjacent areas (1.6%). This allows understanding the impact of this bed form on the reversal of longitudinal drift. The right panel in Figure 5.16 indicates the bed level variation to add to the RB in order to induce the reversal of longitudinal drift along the domain. The most significant bathymetry variations are in RB1_2, because requires more landfill volumes. The necessary volumes are presented in Table 5.7.
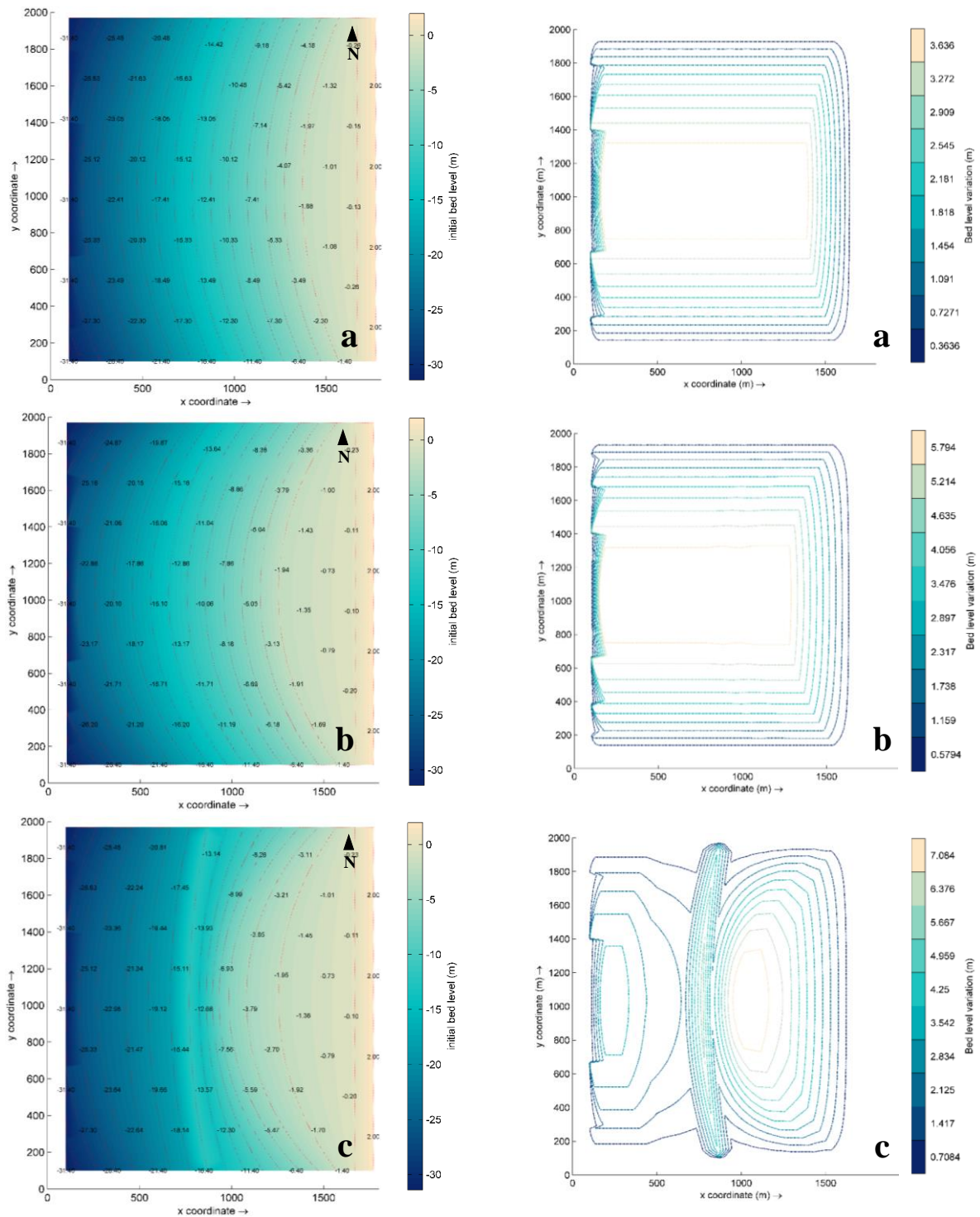
Figure 5.16: Bed level values (left) and variations (right) for scenarios: a) RB1_1; b) RB1_2; and c) RB1_3.

Table 5.7: Volumes for bathymetric changes: RB1_1, RB1_2 and RB1_3.

Characteristics	RB1_1	RB1_2	RB1_3
Volume (m³)	6 512 480.78	10 115 419.82	7 362 629.57

5.4.2.2 RB1_4 and RB1_5

The second group of RB1 bathymetric changes aims to study the effect of a bell-shaped curve (inspired by CERC, 1984) on the reversal of longitudinal drift. In Figure 5.17a (left panel) the RB1_4 slope exposed to wave climate action is 4% along the ledge and changes in bathymetry cover practically the entire domain. In Figure 5.17b (left panel), the intervention is less considerable as bathymetry changes only start in the middle of the RB1_5 domain. In this case, the slope is steeper (14%) than the RB1_4 at the same location. These scenarios allow understanding the impact of the proposed bell-shape curve and their slopes exposed to wave climate action on the reversal of longitudinal drift. The right panel in Figure 5.17 indicates the bed level variation to add to the RB. The most significant bathymetry variations are in RB1_4, because requires more landfill and excavation volumes (Table 5.8).
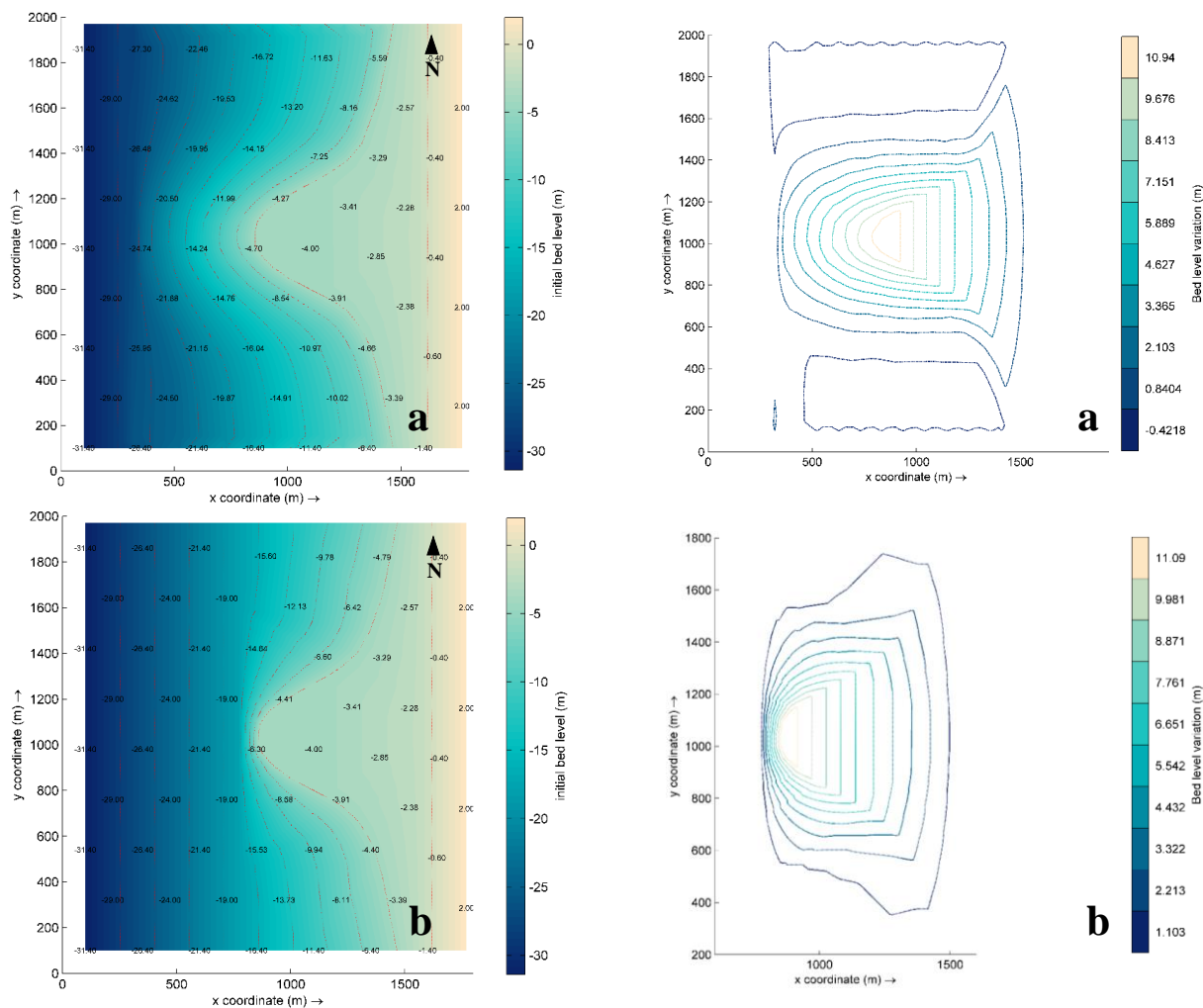
Figure 5.17: Bed level values (left) and variations (right) for scenarios: a) RB1_4; and b) RB1_5.

Table 5.8: Volumes for bathymetric changes: RB1_4 and RB1_5.

Characteristics	RB1_4	RB1_5
Volume (m³)	4 473 099.65 (landfill) -284704.3851 (excavation)	2 759 007.71

5.4.2.3 RB1_6

The RB1_6 seeks to study the effect of an emerged shape on the reversal of longitudinal drift. Figure 5.18 (left panel) depicts that the bathymetry changes cover much of the domain and that the longer slope exposed to wave climate action along the ledge (from 370 m and 560 m) is 11.8% and 1.9% between the longer slope and the -1.5 m platform (from 560 m and 720 m). The elevated crest of the bathymetric change is +1.5 m relatively to MSL. Figure 5.18 (right panel) also indicates the bed level variation to add to the RB. The necessary volumes are presented in Table 5.9. This scenario presents the most significant bed level variation volume of all RB1 bathymetric changes.
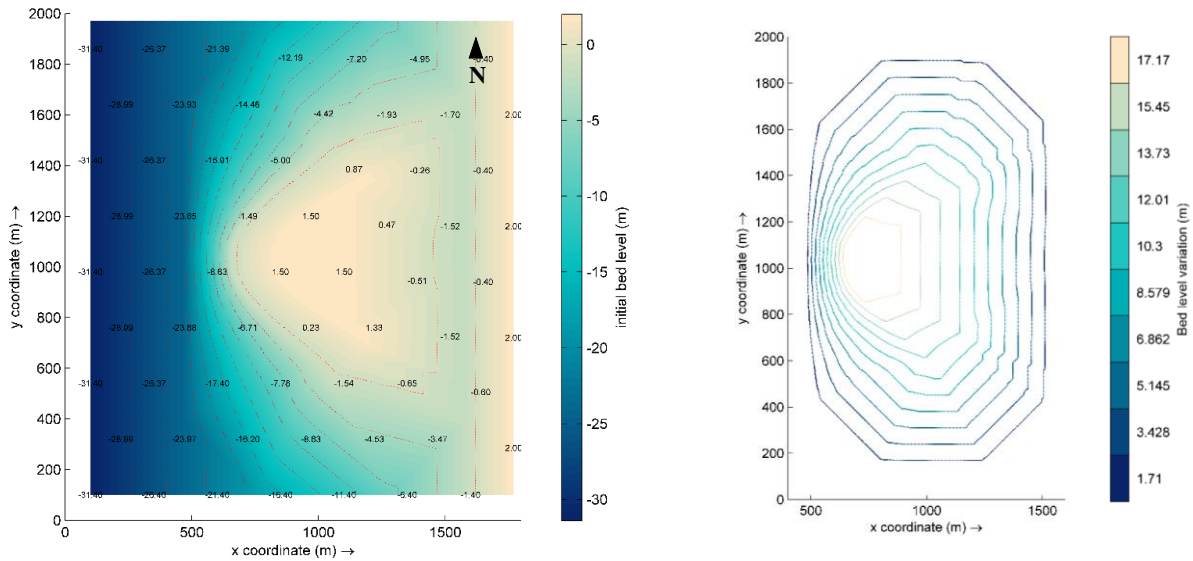
Figure 5.18: Bed level values (left) and variations (right) for scenario RB1_6.

Table 5.9: Volume for bathymetric changes: RB1_6.

Characteristics	RB1_6
Volume (m³)	11 615 447.12

5.4.2.4 Hydrodynamics. Results and discussion

In this section, hydrodynamics results for the RB1 bathymetric changes scenarios (RB1_1, RB1_2 and RB1_3; RB1_4 and RB1_5; and RB1_6) are presented and analysed based on the main outcomes and differences between them.

Figures 5.19, 5.20 and 5.21 present the decrease of significant wave heights from offshore to shoreline (wave energy dissipation) and their mean directions based on the bed level changes (bathymetric changes) created for each scenario. The wave climate conditions are identical to all scenarios. Figures 5.19a, 5.19b and 5.19c present results for RB1_1, RB1_2 and RB1_3, respectively. Figures 5.20a and 5.20b depict results for RB1_4 and RB1_5, respectively. Figure 5.21 presents results for RB1_6.

In Figure 5.19, the different curvatures of the contour lines that were tested demonstrate a greater reversal of the longitudinal drift in RB1_2 and RB1_3 (Figures 5.19b and 5.19c), which indicates that the greater the curvature, the more evident is the effect of the reversal. This effect is more apparent in RB1_3, since the significant wave height mean direction vectors present a greater rotation at a position farther away from the shoreline, compared to the other two scenarios. This is justified by the sudden change in slopes between positions 800 m and 900 m and the curvature of the bed level.

Regarding the results of significant wave heights, a greater wave shoaling (H_s = 4.5 m) is visible in RB1_1 (Figure 5.19a) and RB1_2, while in RB1_3 this effect is less extensive and more located near the north boundary, as already mentioned. Regarding energy dissipation, the waves start breaking at approximately the same position in the three scenarios (RB1_1: 1200 m, RB1_2: 1100 m and RB1_3: 1050 m) and wave heights vary between 4.5 m and 0 m.
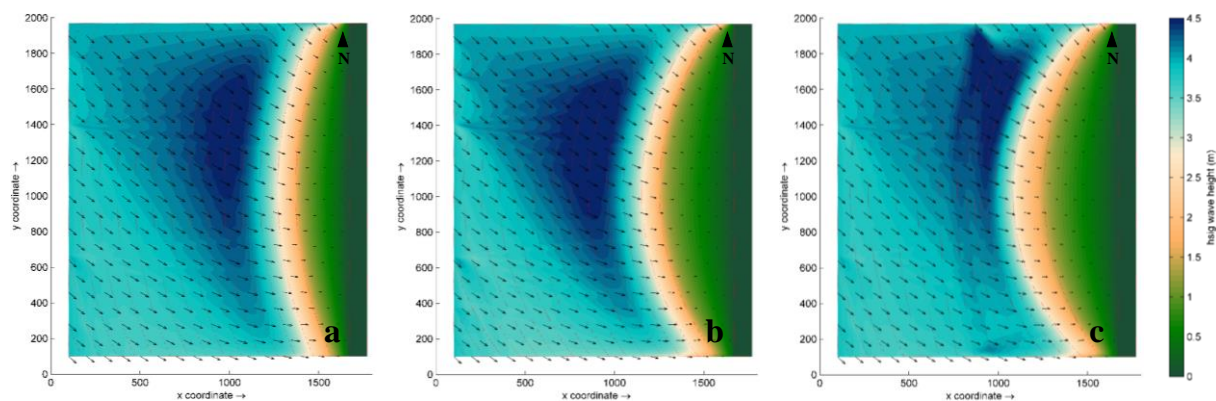
Figure 5.19: H_s for scenarios: a) RB1_1; b) RB1_2; and c) RB1_3.

In the set of scenarios RB1_4 and RB1_5 (Figures 5.20a and 5.20b), the waves start breaking in similar positions in both cases (RB1_4: 860 m and RB1_5: 880 m). The reversal of longitudinal drift reflected by the rotation effect of significant wave height mean direction vectors is more limited in RB1_5 between positions 800 m and 870 m near the ledge, due to the sudden variation of the bed level slope. This sudden and exaggerated slope transition reveals itself in a less extensive area of wave shoaling near the ledge, due to the rapid wave breaking. Conversely, in the RB1_4 scenario as the slope is relatively constant along the ledge, the wave shoaling effect is more extensive. Contrary to

RB1_3 scenario, in RB1_5 the vectors rotation effect downdrift is slightly less noticeable than in RB1_4, which indicates that slope variations should not be so abrupt. The significant wave heights decreasing is clearly presented in both scenarios.
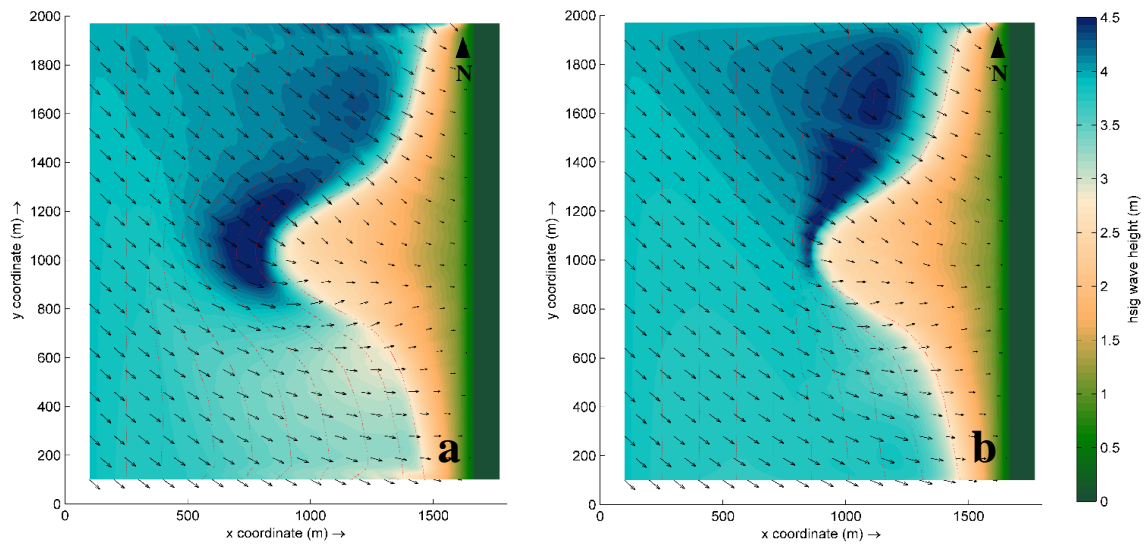
Figure 5.20: H_s for scenarios: a) RB1_4; and b) RB1_5.

In scenario RB1_6 (Figure 5.21), a greater impact of the emerged shape elevation on the decreasing of significant wave heights is visible, as it would be expected.
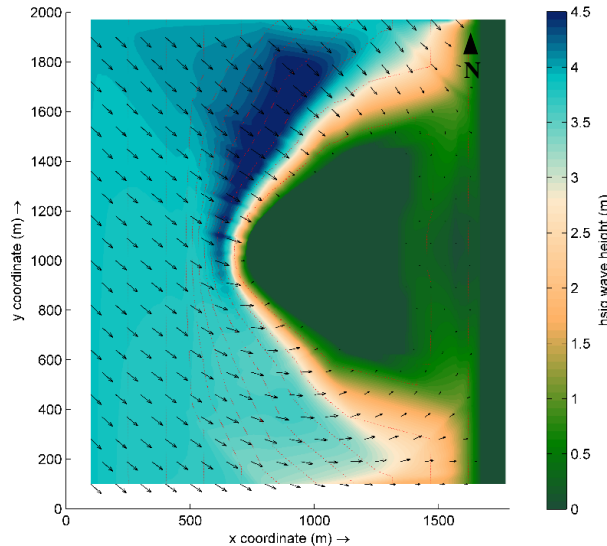
Figure 5.21: H_s for scenario RB1_6.

The more rounded shape of this bathymetric change, compared to the bell-shaped curves (RB1_4 and RB1_5), points to a greater reversal of longitudinal drift by the greater rotation of the significant wave height mean direction vectors downdrift. The waves start breaking at the 650 m position due to the slopes variation, where significant wave heights of 4.5 m start decreasing until the 730 m position near

the ledge zone where waves reach null values due to the emerged shape. The mean direction of significant wave height vectors from positions 1400 m to 1600 m indicate the waves' transmission due to the waves surrounding the emerged shape (diffraction).

The RB1_6 bathymetric change presents good results for the reversal of longitudinal drift as well as for the waves energy dissipation; however, since one of the objectives of this Thesis is to minimize the environmental visual impact of the proposed solutions, the following scenarios will try to reconcile these two concerns, as submerged solutions are more appealing. Due to the extensive bathymetric changes, it is necessary to enlarge the domain in order to analyse the results downdrift of the intervened area.

5.4.3 RB1 structures

The right column presented in Table 5.3 indicates the scenarios with structures. In the following Sections, several structures geometries are tested based on the results from the previous bathymetric changes in order to assess their influence on the reversal of longitudinal drift and on the decreasing of significant wave heights. The domain extension is also analysed in terms of requirements for the downdrift analysis. The reversal of longitudinal drift is presented in the results section through the vectors of significant wave height and the analysis is conducted in four groups: i) RB1_S1, RB1_S2 and RB1_S3; ii) RB1_S4, RB1_S6, RB1_S8, RB1_S10 and RB1_S12; iii) RB1_S5, RB1_S7, RB1_S9, RB1_S11 and RB1_S13; and iv) RB1_S14. The scenarios are grouped based on the structures similarities. Each structure is placed in the RB1, which is characterized by a 2% constant slope.

The first group presents three different tapered structures similar to the MFAR geometry, while the second presents a semi-circular geometry with a variable crest elevation and the third group features the same geometries presented in the second group but with a fixed crest level at -1.5 m relatively to MSL. The fourth group only presents a scenario for an ellipse shaped structure with a variable crest elevation.

5.4.3.1 RB1_S1, RB1_S2 and RB1_S3

The first three structures geometries are represented in Figure 5.22. The left panel presents the initial bed level along the domain, while the right panel depicts the initial bed level variations between the structure and the RB1 (without any structure). Out of the three geometries, RB1_S1 (Figure 5.22a) is the least tapered and the RB1_S3 (Figure 5.22c) the most one. All structures are submerged with a crest level at -1.5 m relatively to MSL and a constant slope of 1:10 (based on the MFAR geometry).

RB1_S1 is the closest to shoreline (310 m), while RB1_S2 (Figure 5.22b) and RB1_S3 are the farthest (340 m). Regarding the volumes, RB1_S1 is the greatest (945K m³) and RB1_S3 the smallest out of the three (589K m³).
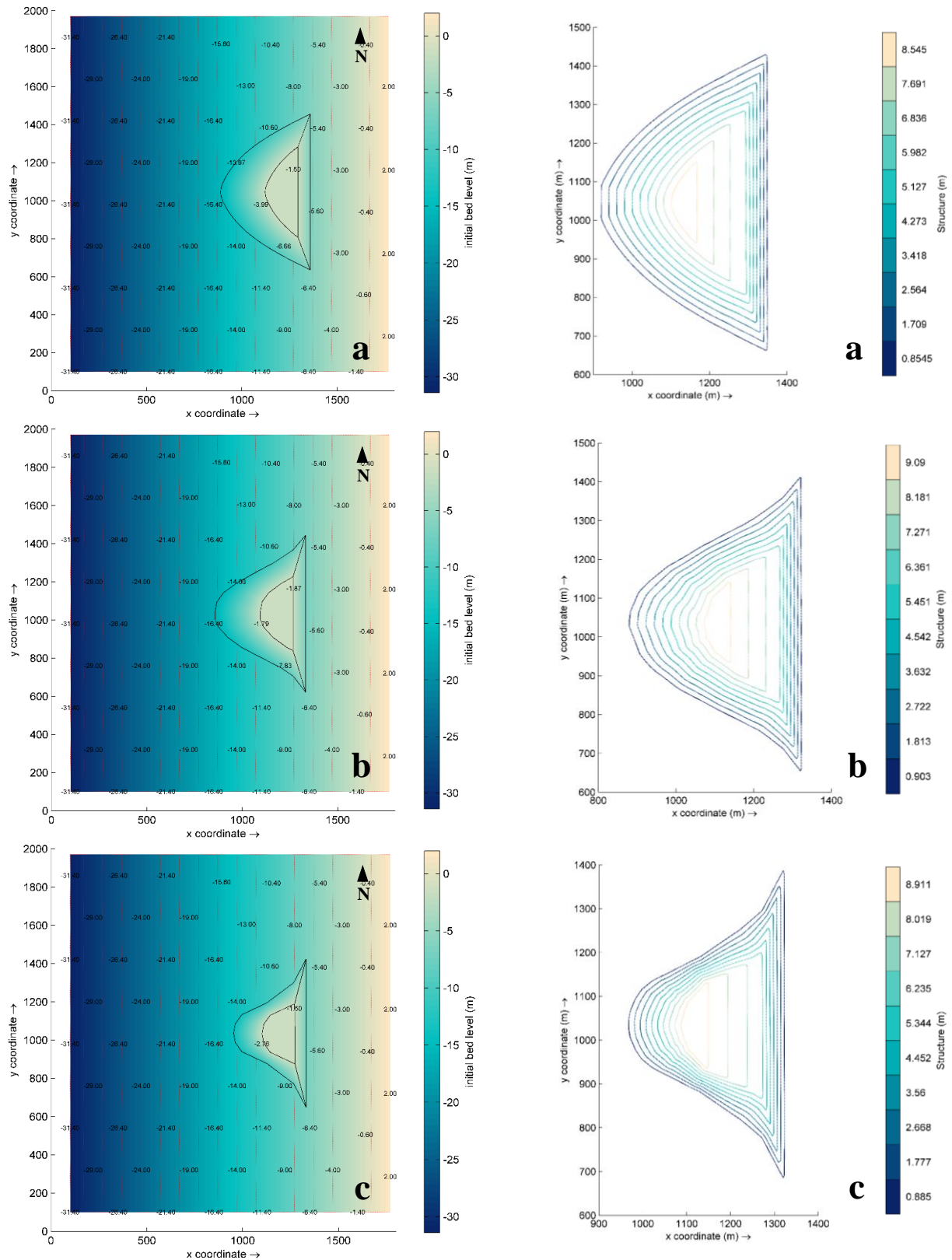
Figure 5.22: Bed level values (left) and variations (right) for scenarios: a) RB1_S1; b) RB1_S2; and c) RB1_S3.

Figure 5.23 depicts the geometrical schematization of each structure where inward stands for coastal side and outward stands for ocean side. The structures characteristics are summarized in Table 5.10.
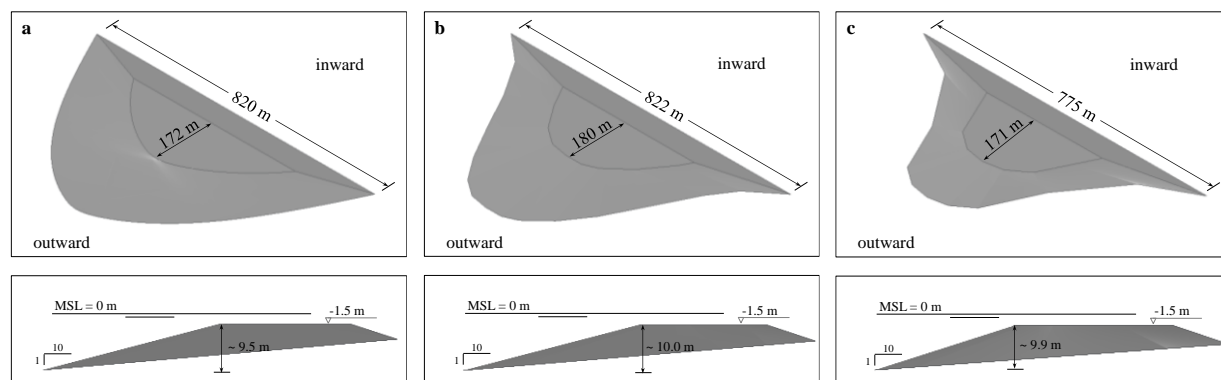
Figure 5.23: Geometrical schematization for: a) RB1_S1; b) RB1_S2; and c) RB1_S3.

Table 5.10: Structures characteristics for RB1_S1, RB1_S2 and RB1_S3.

Characteristics	RB1_S1	RB1_S2	RB1_S3
Length (m)	820.0	822.29	774.92
Width (m)	171.76	179.50	170.92
Slope	1:10	1:10	1:10
Max. height (m)	9.44	10.0	9.88
Crest level (m)	-1.5	-1.5	-1.5
Distance to shoreline (m)	310.0	340.0	340.0
Volume (m³)	945 030.90	881 239.40	588 986.83

5.4.3.2 RB1_S4, RB1_S6, RB1_S8, RB1_S10 and RB1_S12

The second group of scenarios presents a semi-circular geometry with a variable crest elevation, i.e., with a leaning crest. The structures presented in Figure 5.24 have similar geometries only with altered orientations relatively to shoreline. RB1_S4 (Figure 5.24a) and RB1_S6 (Figure 5.24b) are oriented 48° and 0° relatively to shoreline. RB1_S8 (Figure 5.24c), RB1_S10 (Figure 5.24d) and RB1_S12 (Figure 5.24e) have their orientations performed by rotating RB1_S4 90°.
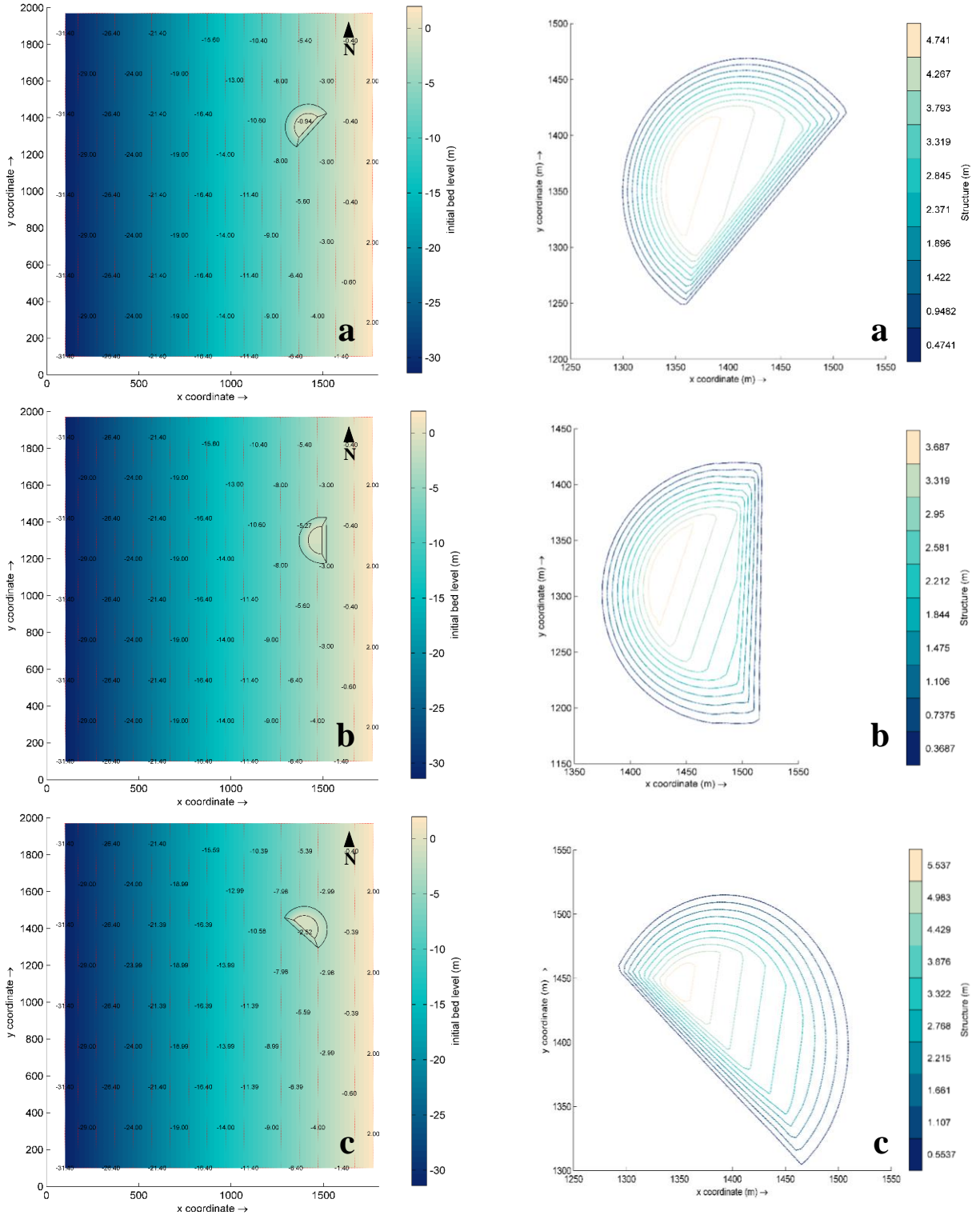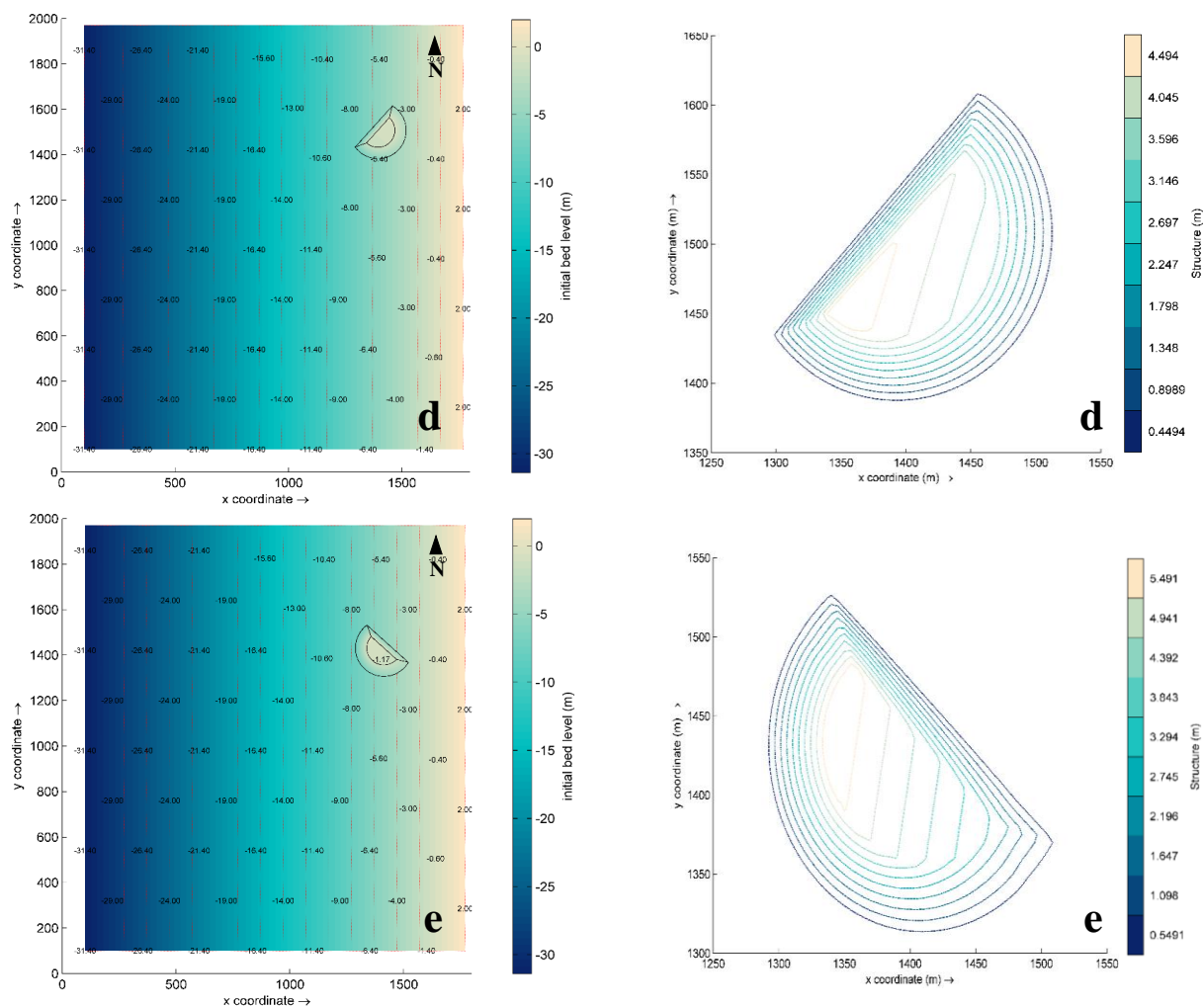
Figure 5.24: Bed level values (left) and variations (right) for scenarios: a) RB1_S4; b) RB1_S6; c) RB1_S8; d) RB1_S10; and e) RB1_S12.

The left panel presents the initial bed level along the domain, while the right panel depicts the initial bed level variations between the structure and the RB1 (without any structure). All structures have a constant slope of 1:10 and the north extremity of the crest level is at -0.5 m and the south extremity at -1.5 m for all scenarios (relatively to MSL). Their positions relatively to shoreline are approximately the same (250 m). Regarding the volumes, RB1_S12 is the greatest (77K m³) and RB1_S6 the smallest out of the five structures (54K m³). All summarized characteristics for each structure are detailed in Figure 5.25 and Table 5.11.
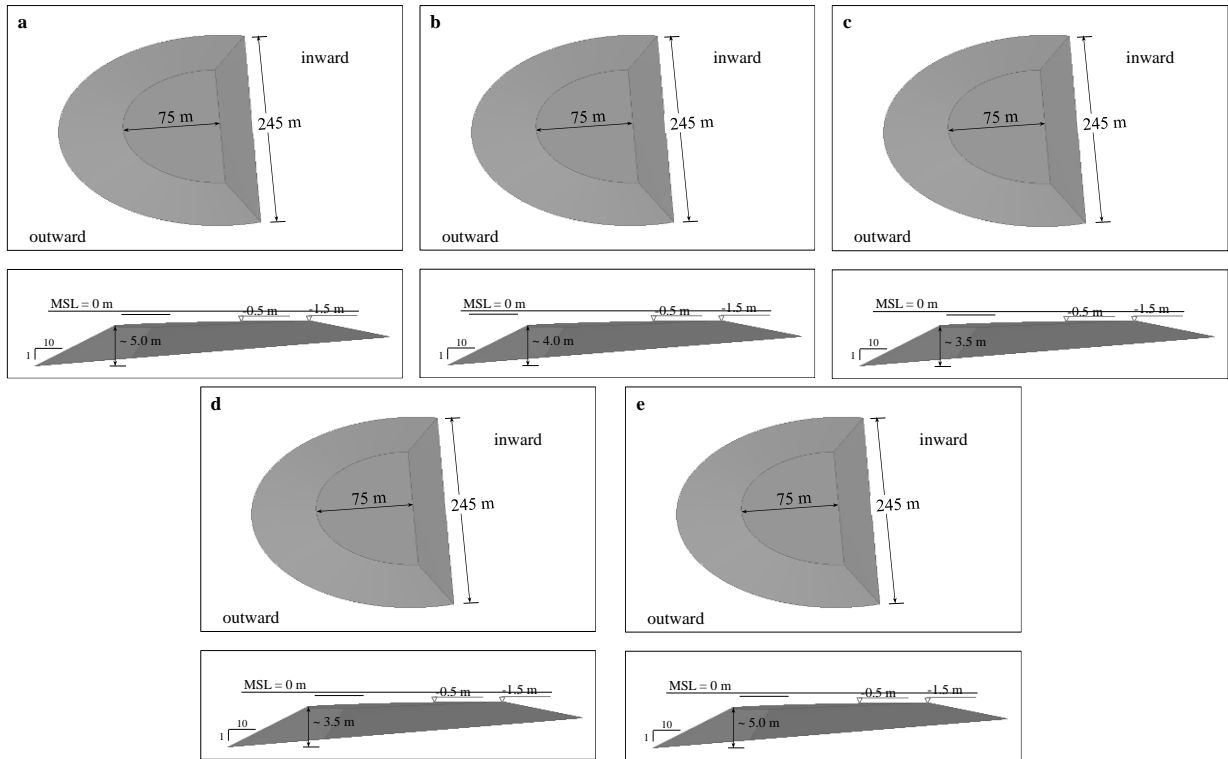
Figure 5.25: Geometrical schematization for: a) RB1_S4; b) RB1_S6; c) RB1_S8; d) RB1_S10; and e) RB1_S12.

Table 5.11: Structures characteristics for RB1_S4, RB1_S6, RB1_S8, RB1_S10 and RB1_S12.

Characteristics	RB1_S4	RB1_S6	RB1_S8	RB1_S10	RB1_S12
Length (m)	244.95	244.95	244.95	244.95	244.95
Width (m)	75.0	75.0	75.0	75.0	75.0
Slope	1:10	1:10	1:10	1:10	1:10
Max. height (m)	5.0	4.0	3.5	3.5	5.0
Crest level (m)	-0.5 (North); -1.5 (South)	-0.5 (North); -1.5 (South)	-0.5 (North); -1.5 (South)	-0.5 (North); -1.5 (South)	-0.5 (North); -1.5 (South)
Distance to shoreline (m)	250.0	250.0	250.0	250.0	250.0
Volume (m³)	76 760.55	53 579.18	67 748.89	68 203.05	77 449.04

5.4.3.3 RB1_S5, RB1_S7, RB1_S9, RB1_S11 and RB1_S13

The third group of scenarios assembles the same semi-circular geometry presented in Section 5.4.3.2 but with a fixed crest level at -1.5 m (MSL). All structures presented in Figure 5.26 have similar geometries with the same orientations as presented before, the same constant slopes of 1:10 and the same positions relatively to shoreline (250 m). The left panel presents the initial bed level along the domain, while the right panel depicts the initial bed level variations between the structure and the RB1 (without any structure). Figures 5.26a, 5.26b, 5.26c, 5.26d and 5.26e depict the RB1_S5, RB1_S7, RB1_S9, RB1_S11 and RB1_S13, respectively.
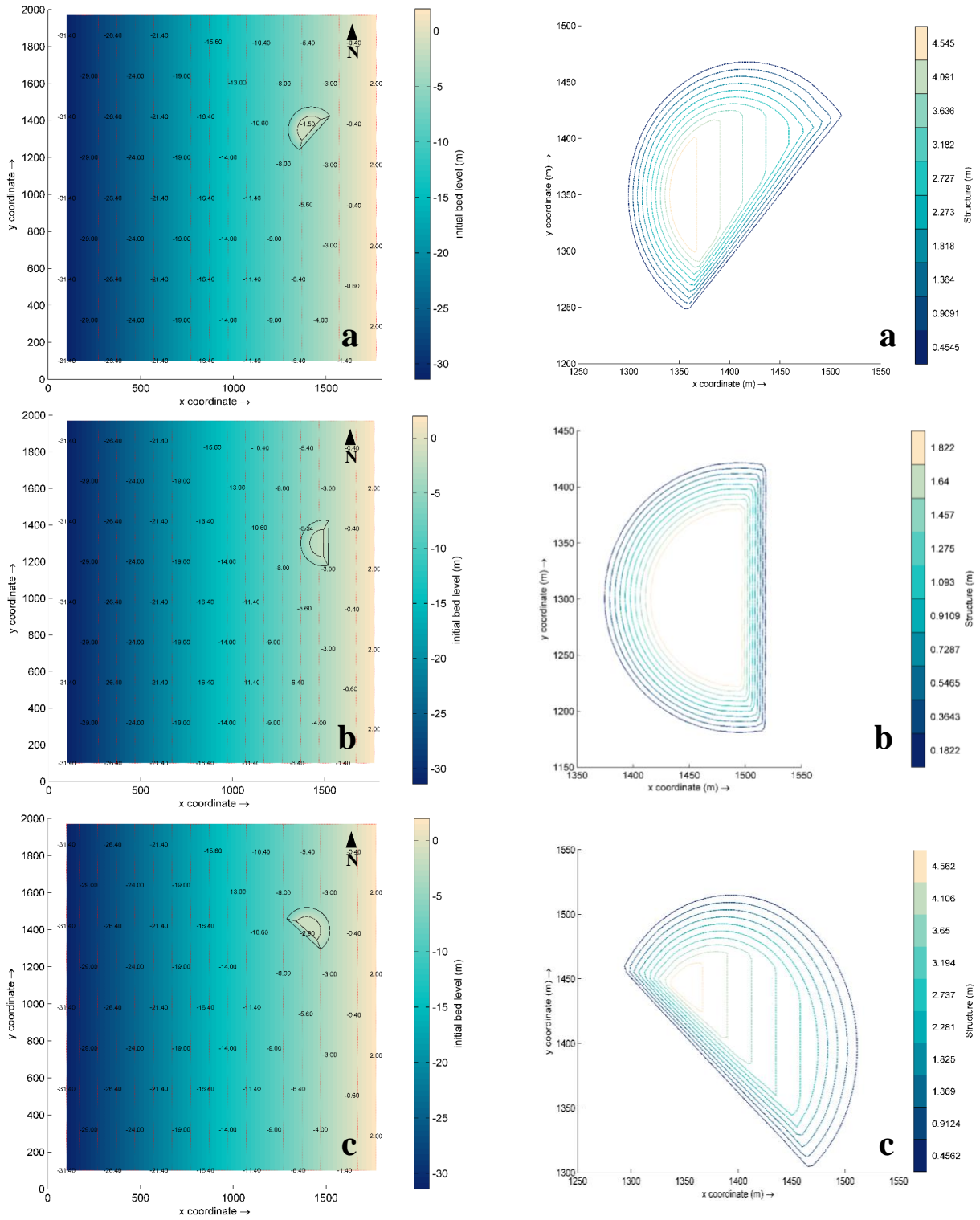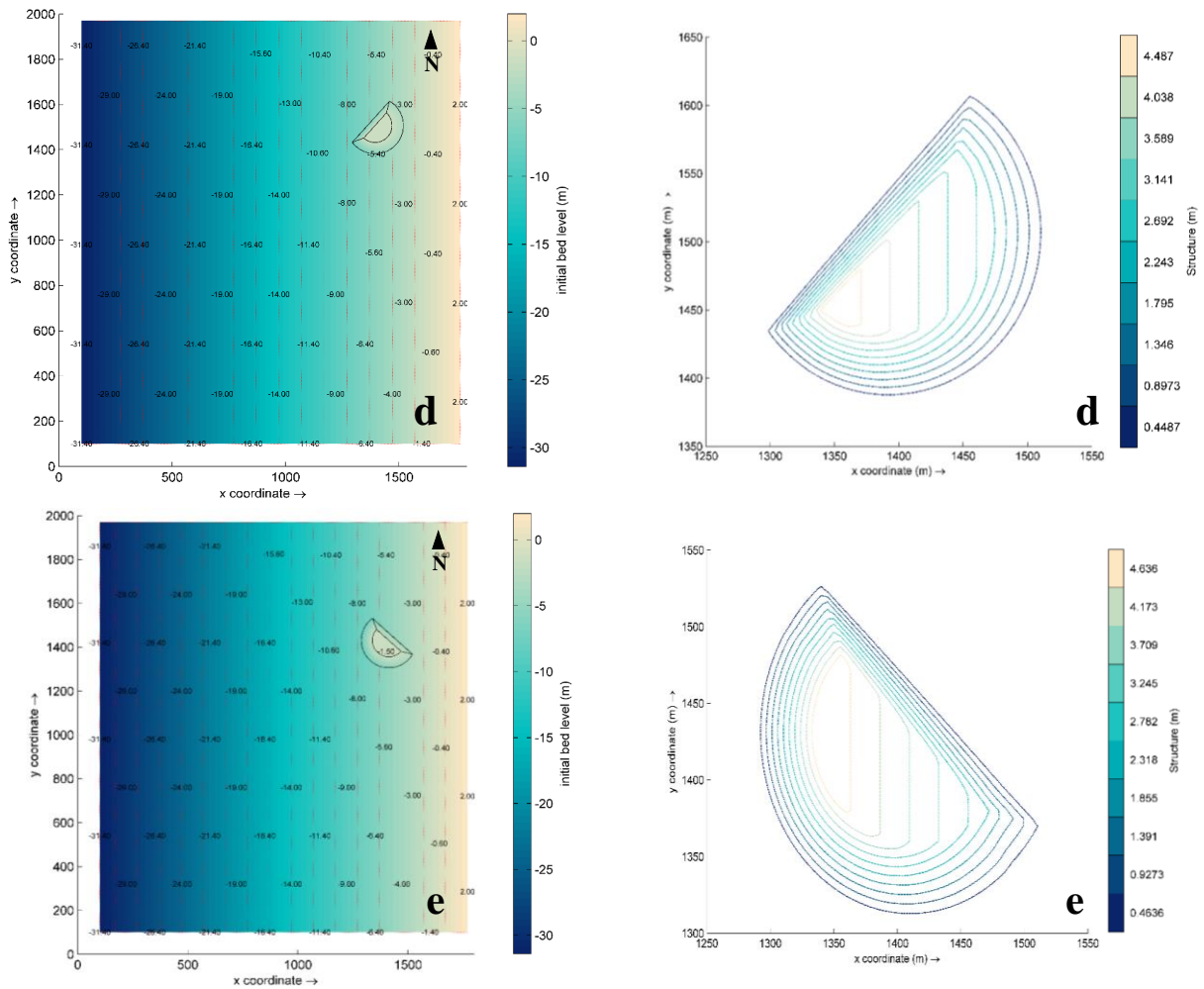
Figure 5.26: Bed level values (left) and variations (right) for scenarios: a) RB1_S5; b) RB1_S7; c) RB1_S9; d) RB1_S11; and e) RB1_S13.

Regarding the volumes, RB1_S13 is the greatest (69K m³) and RB1_S7 the smallest out of the five structures (34K m³). All summarized characteristics for each structure are detailed in Figure 5.27 and Table 5.12.
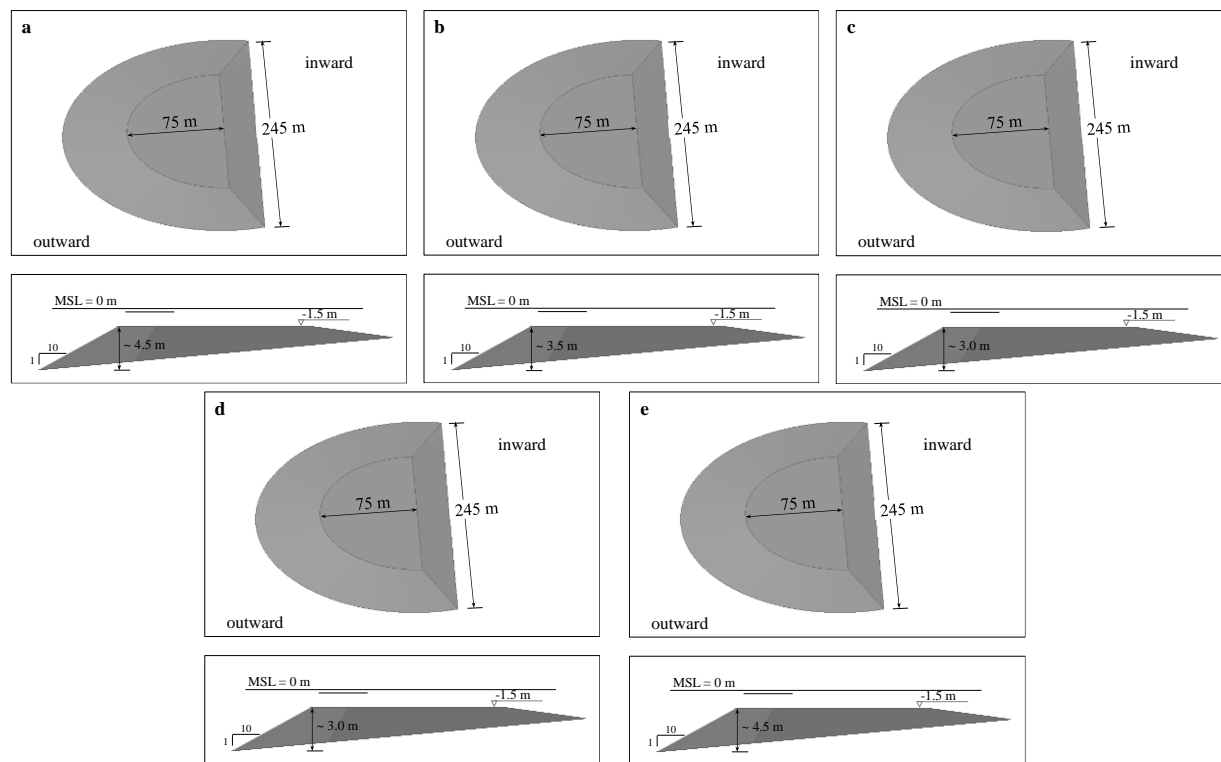
Figure 5.27: Geometrical schematization for: a) RB1_S5; b) RB1_S7; c) RB1_S9; d) RB1_S11; and e) RB1_S13.

Table 5.12: Structures characteristics for RB1_S5, RB1_S7, RB1_S9, RB1_S11 and RB1_S13.

Characteristics	RB1_S5	RB1_S7	RB1_S9	RB1_S11	RB1_S13
Length (m)	244.95	244.95	244.95	244.95	244.95
Width (m)	75.0	75.0	75.0	75.0	75.0
Slope	1:10	1:10	1:10	1:10	1:10
Max. height (m)	4.5	3.5	3.0	3.0	4.5
Crest level (m)	-1.5	-1.5	-1.5	-1.5	-1.5
Distance to shoreline (m)	250.0	250.0	250.0	250.0	250.0
Volume (m³)	67 742.55	33 819.47	59 291.83	58 944.05	69 371.27

5.4.3.4 RB1_S14

Lastly, Figure 5.28 (RB1_S14) presents an ellipse geometry with a variable crest elevation ranging from -1.4 m (North) to -3.8 m (South). Relatively to shoreline, the structure orientation is the same as the RB1_S4 and RB1_S5 (48°) and has a constant slope of 1:10. The structure is located 390 m off the shoreline. In Figure 5.28, the left panel presents the initial bed level along the domain, while the right panel depicts the initial bed level variations between the structure and the RB1 (without any structure). Regarding the volume, RB1_S14 has approximately 87K m³. All summarized characteristics for this structure is detailed in Figure 5.29 and Table 5.13.
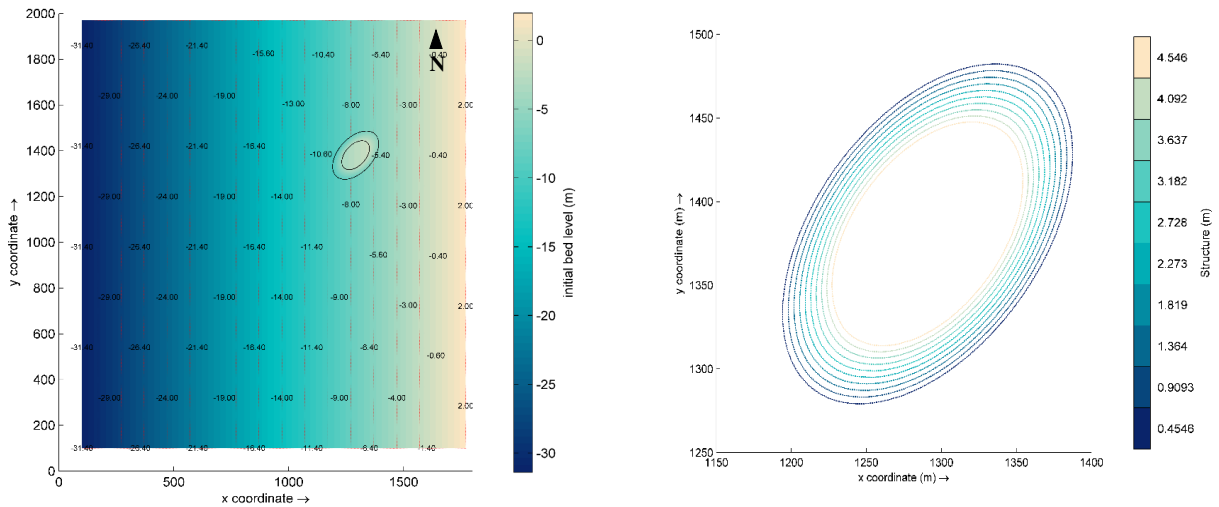
Figure 5.28: Bed level values (left) and variations (right) for scenario RB1_14.
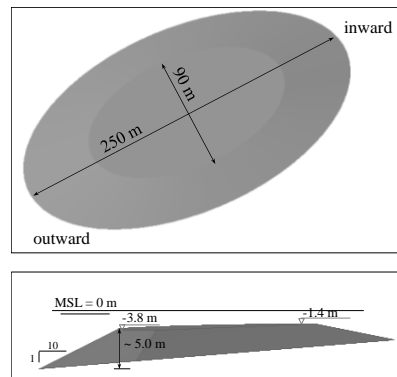
Figure 5.29: Geometrical schematization for RB1_S14.

Table 5.13: Structures characteristics for RB1_S14.

Characteristics	RB1_S14
Length (m)	250.0
Width (m)	90.0
Slope	1:10
Max. height (m)	5.0
Crest level (m)	-1.4 (North) to -3.8 (South)
Distance to shoreline (m)	390.0
Volume (m³)	86 590.16

5.4.3.5 Hydrodynamics. Results and discussion

In this section, hydrodynamics results for the RB1 structures scenarios (RB1_S1, RB1_S2 and RB1_S3; RB1_S4, RB1_S6, RB1_S8, RB1_S10 and RB1_S12; RB1_S5, RB1_S7, RB1_S9, RB1_S11 and RB1_S13; and RB1_S14) are presented and analysed based on the main outcomes and differences between them.

Figures 5.30, 5.31, 5.32 and 5.33 present the decrease of significant wave heights from offshore to shoreline (wave energy dissipation) and their mean directions based on the structures shapes created for each scenario. The wave climate conditions are identical to all scenarios. Figures 5.30a, 5.30b and 5.30c present results for RB1_S1, RB1_S2 and RB1_S3, respectively. Figures 5.31a, 5.31b, 5.31c, 5.31d and 5.31e depict results for RB1_S4, RB1_S6, RB1_S8, RB1_S10 and RB1_S12, respectively. Figures 5.32a, 5.32b, 5.32c, 5.32d and 5.32e depict results for RB1_S5, RB1_S7, RB1_S9, RB1_S11 and RB1_S13, respectively. Figure 5.33 presents results for RB1_S14. In each Figure 5.30, 5.31, 5.32 and 5.33, the left panel presents results for the entire domain, while the right panel depicts results that are more detailed around the structures. All structures have a detached shape from the shoreline.

In the first group of structures, results for significant wave heights near shoreline are relatively similar for all scenarios (Figure 5.30). However, of all three, results in RB1_S1 (Figure 5.30a) can be highlighted as the most favourable in terms of wave energy dissipation, since significant wave height values between 1360 m and 1600 m are less significant (1.2 m) than those presented in RB1_S2 (Figure 5.30b) (1.5 m) and RB1_S3 (Figure 5.30c) (1.8 m). Since, at the same location, results in RB1_S3 present slightly greater values of significant wave heights, it is clear that a greater distance from shoreline reflects in a less noticeable effect of wave energy dissipation near the shoreline. As the slopes exposed to wave climate action near the ledge are similar, the wave breaking occurs roughly at the same location.

Regarding the reversal of longitudinal drift, near shoreline this phenomenon is also more noticeable in RB1_S1 and less significant in RB1_S3. This effect is demonstrated in the shadow zone by the SW orientation of the mean wave direction vectors in RB1_S1. These results indicate that a structure that is closer to shoreline with a less tapered shape is more favourable to achieve the intended objectives. For this reason, structures with a more circular shape need to be tested. In addition, due to the significant volumes, less bulkier solutions than the ones presented should be considered to avoid high construction costs.

Figure 5.30: H$_s$ for the entire domain (left) and around the structure (right) for scenarios: a) RB1_S1; b) RB1_S2, and c) RB1_S3.

Figure 5.31 assembles five structures with similar geometries and locations but with different orientations relatively to shoreline. All structures have a variable crest elevation with a deeper crest level in the south extremity.

All scenarios present a clear influence of the structures on the significant wave heights decreasing, however, regarding the best ability for wave energy dissipation, results point RB1_S6 (Figures 5.31b) as the most favourable scenario, due to a larger shadow zone area with mean values of significant wave heights of 0.5 m.

Regardless of the structures' orientation, waves start breaking from position 1400 m due to the structure's presence, but with different patterns of wave energy dissipation in each scenario.

For all scenarios, with the exception of RB1_S6, significant wave heights reach their lowest values near the structure at the alignment of the north extremity, where the structure's elevation is the highest (-0.5 m). In RB1_S6, the wave energy dissipation occurs along the entire length of the structure due to the large area of the exposed slope to wave climate action.

Results for RB1_S4 (Figure 5.31a) and RB1_S10 (Figure 5.31d) present similar results patterns between 1550 m and 1650 m positions. The fact that the larger dimensions of both structures face the wave climate action yields great areas of impact to waves' action. Due to their orientations, scenarios RB1_S8 (Figure 5.31c) and RB1_S12 (Figure 5.31e) depict outcomes with higher significant wave heights in the shadow zone and smaller shadow zone areas between the same locations, with RB1_S12 being the least effective scenario ($H_s \approx 1.9$ m $vs.$ $H_s \approx 1.2$ m). This occurs because the area of the structures that offers resistance to wave climate action is smaller than in scenarios RB1_S4, RB1_S6 and RB1_S10.

In scenarios RB1_S4, RB1_S6 and RB1_S10, no wave shoaling before the structure is evident because of the smooth slope of 1:10. In RB1_S8 and RB1_S12, since the structure highest crest elevation zone (-0.5 m) is oriented to wave climate, wave shoaling occurs due to a greater variation in depth.

Regarding the reversal of longitudinal drift, despite scenarios RB1_S6 and RB1_S8 being the only to present a rotation of the significant wave height mean direction vectors near shoreline, RB1_S6 stands out as the best scenario, because of a greater rotation (SW) near this location. In contrast, scenarios RB1_S4, RB1_S10 and RB1_S12 do not present any rotation near shoreline, since the vectors orientation indicates a rotation limited to the structures location, around their slopes.
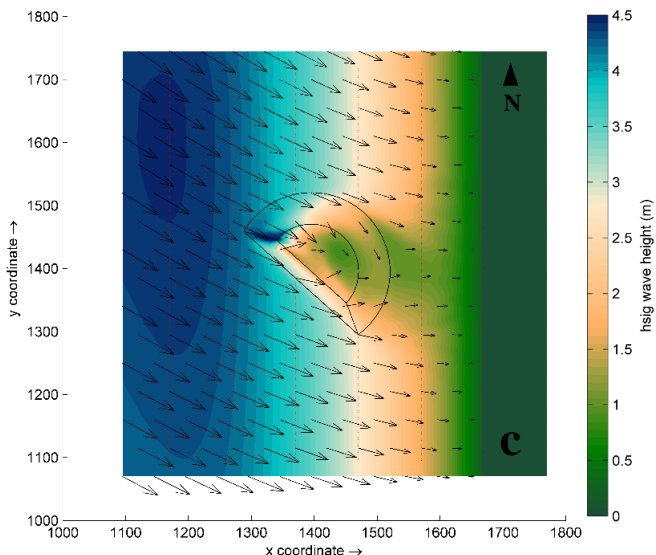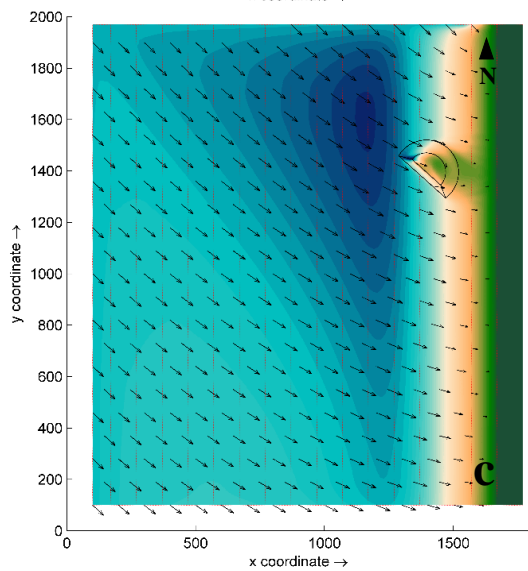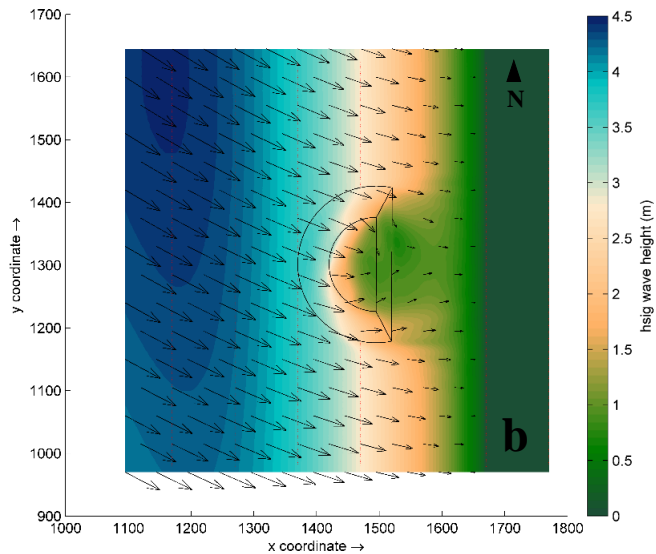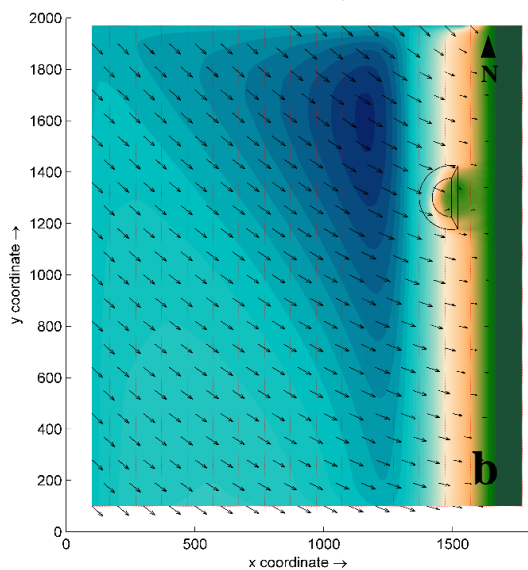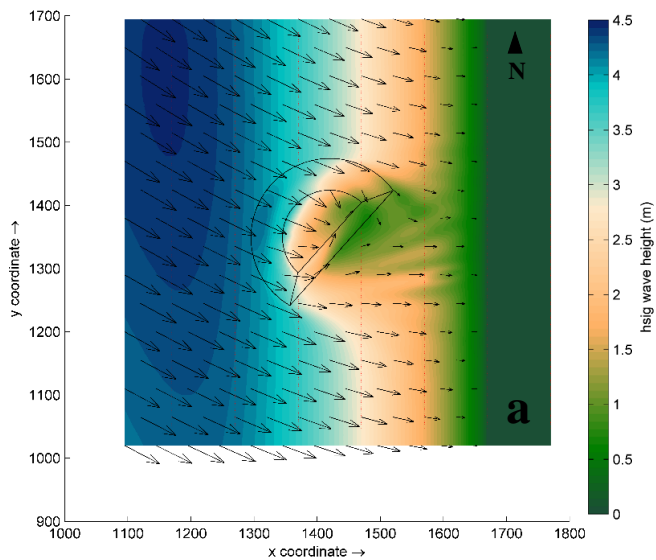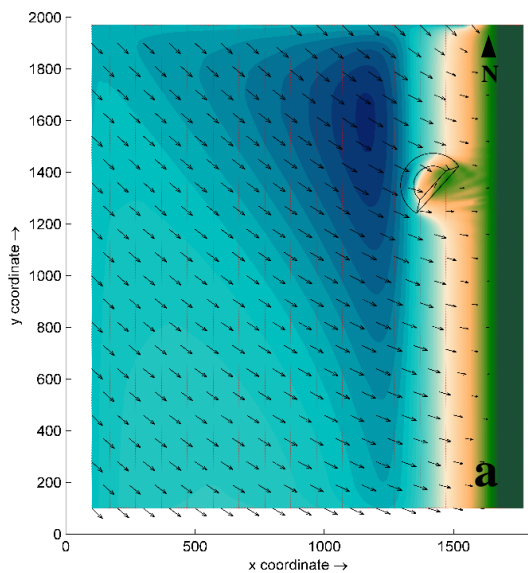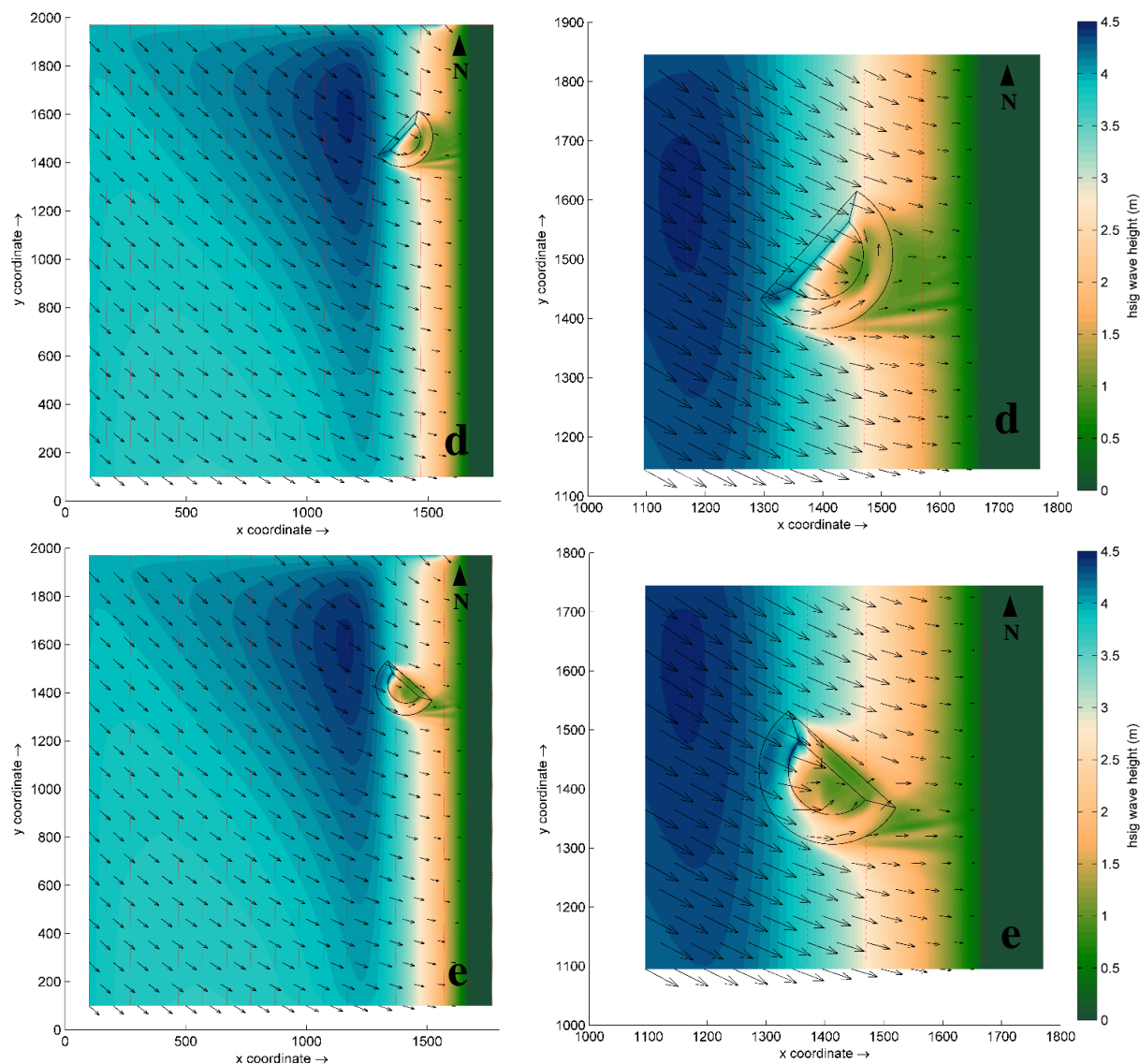
Figure 5.31: H$_s$ for the entire domain (left) and around the structure (right) for scenarios: a) RB1_S4; b) RB1_S6, c) RB1_S8, d) RB1_S10, and e) RB1_S12.

Figure 5.32 assembles five structures with geometric characteristics similar to those presented in Figure 5.31; however, structures in this case have a fixed crest level at -1.5 m.

Due to their similarities, the wave energy dissipation results patterns presented in RB1_S5 (Figure 5.32a), RB1_S7 (Figure 5.32b), RB1_S9 (Figure 5.32c), RB1_S11 (Figure 5.32d) and RB1_S13 (Figure 5.32e) are similar to those previously presented. Nevertheless, the significant wave heights values in the shadow zones are clearly higher in Figure 5.32 (H$_s$ ≈ 1.5 m *vs.* H$_s$ ≈ 1.0 m), because of the lowest fixed position of the crest level. This indicates that although a fixed elevation for the crest presents the same results patterns, this crest level contributes to less wave energy dissipation due to greater submerged levels.
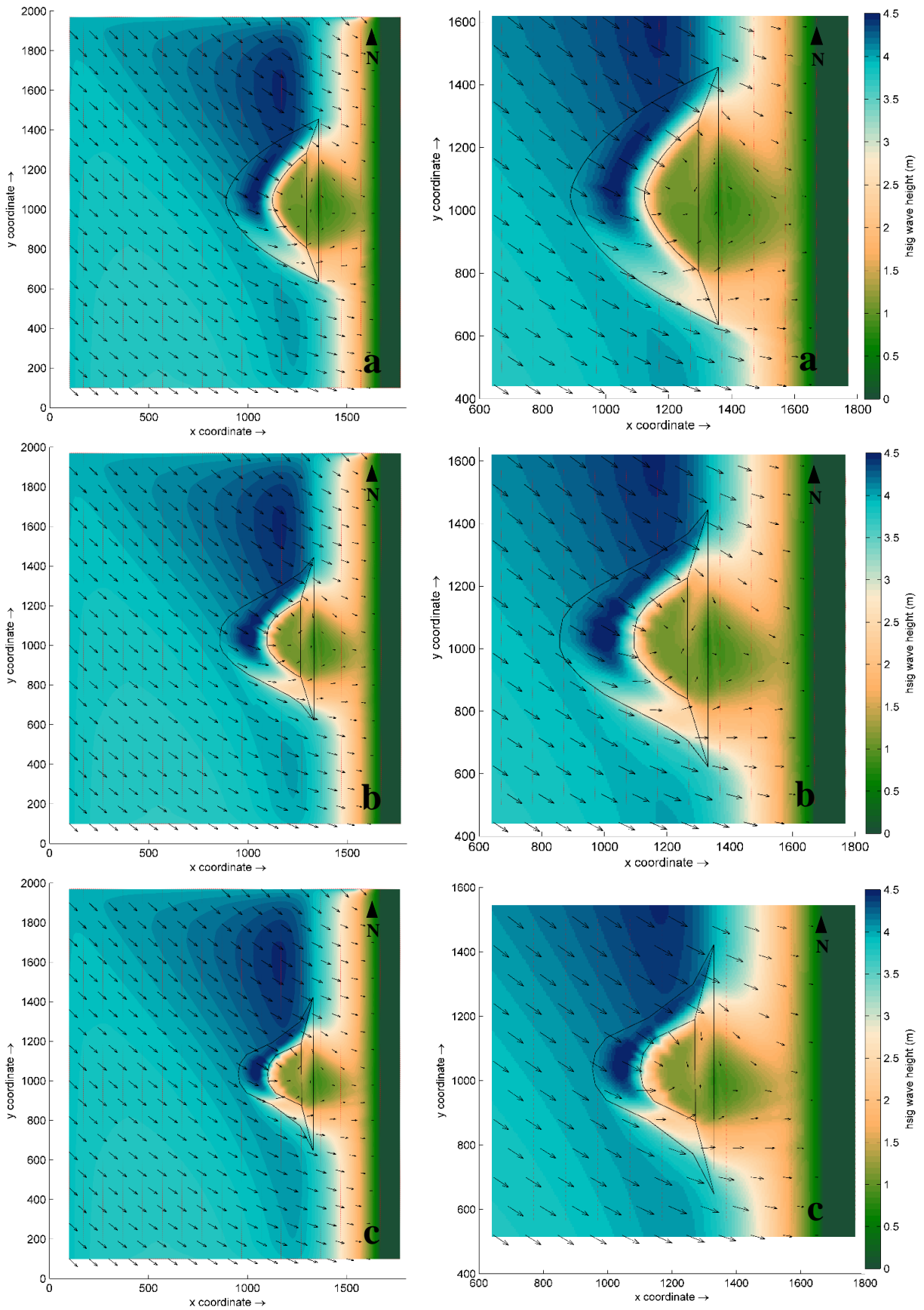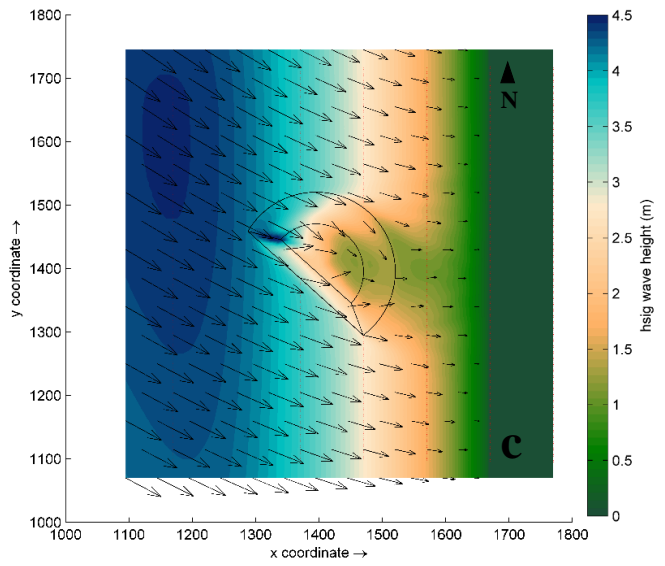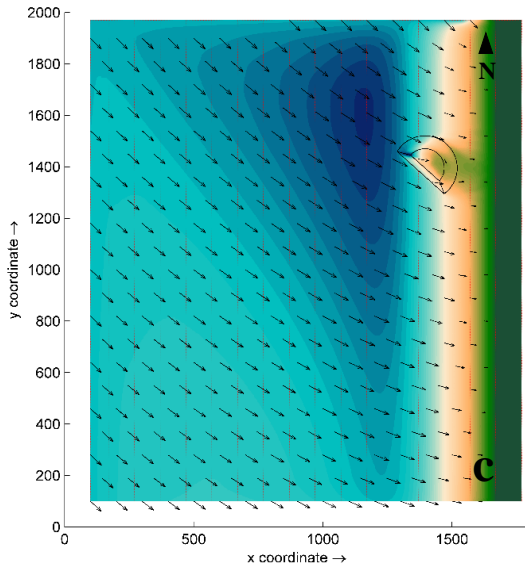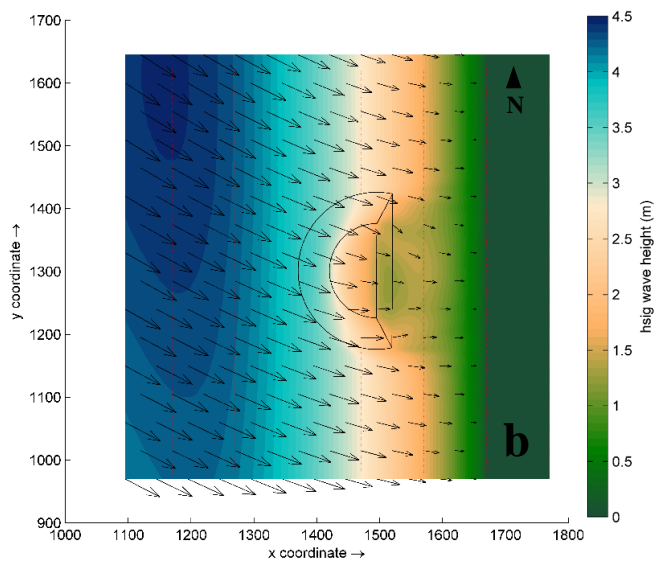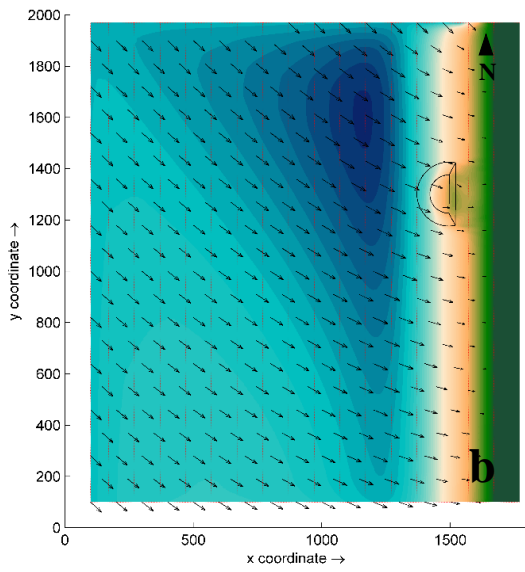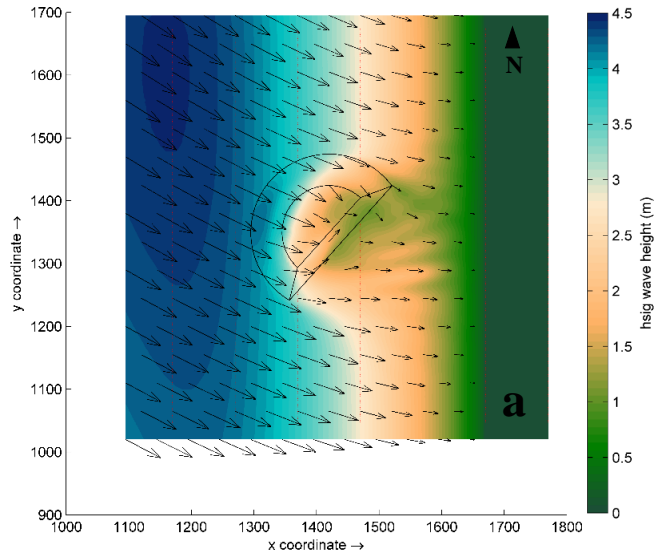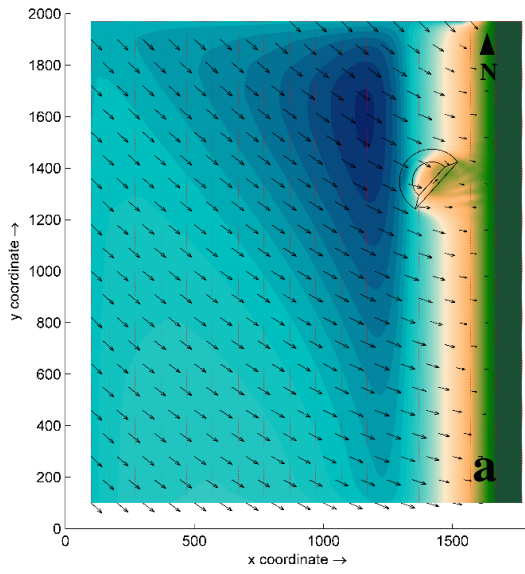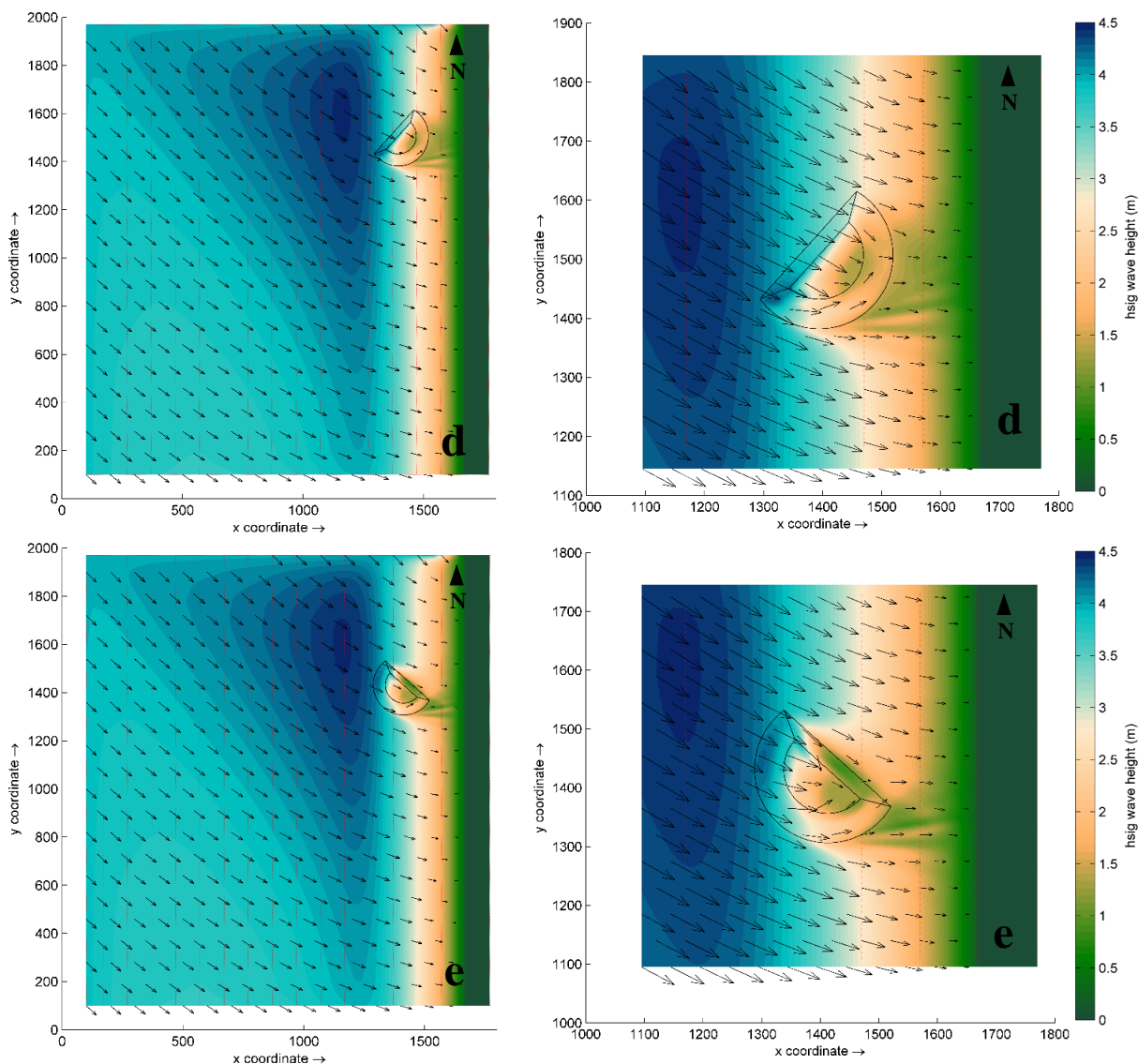
Figure 5.32: H$_s$ for the entire domain (left) and around the structure (right) for scenarios: a) RB1_S5; b) RB1_S7, c) RB1_S9, d) RB1_S11, and e) RB1_S13.

RB1_S14 (Figure 5.33) presents results for an ellipse-shaped structure. In this scenario, waves start breaking at the 1250 m position due to the presence of the structure until reaching null values near shoreline.

In order to understand the reversal effect originated by this structure shape, the submergence levels and the structure position were altered relatively to previous scenarios. Nonetheless, the orientations of significant wave height mean direction vectors also show a limited effect of longitudinal drift reversing around the structure's slope. When compared to RB1_S4, RB1_S6, RB1_S8, RB1_S10 and RB1_S12, RB1_S14 (Figure 5.31), results for significant wave heights in Figure 5.33 present higher values in the shadow zone (H$_s$ ≈ 2.0 m *vs.* H$_s$ ≈ 1.0 m), which indicates that this scenario does not provide a great wave energy dissipation.
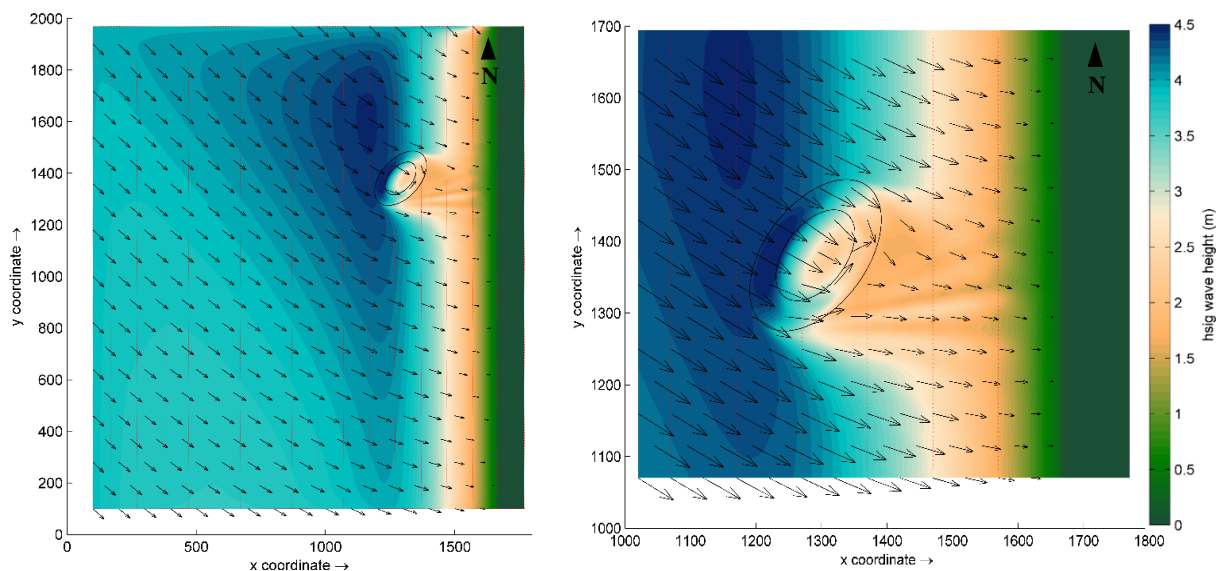
Figure 5.33: H$_s$ for the entire domain (left) and around the structure (right) for scenario RB1_S14.

5.4.4 RB2 bathymetric changes

The large dimension of seabed changes together with the small domain extension to analyse results downdrift highlighted the need to increase the simulations domain. In this way, the domain is increased in order to assess the most appropriate dimensions.

5.4.4.1 RB2_1

Figure 5.34 (left panel) depicts a bathymetric change with a constant elevation of -2.0 m from near shoreline until the 500 m position. The current scenario intends to study the effect of this shape on the reversal of longitudinal drift and to test if the domain resolution is sufficient to analyse this phenomenon downdrift. The longer slope exposed to wave climate action at the ledge (from 0 m to 250 m) is 10.6% and 1.9% between the longer slope and the -2.0 m platform (from 250 m to 410 m). Changes in bathymetry cover practically the entire domain.

The right panel in Figure 5.34 indicates the bed level variation to add to the RB and their necessary volumes are presented in Table 5.14.
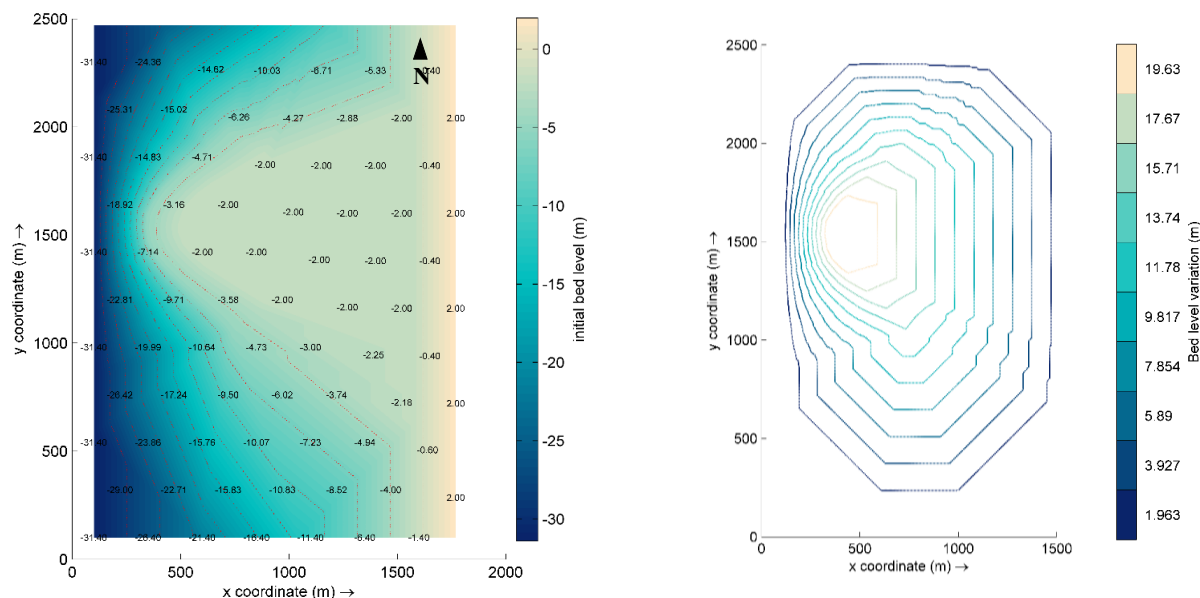
Figure 5.34: Bed level values (left) and variations (right) for scenario RB2_1.

Table 5.14: Volume for bathymetric changes: RB2_1.

Characteristics	RB2_1
Volume (m³)	19 520 629.94

5.4.4.2 Hydrodynamics. Results and discussion

Figure 5.35 depicts results for the RB2_1 scenario characterized by a shape similar to RB1_4 and RB1_5. The main differences between them are in a wider shape and an extensive -2.0 m platform along the domain. Results for RB2_1 show that in this scenario, waves start breaking at the 380 m position in the ledge zone, due to slopes variation, where significant wave heights decrease from 4.5 m to 0.8 m along the submerged platform until reaching null values near shoreline at the 1660 m position. This solution presents good results for wave energy dissipation due to its geometry, particularly for its long and wide dimensions. Regarding the reversal of the longitudinal drift, a significant rotation of significant wave heights vectors is notable, due to the combination of subtle slope variations with the bed level curved shape downdrift, which guarantees a relatively large reversal in this region.

As for the domain resolution, although the current domain has already been extended, another domain enlargement is necessary for an additional sound analysis downdrift, especially for morphodynamics.

Concerning the bathymetric changes, regardless the upcoming results, it is important to mind the shapes dimensions, because significant volumes will reflect on very high construction costs.
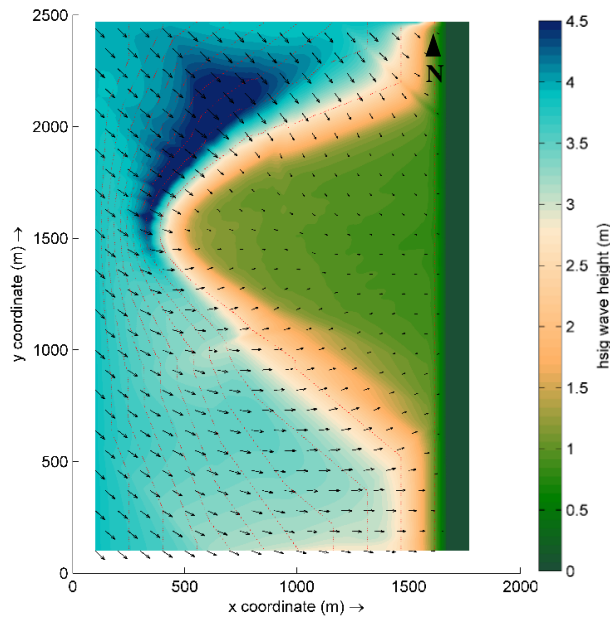
Figure 5.35: H$_s$ for scenario RB2_1.

5.4.5 RB3 bathymetric changes

Similar to Table 5.3, in Table 5.5 the left column presents the scenarios of bathymetric changes without structure. In the following Sections, several scenarios are tested in order to analyse the reversal of longitudinal drift and to define a favourable structure geometry to replicate this phenomenon. This reversal is presented in the results section through the vectors of significant wave height. Based on RB2_1, the following scenarios have less bathymetric variations (less volumes) and since the domain resolution was not yet sufficient for an analysis downdrift, the domain has been increased. The analysis is conducted in two groups, based on bathymetric changes similarities: i) RB3_1, RB3_2 and RB3_3; and ii) RB3_4 and RB3_5. The current scenarios aim to analyse the most adequate solution to serve as basis to propose effective structures to induce the reversal of longitudinal drift.

5.4.5.1 RB3_1, RB3_2 and RB3_3

Figures 5.36a, 5.36b, and 5.36c (left panel) indicate that the seabed changes for RB3_1, RB3_2 and RB3_3 have a constant elevation of -2.0 m from near shoreline until the rim of the salience (variable position, depending on the scenario). The slopes exposed to wave climate action at the ledge are 4.5%, 2.6% and 3.2%, respectively.

The most significant bathymetry variations are in RB3_1 and RB3_3, because of greater landfill volumes. The right panel in Figure 5.36 indicates the bed level variation to add to the RB and their necessary volumes are presented in Table 5.15.
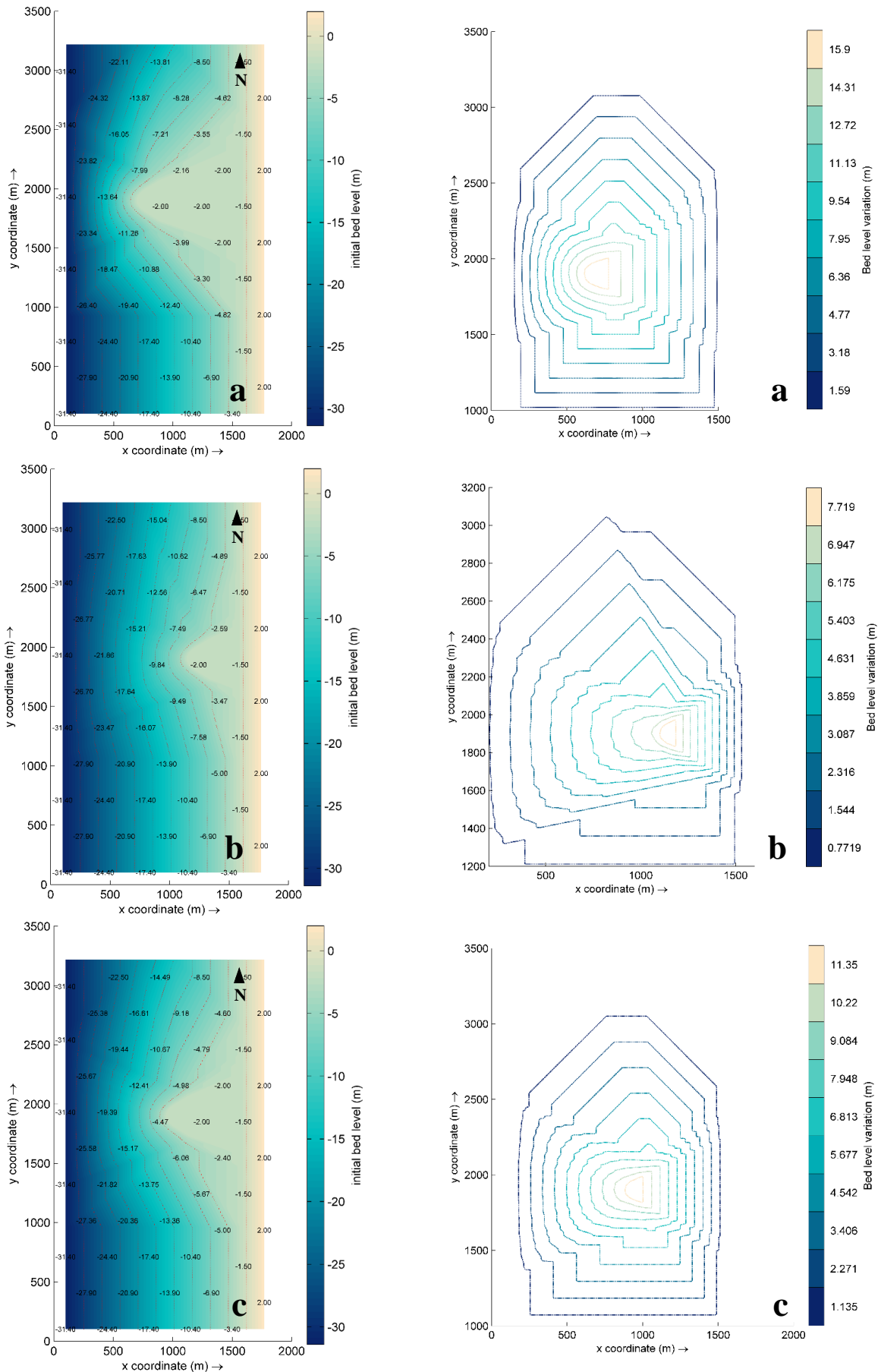
Figure 5.36: Bed level values (left) and variations (right) for scenarios: a) RB3_1; b) RB3_2; and c) RB3_3.

Table 5.15: Volumes for bathymetric changes: RB3_1, RB3_2 and RB3_3.

Characteristics	RB3_1	RB3_2	RB3_3
Volume (m³)	13 429 588.42	4 403 610.59	8 181 426.87

5.4.5.2 RB3_4 and RB3_5

Regarding Figure 5.37a, for RB3_4, the longer slope exposed to wave climate action at the ledge (from 370 m to 560 m) is 10% and 3% between the longer slope and the crest at -2.0 m (from 560 m to 660 m). RB3_5 (Figure 5.37b) has a constant elevation of -2.0 m from near shoreline until the rim of the salience and the slope exposed to wave climate action at the ledge is 8.7%.
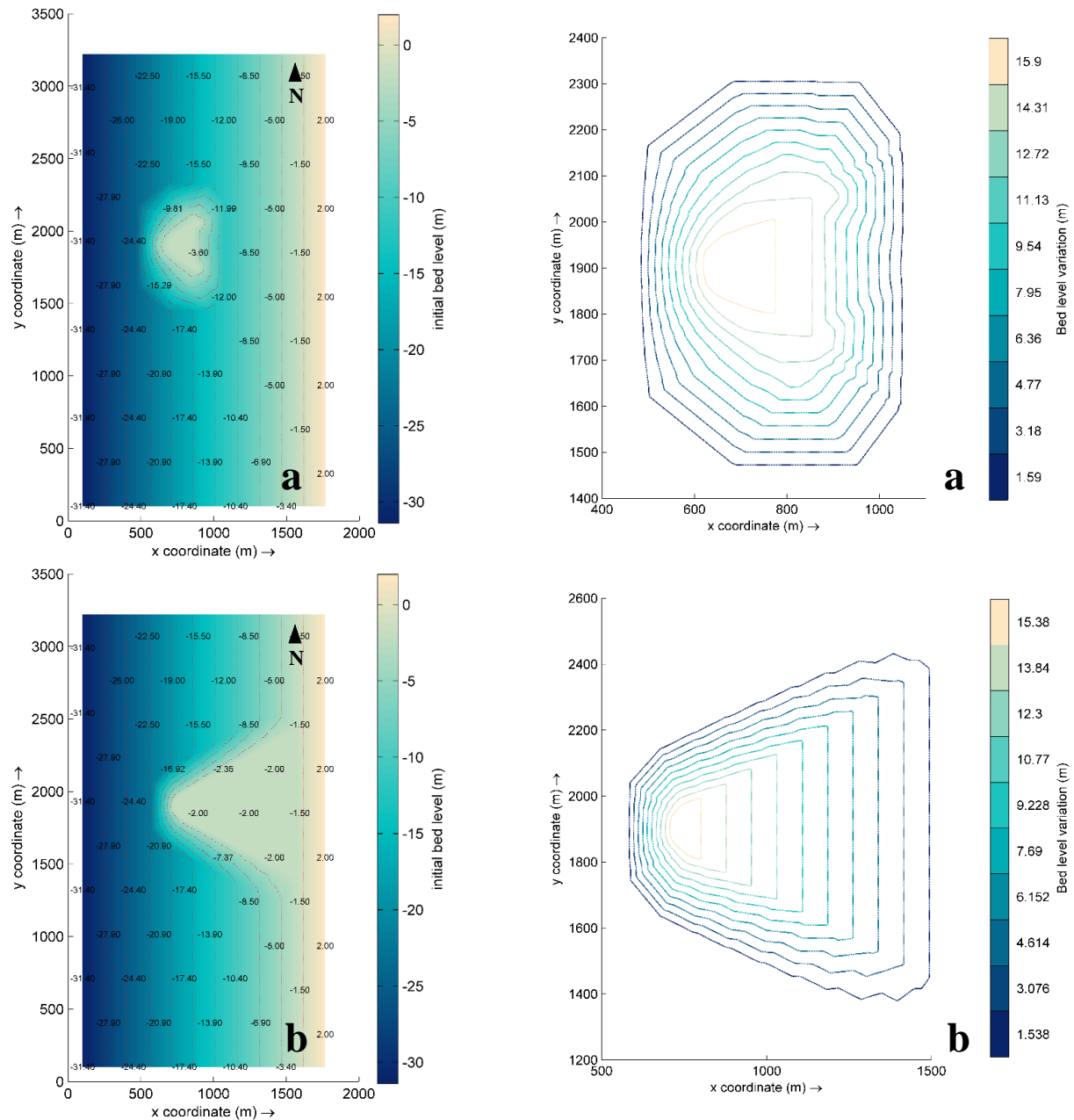
Figure 5.37: Bed level values (left) and variations (right) for scenarios: a) RB3_4; and b) RB3_5.

RB3_4 has more located bathymetric changes than the previous scenarios and was inspired by rocky outcrops shapes. RB3_5 derives from RB3_4 by enlarging the area of intervention, maintaining a similar exposed slope and considering a -2.0 m platform from the ledge to near shoreline. The right panel in Figure 5.37 indicates the bed level variation to add to the RB and their necessary volumes are presented in Table 5.16. These scenarios present the less significant bed level variation volume of all RB3.

Table 5.16: Volumes for bathymetric changes: RB3_4 and RB3_5.

Characteristics	RB3_4	RB3_5
Volume (m³)	3 262 051.62	4 273 586.50

5.4.5.3 Hydrodynamics. Results and discussion

In this section, hydrodynamics results for the RB3 bathymetric changes scenarios (RB3_1, RB3_2 and RB3_3; and RB3_4 and RB3_5) are presented and analysed based on the main outcomes and differences between them.

Figures 5.38 and 5.39 present the decrease of significant wave heights from offshore to shoreline (wave energy dissipation) and their mean directions based on the bed level changes (bathymetric changes) created for each scenario. The wave climate conditions are identical to all scenarios.

Figures 5.38a, 5.38b and 5.38c present results for RB3_1, RB3_2 and RB3_3, respectively. Figures 5.39a and 5.39b depict results for RB3_4 and RB3_5, respectively.

The first group of scenarios (RB3_1, RB3_2 and RB3_3) presented in Figure 5.38 assembles bathymetric changes in an increased domain with shapes similar to the one shown in RB2_1, only with variations in their widths.

Results for significant wave heights show that waves start breaking at different positions in relation to their ledge position. RB3_1 (Figure 5.38a) wave breaking occurs at 650 m position, RB3_2 (Figure 5.38b) at 1100 m, and RB3_3 (Figure 5.38c) at 900 m.

Each scenario presents a solution that contributes to great wave energy dissipation along the domain, as the -2.0 m platform contributes to a calm area corroborated by the vectors small intensities. Significant wave heights decrease from 4.5 m to 0.8 m along the submerged platform until reaching null values near shoreline at the 1660 m position.

Regarding the reversal of longitudinal drift, mean direction vectors orientations show that all proposed bathymetric changes contribute to large areas of longshore drift reversal. Although results do not differ much from each scenario, RB3_1 presents the most noticeable reversal, while in RB3_2 the vectors

orientation indicate this scenario as the least effective. The most intense reversal is justified by a wider geometry, a more curved bed level shape and a slightly steeper slope downdrift.

Despite RB3_1 presenting the best results, the necessary volume to induce the reversal is the most significant out of the three. For this reason, the consideration for smaller seabed changes with the ability to induce the reversal of longitudinal drift is necessary to prevent high construction costs.
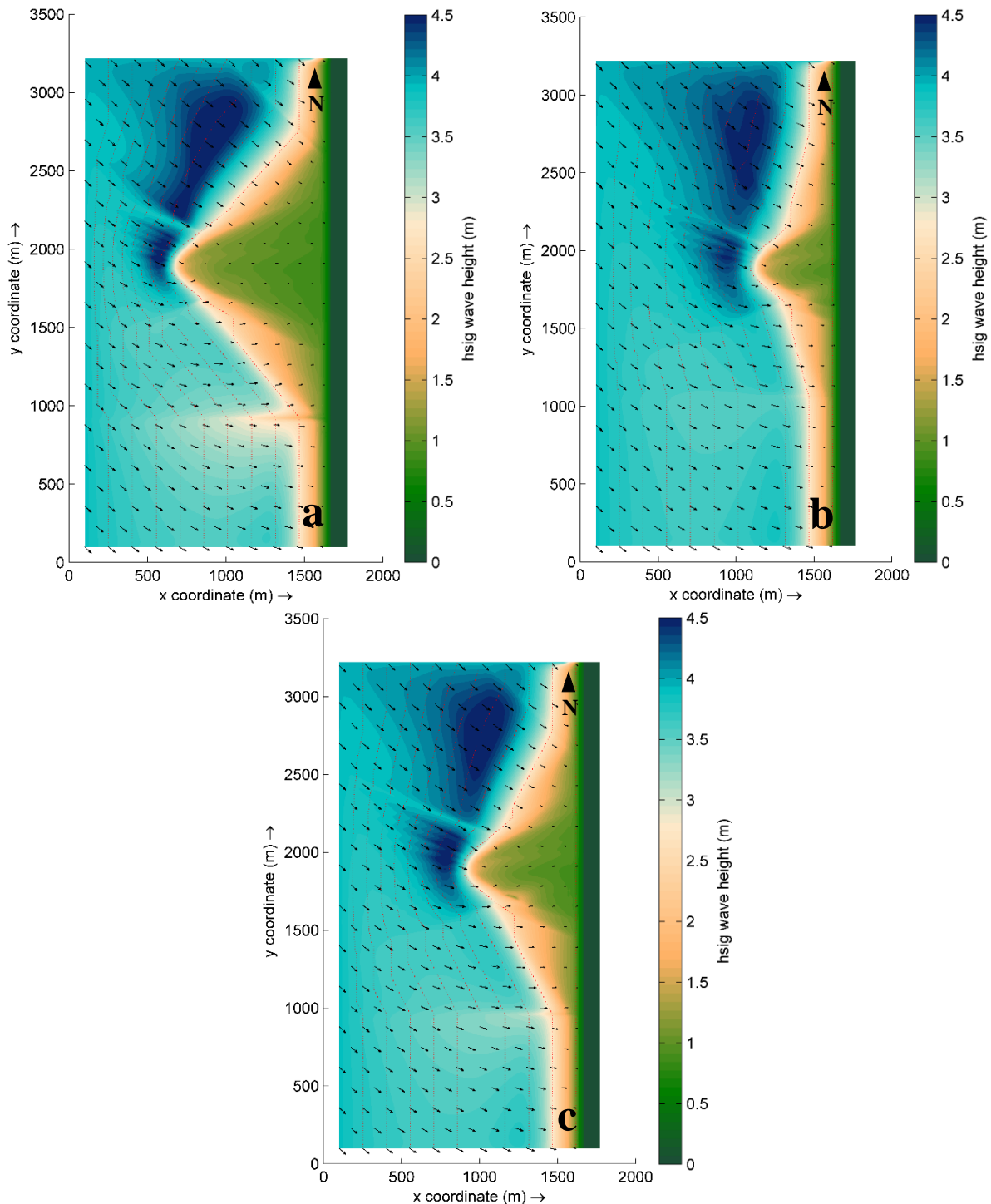
Figure 5.38: Hₛ for scenarios: a) RB3_1; b) RB3_2; and c) RB3_3.

In order to reduce the volumes of bathymetric changes without overlooking the effect of the longshore drift reversal, RB3_4 (Figure 5.39a) was shaped based on the effects of rocky outcrops, which in turn served as basis to the RB3_5 scenario (Figure 5.39b).
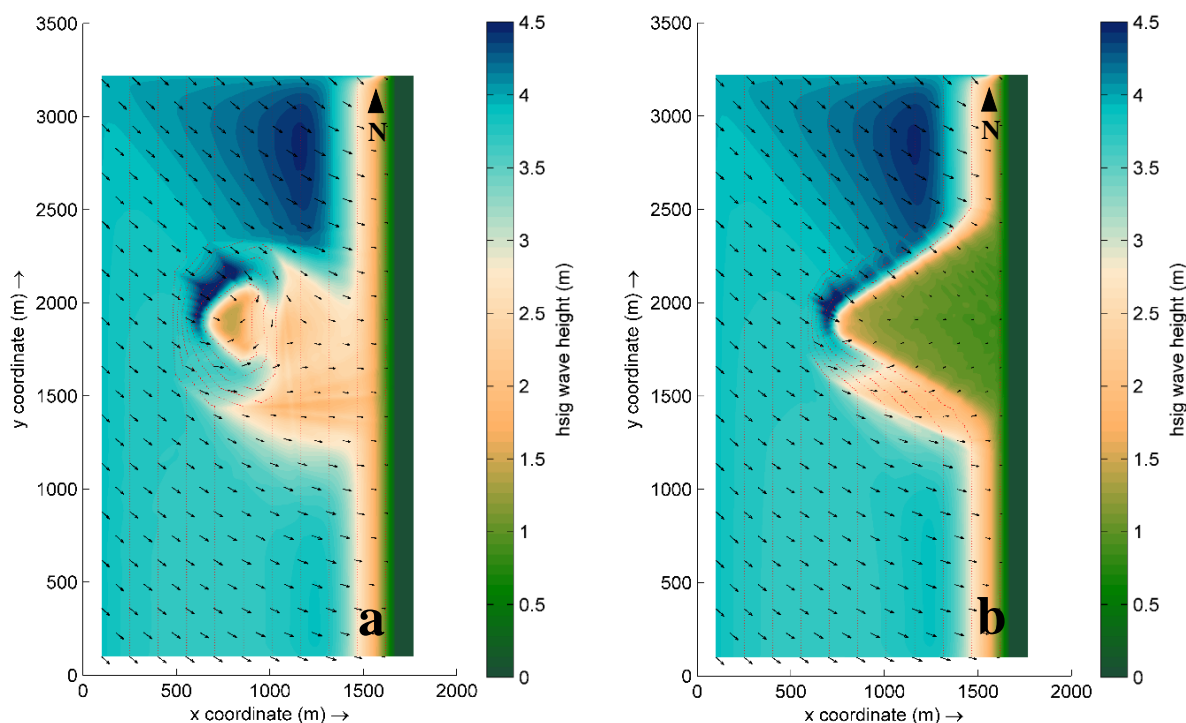
Figure 5.39: H$_s$ for scenarios: a) RB3_4; and b) RB3_5.

Due to the nature of their geometries, in Figure 5.39, results for RB3_4 significant wave heights are considerably different from the ones presented in RB3_5. RB3_4 bathymetric changes results are relatable to those of a detached structure, while RB3_5 results are similar to those of a groin, due to the wide -2.0 m platform. Because seabed changes have slightly different locations in the domain, in RB3_4 waves start breaking at the 650 m position, while in RB3_5 they start at 730 m. In RB3_4 significant wave heights decrease from 4.5 m to 1.5 m near the crest (positions 550 m to 760 m). From positions 760 m to 990 m, because of the waves breaking and the waves' transmission around the structure (diffraction represented by the mean direction vectors), the significant wave heights slightly tend to increase due to shoaling. From 990 m and 1310 m the significant wave heights have a constant value of 2.5 m, and as waves get closer to shoreline and depth decreases, the waves start breaking until reaching null values.

In RB3_5, the wave energy dissipation is similar to that presented in RB3_1, RB3_2 and RB3_3, and near shoreline, due to the large submerged platform, significant wave heights are less intense than those in RB3_4 at the same location.

Regarding the reversal of longitudinal drift, in RB3_5, the phenomenon covers a large area, whilst in RB3_4 the effect is more limited around the shape.

Since RB3_5 presents results similar to the ones presented in RB3_1, RB3_2 and RB3_3 but with lesser volumes, this scenario will serve as basis to the following RB3 proposed structures.

5.4.6 RB3 structures

Similar to Table 5.3, in Table 5.5 the right column presents the scenarios with structures. In the following Sections, several structures geometries are tested based on the previous bathymetric changes in order to assess their influence on the reversal of longitudinal drift and on the decreasing of significant wave heights. The domain extension is also analysed in terms of requirements for the downdrift analysis. The reversal of longitudinal drift is presented in the results section through the vectors of significant wave height and the analysis is conducted in four groups: i) RB3_S1, RB3_S3, RB3_S5 and RB3_S7; ii) RB3_S2, RB3_S4, RB3_S6, and RB3_S8; iii) RB3_S9, RB3_S10 and RB3_S11; and iv) RB3_S12, RB3_S13 and RB3_S14. The scenarios are grouped based on the structures similarities. Each structure is implanted in the RB3, which is characterized by a 2% constant slope.

The first group presents four different structures with large dimensions, while the second features the same geometries presented in the first group but with smaller dimensions. The third group presents three structures with similar geometries but with different crest levels and locations relatively to shoreline. Lastly, the fourth group assembles three groups of structures also with similar geometries but with different spacing (gaps width) and locations relatively to shoreline.

5.4.6.1 RB3_S1, RB3_S3, RB3_S5 and RB3_S7

The first group presents four structures geometries (Figure 5.40) with large dimensions based on the previous bathymetry changes results. Within these four structures, two major groups can be highlighted by their similar characteristics: RB3_S1 and RB3_S5 (Figures 5.40a and 5.40c), which have the largest width and narrower head; and RB3_S3 and RB3_S7 (Figures 5.40b and 5.40d), which have a width that is half the width of RB3_S1 and RB3_S5 and a wider head. The main difference between RB3_S1 and RB3_S5, and RB3_S3 and RB3_S7 is related to their slopes: RB3_S1 and RB3_S3 are wall-type structures (Figures 5.41a and 5.41b), while RB3_S5 and RB3_S7 have a 1:2 slope, which is commonly considered for coastal protection structures (Figures 5.41c and 5.41d). All structures share the same crest levels at -2.0 m relatively to MSL and a 100 m distance from shoreline. Similar to previous scenarios, in Figure 5.40, the left panel presents the initial bed level along the domain, while the right

panel depicts the initial bed level variations between the structure and the RB3 (without any structure). In Figure 5.41, the left panel presents a more detailed representation of the structure in the domain, while the right panel depicts the cross section traced along the ledge of the structure (denominated as profiles, P).

Regarding the volumes, RB3_S1 is the greatest (2.7M m³) and RB3_S7 the smallest out of the four (928K m³). The presented structures are the bulkier of all the ones already tested.

All summarized characteristics for each structure are detailed in Figure 5.42 and Table 5.17.
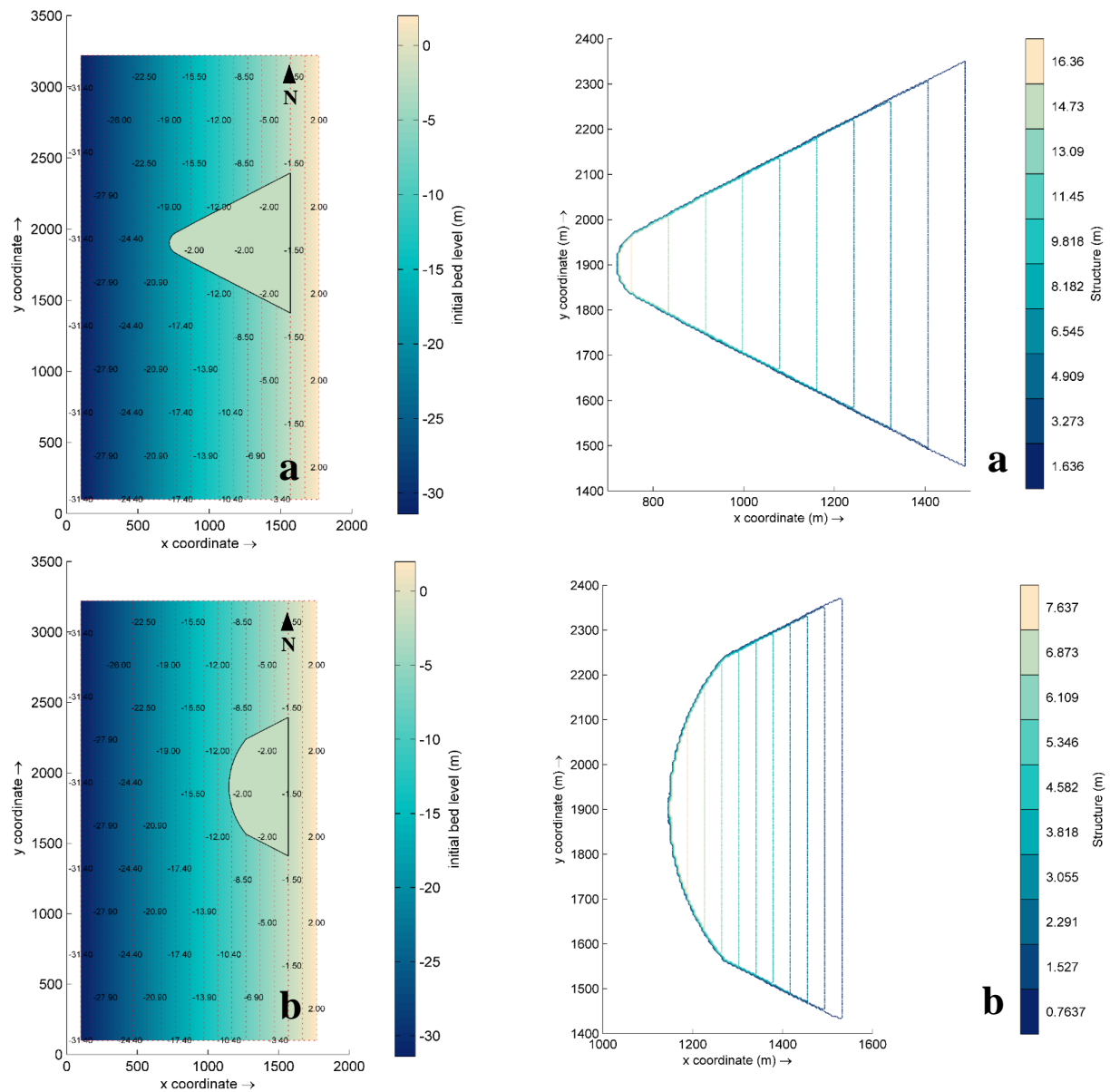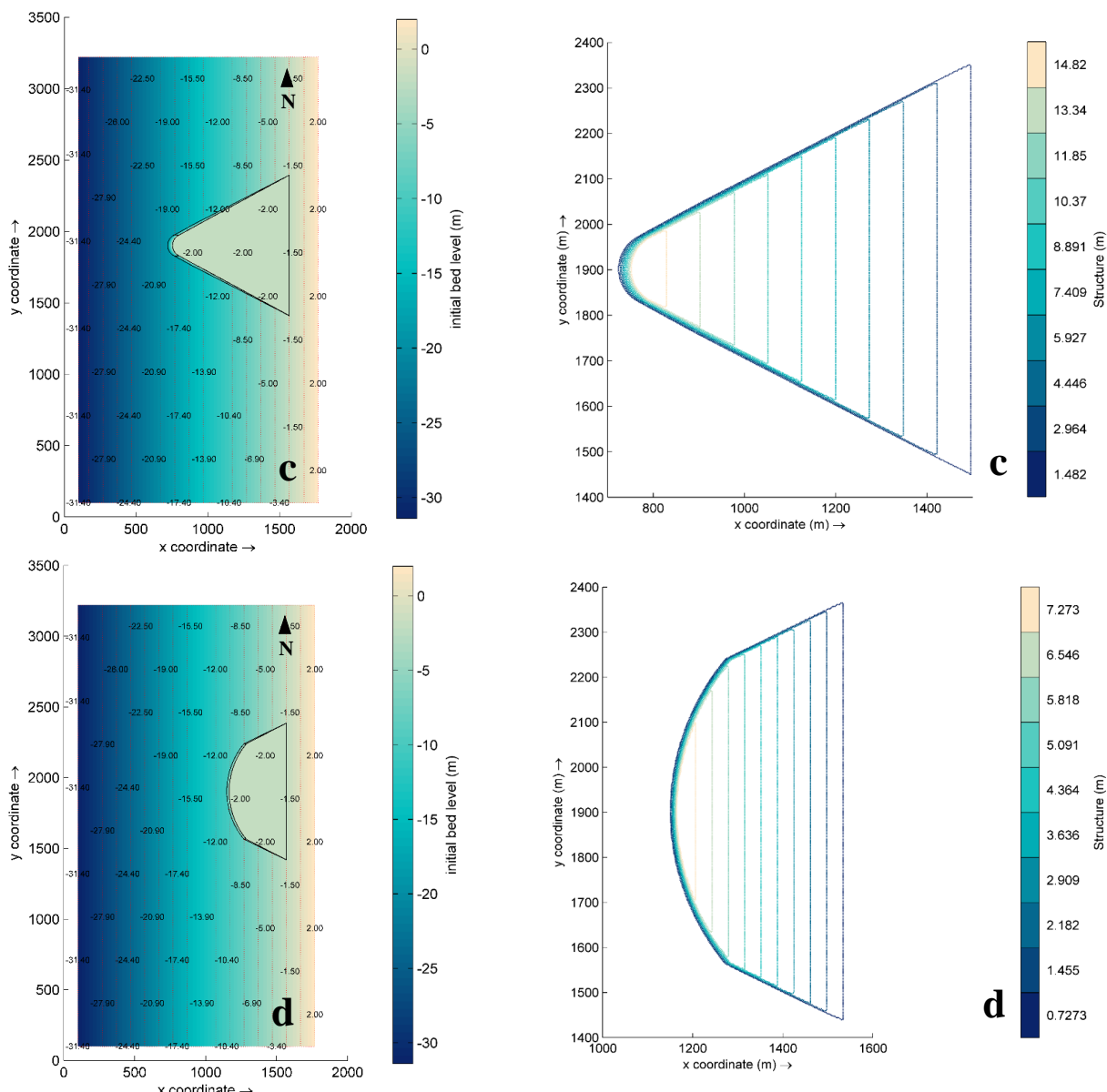
Figure 5.40: Bed level values (left) and variations (right) for scenarios: a) RB3_S1; b) RB3_S3; c) RB3_S5; and d) RB3_S7.
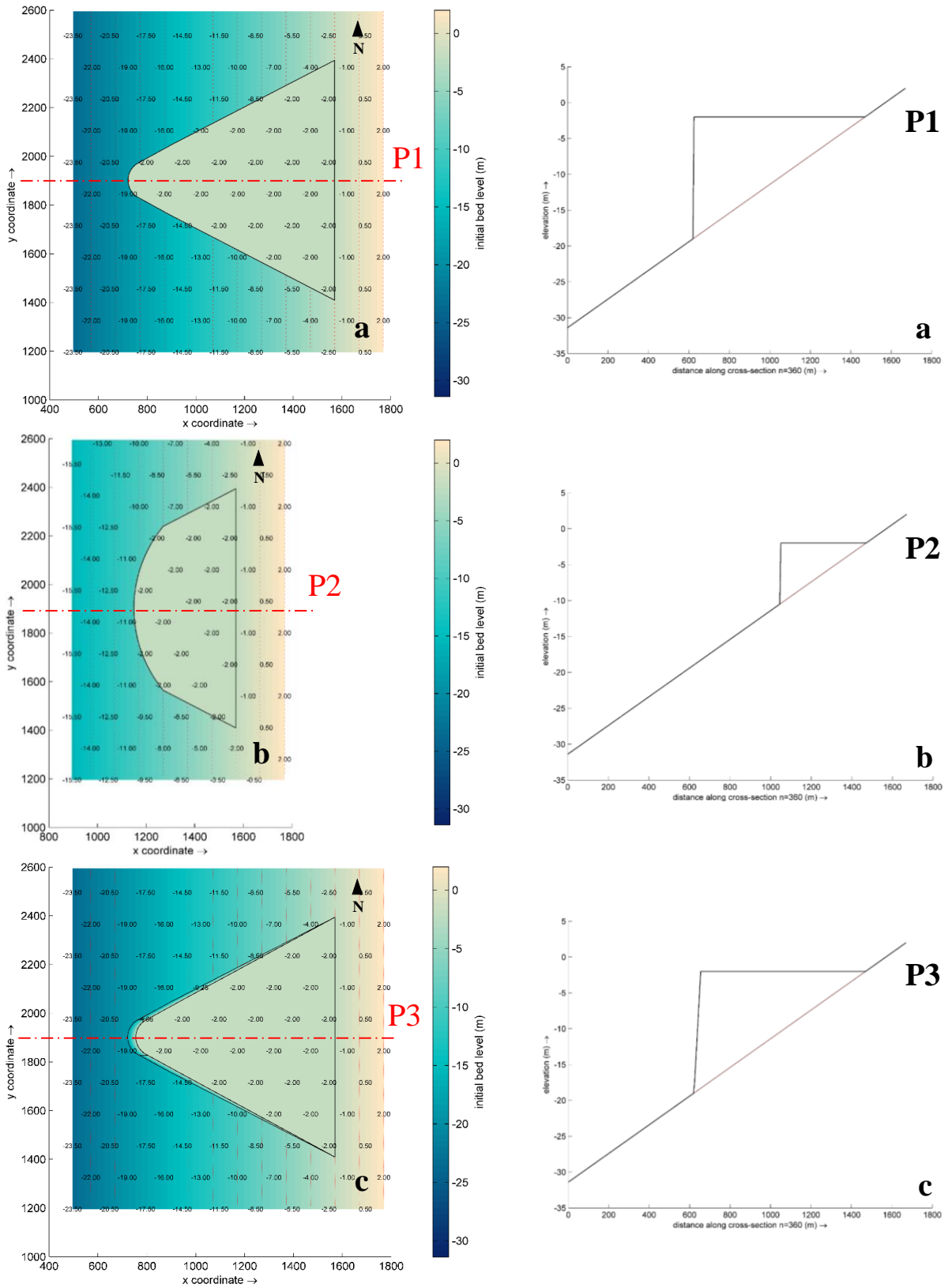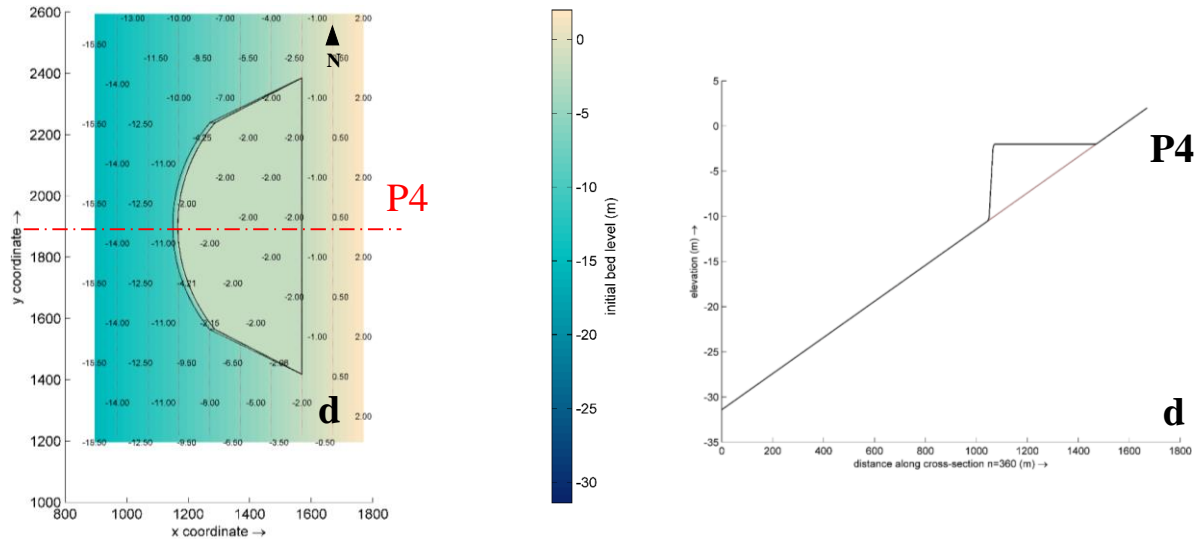
Figure 5.41: Bed level values around the structure (left) and cross section along the crest (right) for scenarios: a) RB3_S1; b) RB3_S3; c) RB3_S5; and d) RB3_S7.

Figure 5.42: Geometrical schematization for: a) RB3_S1; b) RB3_S3; c) RB3_S5; and d) RB3_S7.

Table 5.17: Structures characteristics for RB3_S1, RB3_S3, RB3_S5, and RB3_S7.

Characteristics	RB3_S1	RB3_S3	RB3_S5	RB3_S7
Length (m)	985.47	985.47	985.47	968.38
Width (m)	849.11	420.50	815.44	403.99
Slope	90° (wall)	90° (wall)	1:2	1:2
Max. height (m)	16.98	8.41	16.31	8.08
Crest level (m)	-2.0	-2.0	-2.0	-2.0
Distance to shoreline (m)	100.0	100.0	100.0	100.0
Volume (m³)	2 668 213.23	973 700.03	2 389 818.65	927 776.94

5.4.6.2 RB3_S2, RB3_S4, RB3_S6 and RB3_S8

Due to the high volumes required to implement the structures presented in the first group, the following group aims to analyse similar geometries as the ones presented in the first group but with smaller dimensions. This group assembles four structures geometries (Figure 5.43) that are also subdivided in two groups based on their similarities. Thus, RB3_S2 and RB3_S6 (Figures 5.43a and 5.43c), which have the largest width and narrower head can be assembled into one subgroup, and RB3_S4 and RB3_S8 (Figures 5.43b and 5.43d), which have a width that is half the width of RB3_S2 and RB3_S6 and a wider head can be assembled to another subgroup. RB3_S2 and RB3_S4 are wall-type structures (Figures 5.44a and 5.44b), while RB3_S6 and RB3_S8 have a 1:2 slope (Figures 5.44c and 5.44d). All structures share the same crest levels at -2.0 m relatively to MSL and a 100 m distance from shoreline. In Figure 5.43, the left panel presents the initial bed level along the domain, while the right panel depicts the initial bed level variations between the structure and the RB3 (without any structure). Figure 5.44 presents a more detailed representation of the structure in the domain in the left panel, while the right panel depicts the cross section traced along the ledge of the structure (denominated as profiles, P).

Regarding the volumes, RB3_S4 is the greatest (62K m³) and RB3_S6 the smallest out of the four (37K m³). The presented structures are significantly smaller than the ones mentioned in the first group.

All summarized characteristics for each structure are detailed in Figure 5.45 and Table 5.18.
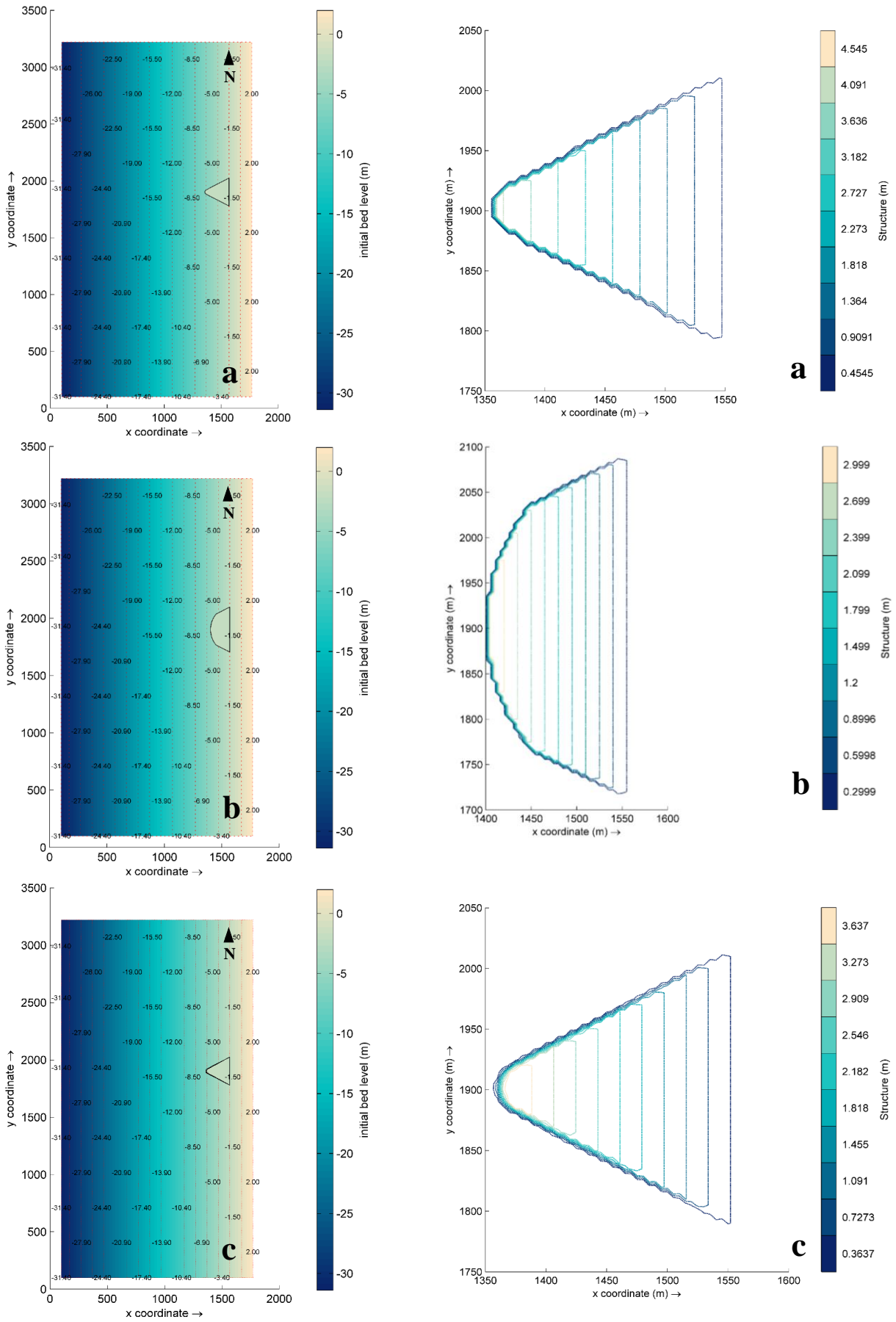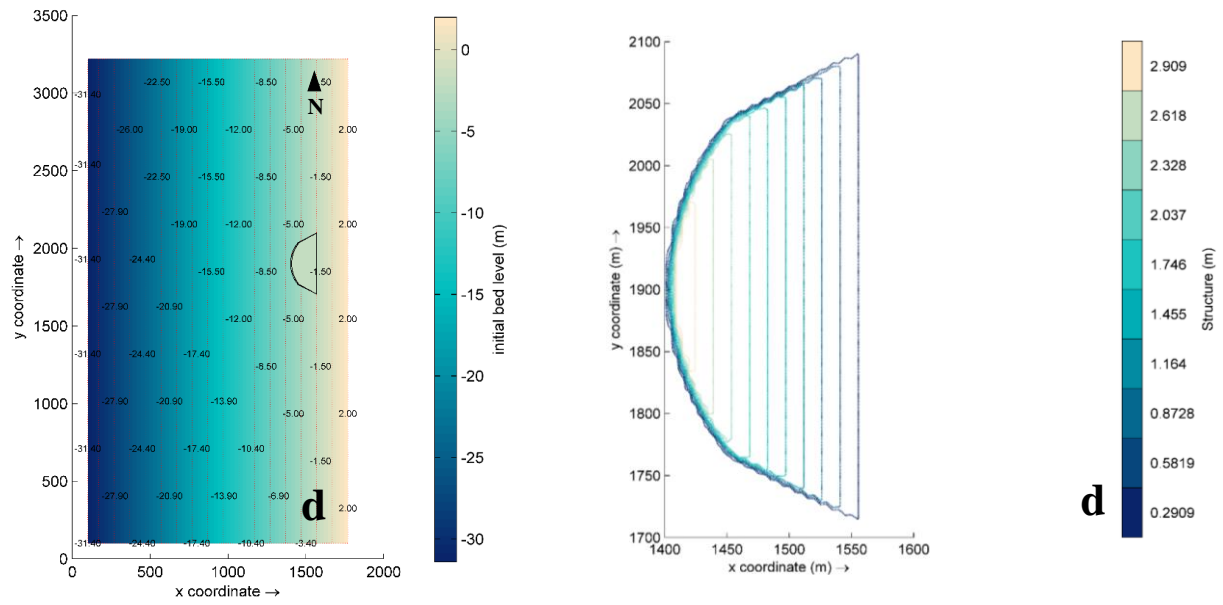
Figure 5.43: Bed level values (left) and variations (right) for scenarios: a) RB3_S2; b) RB3_S4; c) RB3_S6; and d) RB3_S8.
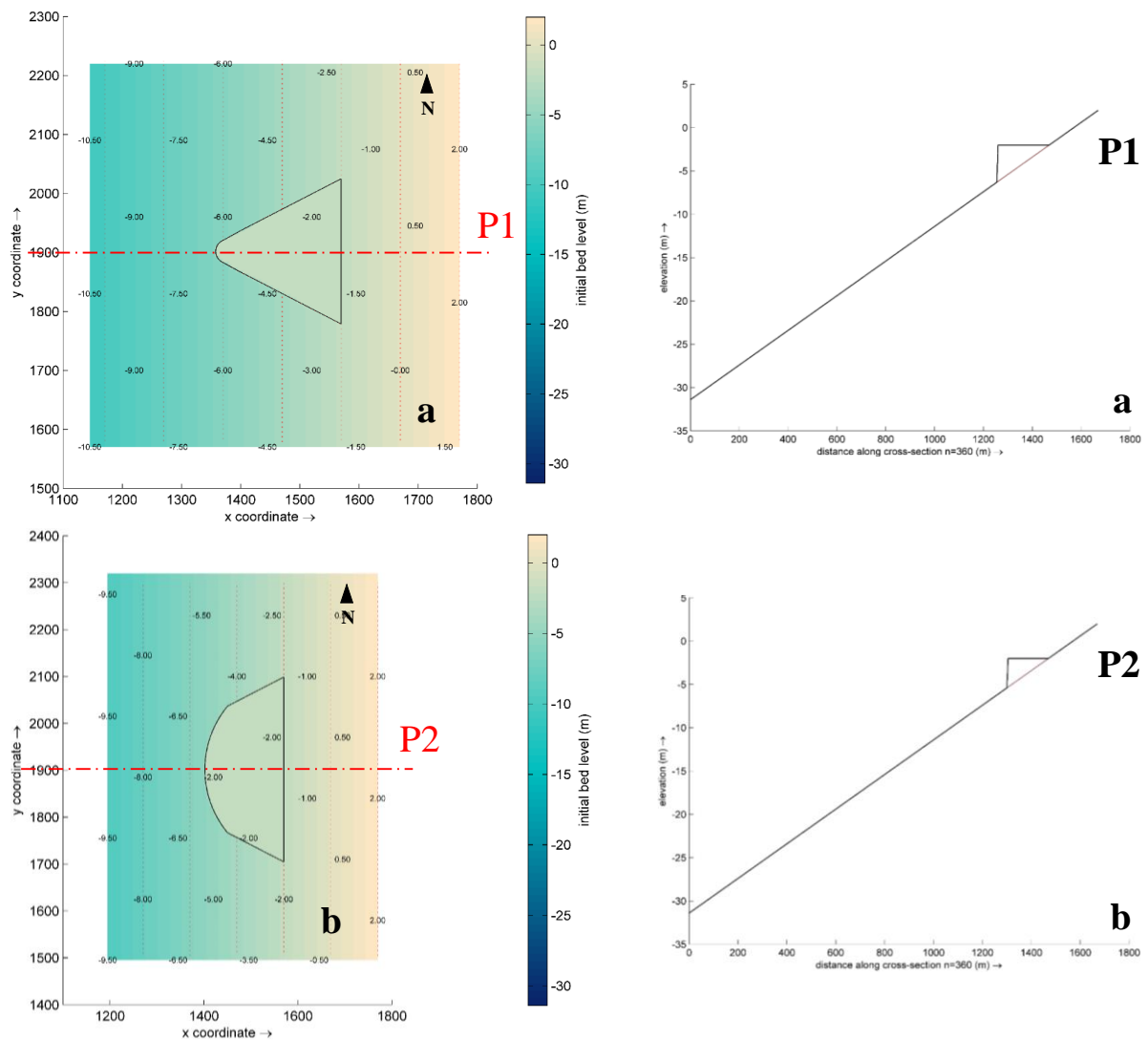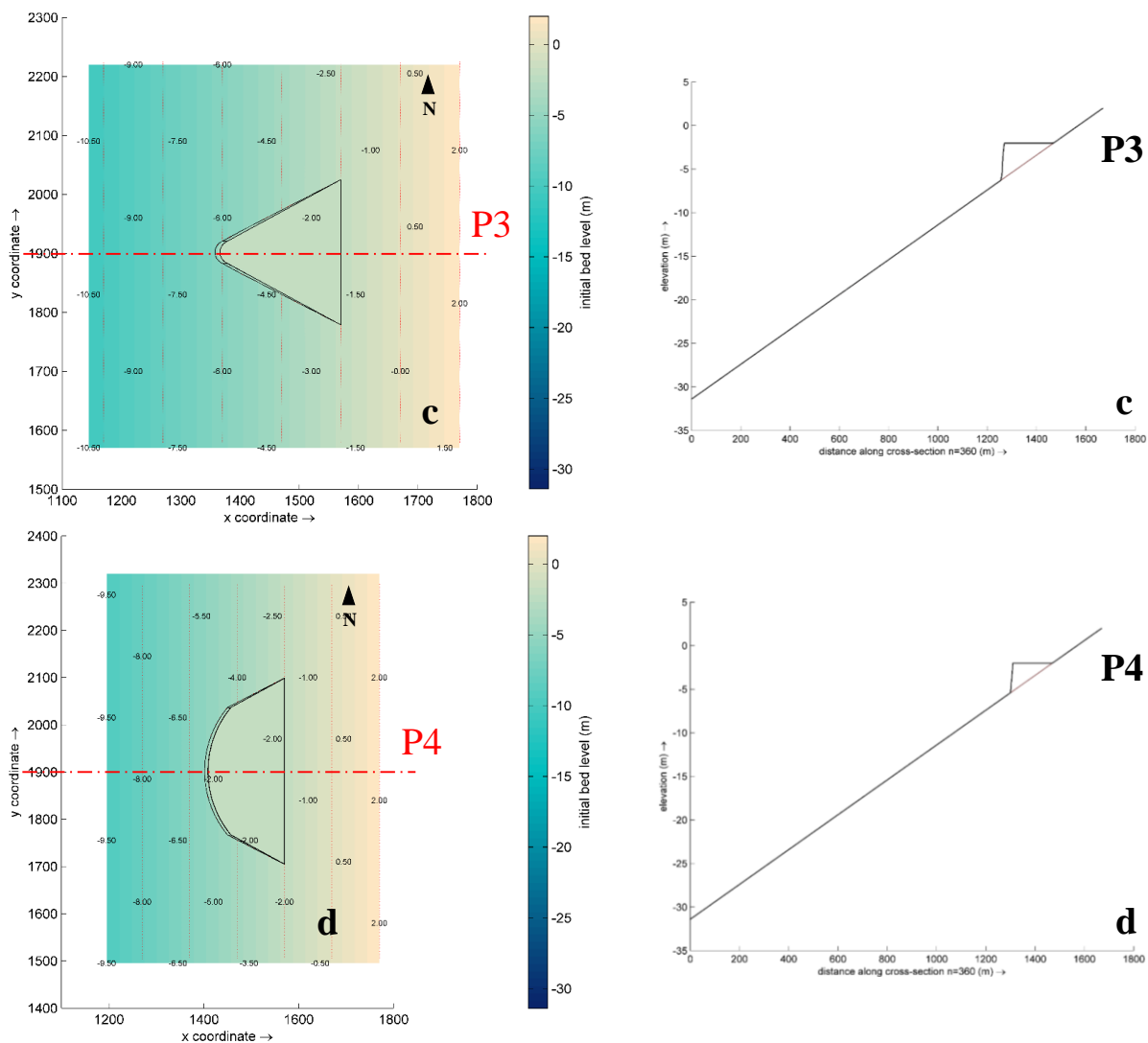
Figure 5.44: Bed level values around the structure (left) and cross section along the crest (right) for scenarios: a) RB3_S2; b) RB3_S4; c) RB3_S6; and d) RB3_S8.

Figure 5.45: Geometrical schematization for: a) RB3_S2; b) RB3_S4; c) RB3_S6; and d) RB3_S8.

Table 5.18: Structures characteristics for RB3_S2, RB3_S4, RB3_S6 and RB3_S8.

Characteristics	RB3_S2	RB3_S4	RB3_S6	RB3_S8
Length (m)	246.37	394.19	246.37	394.19
Width (m)	212.28	168.20	203.86	161.47
Slope	90° (wall)	90° (wall)	1:2	1:2
Max. height (m)	4.25	3.36	4.08	3.23
Crest level (m)	-2.0	-2.0	-2.0	-2.0
Distance to shoreline (m)	100.0	100.0	100.0	100.0
Volume (m³)	46 537.95	62 255.79	37 337.96	59 583.23

5.4.6.3 RB3_S9, RB3_S10 and RB3_S11

The third group assembles three structures with similar geometries, represented in Figure 5.46. All structures have the same slopes (1:10), however their position relatively to shoreline as well as their crest levels are different from each other. The major differences between them are: i) RB3_S9 (Figure 5.46a) is located 100 m offshore, while RB3_S10 (Figure 5.46b) and RB3_S11 (Figure 5.46c) are implanted on the beach; ii) RB3_S10 is the structure with the largest width, while RB3_S9 and RB3_S11 share the same width; and iii) RB3_S9 crest level is at -2.0 m (Figure 5.47a), while RB3_S10 (Figure 5.47b) and RB3_S11 (Figure 5.47c) have it at 0 m relatively to MSL. Similar to previous scenarios, in Figure 5.46, the left panel presents the initial bed level along the domain, while the right panel depicts the initial bed level variations between the structure and the RB3 (without any structure).
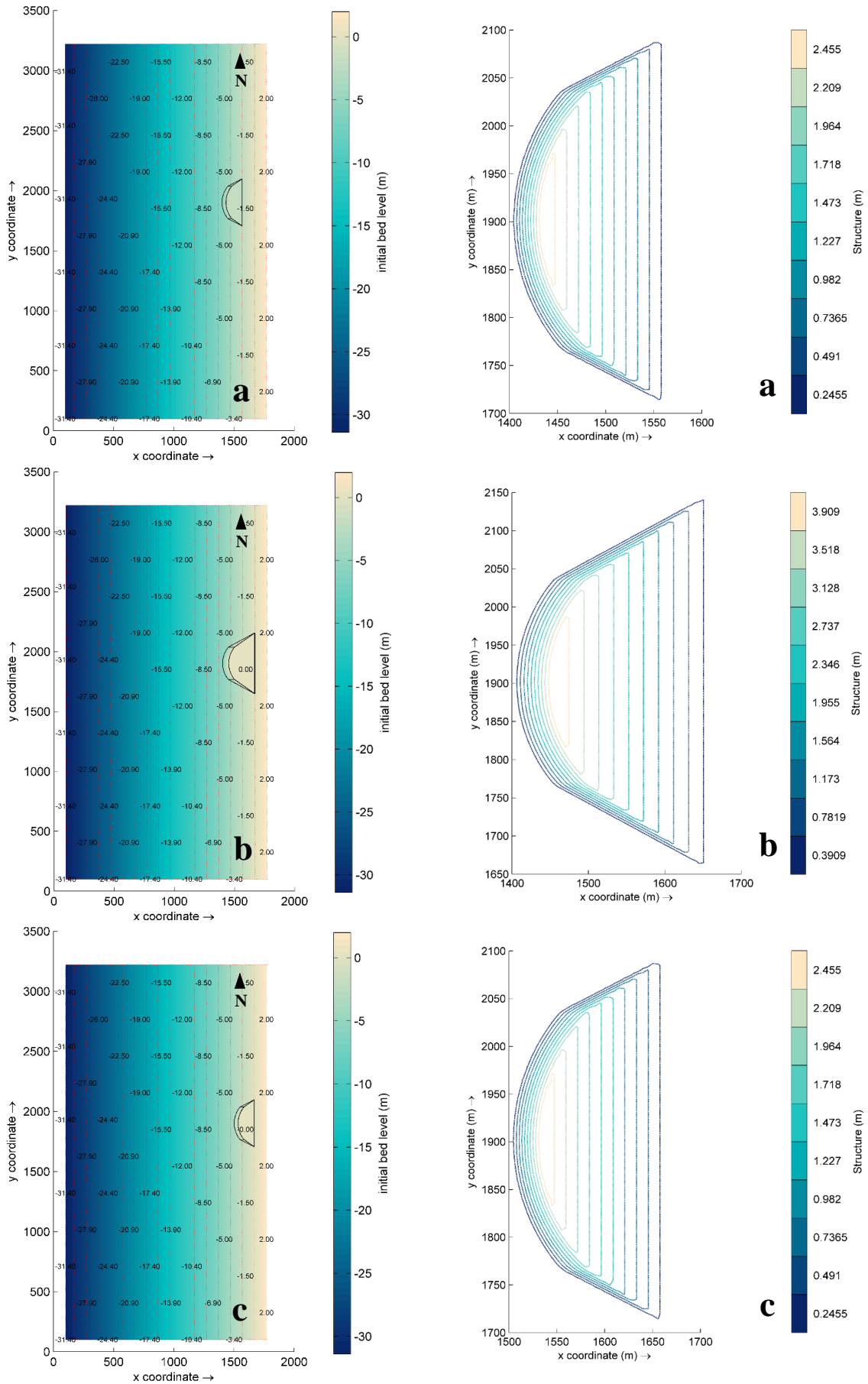
Figure 5.46: Bed level values (left) and variations (right) for scenarios: a) RB3_S9; b) RB3_S10; and c) RB3_S11.

In Figure 5.47, the left panel presents a more detailed representation of the structure in the domain, while the right panel depicts the cross section traced along the ledge of the structure (denominated as profiles, P). Regarding the volumes, RB3_S10 is the greatest (150K m^3) and RB3_S11 the smallest out of the three (49K m^3). Characteristics for each structure are detailed in Figure 5.48 and Table 5.19.
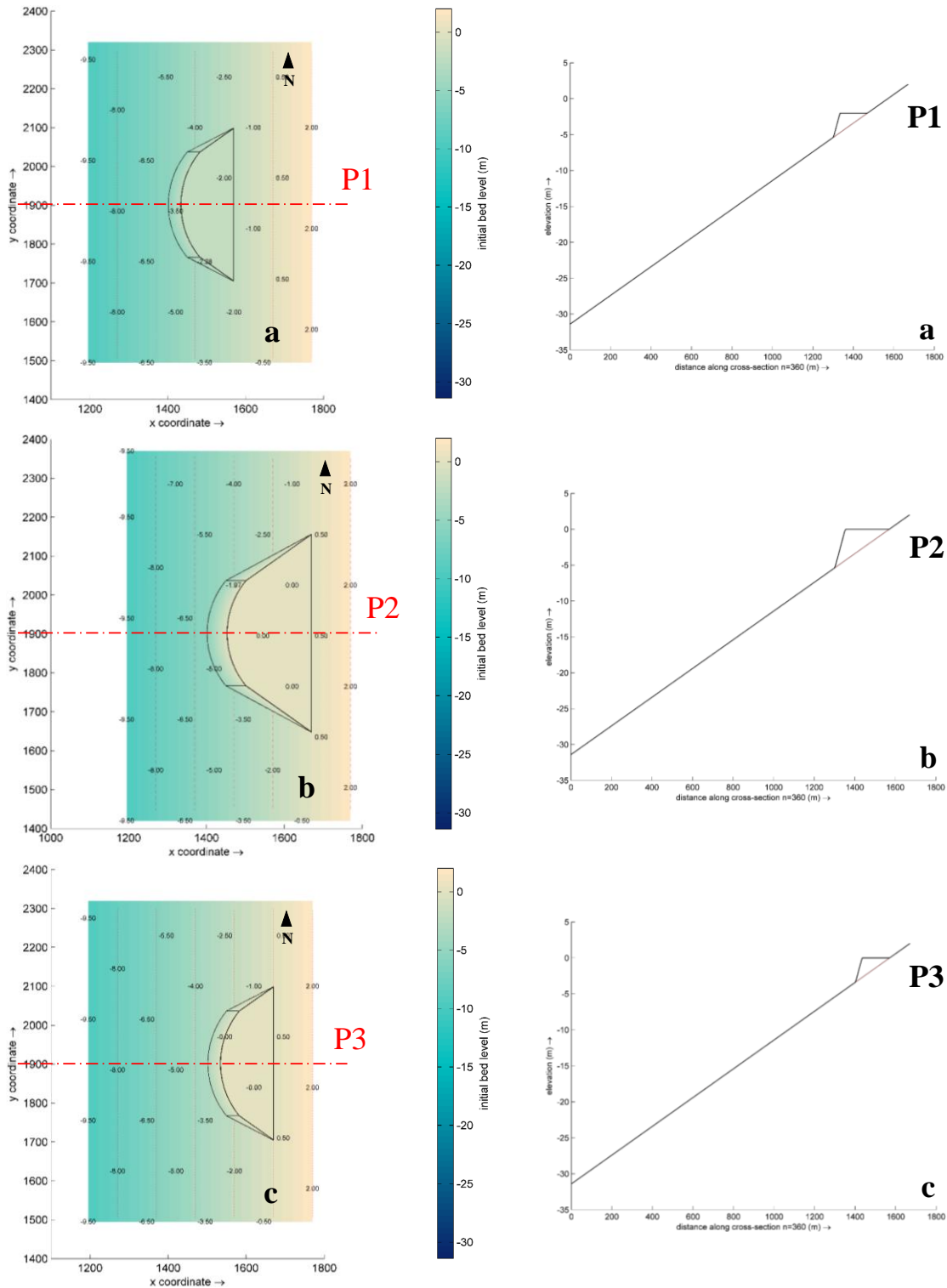
Figure 5.47: Bed level values around the structure (left) and cross section along the crest (right) for scenarios: a) RB3_S9; b) RB3_S10; and c) RB3_S11.
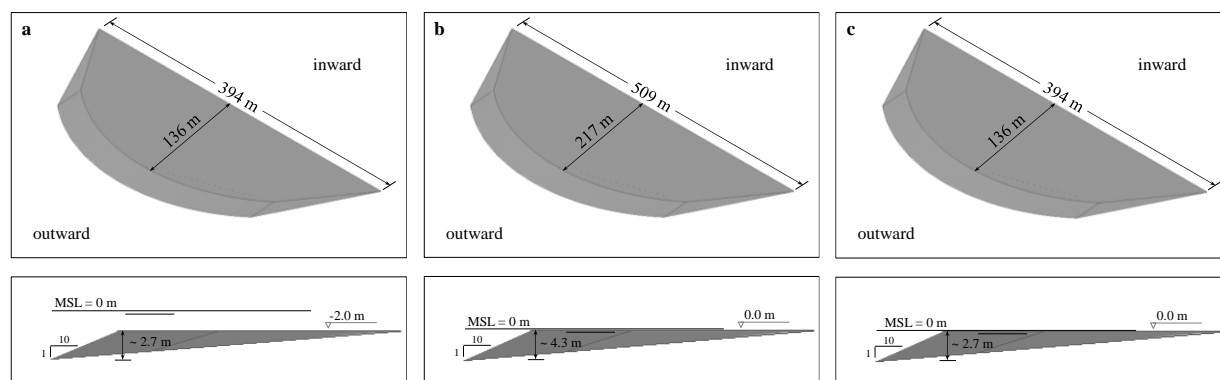
Figure 5.48: Geometrical schematization for: a) RB3_S9; b) RB3_S10; and c) RB3_S11.

Table 5.19: Structures characteristics for RB3_S9, RB3_S10 and RB3_S11.

Characteristics	RB3_S9	RB3_S10	RB3_S11
Length (m)	394.19	508.72	394.19
Width (m)	136.17	217.28	136.17
Slope	1:10	1:10	1:10
Max. height (m)	2.73	4.34	2.72
Crest level (m)	-2.0	0.0	0.0
Distance to shoreline (m)	100.0	0.0	0.0
Volume (m³)	49 059.81	149 944.64	48 929.77

5.4.6.4 RB3_S12, RB3_S13 and RB3_S14

The last assemble focuses on three groups of structures with similar geometries but with different locations relatively to shoreline, crest levels, as well as gaps widths (Figure 5.49). Despite all structures having the same 1:10 seaward slopes, the main characteristics that differ between them are: i) RB3_S12 (Figure 5.49a) and RB3_S14 (Figure 5.49c) are located 100 m offshore, while RB3_S13 (Figure 5.49b) is implanted on the aerial beach; RB3_S12 and RB3_S14 share the same width, while RB3_S13 is the structure with the largest width; iii) RB3_S12 (Figure 5.50a) and RB3_S14 (Figure 5.50c) share the same crest levels at -2.0 m, while RB3_S13 (Figure 5.50b) has its crest level at 0 m relatively to MSL; and iv) gaps between the structures are different for each group of structures.

The gaps width can be calculated recurring to the DEFRA (2010) guidance for outline design of nearshore structures. Although this is specific for detached breakwaters, it can serve as basis to estimate adequate dimensions for the current structures geometries. Accordingly, the gaps width can be estimated based on the maximum shoreline erosion allowed, which can be determined by using existing design curves (Vieira, 2014). The maximum shoreline erosion is given by Equation (5.1):

$$max. shoreline\ erosion = G/X \tag{5.1}$$

where G is the gap width between structures, and X is the distance from the beach to the centre line of the structure.
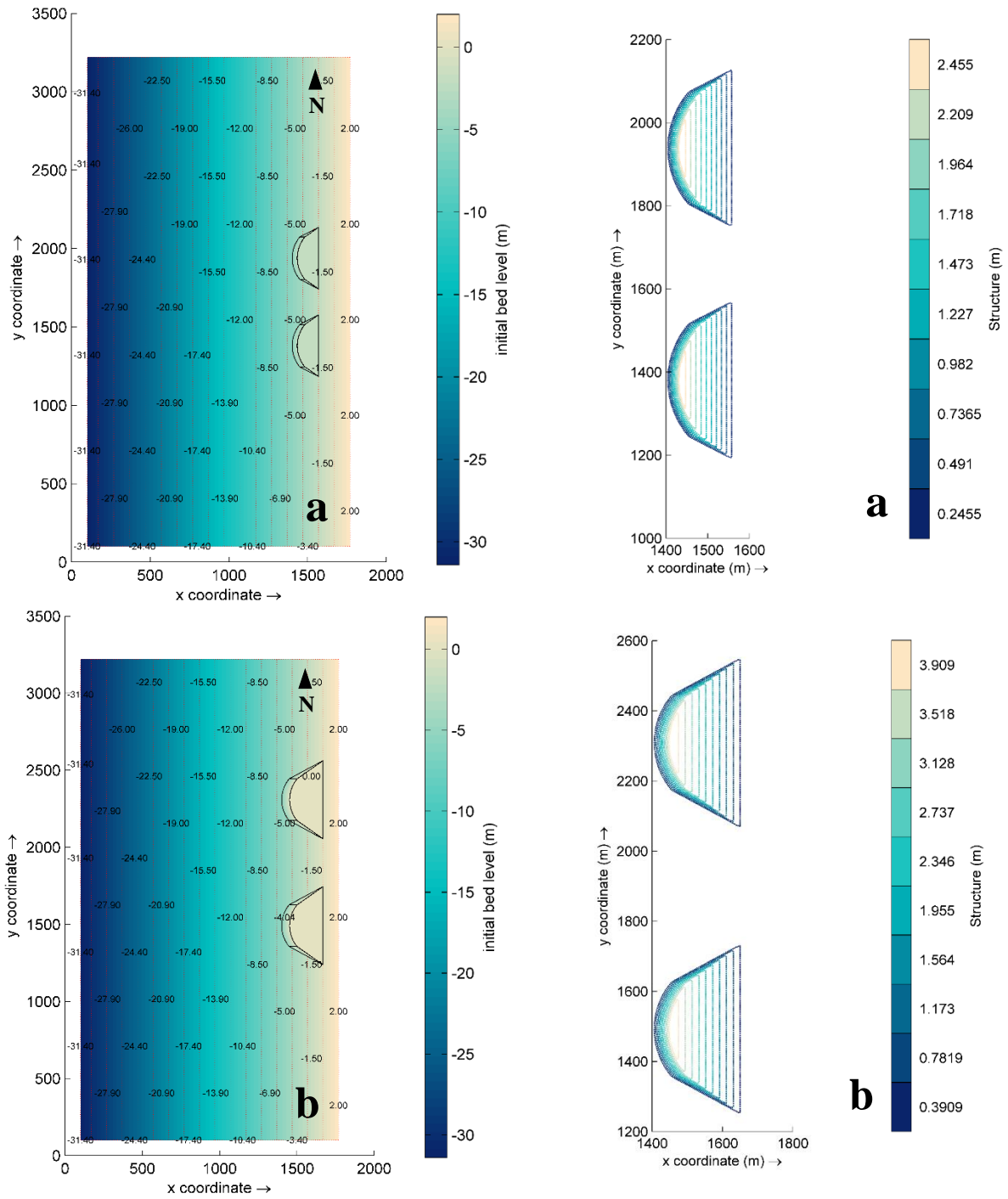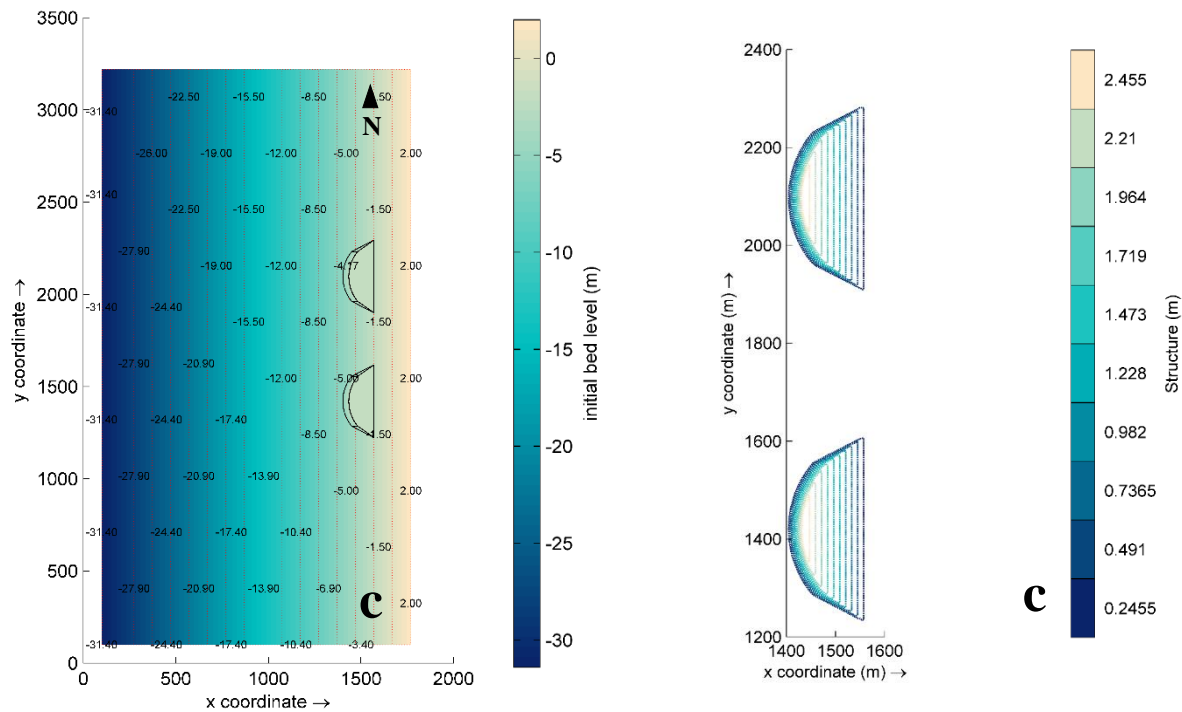
Figure 5.49: Bed level values (left) and variations (right) for scenarios: a) RB3_S12; b) RB3_S13; and c) RB3_S14.

Due to the structures significant dimensions and their non-symmetry along the y-axis (contrary to detached breakwaters), it has been decided that, for this case, X should be measured as the distance from the beach to the ledge of the structure. The X value is then determined by adding the width of the structure to the distance from the structure to shoreline.

An adequate gap width is important to avoid large erosion areas. For a "no erosion" condition, the selected maximum shoreline erosion is 0.7, while for a "possible erosion" and a "certain erosion" the selected values are 1.2 and 1.4, respectively (Vieira, 2014). Thus, the RB3_S12, RB3_S13 and RB3_S14 gap widths are 165.3 m [(100+136.17) x 0.7], 304.2 m [(0+217.28) x 1.4], and 283.4 m [(100+136.16) x 1.2], respectively (Table 5.20).

Similar to previous scenarios, in Figure 5.49, the left panel presents the initial bed level along the domain, while the right panel depicts the initial bed level variations between the group of structures and the RB3 (without any structure). In Figure 5.50, the left panel presents a more detailed representation of the group of structures in the domain, while the right panel depicts the cross section traced along the ledge of the north structure (denominated as profiles, P).

Regarding the volumes, RB3_S13 is the greatest (300K m³), while both RB3_S12 and RB3_S14 have 98K m³. All summarized characteristics for each structure are detailed in Figure 5.51 and Table 5.20.
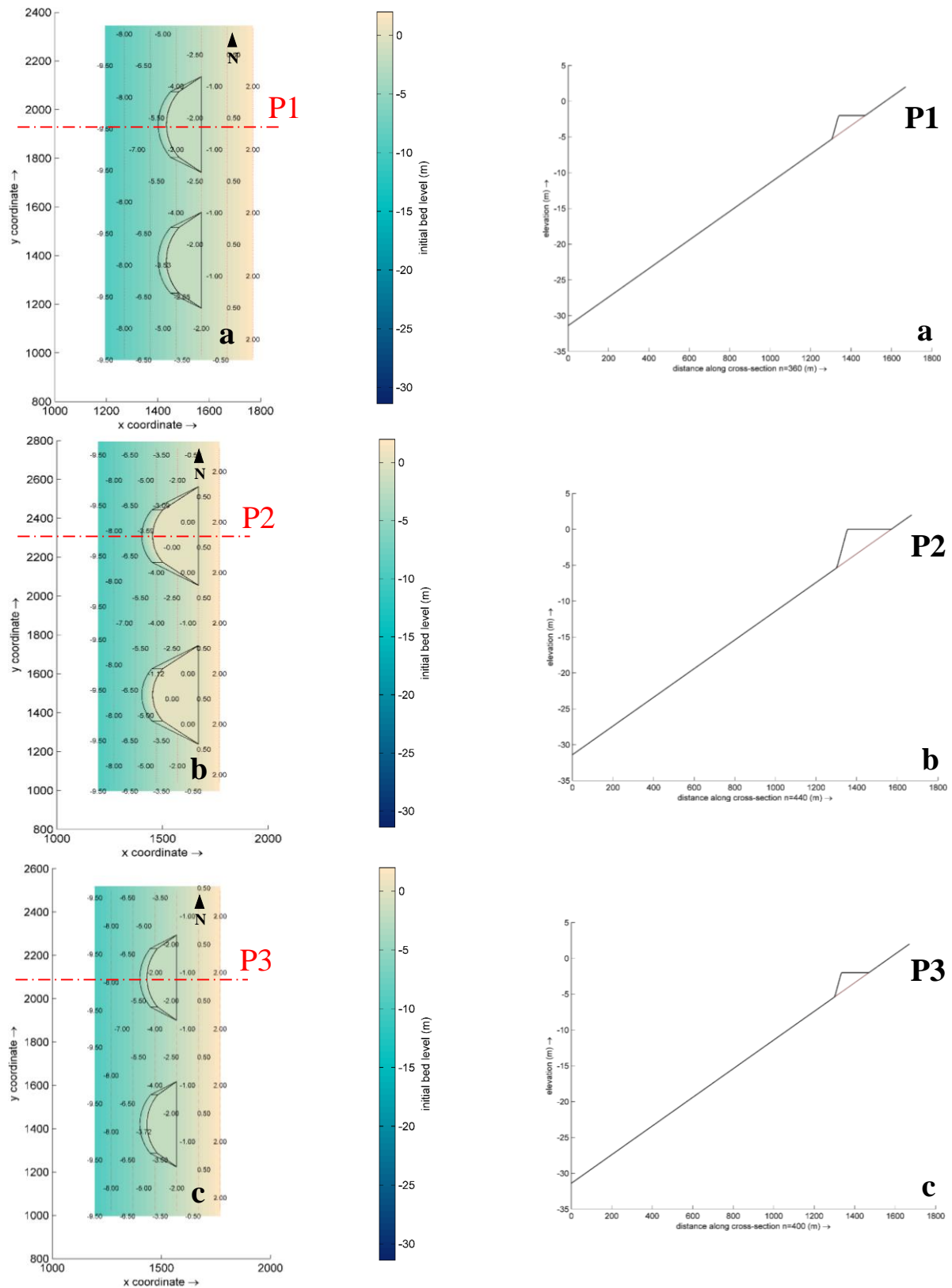
Figure 5.50: Bed level values around the structure (left) and cross section along the crest (right) for scenarios: a) RB3_S12; b) RB3_S13; and c) RB3_S14.
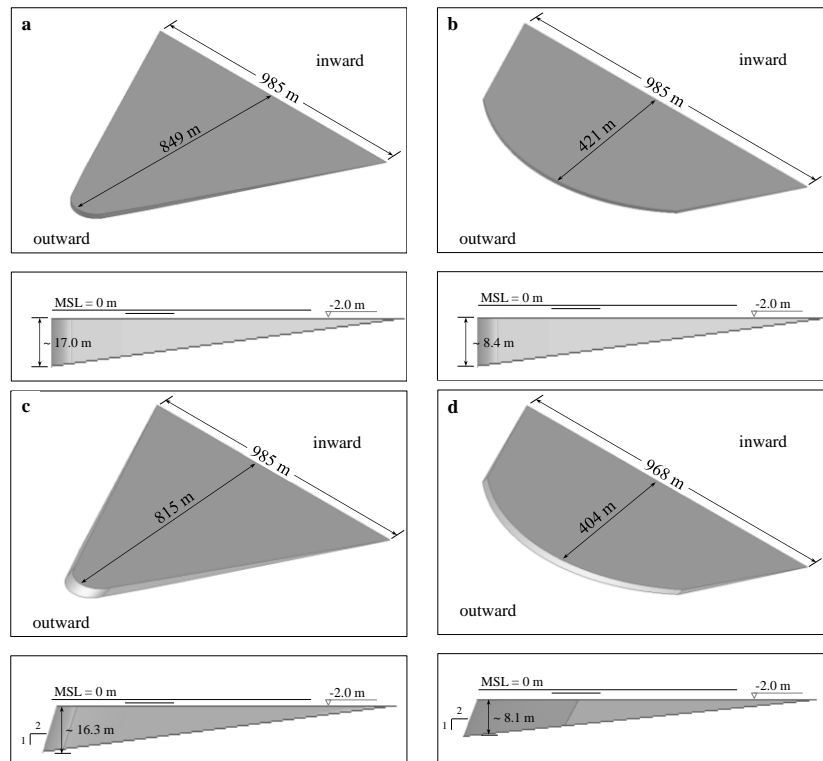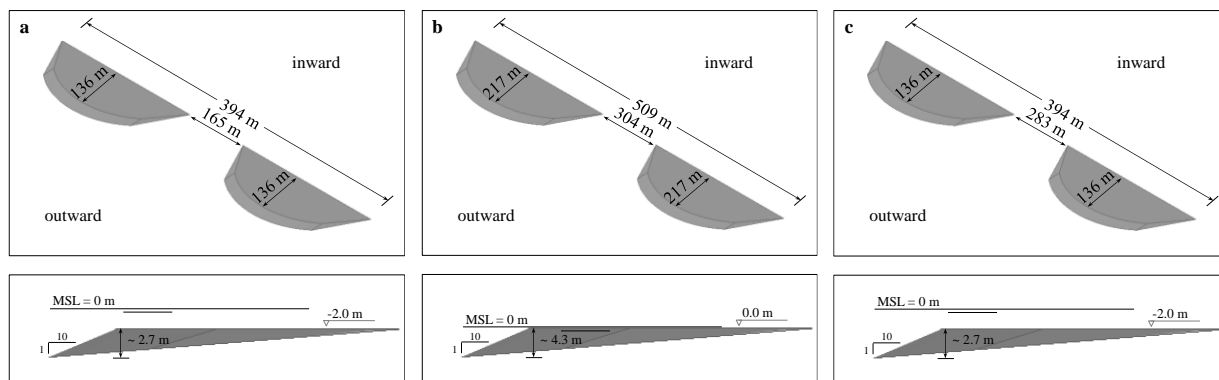
Figure 5.51: Geometrical schematization for: a) RB3_S12; b) RB3_S13; and c) RB3_S14.

Table 5.20: Structures characteristics for RB3_S12, RB3_S13 and RB3_S14.

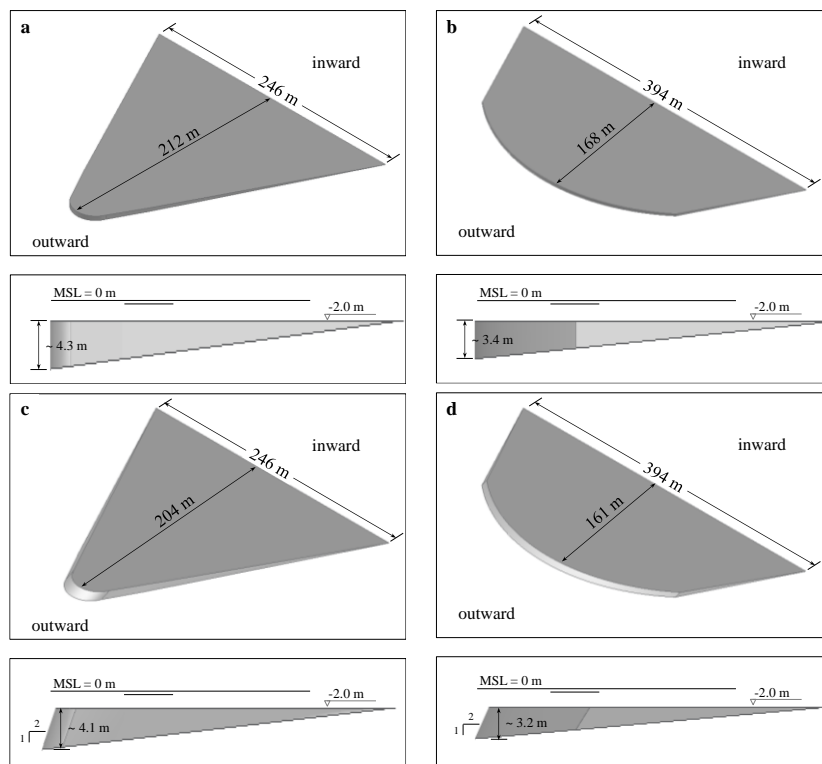| Characteristics	RB3_S12	RB3_S13	RB3_S14
Length (m)	394.19	508.72	394.19
Width (m)	136.17	217.28	136.16
Slope	1:10	1:10	1:10
Max. height (m)	2.73	4.34	2.73
Crest level (m)	-2.0	0.0	-2.0
Gap width (m)	165.3	304.2	283.4
Distance to shoreline (m)	100.0	0.0	100.0
Volume (m³)	98 118.78	299 916.95	98 135.69

5.4.6.5 Hydrodynamics. Results and discussion

In this section, hydrodynamics results for the RB3 structures scenarios (RB3_S1, RB3_S3, RB3_S5 and RB3_S7; RB3_S2, RB3_S4, RB3_S6 and RB3_S8; RB3_S9, RB3_S10 and RB3_S11; and RB3_S12, RB3_S13 and RB3_S14) are presented and analysed based on the main outcomes and differences between them.

Figures 5.52, 5.53, 5.54 and 5.55 present the decrease of significant wave heights from offshore to shoreline (wave energy dissipation) and their mean directions based on the structures shapes created for each scenario. The wave climate conditions are identical to all scenarios. Figures 5.52a, 5.52b, 5.52c and 5.52d present results for RB3_S1, RB3_S3, RB3_S5 and RB3_S7, respectively. Figures 5.53a, 5.53b, 5.53c and 5.53d depict results for RB3_S2, RB3_S4, RB3_S6 and RB3_S8, respectively. Figures 5.54a, 5.54b and 5.54c depict results for RB3_S9, RB3_S10 and RB3_S11, respectively. Figures 5.55a, 5.55b and 5.55c, present results for RB3_S12, RB3_S13 and RB3_S14, respectively. In each Figure 5.52, 5.53, 5.54 and 5.55, the left panel presents results for the entire domain, while the right panel depicts results that are more detailed around the structures. All structures have a detached shape from the shoreline, except for RB3_S10, RB3_S11 and RB3_S13.

In the first group of structures (Figure 5.52), results for significant wave heights are very similar regardless of their types. Figure 5.52 presents two scenarios with wall-type structures (RB3_S1 and RB3_S3, in Figures 5.52a, and 5.52b) and two scenarios with slope-type structures (RB3_S5 and RB3_S7, in Figures 5.52c, and 5.52d). The main results difference between RB3_S1 and RB3_S5, and RB3_S3 and RB3_S7 lies in the smoother decreasing of significant wave heights in the wave-breaking region for scenarios RB3_S5 and RB3_S7 due to their 1:2 slope. The wave shoaling in the wall-type structures has an abrupt effect, while in slope-type structures the wave shoaling is more extensive. The waves breaking starts at positions 780 m for RB3_S1 and RB3_S5, and at 1180 m for RB3_S3 and RB3_S7.

The submerged platform at -2.0 m with a 100 m shoreline detachment proves to be a good strategy to reduce significant wave heights, since all scenarios present significant wave height values with a mean of 1.0 m on the platform, and a mean of 0.8 m near shoreline.

In terms of the reversal of longitudinal drift, the RB3_S3 and RB3_S7 scenarios present a more evident rotation of the significant wave height mean direction vectors along the head of the structures, due to their wider and more round shape. Downdrift, the four scenarios present similar results along the slopes/walls length and the domain resolution proves to be appropriate for the results analysis.

Since results for the wave energy dissipation and the reversal of longitudinal drift are favourable, scenarios with less bulky structures are necessary to avoid high construction costs.
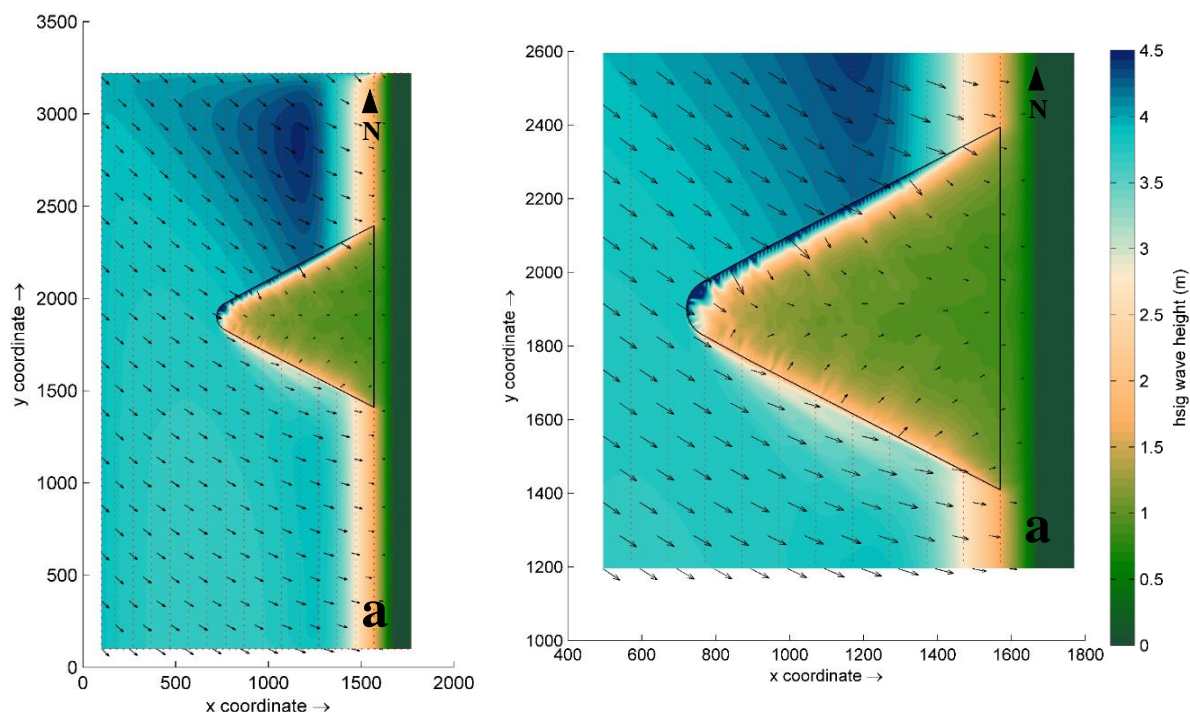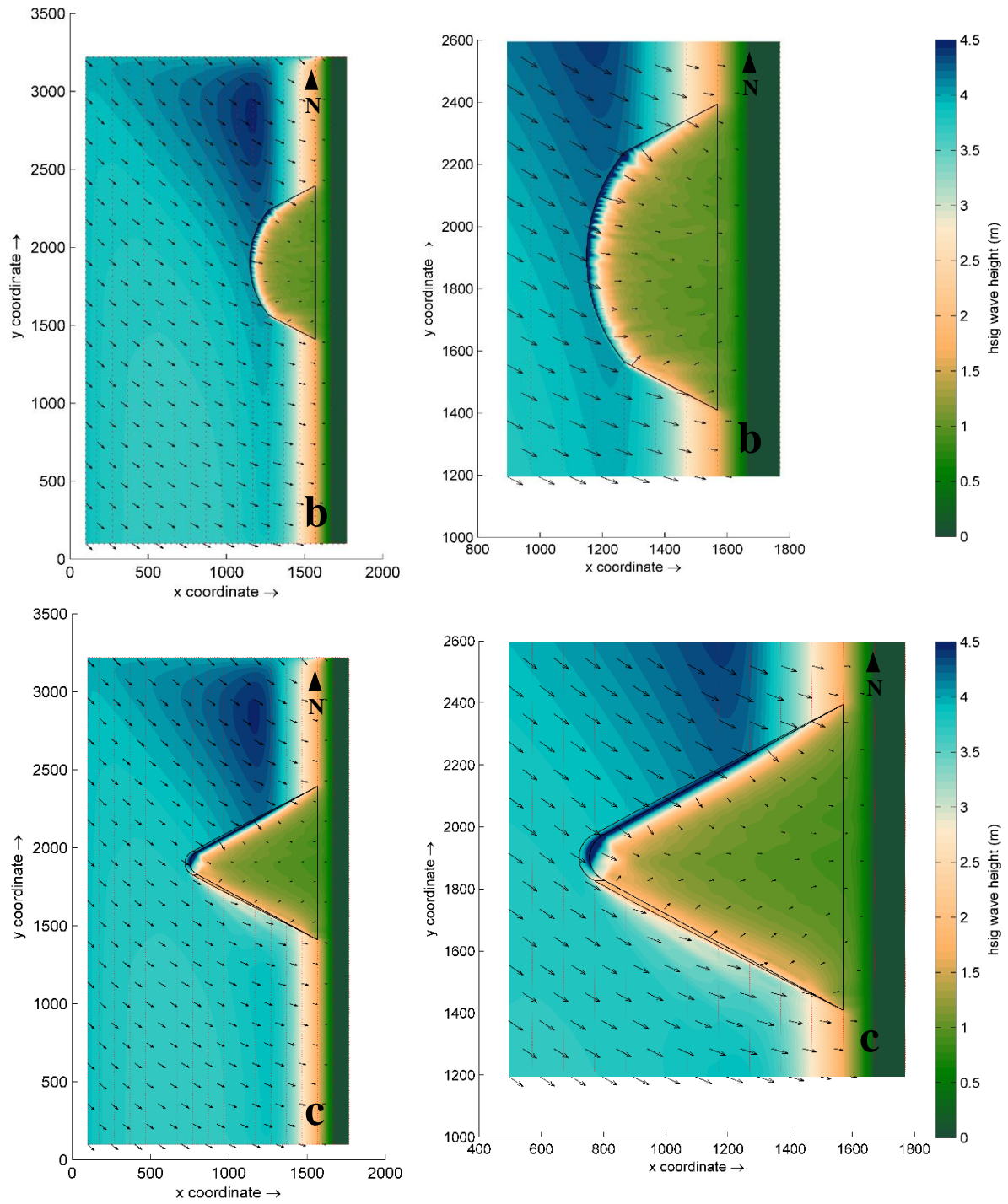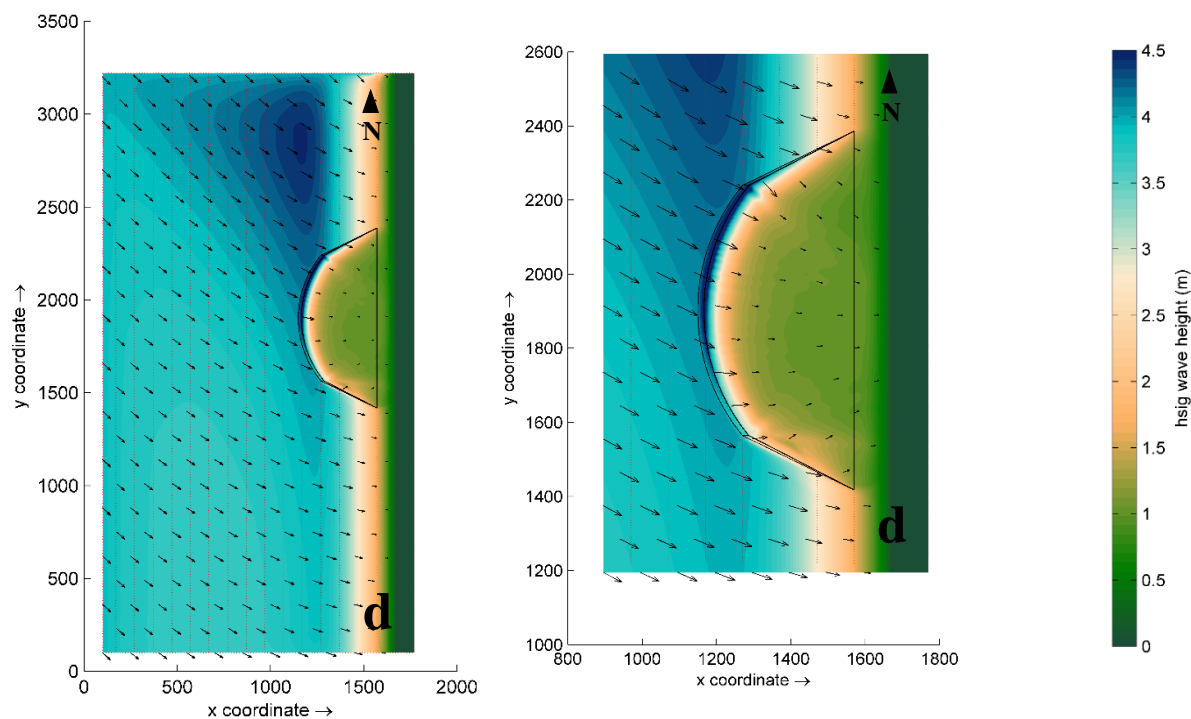
Figure 5.52: H_s along the domain (left) and detailed around the structure (right) for scenarios: a) RB3_S1; b) RB3_S3; c) RB3_S5; and d) RB3_S7.

The second group of structures (Figure 5.53) assembles four structures with geometric shapes similar to those presented in Figure 5.52; however, with significantly smaller dimensions. Scenarios RB3_S2 (Figure 5.53a) and RB3_S4 (Figure 5.53b) are wall-type structures, while RB3_S6 (Figure 5.53c) and RB3_S8 (Figure 5.53d) are slope-type structures with a 1:2 slope. In this group of structures, it is also noticeable that regardless of their type, results for significant wave heights are very similar.

In terms of the significant wave heights decreasing in the wave-breaking region and the wave shoaling effect, scenarios RB3_S6 and RB3_S8 present a smoother decreasing with a slightly more extensive wave shoaling due to their slopes. The waves breaking starts at positions 1400 m for RB3_S2 and RB3_S6, and at 1410 m for RB3_S4 and RB3_S8.

Due to the similar shapes, patterns for wave energy dissipation results presented in Figure 5.53 are similar to those previously presented in Figure 5.52. Even though in Figure 5.53 significant wave heights results are slightly higher in the shadow zones, difference is almost negligible, as results do not differ much in both cases for all scenarios ($H_s \approx 1.3$ m *vs.* $H_s \approx 1.0$ m on the platform; $H_s \approx 0.9$ m *vs.* $H_s \approx 0.8$ m near shoreline). Thus, results indicate that these structures characteristics also provide good wave energy dissipation.

Relatively to the reversal of longitudinal drift, the wider and more round shapes (RB3_S4 and RB3_S8) present a more evident rotation of the significant wave height mean direction vectors along the head of the structures. Downdrift, the four scenarios also present similar results along the slopes/walls length. Overall, in both groups of structures results indicate that a submerged platform at -2.0 m with a 100 m shoreline detachment is a good solution regardless of the structure size. In order to reduce even more the structures volumes and the wave shoaling, smoother slopes should be tested.
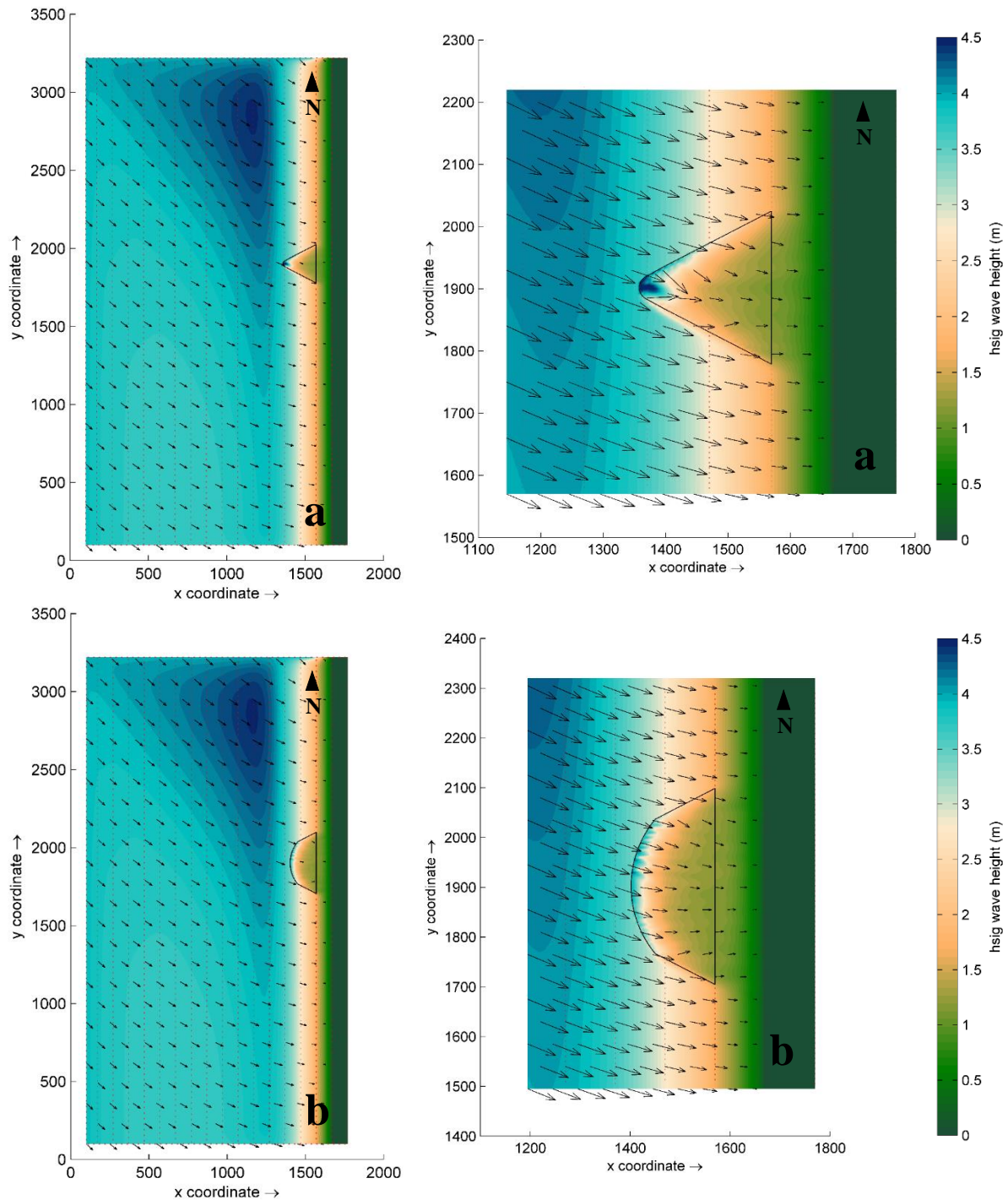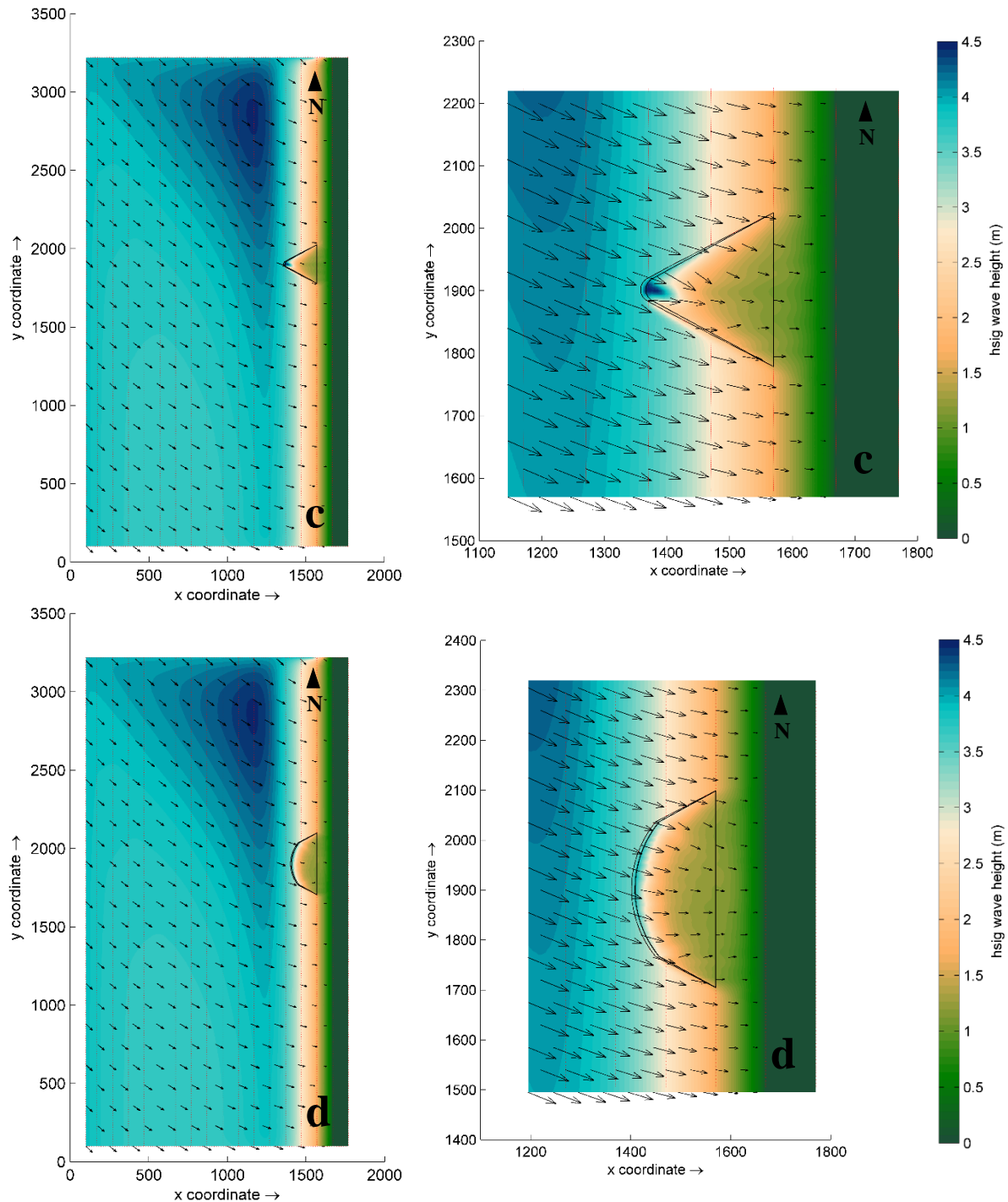
Figure 5.53: H$_s$ along the domain (left) and detailed around the structure (right) for scenarios: a) RB3_S2; b) RB3_S4; c) RB3_S6; and d) RB3_S8.

Figure 5.54 groups three structures with geometries similar to RB3_S8 except with a 1:10 slope and/or with different distances from shoreline and crest levels. Results for RB3_S9 (Figure 5.54a), RB3_S10 (Figure 5.54b) and RB3_S11 (Figure 5.54c) demonstrate that the 1:10 slope does not cause wave shoaling before the structure, and that, out of the three scenarios, RB3_S9 is the one that presents similar results for significant wave heights and mean direction vectors orientations to those depicted in

RB3_S8. On the -2.0 m platform, significant wave heights are approximately 1.3 m and 0.9 m near shoreline.

Contrary to the results depicted in RB3_S9, scenarios RB3_S10 and RB3_S11 present null values on the platforms area, which indicate that at this location significant wave heights are lower than the crest levels (0 m) and no waves transmission over the structures occurs (wave-overtopping). However, these results should be analysed very cautiously, since SWAN does not present reliable results in shallow waters. In fact, in this area, a slight water level due to wave-overtopping may exist since significant wave heights before the structures crests are relatively high (3.0 m for RB3_S10 and 2.0 m for RB3_S11) and waves decreasing is quite abrupt for a 1:10 slope. Nevertheless, the crest levels provide the structures with an emerged structure similar behaviour and the entire platform area guarantees great protection on the adjacent coastal zone for a 0 m tidal level. In addition, crest levels in RB3_S10 and RB3_S11 contribute to the structure environmental visual impact concern because the structures are cyclically emerged and submerged depending on the tidal level.

Consequently, when compared to completely submerged structures, RB3_S10 and RB3_S11 not only are adequate for protecting the shoreline while being visually appealing, but they also stand out for safeguarding tidal variations caused by storm surges and the mean sea level rise due to climate changes. These structures thus become relevant alternative solutions for coastal protection, due to their great wave energy dissipation.
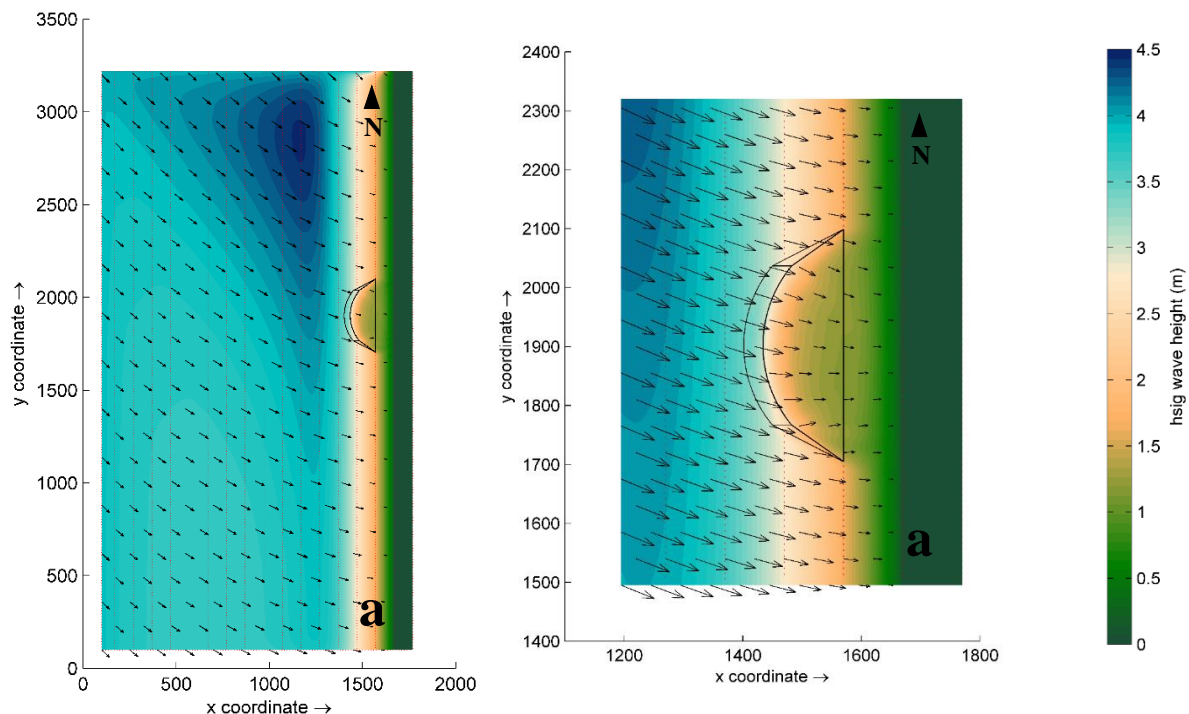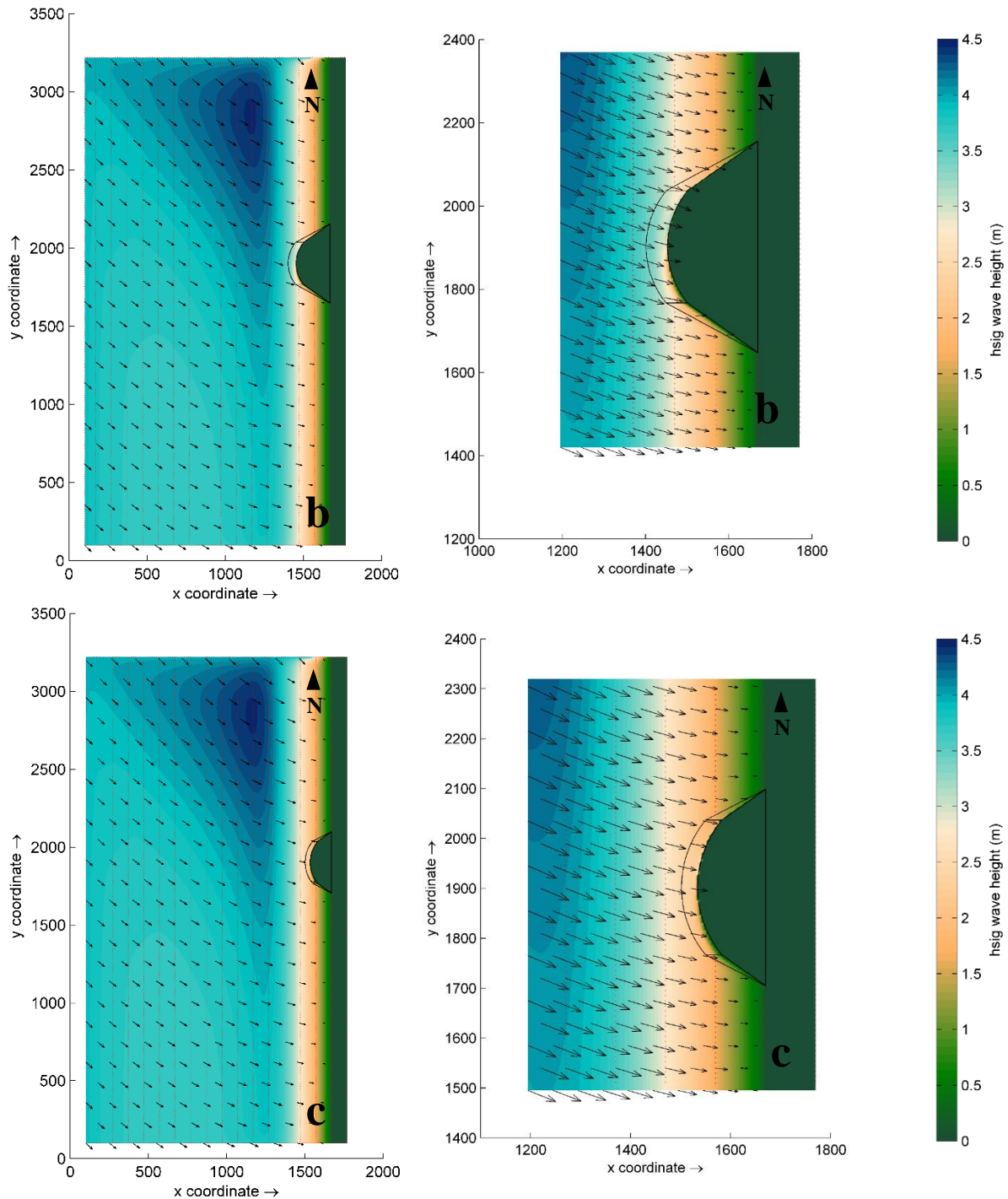
Figure 5.54: H$_s$ along the domain (left) and detailed around the structure (right) for scenarios: a) RB3_S9; b) RB3_S10; and c) RB3_S11.

Although the main difference between RB3_S10 and RB3_S11 relates to the platform width, SWAN hydrodynamics results do not show any differences between them. However, for better understanding their behaviour, these solutions will have to be analysed for different tidal levels through morphodynamics.

In terms of the reversal of longitudinal drift, all scenarios present a rotation of the significant wave height mean direction vectors along the head of the structures.

Figure 5.55 presents results for three scenarios for groups of structures. The structures depicted in RB3_S12 (Figure 5.55a) and RB3_S14 (Figure 5.55c) have similar geometric characteristics to RB3_S9, while structures in RB3_S13 (Figure 5.55b) have similarities to RB3_S10. The main difference between RB3_S12 and RB3_S14 lies in the gap between the structures, while the main differences between them and RB3_S13 are their locations relatively to shoreline, crest levels, and gaps widths.

Due to the geometric similarities, in scenarios RB3_S12, RB3_S13 and RB3_S14 hydrodynamics results are similar to those previously presented (RB3_S9 and RB3_S10), regardless of the gaps widths. This indicates that in terms of significant wave height decreasing and the reversal of longitudinal drift, the number of structures does not affect the hydrodynamics outcomes in SWAN. However, these solutions will have to be analysed for morphodynamics, in order to understand better their differences.
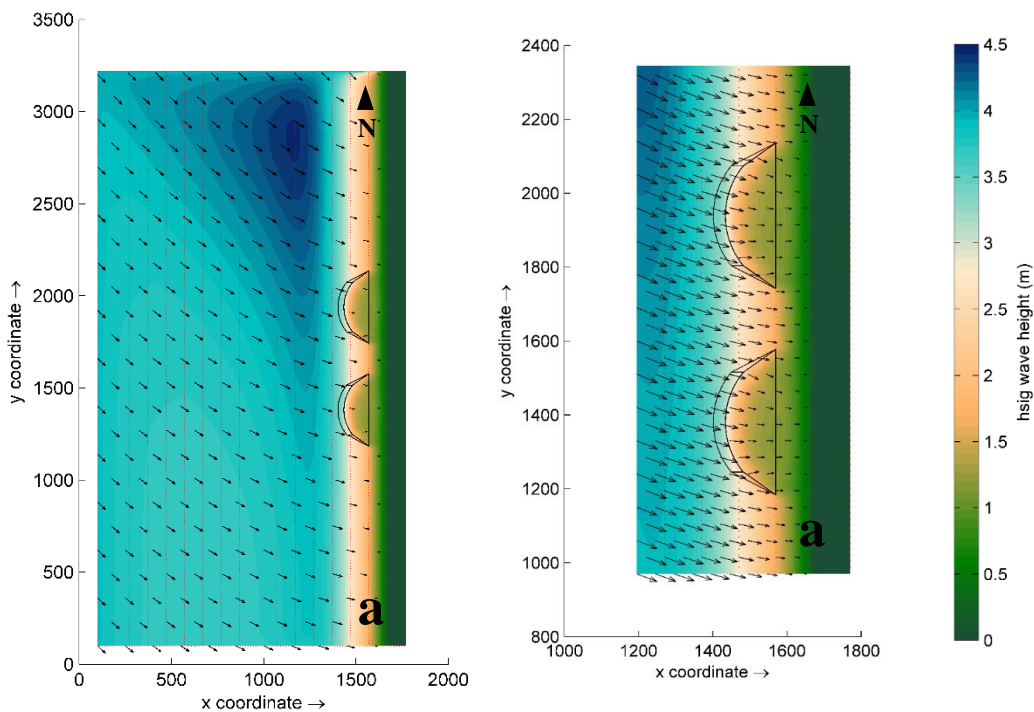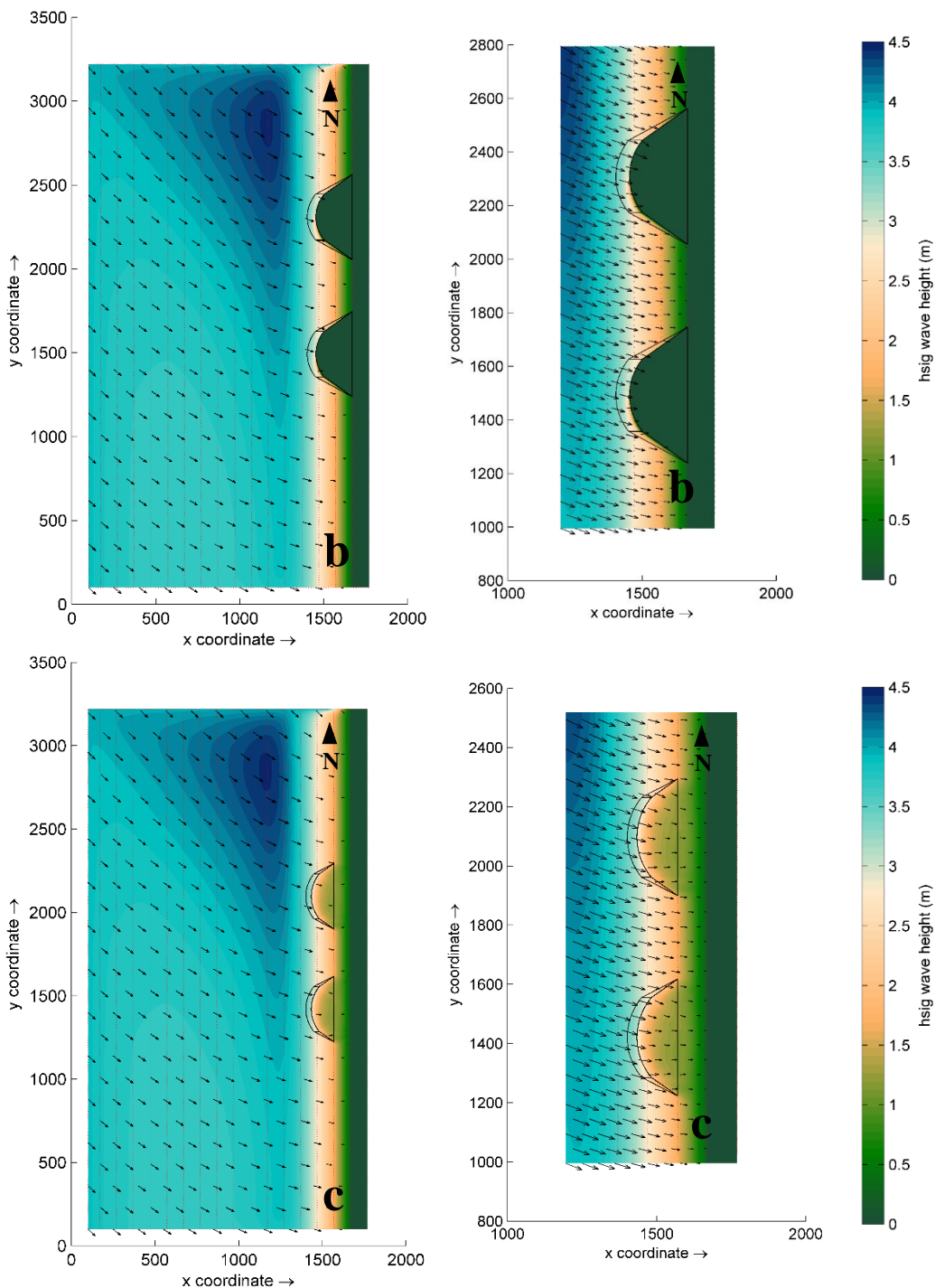
Figure 5.55: H$_s$ along the domain (left) and detailed around the structure (right) for scenarios: a) RB3_S12; b) RB3_S13; and c) RB3_S14.

5.4.7 Parametric analysis and RB3_Groin scenario

Although the most favourable hydrodynamics results for the reversal of longitudinal drift and wave energy dissipation for the smallest structures were achieved for RB3_S10 and RB3_S11, the best morphodynamics results in studying these structures were obtained for RB3_S10 scenario, as it will be

presented in Section 5.4.8.6. Consequently, the parametric analysis was performed for the hydrodynamics behaviour under the scenario RB3_S10.

This analysis considered four categories that intend to analyse the influence of: i) wave climate directions; ii) tidal levels; iii) sand dimensions; and iv) an intense storm. In the following Sections, the reversal of longitudinal drift and the decreasing of significant wave heights are analysed for three groups. As the sediments characteristics only affect the sediments transport (morphodynamics), the third group (sand dimensions) is analysed in Section 5.4.8.6.

Table 5.21 presents the reference bathymetry scenarios without structure (first column) and the structures scenarios (second column) studied. All conditions are summarized in the third column. The first group aims to analyse the influence of southwest (RB3_SW and RB3_SW_S10) and west (RB3_W and RB3_W_S10) wave climate directions with 225° and 270°, respectively. The second group assembles the analysis for high tide (RB3_H and RB3_H_S10) with +2 m and low tide (RB3_L and RB3_L_S10) with -2.0 m, relatively to MSL. The third group focuses on the influence of coarse (RB3_C and RB3_C_S10) and medium (RB3_M and RB3_M_S10) sand dimensions with D_{50} = 1.0 mm and D_{90} = 1.7 mm for medium sand, and D_{50} = 3.6 mm and D_{90} = 4.6 mm for coarse sand. Based on the depth criterion mentioned in Section 5.4 (Figure 5.13 in a black dotted line), the fourth group tests the influence of the selected structure under an intense storm (RB3_Storm10 and RB3_Storm10_S10) of H_s = 10 m. The adopted T_p of 19 s is retrieved from the Iberian_HP scenario results.

For the high tide and storm scenarios, the right boundary has to be increased to a maximum coastal elevation of +4 m (Figure 5.56). This allows a sound analysis of the hydro- and morphodynamics' influence on the beach, since the tidal level is set to +2 m and the H_s will affect a more considerable beach area. The maximum offshore depth and the beach slope remain with the same characteristics.

Table 5.21: RB3 scenarios: parametric analysis.

RB3 (334 × 624)		
Reference Bathymetry	**Structures**	**Conditions**
RB3_SW	RB3_SW_S10	Wave climate direction = 225°
RB3_W	RB3_W_S10	Wave climate direction = 270°
RB3_H	RB3_H_S10	High tide = +2 m
RB3_L	RB3_L_S10	Low tide = -2 m
RB3_C	RB3_C_S10	D_{50} = 3.6 mm | D_{90} = 4.6 mm
RB3_M	RB3_M_S10	D_{50} = 1.0 mm | D_{90} = 1.7 mm
RB3_Storm10	RB3_Storm10_S10	H_s = 10 m | T_p = 19 s
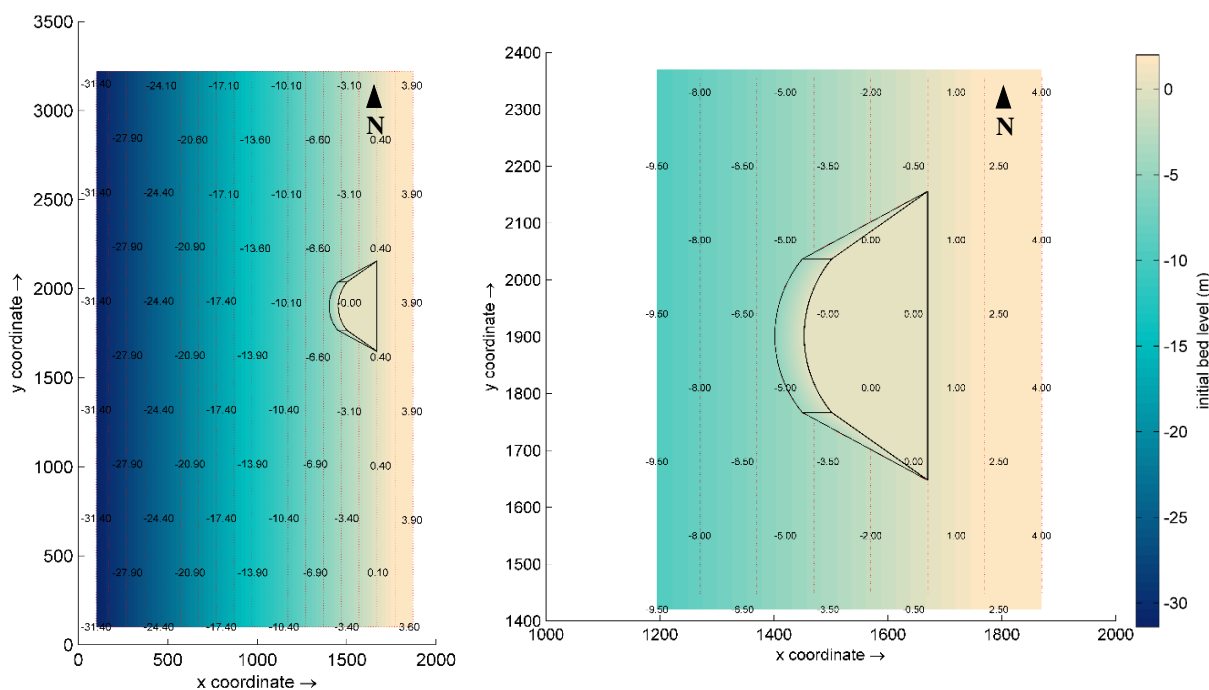
Figure 5.56: Bed level values along the domain (left) and detailed around the structure (right) for RB3_H_S10 and RB3_Storm10_S10 scenarios.

Similar to groins, RB3_S10 is a structure perpendicularly implanted on shoreline. In order to compare results on their individual influence on hydro- and morphodynamics, numerical simulations for a traditional groin (Table 5.22) are conducted.

The groin geometry (RB3_Groin), represented in Figure 5.57, is characterized by a constant crest width of 10 m with a crest level at +4 m relatively to MSL. The groin has a wider head offshore and a narrower head on the shoreline due to the constant slope of 1:2.

Similar to previous scenarios, in Figure 5.57, the left panel presents the initial bed level along the domain, while the right panel depicts the initial bed level variations between the groin and the RB3 (without any structure). In Figure 5.58, the left panel presents a more detailed representation of the groin in the domain, while the right panel depicts the cross section traced along the groin centre line (denominated as profile, P).

Regarding the volume, RB3_Groin has 33K m³, which indicates a significantly less volume than the RB3_S10 (150K m³).

Figures 5.59a and 5.59b, and Table 5.23 present a schematization of the RB3_S10 scenario under low tide (RB3_L_S10) and high tide (RB3_H_S10).

All summarized groin characteristics are detailed in Figure 5.59c and Table 5.23.

Table 5.22: RB3 scenario: Groin.

RB3 (334 × 624)		
Structure		
RB3_Groin		
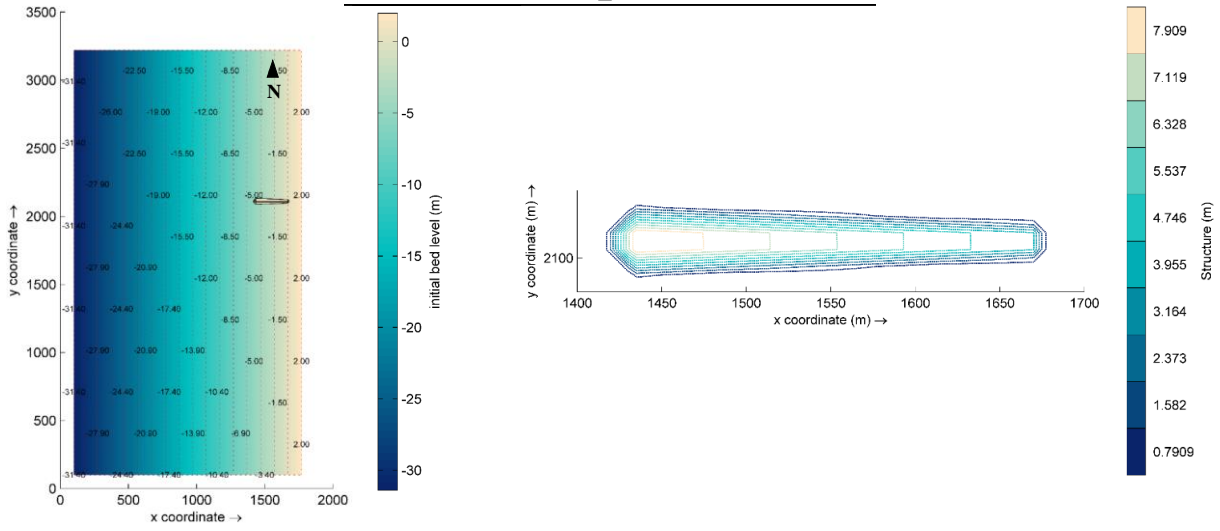
Figure 5.57: Bed level values (left) and variations (right) for RB3_Groin scenario.
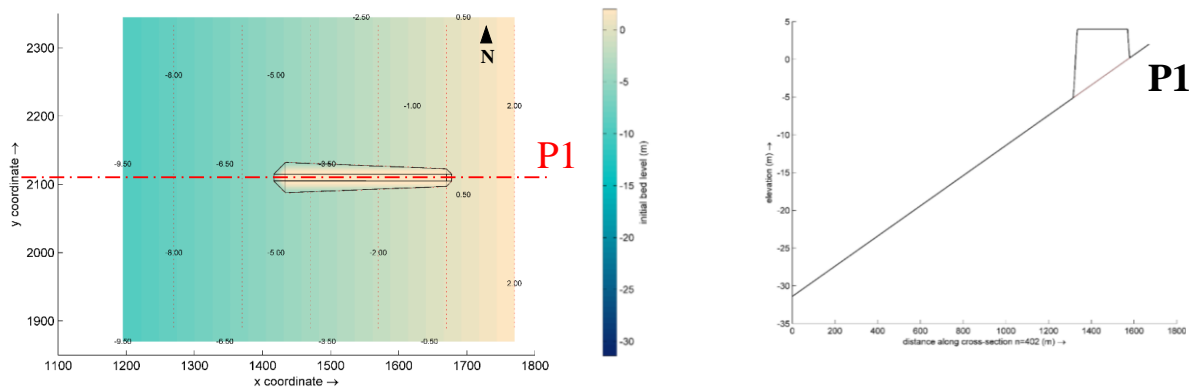
Figure 5.58: Bed level values around the structure (left) and cross section along the crest (right) for RB3_Groin scenario.
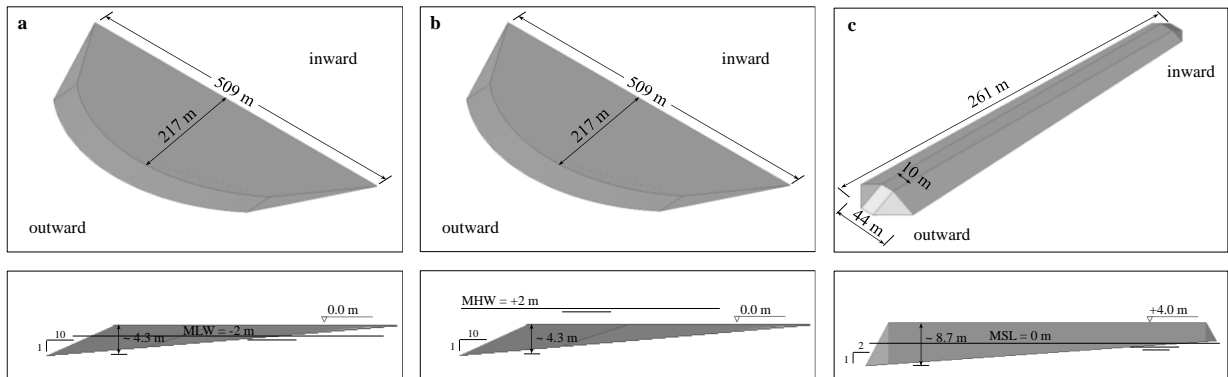
Figure 5.59: Geometrical schematization for: a) RB3_L_S10; b) RB3_H_S10; and c) RB3_Groin.

Table 5.23: Structures characteristics for RB3_L_S10, RB3_H_S10 and RB3_Groin.

Characteristics	RB3_L_S10	RB3_H_S10	RB3_Groin
Length (m)	508.72	508.72	261.29
Crest width (m)	217.28	217.28	10.0
Crest level (m)	0.0	0.0	+4.0
Width (m)	–	–	44.25 (offshore) ; 25.75 (nearshore)
Slope	1:10	1:10	1:2
Max. height (m)	4.34	4.34	8.72
Tidal level (m)	-2.0	+2.0	0.0
Volume (m³)	149 944.64	149 944.64	33 244.43

5.4.7.1 Hydrodynamics. Results and discussion

In this section, initial bed level information and hydrodynamics results for RB3_Groin and all RB3_S10 parametric analysis scenarios mentioned in Table 5.21 are presented and analysed based on the main outcomes and differences between them.

Figure 5.60 presents the reference bathymetry scenarios for the parametric analysis, where the left panel depicts the initial bed levels, and the right panel shows results for hydrodynamics along the domain.

Figure 5.61 depicts the structures scenarios results for the parametric analysis, while Figure 5.62 presents results for the groin scenario. Figures 5.61 and 5.62 depict results for the decrease of significant wave heights from offshore to shoreline (wave energy dissipation) and their mean directions based on the conditions created for each scenario. In each Figure 5.61 and 5.62, the left panel presents results for the entire domain, while the right panel depicts results that are more detailed around the structures.

Figures 5.60a, 5.60b, 5.60c, 5.60d, 5.60e present results for RB3_SW; RB3_W; RB3_H; RB3_L; and RB3_Storm10, respectively. Figures 5.61a, 5.61b, 5.61c, 5.61d, 5.61e depict results for RB3_SW_S10; RB3_W_S10; RB3_H_S10; RB3_L_S10; and RB3_Storm10_S10, respectively. Figure 5.62 presents results for RB3_Groin.

Regarding Figure 5.60, in the left panel, Figures 5.60a, 5.60b and 5.60d indicate the maximum offshore depth of -31.4 m and the maximum coastal elevation of +2 m for RB3_SW, RB3_W, and RB3_L. In Figures 5.60c and 5.60e, domains were enlarged for RB3_H and RB3_Storm10, and the maximum coastal elevation was set to +4.0 m, while maintaining the same maximum offshore depth. All bathymetries have a constant slope of 2% and each RB3 serves as basis to the corresponding scenario with structure. In the right panel, Figures 5.60a, 5.60b and 5.60e depict results different from those presented for the RB3 initial scenario, due to different wave directions, represented by the vectors

(RB3_SW and RB3_W) and storm conditions (RB3_Storm10). Scenarios depicted in Figures 5.60c and 5.60d indicate that tidal level variations near shoreline do not affect significant wave heights results in SWAN.

For all scenarios presented in Figure 5.60, except RB3_Storm10, significant wave heights tend to decrease gradually from position 1400 m onwards until reaching a significant wave height of 0 m. Instead, in RB3_Storm10, waves breaking starts at an earlier position (800 m) due to higher significant wave heights. Results for significant wave height and their mean directions vectors demonstrate an extended wave shoaling due to the consideration of waves entering through boundaries with the same significant wave height at: i) south boundary for RB3_SW (Figure 5.60a); ii) north boundary for RB3_H (Figure 5.60c), RB3_L (Figure 5.60d), and RB3_Storm10 (Figure 5.60e); and iii) north and south boundaries for RB3_W (Figure 5.60b). This phenomenon tends to scatter along the domain, which has already been mentioned in Section 5.4.1.1. Contrarily, for RB3_W, this dissipation effect is distributed along the domain, because west waves contribute to north and south boundary instabilities.
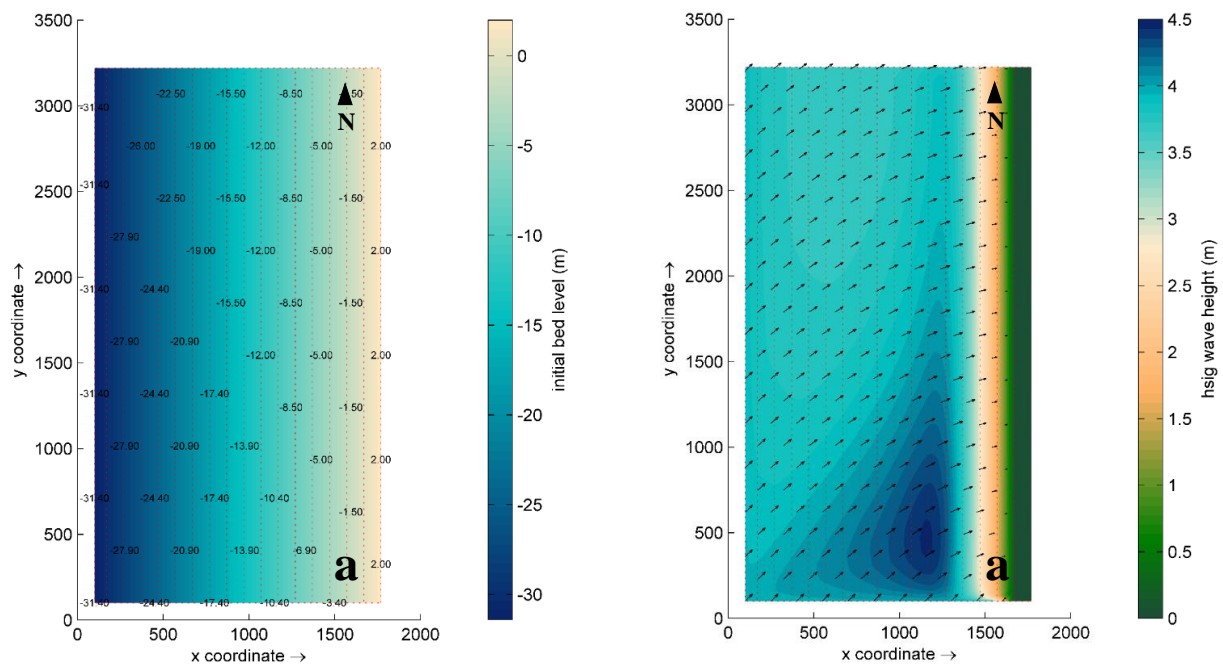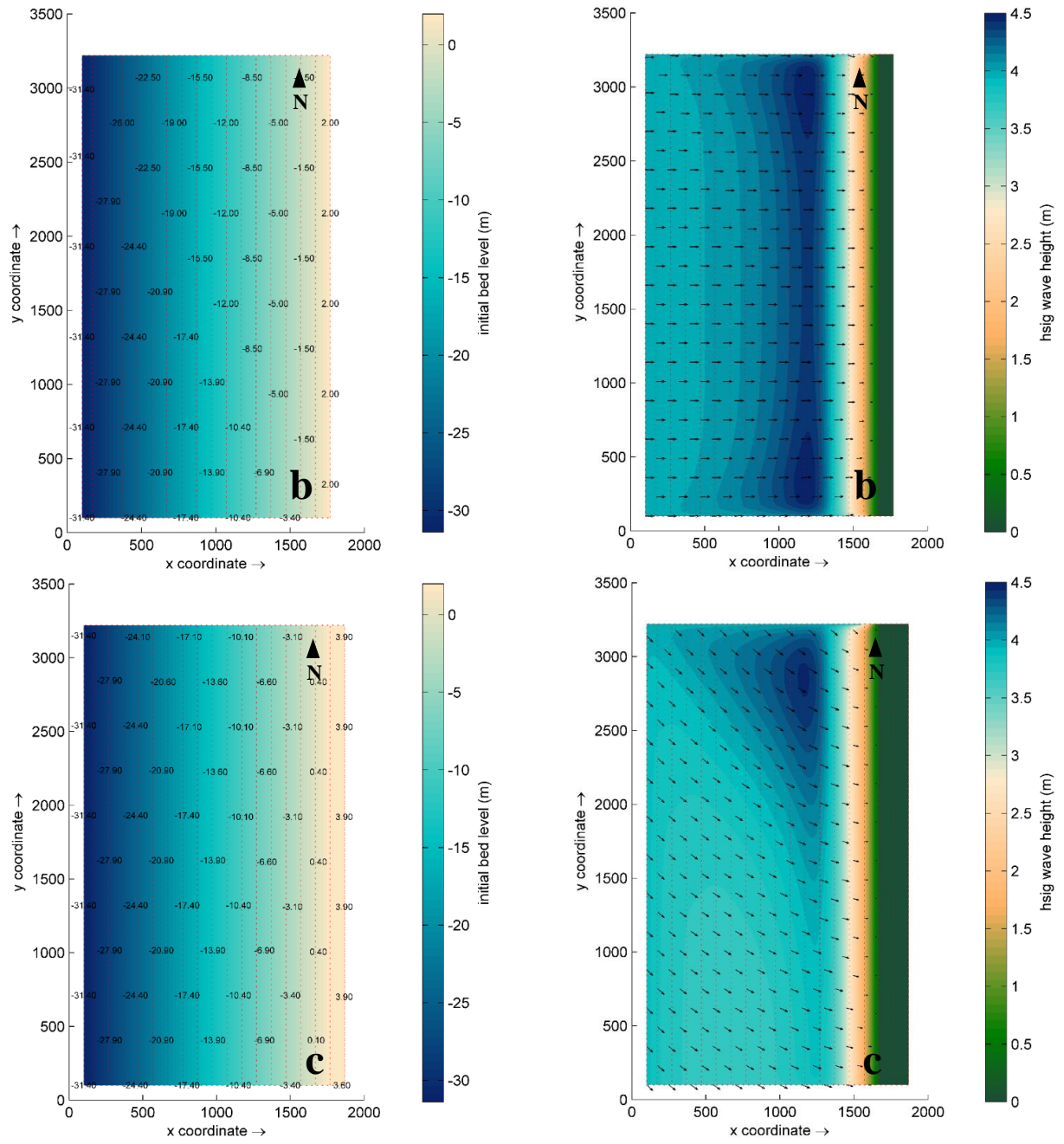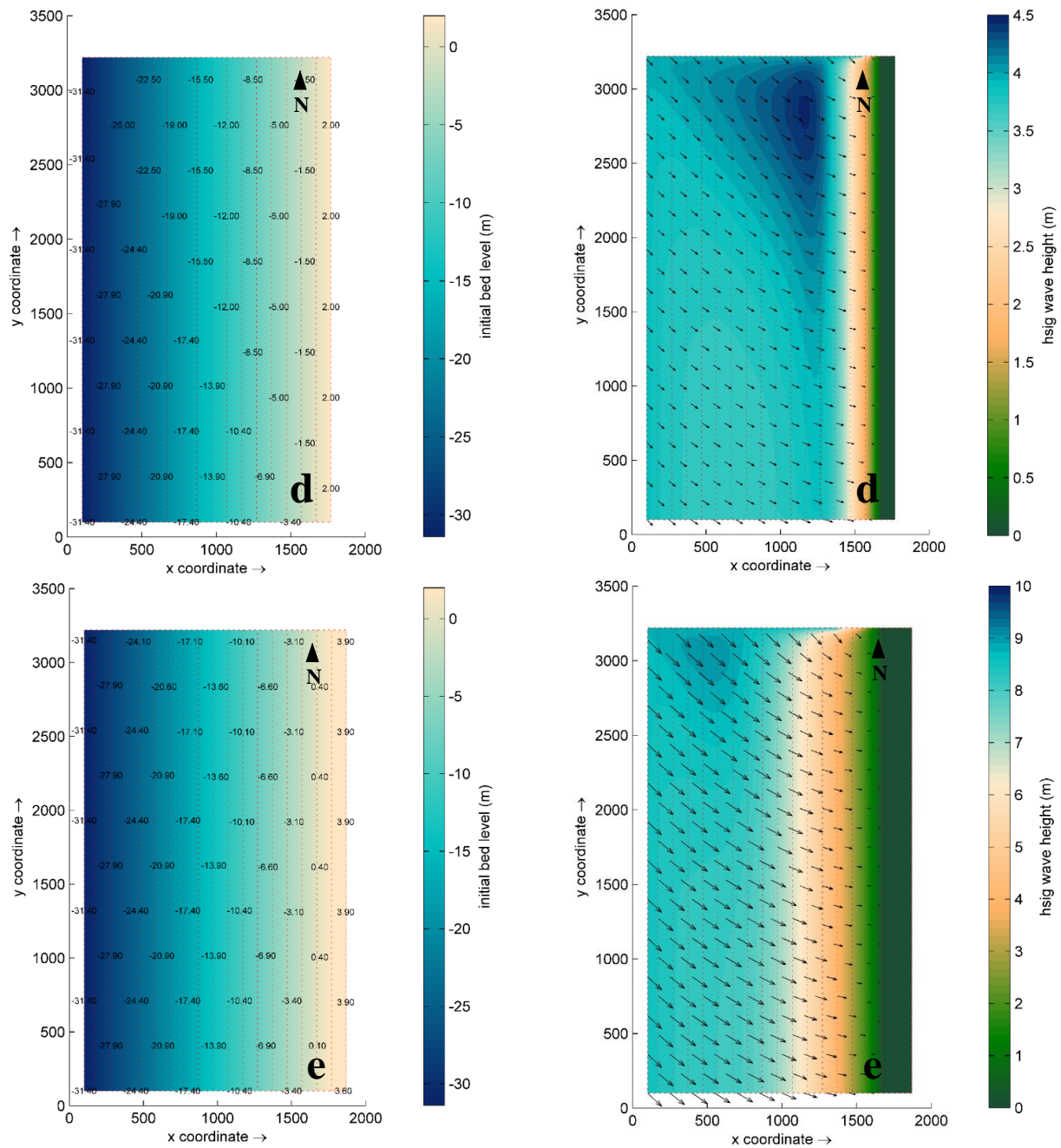
Figure 5.60: Bed level values (left) and Hs along the domain (right) for reference bathymetry scenarios: a) RB3_SW; b) RB3_W; c) RB3_H; d) RB3_L; and e) RB3_Storm10.

Figure 5.61 depicts the significant wave heights and their mean direction vectors results for parametric analysis of structures scenarios. For all scenarios, except RB3_Storm10_S10 (Figure 5.61e), results for wave energy dissipation present no substantial differences along the domain and results are similar to those presented in RB3_S10. On the platforms area, no waves transmission over the structures occurs (wave-overtopping), which shows the crest levels provide great protection on the adjacent coastal zone, regardless of the scenario. However, since the tidal variation effect is not reflected in SWAN, for better

understanding the structures behaviour, results for each solution will have to be analysed for different tidal levels through morphodynamics.

In RB3_Storm10_S10, since the wave breaking occurs in a region farther away from the coast due to higher significant wave heights, the waves approaching the structure present lower significant wave heights. Nevertheless, the pattern of wave energy dissipation is similar to the previous scenarios and the structure platform also presents null significant wave heights. However, as previously mentioned, these results should be analysed very cautiously, since SWAN does not present reliable results in shallow waters.

Regarding the reversal of longitudinal drift, all scenarios present a rotation of the significant wave height mean direction vectors along the head of the structures, regardless the wave climate direction.

Overall, results indicate that wave directions, tidal levels, as well as an intense storm do not affect results for wave energy dissipation through SWAN analysis. For this reason, morphodynamic analysis is crucial to understand the influence of different conditions on shallow waters.
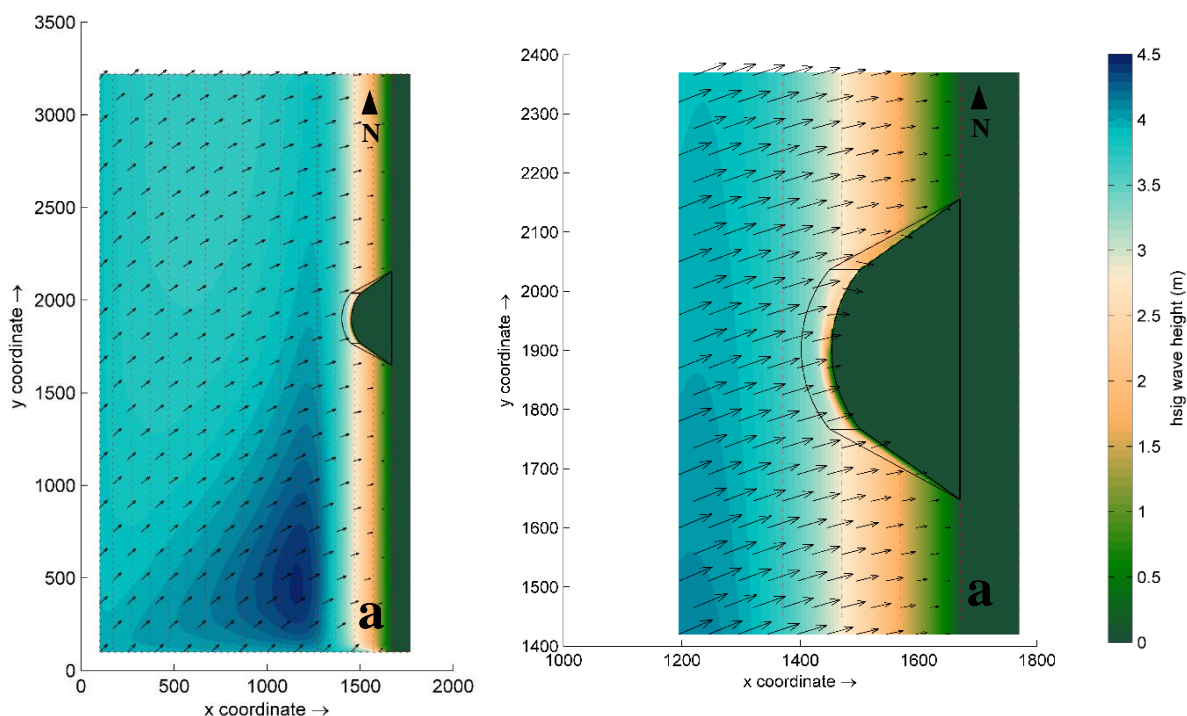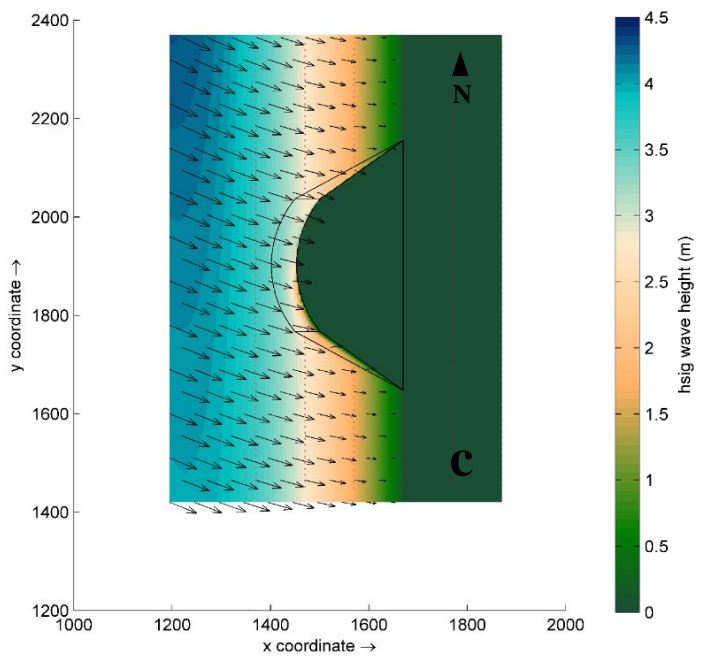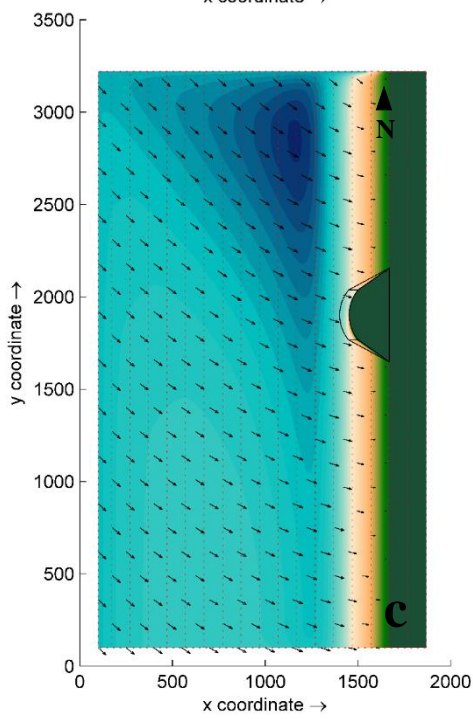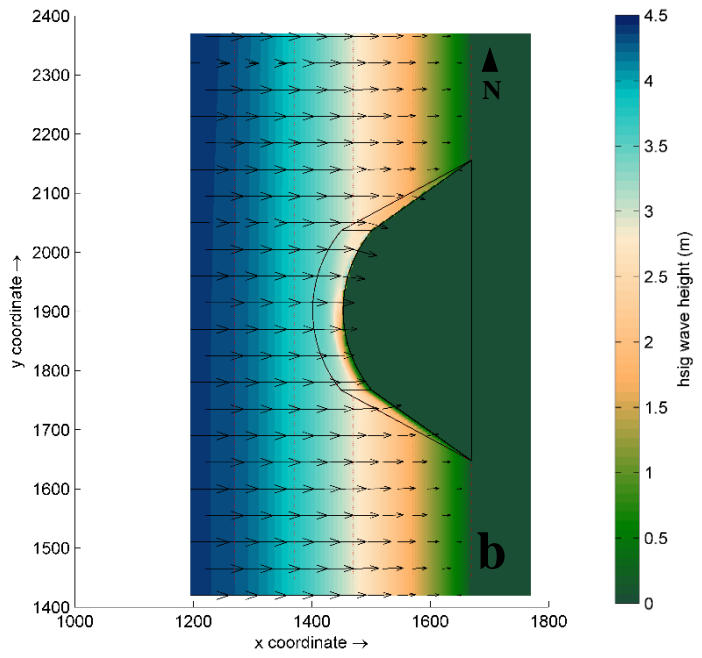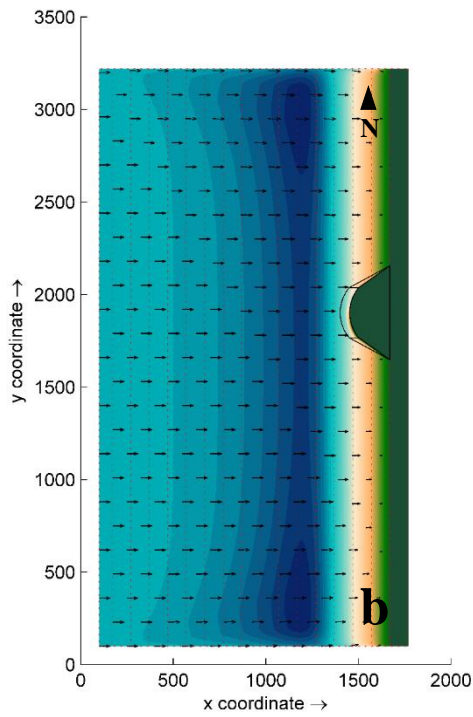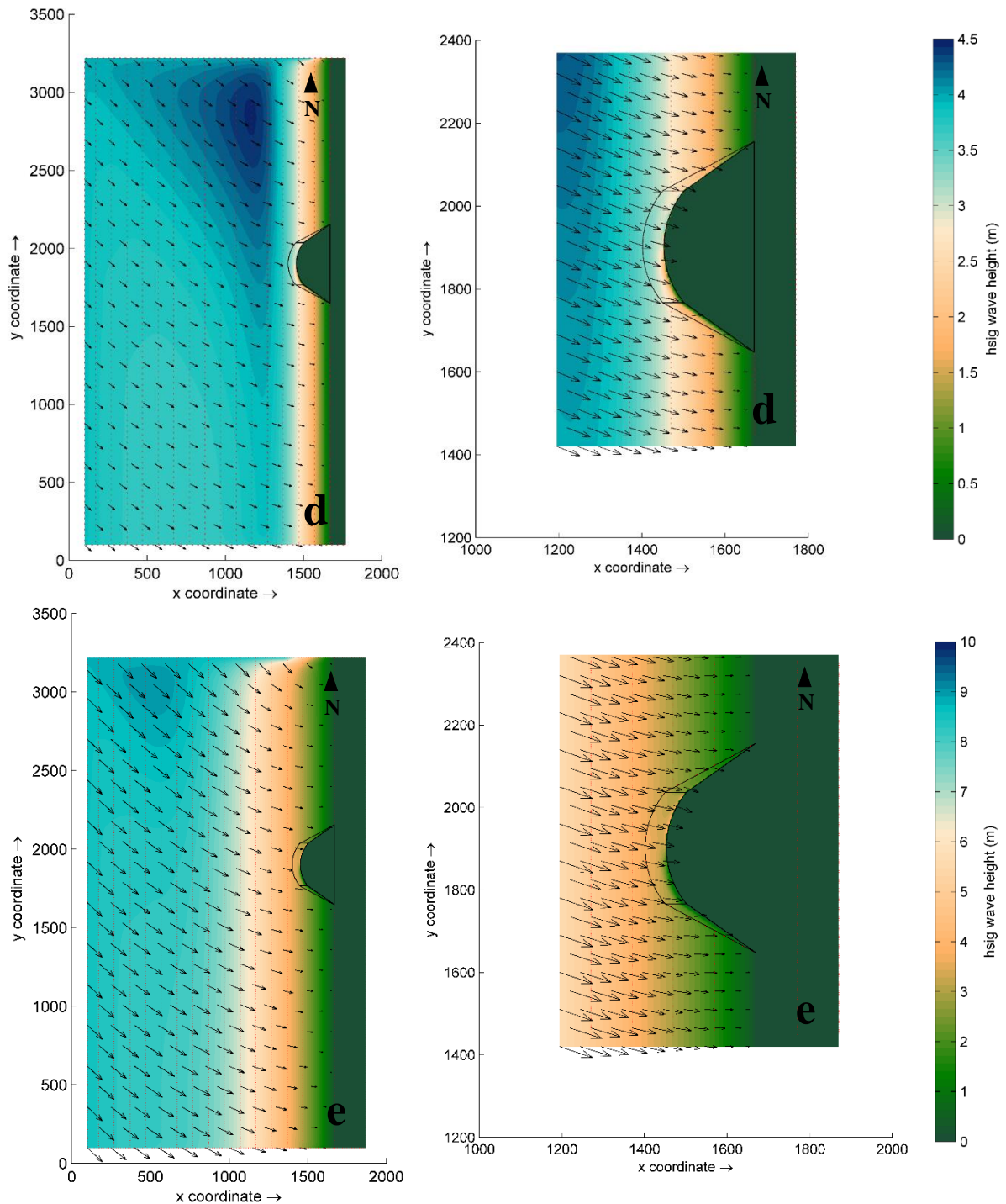
Figure 5.61: H$_s$ along the domain (left) and detailed around the structure (right) for scenarios: a) RB3_SW_S10; b) RB3_W_S10; c) RB3_H_S10; d) RB3_L_S10; and e) RB3_Storm10_S10.

Figure 5.62 depicts the results for RB3_Groin significant wave heights as well as their mean direction vectors orientations. In this case, the structure provides a small shadow zone between 2080 m and 2100 m (y-coordinates) where significant wave heights are approximately 1.0 m. Significant wave heights at the same location updrift are approximately 2.3 m.

Relative to the significant wave heights mean direction vectors, a small diffraction is observable near the groin's head and a local reversal of longitudinal drift is observable near the downdrift slope. Along the domain, this structure does not reverse the longitudinal drift, as vectors orientations display the same direction. Near the head, a small wave shoaling is noticeable and waves break without overtopping the structure crest, which means the crest level (+4.0 m) is higher than the approximate significant wave height (2.5 m) at that location. Nonetheless, for these type of structures, the influence on wave energy dissipation is local and alternative solutions for coastal protection are necessary to improve these results.
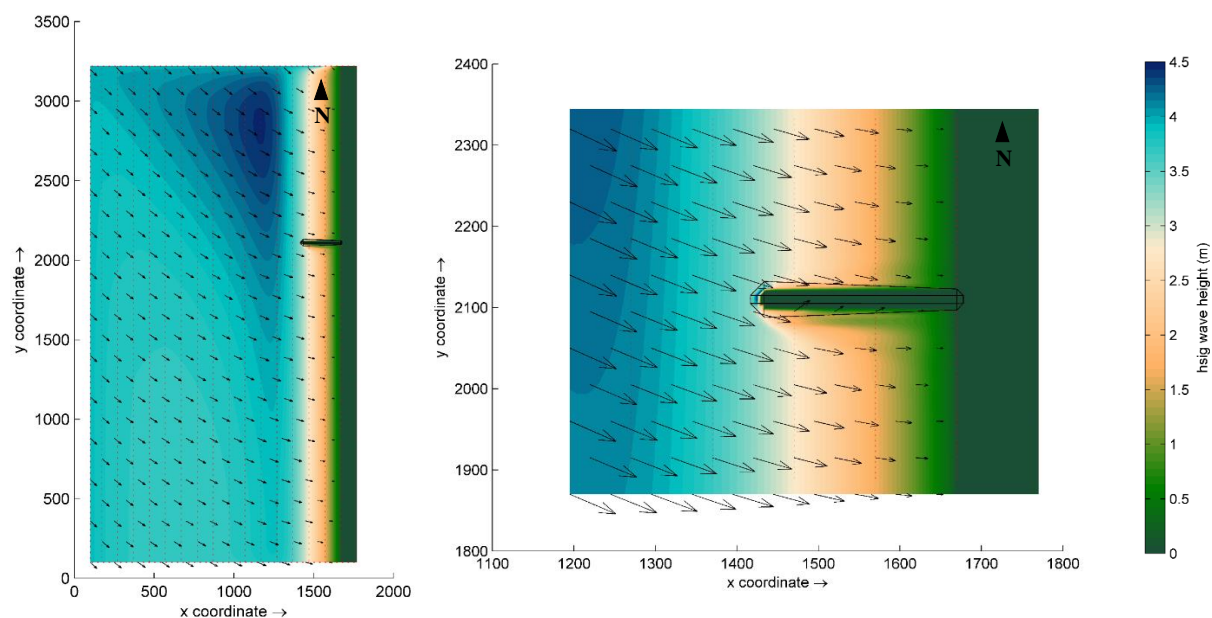
Figure 5.62: H_s along the domain (left) and detailed around the structure (right) for RB3_Groin scenario.

5.4.8 Morphodynamics. Results and discussion

In order to understand sedimentary dynamics behaviour for structures with the best hydrodynamic performances, the morphodynamic analyses with XBeach are performed for scenarios RB3_S1 to RB3_S14. Similar to the previous analysis, results are assembled using groups of scenarios based on the structures similarities for the same four groups. The first group (RB3_S1, RB3_S3, RB3_S5 and RB3_S7) presents four different structures with large dimensions, while the second (RB3_S2, RB3_S4, RB3_S6 and RB3_S8) features the same geometries presented in the first group but with smaller dimensions. The third group (RB3_S9, RB3_S10 and RB3_S11) presents three structures with similar geometries but with different crest levels and locations relatively to shoreline. Lastly, the fourth group (RB3_S12, RB3_S13 and RB3_S14) assembles three groups of structures also with similar geometries but with different gaps width and locations relatively to shoreline.

A parametric analysis for RB3_S10 is also developed for better understanding the influence of wave climate directions (southwest and west), tidal levels (high and low), sediments dimensions (coarse and medium sand) and an intense storm on the morphodynamics. For the sediments dimension, in Section 5.4.8.6 the selection method for the sand dimensions is presented (Figure 5.72).

In this section, morphodynamics results for the entire domains of RB3 structures scenarios are presented and analysed based on the main outcomes and differences between them. The morphodynamics focus the cumulative sedimentation/erosion results, as well as the mean suspended sediments transport (represented by vectors) for the entire domain. The mean suspended sediments transport represents a key factor for the longitudinal drift, where the erosion and accretion bars near shoreline are formed. For the accretion/erosion results, several profiles are considered along the domain for each scenario that depict the sediments variation from deepest locations to the beach. These profiles are drawn according to areas of greater accumulation of sediments or erosion areas near the structures and/or the shoreline, and for each group of scenarios, results for each profile are compared with RB3 (without any structure) results. In this way, through the profiles analysis, the comparison of results and the assessment for the best solution is performed more accurately and with greater sensitivity, especially near shoreline. The northern- and southernmost profiles are named PN and PS, respectively. The identification of the remaining profiles is done in ascending order from north to south boundaries.

Thus, results for the cumulative sedimentation/erosion and the mean suspended sediments transport for the reference bathymetry, structures scenarios and the parametric analysis are presented in Figures 5.63, 5.64, 5.66, 5.68, 5.70, 5.73, 5.75, 5.77, 5.79 and 5.81. The wave climate conditions are identical to all scenarios, except for the parametric analysis (Figures 5.73, 5.75, 5.77 and 5.79). The profiles results for all scenarios including the RB3 (without any structure) are depicted in Figures 5.65, 5.67, 5.69, 5.71, 5.74, 5.76, 5.78, 5.80 and 5.82. The different scales in each profile are defined according to the magnitude of results in different locations of the domain. For the cumulative sedimentation/erosion results, the -0.2 m to 0.2 m scale allows analysing the results near shoreline with more detail.

The morphodynamic analyses with XBeach are performed considering the same wave storm conditions using a JONSWAP spectrum, since it is more reliable compared to stationary waves, which presents the same energy over time. All RB3 domains have the same dimensions and grid spacing as the hydrodynamics simulations. The total simulation time is 2.4 hours with a morphological acceleration factor (morfac) of 10, which corresponds to a 24 hour-duration storm. Contrary to previous

morphodynamics simulations, the morfac of 100 is not considered, as the focus in this Section is to study one long period storm. The waves' statistics developed in Chapter 3 indicate that for a location near the Lima estuary mouth (station W3) the mean storm duration is 22 hours for HP and RCP4.5_end, and 23 hours for the RCP8.5_end. Therefore, for this reason, the selection of a critical scenario of 24 hour-storm seemed adequate to conduct the morphodynamics.

Regarding seabed composition, the sediments dimensions are 0.2 mm for D_{50} and 0.3 mm for D_{90}, which corresponds to a fine sand, according to the Unified Soils Classification of sediments (Bosboom and Stive, 2022).

Boundary conditions for XBeach model are defined as absorbing-generating (weakly-reflective) in 2D (abs_2d) for front and back boundaries, and Neumann for left and right boundaries. The Neumann boundary condition, which indicates there is locally no change in elevation and velocity, allows simulating a continuous environment throughout the boundaries without instabilities near left and right boundaries. For this reason, the wall type boundary condition (simple no flux) used in Chapter 4 was not considered for the following simulations.

XBeach morphology files also allow indicating areas as erodible and non-erodible. Thus, all domain is set as erodible, while the structures area is defined as non-erodible due to the concrete nature of the armour units.

Summarised information regarding the input conditions for the RB3 scenarios (from RB3_S1 to RB3_S14) using XBeach are presented in Table 5.24. For the parametric analysis, only some conditions are changed, which are the same as those presented in Table 5.21.

Table 5.24: XBeach numerical model conditions for RB3 scenarios (from RB3_S1 to RB3_S14).

XBeach Numerical Model Conditions	
Parameters	**RB3 (from RB3_S1 to RB3_S14)**
Tidal level (m)	0
Wave condition	Storm
Wave direction	Northwest
Boundary conditions	Front and back: abs_2d Left and right: neumann
Sediments dimensions (mm)	$D_{50} = 0.2$ $D_{90} = 0.3$
Morphological acceleration factor (morfac)	10
Wave type conditions	JONSWAP spectrum
Simulation time (hours)	2.4
Computational domain (m)	1670×3120 (cross-shore $\times$ longshore)
Grid spatial resolution (m)	dx=dy=5
Computational grid	334×624

5.4.8.1 Reference bathymetry: RB3

In this section, Figure 5.63 depicts results for the cumulative sedimentation/erosion and the mean suspended sediments transport (represented by vectors) for the entire domain of the reference bathymetry scenario (RB3). Although in Figure 5.63 this scenario is subdivided into four parts, results are the same in all cases. The only difference between them lies in the location and/or number of profiles traced that will serve as basis for comparing RB3 scenario with the structures scenarios. Thus, Figures 5.63a, 5.63b, 5.63c and 5.63d present the profiles locations to analyse and compare scenarios results for: a) RB3_S1, RB3_S3, RB3_S5, and RB3_S7; b) RB3_S2, RB3_S4, RB3_S6, and RB3_S8; c) RB3_S9, RB3_S10, and RB3_S11; and d) RB3_S12, RB3_S13, and RB3_S14.

Regarding the outcomes, overall, RB3 morphodynamics reveal an accretion bar along the entire domain near shoreline roughly from 1580 m and 1675 m with a mean of +0.16 m, and an erosion bar approximately located between 1675 m and 1735 m with a mean of -0.30 m, also along the entire domain near shoreline.

The areas with greater accumulation are between PN and P3 in Figures 5.63a, 5.63b and 5.63c, and PN and P4 in Figure 5.63db, with a mean of +0.22 m. The areas with lesser erosion are between P3 and P5 in Figures 5.63a, 5.63b and 5.63c, and between P4 and P7 in Figure 5.63d with a mean of -0.28 m. The areas with lesser accumulation are between P3 and P5 in Figures 5.63a, 5.63b and 5.63c, and P4 and P7 in Figure 5.63d with a mean of +0.10 m. The areas with greater erosion are between PN and P3 in Figures 5.63a, 5.63b and 5.63c, PN and P4 in Figure 5.63d with a mean of -0.30 m, and in PS (Figures 5.63a, 5.63b, 5.63c and 5.63d) with an erosion of -0.30 m. These results indicate that in locations with great erosions, also great accretions are observable; and in locations of lesser sedimentations, there are also lesser erosions. However, in both cases, the accretion does not compensate for the erosion areas. It is expected the coastal stretch protected by a coastal structure to have a larger extension of sediments accumulation and a reduction in the erosion areas.

Overall, the accretion bars have a mean width of 95 m, except in the areas comprised by P3 and P5 (Figures 5.63a, 5.63b and 5.63c), and P4 and P7 (Figure 5.63d), where the sedimentation width is 90 m. In PS, the accretion bar is the widest with 120 m. The erosion bars have a mean width of 65 m except between PN and P3 (Figures 5.63a, 5.63b and 5.63c), and PN and P4 (Figure 5.63d) where the erosion has a width of 80 m. These results indicate that locations with lower sedimentation values have a smaller area, and locations with higher erosion values have a larger area.

In the area comprised by P3 and P5 (Figures 5.63a, 5.63b and 5.63c), and P4 and P7 (Figure 5.63d), vectors for the mean suspended sediments transport display a change in their directions that reflect a

decrease of sediments accretion in this area. Since this phenomenon is located exactly in the mid area of the domain and no changes were made to the bed level, these results may indicate a lesser influence of the boundary conditions on this location, as this area is the farthest from each Neumann boundaries (left and right, or North and South).

A slight accretion is also visible for all profiles from 1290 m to 1530 m with 0.05 m.
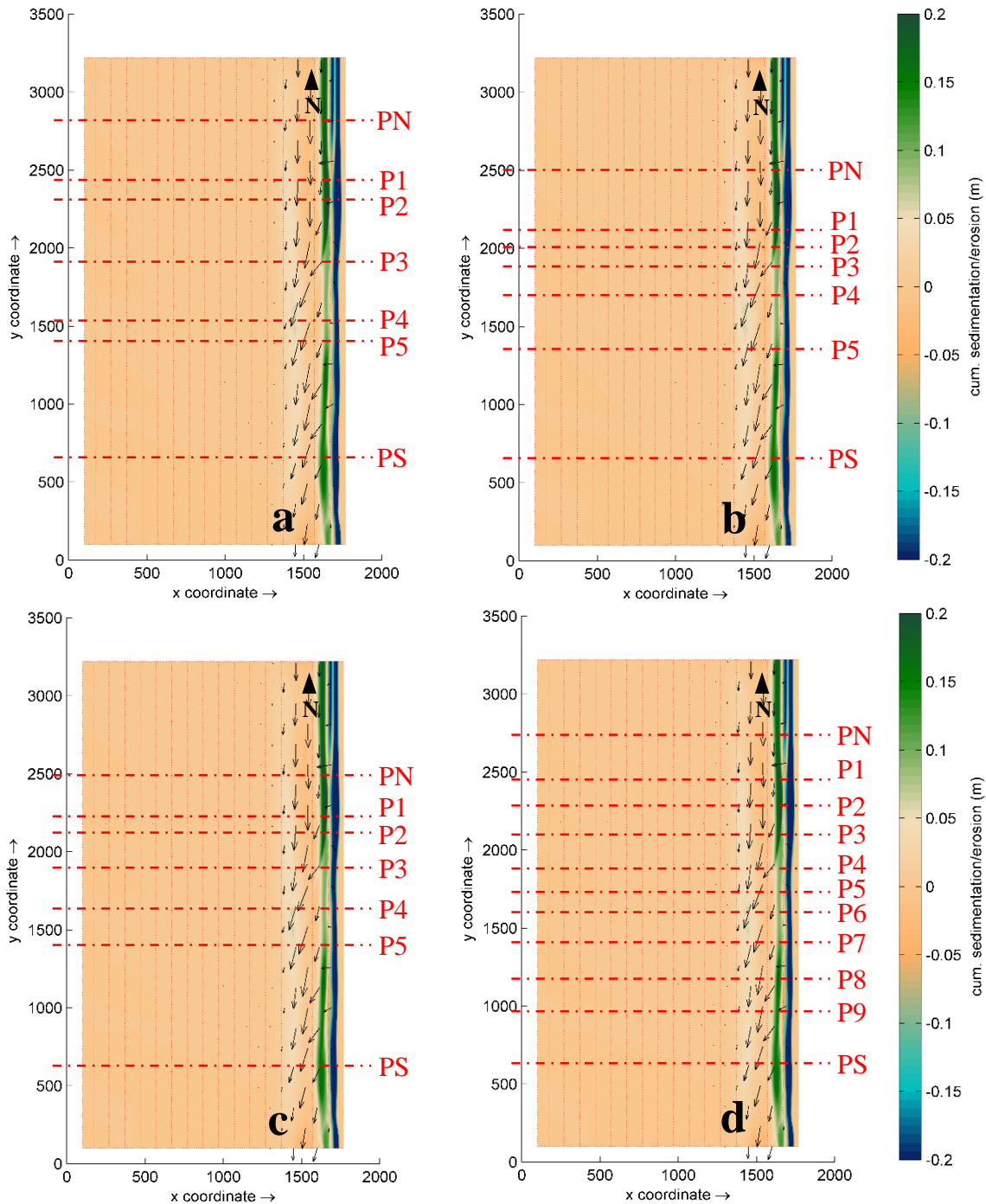
Figure 5.63: Cumulative sedimentation/erosion results for the reference bathymetry RB3 and profile locations to analyse and compare scenarios results for: a) RB3_S1, RB3_S3, RB3_S5, and RB3_S7; b) RB3_S2, RB3_S4, RB3_S6, and RB3_S8; c) RB3_S9, RB3_S10, and RB3_S11; and d) RB3_S12, RB3_S13, and RB3_S14.

5.4.8.2 RB3_S1, RB3_S3, RB3_S5 and RB3_S7

Figures 5.64a, 5.64b, 5.64c and 5.64d depict results for the cumulative sedimentation/erosion and the mean suspended sediments transport (represented by vectors) for the entire domain of structures scenarios RB3_S1, RB3_S3, RB3_S5 and RB3_S7, respectively. Figure 5.65 depicts results along all profiles for RB3_S1, RB3_S3, RB3_S5 and RB3_S7.

Near the structures, the greatest areas of sediments accumulation occur in the updrift zone of the four scenarios (covered in P1 and P2); along the up- and downdrift structures walls in RB3_S1 and RB3_S3 (covered in P2 and P4, respectively); and at the ledge in RB3_S3 (covered in P3).

In RB3_S3 and RB3_S7, great sediments accumulation between 1290 m to 1530 m (between P5 and PS, not covered by any profile) is observable in an area away from the structures and the shoreline, which indicates these structures shapes allow great sediments transport from North to South because of their smaller width. Results for the mean suspended sediments transport vectors also corroborate the lesser sediment disruption, as vectors are more intense in this location. Between scenarios RB3_S1 and RB3_S5, the slope-type structure (RB3_S5) allows greater sediments transport to the South than the wall-type structure in RB3_S1, due to greater vectors intensity downdrift the structure. However, the shadow zone provided by the RB3_S5 structure is not sufficient for the sediments accretion at this location. On the contrary, near the structure wall in RB3_S1, great sediments retention downdrift is visible, due to the enhanced effect by the shadow zone of the wall, which is also observable in RB3_S3 (covered in P4). These results indicate that the wall type structures favour a sediments accretion next to the structure wall downdrift.

Regarding erosion near structures, all scenarios display erosion areas at the up- and downdrift extremities (covered in P1 and P5). In RB3_S1 and RB3_S3, structures have great erosion areas at the ledge (covered in P3), and along the walls most exposed to wave climate (covered in P2 and P4), due to the abrupt waves breaking on this type of structures, especially in RB3_S1 (-5.0 m). In the case of slope type structures (RB3_S5 and RB3_S7), this effect is negligible.

At the downdrift structure extremities, scenarios with less wide structures (RB3_S3 and RB3_S7) present the greatest erosion areas, which means the effect of the reversal of longitudinal drift in these cases causes greater scouring close to the structures (covered in P4 and P5) than in RB3_S1 and RB3_S5. In terms of intensity, RB3_S7 depicts the greatest erosion (-2.30 m in P4), which means the erosion effect at this location is greater in less widely slope type structures. Erosion patterns next to structures are similar in scenarios with similar geometric shapes (RB3_S1 and RB3_S5, and RB3_S3 and RB3_S7).

At the structures shadow zones near shoreline, all scenarios present less erosion between 1680 m and 1750 m (covered in P2 and P3), compared to the reference bathymetry RB3. However, in P3 between 1585 m and 1680 m the erosion effect is intensified in all scenarios, except in RB3_S1. In P4, all scenarios show high sedimentation (+0.20 m) between 1585 m and 1680 m and low erosion between 1680 m and 1750 m, when compared to RB3, which indicates the structures provide a good level of protection at these locations, especially in RB3_S7. In P1 and P5 near shoreline, all structures also present a reduction in erosion, with an emphasis on RB3_S7, which presents the lowest values of erosion close to shoreline (-0.18 m). However, in P5, between 1585 m and 1680 m, the less wide structures (RB3_S3 and RB3_S7) present less sediments accumulation, while the wider structures (RB3_S1 and RB3_S5) present the greatest sediments accumulation, when compared to RB3.

In PN and PS, results are relatively similar in all cases, since these profiles are farther away from the structures, which means that the structures influence is reflected on a smaller scale. However, PN presents greater sediments accumulation in all scenarios between 1275 m and 1680 m, relatively to RB3. In addition, PS plots great sedimentation in RB3_S3 and RB3_S7 (less wide structures) between 1275 m 1610 m.

In short, less wide structures allow greater sediments transport from North to South than wider structures; however, at the downdrift extremities of those structures significant erosions occur, especially in the slope type structure (RB3_S7: -2.30 m and -0.37 m). At the updrift extremities, large sediments accretion in all scenarios occurs; however, with immediate high erosion areas, especially in wall type structures (RB3_S1: -1.0 m and -5.0; and RB3_S3: -1.0 m). Along the more exposed wave climate structure faces, results demonstrate greater erosion in wall-type than in slope-type structures. Near shoreline, all scenarios depict a reduction in erosion downdrift, especially in RB3_S7, as well as great sediments accumulation in all scenarios relatively to RB3. Close to the beach, at the structure alignment, a reduction in erosion is depicted in all structures.

Figure 5.64: Cumulative sedimentation/erosion results and profile locations for scenarios: a) RB3_S1; b) RB3_S3; c) RB3_S5; and d) RB3_S7.

Figure 5.65: Cumulative sedimentation/erosion results along the profiles for RB3, RB3_S1, RB3_S3, RB3_S5, and RB3_S7.

5.4.8.3 RB3_S2, RB3_S4, RB3_S6 and RB3_S8

Figures 5.66a, 5.66b, 5.66c and 5.66d depict results for the cumulative sedimentation/erosion and the mean suspended sediments transport (represented by vectors) for the entire domain of structures scenarios RB3_S2, RB3_S4, RB3_S6 and RB3_S8, respectively. Figure 5.67 depicts results along all profiles for RB3_S2, RB3_S4, RB3_S6 and RB3_S8.

The results observation in Figure 5.66 quickly allow concluding that, despite the structures shape being the same as the previously analysed, the influence of their dimensions on sediments transport along the domain has a completely different behaviour. In this case, all structures regardless of their widths allow great sediments transport from North to South; however, this effect is still more noticeable in less wide structures (RB3_S4 and RB3_S8), where a maximum of sediments accumulation of +0.17 m occurs between 1290 m and 1680 m (covered in P5). This effect is also corroborated by the intensities of the mean suspended sediments transport vectors. Between the scenarios RB3_S2 and RB3_S6, the slope-type structure (RB3_S6) also presents greater sediments transport to the South than the wall-type structure in RB3_S2. Downdrift the structures, contrary to previous results, no sediments accretion occurs along the wall/slope, because sediments outline the structures more easily due to their smaller dimensions and settle farther in the domain.

Near the structures, the greatest areas of sediments accretion occur updrift the structure (+0.10 m) between 1280 m and 1510 m for all scenarios (covered in P1); at the ledge of the four structures (covered in P3); and at the most exposed wave climate structure faces updrift (covered in P2). In wall type structures, the sediments accretion is more noticeable at the ledge, with a maximum of +2.68 m in RB3_S2 and +1.17 m in RB3_S4.

In relation to erosion near structures, scenarios with wall type structures (RB3_S2 and RB3_S4) display erosion areas at the walls most exposed to wave climate due to the abrupt waves breaking on this type of structures, and the less wide structures (RB3_S4 and RB3_S8) present erosions at the updrift extremities (covered in P2). RB3_S6 structure presents no erosion in these areas. In all scenarios, at the structures ledge, the erosion areas are inexistent. At the downdrift extremities, erosion occurs in all structures (covered in P4), although with more significant results for the less wide structures (RB3_S4: -1.1 m and RB3_S8: -1.3 m), which allows to conclude that the reversal of longitudinal drift in these structures intensifies the erosion near this location, especially in the slope type structure. Erosion patterns next to structures are similar in scenarios with similar geometric shapes (RB3_S2 and RB3_S6, and RB3_S4 and RB3_S8).

Near shoreline updrift the structure, between 1680 m and 1750 m, all scenarios present no improvements in erosion compared to RB3 (covered in P1 and P2). However, at the alignment and downdrift the structure at the same location (covered in P3, P4 and P5), the erosion is less intense for the less wide structures (RB3_S4 and RB3_S8) and it gets slightly aggravated for the wider structures (RB3_S2 and RB3_S6). Between 1585 m and 1680 m, all structures plot less sediments accretion in P1, however in P2 all scenarios present more sediments accumulation due to the structures influence near shoreline. At the alignment of the structure (covered in P3), between the same positions, the wider structures (RB3_S2 and RB3_S6) present more sedimentation than in RB3, while the less wide structures (RB3_S4 and RB3_S8) plot erosion and sedimentation areas. However, downdrift the structure (covered in P4), all structures depict less sediments accretion than in RB3 at this location, especially RB3_S4 and RB3_S8. At a farther distance from the structure downdrift (covered in P5), between 1290 m and 1680 m, results present large sedimentations for all scenarios, especially for the less wide structures (RB3_S4 and RB3_S8).

In PN and PS, results are also relatively similar in all cases. However, in PN, results plot a slight improvement in the erosion reduction for RB3_S4 and RB3_S8 near shoreline.

In short, similar to what has been concluded before in previous results, less wide structures provide the greatest sediments transport from North to South; however, with significant erosion areas at their downdrift extremities, especially in the slope-type structure (RB3_S8). At the updrift structures extremities, relatively to erosion results, the same conclusions as before can be addressed, as more intense erosion areas occur in the less wide structures, with higher values for the wall-type structure (RB3_S4). In addition, along the more exposed wave climate structure faces, results demonstrate, once more, that greater erosion occurs in wall-type structures rather than in slope-type structures. Near shoreline, in the structures alignment, a slight improvement in erosion occurs for the less wide structures (especially in RB3_S8), and a great sediments accumulation for the wider structures, relatively to RB3. Near the beach, downdrift the structure, significant changes only occur at a farther location from the structure, while updrift, great sediments accretion occurs for all scenarios.

Figure 5.66: Cumulative sedimentation/erosion results and profile locations for scenarios: a) RB3_S2; b) RB3_S4; c) RB3_S6; and d) RB3_S8.
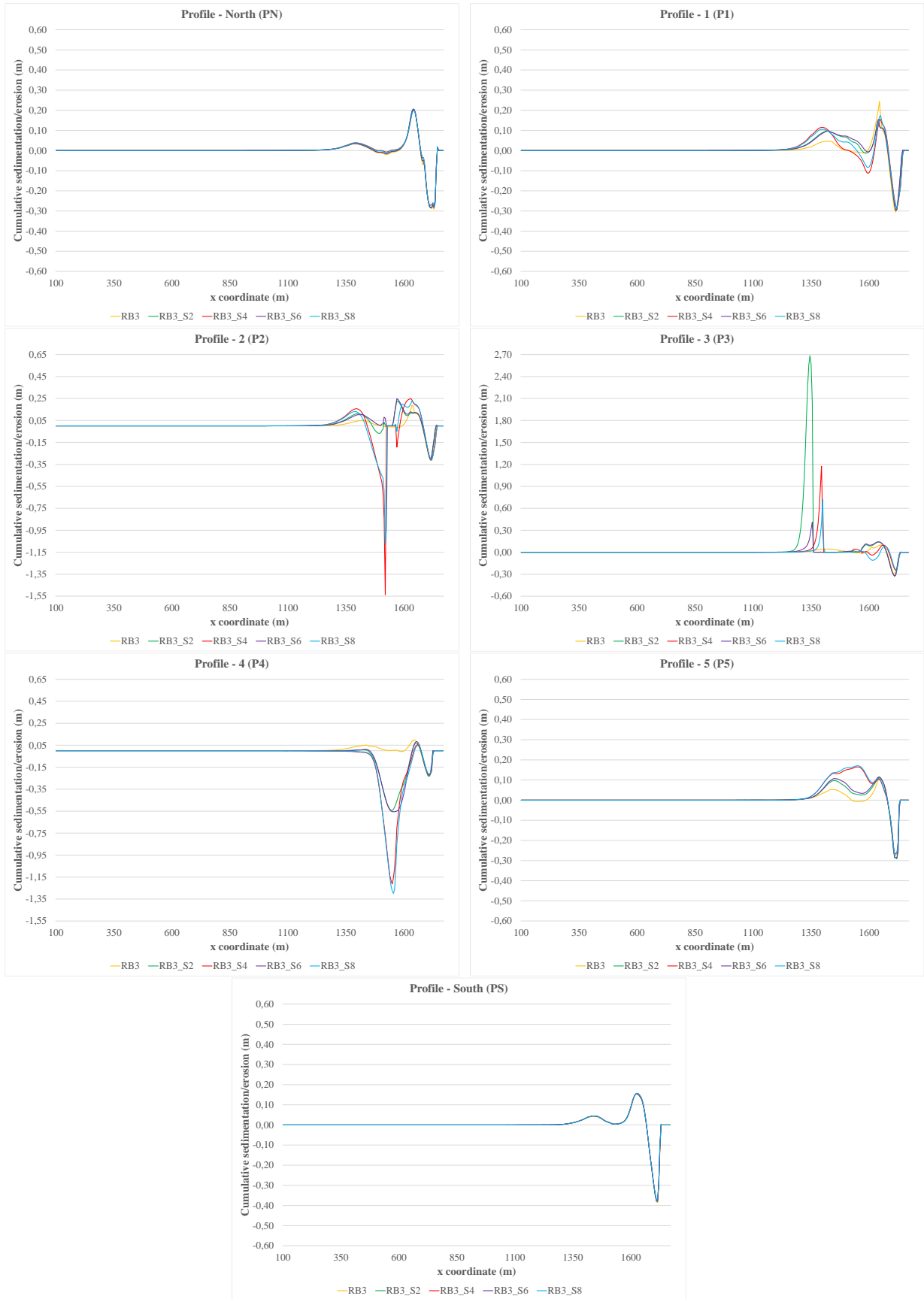
Figure 5.67: Cumulative sedimentation/erosion results along the profiles for RB3, RB3_S2, RB3_S4, RB3_S6, and RB3_S8.

5.4.8.4 RB3_S9, RB3_S10 and RB3_S11

Figures 5.68a, 5.68b and 5.68c depict results for the cumulative sedimentation/erosion and the mean suspended sediments transport (represented by vectors) for the entire domain of structures scenarios RB3_S9, RB3_S10 and RB3_S11, respectively. Figure 5.69 depicts results along all profiles for RB3_S9, RB3_S10 and RB3_S11.

The following scenarios indicate resembling results patterns due to similar structures shape; however, each profile presents some particularities, depending on the structure. For this reason, the analysis will follow the profiles order from P1 to P5.

Results covered in P1, indicate great sediments accumulation updrift the structures for all scenarios, especially for structures closer to shoreline with a 0 m crest level (RB3_S10 and RB3_S11). The greatest sediments accretion is observable for the widest structure (RB3_S10: +0.49 m). Nevertheless, structures in RB3_S10 and RB3_S11 present more erosion (-0.37 m) near shoreline relatively do RB3 and RB3_S9.

Near the structures updrift extremities, in P2, results depict erosion areas in all scenarios; however, the more intense erosion areas are in RB3_S10 and RB3_S11 (especially in RB3_S10 with -1.47 m). Results also indicate that, at this location, the structure farthest from shoreline (RB3_S9) presents greater sediments accumulation near shoreline relatively to the other scenarios, but very similar results to RB3.

At the alignment of the structures, in P3, lesser sediments accretion is visible at the ledge of the RB3_S11 structure than in RB3_S9 and RB3_S10, due to the structure proximity to shoreline and the lesser width. In this case, the structure characteristics provide a reduced barrier effect to the sediments transport downdrift, which is corroborated by the results for the mean suspended sediments transport vectors. Near shoreline, the 0 m crest level structures reveal great sediments accumulation (RB3_S10: +0.16 m and RB3_S11: +0.19 m) and reduction in erosion areas relatively to the RB3_S9 and RB3 scenarios.

Near the structures downdrift extremities, in P4, results indicate that all structures contribute to a significant scouring near this location, especially in RB3_S9 and RB3_S10 (-0.68 m). Nonetheless, near shoreline, the erosion areas are more intense in RB3_S10 and RB3_S11 and a bar of sediments is formed in RB3_S9, because of the farthest position relatively to shoreline that contributes to sediments accretion at this location. However, this sediments bar is less significant than in RB3, and overall, this profile plots worse results than in the RB3, which indicates these structures shape enhance the erosion near the downdrift extremities probably due to the reversal of longitudinal drift.

Relatively to P5, results depict great sediments accretion in all scenarios and similar erosion areas near shoreline relatively to RB3. RB3_S10 (+0.40 m) and RB3_S11 (+0.28 m) present the greatest sediments accumulation in this profile owing to the structures 0 m crest level. Despite RB3_S11 structure having a reduced barrier effect to the sediments transport, the crest level of 0 m contributes to more intense sediments retention at this location than in RB3_S9.

Regarding the PN and PS, results are also relatively similar in all cases. However, in PN, results plot greater sediments accretion in RB3_S10 than in RB3; however, with a slight worsening in erosion near shoreline, and an improvement in erosion in RB3_S9. In PS, RB3_S10 presents a slight improvement in the erosion reduction near shoreline but also a decrease in sedimentation a few meters behind, relatively to RB3.

Since the structure presented in RB3_S8 (from previous results) has a similar shape as the structure in RB3_S9 only with a different slope, the two scenarios can be generically compared. In this case, RB3_S9 presents lesser erosion areas in P1, P2, P4, but lesser sediments accumulation at the ledge of the structure in P3 and at a location farthest from the structure in P5. Overall, these results indicate that structures with a 1:10 slope benefit from less intense erosion areas near the structures' extremities, with negligible differences in sediments accumulation near shoreline.

In short, despite scenarios presenting resembling results patterns due to structures likenesses, each one depicts their particularities. Updrift, results demonstrate the greatest sediments accumulation occurs for structures closer to shoreline, especially with a wider crest (RB3_S10); however, with more intense erosion areas near the structures updrift extremities. At the alignment, structures closer to shoreline with a 0 m crest level present more sediments accretion near shoreline than the structure farthest from shoreline, as well as a reduction in erosion areas relatively to RB3. Near the structures downdrift extremities, overall, results label this location as a critical area, since these structures shape enhance the erosion probably due to the reversal of longitudinal drift. At this site, RB3_S10 presents the largest and most intense area of erosion. Downdrift, results indicate great sediments accretion for structures closer to shoreline with a 0 m crest level, especially in RB3_S10. Near shoreline at this location, relatively to RB3, results depict similar erosion areas; however, with a slight improvement in the erosion reduction in RB3_S10. Comparing structures with similar characteristics but with different slopes (1:2 and 1:10), results indicate that structures with a 1:10 slope benefit from less intense erosion areas near the structures' extremities, with negligible differences in sediments accumulation near shoreline.

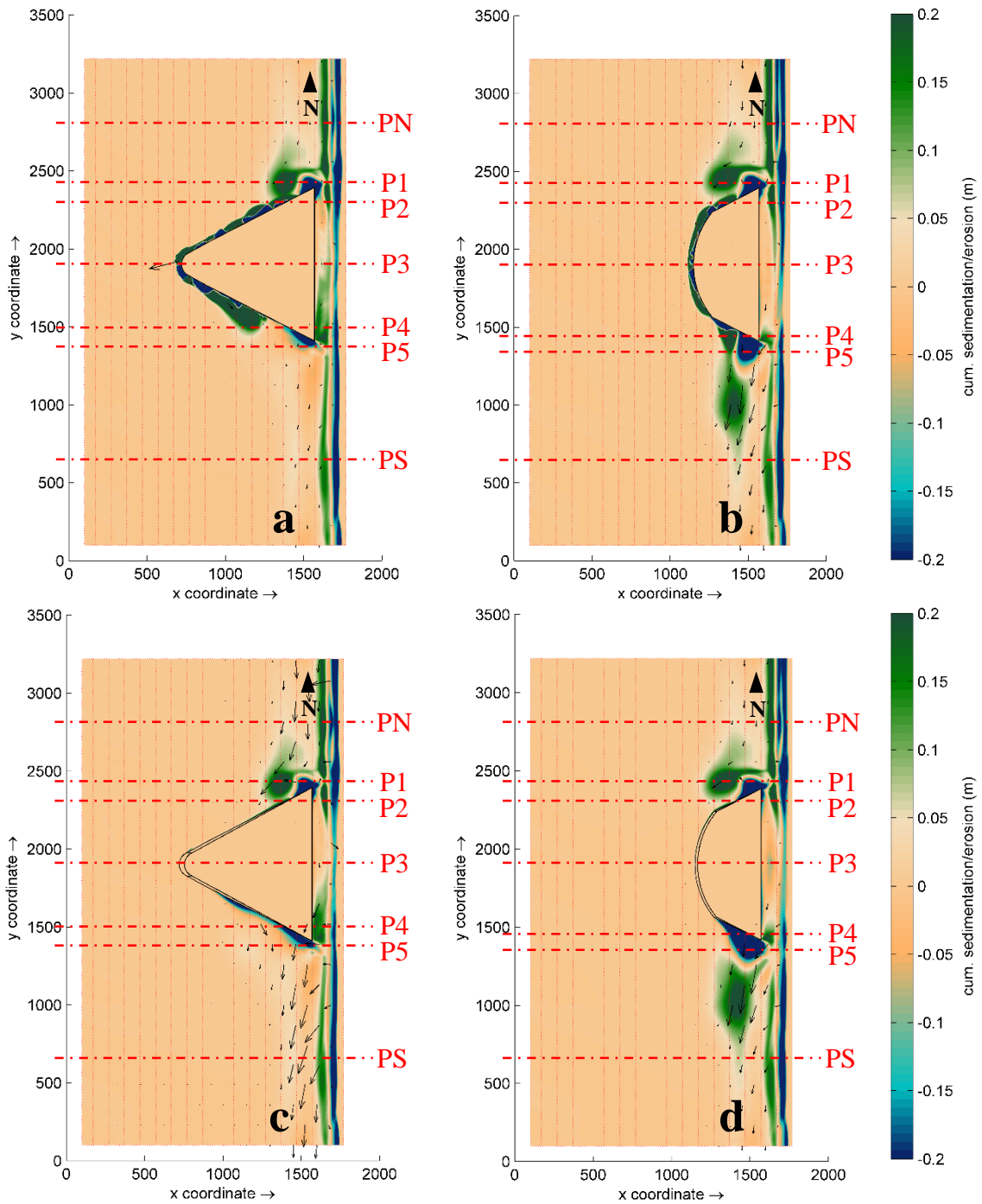**Figure 5.68:** Cumulative sedimentation/erosion results and profile locations for scenarios: a) RB3_S9; b) RB3_S10; and c) RB3_S11.
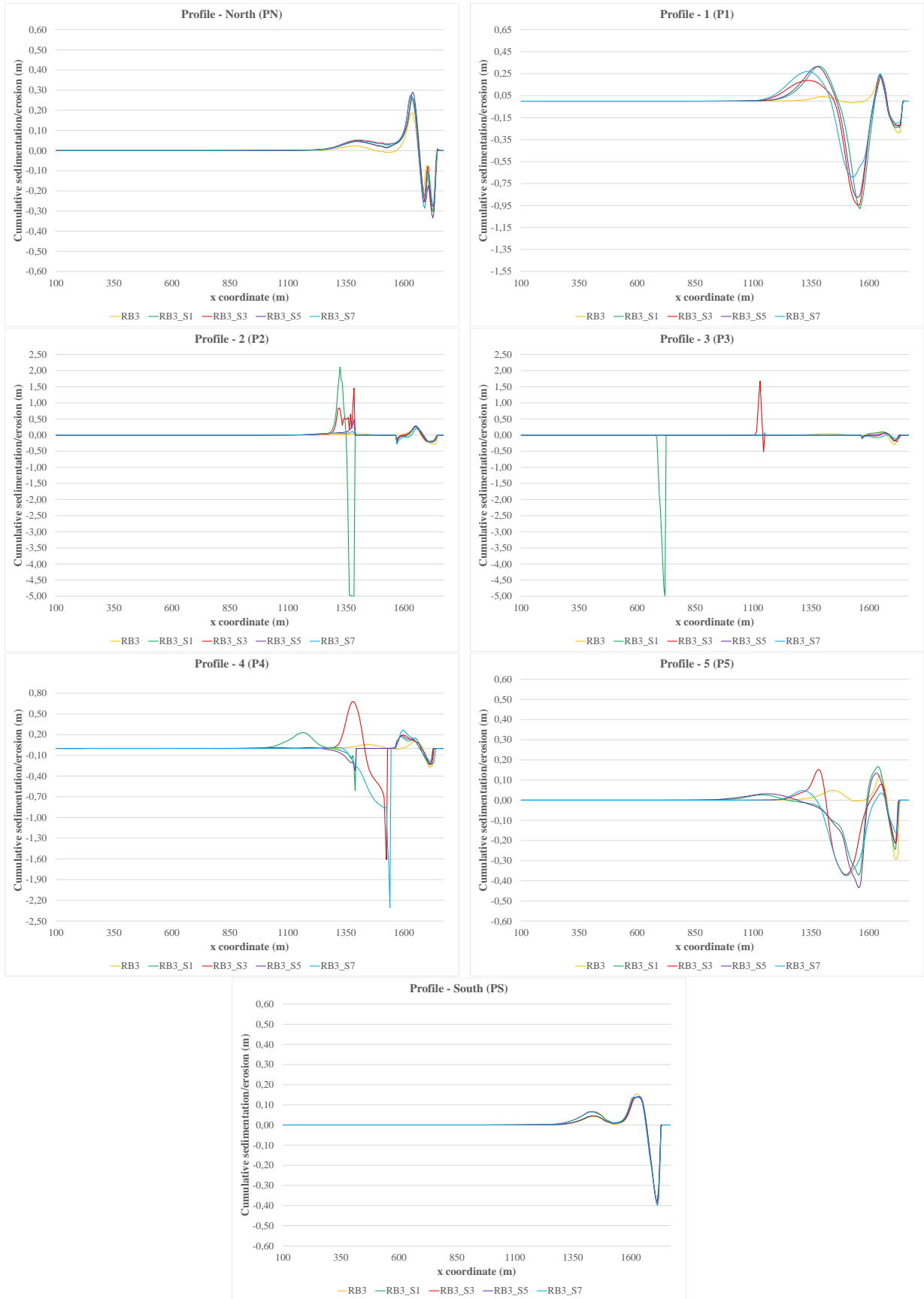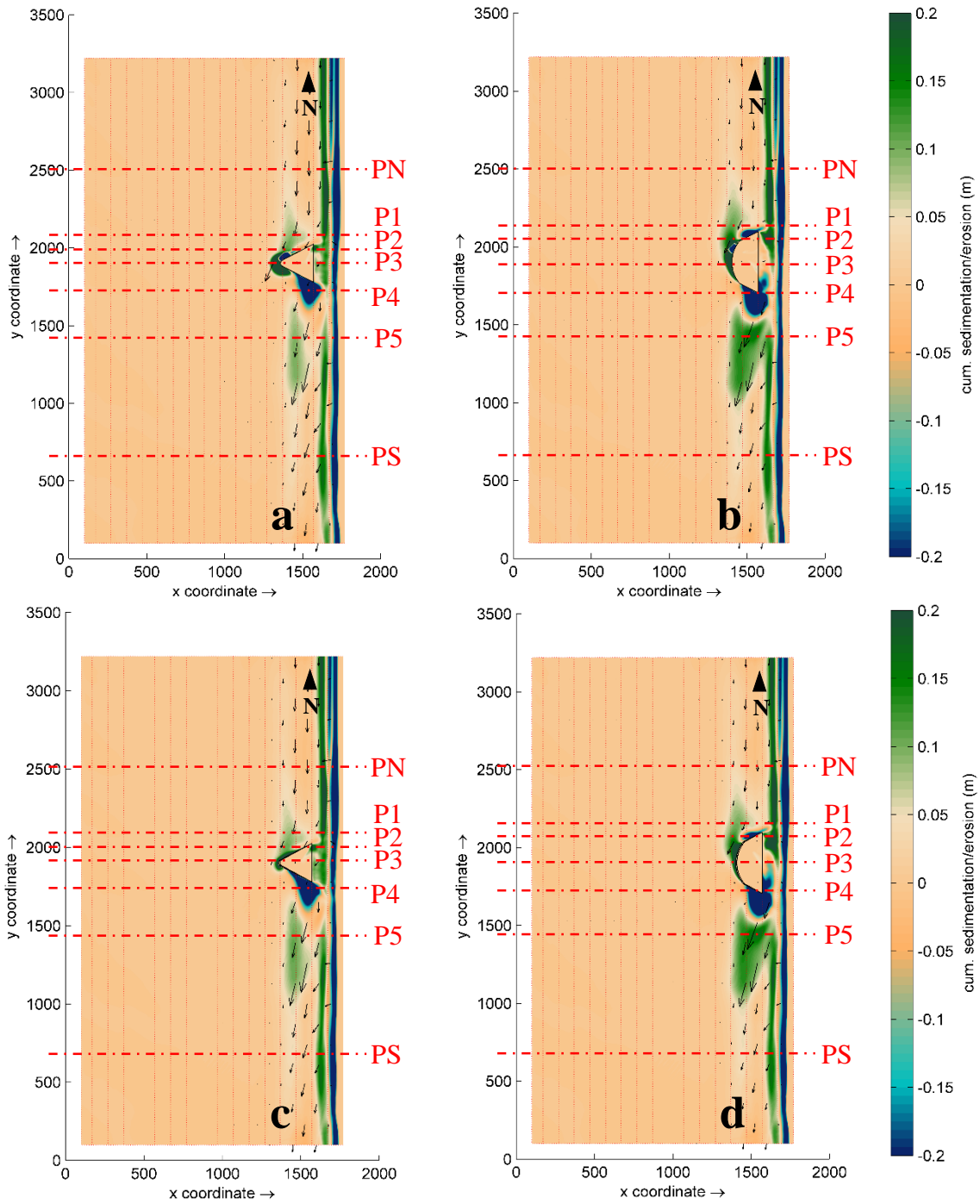
Figure 5.69: Cumulative sedimentation/erosion results along the profiles for RB3, RB3_S9, RB3_S10, and RB3_S11.

5.4.8.5 RB3_S12, RB3_S13 and RB3_S14

Lastly, Figures 5.70a, 5.70b and 5.70c depict results for the cumulative sedimentation/erosion and the mean suspended sediments transport (represented by vectors) for the entire domain of structures scenarios for RB3_S12, RB3_S13 and RB3_S14, respectively. Figure 5.71 depicts results along all profiles for RB3_S12, RB3_S13 and RB3_S14.

In this set of structures, the profiles location is not exactly the same in all scenarios because the structures location is different due to the gap adopted for each group of structures. However, each scenario has the same number of profiles with concordant positions between them, in order to ensure a coherent analysis. Due to the smaller gap between structures in RB3_S12, P5 and P6 depict results for the structures gap as well as the updrift extremities of the south structure.

Starting with PN, results depict a slight difference in results between RB3_S12 and the other structures, indicating lesser erosion near shoreline. However, these results might present discrepancies due to their different location.

Updrift, results in P1 depict sediments accretion and an improvement in erosion near shoreline for all scenarios, especially in the structure closer to shoreline (RB3_S13: +0.52 m). Near the updrift extremities of the north structures (P2), results indicate that the structure closer to shoreline contributes to greater erosion (RB3_S13: -1.52 m) than the other structures (RB3_S12: -0.58 m RB3_S14: -0.43 m) and that all slopes most exposed to wave climate tend to retain sediments. Between the structures and the shoreline, results depict sediments accumulation in RB3_S12 and RB3_S14.

At the alignment of the structures (P3), results present for all structures great sediments accumulation at the ledge of the structures, as well as in between the structures and the shoreline; however, with a lesser magnitude than in RB3. Relatively to the erosion near shoreline, an improvement in all scenarios occurs, especially in RB3_S13.

At the downdrift extremities of the north structures (P4), results depict great erosion areas for all scenarios with higher intensities in RB3_S12 and RB3_S14, but with a more extended area in RB3_S13, due to the proximity of this structure to shoreline. Similar to what has been concluded before, overall, this location presents a worsen situation than in RB3, because of the reversal of longitudinal drift.

At the structures gap (P5), great sediments accumulation occurs for all scenarios, especially in RB3_S13, which indicates that this spacing between structures allied to a 0 m crest level contribute to greater sediments accretion. Between the structures with most geometric similarities (RB3_S12 and RB3_S14), results indicate that the structure with the largest gap (RB3_S14) contributes to a larger

area of sediments accretion; however, with lesser intensity. In relation to the erosion near shoreline, comparatively to RB3, all results show a worsening in erosion, except in RB3_S14.

Near the updrift extremities of the south structures (P6), results in RB3_S12 and RB3_S14 present a reduction in the erosion areas that are commonly seen at the upper extremities of these type of structures (as presented in P2), as well as a great sediments accretion. Therefore, results at this location reflect no erosion in RB3_S12 and a lesser erosion in RB3_S14. In RB3_S13, however, this effect is slightly aggravated, which again indicates that a structure closer to shoreline tends to enhance the erosion at the structures extremities, and that although the gap between structures contributes to sediments accretion at this location, it is still not sufficient to compensate this erosion. Near shoreline, all scenarios contribute to an improvement in the erosion at this location, especially in RB3_S13, which indicates that despite promoting significant erosion near the extremities, near shoreline this scenario presents better results.

At the alignment of the south structures (P7), results demonstrate great sediments accretion at the ledge of the structures and comparatively to P3, results indicate an improvement in sediments accretion for all structures. Contrary to what has been observed in P3, the sediments accretion between the structures and the shoreline for all structures present better results than in RB3, especially in RB3_S13. Near shoreline, structures with greater distance from shoreline (RB3_S12 and RB3_S14) depict more erosion, while RB3_S13 plots an improvement in erosion relatively to RB3.

Near the downdrift extremities of the south structures (P8), results are very similar to those already analysed in P4. At this location, results also depict significant scouring for all scenarios with higher intensities in RB3_S12 and RB3_S14, but with a more extended area in RB3_S13, due to the proximity of this structure to shoreline. As expected, and similar to what has already been concluded before, this is a critical location for these types of structures probably due to the reversal of longitudinal drift, regardless of the number of structures layered in the domain.

Relatively to P9, great sediments accretion occurs for all scenarios, especially in RB3_S13, which again indicates that the 0 m crest level contributes to greater sediments accumulation. Between the structures with most geometric similarities (RB3_S12 and RB3_S14), no significant differences are depicted. As expected, the magnitude of sediments accretion at this location is less significant than in P5. In relation to the erosion near shoreline, results plot no major differences between the structures and to RB3.

Regarding the PS, overall, results are relatively the same between all structures, especially in RB3_S12 and RB3_S14 because of the structures similarities. In addition, comparatively to RB3, all structures

contribute to greater sediments accretion, yet near shoreline, no improvements in erosion are observable.

In short, as in previous conclusions, updrift of the north structures, results demonstrate that the greatest sediments accumulation and improvement in erosion near shoreline occurs for the structure closer to shoreline with a wider crest (RB3_S13). However, this structure also induces more erosion near the structures updrift extremities. At the alignment of the structures, the structure closer to shoreline (RB3_S13) also presents the best improvement in the erosion near shoreline and great sediments accretion between the structure and the shoreline. Near the structures downdrift extremities of the north structures, results again indicate this area as prone to scouring probably due to the reversal of longitudinal drift. In addition, results also demonstrate that the structure closer to shoreline (RB3_S13) presents the largest area of erosion, however with lesser intensity than in the other structures. At the structures gap, results present great sediments accumulation for all scenarios with the greatest intensity for the structure closer to shoreline with a 0 m crest level. Results at this location also indicate that for the structures farther from shoreline, the greater the gap, the larger the area of sediments accretion; however, with lesser intensity. At the updrift extremities of the south structures, results indicate that the erosion areas commonly seen at the upper extremities are reduced, except for the structure closer to shoreline (RB3_S13), which, again, means these structure characteristics tend to enhance the erosion at this location regardless of the intensity in sediments accretion at the gap. Nevertheless, near shoreline this structure presents better results at reducing the erosion, relatively to RB3. At the alignment of the south structures, the presented results are similar to those in the north structure, however with higher intensities and better results relatively to RB3. Near the downdrift extremities of the south structures, no variations relatively to the north structures are depicted. Downdrift in the domain, all scenarios present great sediments accretion, especially for the structure closer to shoreline (RB3_S13), which indicates that these structures characteristics allow good sediments transport along the domain. Near shoreline, however, no significant differences occur relatively to RB3.
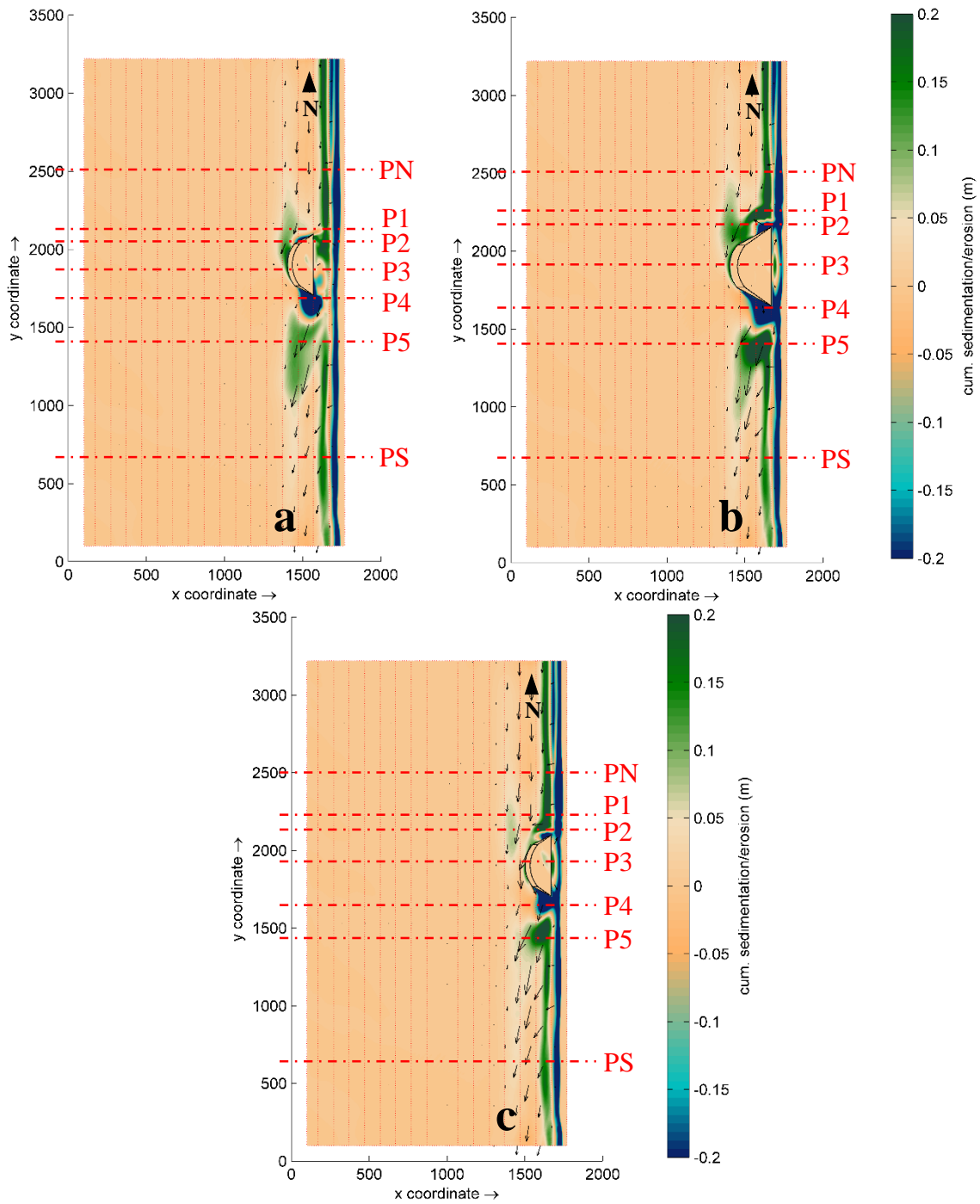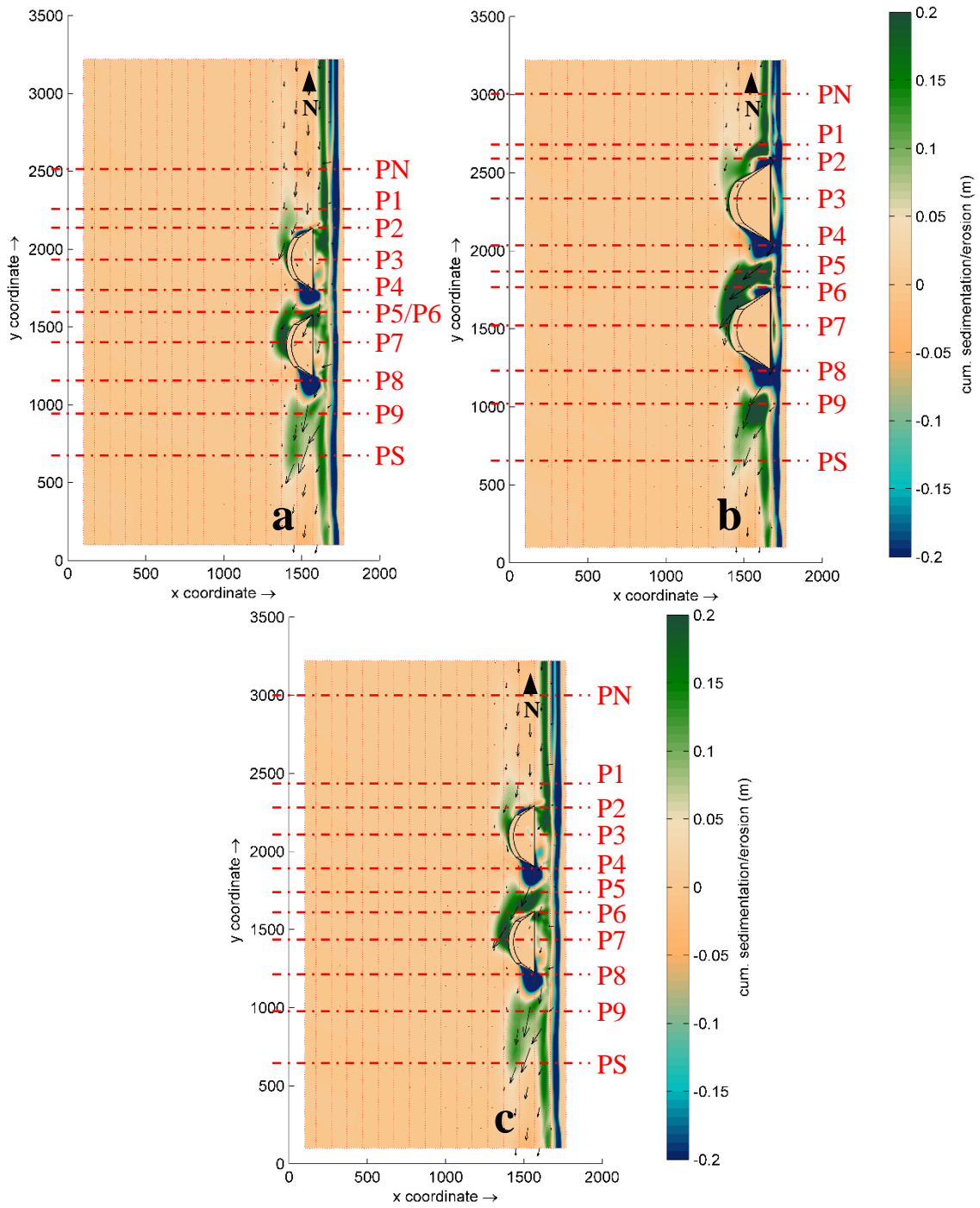
Figure 5.70: Cumulative sedimentation/erosion results and profile locations for scenarios: a) RB3_S12; b) RB3_S13; and c) RB3_S14.
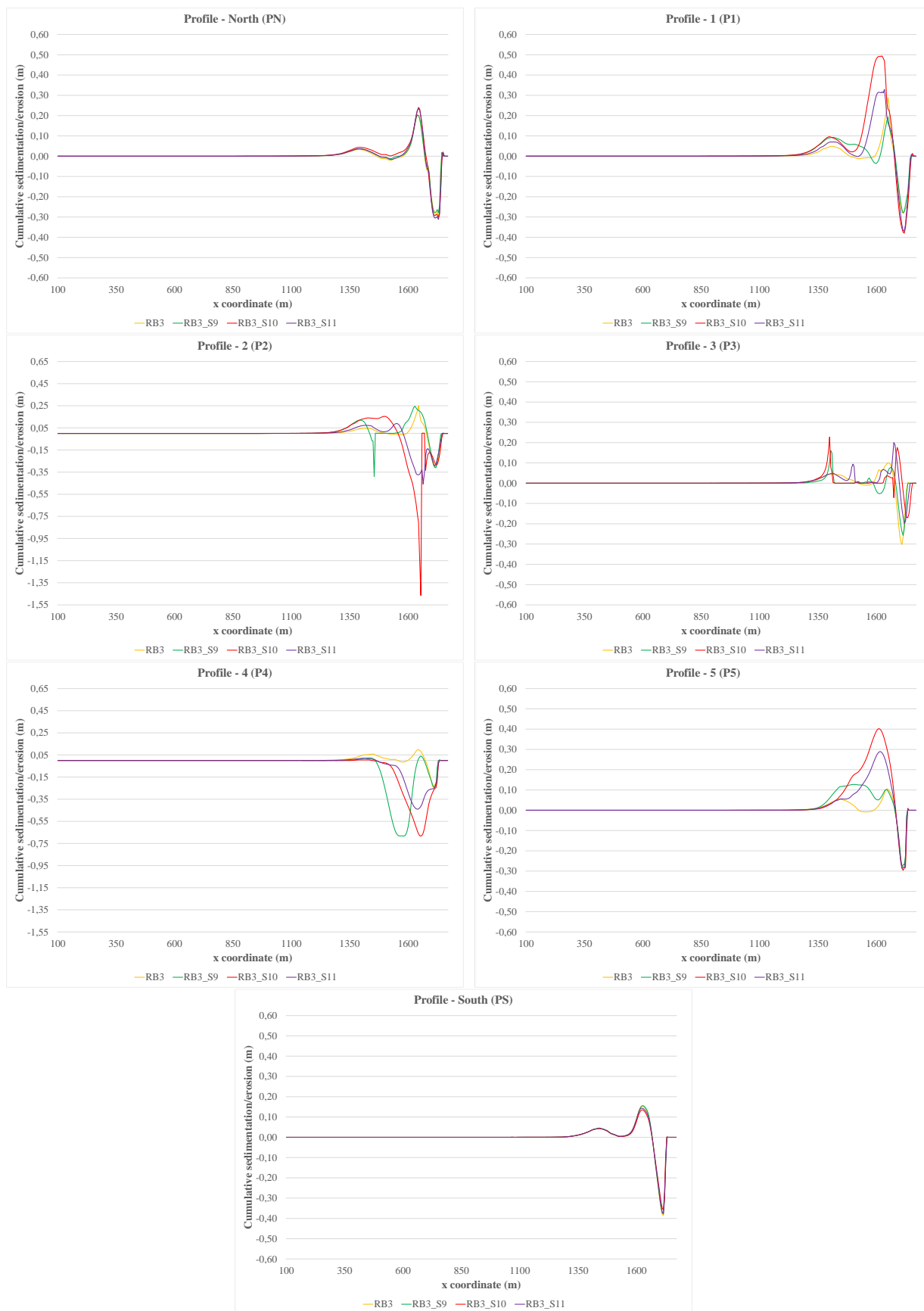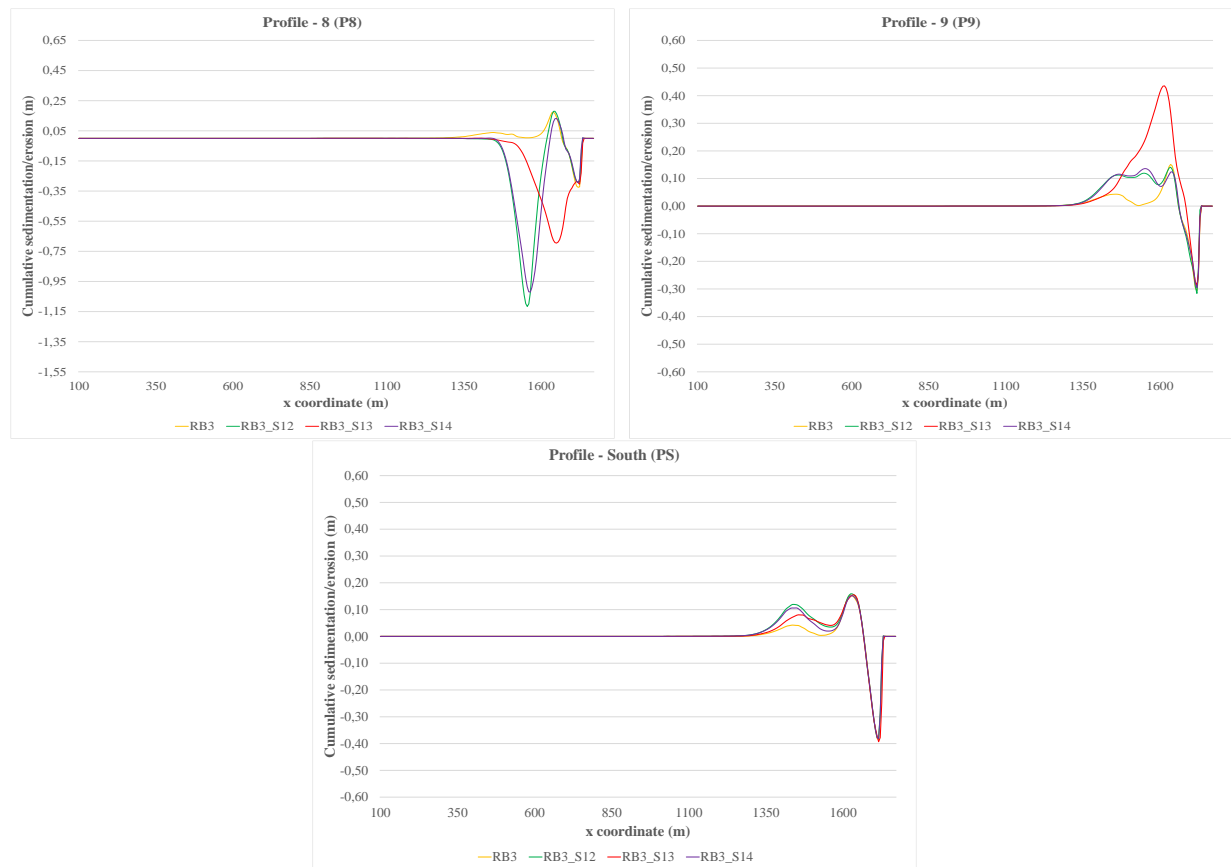
Figure 5.71: Cumulative sedimentation/erosion results along the profiles for RB3, RB3_S12, RB3_S13, and RB3_S14.

5.4.8.6 Parametric analysis and RB3_Groin scenario

Since the most favourable results for the hydro- and morphodynamics were achieved for RB3_S10, for better understanding the structure behaviour, it is important to study the influence of different conditions on this scenario. Results for the parametric analysis are organized as follows: the upper panels of each Figure depict the results for the reference bathymetry (without any structure), while the lower panels represent the outcomes with structures.

In order to compare morphodynamics results between the innovative solution and a groin, and to analyse their individual influence on sediments transport, numerical simulations for a traditional groin are also conducted.

As previously mentioned in Section 5.4.7, the third group focuses on the sediments dimension effect on the accretion/erosion patterns. Since the main conducted scenarios assumed fine sands for the bed level composition (D_{50} = 0.2 mm and D_{90} = 0.3 mm), the parametric analysis focuses on coarse (RB3_C and RB3_C_S10) and medium sands (RB3_M and RB3_M_S10). The selected sand characteristics for these scenarios are based on the Unified Soils Classification (Bosboom and Stive, 2022) and the selected dimensions are identified in Figure 5.72. The nominal diameters selection for D_{50} and D_{90} are

calculated by assuming the mean and the percentile 90 for each class, respectively. Thus, for coarse sand, D_{50} = 3.6 mm and D_{90} = 4.6 mm, and for fine sand, D_{50} = 1.0 mm and D_{90} = 1.7 mm.

Figure 5.72: Unified Soils Classification for medium and coarse sand nominal diameter selection (Bosboom and Stive, 2022).

Regarding the wave climate conditions, Figures 5.73a and 5.73b depict results for the entire domain for SW and W wave climate directions, while Figure 5.74 plots results along all profiles (RB3_SW, RB3_SW_S10; RB3_W, RB3_W_S10; and RB3_S10).

The first analysed parameter demonstrates that results in RB3_SW_S10 depict an inverted pattern relatively to RB3_S10, as it would have been expected, and that in RB3_W_S10 the patterns for sediments deposition as well as the erosion areas are relatively symmetrical relatively to the alignment of the structure.

Results for RB3_SW_S10 indicate great sediments accretion in PN with a reduction in erosion near shoreline, but aggravated erosion in P1 and P2, due to scouring from the reversal of longitudinal drift, as previously mentioned. At the alignment of the structure (P3), results reveal sediments accretion at the ledge of the structure as well as an improvement in erosion reduction near shoreline, with a slight sediments accumulation, relatively to RB3_SW. In P4, results depict sediments accretion near the structure slope, but also significant erosion areas near the structure updrift extremity; however, with an improvement in erosion near shoreline, relatively to RB3_SW. Updrift (P5 and PS), an improvement in sediments accretion is observable as well as in the erosion reduction, comparatively to RB3_SW.

In RB3_W_S10, results in PN depict a larger area of sediments accretion than in RB3_W and RB3_S10; and an aggravation of erosion near shoreline relatively to RB3_S10. Updrift the structure in P1, results indicate lesser sediments accretion relatively to RB3_W and RB3_S10; however, next to shoreline the W wave results indicate an improvement in erosion near shoreline, comparatively to

RB3_S10. Near the structure upper extremity (P2), results for RB3_W_S10 indicate a worsen scenario than in RB3_S10 and RB3_W in terms of erosion.
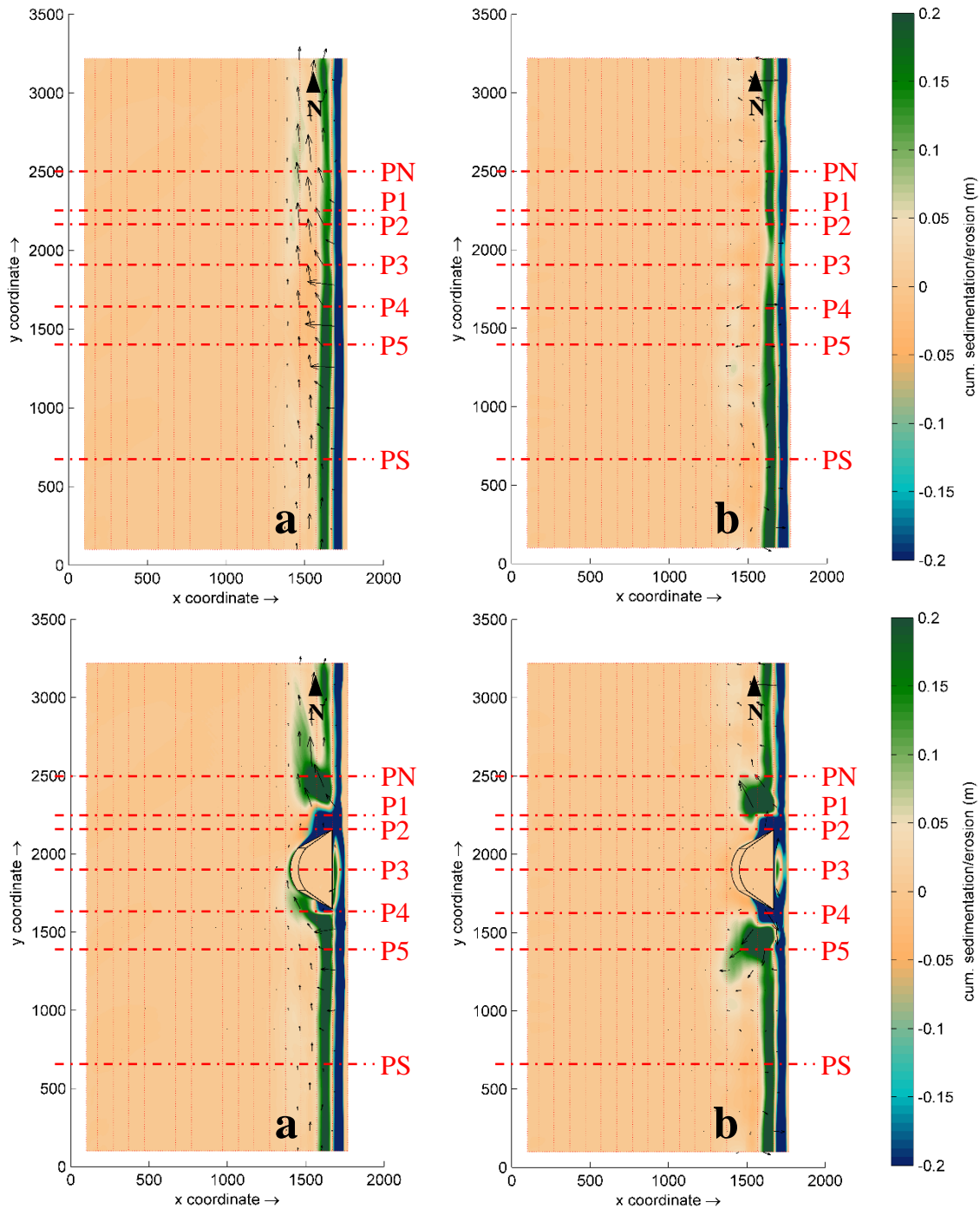
Figure 5.73: Cumulative sedimentation/erosion results and profile locations for scenarios: a) RB3_SW (upper panel) and RB3_SW_S10 (lower panel); and b) RB3_W (upper panel) and RB3_W_S10 (lower panel).

At the alignment of the structure (P3), an improvement in sediments accumulation and in erosion reduction occurs near shoreline relatively to RB3_W; but along the ledge of the structure due to the nature of the wave climate no sediments settle at this location. Near shoreline, results are also better in RB3_W_S10 than in RB3_S10.
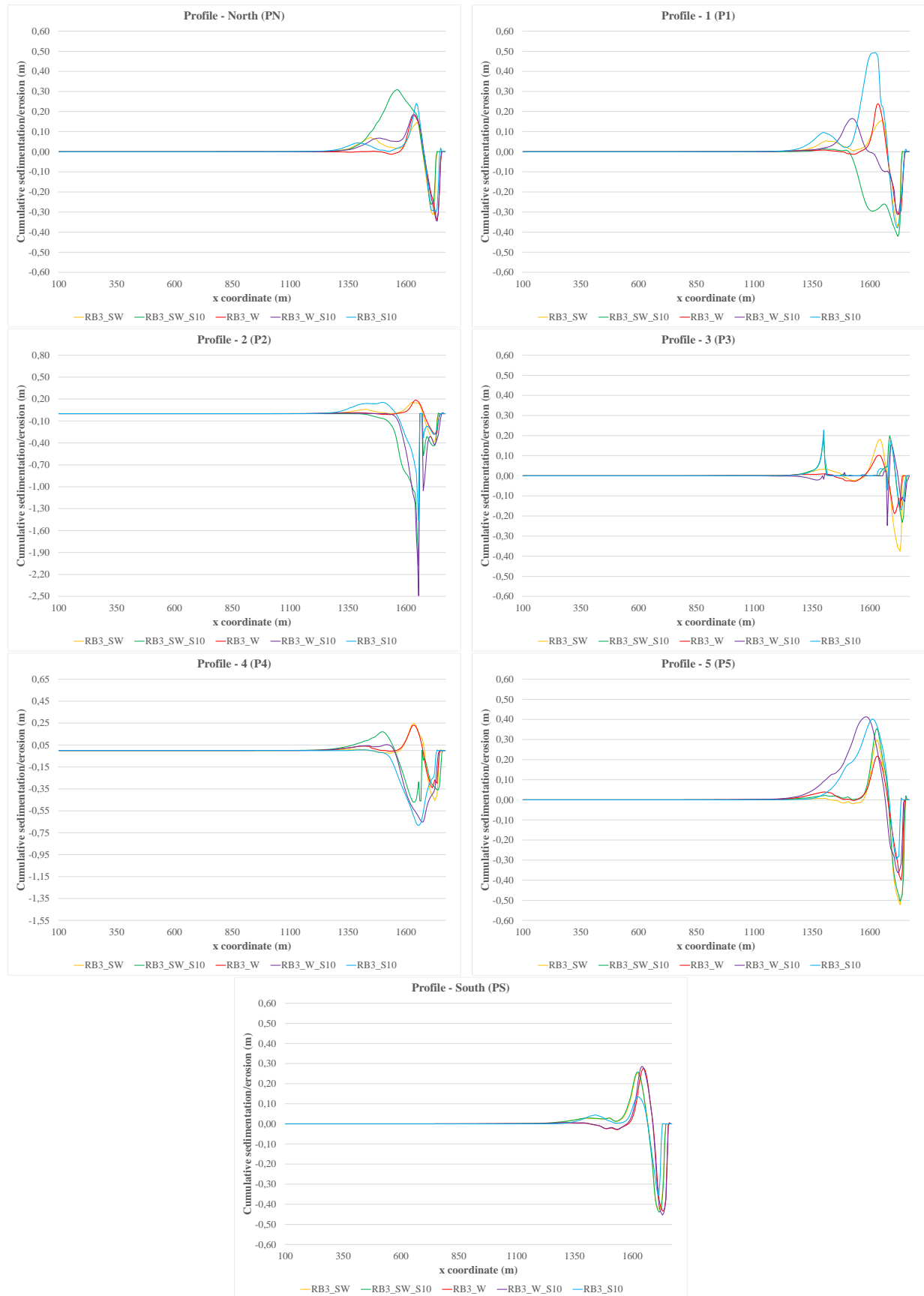
Figure 5.74: Cumulative sedimentation/erosion results along the profiles for RB3_SW, RB3_SW_S10, RB3_W, RB3_W_S10, and RB3_S10.

Near the structure lower extremity (P4), results in RB3_W_S10 are similar to those in RB3_S10; however, these scenarios present an aggravated erosion relatively to RB3_W. Downdrift (P5), results in RB3_W_S10 are also similar to those in RB3_S10; however, with an aggravation in erosion near shoreline. Comparatively to RB3_W, results in RB3_W_S10 present greater sediments accumulation and an improvement in erosion reduction near shoreline. In PS, results in RB3_W_S10 are similar to those in RB3_W, with a slight improvement in sediments accumulation relatively to RB3_S10. However, near shoreline, in the W wave climate results present an aggravation in erosion relatively to RB3_S10.

Concerning the different sand dimensions, Figures 5.75a and 5.75b present results for the entire domain for coarse and medium sand, while Figure 5.76 plots results along all profiles (RB3_C, RB3_C_S10; RB3_M, RB3_M_S10; and RB3_S10).

The second analysed parameter demonstrates that results in RB3_C_S10 and RB3_M_S10 present less suspended sediments along the domain due to the nature of sediments, and that in all profiles the sedimentation and erosion are less intense than in RB3_S10 (with finer sediments). When analysing RB3_C_S10 and RB3_M_S10, overall, the same can be concluded, as coarse sediments present less intense sedimentation as well as less significant erosion areas.

Starting with the farthest profiles in the domain (PN and PS), results indicate that, relatively to RB3_C and RB3_M, no variations occur in RB3_C_S10 and RB3_M_S10, which means no influence of the structure takes place at these locations. Updrift, in P1, relatively to RB3_C and RB3_M, a larger area of sediments accretion in RB3_C_S10 and RB3_M_S10 occurs, while in P2 the commonly erosion near the structure extremity is visible; however, with lesser intensity than in RB3_S10. In addition, an improvement in erosion near shoreline is also observable. At the alignment of the structure (P3), near shoreline, the erosion in RB3_C_S10 and RB3_M_S10 is also improved relatively to RB3_C and RB3_M. Near the downdrift structure extremity (P4), the erosion probably due to the reversal of longitudinal drift is also present and more significant in RB3_S10; however, near shoreline the erosion effect in RB3_M_S10 and RB3_C_S10 is lessen, relatively to RB3_C and RB3_M. In P5, the sediments accumulation downdrift is also visible for all cases, with higher values in RB3_S10, but with more aggravated erosion near shoreline.
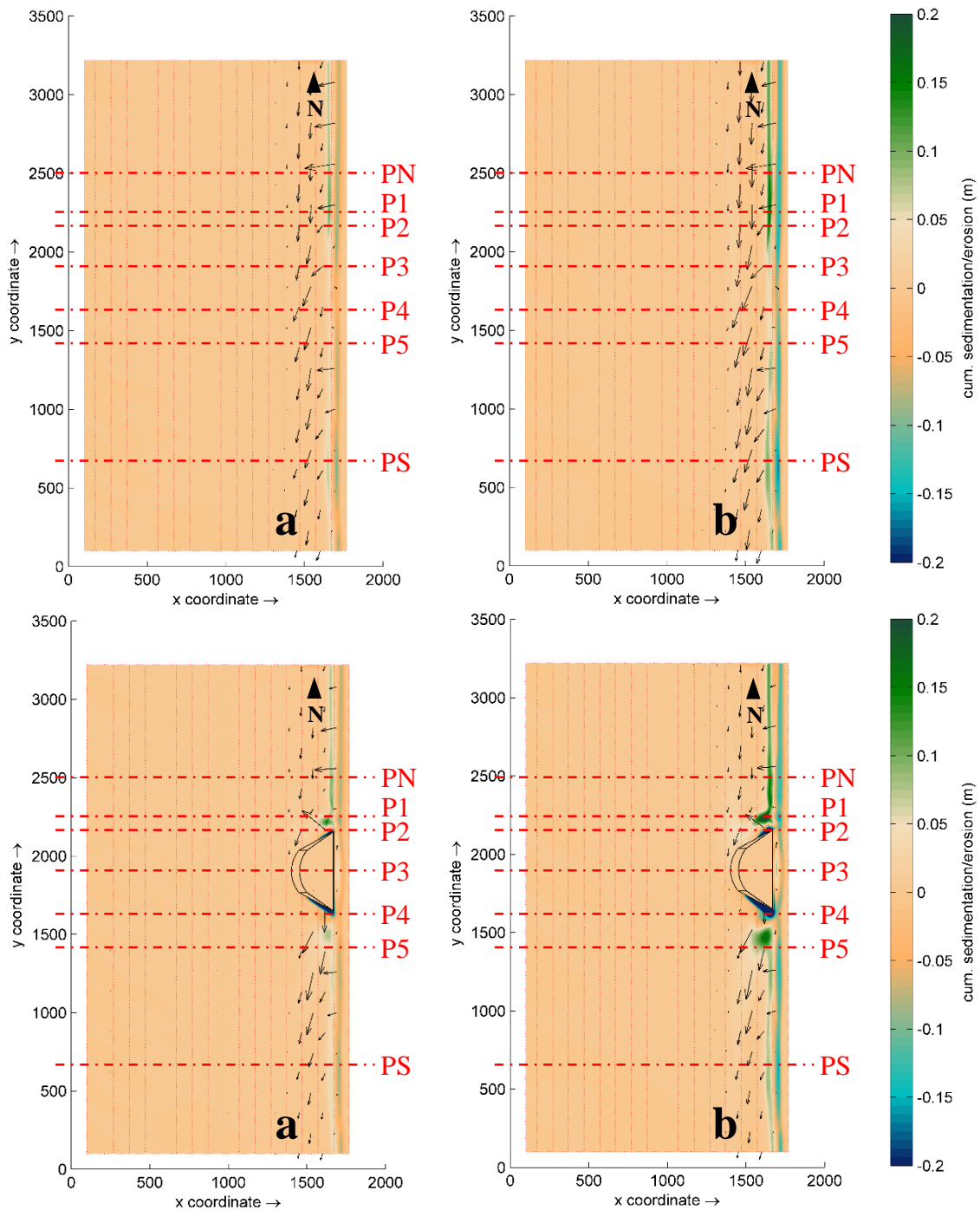
Figure 5.75: Cumulative sedimentation/erosion results and profile locations for scenarios: a) RB3_C (upper panel) and RB3_C_S10 (lower panel); and b) RB3_M (upper panel) and RB3_M_S10 (lower panel).
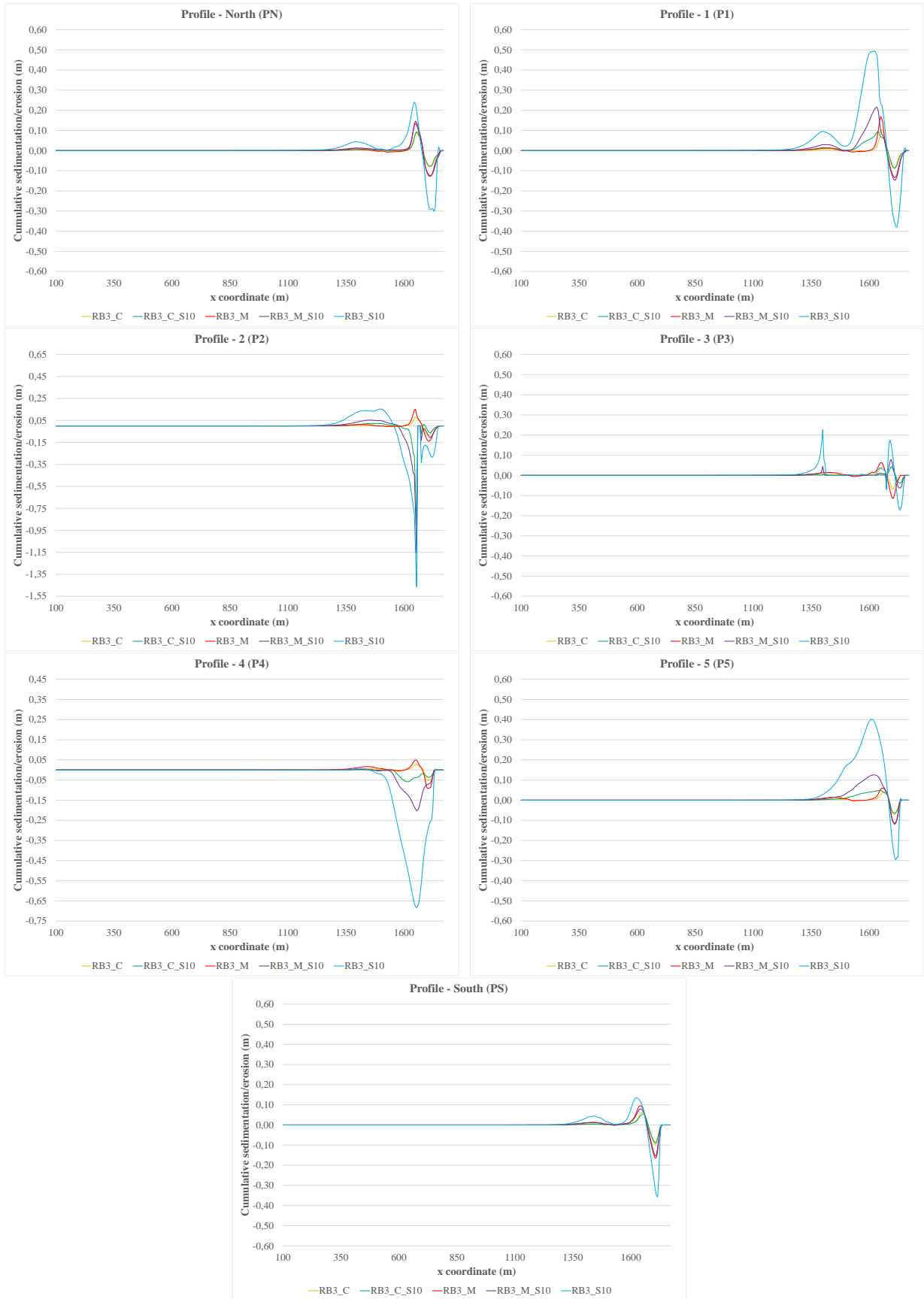
Figure 5.76: Cumulative sedimentation/erosion results along the profiles for RB3_C, RB3_C_S10, RB3_M, RB3_M_S10, and RB3_S10.

In regards to tidal levels conditions, Figures 5.77a and 5.77b show results for the entire domain for high tide and low tide, while Figure 5.78 plots results along all profiles (RB3_H, RB3_H_S10; RB3_L, RB3_L_S10; and RB3_S10).

The third analysed parameter demonstrates that, in all profiles, sediments accumulation and erosion areas occur at a farthest location relatively to shoreline in a low tide, and in a high tide, results plot these effects closer to shoreline. In addition, larger areas of sediments accretion and erosion are more notorious in RB3_H_S10 than in RB3_L_S10.

Starting with PN and PS, results depict no significant variations at the farthest locations from the structure, except in PN for RB3_L_S10, where the sediments accumulation and the erosion near shoreline is the most intense. Updrift, in P1, despite RB3_H_S10 having a larger area of sediments accumulation, RB3_L_S10 presents greater results for sediments accumulation and an improvement in erosion reduction near shoreline, relatively to RB3_L and the high tide results. Relatively to RB3_S10, high tide and low tide results have lesser intensities in sediments accretion and in erosion near shoreline. These results indicate that the 0 m crest level of the structure has a better performance at retaining sediments at this location when the tide level is 0 m than in a low tide or a high tide. In P2, RB3_H_S10 and RB3_L_S10 results depict an improvement in sediments accretion relatively to RB3_H and RB3_L; however, near the updrift structure extremity intense erosions are visible, especially in RB3_H_S10 (-1.18 m). Nonetheless, results in RB3_S10 present the most intense erosion near the structure extremity (-1.47 m). At the alignment of the structure (P3), in RB3_L_S10 results indicate a slight sediments accretion at the ledge of the structure, and that near shoreline, the erosion area depicted in RB3_L is no longer observed, because the structure's presence avoids erosion at this location due to the low tide. In RB3_H_S10, results demonstrate that at the ledge of the structure no sediments accretion occurs and that near shoreline an improvement in erosion occurs relatively to RB3_H. RB3_S10 presents the greatest sediments accumulation at the ledge of the structure, and near shoreline, results indicate more sedimentation and less erosion relatively to high tide results. Near the downdrift structure extremity (P4), the erosion probably due to the reversal of longitudinal drift is less significant in low tide and more significant in RB3_H_S10, which means that at this location, the higher the tide, the greater the erosion. Near shoreline, results depict no variations relatively to the reference bathymetries. In P5, the sediments accumulation downdrift is also visible for all cases, with greater sediments accretion in RB3_S10 than in RB3_H_S10 and lesser values in RB3_L_S10.
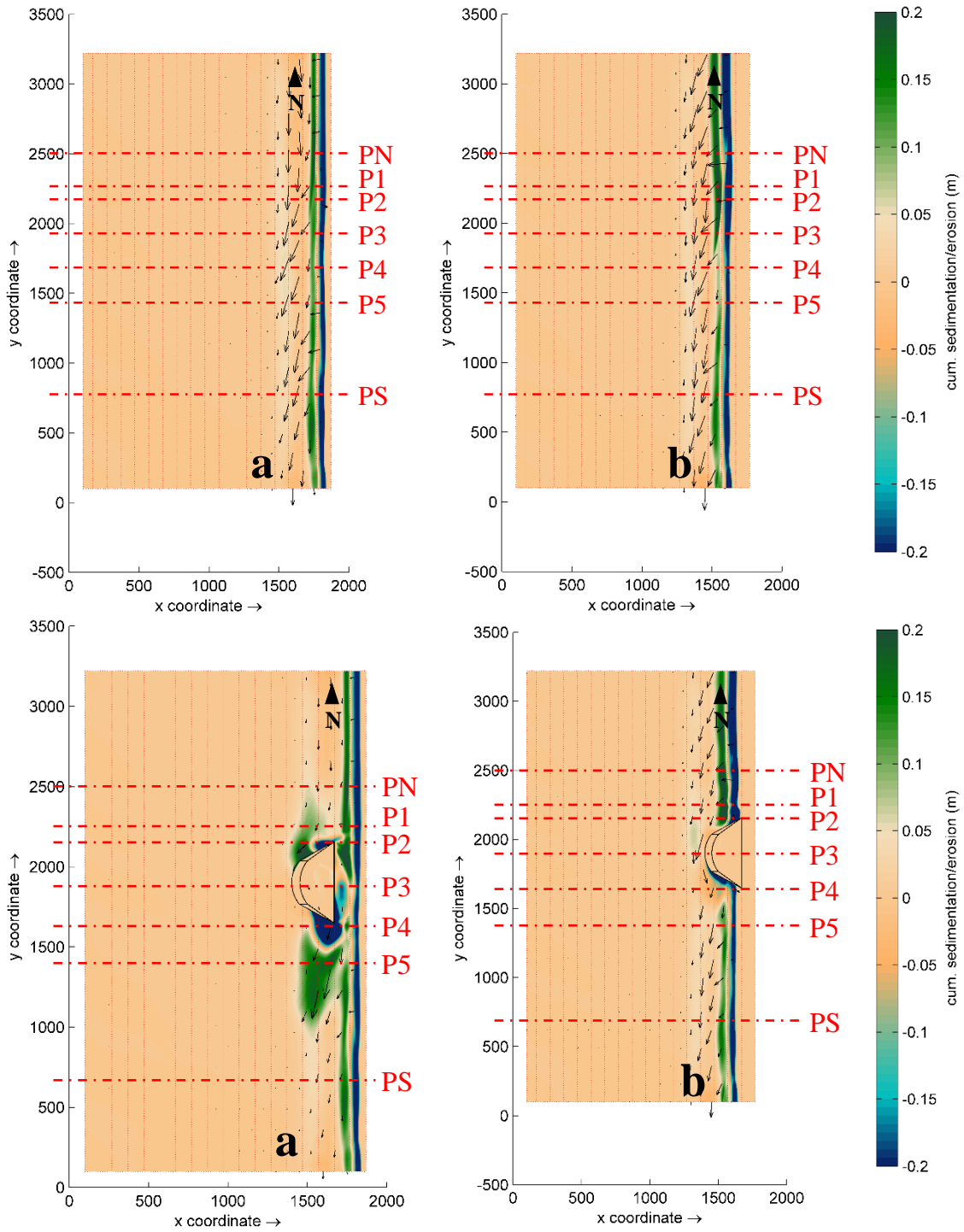
Figure 5.77: Cumulative sedimentation/erosion results and profile locations for scenarios: a) RB3_H (upper panel) and RB3_H_S10 (lower panel); and b) RB3_L (upper panel) and RB3_L_S10 (lower panel).

Figure 5.78: Cumulative sedimentation/erosion results along the profiles for RB3_H, RB3_H_S10, RB3_L, RB3_L_S10, and RB3_S10.

Lastly, as to the influence of an intense storm, Figure 5.79 depicts results for the entire domain for scenarios RB3_Storm10 (left panel) and RB3_Storm10_S10 (right panel), while Figure 5.80 plots results along all profiles for the same scenarios as well as in RB3_S10.

Overall, results depict more intense sediments accretion and erosion along the domain than in RB3_S10. However, in some locations the sediments accumulation and erosion are not as significant when compared to RB3_S10.

Updrift, PN and P1 depict greater sediments accumulation and erosion areas in RB3_Storm10_S10 than in RB3_S10 and RB3_Storm10; while in P2, results indicate similar sediments accretion at the structures slopes in RB3_Storm10_S10 and RB3_S10, and more significant erosion near the structure upper extremity in RB3_S10. Near shoreline, results plot an aggravation in erosion in RB3_Storm10_S10 relatively to RB3_Storm10 and RB3_S10. At the alignment of the structure (P3), results indicate similar sediments accumulation at the ledge of the structure in RB3_Storm10_S10 and RB3_S10, and an aggravation in erosion near shoreline in RB3_Storm10_S10 relatively to RB3_S10. However, in an intense storm condition, the structure in RB3_Storm10_S10 contributes to an improvement in erosion reduction near shoreline when compared to the reference bathymetry (RB3_Storm10).
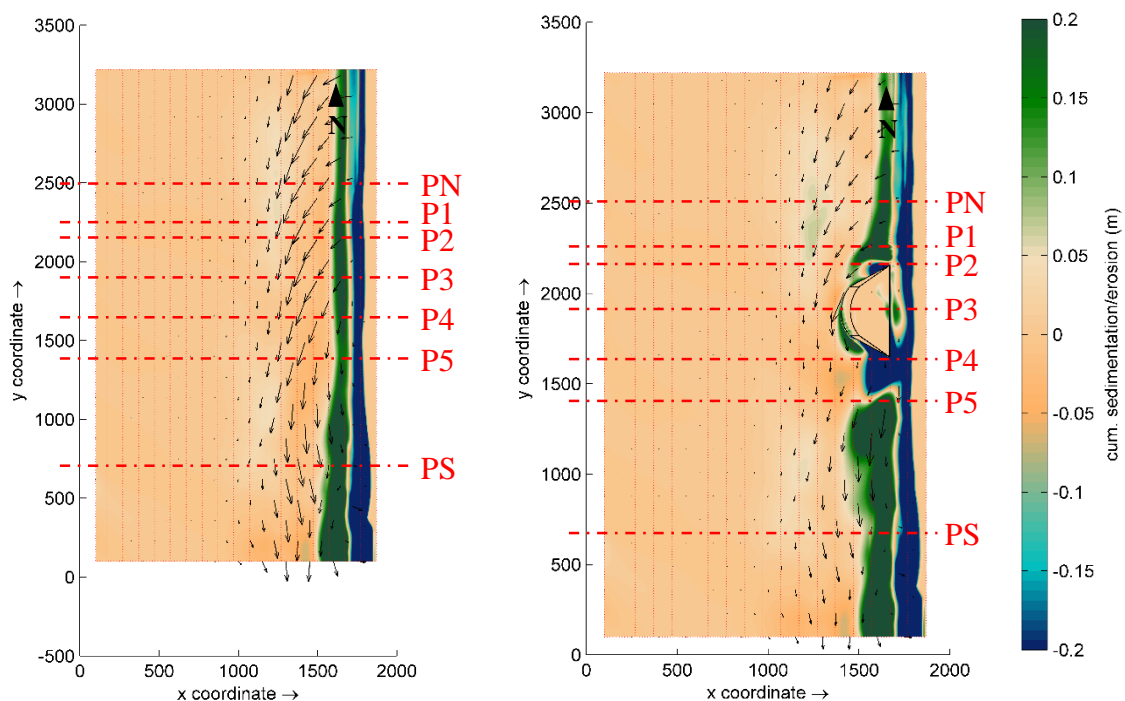
Figure 5.79: Cumulative sedimentation/erosion results and profile locations for scenarios RB3_Storm10 (left) and RB3_Storm10_S10 (right).

Figure 5.80: Cumulative sedimentation/erosion results along the profiles for RB3_Storm10, RB3_Storm10_S10, and RB3_S10.

Near the downdrift structure extremity (P4), RB3_Storm10_S10 presents the most intense erosion (-1.30 m) probably due to the reversal of longitudinal drift; while in P5, results depict greater sediments accretion and an improvement in erosion relatively to RB3_Storm10. In addition, at this location, RB3_S10 presents the most intense sediments accretion and the less intense erosion near shoreline. In PS, results between RB3_Storm10_S10 and RB3_Storm10 are fairly the same, while comparatively to RB3_S10, the sediments accumulation and erosion are more intense.

The left panel of Figure 5.81 presents the results for RB3 (without any structure), while the right panel depict results for the entire domain for RB3_Groin. Figure 5.82 plots results along all profiles for scenarios RB3, RB3_Groin and RB3_S10.

Comparing the groin with the innovative structure, RB3_S10 presents a good performance overall, with some locations having an improvement in the erosion near shoreline and greater sediments accumulation along the domain. Nonetheless, some locations, especially near the structures extremities, the results are not so favourable to RB3_S10.

Starting updrift, in PN, results present no significant differences between RB3_S10 and RB3_Groin, while in P1, RB3_S10 presents better results than in RB3_Groin with greater sediments accumulation and an improvement in erosion near shoreline. In P2, however with less intensity than in RB3_Groin, results depict a great sediments accumulation area in RB3_S10. Near shoreline, results indicate less erosion area in RB3_S10, however with more intensity than in RB3_Groin. In P3, despite the RB3_Groin profile being located at a different position than P3 in RB3_S10, the innovative structure presents less sediments accumulation area and a slight aggravation in erosion near shoreline, relatively to RB3_Groin. Downdrift the structure, P4 is yet the location with the most intense erosion results in RB3_S10, probably due to the reversal of longitudinal drift. However, in P5, results indicate RB3_S10 with the most intense sediments accretion and similar erosion results near shoreline, relatively to RB3_Groin. Finally, in PS, RB3_S10 results show lesser sediments accumulation and erosion near shoreline, comparatively to RB3_Groin.
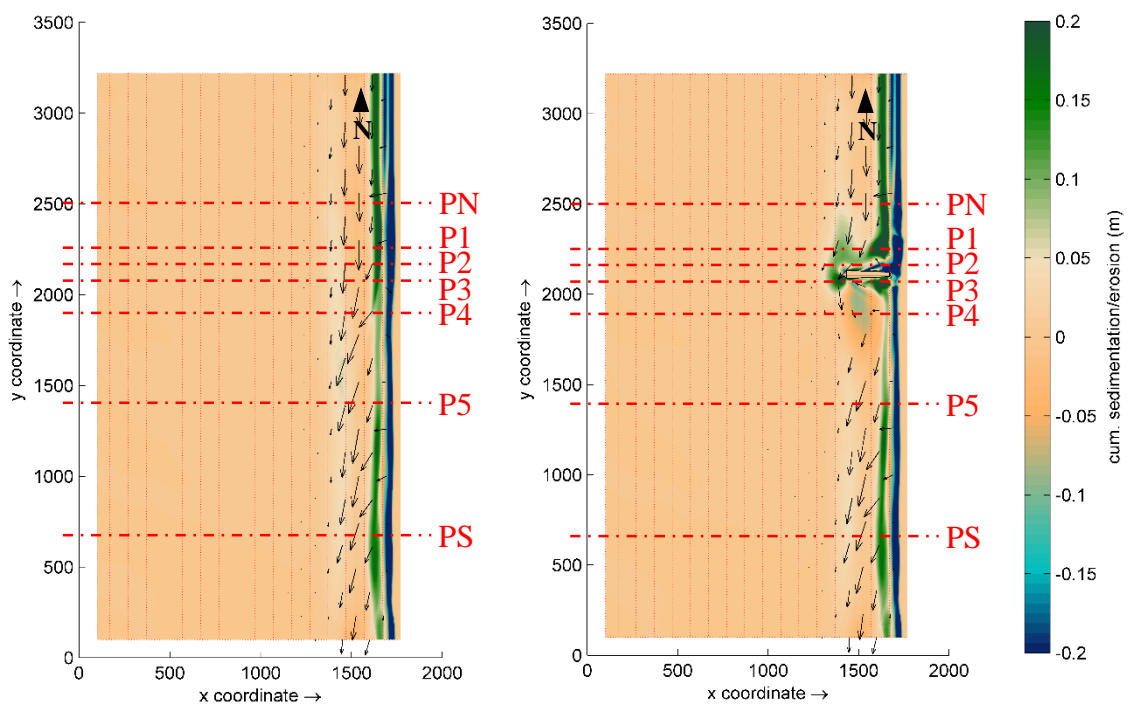
Figure 5.81: Cumulative sedimentation/erosion results and profile locations for scenarios RB3 (left) and RB3_Groin (right).

Regarding the influence of the groin in the reference bathymetry (RB3), results demonstrate an improvement in sediments accretion and erosion reduction near shoreline in PN, and similar results downdrift (P5 and PS). In P1, results show significant sediments accretion parallel to the groin slope, but an aggravation in erosion near shoreline. In P2, although sediments accumulation near the groin slope location is more intense in RB3_Groin than in RB3, results depict the worst erosion results in RB3_Groin near shoreline (-1.33 m). Downdrift in P3, results in RB3_Groin present a significant improvement in erosion reduction near shoreline, and a great sediments accretion parallel to the groin slope, however, with an erosion area visible between 1445 m and 1510 m. Finally, in P4, an erosion area is formed between 1380 m and 1620 m, but near shoreline, the erosion is reduced relatively to RB3.
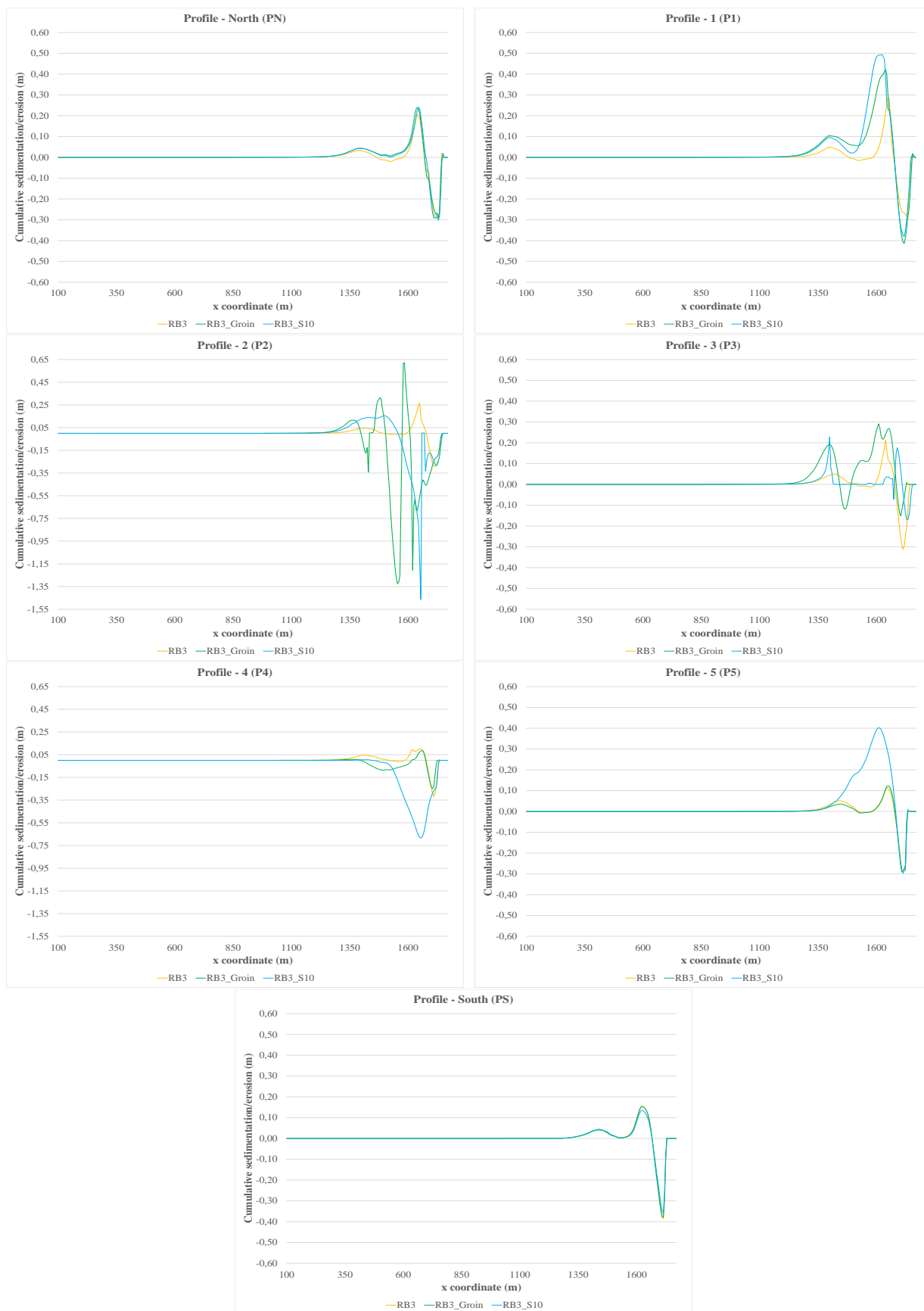
Figure 5.82: Cumulative sedimentation/erosion results along the profiles for RB3, RB3_Groin and RB3_S10.

5.5 Summary and conclusions

Hydro- and morphodynamic studies under storm conditions have been developed in order to obtain optimized geometries for maritime protection structures that have the capacity to induce a longitudinal drift reversal.

The observation of waves' behaviour at river mouths environments, where usually the reversal of longitudinal drift occurs, served as a basis for estimating the dimensions to consider in an artificial ebb tidal delta simulated with bathymetric changes and in the protection structures.

The storm conditions for application of hydro- and morphodynamics models required the consideration of previously obtained results for the wave heights with a return period of 100 years for HP, RCP4.5_end and RCP8.5_end. For this, it was necessary to nest models that involved the entire region of the Atlantic littoral of the Iberian Peninsula and the river Lima mouth was the selected location to estimate the wave characteristics, through the application of Delft Dashboard and D3D. Considered storm conditions are: $H_s = 4$ m and $T_p = 15$ s, and for a more intense storm condition is: $H_s = 10$ m and $T_p = 19$ s.

Results from this analysis demonstrated that:

- Along the western coast of Iberian Peninsula, the wave climate tends to be less energetic as the latitude decreases;

- The significant wave heights have similar behaviours along the selected location regardless of the scenario, as they remain constant until a more abrupt variation of the beach slope where the waves tend to break;

- Near the coast, for the HP and RCPs scenarios, the obtained results are very similar, despite of their input values being different.

Hydrodynamics modelling with D3D was considered to simulate the effect of the wave regime in wave energy dissipation and in the reversal of longitudinal drift in different bathymetric conditions when the domain was considered without implantation of structures or when structures with different geometries were considered.

Morphodynamics modelling with XBeach was developed to describe sediments transport (accretion and erosion) behaviour for new protection structures with the best hydrodynamics performance related to the reversal of longitudinal drift.

The main objective of this study was to ensure that the optimized structure dissipates energy and reorients the waves, since the incident waves orientation influences the sediments transport. Artificial

headland shapes were explored based on the necessary horizontal and vertical dimensions, from observations of real cases, in order to induce the reversal of the longitudinal drift. Despite having the possibility of being constructed from land and inducing sedimentary accumulations, this shape has excessive dimensions, which will entail great costs and be an expensive solution. For this reason, structures with similar shapes but with lesser dimensions were studied.

In addition, the intention of this study was to ensure that the structures defend the beach and that the erosion bar near shoreline is reduced.

From the hydrodynamics modelling results, it can be concluded that:

a) For RB1 and RB2:

- The greater the curvature of shapes, the more evident the effect of the reversal of longitudinal drift;

- Seaward slope variations should not be too abrupt, in order to benefit from the reversal of longitudinal drift;

- Emerged shapes and more elevated submerged crest levels have greater energy waves dissipation;

- A structure that is closer to shoreline with a more rounded shapes is more favourable to the reversal of longitudinal drift than the bell-shaped curves;

- The best results for wave energy reduction are for structures that have a parallel orientation relatively to shoreline with the larger dimensions facing the wave action, since they yield greater areas for the shadow zone;

- The best results for the reversal of longitudinal drift and wave energy dissipation are for long and wide shapes with a fixed platform near shoreline;

- The combination of subtle slope variations with the bed level curved shape downdrift guarantees a relatively large reversal in this region.

b) For RB3:

- The most suitable domain extensions for the simulations was RB3;

- The most intense reversal is justified by a wider geometry with a more curved shape;

- The rocky outcrop inspired shape presents results that are relatable to those of a detached structure, and the triangular and curved shapes results are similar to those of a groin;

- Detached shapes present a reversal of longitudinal drift more limited around the shape, while the platform shapes induce the reversal in a larger area;

- Slope-type structures present smoother decreasing of significant wave heights in the wave-breaking region and more extensive wave shoaling than in wall-type structures;

- Submerged platforms at -2.0 m present good results for reducing the significant wave heights. However, they transmit more wave energy to the beach, when compared to structures with 0 m crest levels;

- The more rounder and wider shapes provide more evident reversal of the longitudinal drift along their slopes/walls;

- Small scale structures present similar wave energy dissipation results in the shadow zones as those in large scale structures;

- Regardless of their width, structures constructed on shoreline with 0 m crest level present no waves' transmission over the structures for a tidal level of 0 m, and are cyclically emerged and submerged depending on the tidal level. Compared to completely submerged structures, those structures are not also visually appealing, but they also stand out for safeguarding tidal variations caused by storm surges and the mean sea level rise due to climate changes. Results for these structure should be, however, analysed very cautiously at this location and complemented with morphodynamics simulated with XBeach;

- Group of structures results indicate that in terms of significant wave height decreasing and the reversal of longitudinal drift, the number of structures does not affect the hydrodynamics outcomes in SWAN, and that morphodynamics simulations are necessary to understand their influence along the domain;

- The hydrodynamics parametric analysis results for the most efficient structure depicts results similar to those presented for RB3_S10;

- The groin does not contribute to the reversal of longitudinal drift;

- Morphodynamic analysis is crucial to understand the influence of different conditions on shallow waters.

From the morphodynamics modelling results, it can be concluded that for RB3:

- The scenarios without structures form erosion and sedimentation bars near shoreline along the entire domain. In locations with great erosions, great accretions are also observable; and in locations of lesser sedimentations, there are also lesser erosions. Regarding the bars widths, locations with lower sedimentation values have a smaller area, and locations with higher

erosion values have a larger area. However, in both cases, the accretion does not compensate for the erosion areas;

— Less wide structures provide greater sediments transport from North to South than wider structures; however, at the downdrift extremities of those structures significant erosions occur, especially in the slope-type structure;

— Along the more exposed wave climate structure faces, results demonstrate greater erosion in wall-type than in slope-type structures;

— Comparing structures with similar characteristics but with different slopes (1:2 and 1:10), results indicate that structures with a 1:10 slope benefit from less intense erosion areas near the structures' extremities, with negligible differences in sediments accumulation near shoreline. In fact, the slope does not greatly influence the sediments results, but the structure crest level does;

— At the structures updrift extremities, large sediments accretion in all scenarios occurs; however, with immediate high erosion areas, especially in the less wide wall-type structures. The greatest sediments accumulation occurs for structures closer to shoreline, especially with a wider crest with a crest level of 0 m; however, with also intense erosion areas near the structures updrift extremities;

— At the alignment, structures closer to shoreline with a 0 m crest level present more sediments accretion near shoreline than the structure farthest from shoreline, as well as a reduction in erosion areas relatively to RB3. At the alignment of the south structures (for the group of structures), the results are similar; however, with higher intensities and better results relatively to RB3;

— The structures downdrift extremities for scenarios RB3_S1 to RB3_S14, overall, are labelled as critical areas, since these structures shape enhance the erosion probably due to the reversal of longitudinal drift and contribute to structures' scouring at this location. For the group of structures, the south structure presents no variations relatively to the north structures;

— Near shoreline, at the structures alignment, all scenarios depict a reduction in erosion, especially in the less wide slope-type structures, as well as great sediments accumulation in all scenarios;

— Near the beach, at a farther location downdrift the structures, most structures present significant sediments accretion, especially for structures closer to shoreline with a 0 m crest

level. This indicates that these structures characteristics allow the sediments transport along the domain;

— At the structures gap (for the group of structures), results present great sediments accumulation for all scenarios with the greatest intensity for the structure closer to shoreline with a 0 m crest level. Results at this location also indicate that the greater the gap, the larger the area of sediments accretion; however, with lesser intensity;

— At the updrift extremities of the south structures (for the group of structures), results indicate that the erosion areas commonly seen at the upper extremities are reduced, except for the structure closer to shoreline, which, means these structure characteristics tend to enhance the erosion at this location regardless of the intensity in sediments accretion at the gap;

— The most efficient structure is presented in RB3_S10.

From the morphodynamics modelling results for the parametric and groin analysis, it can be concluded that for RB3:

— Results with a SW wave climate direction depict an inverted pattern relatively to RB3_S10, as it would have been expected, and that in a scenario with a wave climate incoming from W, the patterns for sediments deposition as well as the erosion areas are relatively symmetrical relatively to the alignment of the structure;

— Regarding the sediments dimensions, results demonstrate that coarser and medium sands present less suspended sediments along the domain due to the nature of sediments, and that in all profiles the sedimentation and erosion are less intense than in RB3_S10 (with finer sediments). Between the coarser and medium sands, the same can be concluded, as coarse sediments present less intense sedimentation as well as less significant erosion areas;

— In low tide and high tide, results show that sediments accumulation and erosion areas occur at a farther location relatively to shoreline in a low tide, and closer to shoreline in a high tide. In addition, larger areas of sediments accretion and erosion are more notorious in high tide than in low tide;

— During an intense storm, results indicate that overall, more intense sediments accretion and erosion occur along the domain than in RB3_S10. However, in some locations the sediments accumulation and erosion are not as significant when compared to RB3_S10;

— Comparing the groin with the innovative structure, RB3_S10 presents a good performance overall, with some locations having an improvement in the erosion near shoreline and greater

sediments accumulation along the domain. Nonetheless, some locations, especially near the structures extremities, the results are not so favourable to RB3_S10.

The selected innovative structure presents a similar shape to the MFAR; however, in RB3_S10, the structure is attached to shoreline, has a rounded ledge, and its length is almost double that of MFAR. This structure could be adequate for protecting buildings near coastal zones, since there is no interruption of the longitudinal drift, and downdrift, the structure contributes to sediments accumulation, near shoreline. Overall, the sedimentary distribution of this structure is good, except for the scouring next to the extremities. Nonetheless, the structure stability is ensured, if knowing its intensity by making sure the foundation is at a deeper elevation than the erosion level. This erosion does not affect the beach; it only affects the structure.

Nevertheless, despite not being the best solution, it presents improvements at certain locations, when compared to groins. While groins interrupt the transport of sediments from North to South, being sediments accumulation only visible at a farthest location downdrift, with the proposed structure, sediments accumulation is noticeable up- and downdrift. This particular phenomenon presents the main advantage of this innovative structure, and it is also important to note that realistically, the wave, the tide and the sedimentary conditions are variable and locations pointed as critical, may become less intense with the combination of different conditions, which will be determinant to estimate the protection extension of the structure.

The overall results of the developed hydro-morphodynamic studies allow concluding that the tested innovative structures helped overcoming some problems and weaknesses of traditional protection structures. However, these innovative solutions for protection structures have some weaknesses, particularly at their extremities, which is a matter for further research.

5.6 References for Chapter 5

Bio, A.; Gonçalves, J.A.; Pinho, J.; Vieira, L.; Vieira, J.; Smirnov, G.; and Bastos, L. (2020). Indicadores de vulnerabilidade de erosão costeira: Um estudo de caso no Norte de Portugal. *Revista de Gestão Costeira Integrada - Journal of Integrated Coastal Zone Management*, *20*(3), 197–209. https://doi.org/10.5894/rgci-n337.

Bosboom, J.; and Stive, M.J.F. (2022). *Coastal Dynamics*. TU Delft Open. https://doi.org/https://doi.org/10.5074/T.2021.001.

CERC. (1984). *Coastal Engineering Research Center. US Army Corps of Engineers - Shore Protection Manual Volume 1* (4th Ed.). Washington, DC, USA: U.S. Government Printing Office. Retrieved from https://luk.staff.ugm.ac.id/USACE/USACE-ShoreProtectionManual1.pdf.

DEFRA. (2010). *Department for Environment Food and Rural Affairs - Guidance for outline design of nearshore detached breakwaters on sandy macro-tidal coasts*. Environment Agency of United Kingdom.

Ferreira, M.; Fernández-Fernández, S.; Coelho, C.; and Silva, P.A. (2021). Caracterização de tempestades e da deriva litoral no litoral de Aveiro, em cenários de alterações climáticas. In *15º Congresso da Água, 22 a 26 de Março 2021*. Lisboa, Portugal. Retrieved from https://www.aprh.pt/congressoagua2021/docs/15ca_17.pdf.

Pinho, J.; Vieira, L.; Vieira, J.; Smirnov, G.; Gomes, A.; Bio, A.; Gonçalves, J.A.; and Bastos, L. (2020). Modelação da hidrodinâmica e da morfodinâmica na costa Noroeste de Portugal em cenários de alterações climáticas. *Journal of Integrated Coastal Zone Management / Revista de Gestão Costeira Integrada*, *20*(2), 89–102. https://doi.org/10.5894/rgci-n297.

van Ormondt, M.; Nederhoff, K.; and van Dongeren, A. (2020). Delft Dashboard: a quick set-up tool for hydrodynamic models. *Journal of Hydroinformatics*, *22*(3), 510–527. https://doi.org/10.2166/hydro.2020.092.

Vieira, B.F.V. (2014). *Wave hydrodynamics in coastal stretches influenced by detached breakwaters*. MSc Thesis in Civil Engineering, University of Minho: Guimarães, Portugal. Retrieved from http://hdl.handle.net/1822/36113.

(Page intentionally left blank)

CHAPTER 6

Design of innovative RSFRC armour unit:

A thermo-mechanical analysis

"Every great advance in science has issued from a new audacity of imagination"

John Dewey. American philosopher and psychologist (1859-1952)

(Page intentionally left blank)

CHAPTER 6   DESIGN OF INNOVATIVE RSFRC ARMOUR UNIT: A THERMO-MECHANICAL ANALYSIS

6.1 Innovative concrete armour unit shape and techniques: a proposal

Inspired by the specific breakwater armour units characteristics presented in Chapter 2, as well as the benefits of the use of fibre reinforcement, the present Section intends to propose the preliminary development of an innovative shape for concrete blocks used in coastal erosion protection. Moreover, the geometric preliminary design of the proposed armour units is presented, as well as some recommendations regarding their placement, aggregates and fibres dimensions.

6.1.1 Shape, placement and materials

Towards the search for better solutions for concrete armour units used in maritime protection structures, the proposed solution combines the advantages of the resilience associated to robust blocks and the interlocking abilities inspired by the recent shapes developed during the past years. For the design of the concrete armour unit, a fibre reinforced concrete with certain thermo-mechanical properties will be proposed, which can be accomplished by using commercial or recycled fibres. Proper experimental programs should be carried out according to the recommendations of fib Model Code 2010 (Fédération internationale du béton, 2013) in order to ensure these properties are attained.

As previously mentioned, there are three main types of concrete armour units (bulky, interlocking and hollow). Briefly, bulky armour units are mainly stabilised by their own weight and have limited interlocking capabilities. Interlocking blocks are slender than the bulky elements and are stabilised by their own weight as well as by the surrounding elements. Both solutions dissipate wave energy and reduce wave run-up due to the voids created between each armour unit. On the other hand, hollow armour units have voids within the blocks that contribute to wave energy dissipation. This type of blocks gain their stability partially from their own weight but mainly from the friction between surrounding units. Despite being very stable, the complex blocks placement limits their applications for structures below water.

Considering the characteristics associated to each type of armour units, the proposed solution aims to comprise part of advantages of the three main types of concrete blocks into one and suggest an innovative shape for the armour units. Since bulky elements have better weight stability to withstand wave forces than slender shapes (better structural capabilities), which will probably reduce the maintenance costs due to their less breakable nature, the proposed solution will focus on the

improvement of bulky elements by increasing interlocking features (hydraulic stability) and incorporating holes to allow better wave energy dissipation.

Inspired by the Antifer cube, the proposed armour unit has a cube-like shape with a cross section with round edges to avoid chipping and a convex shape at the centre parts to allow a better interlocking with the surrounding blocks.

To increase the interlocking capabilities, the suggested solution includes two types of armour units that complement each other: the base blocks that have an indentation to allow the top blocks to engage them, and the top ones that include a convex shape at the bottom to interlock with the base blocks. In order to increase the wave energy dissipation, both types have holes in each face to allow seawater circulation. In addition, these holes can contribute to anchoring natural fibre ropes around the armour unit, as well as help decreasing the hydration heat that can lead to crack formation during the concrete hardening process.

Similar to traditional cubes and Antifer cube placements, the proposed solution intends to include a two-layer system. As aforementioned, although the second layer blocks do not provide extra safety, it offers better interlocking behaviour. Nonetheless, special attention should be given to the rocking phenomena, since the second layer blocks tend to rock and aggravate the risk of armour units breaking. It is also important to note that the existence of early age cracks formed due to temperature variations associated with the concrete hardening process can aggravate the risk of breaking due to rocking and its application is not recommended in this situation. For this reason, and because cracks have a detrimental effect on the concrete mechanical properties, a thermo-mechanical analysis becomes imperative to understand and locate eventual fragilities related to the proposed armour unit.

In this study, the consideration of RSF is suggested as the preferable type of reinforcement for this innovative solution, as it contributes to the improvement of the post cracking behaviour and to a positive ecological aspect. The recommended fibre length for the immense heavy blocks used in coastal protection should be at least 3 times larger than the maximum aggregate size. The selection of aggregates should include small aggregates (less than 4 mm) to contribute to a more uniform fibres distribution and coarse aggregates (between 18 and 38 mm). The use of larger coarse aggregates allows the reduction of the cement paste, which results in a more ecological solution and less shrinkage. The increase in the aggregates component, in relation to the cement paste induces the reduction of shrinkage, which is a key factor for the armour units volumetry. Therefore, in order to attain the full potential of the fibre reinforcement, the fibre length should be in the interval 54-114 mm. Concerning the post-cracking, the RSFRC behaviour depends on fibre percentage, nature of the fibres, fibres

orientation and distribution, which in turn depends on the casting technology adopted, geometry of the element and rheological properties of the RSFRC. The use of steel fibres ensures a post-cracking tensile capacity that avoids the occurrence of cracks of width higher than the admissible one, mainly during the concrete curing process.

However, since experimental data is beyond the scope of this research work, mechanical properties of RSFRC of common structural elements (columns, beams and slabs) were adopted, assuming that they remain valid for large armour units.

In addition to the proposed shape, an innovative technique using rope confinement is suggested in order to soften the rocking, help improve the stability of the blocks, and enhance the mechanical properties of the concrete armour units. Since this study only focuses on the crack risk analysis during the construction phase, the efficiency analysis of the carrying capacity in service of the armour unit in the hardened state, as well as the detailing on the rope confinement process and design will not be analysed, as this is still a first stage idea for improving armour units. Nevertheless, at the end of this Chapter, a general view on rope confinement techniques and their main advantages is presented.

6.1.2 Preliminary design

Assuming the macro-structure is placed at the NW coast of the Iberian Peninsula, the design parameters for the proposed maritime structure will be based on the criteria presented in Figure 5.13. By this means, the selected range of significant wave heights for the design H_s at the toe of the structure is from 4 m up to 10 m. In a study developed by Taveira-Pinto and Cunha (2010), the recommended design H_s for the Leixões harbour (located at the NW coast of the Iberian Peninsula) is defined for a range between 5 m and 10 m, which proves the range of values is very similar in both cases. In order to ensure an appropriate value for this purpose, the design H_s is selected for an upper intermediate value of 8 m with a corresponding T_p of 17.7 s, which is retrieved from the Iberian_HP scenario results.

The geometrical preliminary design of the proposed armour units is conducted by using the van der Meer formula adapted for cubes due to the shapes similarity.

Regarding cubic-shaped blocks, van der Meer (1988) suggested the formula presented in Table 2.7 (Equation 2.10), which is considered acceptable but conservative for the Antifer cubes (Freitas, 2013). The recommended N_{od} for cubes should be between 0 and 2, where 2 corresponds to the ruin damage level, and the N_z should be between 1000 and 7000. Greater values of N_z indicate more

severity of the wave climate action that will lead to more instability, which means the unit weight of the blocks will be also greater.

Despite the applicability of the formula having inherent limitations (e.g., cotgθ of 1.5), Equation (2.10) is applied for the armour unit design, and summarized considerations are presented in Table 6.1. The proposed D_n is approximately 2.5 m, which equals a mass of 36 tonnes for a regular cube. Since the proposed armour unit presents holes, the design focused in considering a total mass of approximately 36 tonnes.

Table 6.1: Considerations for the armour unit characteristics design.

Parameter	Value
H_s **(m)**	8
T_p **(s)**	17.7
s_m	0.02
N_{od} **(between 0 and 2)**	1
N_z **(between 1000 and 7000)**	3000
cotgθ	1.5
ρ_a **(kg/m³)**	2400
ρ_w **(kg/m³)**	1025
Δ	1.3

The motive behind the consideration for the van der Meer formula resulted from the more conservative design, due to the innovative geometry of the proposed armour unit. It is uncertain that the application of this formula for the special characteristics of the proposed block is adequate or whether it results in under or overdesigned blocks. However, it is important to note that this is a preliminary study and that the application of predesign formulas are a first analysis for the armour units' weight. Further studies using Computational Fluid Dynamics (CFD) numerical modelling should also be conducted as complementary means to help predicting the uncertainty related to the structural behaviour under severe wave climate conditions. In addition, composite modelling using experimental and numerical research should be engaged to fully understand the applicability of this formula on the design of the proposed blocks. Nonetheless, armour units weights considered in maritime structures in the NW coast of the Iberian Peninsula present a range of values from 25 tonnes to 45 tonnes (Azenha *et al.*, 2011; Medina *et al.*, 2022; Taveira-Pinto and Cunha, 2010), depending on their types. For comparison purposes, the Leixões harbour plain concrete Tetrapods have a weight of 40 tonnes.

As aforementioned, the proposed solution includes two types of armour units that complement each other. Despite having the same dimensions, each type of block presents different volumes due to their different configurations. Table 6.2 depicts the armour units' dimensions (in meters) in different views.

All hollows in each face have a diameter of 0.5 m. The indentation of the base armour unit and the protuberance of the top armour unit are semi-spherical and have a diameter of 1 m.

Table 6.2. Innovative armour unit shapes and dimensions for the base (left) and top (right) blocks.
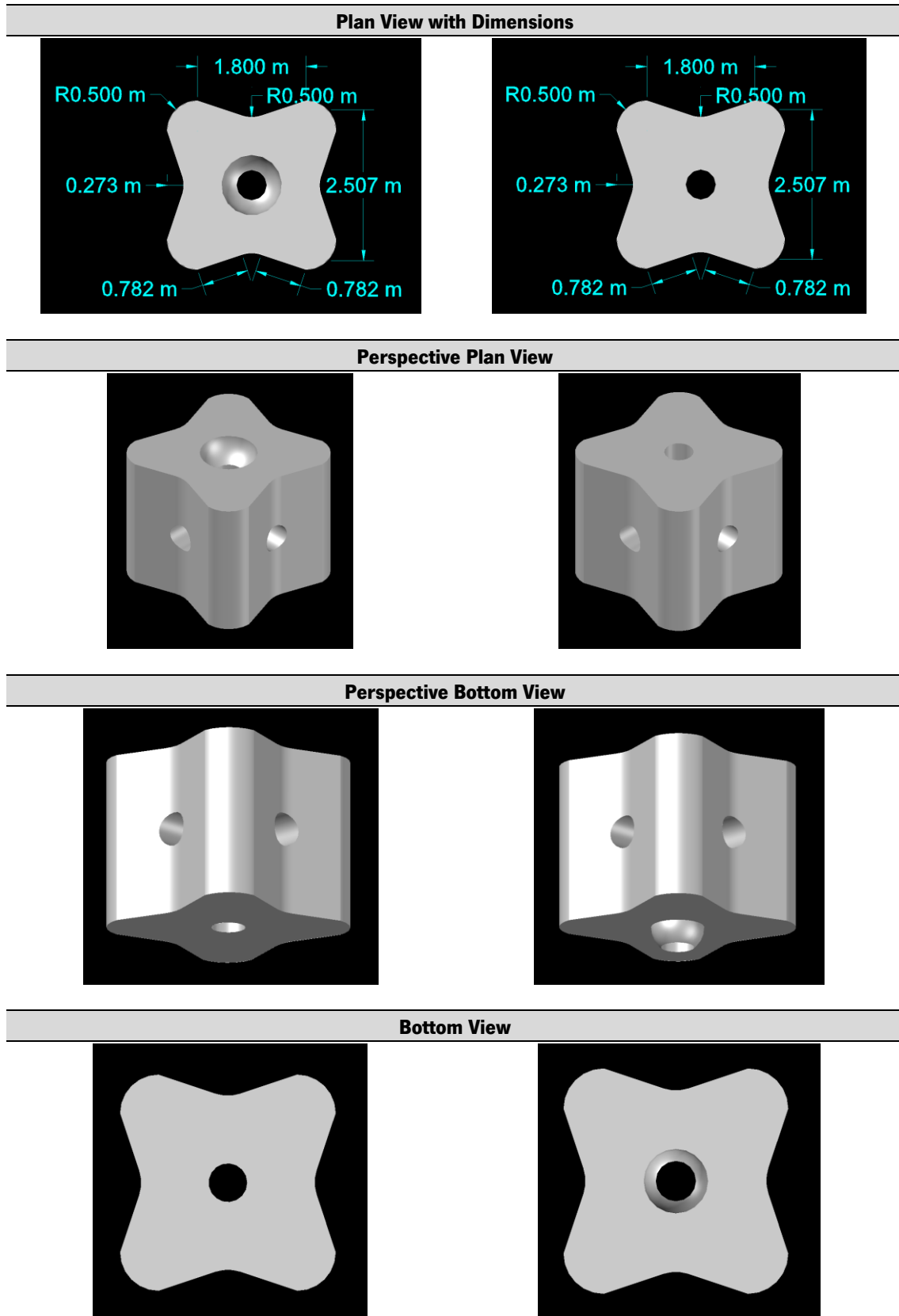
The base armour unit has a volume of 15.01 m³, which totals a mass of 36.0 tonnes, while the top armour unit has a volume of 15.24 m³, which totals a mass of 36.6 tonnes. Both blocks have a height of 2.5 m.

An example of armour units layout in a slope structure is schematically depicted in Figure 6.1, where the proposed two layer solution is displayed in a regular uniform placement pattern. The spaces between adjacent armour units contribute to wave energy dissipation. The toe of the structure can be of rockfill.
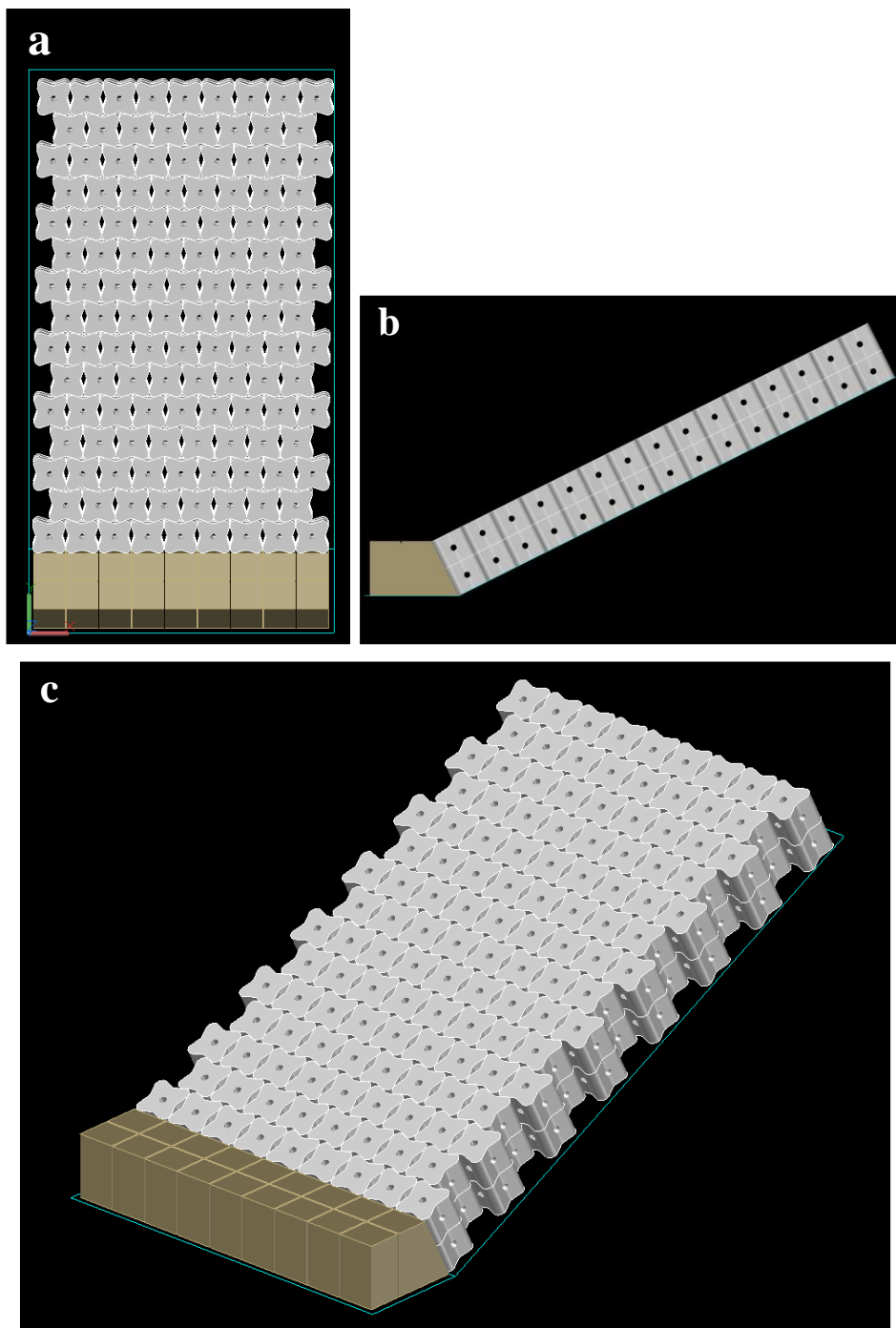
Figure 6.1: Schematic layout for the proposed armour units: a) plan view; b) side view; c) perspective view.

6.2 Thermo-mechanical stress cracking on concrete structures

Despite bulky armour units being less vulnerable than slender elements, the temperature difference between the inside and the outside of these elements during hardening could cause tensile stresses that attains the tensile strength of early age concrete. This type of failure is known as thermal stress cracking, and it can result in a reduction of the element strength and stiffness or even its breakage (van Zwicht, 2009). If the magnitude of tensile stresses due to thermal shrinkage reaches the tensile strength of concrete, then cracks are formed (Figure 6.2). Preventing or controlling the magnitude of these cracks is important for the strength, stiffness and durability of the structure.

ORIGINAL LENGTH

UNRESTRAINED
SHRINKAGE

RESTRAINED SHRINKAGE
DEVELOPS TENSILE STRESS

IF TENSILE STRESS IS GREATER
THAN TENSILE STRENGTH,
CONCRETE CRACKS
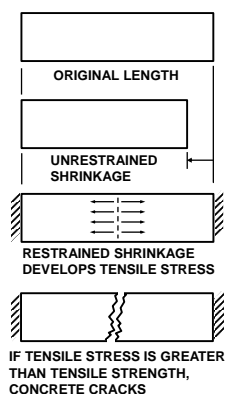
Figure 6.2: Cracking of concrete due to drying shrinkage and restrain (ACI, 1992; Ventura-Gouveia, 2011).

When shrinkage is actuating, cracking in concrete members only appears if they are not free to shrink (Koenigsfeld and Myers, 2003; Ventura-Gouveia, 2011). The degree of shrinkage depends on the w/c ratio, relative humidity associated with the environment temperature, type of cement and geometric characteristics of the element (Ventura-Gouveia, 2011). For these reasons, good quality concrete is required. The best strategies to mitigate shrinkage are (D'Ambrosia *et al.*, 2001; Ventura-Gouveia, 2011; Weiss *et al.*, 1998): (i) to reduce the w/c ratio; (ii) to ensure proper curing conditions; (iii) to use expansive cements to counteract the shrinkage effect; (iv) to use shrinkage reducing admixtures; (v) fibre reinforcement, due to its cracking control efficiency.

Different types of shrinkage can be classified as plastic, drying, autogenous, carbonation and thermal.

Plastic shrinkage is characterized by the loss of water by evaporation in a fresh concrete surface (Ventura-Gouveia, 2011; Weiss *et al.*, 1998).

Drying shrinkage occurs in hardened concrete and it is caused by the loss of water through the surface by the difference between the internal and external relative humidity (Ventura-Gouveia, 2011; Weiss *et al.*, 1998).

Autogenous shrinkage occurs during the hydration reaction of binder materials due to the internal consumption of water (self-desiccation) (Ventura-Gouveia, 2011).

Carbonation shrinkage occurs at the surface of the concrete as a result of the reaction between the carbon dioxide (CO_2) present in the atmosphere and the hydrated cement (Ventura-Gouveia, 2011; Weiss *et al.*, 1998).

Thermal shrinkage occurs as a result of the hydration process during the concrete curing. During this phase, an exothermic reaction occurs with the generation of a large quantity of heat, whose dissipation is faster in thin than in thick structures due to faster hydration heat transfer. After the curing phase, during the concrete cooling process, and since heating/cooling phases can occur simultaneously in distinct parts of a concrete element, tensile stresses are developed (thermal stresses) in the parts that are shrinking, leading to the formation of cracks. Thermal stresses also occur in hardened concrete due to diurnal and seasonal temperature changes, which can also cause the development of cracks (Ventura-Gouveia, 2011; Weiss *et al.*, 1998).

Creep and shrinkage can be defined as the time-dependent increase of strain in concrete subjected to sustained stress that are interrelated and cannot be completely dissociated (ACI, 1992; Ventura-Gouveia, 2011). Weiss *et al.* (1998) explains that when the phenomenon of creep occurs, the stress level decreases due to creep relaxation, thus delaying the cracking age of the concrete. This is a favourable contribution regarding the concrete shrinkage, since the strength increase in this period can avoid the formation of cracks.

Azenha *et al.* (2011) conducted a study on a Tetrapod using a thermo-mechanical numerical simulation tool (3D), based on the finite element method, for the assessment of hydration heat induced stresses. The study intended to understand if the self-induced stresses associated to hydration heat release and consequent temperature variations are partially responsible for the insufficient service-life behaviour usually observed in this kind of element. The Tetrapod behaviour was assessed and compared to alternative solutions, such as reinforced concrete using stainless steel rebar, steel fibre reinforced concrete and reinforced concrete with FRPs. Results have shown that the cracking risk is mainly relevant at the surface regions during the heating stage at early ages and that in the core areas the cracking risk is quite small. The authors concluded that if crack development occurs, it should tend to close during the cooling stage of the concrete and this phenomenon should not be accountable to the damaging of the armour unit that often leads to premature ruptures. The load carrying capacity of the Tetrapod's leg reinforced with steel fibres was 74 % higher than the reference case (plain concrete).

6.2.1 Transient non-linear analysis

Since the risk of cracking at an early age on cement-based materials is likely to occur, the estimation of the heat generated by the hydration process and the induced stress fields should be studied using numerical modelling.

Ventura-Gouveia (2011) developed and integrated a FEM-based heat transfer model in a mechanical model that simulates the crack initiation and propagation in structures discretized with solid finite elements. This time-dependent 3D multi-directional smeared crack model is able to simulate the shrinkage and creep, which is crucial to predict the behaviour of concrete structures from their early ages to the hardened phase, and their concern for service limit states due to crack opening limits. The 3D multi-directional smeared crack model allows simulating the formation of more than one smeared crack per integration point (IP).

The early age heat generation rate of cement-based materials can be obtained with the following Equation (6.1) (Azenha, 2009; Ventura-Gouveia, 2011):

$$\dot{Q} = f(\alpha_T) A_T e^{\frac{E_a}{R(273.15+T)}} \tag{6.1}$$

where $\dot{Q}$ is the heat generation rate; $f(\alpha_T)$ is the normalized heat generation function; A_T is a rate constant; E_a is the apparent activation energy that depends on the type of cement (Jmol[-1]); R is the universal gas constant (8.314 Jmol[-1]K[-1]); and T is the temperature (°C).

The values that characterize the heat generation rate defined by Equation (6.1) are dependent on the type of cement used in the experiment.

The $f(\alpha_T)$ function describes the relative amount of heat generation due to cement hydration and is obtained directly from experiments. This rate is a function of the degree of heat development α_T, given by Equation (6.2) (Azenha, 2009):

$$\alpha_T = \frac{Q(t)}{Q_{total}} \tag{6.2}$$

where $Q(t)$ is the accumulated heat generated until a certain instant t, and Q_{total} is the final accumulated heat of the cement hydration.

The value of the heat transfer coefficient, h_{cr}, assigned to the face in contact with the environment is 10.0 Wm[-2]K[-1], and for the other faces an equivalent heat transfer coefficient, h_{eq}, is used to account for the formwork material given by Equation (6.3).

$$h_{eq} = \left[\frac{1}{h_{cr}} + \sum_{i=1}^{n} \frac{L_i}{k_i}\right]^{-1} \tag{6.3}$$

where L_i and k_i are the thickness and the thermal conductivity of the ith layer of the material located between the concrete and the environment, respectively.

The predictive performance of the thermal transient nonlinear model was demonstrated on a concrete cube analysed in Ventura-Gouveia (2011).

6.2.2 Time-dependent deformations

The total strain of a concrete member loaded in an uniaxial direction at time t with constant stress σ can be expressed by Equation (6.4) (Póvoas, 1991; Ventura-Gouveia, 2011):

$$\varepsilon(t) = \varepsilon^{in}(t_0) + \varepsilon^c(t) + \varepsilon^s(t) + \varepsilon^T(t) \tag{6.4}$$

where $\varepsilon^{in}(t_0)$ is the initial strain at loading, $\varepsilon^c(t)$ is the creep strain at time $t>t_0$, $\varepsilon^s(t)$ is the shrinkage strain and $\varepsilon^T(t)$ is the thermal strain.

The strains $\varepsilon^{in}(t_0)$ and $\varepsilon^c(t)$ are called mechanical strains, because they are caused by applied stresses, while the strains $\varepsilon^s(t)$ and $\varepsilon^T(t)$ are independent from the stress field. The thermal strain $\varepsilon^T(t)$ can be obtained from the temperature field at a certain instant by using Equation (6.5) (Ventura-Gouveia, 2011):

$$\varepsilon^T(t) = \alpha\Delta T \tag{6.5}$$

where α is the coefficient of thermal expansion and ΔT is the temperature variation.

The total shrinkage $\varepsilon^s(t)$ and creep $\varepsilon^c(t)$ strains expressions are given by Equations (6.6) and (6.7). Additional information can be found in the Eurocode 2 (EC2, 2004) and in Ventura-Gouveia (2011).

$$\varepsilon^s(t) = \varepsilon_{ca}(t) + \varepsilon_{cd}(t, t_s) \tag{6.6}$$

where $\varepsilon_{ca}(t)$ is the autogenous shrinkage strain at time t, and $\varepsilon_{cd}(t, t_s)$ is the drying shrinkage strain at time t.

$$\varepsilon^c(t) = \phi(t, t_0)\frac{\sigma_c}{E_c} \tag{6.7}$$

where σ_c is the constant stress applied at a concrete age t_0, E_c is the tangent modulus of concrete ($1.05E_{cm}$, being E_{cm} the secant modulus of elasticity of concrete at 28 days), and $\phi(t, t_0)$ is the creep coefficient.

The strain components of the 3D multi-fixed smeared crack model are the addition of the strain components in the smeared cracks, $\underline{\varepsilon}^{cr}$, with the strain components in the uncracked concrete between cracks, $\underline{\varepsilon}^{co}$ (Equation 6.8).

$$\underline{\varepsilon} = \underline{\varepsilon}^{co} + \underline{\varepsilon}^{cr} \tag{6.8}$$

The strain vector of the uncracked concrete is decomposed in order to include time-dependent effects. Thus, the Equation (6.4) is adapted and results in Equation (6.9):

$$\underline{\varepsilon}(t) = \underline{\varepsilon}^e(t_0) + \underline{\varepsilon}^c(t) + \underline{\varepsilon}^s(t) + \underline{\varepsilon}^T(t) + \underline{\varepsilon}^{cr}(t) \tag{6.9}$$

where $\underline{\varepsilon}^{e}$, $\underline{\varepsilon}^{c}$, $\underline{\varepsilon}^{s}$, and $\underline{\varepsilon}^{T}$ are the elastic, creep, shrinkage and thermal strain vectors, and $\underline{\varepsilon}^{cr}$ is the crack strain vector. Additional information can be found in Ventura-Gouveia (2011).

The predictive performance of the thermo-mechanical model analysing a U-shaped cross section of a prefabricated beam was demonstrated in Ventura-Gouveia (2011).

6.3 Modelling thermo-mechanical behaviour of RSFRC armour unit

During the hardening phase, the concrete is subjected to temperature variations due to the heat of hydration. The impact of the thermal loads on the concrete will cause stresses that can origin cracking and significant damage to the structure. On the other hand, at the same time during this process, an evolution of the concrete properties, such as modulus of elasticity, E, tensile and compressive strengths also occur.

In this Section, the thermo-mechanical stress crack formation during the concrete hardening process is analysed using GID-FEMIX for the proposed amour unit for the maritime protection structure. The thermal analysis will allow understanding the effect of different cement types and contents in the concrete mixture on temperature variations. The mechanical analysis will consist on assessing the evolution of strain and stress fields, concrete strength and stiffness, and the simulation of cracking formation and propagation in zones where the maximum principal tensile stress attains the local concrete tensile strength. Thus, the analysis conducted in FEMIX will allow deciding which type of cement and cement content in the concrete mixture develop greater temperature variations, and consequently which one is the most prone to crack formation. The mesh refinement is also analysed in order to decide the most adequate mesh for this block. For the simulation results with the highest number of cracks, an additional analysis of different armour unit sizes (for 18 tonnes and 60 tonnes) is conducted to allow understanding the impacts of temperature and stress variations and crack formation on smaller and greater armour units. Moreover, a comparative study between the most susceptible scenario and a scenario with plain concrete is developed in order to understand the influence of RSFRC on the crack evolution.

6.3.1 Creating the mesh for the armour unit

Despite the two geometries presented in this study, only the base armour unit is selected to perform the thermal and mechanical numerical modelling analysis, as results would not differ much from each block due to the shape similarity. In order to reduce calculation time, the numerical modelling is conducted for only a quarter of the original block, since the double symmetry of the armour unit

geometry (Figure 6.3) allows this simplification. The structured mesh for the quarter of the block is discretized with quadratic hexahedra finite elements with 20 nodes (Figure 6.4) and the mesh is developed using GID 14.1.8d.
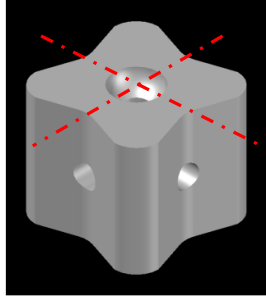
Figure 6.3: Armour unit shape double symmetry.
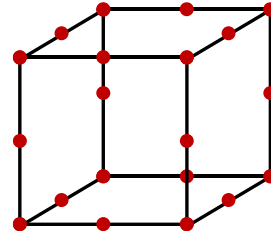
Figure 6.4: Schematic representation of a quadratic hexahedra element.

With the purpose of understanding the influence of the mesh refinement on the modelling results, three meshes are created considering the following element sizes: 0.05 m (Figure 6.5a), 0.1 m (Figure 6.5b) and 0.15 m (Figure 6.5c). The mesh refinement analysis will be conducted for the thermal and mechanical nonlinear problems.
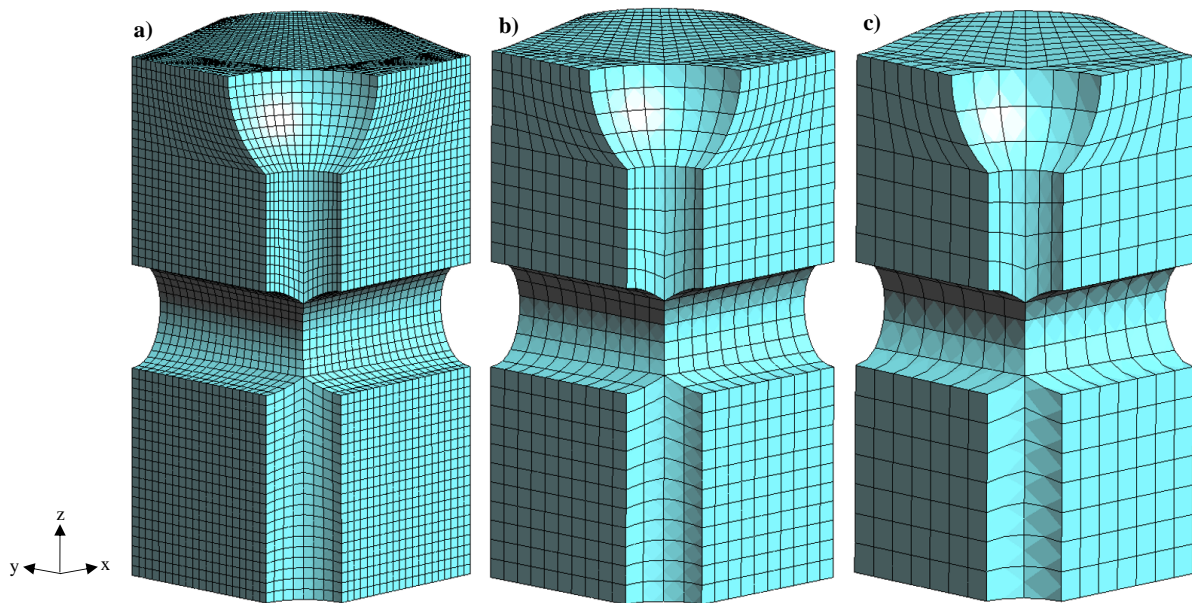
Figure 6.5: Mesh refinement used in the numerical simulations: a) 005; b) 01; c) 015.

6.3.2 Thermal problem

6.3.2.1 Pre-processing

After the mesh conception using GiD-FEMIX, the first step consists of attributing the material and element properties, load and supporting conditions to the block. The selected material is recycled steel

fibre reinforced concrete with a density of 2400 kg/m³; the mesh element type is solid hexahedra; and the loads are thermal loads that are input in the model as boundary conditions by assigning the surface convection heat transfer in each face (Figure 6.6). The considerations for the assignment of the heat transfer coefficients for each boundary face are as follows:

− The symmetry planes correspond to the inner area of the concrete block, which means no heat exchange between surfaces will occur, as there is no contact between different materials (conductivity is null);

− The outer curved, bottom and inner curved faces have contact with the steel formwork (steel conductivity is 50 Wm⁻¹K⁻¹). The equivalent heat transfer coefficient, h_{eq}, calculated by Equation (6.3), is 9.98 Wm⁻²K⁻¹. The steel formwork has a thickness of 0.008 m;

− The top face has contact with the environment. The heat transfer coefficient, h_{cr}, assigned to this face is 10 Wm⁻²K⁻¹.

The initial temperature is 20°C, which is the ambient temperature.
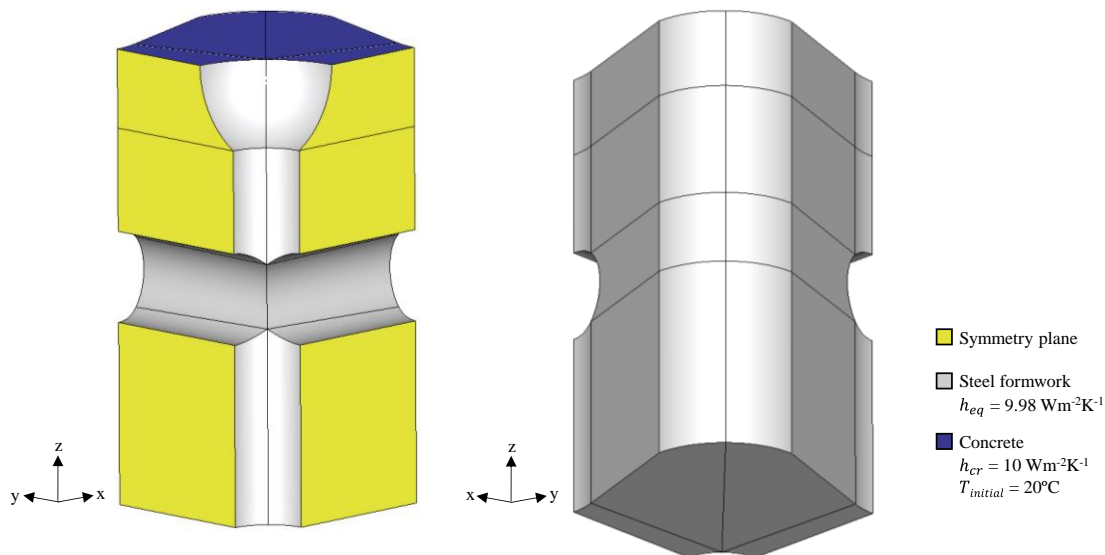
Figure 6.6: Boundary conditions for the thermal analysis.

Regarding the concrete thermal characteristics, the thermal conductivity, k, is 2.6 Wm⁻¹K⁻¹ and the specific heat capacity, ρc, is 1000 Jkg⁻¹K⁻¹. The specific heat capacity describes the quantity of heat (J) absorbed per unit mass of the material (kg) when its temperature increases 1K (Guo and Shi, 2011).

The adopted simulation time for the thermal numerical modelling is 8 days (192 hours), which seems adequate to allow the temperatures to stabilize towards the ambient temperature (20°C).

The Newton-Raphson method was used to determine the unknowns at each time step of this thermal analysis, while the system of equations was solved by the conjugate gradient method due to the

relatively large size of this system. The time integration scheme selected for the solution of differential equations is the Backward-Euler (Ventura-Gouveia, 2011).

6.3.2.2 Simulation scenarios

In this study, the influence of the types of cement and their contents in the concrete mixture on the thermal behaviour during the concrete hardening phase is conducted by defining different scenarios. The types of cement are generally categorized as normal (N), fast (R) or slow hardening (S).

The selected types of cement for the numerical modelling are CEM I 42.5R, CEM IV 32.5N and CEM I 52.5R, due to their established suitability for use in maritime environment (CIMPOR, 2021). The selected cement contents are 400 kg/m³, 310 kg/m³, 368 kg/m³, and 435 kg/m³. This selection criterion is based on the minimum (310 kg/m³), maximum (435 kg/m³) and mean (368 kg/m³) armour units cement values referred in the studies presented in Appendices 1A and 1B. The 400 kg/m³ cement content corresponds to an intermediate value between the maximum and the mean values and serves as a control group to help deciding the best mesh refinement.

Table 6.3 presents the thermal parameters associated to the selected different types of cement to be adopted in the numerical modelling.

The numerical simulations for the thermal analysis are conducted for six scenarios (SCs), which are summarized in Table 6.4.

The first scenario (SC1) is subdivided into three (SC1.1, SC1.2 and SC1.3) for the same type of cement (CEM I 42.5R) and the same cement content (400 kg/m³). These scenarios are control groups intended to analyse the influence of the mesh refinements on thermal results (presented in Figure 6.5 in Section 6.3.1). The results comparison is conducted by selecting 4 observation points at matching locations for the three meshes (005, 01 and 015) and assessing the differences in temperatures evolution through the simulation time at these locations. The observation points are selected for the locations where the temperatures reached higher values.

SC2, SC3 and SC4 have the same type of cement (CEM I 42.5R) but different cement contents (310, 368 and 435 kg/m³, respectively). The last two scenarios (SC5 and SC6) have the same cement contents (368 kg/m³) but different types of cement (CEM IV 32.5N and CEM I 52.5R). For SC2 to SC6, the analysis of temperature evolution is conducted by selecting 2 observation points at locations where the temperatures reach higher values.

For the control group scenarios (SC1.1 to SC1.3), the time step is 3600 s (1 hour), which totals 192 time steps. For SC2 to SC6, the first time step is 10800 s (3 hours), while the remaining are 3600 s (1

hour), which totals 190 time steps. This adaptation is necessary to avoid numerical modelling instabilities for the mechanical model, as this prevents the RSFRC strength values from being extremely low and close to the tolerances considered by FEMIX for the opening and closing of the cracks during the first time steps. FEMIX considers that a crack opens when the maximum principal tensile stress attains the material tensile strength at less than a tolerance assumed adequately small enough, while a crack closes when the strain normal to the crack is less than a very small strain-based tolerance. The simulation time is 8 days for all scenarios.

Table 6.3: Thermal parameters associated to different types of cement (per kg of cement) (adapted from Azenha, 2009).

Thermal Parameters	Cement Type		
	CEM I 42.5R	CEM IV 32.5N	CEM I 52.5R
Cement content (kg/m³)	400; 310; 368; 435	368	368
A_T	2.645E+07	1.831E+07	7.400E+08
E_a (J/mol)	38.38E+03	38.07E+03	46.18E+03
Q_{Total} (J/kg)	355.2E+03	279.5E+03	386.3E+03

Thermal Parameters			
α_T	$f(\alpha_T)$ for CEM I 42.5R	$f(\alpha_T)$ for CEM IV 32.5N	$f(\alpha_T)$ for CEM I 52.5R
0.00	0.00	0.00	0.00
0.05	0.65	0.62	0.62
0.10	0.91	0.85	0.88
0.15	1.00	0.98	0.99
0.20	0.98	0.99	1.00
0.25	0.94	0.92	1.00
0.30	0.86	0.82	0.95
0.35	0.75	0.72	0.85
0.40	0.63	0.58	0.70
0.45	0.51	0.41	0.56
0.50	0.41	0.27	0.45
0.55	0.32	0.19	0.36
0.60	0.24	0.15	0.28
0.65	0.18	0.12	0.23
0.70	0.13	0.10	0.18
0.75	0.09	0.08	0.13
0.80	0.06	0.05	0.08
0.85	0.04	0.03	0.04
0.90	0.02	0.02	0.02
0.95	0.01	0.01	0.01
1.00	0.00	0.00	0.00

Table 6.4: Thermal scenarios.

Thermal Scenarios | Simulation Time: 192 h (8 days)				
Scenario	**Mesh**	**Cement Content (kg/m³)**	**Cement Type**	**Observation Points**
SC1.1	005	400	CEM I 42.5R	4
SC1.2	01	400	CEM I 42.5R	4
SC1.3	015	400	CEM I 42.5R	4
SC2	015	310	CEM I 42.5R	2
SC3	015	368	CEM I 42.5R	2
SC4	015	435	CEM I 42.5R	2
SC5	015	368	CEM IV 32.5N	2
SC6	015	368	CEM I 52.5R	2

6.3.2.3 Results and discussion

SC1.1, SC1.2 and SC1.3

The analysis for the influence of mesh refinement on the temperatures evolution results is conducted for the control group scenarios (SC1.1, SC1.2 and SC1.3) by selecting 4 observation points for each mesh, considering the same type and contents of cement. In order to understand the temperatures inside the block, the meshes are cut in half and the results for the temperature field are depicted in Figure 6.7 for the time step when the temperatures are higher. The comparison of results for the temperatures evolution at each observation point is represented in Figure 6.8 for the three mesh refinements.
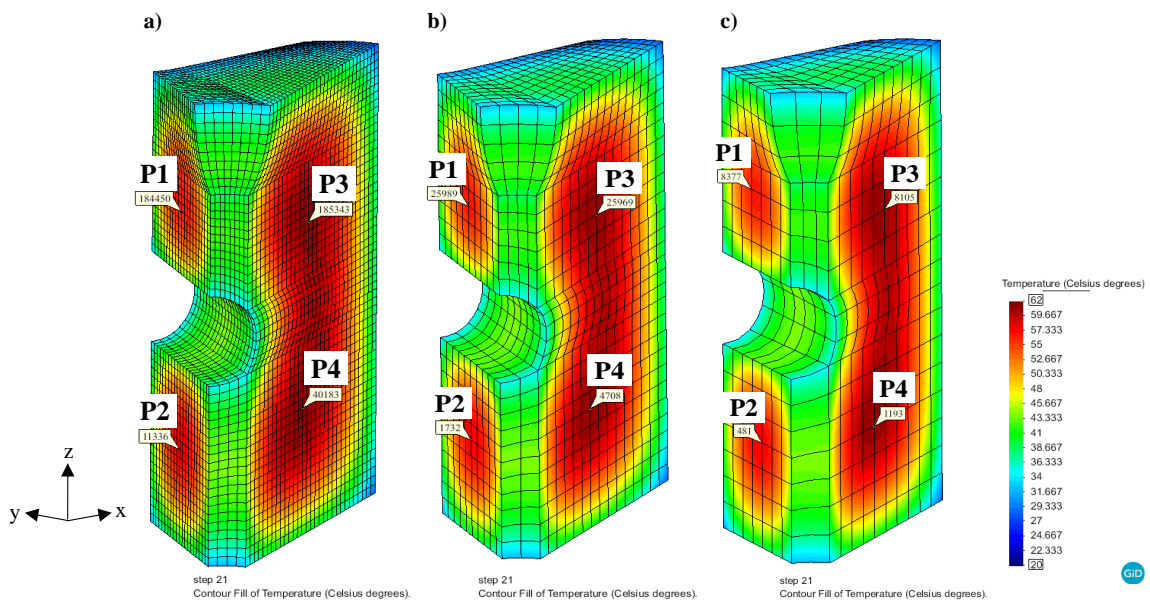
Figure 6.7: Location of the observation points P1, P2, P3, and P4, and results for the temperature field 21 h after the casting for mesh: a) 005; b) 01; c) 015.
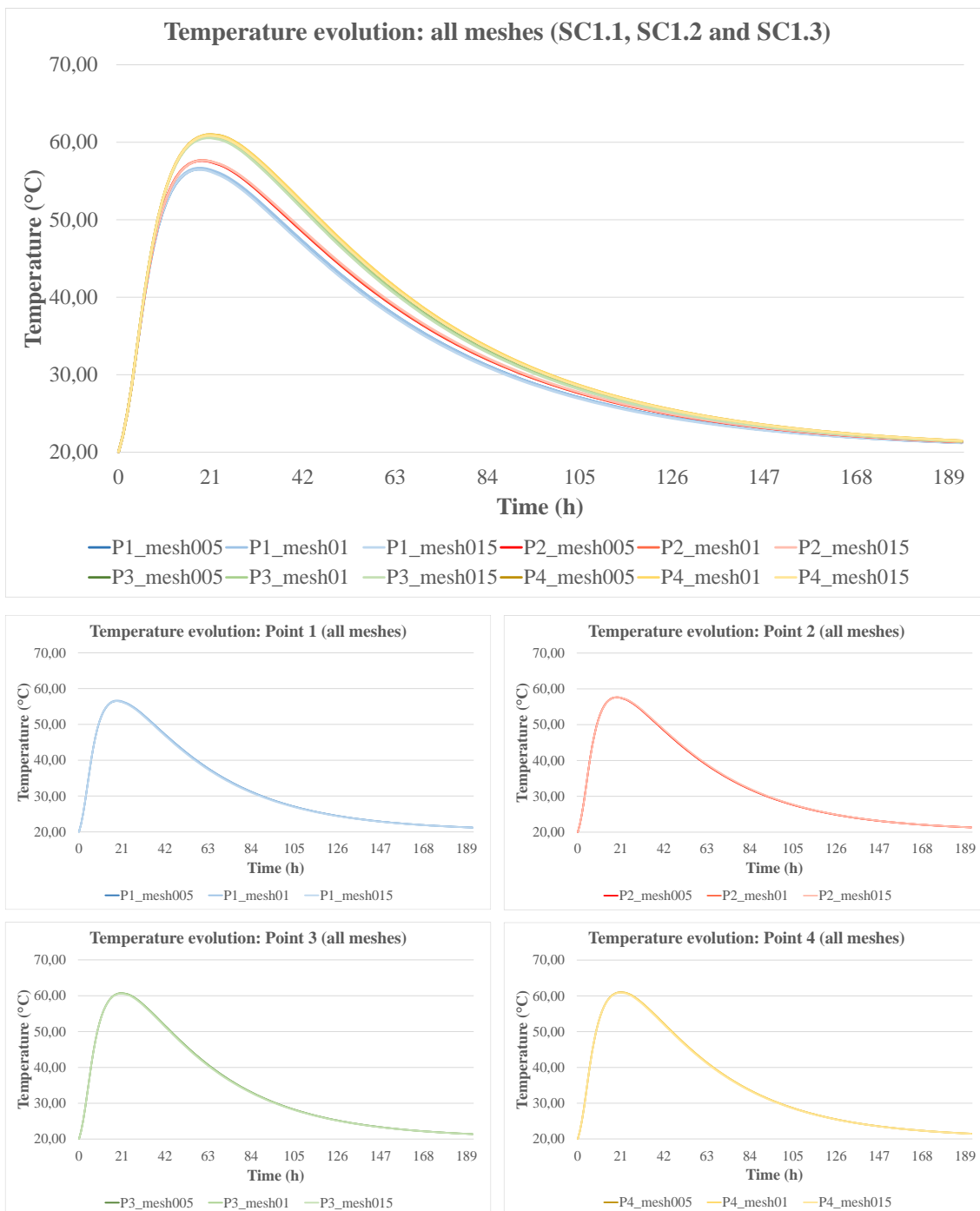
Figure 6.8: Comparison results between the different meshes for temperatures evolution during 8 days of curing for each observation point.

Results from Figure 6.7 demonstrate that the three meshes present maximum temperatures 21 hours after the casting and that, regardless of their refinements, the temperature field patterns are similar between the three meshes. The greatest temperature gradient is depicted for the inner part of the block, where temperature reach maximum values around 61°C in P3 and P4. The observation points P1 and

P2 register maximum temperatures of 57°C and 58°C, respectively. Additional information retrieved from the obtained results can be found in Appendix 4A.

Nonetheless, despite the high temperature values in the core of the block, with time, temperatures will tend to the ambient temperature, as depicted in the asymptotic shape of results presented in Figure 6.8. From the comparison results, it is clear that the coarser mesh refinement (mesh 015) predicts perfectly the same temperature evolution results as the finer refinements (meshes 01 and 005), since their differences are practically null. Thus, in order to reduce the numerical modelling calculation time, the coarser mesh (015) is selected for the subsequent numerical simulations.

Regarding the observation points, since results between P1 and P2, and P3 and P4 do not differ much due to similar symmetry conditions, henceforth, for SC2 to SC6, the selected locations for the observation points are around P2 and P4, where the highest temperatures are attained.

SC2, SC3 and SC4

In order to understand the influence of different cement contents (310, 368 and 435 kg/m³) on temperatures evolution, SC2 to SC4 have the same type of cement (CEM I 42.5R) and the analysis is conducted by comparing each scenario results for 2 observation points. As previously explained, the mesh refinement is 015 and the mesh is also cut in half to allow retrieving temperature values in the core. Figure 6.9 depicts each scenario's temperature field results for the time step when temperatures are higher, while Figure 6.10 plots the temperature evolution results for each scenario and observation point.
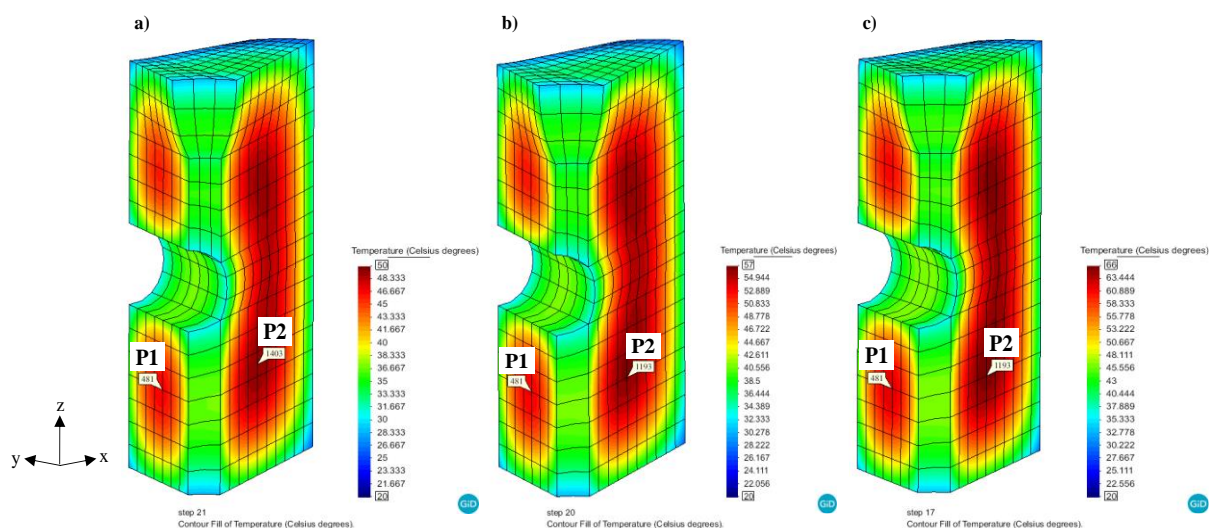
Figure 6.9: Location of the observation points P1 and P2, and results for the temperature field for the time step when temperatures are higher in: a) SC2; b) SC3; c) SC4.
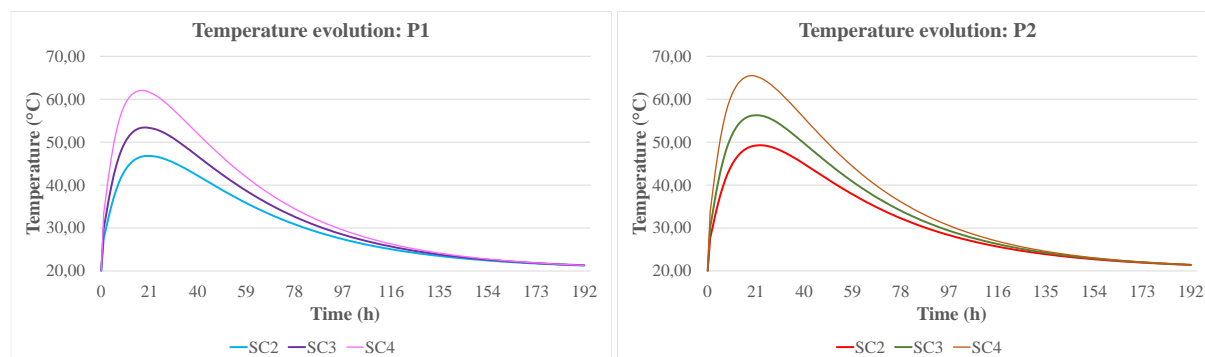
Figure 6.10: Results for temperatures evolution during 8 days of curing for each observation point for SC2, SC3, and SC4.

Results from Figure 6.9 demonstrate that for each scenario, the greatest temperature gradient occurs in the inner part of the block (P2), where temperatures reach maximum values around 49°C, 56°C and 66°C in SC2, SC3 and SC4, respectively (Figure 6.10). This demonstrates that, as expected, temperature increases with the content of cement and that consequently, temperature variation that results from hydration is more abrupt for higher contents of cement.

Therefore, this analysis allows concluding that the evolution of the maximum temperature is a function of the amount of cement used in the casting. Appendix 4A presents additional information retrieved from the obtained results.

SC5 and SC6

The last two scenarios (SC5 and SC6) intend to analyse the influence of different types of cement on the temperatures evolution by comparing each scenario results for 2 observation points. In order to understand the temperatures behaviour, the same cement content (368 kg/m³) is attributed to CEM IV 32.5N and CEM I 52.5R. The obtained results from these numerical simulations will be compared to SC3, which has the same cement content (368 kg/m³), but different type of cement (CEM I 42.5R). Figure 6.11 presents the results for SC5 and SC6 temperature field for the time step when temperatures are higher. Figure 6.12 plots the results for the temperature evolution for each scenario and observation point.
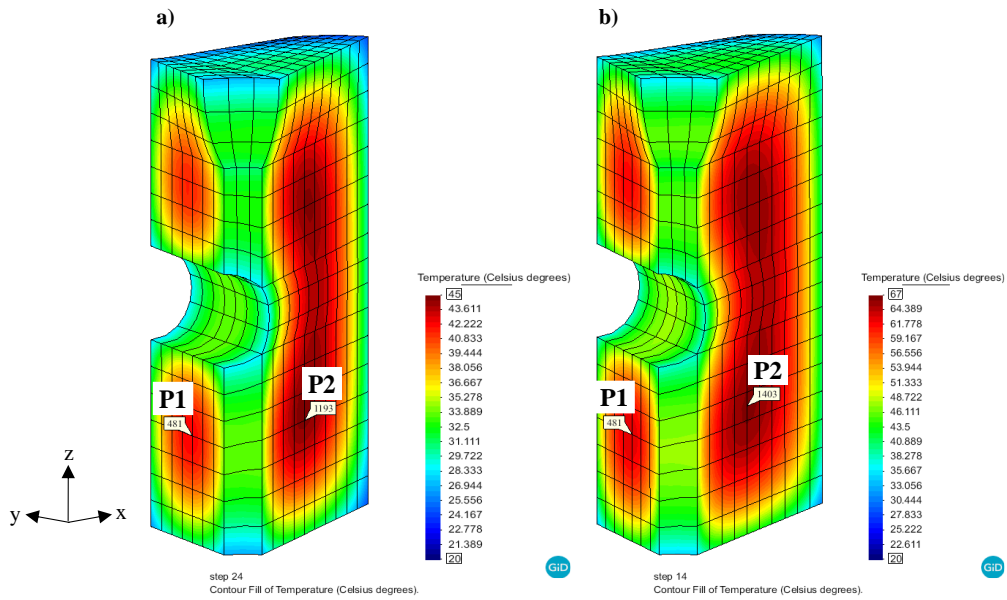
Figure 6.11: Location of the observation points P1 and P2, and results for the temperature field for the time step when temperatures are higher in: a) SC5; b) SC6.
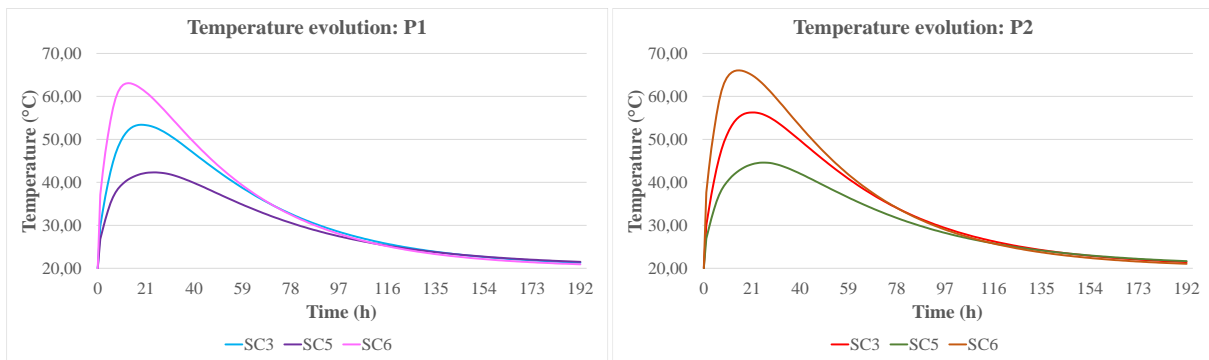
Figure 6.12: Results for temperatures evolution during 8 days of curing for each observation point for SC3, SC5 and SC6.

Results in Figure 6.11 show that for each scenario, the greatest temperature gradient is registered in the inner part of the block, where temperatures reach maximum values in P2 of approximately 56°C for SC3, 45°C for SC5 and 66°C for SC6 (Figure 6.12). These results indicate a substantial influence of the type of cement on the maximum temperature values. Regarding the temperature variation, SC6 presents a more abrupt temperature rise when compared to SC5, since temperature reaches its maximum at an earlier age, which means greater temperature variations are predicted in CEM I 52.5R. Appendix 4A presents additional information retrieved from the obtained results.

Comparing these results with the obtained for SC3, it can be concluded that the maximum temperature for CEM I 42.5R (56°C) is higher than the maximum temperature registered for CEM IV 32.5N (45°C), but lower than that of the CEM I 52.5R (66°C). Similarly, temperature variation in SC3 is higher than that registered in SC5 (CEM IV 32.5N), and lower than that in SC6 (CEM I 52.5R). This behaviour will

be relevant to understand the probability of cracks formation in the mechanical analysis, since the higher the temperatures, the most likely the increase of cracking risk will be due to the increase of tensions in the concrete.

This analysis allows concluding that the evolution of the maximum temperature is a function of the type of cement used in the casting due to the cement constituents.

6.3.3 Mechanical problem

6.3.3.1 Pre-processing

For the mechanical model conception, the defining conditions of the mesh, the types of cement and their contents in the concrete mixture, and the iterative algorithm are the same as for the thermal model. By taking advantage of the double structural symmetry, the support conditions for the mechanical analysis are schematically represented in Figure 6.13. The simulation time for the mechanical model is the same as for the thermal numerical simulations (192 h), since thermal results demonstrated that in the last time step the temperatures are close to the ambient temperature. The 8 days simulation will allow observing cracks formation, as well as identifying areas where cracks will be closing due to cooling. The loads considered for the mechanical analysis are the temperature variations retrieved from the thermal model. These results are obtained from the FEMIX output files, as FEMIX writes information regarding the temperature variations for each element node of the mesh for each time step. Thereby, the temperature variations results are the input loads for the mechanical model that will allow predicting the corresponding stress field.

□ Constraints for x displacements
□ Constraints for y displacements
□ Constraints for z displacements
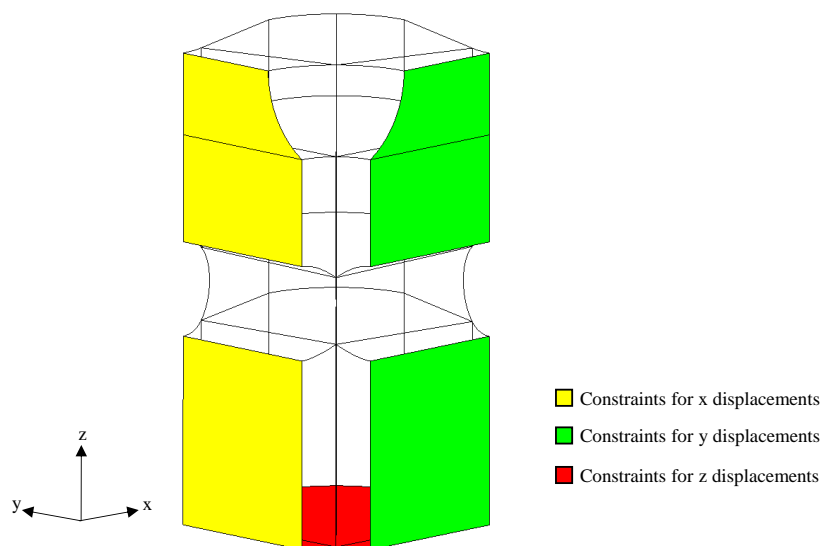
Figure 6.13: Support conditions for the mechanical analysis.

The mechanical model developed by Ventura-Gouveia (2011) simulates the cracks formation and their evolution according to the fracture properties indicated in the model initial conditions. If tensile stresses are lower than the concrete tensile strength, the material does not crack; however, if tensile stresses reach the concrete tensile strength, a crack will form and the stress evolution will depend on the tensile-softening diagram that characterizes the post-cracking behaviour for the RSFRC.

The propagation of the crack opening can be simulated with trilinear or quadrilinear tensile-softening diagrams that relate stresses with strains by defining α_i and ξ_i parameters (Figure 6.14). These parameters (Equations 6.10 and 6.11) define the shape of the tensile-softening diagram and depend significantly on the composition of the RSFRC. The determination of these parameters is based on experimental data analysis by performing inverse analysis. Detailed information about this methodology can be found elsewhere (Ventura-Gouveia, 2011).

$$\alpha_i = \sigma_{n,i+1}^{cr}/\sigma_{n,1}^{cr} \tag{6.10}$$

$$\xi_i = \varepsilon_{n,i+1}^{cr}/\varepsilon_{n,u}^{cr} \tag{6.11}$$

The ultimate crack normal strain, $\varepsilon_{n,u}^{cr}$, is defined as a function of the α_i and ξ_i parameters, the fracture energy, G_f^I, the RSFRC tensile strength, $\sigma_{n,1}^{cr} = f_{ct}$, and the crack bandwidth, l_b. The fracture energy is obtained from experimental tests. The crack bandwidth, l_b, is a length entity relating the crack width and the crack normal strain in order to ensure that the fracture energy is dissipated by the cracks smeared along this length. In an attempt of ensuring the results from the simulations with this type of cracking constitutive model are not dependent on the refinement of the finite element mesh, the crack bandwidth is related to a length entity of the finite elements adopted. In the present simulations, the crack bandwidth was considered as the cubic root of the volume of the finite element IP (Valente, 2019; Ventura-Gouveia, 2011).
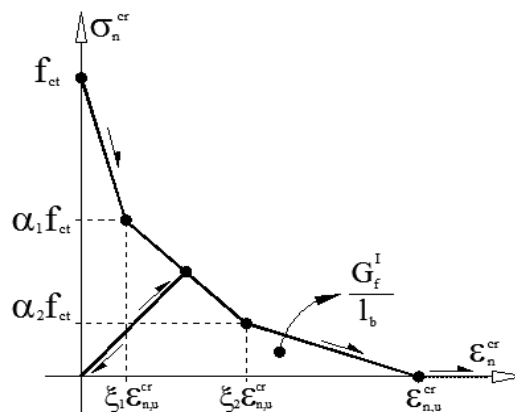
Figure 6.14: Schematic representation of trilinear tensile-softening diagram (Valente, 2019).

Based on the fib Model Code 2010 (Fédération internationale du béton, 2013), the two most important parameters for the crack opening limits that define the constitutive laws of the RSFRC and the toughness class are the f_{R1k} and f_{R3k}, which are the characteristic residual tensile strength for serviceability and ultimate conditions for crack openings with 0.5 mm (w_{SLS}) and 2.5 mm (w_{ULS}), respectively.

The toughness class is defined from the f_{R1k} and a letter corresponding to the ratio between f_{R3k} and f_{R1k} (Table 6.5). For example, if the RSFRC has a toughness class of 5c, it means the f_{R1k} is between 5 MPa and 5.9 MPa and that f_{R3k}/f_{R1k} ranges between 0.9 and 1.1.

Table 6.5: RSFRC toughness classification based on the post-cracking residual strength given by f_{R1k} and f_{R3k}.

Strength Interval (MPa)	Residual Strength Ratios
Given by two subsequent numbers in the series: 1.0, 1.5, 2.0, 2.5, 3.0, 4.0, 5.0, 6.0, 7.0, 8.0, …	**a** if $0.5 \leq f_{R3k}/f_{R1k} < 0.7$ **b** if $0.7 \leq f_{R3k}/f_{R1k} < 0.9$ **c** if $0.9 \leq f_{R3k}/f_{R1k} < 1.1$ **d** if $1.1 \leq f_{R3k}/f_{R1k} < 1.3$ **e** if $1.3 \leq f_{R3k}/f_{R1k}$

Since the armour unit has a large volume and the probability of having weaknesses, such as segregation of aggregates or fibres and concentration of voids is higher than in regular structural elements, it is advisable to adopt the $f_{ctk,min}$ instead of f_{ctm} for the quadrilinear tensile-softening diagram, as it is the minimum characteristic tensile strength of concrete at 28 days of age.

For the parametric study, different RSFRC toughness classifications and strength classes will be defined for the simulated scenarios presented in Section 6.3.3.2.

Based on the considered adaptations, Figure 6.15 depicts the representation of the quadrilinear diagram used in this study, which includes four branches:

- $\overline{BQ}$, which corresponds to the plain concrete behaviour presented in the first branch in Figure 6.16;
- $\overline{CD}$, which is a constant level considered to avoid an odd behaviour when performing the "CD" interpolation as indicated in the Model Code 2010 (Fédération internationale du béton, 2013);
- $\overline{DE}$, which corresponds to the post-cracking behaviour between w_{SLS} (0.5 mm) and w_{ULS} (2.5 mm);
- The stress cut-off branch, which is determined by $1.1 \times w_{ULS}$.
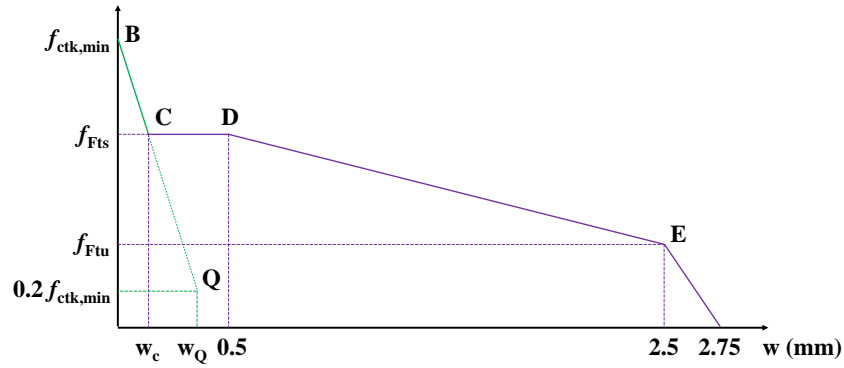
Figure 6.15: Schematic representation of quadrilinear tensile-softening diagram.
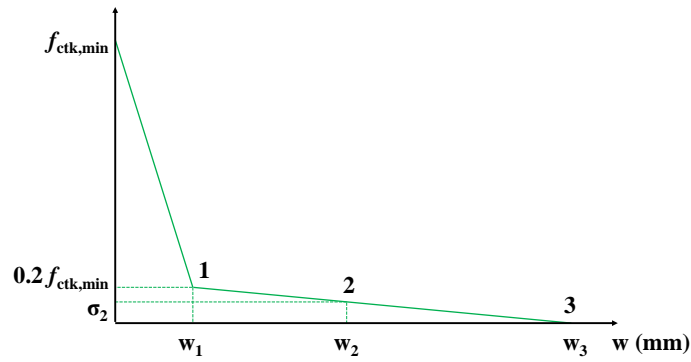
Figure 6.16: Schematic representation of stress-crack opening relation for plain concrete.

The f_{Fts} and f_{Ftu} correspond to the serviceability and ultimate residual strengths (post-cracking strength for serviceability and ultimate crack openings), respectively, and are obtained with Equations 6.12 and 6.13 (Fédération internationale du béton, 2013; Valente, 2019):

$$f_{Fts} = 0.37 \times f_{R1k} \tag{6.12}$$

$$f_{Ftu} = f_{Fts} - (f_{Fts} - 0.57 f_{R3k} + 0.26 f_{R1k}) \geq 0 \tag{6.13}$$

The crack width in point C, w_C, (Figure 6.15) is obtained by defining $\overline{BQ}$, while the crack widths in point Q, w_Q, (Figure 6.15) and point 3, w_3, (Figure 6.16) are given by Equations 6.14 and 6.15:

$$w_Q = w_1 = G_f^I / f_{ctk,min} \tag{6.14}$$

$$w_3 = 5 \, G_f^I / f_{ctk,min} \tag{6.15}$$

Being the fracture energy, G_f^I, the area under the stress-crack opening relation obtained with Equation 6.16:

$$G_f^I = 73 \, f_{cm}^{0.18} / 1000 \tag{6.16}$$

where f_{cm} is the mean compressive strength of concrete at 28 days of age.

The parameters α_i and ξ_i for points C,D and E are given by Equations 6.17 and 6.18, respectively:

$$\alpha_C = f_{Fts} / f_{ctk,min} \tag{6.17a}$$

$$\alpha_D = f_{Fts}/f_{ctk,min} \tag{6.17b}$$

$$\alpha_E = f_{Ftu}/f_{ctk,min} \tag{6.17c}$$

$$\xi_C = w_C/2.75 \tag{6.18a}$$

$$\xi_D = 0.5/2.75 \tag{6.18b}$$

$$\xi_E = 2.5/2.75 \tag{6.18c}$$

For the mechanical analysis of RSFRC, the $f_{ctk,min}$ has to be determined based on the toughness of the material.

6.3.3.2 Simulation scenarios

This analysis intends to understand the influence of the types of cement and their contents in the concrete mixture on the mechanical behaviour during the concrete hardening phase. The scenarios selected for the mechanical simulations are the same as the analysed for the thermal simulations, but the influence of the mesh refinement is limited to the two refinement corresponding to those adopted in SC1.2 and SC1.3. The subsequent scenarios will be based on the most adequate mesh.

The mechanical simulations are performed for three numerical analysis considering the: i) concrete with elastic behaviour (linear); ii) crack constitutive model (nonlinear); and iii) the crack constitutive model with the autogenous shrinkage and creep. The evolution of the material properties, such as the modulus of elasticity, and the compressive and tensile strengths during the curing time are simulated by the concrete maturity model, which is included in all numerical simulations. Details on the formulation for these models can be found in Ventura-Gouveia (2011).

Equation 6.19 presents the notional size of the cross section, h_0, that has to be defined for the shrinkage and creep model.

$$h_0 = 2\,A_c/u \tag{6.19}$$

where A_c is the concrete cross sectional area (mm²), and u is the perimeter of the part of the cross section exposed to drying (mm). For the proposed armour unit the A_c is 1.44E+06 mm² and u is 2.67E+03 mm.

The control group scenarios (SC1.2 and SC1.3) will serve as a basis for the parametric study that focus on the analysis of the concrete behaviour for mechanical linear, nonlinear, and shrinkage and creep simulations. Firstly, the mesh refinement analysis will be conducted for the mechanical nonlinear analysis considering a maximum number of 1 crack allowed per IP (MNL1) in order to infer if the coarser mesh (015) in SC1.3 (MNL1_SC1.3) predicts similar results as to the mesh 01 in SC1.2 (MNL1_SC1.2). If results differences are not significant, mesh 015 will be adequate for the subsequent

mechanical nonlinear, and shrinkage and creep numerical simulations. The results comparison is conducted by selecting 6 observation points (two per each direction) at matching locations for the two meshes and assessing the differences in normal stress evolution through the simulation time at these locations. The observation points are selected for the locations where the stresses reached higher and lower values.

Secondly, a mechanical linear analysis in SC1.3 (ML_SC1.3) will be conducted in order to verify if the maximum compressive stress never exceeds 50% of the compressive strength of the RSFRC, and to understand the tensile stresses behaviour.

Thirdly, in order to decide the most adequate maximum number of cracks allowed per IP, for the mechanical nonlinear analysis (MNL), two simulations in SC1.3 are considered: one for a maximum value of 1 crack; and other for a maximum value of 2 cracks (MNL1_SC1.3 and MNL2_SC1.3, respectively). The results for the evolution of the maximum tensile stress and the RSFRC tensile strength are analysed for the observation points where stresses reached maximum values. The most reasonable results between the two simulations (MNL1_SC1.3 and MNL2_SC1.3) will dictate the selected maximum number of cracks allowed per IP for the shrinkage and creep analysis. From the obtained results, the risk of crack formation and a relation between the crack width and the temperature evolution will be analysed.

Lastly, the shrinkage and creep (SC) numerical simulations will be conducted for scenarios SC1.3 to SC6, where results for the evolution of the maximum tensile stress and the RSFRC tensile strength are analysed, as well as the risk of crack formation and a relation between the crack width and the temperature evolution. The simulation results with the highest number of cracks, will serve as basis for the analysis of two different volumes for the armour unit: one is half the volume and the other is less than twice the volume of the proposed block (18 tonnes and 60 tonnes, respectively). In addition, a comparison between the cracking results for a RSFRC and for a plain concrete will be performed.

Regarding the shrinkage, only the autogenous shrinkage is simulated, as the drying shrinkage is not significant during the first 8 days of curing.

The mechanical analysis adopted the same time steps and simulation time as considered in the thermal model.

Regarding the RSFRC toughness and strength, since concrete properties are influenced by the cement type and content, different parameters that characterize the properties for the adopted RSFRC are determined recurring to the proposed expressions in the fib Model Code 2010 (Fédération internationale du béton, 2013). However, for the control group scenarios, the values are retrieved from

an independent experimental study using fibres with 20 to 25 mm and aggregates with maximum dimension of 12 mm (Frazão, 2019). For the remaining scenarios, since no experimental tests were conducted, the concrete strength classes attributed for each scenario is based on the expected characteristics for the combination of the cement content and the type of cement. This way, the post-cracking constitutive laws defined for each scenario are consistent with the parametric studies. Similar assumptions are considered for the attribution of the toughness classes.

It is important to note that the concrete considered for the armour unit should have larger aggregates and fibres than those that are usually considered for structural elements. However, because the experimental evaluation is complex and beyond the scope of the present work, no experimental data was conducted. Thus, because reliable research and experimentation data is unavailable for a RSFRC with aggregates and fibres of dimensions adequate for this relatively large elements, the properties of the RSFRC developed by Frazão (2019) were adopted in the present simulations.

The following correspondence between content and type of cement and concrete strength class was assumed:

- − SC2: 310 kg/m³ cement CEM I 42.5R should correspond to class C20/25;
- − SC3: 368 kg/m³ cement CEM I 42.5R should correspond to class C35/45;
- − SC4: 435 kg/m³ cement CEM I 42.5R should correspond to class C50/60;
- − SC5: 368 kg/m³ of cement CEM IV 32.5N should correspond to class C30/37;
- − SC6: 368 kg/m³ of cement CEM I 52.5R should correspond to class C40/50.

The following correlation between type and content of cement and toughness class of the RSFRC was assumed:

- − SC2: 310 kg/m³ of cement CEM I 42.5R should correspond to class 3b;
- − SC3: 368 kg/m³ of cement CEM I 42.5R should correspond to class 4c;
- − SC4: 435 kg/m³ of cement CEM I 42.5R should correspond to class 5e;
- − SC5: 368 kg/m³ of cement CEM IV 32.5N should correspond to class 3b;
- − SC6: 368 kg/m³ of cement CEM I 52.5R should correspond to class 5e.

Table 6.6 summarises the information regarding the simulated scenarios for the mechanical analysis. Once the RSFRC toughness and strength classes are defined, the material properties attributed to the numerical simulations in Table 6.7 are retrieved and calculated from the fib Model Code 2010 recommendations (Fédération internationale du béton, 2013).

For the formation of a new crack in an already cracked integration point, the maximum principal tensile stress should attain the tensile strength of the material and the angle between this principal tensile stress and the existing cracks should be higher than a threshold angle, α_{th}, whose recommended value should be in the interval of 30° and 60° (Ventura-Gouveia, 2011). In this study, a α_{th}=30° was adopted. The Poisson's ratio, ν, is 0.2 for all scenarios.

Table 6.6: Mechanical scenarios.

Mechanical Scenarios | Simulation Time: 192 h (8 days)						
Scenario	Mesh	Cement content (kg/m³)	Cement type	Concrete strength class	RSFRC toughness class	Analysis type
SC1.2	01	400	CEM I 42.5R	C40/50	4d	MNL1
SC1.3	015	400	CEM I 42.5R	C40/50	4d	ML; MNL1; MNL2; SC
SC2	015	310	CEM I 42.5R	C20/25	3b	SC
SC3	015	368	CEM I 42.5R	C35/45	4c	SC
SC4	015	435	CEM I 42.5R	C50/60	5e	SC
SC5	015	368	CEM IV 32.5N	C30/37	3b	SC
SC6	015	368	CEM I 52.5R	C40/50	5e	SC

Table 6.7: Values of the parameters of the constitutive model used in the mechanical numerical simulations.

Parameters	Scenarios					
	SC1.2; SC1.3	SC2	SC3	SC4	SC5	SC6
ρ_a (kg/m³)	2.40E-03	2.40E-03	2.40E-03	2.40E-03	2.40E-03	2.40E-03
E_{cm} (MPa)	30.9E+03	30.3E+03	35.0E+03	38.6E+03	33.6E+03	36.3E+03
f_{cm} (MPa)	64.2	28.0	43.0	58.0	38.0	48.0
f_{ctm} (MPa)	3.67	–	–	–	–	–
$f_{ctk,min}$ (MPa)	–	1.50	2.20	2.90	2.00	2.50
α_C	0.28	0.74	0.67	0.64	0.56	0.74
ξ_C	0.23	0.01	0.01	0.01	0.01	0.01
α_D	0.19	0.74	0.67	0.64	0.56	0.74
ξ_D	0.39	0.18	0.18	0.18	0.18	0.18
α_E	0.10	0.28	0.46	0.83	0.21	0.96
ξ_E	0.74	0.91	0.91	0.91	0.91	0.91
G_f^I (MN/m)	4.56E-03	2.14E-03	3.37E-03	5.49E-03	2.15E-03	5.49E-03
α_{th} (°)	30	30	30	30	30	30
ν	0.2	0.2	0.2	0.2	0.2	0.2

6.3.3.3 Results and discussion

MNL1_SC1.2 and MNL1_SC1.3

The first step of this analysis is to select the most adequate mesh refinement by comparing results of normal stress evolution for the MNL1_SC1.2 and MNL1_SC1.3 at 6 matching observation points (two per each direction) where stresses reach maximum tensile and compressive values.

Since the adopted methodology is similar to the presented in the thermal problem, only the comparison results for the stresses evolution at each observation point are depicted for the two mesh refinements (Figure 6.17). For this analysis, the observation points defined as P1, P3 and P5 are located where stresses reach maximum tensile values in x, y and z directions, while P2, P4, and P6 are located where stresses reach maximum compressive values also for each direction. The positive values correspond to tensile stresses, while the negative to compressive stresses.

Results from Figure 6.17 demonstrate that MNL1_SC1.2 and MNL1_SC1.3 present maximum stresses at similar time-steps for each direction, and that the maximum stresses are registered in P5 (4.04 MPa and 3.95 MPa) for the tensile stresses and P6 (-2.68 MPa and -2.73 MPa) for the compressive stresses. After reaching their peaks, tensile and compressive stress values tend to decrease overtime due to the temperature variation, and at the end of the simulation time, locations where tensile stresses were high depict compressive stresses and locations where compressive stresses were high present tensile stresses.

From the comparison results, it is clear that the coarser mesh refinement (mesh 015) predicts perfectly the same stress evolution results as the mesh 01, since their differences are practically null. Thus, in order to reduce the numerical modelling calculation time, the coarser mesh (015) is selected for the subsequent numerical simulations, and for the following results, only the observation points' results where tensile and compressive stresses reach their maximum values are presented.
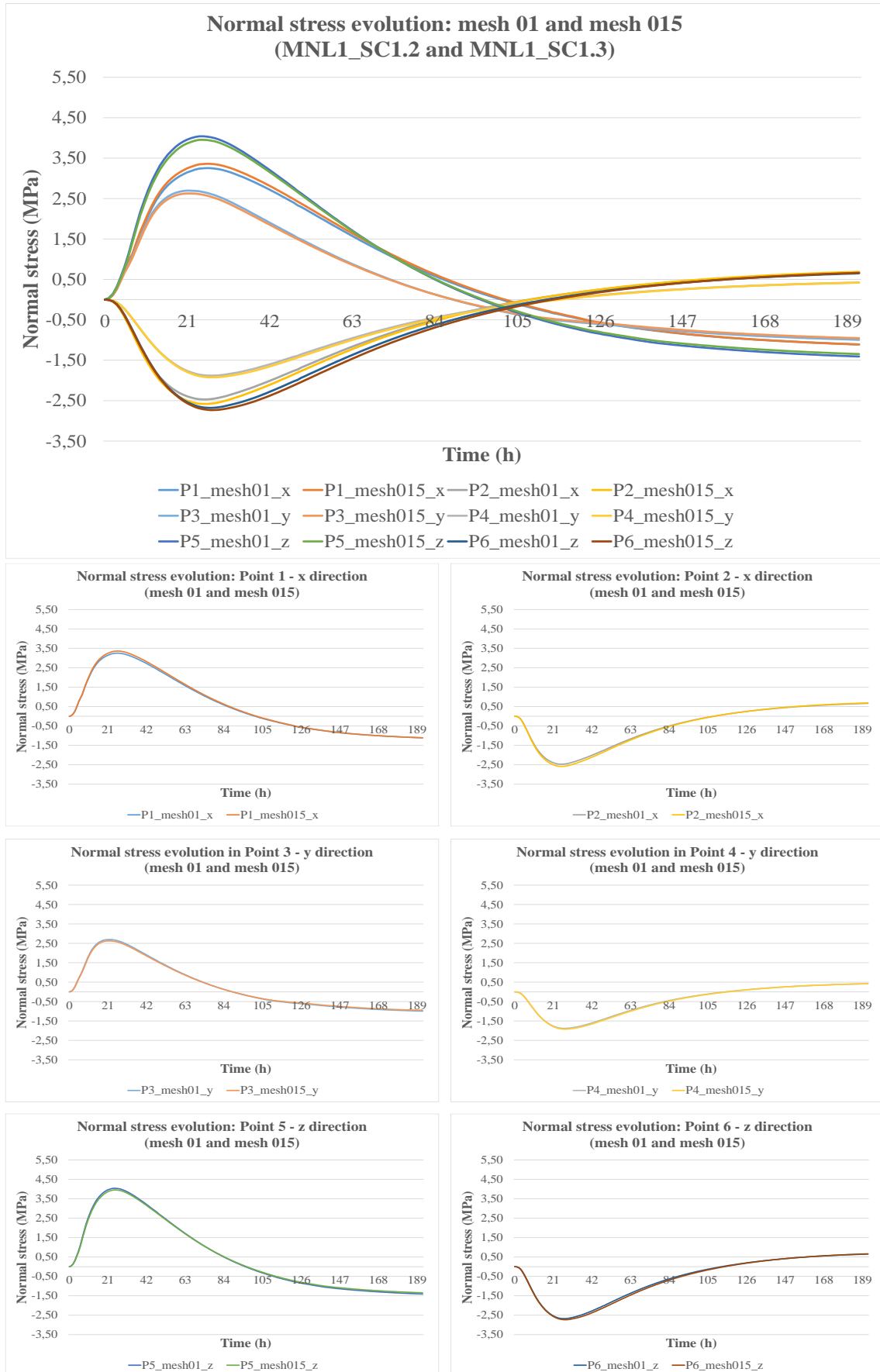
Figure 6.17: Comparative results for two meshes for stresses evolution during 8 days of curing for each observation point.

ML_SC1.3

This analysis intends to understand if the maximum tensile stress exceeds the RSFRC tensile strength, and if the maximum compressive stress never exceeds 50% of the compressive strength of the RSFRC. Table 6.8 presents the maximum values for tensile and compressive stresses in P1 (x direction) and P6 (z direction), as well as the values for the tensile and compressive strengths at 28 days. Figure 6.18 presents the evolution of the normal stress for P1 and P6 with the indication of the tensile strength. Additional information retrieved from the obtained results can be found in Appendix 4B.

Table 6.8: Maximum normal stress in P1 and P6 and tensile and compressive strength values for ML_SC1.3.

Obs. Point	Element	IP	Max. Normal Stress (MPa)	Time (h)	f_{ct} (MPa)	f_{cm} (MPa)
P1	49	1	4.64	23	3.67	64.20
P6	924	3	-3.10	27		
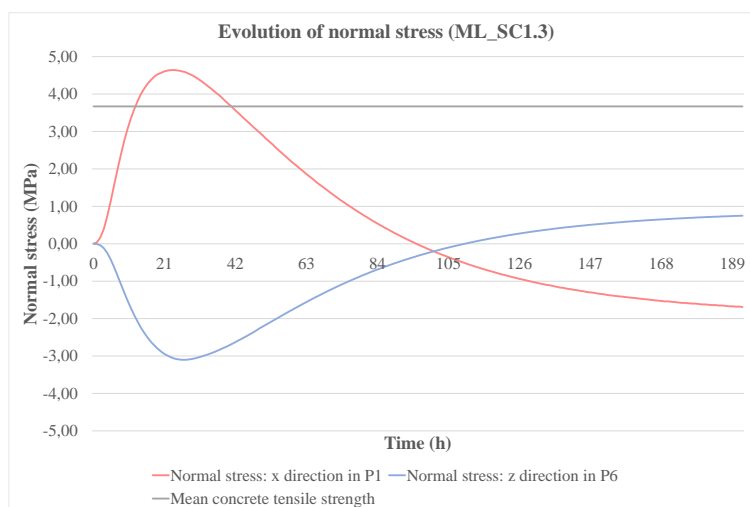
Figure 6.18: Evolution of the normal stress in P1 and P6 for ML_SC1.3 and representation of the f_{ct} value.

Results from Table 6.8 and Figure 6.18 show that the maximum compressive stress is very low (-3.10 MPa) relatively to the compressive strength (64.20 MPa), which allows assuming the compression behaviour is linear. Hence, all subsequent simulations will assume this elastic behaviour of the concrete. Regarding the maximum tensile stress, the elastic behaviour predicts an unrealistic behaviour, because the stress field reaches higher values than the tensile strength. For this reason, the following simulations will consider a nonlinear behaviour.

MNL1_SC1.3 and MNL2_SC1.3

Nonlinear analysis considers the possibility of crack formation. In order to understand the influence of a maximum of 1 and 2 cracks per IP in the numerical simulations, two simulations for SC1.3 were

performed (MNL1_SC1.3 and MNL2_SC1.3). The analysis is conducted for the observation points where stresses reach maximum tensile and compressive values and the selection of the maximum number of cracks allowed per IP depends on the results for the evolution of the maximum tensile stress and the tensile strength. From the obtained results, the risk of crack formation and a relation between the crack width and the temperature evolution is also analysed. As previously explained, the mesh refinement is 015 and the mesh is cut in half to allow retrieving stresses values in the core. Figure 6.19 depicts the MNL1_SC1.3 stress field results for the time step and direction where stresses are higher.
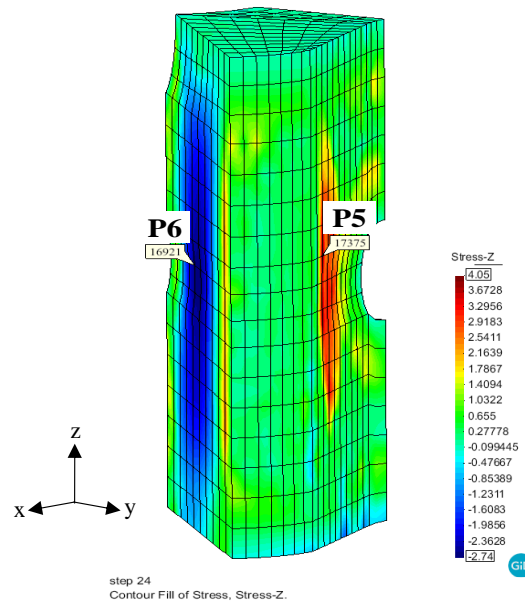
Figure 6.19: Location of the observation points P5 and P6, and results for the stress field for the time step and direction where stresses are higher in MNL1_SC1.3.

For MNL1_SC1.3, the maximum stresses retrieved from GID are registered in P5 (3.95 MPa) for the tensile stresses, and P6 (-2.73 MPa) for the compressive stresses. Additional information retrieved from the obtained results can be found in Appendix 4B.

It is important to note that the results from the stress fields retrieved from GID are obtained by extrapolation of the IP results given by the FEMIX model and, for this reason, GID results do not correspond to the realistic values FEMIX calculates. In order to analyse the maximum stress values, the following observation points' results present the FEMIX outcomes for the IP of the element closest to the corresponding GID mesh node.

Table 6.9 presents the maximum values for tensile and compressive stresses retrieved from FEMIX in P5 (z direction) and P6 (z direction) for the IP of the mesh element closest to the corresponding GID mesh node, as well as the values for the corresponding tensile and compressive strengths. Figure 6.20 plots the evolution of the normal stress for P5 and P6 and the tensile strength.

Table 6.9: Maximum normal stress in P5 and P6 and tensile and compressive strength values for MNL1_SC1.3.

Obs. Point	Element	IP	Max. Normal Stress (MPa)	Time (h)	f_{ct} (MPa)	f_{cm} (MPa)
P5	2460	7	3.04	25	2.33	–
P6	924	7	-2.68	26	–	-49.29
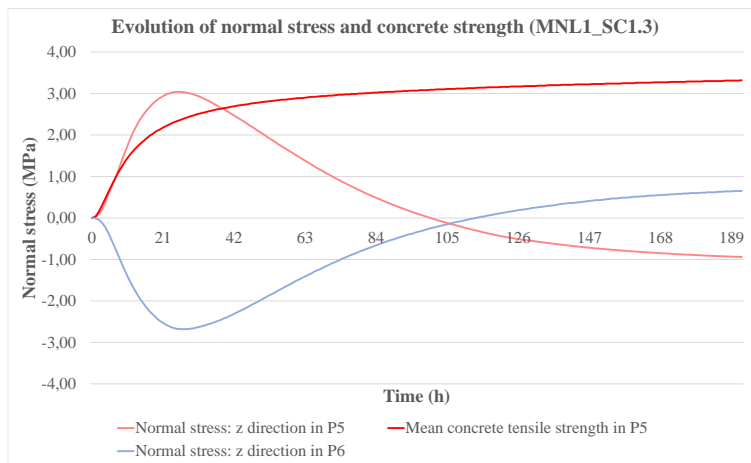
Figure 6.20: Evolution of the normal stress in P5 and P6 for MNL1_SC1.3 and its tensile strength.

Using the nonlinear model with a maximum of 1 crack per IP, results in Figure 6.20 demonstrate that by do not allowing more than 1 crack, tensile stress in z direction in P5 has exceeded the material's tensile strength. This can conduct to unsafe predictions, since the degradation of stiffness, due to proper simulation of cracking, is not being well captured.

Thus, in the MNL2_SC1.3 simulation, a maximum of 2 cracks per IP is adopted. Figure 6.21 depicts the MNL2_SC1.3 stress field results for the time step and directions where the highest stresses have occurred.

For MNL2_SC1.3, the maximum stresses retrieved from GID are registered in P3 (2.72 MPa) for the tensile stresses, and P6 (-2.71 MPa) for the compressive stresses. Additional information retrieved from the obtained results can be found in Appendix 4B.

Table 6.10 presents the maximum values for tensile and compressive stresses retrieved from FEMIX in P3 (y direction) and P6 (z direction) for the IP of the mesh element closest to the corresponding GID mesh node, as well as the values for the corresponding tensile and compressive strengths. Figure 6.22 plots the evolution of the normal stress for P3 and P6 and the tensile strength.

Results in Table 6.10 show that the maximum tensile stress in MNL2_SC1.3 is lower than that of MNL1_SC1.3, and that for the maximum compressive stress the results reach very similar values.

Using the nonlinear model with a maximum of 2 cracks per IP, results in Figure 6.22 demonstrate that the stresses in P3 do not exceed the tensile strength.

Figure 6.21: Location of the observation points P3 and P6, and results for the stress field for the time step and directions where stresses are higher in MNL2_SC1.3.

Table 6.10: Maximum normal stress in P3 and P6 and tensile and compressive strength values for MNL2_SC1.3.

Obs. Point	Element	IP	Max. Normal Stress (MPa)	Time (h)	f_{ct} (MPa)	f_{cm} (MPa)
P3	21	3	1.79	20	2.13	–
P6	924	7	-2.65	26	–	-49.29
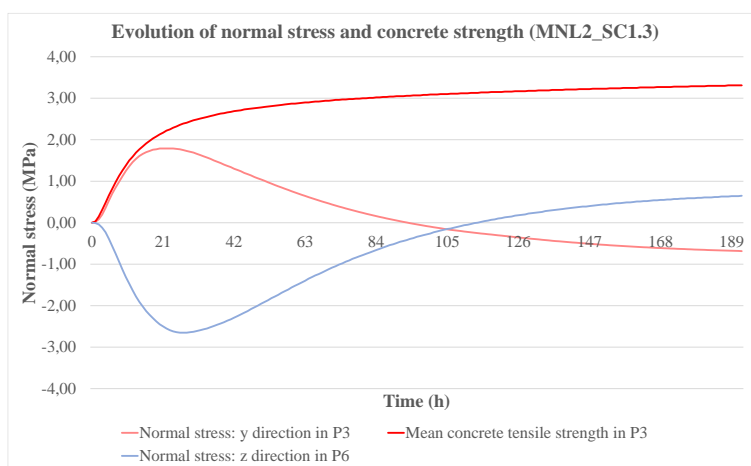
Figure 6.22: Evolution of the normal stress in P3 and P6 for MNL2_SC1.3 and its tensile strength.

In order to analyse the stress behaviour for a critical location, since the FEMIX results for the selected IP of the mesh element closest to the mesh node in GID does not originate cracking, a different IP for the same element is selected. Therefore, results for the evolution of tensile stress and tensile strength in a location where the crack formation occurs are depicted in Figure 6.23. Table 6.11 presents the information related to the crack evolution provided in FEMIX.
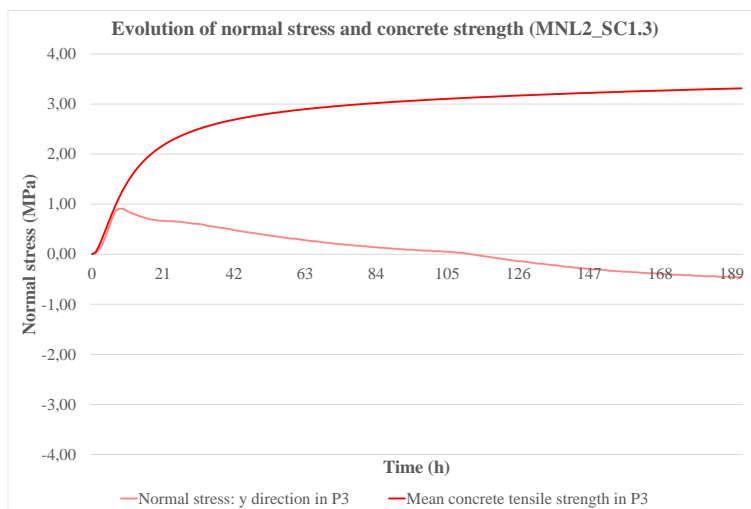
Figure 6.23: Evolution of the tensile stress for a critical location in MNL2_SC1.3 and its tensile strength.

Table 6.11: Crack evolution in MNL2_SC1.3.

Element 21 - Integration Point 7, near P3						
Time (h)	Normal Stress: y Direction (MPa)	Mean Tensile Strength (MPa)	Crack Status	No. of Cracks	Crack Normal Strain (%)	Crack Band Width (m)	Crack Width (m)
7	0.87	0.98	OPENING	1	1.43E-06	0.0733	1.05E-07
24	0.66	2.29	CLOSING	1	1.28E-04	0.0733	9.38E-06
111	0.01	3.13	CLOSED	1	-4.87E-21	0.0733	-3.57E-22

Results in Figure 6.23 demonstrate that for a location where the formation of crack occurs, the stresses near P3 reach the tensile strength without ever exceeding its value. This simulation suggests that the consideration for a maximum of 2 cracks per IP captures a realistic stress development curve, since the stress values start decreasing when the concrete cracks. The maximum tensile stress registered is 0.87 MPa for an age of 7 hours after casting.

Results from Table 6.11 show that near P3 only 1 crack develops during the simulation time and that the maximum crack width is reached 24 hours after casting (9.38E-06 m). Nonetheless, 111 hours after the casting, the crack closes. Crack widths below the critical value of 50 μm (5.00E-05 m) are negligible. In order to analyse the crack patterns, Figure 6.24 depicts the crack pattern and the different crack status for two different timings: i) 20 hours after casting (when the maximum tensile stress is reached, as presented in Table 6.10); and ii) at the end of the simulation time (192 hours).

t = 20 h   **t = 192 h**
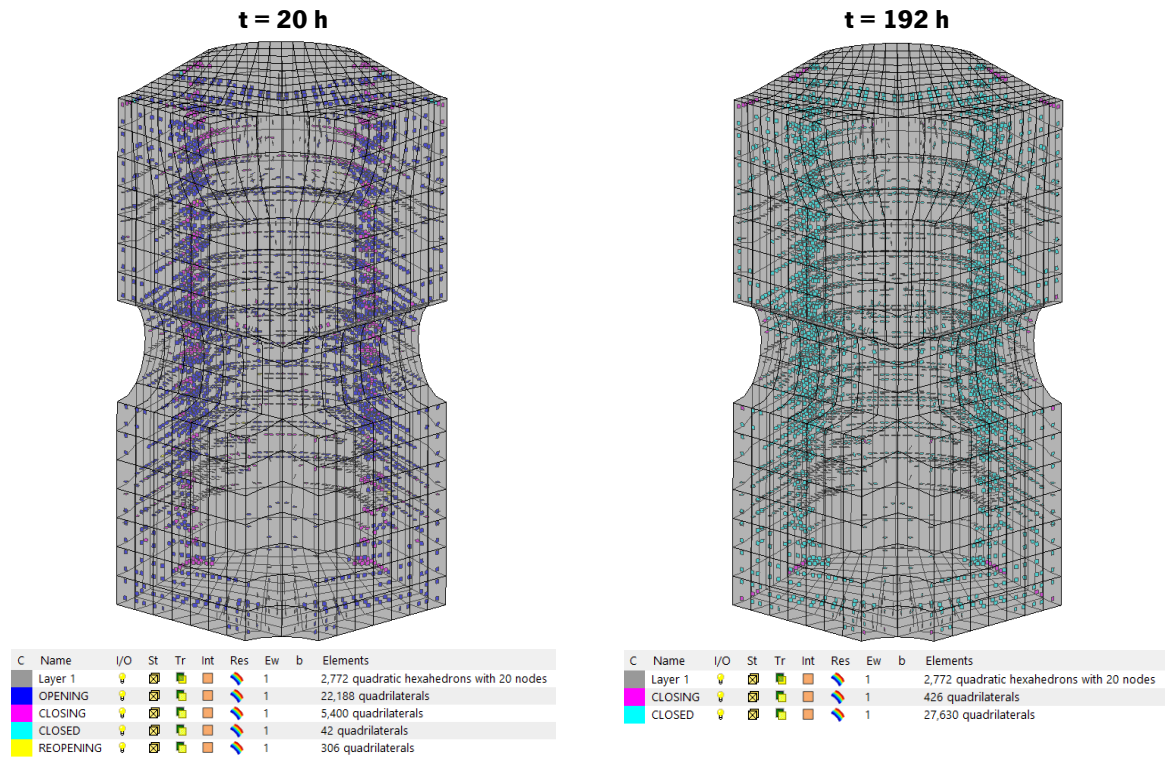
Figure 6.24: Crack pattern and crack status for different time steps in MNL2_SC1.3.

Results in Figure 6.24 depict that during the simulation time, the cracks reach various status and that although in t = 20 h some cracks reopen, at the end of simulation (8 days after the casting) all cracks are either closing or closed due to the temperature decreasing. These results indicate that the durability of this block is not compromised, since the maximum crack width at the final of the curing stage will be sufficiently small for not decreasing the stiffness of the block. The cracks that are forming at t = 20 h are mainly located in areas near the steel formwork or in contact with the ambient temperature, which are locations where the maximum tensile stresses are registered. Figure 6.25 plots the evolution of temperature and crack width for the maximum crack opening value registered in t = 20 h.

Results from Figure 6.25 demonstrate that the crack width tends to increase with temperature and that after the temperature has reached its maximum value, the crack starts closing. The maximum values for temperature and crack width are 31.69°C and 1.31E-04 m, respectively. Appendix 4C presents additional information retrieved from the obtained results.
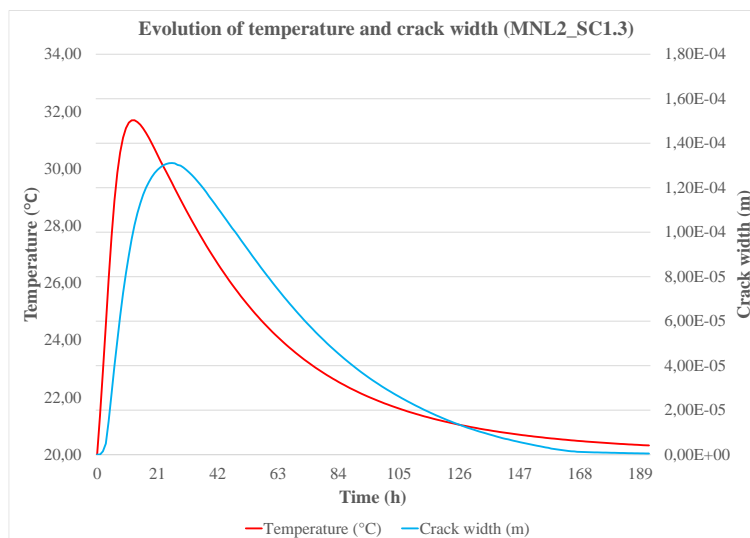
Figure 6.25: Relation between temperature and crack width evolution for MNL2_SC1.3.

SC1.3

Regarding the mechanical nonlinear scenarios considering the shrinkage and creep phenomena, the maximum of 2 cracks per IP is selected, since results demonstrated this condition predicts a realistic stress development. The methodology for the analysis of shrinkage and creep numerical modelling is the same as the presented for the mechanical nonlinear simulations, as it intends to understand if the maximum tensile stress exceeds the RSFRC tensile strength. Moreover, the risk of crack formation and the relation between the crack width and the temperature evolution are also analysed.

Results for SC1.3 stress field are depicted in Figure 6.26 for the time steps and directions where the stresses are higher.

Results from Figure 6.26 indicate that in locations where temperatures reached their maximum values, the compressive stresses are also the greatest. This effect is directly associated to the increasing of temperatures and the restrictive conditions provided by the support and symmetry boundaries that limit the expansion of concrete. Concerning the tensile stresses, the maximum values are reached in the faces in contact with the steel formwork and the environment, which are the locations where lower temperatures were presented. These results demonstrate that temperature decrease leads to the development of tensile stresses when the retraction of concrete is restricted.

For SC1.3, the maximum stresses retrieved from GID are registered in P3 (2.50 MPa) for the tensile stresses, and P6 (-2.46 MPa) for the compressive stresses. Additional information retrieved from the obtained results can be found in Appendix 4B.
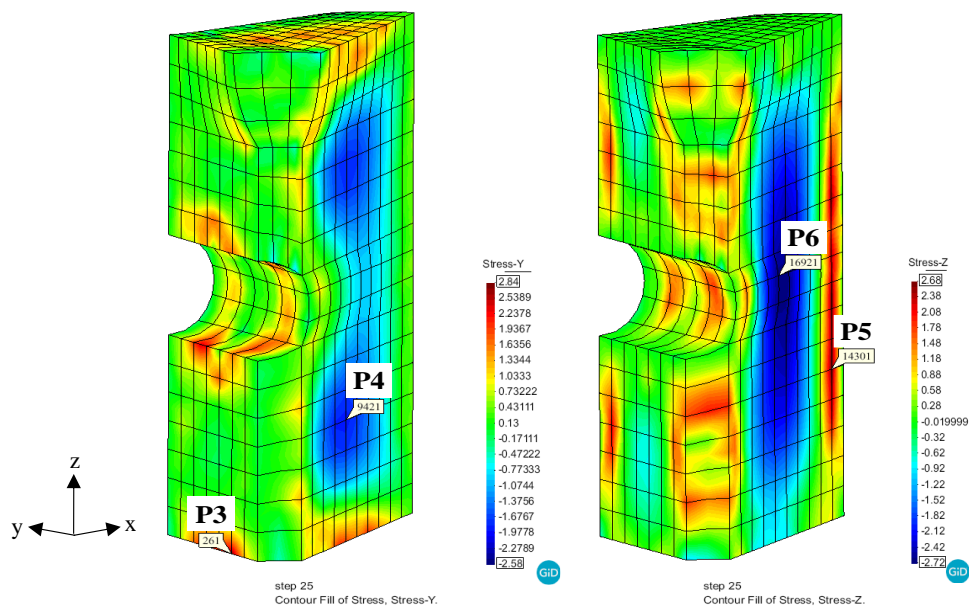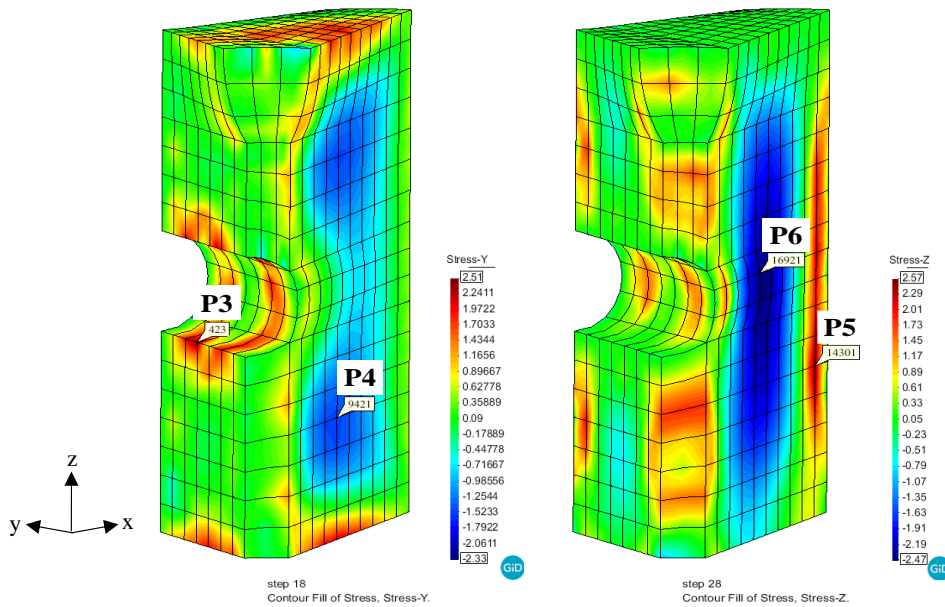
Figure 6.26: Location of the observation points P3 and P6, and results for the stress field for the time steps and directions where stresses are higher in SC1.3.

Table 6.12 presents the maximum values for tensile and compressive stresses retrieved from FEMIX in P3 (y direction) and P6 (z direction) for the IP of the mesh element closest to the corresponding GID mesh node, as well as the corresponding values for the tensile and compressive strengths. Figure 6.27 plots the evolution of the normal stress for P3 and P6 and the tensile strength.

Table 6.12: Maximum normal stress in P3 and P6 and tensile and compressive strength values for SC1.3.

Obs. Point	Element	IP	Max. Normal Stress (MPa)	Time (h)	f_{ct} (MPa)	f_{cm} (MPa)
P3	29	4	1.79	19	2.18	–
P6	924	7	-2.41	25	–	-48.71
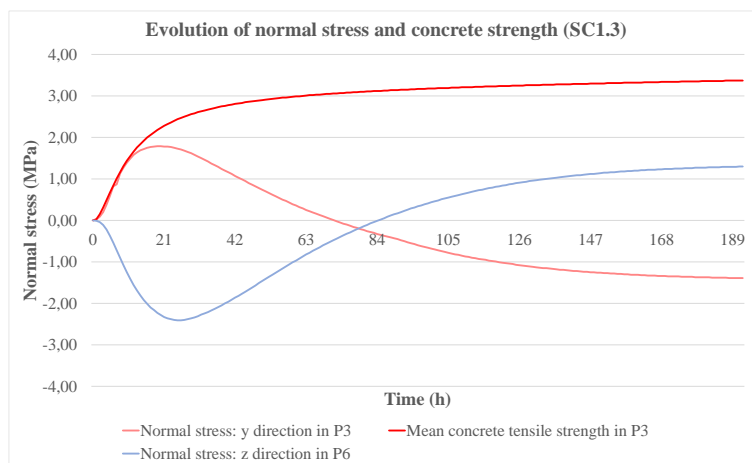
Figure 6.27: Evolution of the normal stress in P3 and P6 for SC1.3 and its tensile strength.

Results in Table 6.12 show that the maximum tensile stress in SC1.3 is the same as that of MNL2_SC1.3, and that for the maximum compressive stress the results reach similar values.

Regarding the results in Figure 6.27, the stresses in P3 do not exceed the tensile strength. In order to understand the results differences between MNL2_SC1.3 and SC1.3, Figure 6.28 presents the evolution of their normal stresses and strengths.
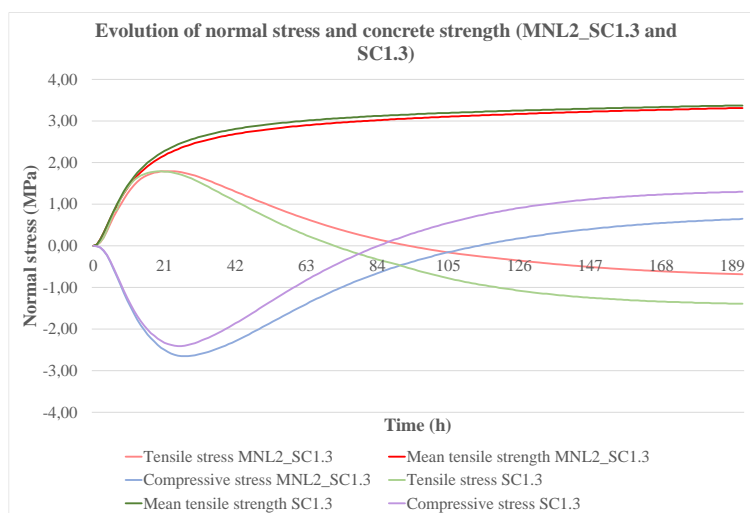
Figure 6.28: Comparison results for evolution of normal stresses and tensile strengths between MNL2_SC1.3 and SC1.3.

Results from Figure 6.28 confirm that the maximum tensile stress values between the two simulations are the same and that the maximum compressive stress is slightly lesser in SC1.3. Regarding the stress evolution behaviour, results demonstrate that before reaching the maximum value, tensile stresses in SC1.3 are greater than in MNL2_SC.13 and that after reaching the maximum value this tendency is inverted. As for the evolution behaviour for the concrete tensile strength, results are similar in both simulations.

Similarly to the methodology adopted in MNL2_SC.13, in order to analyse the stress behaviour for a critical location, a different IP for the same mesh element is selected. Figure 6.29 depicts the results for the evolution of tensile stress and tensile strength at a critical location, while Table 6.13 presents the information related to the crack evolution provided in FEMIX.

Figure 6.29 shows that for a location where the formation of crack occurs, the mechanical nonlinear model considering shrinkage and creep with a maximum of 2 cracks per IP predicts a realistic stress development curve, as the stresses near P3 reach the tensile strength without ever exceeding its value. When this happens, the concrete cracks and stress values starts decreasing. The maximum tensile stress registered is 0.84 MPa for an age of 6 hours after casting.

Results from Table 6.13 show that, near P3, only 1 crack develops during the simulation time and that the maximum crack width is reached 22 hours after casting (5.95E-06 m). Nevertheless, 91 hours after the casting, the crack closes.
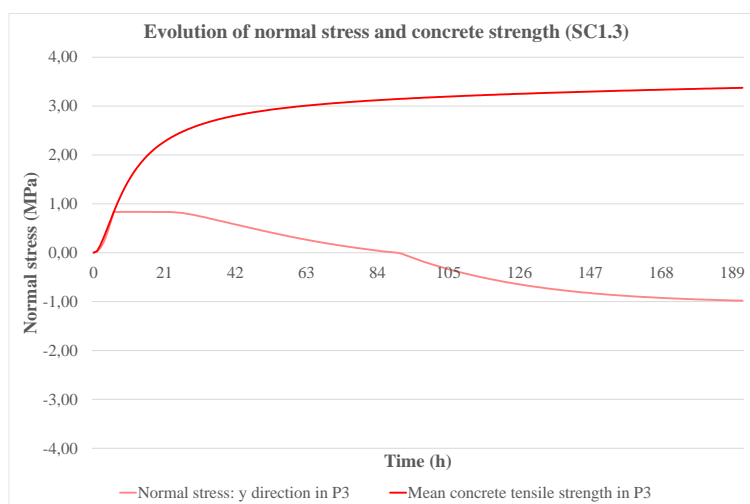
Figure 6.29: Evolution of the tensile stress for a critical location in SC1.3 and its tensile strength.

Table 6.13: Crack evolution in SC1.3.

Element 29 - Integration Point 8, near P3						
Time (h)	Normal Stress: y Direction (MPa)	Mean Tensile Strength (MPa)	Crack Status	No. of Cracks	Crack Normal Strain (%)	Crack Band Width (m)	Crack Width (m)
6	0.84	0.84	OPENING	1	4.15E-07	0.0713	2.96E-08
22	0.84	2.32	CLOSING	1	8.35E-05	0.0713	5.95E-06
91	-0.02	3.15	CLOSED	1	1.06E-22	0.0713	7.56E-24

Figure 6.30 depicts the crack pattern and the different crack status for two different timings: i) 19 hours after casting (when the maximum tensile stress is reached, as presented in Table 6.12); and ii) at the end of the simulation time (192 hours).

Results in Figure 6.30 depict that during the simulation time, the cracks reach various status and that, similarly to MNL2_SC1.3, although in t = 19 h some cracks reopen, at the end of simulation (8 days after the casting) all cracks are completely closed due to the temperature decreasing. These results indicate that the durability of this block is not compromised, since the contribution of the RSFRC is favourable to the temperature and stress variations that occur throughout the curing. The cracks that are forming at t = 19 h are also mainly located in areas near the steel formwork or in contact with the ambient temperature, which are locations where the maximum tensile stresses are registered.

t = 19 h   **t = 192 h**

C	Name	I/O	St	Tr	Int	Res	Ew	b	Elements
	Layer 1						1		2,772 quadratic hexahedrons with 20 nodes
	OPENING						1		18,126 quadrilaterals
	CLOSING						1		4,356 quadrilaterals
	CLOSED						1		24 quadrilaterals
	REOPENING						1		222 quadrilaterals

C	Name	I/O	St	Tr	Int	Res	Ew	b	Elements
	Layer 1						1		2,772 quadratic hexahedrons with 20 nodes
	CLOSED						1		22,806 quadrilaterals
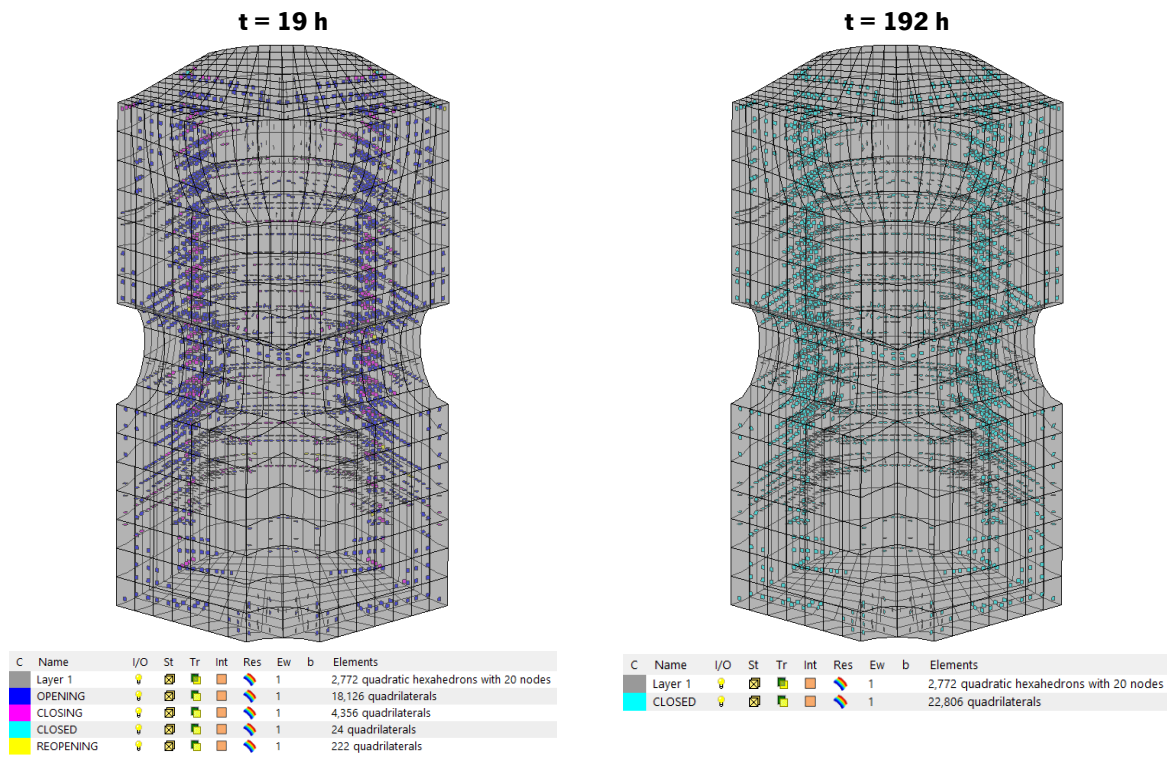
Figure 6.30: Crack pattern and crack status for different time steps in SC1.3

Similar to MNL2_SC1.3, results from Figure 6.31 indicate that crack width increases with temperature and after reaching the maximum temperature, the crack starts closing due to temperature decreasing. The maximum values for temperature and crack width are 31.69°C and 1.47E-04 m, respectively.
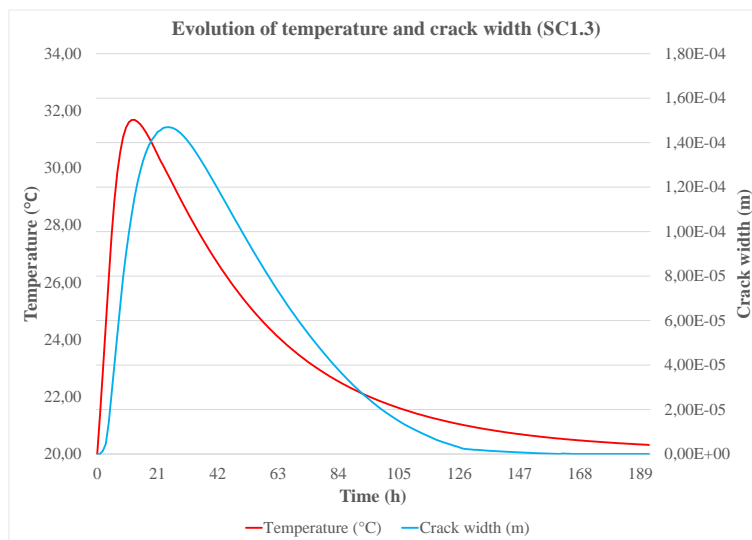
Figure 6.31: Relation between temperature and crack width evolution for SC1.3.

Figure 6.32 demonstrates that comparatively to MNL2_SC1.3, the maximum crack width in SC1.3 is greater, which indicates the obtained results considering shrinkage and creep are relevant, as it leads to

wider cracks. For this reason, the subsequent simulations will consider these phenomena. Appendix 4C presents additional information retrieved from the obtained results.
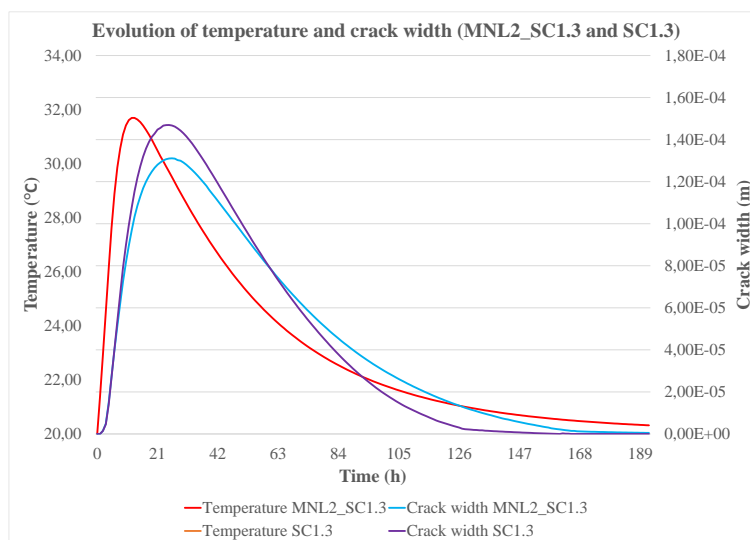
Figure 6.32: Comparison results between temperature and crack width evolution for MNL2_SC1.3 and SC1.3.

SC2, SC3 and SC4

As previously mentioned, the cement content and the type of cement influence the temperatures variation, as well as the concrete strength and the tensile stresses. In order to understand the influence of the cement content on the crack formation, and the evolution of tensile stresses and concrete strength, the mechanical analysis for SC2, SC3 and SC4 is conducted by comparing each scenario results in locations where stresses reach maximum values. In addition, the relation between the crack width and the temperature evolution is also analysed for each scenario.

Figure 6.33 depicts each scenario's stress field results for the time steps and direction where stresses are higher. The number of maximum cracks per IP is also 2, since previous simulation results demonstrated this condition predicts a realistic stress development.

Results from Figure 6.33 demonstrate that regardless of the cement contents, SC2, SC3 and SC4 present similar patterns for the stress field with compressive stresses in the core and tensile stresses at locations in contact with the steel formwork.

For SC2, SC3 and SC4, the maximum stresses retrieved from GID are registered in P5 (0.92 MPa, 1.65 MPa and 2.40 MPa, respectively) for the tensile stresses, and P6 (-1.11 MPa, -2.00 MPa and -2.62 MPa, respectively) for the compressive stresses. These results demonstrate that, for the same type of cement, greater cement contents contribute to higher tensile and compressive stresses in the block. Additional information retrieved from the obtained results can be found in Appendix 4B.
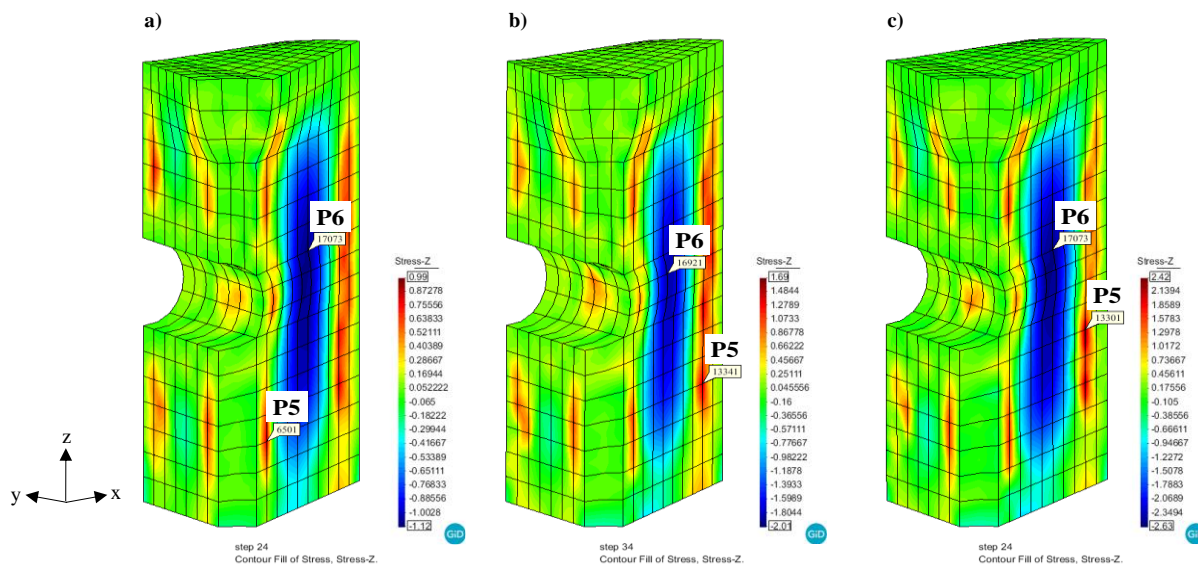
Figure 6.33: Location of the observation points P5 and P6, and results for the stress field for the time steps and direction where stresses are higher in: a) SC2; b) SC3; c) SC4.

Table 6.14 presents the maximum values for tensile and compressive stresses retrieved from FEMIX in P5 (z direction) and P6 (z direction) for the IP of the mesh element closest to the corresponding GID mesh node, as well as the corresponding values for the tensile and compressive strengths for each scenario.

Table 6.14: Maximum normal stress in P5 and P6 and tensile and compressive strength values for SC2, SC3 and SC4.

SC	Obs. Point	Element	IP	Max. Normal Stress (MPa)	Time (h)	f_{ct} (MPa)	f_{cm} (MPa)
SC2	P5	326	2	0.75	18	0.84	–
	P6	854	3	-1.08	24	–	-18.71
SC3	P5	717	8	1.16	21	1.60	–
	P6	924	7	-1.93	26	–	-31.91
SC4	P5	716	5	1.64	26	2.18	–
	P6	854	3	-2.54	24	–	-45.72

Results in Table 6.14 confirm that for the same type of cement, greater cement contents contribute to higher tensile and compressive stresses in the block. SC3 (1.16 MPa) presents higher maximum tensile stress values than in SC2 (0.75 MPa) and lower than that of the SC4 (1.64 MPa).

Figure 6.34 plots the evolution of the normal stress for P5 and P6 and the tensile strength for each scenario, while Figure 6.35 compares stress and strength results between SC2, SC3 and SC4.

In Figure 6.34, results show that for the three scenarios, the tensile stresses in P5 never exceed the tensile strength. Results from Figure 6.35 depict that the evolution of concrete stresses and tensile strength is greater and faster for higher contents of cement due to higher temperatures.
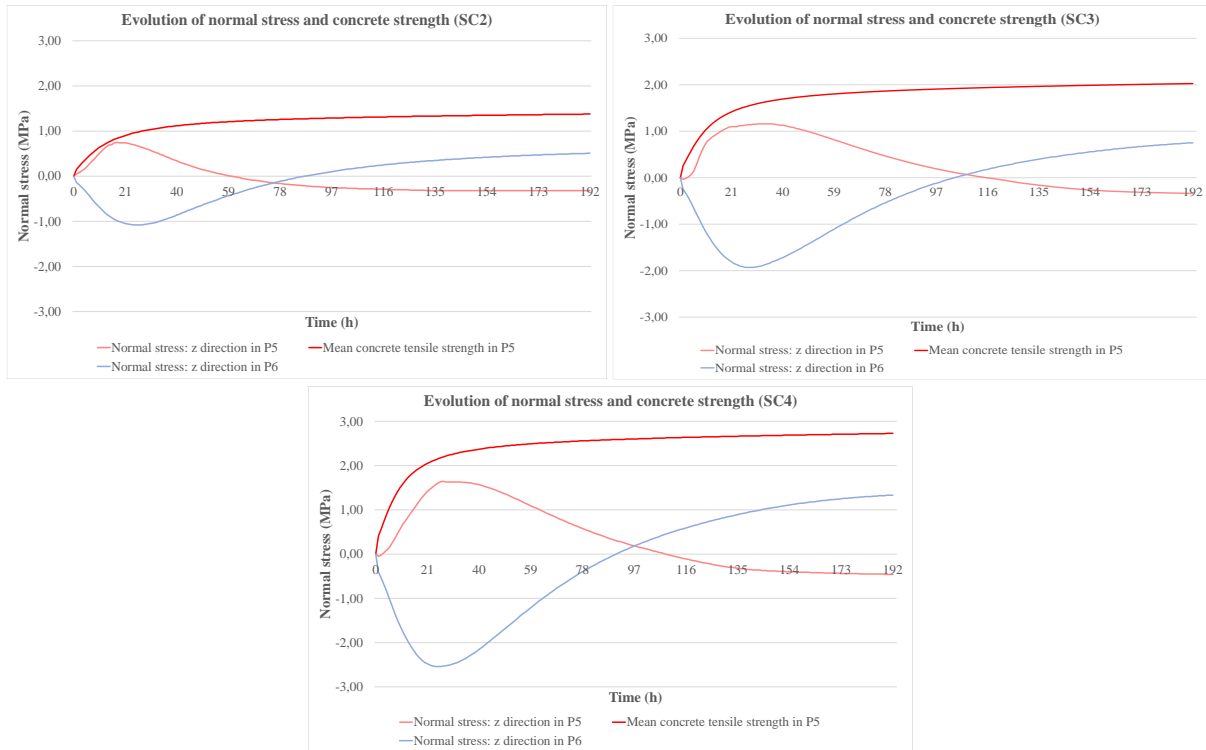
Figure 6.34: Evolution of the normal stress in P5 and P6 for SC2, SC3 and SC4, and their tensile strengths.
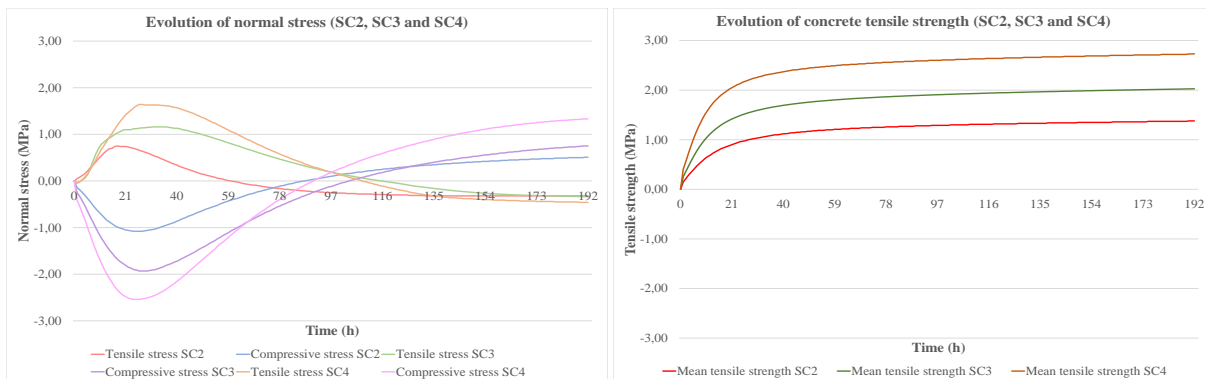
Figure 6.35: Comparison results for the evolution of normal stresses (left) and tensile strengths (right) between SC2, SC3 and SC4.

Since for the selected IPs none of the scenarios develops cracking, in order to analyse the stress behaviour at critical locations, different IPs in SC2, SC3 and SC4 for the same mesh element are selected. Figure 6.36 depicts the results for the evolution of tensile stress and tensile strength in a location where the crack formation occurs in SC2, SC3 and SC4. Table 6.15 presents the information related to the crack evolution provided in FEMIX for each scenario.
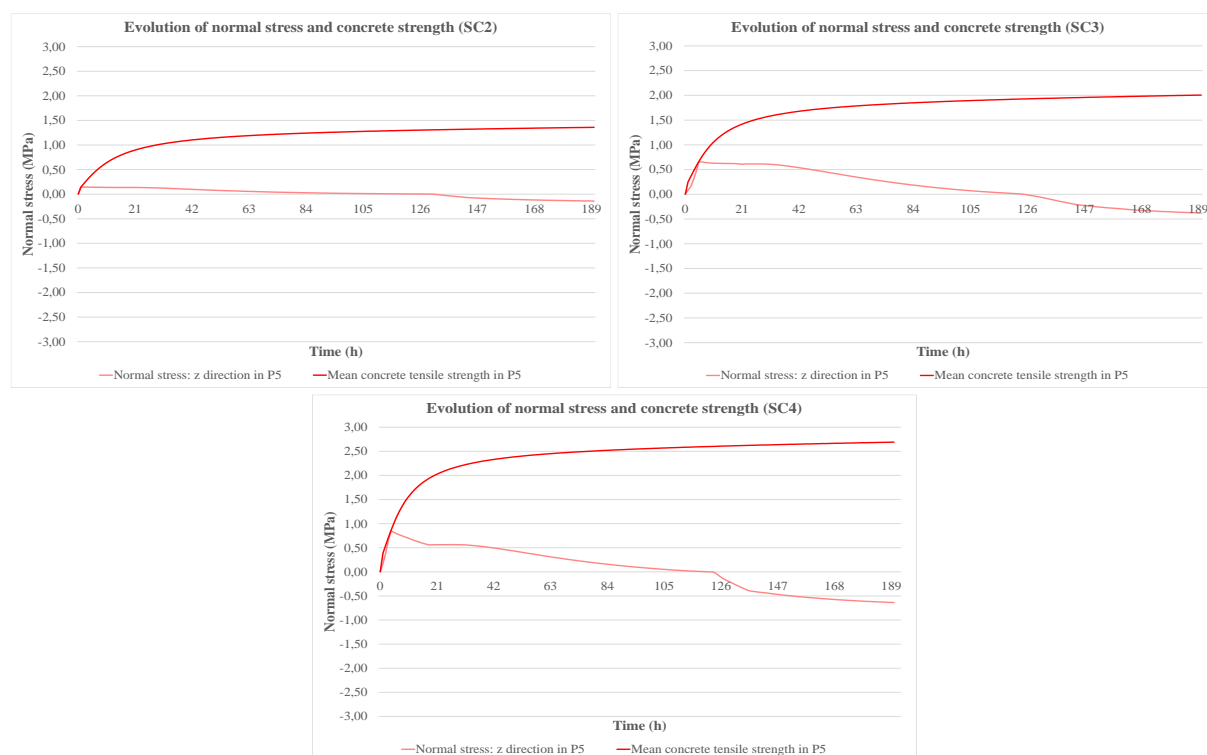
Figure 6.36: Evolution of the tensile stress for a critical location in SC2, SC3 and SC4, as well as their tensile strengths.

Table 6.15: Crack evolution in SC2, SC3 and SC4.

Time (h)	Normal Stress: z Direction (MPa)	Mean Tensile Strength (MPa)	Crack Status	No. of Cracks	Crack Normal Strain (%)	Crack Band Width (m)	Crack Width (m)
SC2 | Element 326 - Integration Point 6, near P5							
3	0.14	0.14	OPENING	1	3.65E-06	0.0663	2.42E-07
19	0.14	0.82	CLOSING	1	1.00E-04	0.0663	6.63E-06
20	0.14	0.84	OPENING	1	1.01E-04	0.0663	6.70E-06
23	0.14	0.90	CLOSING	1	1.03E-04	0.0663	6.83E-06
133	0.00	1.31	CLOSED	1	-7.15E-21	0.0663	-4.74E-22
SC3 | Element 717 - Integration Point 2, near P5							
6	0.66	0.66	OPENING	1	1.70E-05	0.055	9.35E-07
20	0.62	1.35	CLOSING	1	6.93E-05	0.055	3.81E-06
126	0.00	1.93	CLOSED	1	5.29E-23	0.055	2.91E-24
SC4 | Element 716 - Integration Point 4, near P5							
6	0.85	0.86	OPENING	1	1.73E-05	0.0549	9.50E-07
31	0.56	2.19	CLOSING	1	5.18E-04	0.0549	2.84E-05
126	-0.03	2.60	CLOSED	1	1.16E-20	0.0549	6.37E-22

Results in Figure 6.36 demonstrate that the maximum tensile stresses registered in SC2, SC3 and SC4 are 0.14 MPa, 0.66 MPa and 0.85 MPa for an age of 3 and 6 hours after casting.

Results from Table 6.15 show that, near P5, only 1 crack per IP develops during the simulation time. For SC2, SC3 and SC4, the maximum crack widths reach 6.83E-06 m, 3.81E-06 m and 2.84E-05 m at an age of 23 h, 20 h and 31 h after casting, respectively. In SC2, the crack that is forming at an age of

3 hours after casting reopens at an age of 20 hours. Regardless of these results, all cracks close at an age of 133 h for SC2, and 126 h for SC3 and SC4 after casting, which indicates the cracks that are forming in the selected IPs are not significant.

Nonetheless, in order to analyse the crack patterns, Figure 6.37 depicts the crack pattern and the different crack status for two time steps. The first corresponds to when the maximum tensile stress is reached, as presented in Table 6.14 (18 h, 21 h and 26 h after casting for SC2, SC3 and SC4, respectively), and the second at the end of the simulation time (192 hours).

SC2

SC3

t = 21 h	t = 192 h

C	Name	I/O	St	Tr	Int	Res	Ew	b	Elements
	Layer 1							1	2,772 quadratic hexahedrons with 20 nodes
	OPENING							1	29,892 quadrilaterals
	CLOSING							1	41,706 quadrilaterals
	CLOSED							1	318 quadrilaterals
	REOPENING							1	1,518 quadrilaterals

C	Name	I/O	St	Tr	Int	Res	Ew	b	Elements
	Layer 1							1	2,772 quadratic hexahedrons with 20 nodes
	CLOSING							1	12 quadrilaterals
	CLOSED							1	73,506 quadrilaterals

SC4

t = 26 h	t = 192 h

C	Name	I/O	St	Tr	Int	Res	Ew	b	Elements
	Layer 1							1	2,772 quadratic hexahedrons with 20 nodes
	OPENING							1	1,140 quadrilaterals
	CLOSING							1	68,220 quadrilaterals
	CLOSED							1	444 quadrilaterals
	REOPENING							1	378 quadrilaterals

C	Name	I/O	St	Tr	Int	Res	Ew	b	Elements
	Layer 1							1	2,772 quadratic hexahedrons with 20 nodes
	CLOSED							1	70,182 quadrilaterals

Figure 6.37: Crack pattern and crack status for different time steps in SC2, SC3 and SC4.

Results in Figure 6.37 depict that although in the first analysed time step for all scenarios (t = 18 h, 21 h and 26 h) some cracks reopen, at the end of simulation (8 days after the casting) all cracks are either

closing or closed due to the temperature decreasing. From all three scenarios, SC4 is the only to have all cracks closed at t = 192 h, due to the fastest temperature decreasing. These results demonstrate that the durability of this block is not compromised, since the contribution of the RSFRC is favourable to the temperature and stress variations that occur throughout the curing. Regarding the total number of cracks that start opening in the first analysed time step, results depict that SC2 is the scenario with more cracking, and that SC4 is the scenario with less cracking. These results indicate that the greatest and fastest evolution of the concrete tensile strength for higher contents of cement contribute to less cracking.

Figure 6.38 plots the evolution of temperature and crack width for the maximum crack opening value registered in t = 18 h, 21 h and 26 h for SC2, SC3 and SC4, respectively.
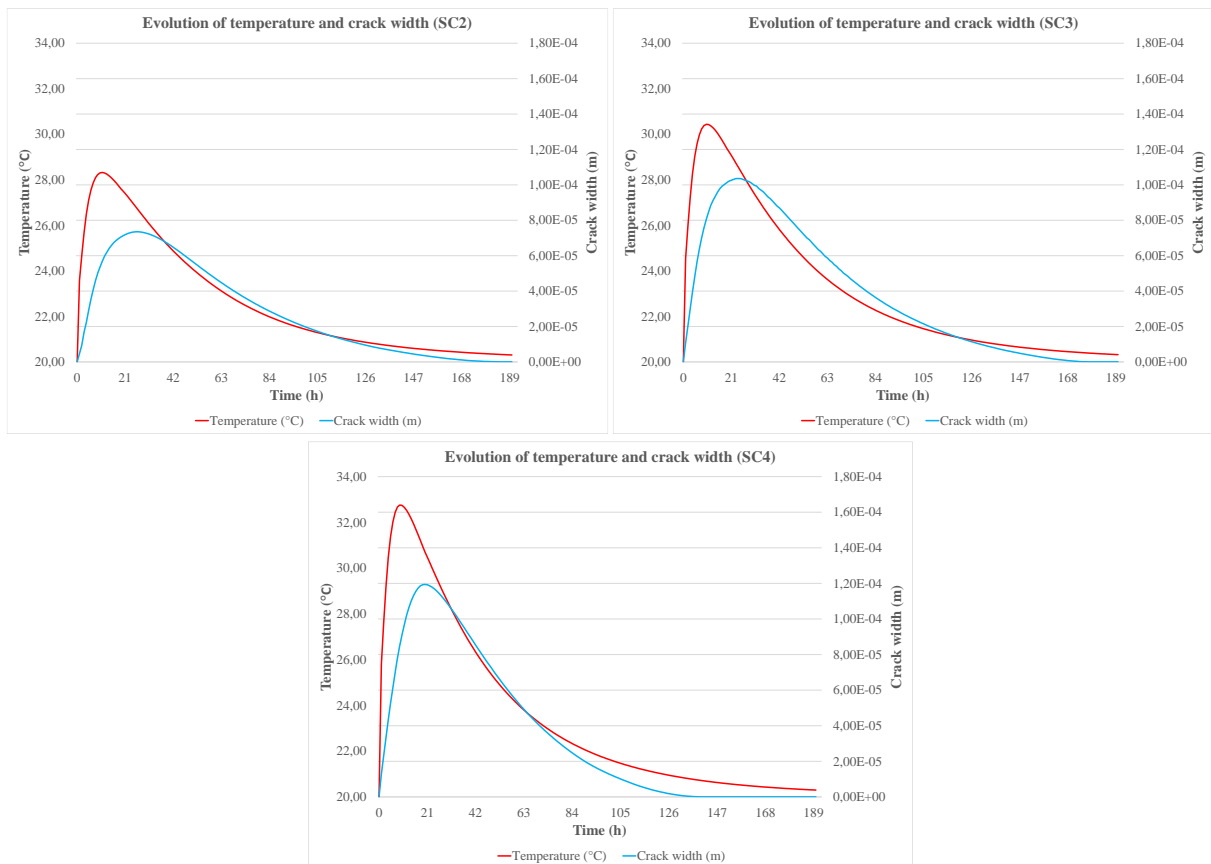
Figure 6.38: Relation between temperature and crack width evolution for SC2, SC3, and SC4.

Results from Figure 6.38 demonstrate that the maximum values for crack width and temperature in SC2 are 7.35E-05 m and 28.32°C; in SC3 are 1.04E-04 m and 30.44°C; and in SC4 are 1.19E-04 m and 32.76°C, respectively. Appendix 4C presents additional information retrieved from the obtained results. Figure 6.39 compares the maximum values for crack width and temperatures between SC2, SC3 and SC4.
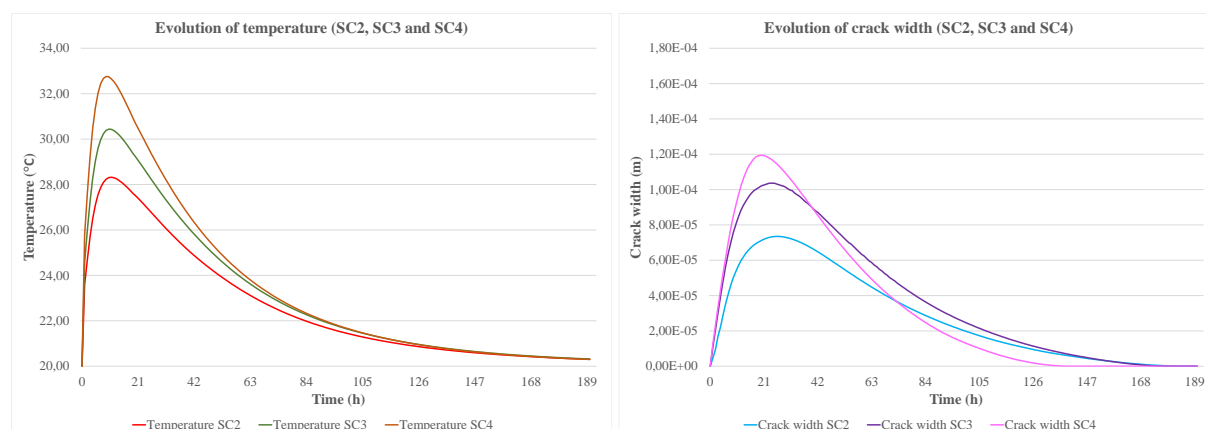
Figure 6.39: Comparison results between temperature (left) and crack width (right) evolution for SC2, SC3 and SC4.

Figure 6.39 demonstrates that higher maximum temperatures from higher cement contents, lead to greater maximum crack widths in earlier ages of curing. SC3 (1.04E-04 m) registers wider cracks than in SC2 (7.35E-05 m) and narrower than in SC4 (1.19E-04 m). Moreover, results demonstrate that fastest temperature decreasing leads to cracks closing at an earlier age, since in SC4 cracks start closing at an earlier age when compared to SC2.

These results suggest that the cement content of 435 kg/m³ is probably the most adequate for this armour unit, since the stresses evolution lead to no cracks at the end of simulation.

Thus, this analysis allows concluding that the evolution of the stresses and crack width, as well as the crack pattern is a function of the amount of cement used in the casting.

SC5 and SC6

The current scenarios intend to analyse the influence of different types of cement on the crack formation, and the evolution of tensile stresses and concrete strength by comparing SC5 and SC6 results in locations where stresses reach maximum values. Moreover, the relation between the crack width and the temperature evolution is also analysed for each scenario. The obtained results from the numerical simulations will also be compared to SC3, which has the same cement content, but different type of cement.

Figure 6.40 depicts SC5 and SC6 stress field results for the time steps and directions where stresses are higher.
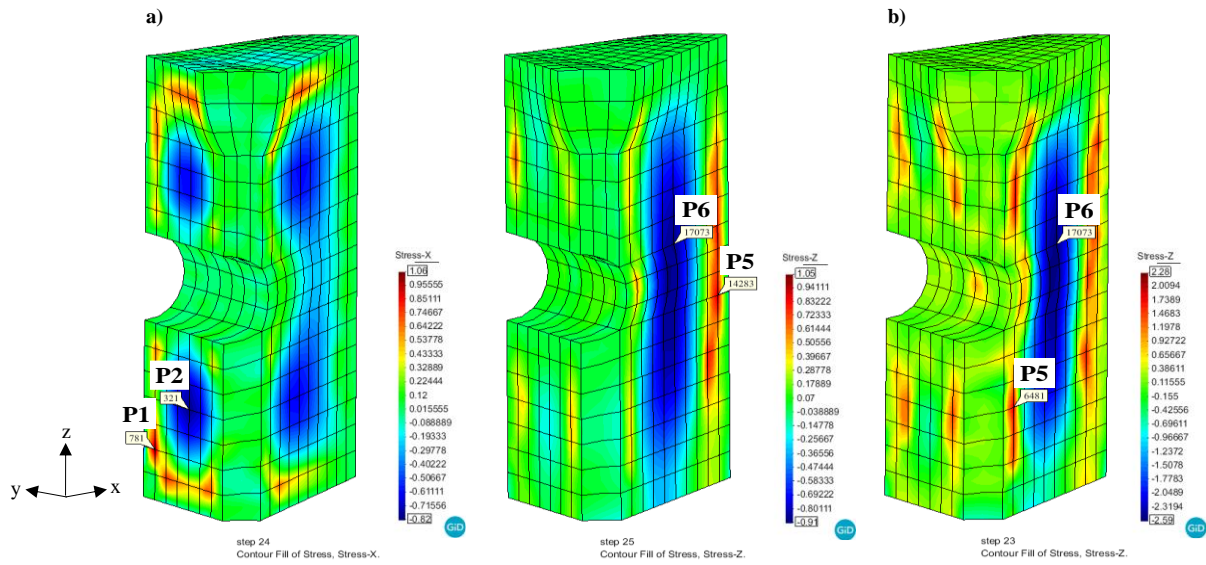
Figure 6.40: Location of the observation points P1 and P6, and P5 and P6, as well as results for the stress field for the time steps and directions where stresses are higher in: a) SC5; b) SC6.

Results from Figure 6.40 indicate that for SC5, the maximum stresses retrieved from GID are registered in P1 (1.05 MPa) for the tensile stress, and P6 (-0.90 MPa) for the compressive stress; for SC6, the maximum tensile stress is registered in P5 (1.99 MPa) and the maximum compressive stress is registered in P6 (-2.58 MPa). These results demonstrate that, for the same cement content, greater types of cement contribute to higher tensile and compressive stresses in the block. Additional information retrieved from the obtained results can be found in Appendix 4B.

Table 6.16 presents the maximum values for tensile and compressive stresses retrieved from FEMIX in P1 (x direction) and P6 (z direction) for SC5, and P5 (z direction) and P6 (z direction) for SC6, as well as the corresponding values for the tensile and compressive strengths for each scenario. The selected IP of the mesh element is the closest to the corresponding GID mesh node. Figure 6.41 plots the evolution of the normal stress for P1 and P6, and P5 and P6, as well as the tensile strength for each scenario. Figure 6.42 compares stress and strength results between SC3, SC5 and SC6.

Table 6.16: Maximum normal stress in P1 and P6 for SC5, and P5 and P6 for SC6, as well as their tensile and compressive strength values.

SC	Obs. Point	Element	IP	Max. Normal Stress (MPa)	Time (h)	f_{ct} (MPa)	f_{ct} (MPa)
SC5	**P1**	47	3	0.89	24	1.00	–
	P6	854	5	-0.87	23	–	-20.91
SC6	**P5**	326	2	1.51	20	1.96	–
	P6	854	3	-2.50	24	–	-41.44
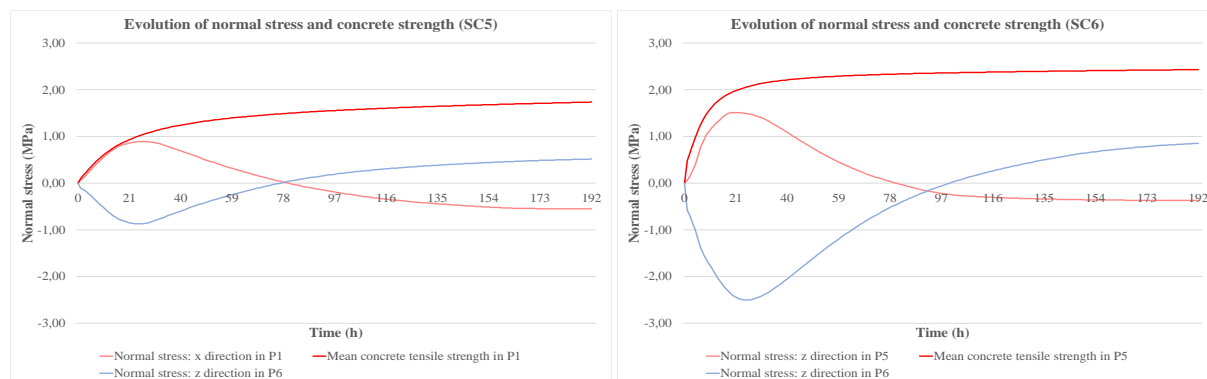
Figure 6.41: Evolution of the normal stress in P1 and P6 for SC5, and P5 and P6 for SC6, as well as their tensile strengths.
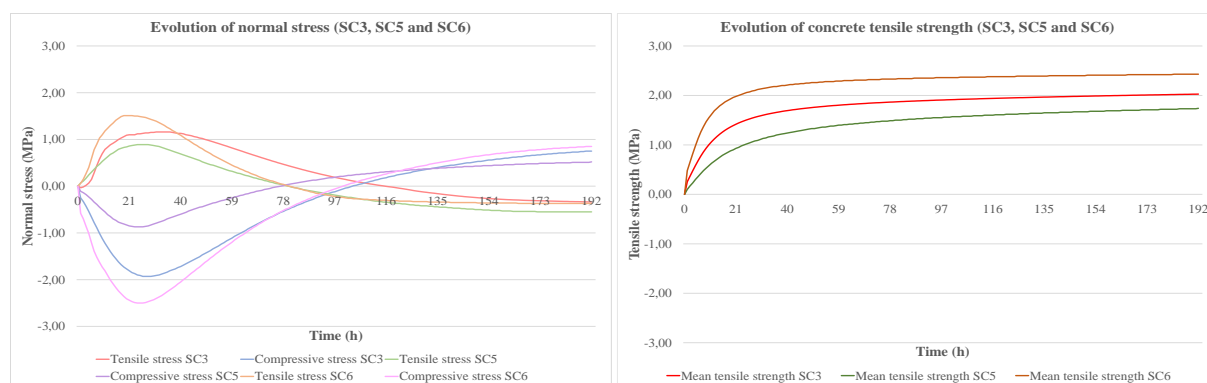
Figure 6.42: Comparison results for the evolution of normal stresses (left) and tensile strengths (right) between SC3, SC5 and SC6.

Results in Table 6.16 and Figure 6.42 confirm that for the same cement content, greater types of cement (CEM I 52.5R) contribute to higher tensile and compressive stresses in the armour unit. In Figure 6.41, results show that for the SC5 and SC6, the tensile stresses in P1 and P5 never exceed the tensile strength. Results from Figure 6.42 indicate that the evolution of concrete tensile strength is greater and faster for the type of cement CEM I 52.5R, because greater types of cement, and consequently higher temperatures, influence the speed evolution of the concrete properties. Conversely, for class N cement (CEM IV 32.5N), the evolution of concrete properties is the slowest, which might contribute to more crack opening at an earlier age when compared to class R cements. Comparing results with the obtained for SC3, it can be concluded that the maximum tensile stress registered in FEMIX for SC3 (CEM I 42.5R: 1.16 MPa) is higher than the maximum stress for SC5 (CEM IV 32.5N: 0.89 MPa), but lower than that of the SC6 (CEM I 52.5R: 1.51 MPa). These results are coincident with the maximum temperature results analysed in Section 6.3.2.3.

In order to analyse the stress behaviour for a critical location in SC5 and SC6, different IPs for the same mesh elements are selected. Figure 6.43 depicts the results for the evolution of tensile stress and tensile strength in a location where the crack formation occurs in SC5 and SC6. Table 6.17 presents the information related to the crack evolution provided in FEMIX for each scenario.
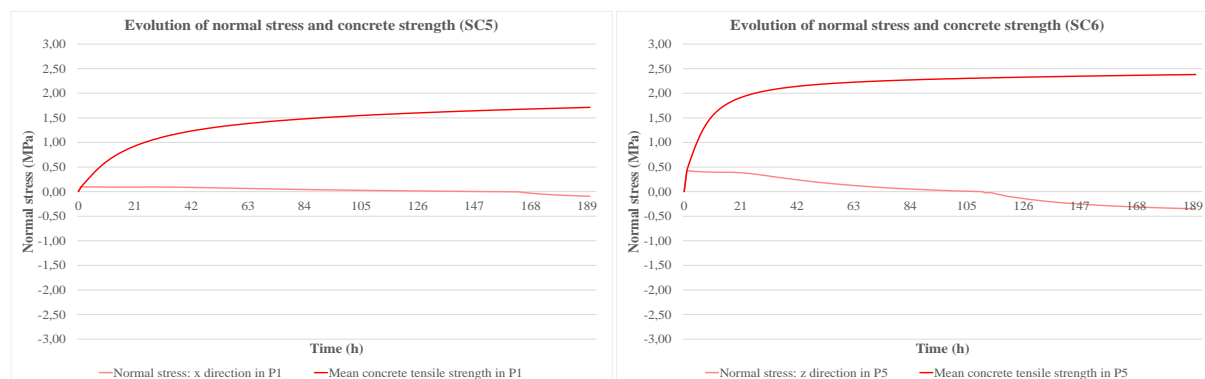
Figure 6.43: Evolution of the tensile stress for a critical location in SC5 and SC6, as well as their tensile strengths.

Table 6.17: Crack evolution in SC5 and SC6.

Time (h)	Normal Stress: x Direction (MPa)	Mean Tensile Strength (MPa)	Crack Status	No. of Cracks	Crack Normal Strain (%)	Crack Band Width (m)	Crack Width (m)
SC5 | Element 47 - Integration Point 1, near P1							
3	0.10	0.10	OPENING	2	7.47E-06	0.0721	5.39E-07
33	0.09	1.10	CLOSING	2	1.06E-04	0.0721	7.64E-06
166	-0.01	1.67	CLOSED	2	8.07E-22	0.0721	5.82E-23
SC6 | Element 326 - Integration Point 6, near P5							
3	0.43	0.43	OPENING	1	1.60E-05	0.0663	1.06E-06
21	0.39	1.87	CLOSING	1	9.96E-05	0.0663	6.60E-06
113	0.00	2.31	CLOSED	1	1.61E-21	0.0663	1.07E-22

Results in Figure 6.43 demonstrate that the maximum tensile stresses registered in SC5 and SC6 are 0.10 MPa and 0.43 MPa for an age of 3 hours after casting.

Results from Table 6.17 show that, near P1 and P5, in SC5 the maximum number of cracks reached 2 cracks, while in SC6 only 1 crack per IP develops during the simulation time. These results suggest that for SC5, the slower evolution of the tensile strength given by CEM IV 32.5N originates more cracking and that the durability of the block during its service life could be compromised, if these cracks will not close.

For SC5 and SC6, the maximum crack widths reach 7.64E-06 m and 6.60E-06 m at an age of 33 h and 21h after casting, respectively. Regardless of these results, all cracks close at an age of 166 h, and 113 h after casting for SC5 and SC6, respectively, which indicates the cracks that are forming in the selected IPs are not significant.

Figure 6.44 depicts the crack pattern and the different crack status for a time step when the maximum tensile stress is reached, as presented in Table 6.16 (24 h and 20 h after casting for SC5 and SC6, respectively), and at the end of the simulation time (192 hours).

SC5

t = 24 h	t = 192 h

C	Name	I/O	St	Tr	Int	Res	Ew	b	Elements
	Layer 1							1	2,772 quadratic hexahedrons with 20 nodes
	OPENING							1	22,878 quadrilaterals
	CLOSING							1	41,460 quadrilaterals
	CLOSED							1	516 quadrilaterals
	REOPENING							1	3,198 quadrilaterals

C	Name	I/O	St	Tr	Int	Res	Ew	b	Elements
	Layer 1							1	2,772 quadratic hexahedrons with 20 nodes
	CLOSING							1	36 quadrilaterals
	CLOSED							1	68,010 quadrilaterals
	REOPENING							1	6 quadrilaterals

SC6

t = 20 h	t = 192 h

C	Name	I/O	St	Tr	Int	Res	Ew	b	Elements
	Layer 1							1	2,772 quadratic hexahedrons with 20 nodes
	OPENING							1	15,300 quadrilaterals
	CLOSING							1	56,826 quadrilaterals
	CLOSED							1	138 quadrilaterals
	REOPENING							1	1,398 quadrilaterals

C	Name	I/O	St	Tr	Int	Res	Ew	b	Elements
	Layer 1							1	2,772 quadratic hexahedrons with 20 nodes
	CLOSED							1	73,710 quadrilaterals
	REOPENING							1	12 quadrilaterals

Figure 6.44: Crack pattern and crack status for different time steps in SC5 and SC6.

In Figure 6.44, results demonstrate that despite most cracks at the end of simulation (8 days after the casting) being either closing or closed due to the temperature decreasing, 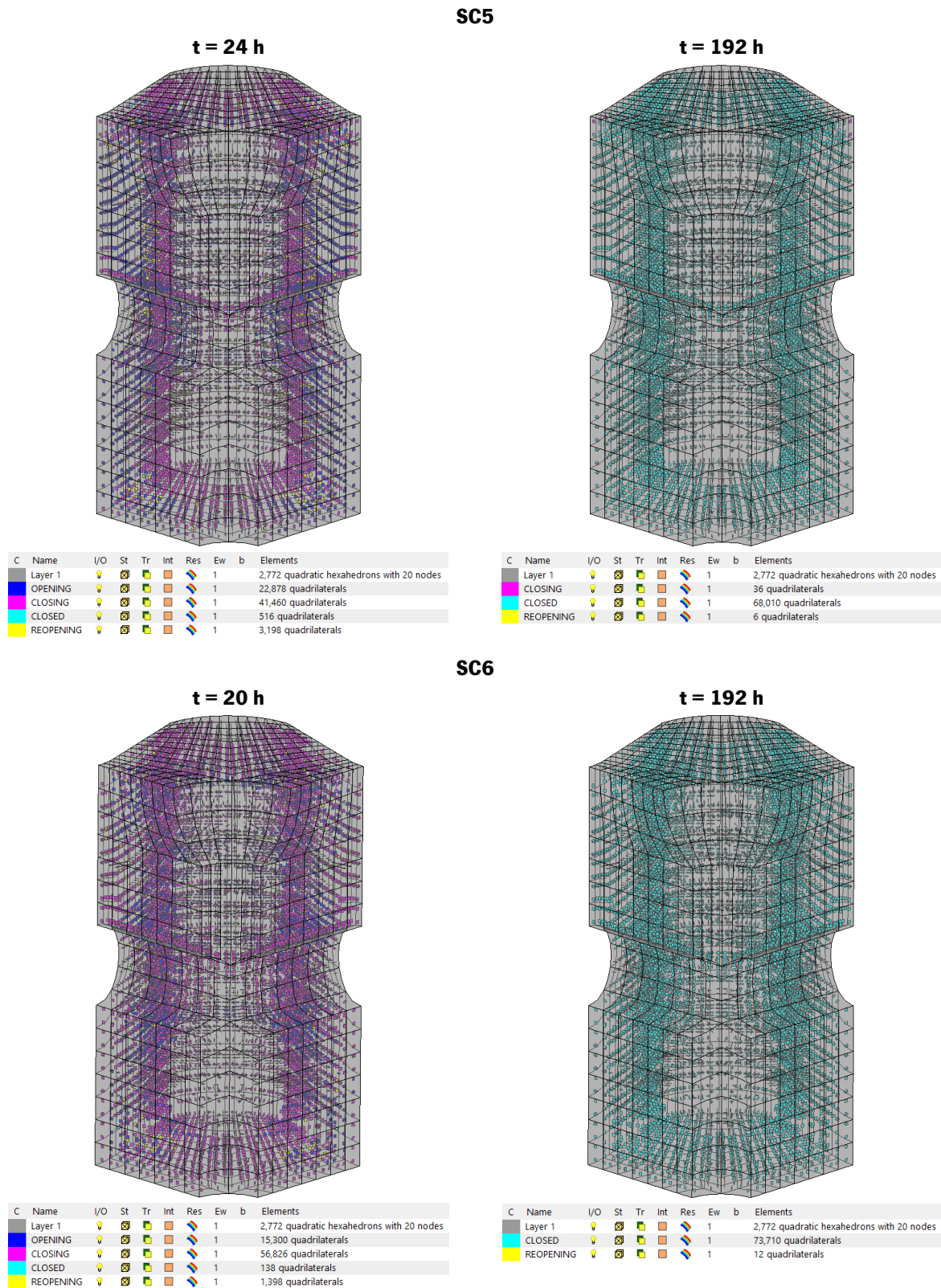some cracks are still reopening, especially in SC6. This suggests that the durability of the block might be compromised when using CEM I 52.R for this type of structure if the cracks will not close until 28 days of age, as this type of cement predicts higher temperatures and consequently more stress variations throughout the curing. Regarding the total number of cracks that start opening in the first analysed time step, results depict that SC5 has more cracking, which suggests that the smaller and slower evolution of the concrete tensile strength for CEM IV 32.5N contributes to more cracking during the first stages of curing, but less cracks reopening 8 days after the casting. Conversely, in the first analysed time step, SC6 presents less cracking due to greater and faster evolution of the concrete tensile strength for CEM I 52.R, but more cracks reopening at an age of 8 days.

Comparing results with the obtained for SC3, no crack reopening occurs in SC3 at the end of simulation, and in the first analysed time step, SC3 results depict more cracks reopening than in SC6 but less than in SC5. These results suggest that slower evolution of the concrete tensile strength contribute to more cracking during the first stages of curing and that the type of cement CEM I 42.5R is probably the most adequate for this armour unit, since the stresses evolution lead to no cracks at the end of simulation.

Figure 6.45 plots the evolution of temperature and crack width for the maximum crack opening value registered in t = 24 h and 20 h for SC5 and SC6, respectively.
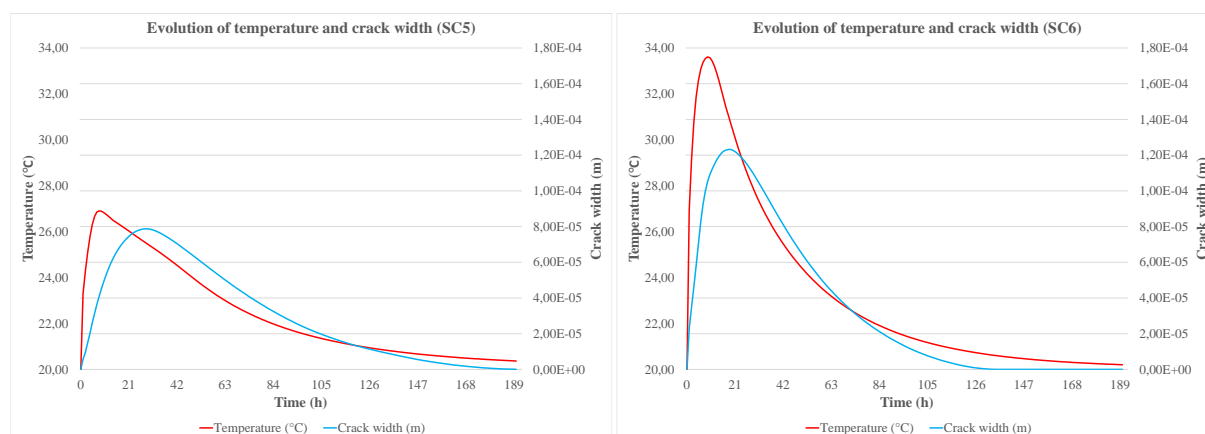
Figure 6.45: Relation between temperature and crack width evolution for SC5 and SC6.

Results from Figure 6.45 demonstrate that the maximum values for crack width and temperature in SC5 are 7.88E-05 m and 26.91°C; and in SC6 are 1.23E-04 m and 33.61°C, respectively. Appendix 4C presents additional information retrieved from the obtained results. Figure 6.46 compares the maximum values for crack width and temperatures between SC3, SC5 and SC6.
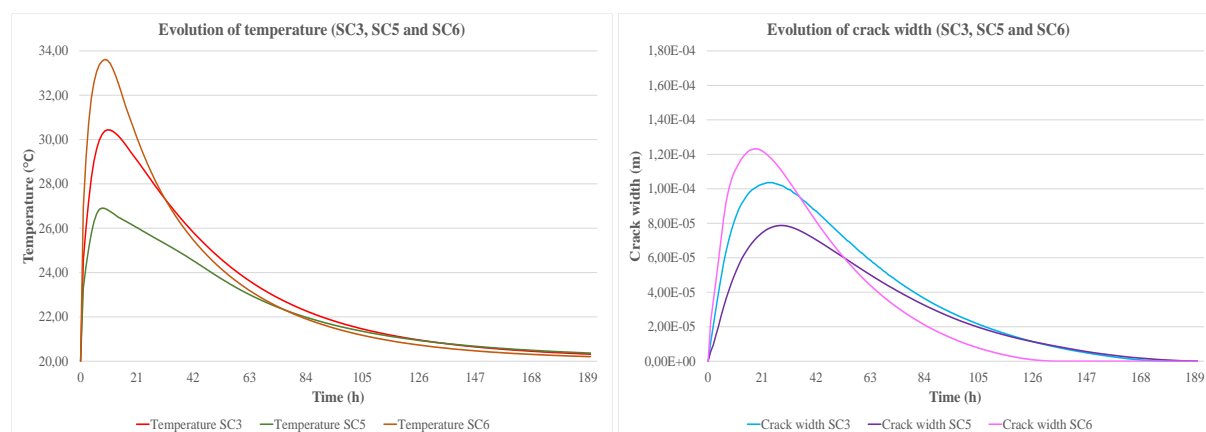
Figure 6.46: Comparison results between temperature (left) and crack width (right) evolution for SC3, SC5 and SC6.

Figure 6.46 demonstrates that higher maximum temperatures from higher types of cement lead to greater maximum crack widths in earlier ages of curing, and that fastest temperature decreasing in SC6 leads to cracks closing at an earlier age when comparing with SC5.

Comparing results with the obtained for SC3, this scenario registers wider cracks (1.04E-04 m) that in SC5 (7.88E-05 m) and narrower cracks than in SC6 (1.23E-04 m).

Thus, this analysis allows concluding that the evolution of the stresses and crack width, as well as the crack pattern is a function of the temperatures and the type of cement used in the casting.

Since the scenario with the most significant maximum crack width value is SC6 (1.23E-04 m), and results for the crack pattern demonstrated that, at the end of the simulation time, a greater number of cracks in the reopening phase is evident, two additional scenarios are conducted for SC6 to analyse different armour unit dimensions (SC6_18 and SC6_60). In addition, a comparative study between SC6 and a scenario with plain concrete (SC6_plain) is also developed.

SC6_18, SC6_60 and SC6_plain: thermo-mechanical analysis

As previously mentioned, the proposed armour unit can serve multiple applications in maritime environments with different design wave conditions. Since results from the crack formation analysis demonstrated that the most susceptible scenario is SC6, the thermo-mechanical behaviour for different armour unit volumes is conducted for two additional scenarios based on SC6. The selected volumes are as follows: one is half the volume and the other is less than twice the volume of the original block. The analysis will allow understanding the influence of block sizes with 18 tonnes and 60 tonnes on the evolution of temperature, stresses and crack formation for SC6 (SC6_18 and SC6_60, respectively). Regarding the maximum dimensions of these two armour units, SC6_18 and SC6_60 present maximum heights of 1.99 m and 2.96 m, respectively. Moreover, a comparative study between SC6

and a scenario with plain concrete (SC6_plain) will also be conducted to understand the contribution of the RSFRC in minimizing the crack evolution.

Thermal numerical simulations to understand the temperature evolution in two different armour unit dimensions are only conducted for SC6_18 and SC6_60, since the only difference between these scenarios is the armour unit size. Since SC6_plain has the same size, cement and thermal simulation conditions as SC6, thermal numerical simulations are not developed for that scenario.

Regarding the numerical simulations for the mechanical analysis, the analysis is conducted for three scenarios (SC6_18, SC6_60 and SC6_plain) and intends to understand the influence of the armour unit size on the stress evolution and crack formation and to compare the RSFRC and the plain concrete behaviours. The numerical conditions for SC6_18 and SC6_60 are the same as in SC6; however, for SC6_plain the parameters of the constitutive model used in the mechanical numerical simulations have to be determined, because of the different post-cracking behaviour for the plain concrete.

In order to define the post-cracking behaviour for SC6_plain, Figure 6.16 in Section 6.3.3.1 depicts a schematic representation of the stress-crack opening relation for plain concrete that allows calculating the parameters α_i and ξ_i that define the trilinear diagram. For SC6_18 and SC6_60, the parameters for the RSFRC are the same as the SC6, since the type of cement and cement contents are the same. Table 6.18 presents the material properties attributed to the mechanical numerical simulations that are retrieved and calculated from the fib Model Code 2010 (Fédération internationale du béton, 2013).

Table 6.18: Values of the parameters used in the mechanical simulations in SC6, SC6_18, SC6_60 and SC6_plain.

Parameters	Scenarios			
	SC6	SC6_18	SC6_60	SC6_plain
ρ_a **(kg/m³)**	2.40E-03	2.40E-03	2.40E-03	2.40E-03
E_{cm} **(MPa)**	36.3E+03	36.3E+03	36.3E+03	36.3E+03
f_{cm} **(MPa)**	48.0	48.0	48.0	48.0
$f_{ctk,min}$ **(MPa)**	2.50	2.50	2.50	2.50
$\alpha_C \mid \alpha_1$	0.74	0.74	0.74	0.20
$\xi_C \mid \xi_1$	0.01	0.01	0.01	0.20
$\alpha_D \mid \alpha_2$	0.74	0.74	0.74	0.15
$\xi_D \mid \xi_2$	0.18	0.18	0.18	0.40
α_E	0.96	0.96	0.96	–
ξ_E	0.91	0.91	0.91	–
G_f^I **(MN/m)**	5.49E-03	5.49E-03	5.49E-03	1.47E-04
α_{th} **(°)**	30	30	30	30
ν	0.2	0.2	0.2	0.2

Regarding the thermal analysis, Figure 6.47 presents the results for the temperature field for the time step when temperatures are higher in 2 observation points for SC6_18 and SC6_60. Figure 6.48 plots the results for the temperature evolution for each scenario and observation point. The obtained results from these numerical simulations will be compared to SC6.
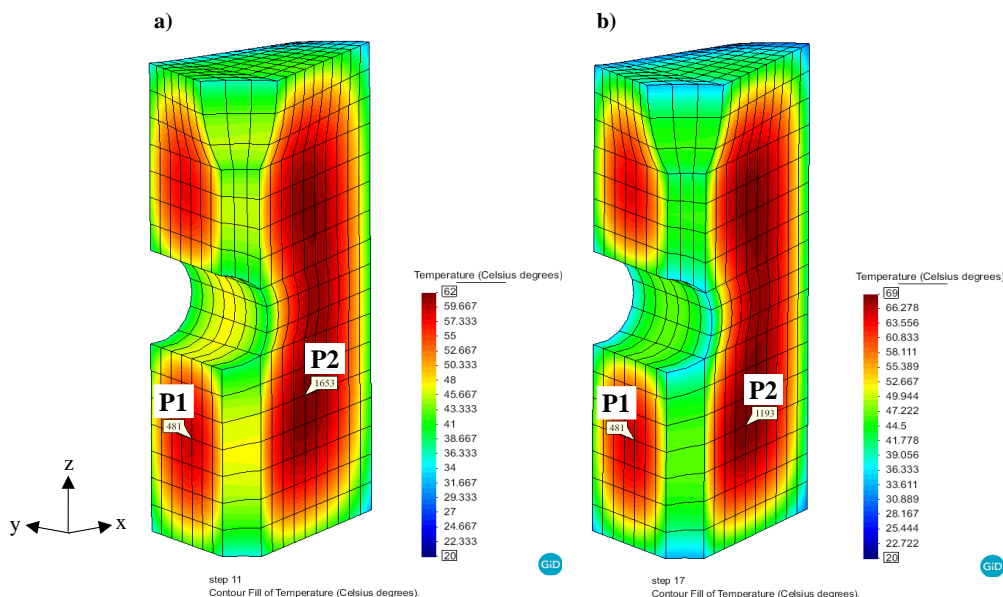
Figure 6.47: Location of the observation points P1 and P2, and results for the temperature field for the time step when temperatures are higher in: a) SC6_18; b) SC6_60.
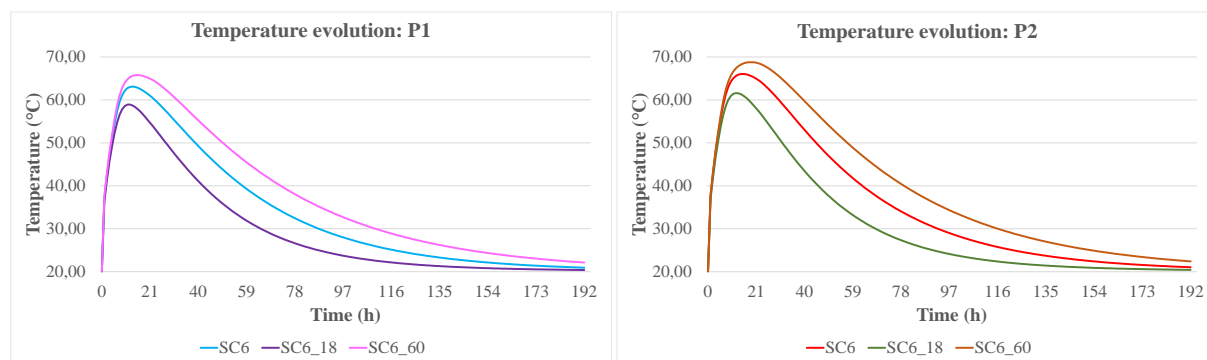
Figure 6.48: Results for temperatures evolution during 8 days of curing for each observation point for SC6, SC6_18 and SC6_60.

Results in Figure 6.47 show that for each scenario, the greatest temperature gradient is registered in the inner part of the block, where temperatures reach maximum values in P2 of approximately 62°C for SC6_18 and 69°C for SC6_60 (Figure 6.48). At the same location for SC6, the maximum temperature in P2 was 66°C. These results indicate that for the same type of cement and cement content, armour units with more volume (SC6_60) originate higher temperatures during the hydration process and that smaller armour units (SC6_18) reach maximum temperature values at a slight earlier age. In addition,

the temperature decrease in SC6_18 is more abrupt than in SC6_60, which suggests that smaller armour units tend to attain ambient temperatures faster.

Comparing these results with the obtained for SC6, it can be concluded that the maximum temperature for SC6 (66°C) is slightly higher than the maximum temperature registered for SC6_18 (62°C), but lower than that of the SC6_60 (69°C). Conversely, the temperature decrease in SC6 is faster than that registered in SC6_60, and slower than that in SC6_18. This behaviour will be relevant to understand the probability of cracks formation, as higher temperatures lead to more cracking due to the increase of tensions in the concrete. Thus, it is expected that SC6_60 presents more cracks than in SC6 and SC6_18. Appendix 4A presents additional information retrieved from the obtained results.

In short, this thermal analysis allows concluding that the evolution of the maximum temperature is a function of the size of the armour unit used in the casting due to the temperature dissipation.

Regarding the mechanical analysis, the numerical simulations for SC6_18, SC6_60 and SC6_plain present results for the evolution of the maximum tensile stress and the RSFRC tensile strength, crack patterns and the relation between the crack width and the temperature evolution. The obtained results from the numerical simulations will also be compared to SC6.

Figure 6.49 depicts SC6_18, SC6_60 and SC6_plain stress field numerical simulations results for the time steps and direction where stresses are higher.

Figure 6.49: Location of the observation points P5 and P6, and results for the stress field for the time steps and direction where stresses are higher in: a) SC6_18; b) SC6_60; c) SC6_plain.
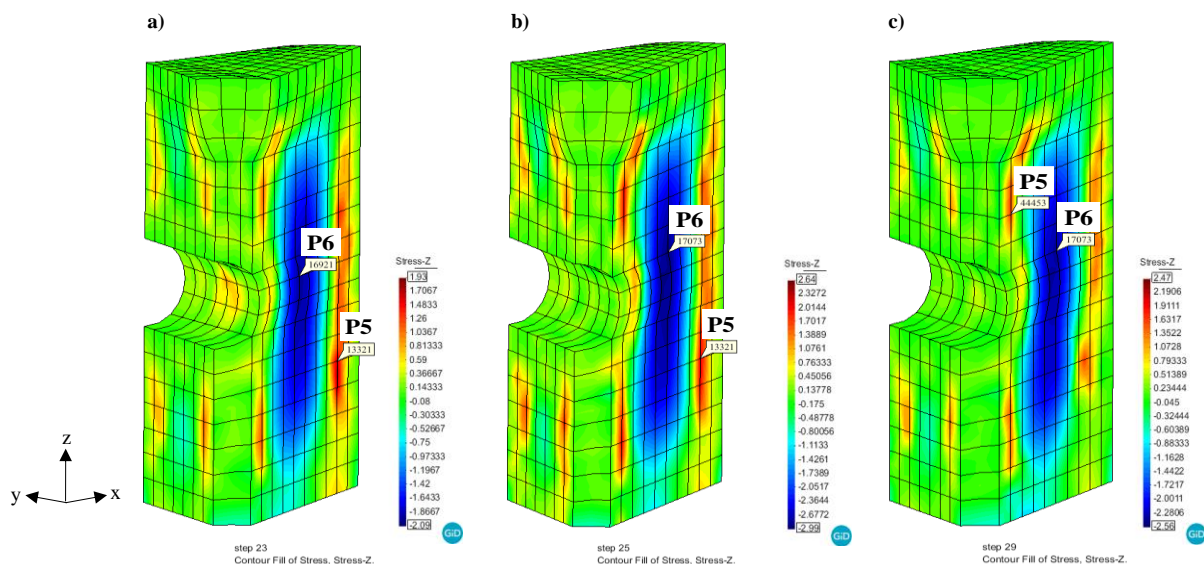
Results from Figure 6.49 indicate that for SC6_18, SC6_60 and SC6_plain, the maximum stresses retrieved from GID are registered in P5 (1.77 MPa, 2.32 MPa and 1.93 MPa) for the tensile stress, and

P6 (-2.08 MPa, -2.98 MPa and -2.55 MPa) for the compressive stress. These results demonstrate that, for the same type of cement and cement content, greater armour units contribute to higher tensile and compressive stresses in the block. Additional information retrieved from the obtained results can be found in Appendix 4B.

Table 6.19 presents the maximum values for tensile and compressive stresses retrieved from FEMIX in P5 (z direction) and P6 (z direction) for the three scenarios, as well as the corresponding values for the tensile and compressive strengths for each scenario. The selected IP of the mesh element is the closest to the corresponding GID mesh node. Figure 6.50 plots the evolution of the normal stress for P5 and P6, as well as the tensile strength for each scenario. Figure 6.51 compares stress and strength results between SC6, SC6_18 and SC6_60, and SC6 and SC6_plain.

Results in Table 6.19 and Figure 6.51 confirm that for the same type of cement and cement content, greater armour units contribute to higher tensile and compressive stresses in the armour unit. Figure 6.50 shows that for the three scenarios, the tensile stresses in P5 never exceed the tensile strength.

Results in Figure 6.51 show that SC6_60 presents higher tensile stresses for the longest time during the simulation and that the evolution of concrete tensile strength in SC6_60 is slightly greater than in SC6_18, because higher temperatures influence the speed evolution of the concrete properties. Comparing results with the obtained for SC6, the maximum tensile stress registered in FEMIX for SC6 (1.51 MPa) is slightly higher than the maximum stress for SC6_18 (1.49 MPa), but lower than that of the SC6_60 (1.99 MPa). These results are coincident with the maximum temperature results analysed in this Section. The tensile strength evolution between SC6 and SC6_60 is very similar.

Regarding the different types of concrete, results show that tensile stresses in SC6_plain are higher (1.68 MPa) than in SC6 (1.51 MPa), and that relatively to compressive stresses results are very similar (around -2.50 MPa).

Table 6.19: Maximum normal stress in P5 and P6 and tensile and compressive strength values for SC6_18, SC6_60, and SC6_plain.

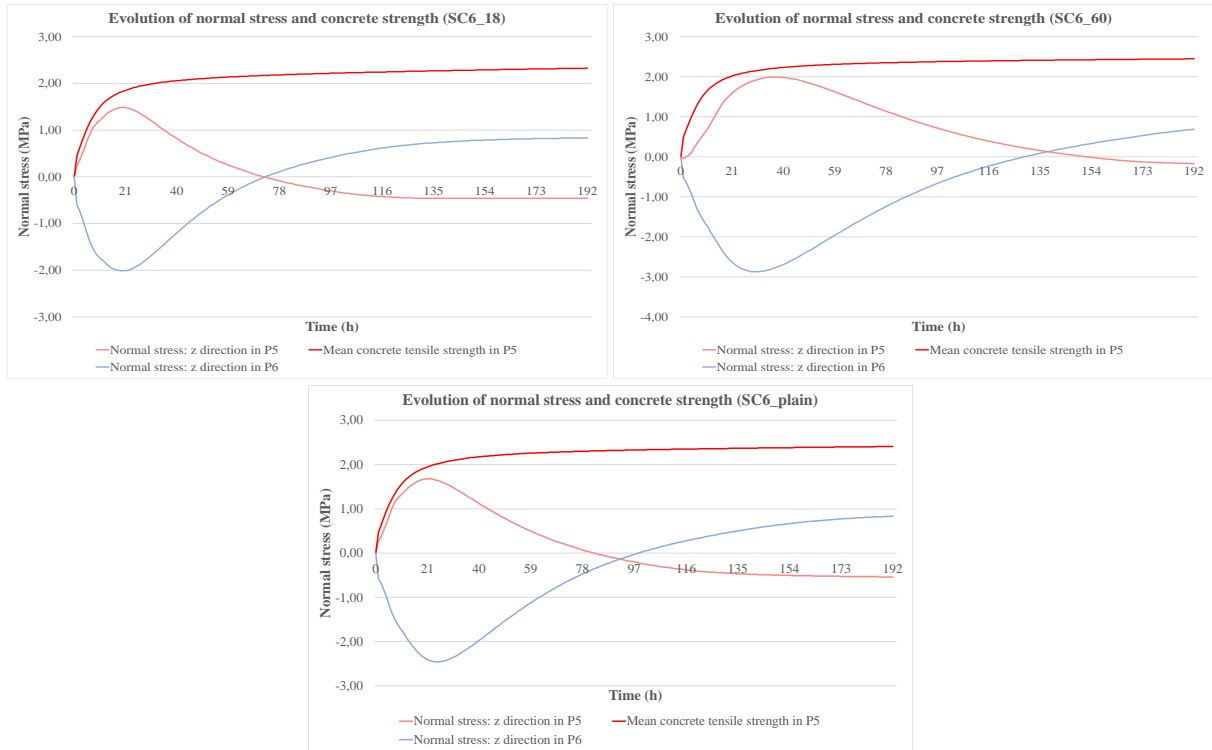| SC	Obs. Point	Element	IP	Max. Normal Stress (MPa)	Time (h)	f_{ct} (MPa)	f_{ct} (MPa)
SC6_18	P5	717	5	1.49	19	1.81	–
	P6	924	7	-2.01	19	–	-37.85
SC6_60	P5	717	6	1.99	35	2.20	–
	P6	854	3	-2.87	28	–	-43.49
SC6_plain	P5	2233	5	1.68	21	1.95	–
	P6	854	5	-2.46	24	–	-41.57

Figure 6.50: Evolution of the normal stress in P5 and P6 for SC6_18, SC6_60, and SC6_plain, and their tensile strengths.
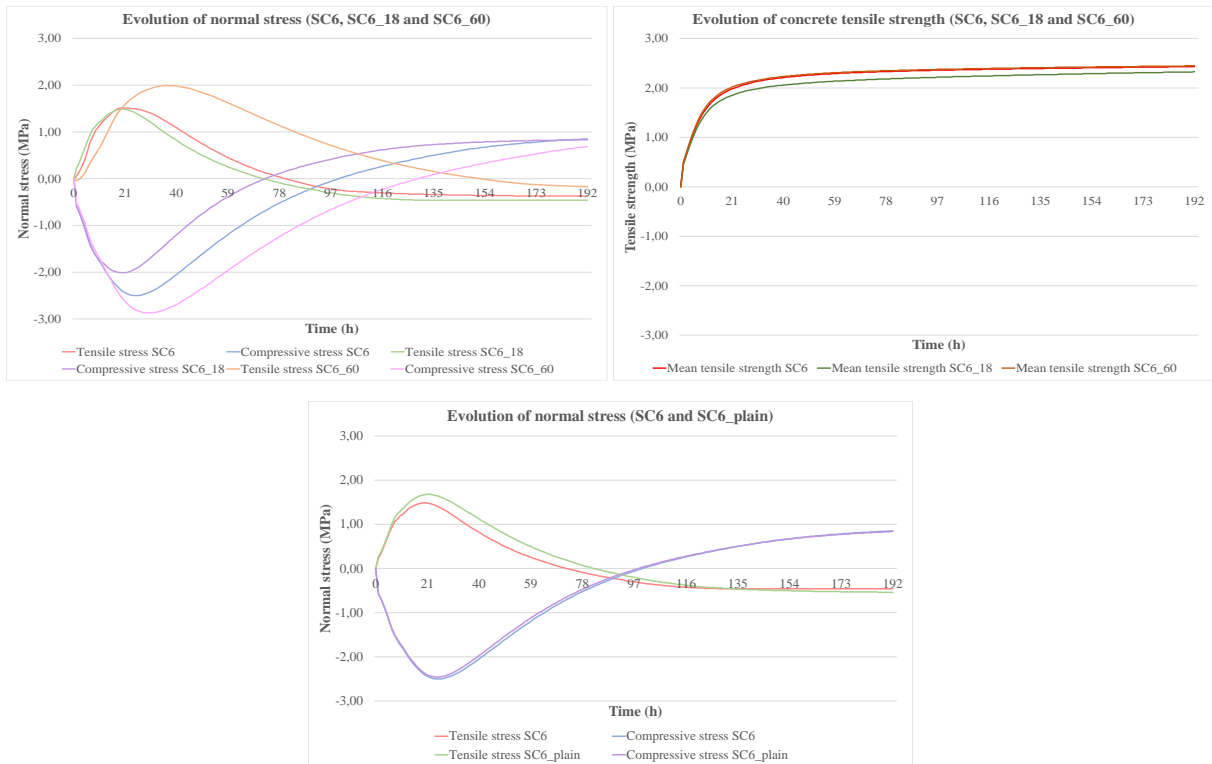
Figure 6.51: Comparison results for the evolution of normal stresses (left) and tensile strengths (right) between SC6, SC6_18 and SC6_60, and the evolution of normal stresses between SC6 and SC6_plain.

In order to analyse the stress behaviour for a critical location in SC6_18, SC6_60 and SC6_plain, different IPs for the same mesh element are selected. Figure 6.52 depicts the results for the evolution of tensile stress and tensile strength in a location where the crack formation occurs in SC6_18, SC6_60 and SC6_plain. Table 6.20 presents the information related to the crack evolution provided in FEMIX for each scenario.
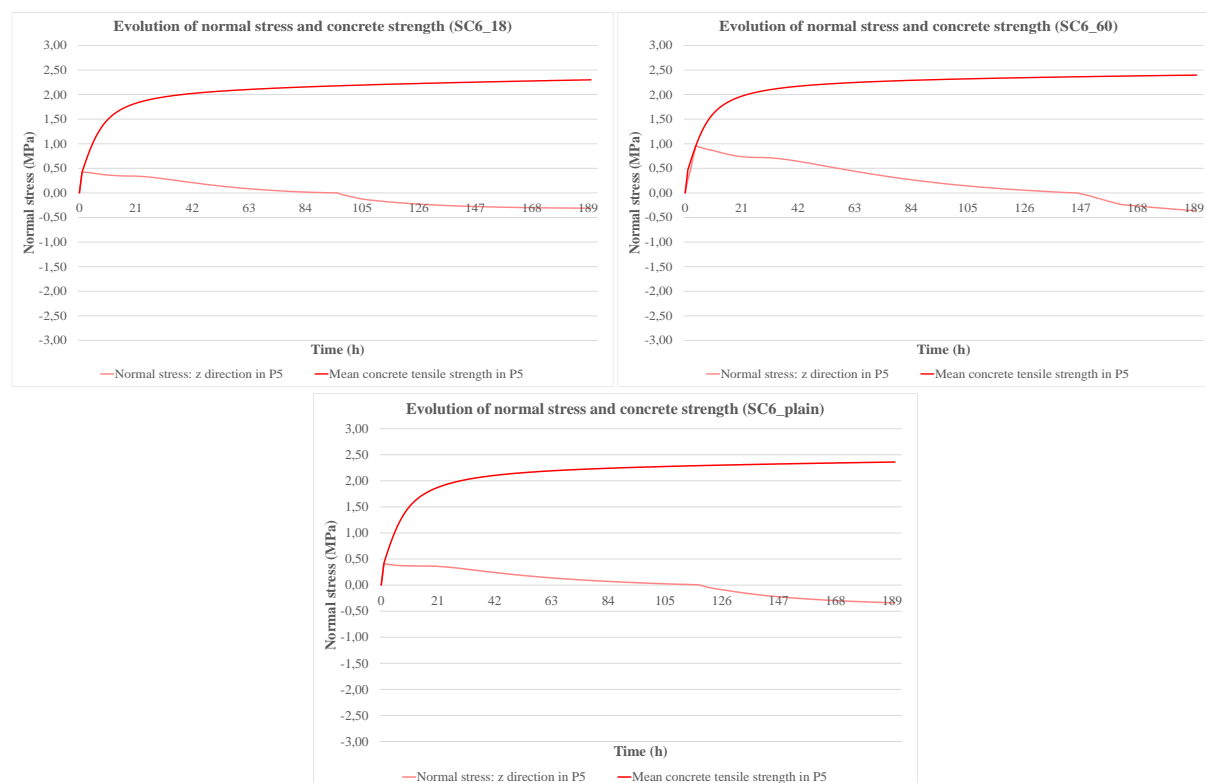
Figure 6.52: Evolution of the tensile stress for a critical location in SC6_18, SC6_60 and SC6_plain, as well as their tensile strengths.

Table 6.20: Crack evolution in SC6_18, SC6_60 and SC6_plain.

Time (h)	Normal Stress: z Direction (MPa)	Mean Tensile Strength (MPa)	Crack Status	No. of Cracks	Crack Normal Strain (%)	Crack Band Width (m)	Crack Width (m)
SC6_18 | Element 717 - Integration Point 4, near P5							
3	0.43	0.43	OPENING	1	1.21E-07	0.0436	5.28E-09
22	0.34	1.81	CLOSING	1	3.25E-04	0.0436	1.42E-05
98	0.00	2.18	CLOSED	1	0.00E+00	0.0436	0.00E+00
SC6_60 | Element 717 - Integration Point 3, near P5							
6	0.96	0.96	OPENING	1	7.47E-07	0.0649	4.85E-08
31	0.72	2.08	CLOSING	1	2.91E-04	0.0649	1.89E-05
148	0.00	2.36	CLOSED	1	2.15E-20	0.0649	1.40E-21
SC6_plain | Element 2233 - Integration Point 6, near P5							
3	0.41	0.42	OPENING	1	2.48E-05	0.0672	1.67E-06
6	0.39	0.88	OPENING	2	7.55E-05	0.0672	5.07E-06
19	0.37	1.78	CLOSING	2	1.24E-04	0.0672	8.33E-06
120	0.00	2.29	CLOSED	2	3.18E-20	0.0672	2.14E-21

Results in Figure 6.52 demonstrate that the maximum tensile stresses registered in SC6_18, SC6_60 and SC6_plain are 0.43 MPa, 0.96 MPa and 0.41 MPa for an age of 3, 6 and 3 hours after casting, respectively.

Results from Table 6.20 show that, near P5, in SC6_plain the maximum number of cracks reached 2 cracks, while in SC6_18 and SC6_60 only 1 crack per IP develops during the simulation time. These results suggest that the plain concrete originates more cracking when compared to RSFRC and that the durability of this armour unit during its service life could be compromised, if these cracks will not close.

For SC6_18, SC6_60 and SC6_plain, the maximum crack widths reach 1.42E-05 m, 1.89E-05 m and 8.33E-06 m at an age of 22 h, 31 h and 19 h after casting, respectively. Regardless of these results, all cracks close at an age of 98 h, 148 h, and 120 h after casting for SC6_18, SC6_60 and SC6_plain, respectively, which indicates the cracks that are forming in the selected IPs are not significant.

Figure 6.53 depicts the crack pattern and the different crack status for the end of the simulation time (192 hours). Results demonstrate that despite most cracks at the end of simulation (8 days after the casting) being either closing or closed due to the temperature decreasing, some cracks in SC6_plain are still reopening. This suggests that the durability of the block might be compromised when using plain concrete for this type of structure if the cracks will not close until 28 days of age. Regarding the total number of cracks that closed, results depict that the greatest armour unit (SC6_60) has the most cracking and that the plain concrete (SC6_plain) also has more cracking when compared to the RSFRC in SC6. In addition, SC6_plain also presents more cracks reopening than in SC6, which indicates that the contribution of the RSFRC is favourable to the stress variations that occur throughout the curing. From all three scenarios, the smallest armour unit (SC6_18) has the less cracking and is the only to have all cracks closed at t = 192 h, due to the fastest temperature decreasing.
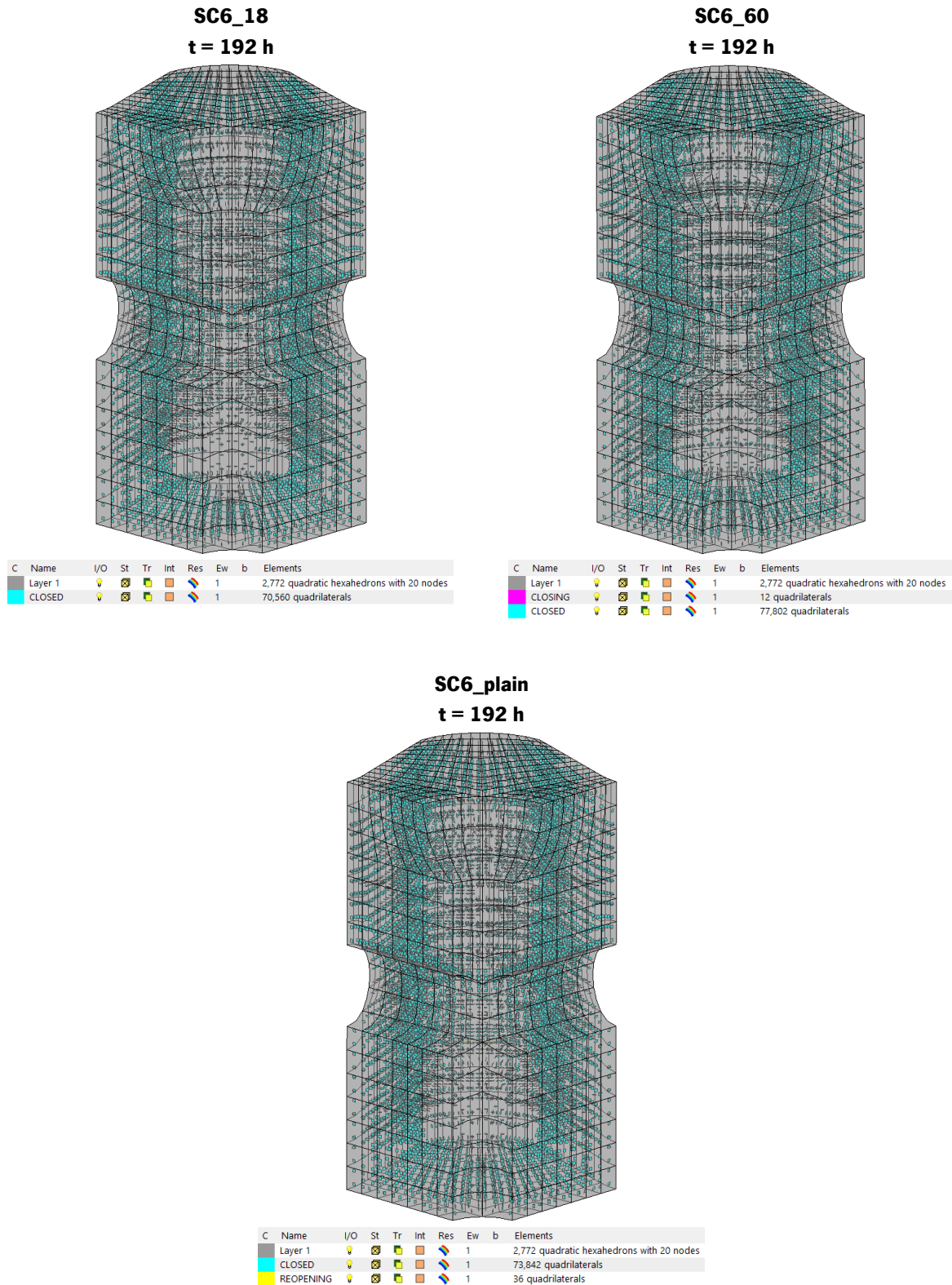
Figure 6.53: Crack pattern and crack status for the last time step in SC6_18, SC6_60 and SC6_plain.

Figure 6.54 plots the evolution of temperature and crack width for the maximum crack opening value registered when the maximum tensile stress is reached in t = 19 h, 35 h and 21 h for SC6_18, SC6_60 and SC6_plain, respectively.

Results from Figure 6.54 demonstrate that the maximum values for crack width and temperature in SC6_18 are 8.65E-05 m and 33.67°C; in SC6_60 are 1.64E-04 m and 33.61°C; and in SC6_plain are 1.52E-04 m and 33.61°C, respectively. Appendix 4C presents additional information retrieved from the obtained results.
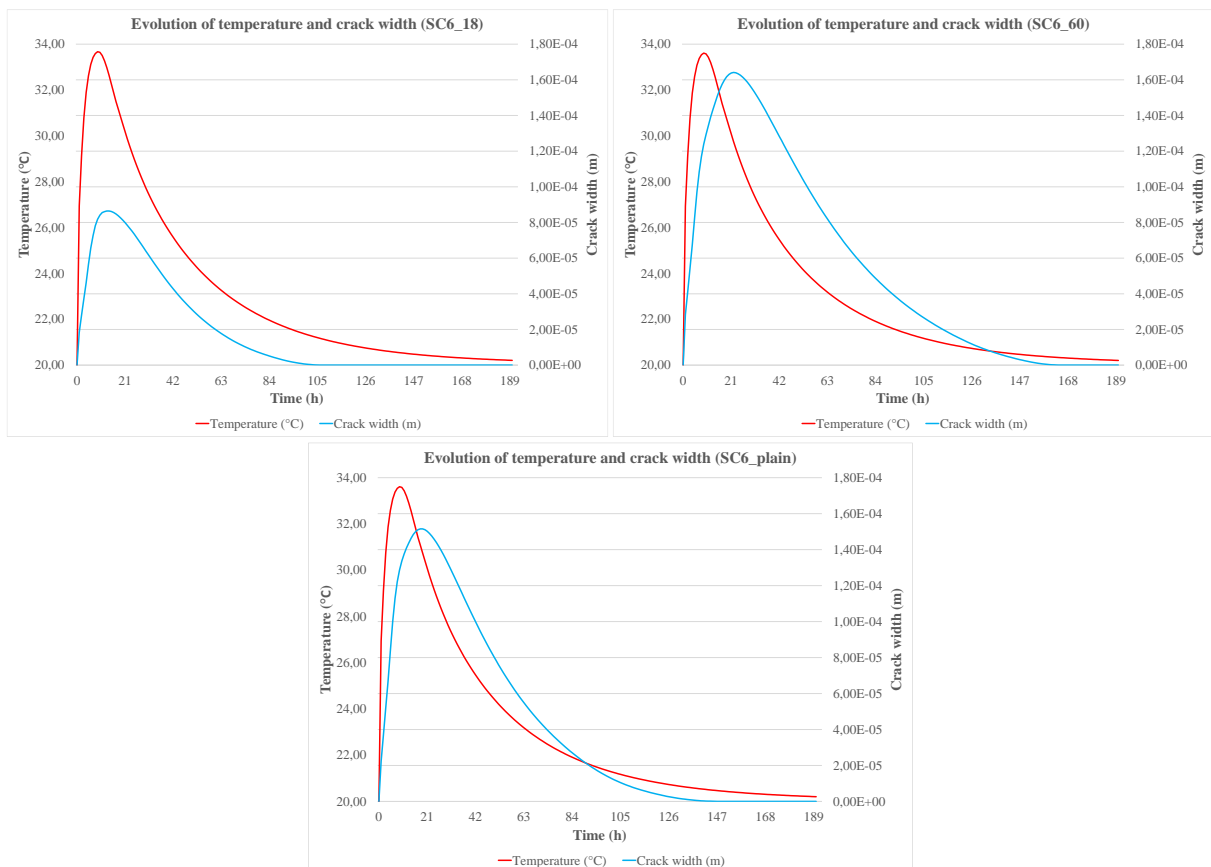
Figure 6.54: Relation between temperature and crack width evolution for SC6_18, SC6_60 and SC6_plain.

Figure 6.55 compares the maximum values for crack width between SC6, SC6_18 and SC6_60, and SC6 and SC6_plain. This Figure demonstrates that greater armour units contribute to greater maximum crack widths and that relatively to the RSFRC in SC6 (1.23E-04 m), the plain concrete (SC6_plain) registers wider cracks (1.52E-04 m). SC6 presents wider cracks than in SC6_18 (8.65E-05 m) and narrower cracks than in SC6_60 (1.64E-04 m). The obtained results allow concluding that, between SC6 and SC6_plain, RSFRC offers greater resistance to crack propagation, as the adopted concrete strength class is the same. In relation to the plain concrete, the lesser maximum crack opening in the

RSFRC armour unit will have an impact on its greater stiffness, lesser susceptibility to rupture when in service, and on the increase of its durability.
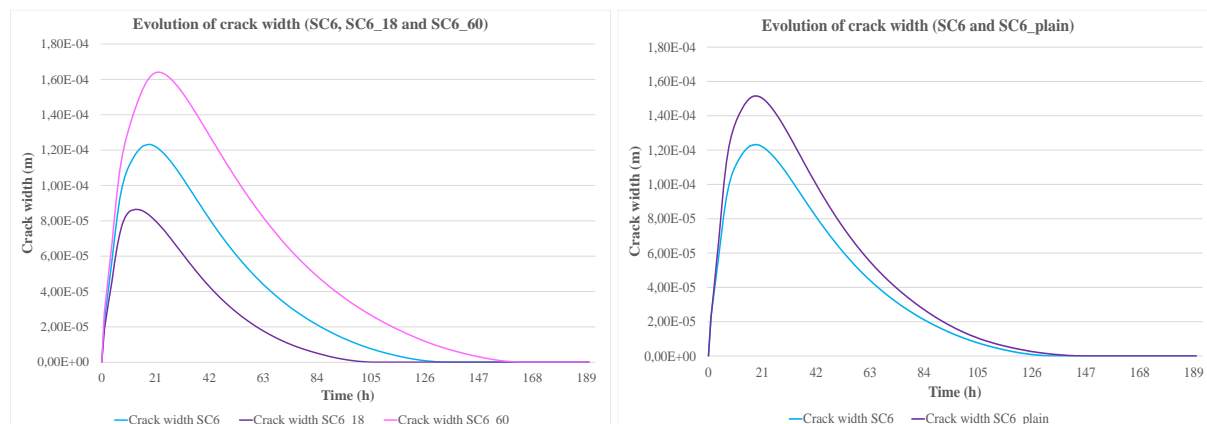
Figure 6.55: Comparison results between crack width evolution for SC6, SC6_18 and SC6_60 (left) and SC6 and SC6_plain (right).

In order to emphasize the beneficial contribution of the fibres and the influence of the armour unit size on the evolution of crack width, Figure 6.56 groups the results for the relation between SC6, SC6_18, SC6_60 and SC6_plain with the crack width during the simulation time.

Thus, this analysis allows concluding that the evolution of the stresses and crack width, as well as the crack pattern is a function of the type of concrete used in the casting, as well as the size of the armour unit.
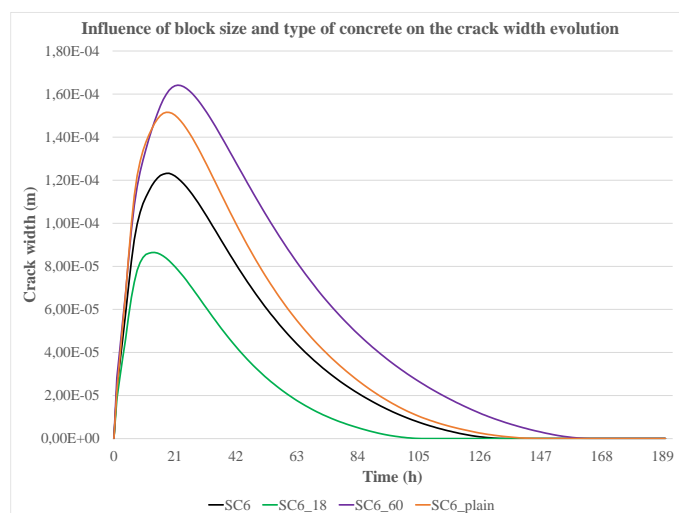
Figure 6.56: Influence of armour unit size and type of concrete on the evolution of crack width for SC6, SC6_18, SC6_60 and SC6_plain.

6.4 Suggestions for the rope confinement of the armour unit

Rope confinement is an innovative technique that contributes to the improving of the stability of the armour units, and to the increase of its axial load and deformation capacity, as well as to the energy absorption from rocking.

The selected confinement material for the ropes is the sisal and the adopted technique includes the wrapping and/or the interlocking of the blocks using ropes through the openings intended for this purpose. The use of FRPs is not wise due to the relatively small confinement effect they can introduce in this high volumetric elements, as well as their high price.

The use of the rope confinement technique will allow the energy absorption of local actions from rocking, and since the spaces created between blocks will be small and the kinetic energy will be too low to induce significant damage, the rope confinement will give the armour units good impact resistance. However, due to the low modulus of elasticity and natural porosity, the associated relaxation of the sisal ropes fibres (loss of tension over time) will occur. Nonetheless, the eventual rotation and displacement of armour units will induce tensions on the ropes of the surrounding blocks that will help prevent breakage of the concrete. The material should also ensure adequate durability during dry-wet cycles.

The armour units can be partially or fully confined and the process can be ensured by using a type of winding machine that is commonly used in concrete column confinement with carbon fibres. The selection of sisal ropes for this purpose is justified by their regular practice in ship mooring and good tensile properties. The consideration of man-made fibres for the rope confinement process in marine environments is not advisable due to environmental concerns, as disintegration of the rope and releasing of harmful elements is a possibility.

The armour units' geometry along with the macro-structure location at the intertidal zone as presented in Chapter 5 (crest level of 0 m, relatively to MSL), provide the means to promote biodiversity in the hollow features, as well as onto the sisal ropes. This is due to the fact that this region is known for being an ecosystem that provides optimal conditions for many marine organisms (e.g., algae, crabs, sea stars, snails, barnacles, mussels), and for being important feeding spots for birds.

In this study, the analysis of the armour unit for the hardened state was not conducted, since the aim was on the crack risk analysis that occurs during the construction phase. Nevertheless, since from a conceptual point of view, the armour units were designed to account for sisal ropes to confine the unit itself and/or to connect the blocks, Figure 6.57 presents a schematic representation of this solution for a single armour unit. The representation includes the sisal ropes around the element (solid line and

solid dots) and the sisal ropes configuration when ropes are tensioned by the transversal ropes and/or other blocks (dotted line). Two alternative armour unit arrangements are shown in Figure 6.58, which are intended to take advantage of the rope confinement technique provided by adjacent blocks.
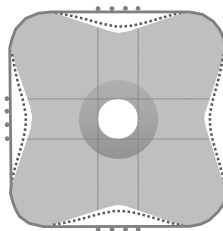
Figure 6.57: Schematic representation for the rope confinement of a single armour unit.
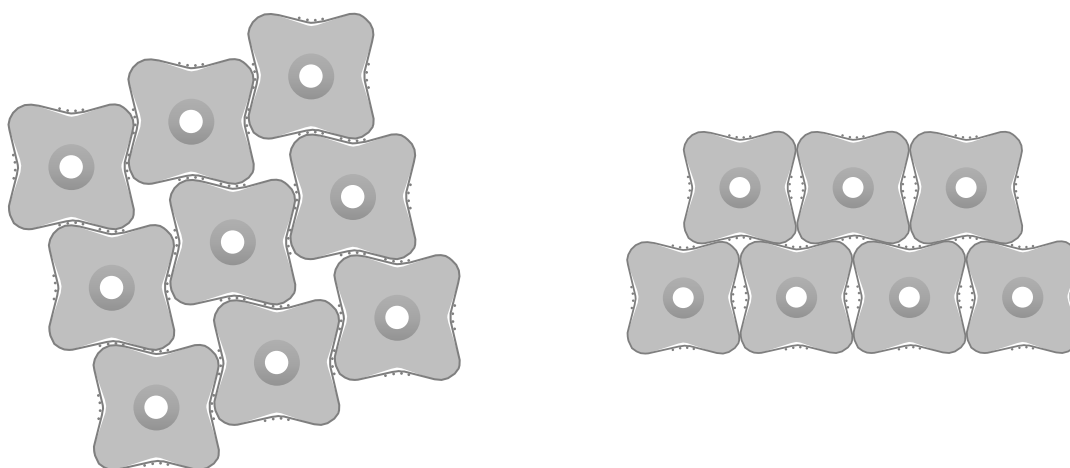
Figure 6.58: Two arrangement alternatives for rope confinement of armour units.

It is important to note that the main sisal rope properties are in the longitudinal direction, because of their fibres distribution. Sisal ropes have an orthotropic behaviour, which means that mechanical and thermal properties are unique and independent in the three directions. The methodology for simulating the rope confinement should account for the pairing between the armour unit and the sisal meshes, as well as for the consideration of interface elements between the two meshes to allow the ropes to move around in all directions.

6.5 Summary and conclusions

Innovative eco-engineering solutions are of paramount importance for the design of breakwater armour units, which should mitigate erosive processes promoting sediments accretion on coastal stretches. A comprehensive state of the art regarding existing solutions served as basis for the conceptualization of the innovative concrete armour unit shapes and geometrical design proposed in this study.

An innovative shape for a concrete armour unit based on good structural and hydraulic stabilities was developed. The proposed solution was designed by applying the van der Meer formula and combines the advantages of the resilience associated to robust blocks and the interlocking abilities in order to obtain good structural and hydraulic stabilities for coastal erosion protection.

The armour unit has a cube-like shape with a cross section with round edges to avoid chipping and a convex shape at the centre parts that will allow a better interlocking with the surrounding blocks. To increase the interlocking capabilities, two different armour unit shapes that complement each other were proposed, in order to ensure good impact resistance guaranteeing that no significant damage due to the collisions of blocks (rocking) will occur. This shape, with holes on its faces, increases the wave energy dissipation and allows the easy attachment of colonies of marine organisms and at the same time allows anchoring the sisal ropes through the holes.

Since the proposed concrete armour units have large dimensions, the generation of high temperatures in the construction phase is recognized as a critical design situation. The formation of cracks during concrete hardening (thermal stress cracking) is a process that occurs due to temperature difference between the inside and the outside of the elements, when tensile stresses reach the strength of early age concrete. In order to evaluate this process, a numerical modelling study for the thermo-mechanical behaviour of the proposed armour unit was applied.

The application of steel fibres as concrete reinforcement had been analysed, since in recent studies results have shown that fibre-reinforced concrete can enhance the post-cracking response and impact resistance of the concrete. From a structural and environmental point of view, the application of recycled steel fibres from tyres is justified by the fact that they exhibit similar mechanical response than the industrial steel fibres with far lesser energy consumption in production with a positive ecological contribution.

The armour units are usually subjected to rocking under heavy wave attack. This phenomenon makes the structure more vulnerable, and compromises its stability. A solution to reduce the rocking and enhance the concrete strength by rope confinement was suggested in order to dissipate energy and to reduce contact stiffness.

The main objective of the proposed armour unit shapes was to overcome some of the fragilities of the existing blocks and to consider an adequate concrete mix with recycled steel fibres that could enhance the concrete mechanical properties, as well as the post-cracking behaviour.

Thermo-mechanical numerical modelling allowed understanding the influence of types of cement and cement contents on the evolution of temperatures, stresses and strength of concrete, as well as on the

crack risk by establishing six different scenarios. Moreover, the most critical scenario served as basis for the analysis of two different volumes for the armour unit (18 tonnes and 60 tonnes), and for the comparative study between RSFRC and plain concrete. The analysis for the numerical modelling mesh refinement demonstrated that the coarser mesh is sufficient to predict the thermo-mechanical evolution. From the thermal modelling results, it can be concluded that:

- The temperature values decreased from the core to extremities, where temperatures reached minimum values close to the ambient temperature, especially around corners;
- The greatest temperature gradient was found in the inner part of the block, where temperature reached maximum values;
- The evolution of the maximum temperature is a function of the cement content used in the casting due to the exothermic reaction between cement and water. Consequently, the temperature variation that results from hydration is more abrupt for higher contents of cement;
- The evolution of the maximum temperature is a function of the type of cement used in the casting due to the cement constituents, which consequently means that the temperature variation is also more abrupt for greater types of cement;
- Higher temperatures imply the increase of cracking risk due to the evolution of tensions in the concrete.

For the mechanical analysis, the defining of RSFRC toughness and the shape of the tensile-softening diagram allowed calculating the stresses and strength of concrete, as well as the evolution of the crack formation. The mechanical model included the simulating of cracking behaviour of the RSFRC as well as the maturity along the curing time. The simulations were performed for three numerical analysis: i) concrete with elastic behaviour (linear); ii) crack constitutive model (nonlinear) for two simulations considering a maximum of 1 and 2 cracks per IP; and iii) the crack constitutive model with the autogenous shrinkage and creep (shrinkage and creep) for a maximum of 2 cracks per IP.

From the linear mechanical modelling results, it can be concluded that:

- The maximum compressive stress never exceeded 50% of the compressive strength of the RSFRC, which allows assuming a linear compression behaviour;
- The elastic behaviour predicted an unrealistic behaviour for the tensile stresses, because the stress field reached higher values than the tensile strength.

From the nonlinear mechanical modelling results, it can be concluded that:

- Considering a maximum of 1 crack per IP, the tensile stress development exceeds the tensile strength, which can lead to unsafe predictions since the degradation of stiffness is not being well captured;

- Considering a maximum of 2 cracks per IP, the realistic stress development curve was captured, since stresses did not exceed the tensile strength and stress values started decreasing when the concrete cracks.

From the nonlinear with shrinkage and creep mechanical modelling results, it can be concluded that:

- In locations where temperatures reached their maximum values, the compressive stresses were also the greatest due to the restrictive conditions provided by the support and symmetry boundaries that limit the expansion of concrete;

- The cracks were mainly located in areas near the steel formwork and/or in contact with the ambient temperature, where the lowest temperatures and the maximum tensile stresses were presented. These results demonstrated that the temperature decrease lead to the development of tensile stresses when the retraction of concrete is restricted;

- The shrinkage and creep model results showed wider cracks than those obtained from the nonlinear model;

- For the same type of cement, the evolution of the stresses and crack width, as well as the crack pattern is a function of the cement content used in the casting due to higher temperatures;

- The greatest and fastest evolution of the concrete tensile strength for higher contents of cement contributed to less cracking;

- For the same cement content, the evolution of the stresses and crack width, as well as the crack pattern is a function of the temperatures and the type of cement used in the casting;

- The evolution of concrete tensile strength was greater and faster for greater types of cement, because the type of cement and high temperatures influence the speed evolution of the concrete properties;

- Despite most cracks at the end of simulation (8 days after the casting) being either closing or closed due to the temperature decreasing, some cracks were still reopening, especially for the greatest type of cement;

- After temperature reaching its maximum value, cracks started closing due to temperature decreasing and that fastest temperature decreasing lead to cracks closing at an earlier age;

- Results suggest that the type of cement CEM I 42.5R and the cement content of 435 kg/m^3 were the most adequate for the proposed armour unit, since the stresses evolution lead to no cracks at the end of simulation.

From the mechanical modelling results for the armour units with different volumes and with plain concrete, it can be concluded that:

- For the same type of cement and cement content, the thermal analysis allows concluding that the evolution of the maximum temperature is a function of the size of the armour unit used in the casting due to the temperature dissipation. Regarding the mechanical analysis, the evolution of the stresses and crack width, as well as the crack pattern is a function of the size of the armour unit, and of type of concrete used in the casting.

- Regarding the different types of concrete, the tensile stresses in the plain concrete were slightly higher and originated more cracking than in the RSFRC, as well as more cracks reopening at the end of the simulation. In addition, the plain concrete registered wider cracks than in RSFRC;

- The evolution of concrete tensile strength in greater armour units was slightly faster than in smaller blocks, because higher temperatures influence the speed evolution of the concrete properties. The speed evolution of the concrete properties between the plain concrete and the RSFRC was very similar;

- Despite most cracks at the end of simulation (8 days after the casting) being either closing or closed due to the temperature decreasing, some cracks in the plain concrete were still reopening;

- From all three scenarios, the smallest armour unit was the only to have all cracks closed at the end of the simulation due to the fastest temperature decreasing, and to reach maximum temperature values at a slight earlier age, thus attaining the ambient temperature faster;

- The contribution of the RSFRC is favourable to the stress variations that occur throughout the curing.

6.6 References for Chapter 6

ACI. (1992). *American Concrete Institute - Prediction of creep, shrinkage, and temperature effects in concrete structures (Reapproved 1997), Technical committee document 209R-92, American Concrete Institute (ACI), Committee 209.*

Azenha, M. (2009). *Numerical simulation of the structural behaviour of concrete since its early ages*. PhD Thesis in Civil Engineering, Faculty of Engineering of the University of Porto, Portugal. Retrieved from http://hdl.handle.net/10216/57587.

Azenha, M.; Sena-Cruz, J.; Camões, A.; and Ferreira, R.M. (2011). Numerical simulation of the structural behaviour of concrete tetrapods subject to imposed deformations and applied loads. In *Congress on Numerical Methods in Engineering, 14th to 17th June 2011*. Coimbra, Portugal. Retrieved from http://hdl.handle.net/1822/12989.

CIMPOR. (2021). Gama de Cimentos. Descrições e Finalidades. Retrieved July 15, 2021, from https://www.cimpor.com/cimento.

D'Ambrosia, M.; Altoubat, S.; and Lange, D. (2001). Early Age Tensile Creep and Shrinkage of Concrete with Shrinkage Reducing Admixtures. In F. Ulm, Z. Bazant, & F. H. Wittman (Eds.), *Proceedings of CONCREEP: Creep, Shrinkage and Durability Mechanics of Concrete and other Quasi-Brittle Materials, 13th to 15th August 2001* (pp. 685–690). Boston, USA. Retrieved from https://www.researchgate.net/publication/237746268_Early_Age_Tensile_Creep_and_Shrinkage_of_Concrete_with_Shrinkage_Reducing_Admixtures.

EC2. (2004). Eurocode 2 - Design of Concrete Structures—Part 1-1: General rules and rules for buildings, CEN, EN 1992-1-1. Brussels, Belgium.

Fédération internationale du béton. (2013). *fib Model Code for Concrete Structures 2010*. John Wiley & Sons.

Frazão, C.M.V. (2019). *Recycled Steel Fiber Reinforced Concrete for Structural elements subjected to chloride attack: Mechanical and Durability performance*. PhD Thesis in Civil Engineering, University of Minho, Portugal. Retrieved from http://hdl.handle.net/1822/66884.

Freitas, P. (2013). *Estabilidade Hidráulica em Cubos Antifer. Estudo em Modelo Físico*. Instituto Superior Técnico Lisboa. Retrieved from https://fenix.tecnico.ulisboa.pt/cursos/mec/dissertacao/2353642435846.

Guo, Z.; and Shi, X. (2011). Chapter 5 - Temperature–Time Curve of Fire and the Equation of Heat Conduction. In Z. Guo & X. B. T.-E. and C. of R. C. at E. T. Shi (Eds.) (pp. 76–90). Boston: Butterworth-Heinemann. https://doi.org/https://doi.org/10.1016/B978-0-12-386962-3.10005-1.

Koenigsfeld, D.; and Myers, J.J. (2003). *Secondary reinforcement for fiber reinforced polymers reinforced concrete panels. Report CIES 03-45*.

Medina, J.R.; Gómez-Martín, M.E.; Peña, E.; and Corredor, A. (2022). Design of the Western Breakwater for the Outer Port at Punta Langosteira, A Coruña, Spain. In *Coastal Structures and Solutions to Coastal Disasters 2015, 9th to 11th September 2015* (pp. 828–837). Boston, Massachusetts, USA. https://doi.org/doi:10.1061/9780784480304.086.

Póvoas, R.H.C.F. (1991). *Modelos não-lineares de análise e dimensionamento de estruturas laminares de betão incluindo efeitos diferidos*. PhD Thesis in Civil Engineering, Faculty of Engineering of University of Porto, Portugal.

Taveira-Pinto, F.; and Cunha, P. (2010). Dimensionamento Optimizado de Quebramares de Taludes. Optimized Design of Rubble Mound Breakwaters. In *5as Jornadas de Hidráulica, Recursos Hídricos e Ambiente, 25 Outubro 2010*. Porto, Portugal. Retrieved from https://paginas.fe.up.pt/~shrha/publicacoes/pdf/JHRHA_5as/2_FTPinto_Dimensionamento.pdf.

Valente, T. (2019). *Advanced tools for design and analysis of fiber reinforced concrete structures*. PhD Thesis in Civil Engineering, University of Minho, Portugal. Retrieved from http://hdl.handle.net/1822/65870.

van der Meer, J.W. (1988). Stability of Cubes, Tetrapodes and Accropodes. In *Proceedings of the Breakwaters '88 Conference, London, UK* (pp. 71–80).

van Zwicht, B.N.M. (2009). *Effect of the concrete density on the stability of Xbloc armour units*. MSc Thesis in Coastal Engineering, Faculty of Civil Engineering and Geosciences, Delft University of Technology, The Netherlands. Retrieved from http://resolver.tudelft.nl/uuid:8866d0ca-1ecf-4ea0-bb91-f0623a14de94.

Ventura-Gouveia, A. (2011). *Constitutive models for the material nonlinear analysis of concrete structures including time-dependent effects*. PhD Thesis in Civil Engineering, University of Minho, Portugal. Retrieved from http://hdl.handle.net/1822/19653.

Weiss, W.J.; Yang, W.; and Shah, S.P. (1998). Shrinkage Cracking of Restrained Concrete Slabs. *Journal of Engineering Mechanics*, *124*(7), 765–774. https://doi.org/10.1061/(ASCE)0733-9399(1998)124:7(765).

CHAPTER 7

Conclusions and Future Research

"*Research is seeing what everybody else has seen and thinking what nobody else has thought*"
Albert Szent-Györgyi. Hungarian pharmacologist. Nobel Prize in Physiology or Medicine in 1937 (1893-1986)

(Page intentionally left blank)

CHAPTER 7   CONCLUSIONS AND FUTURE RESEARCH

7.1 Main conclusions

Hydro-morphodynamics of highly dynamic estuarine and coastal zones systems are directly influenced by natural driving forces (e.g., waves, tidal currents, wind, river discharges and sea level changes) and human-induced impacts (e.g., coastal morphological modifications and sediment supply changes). Understanding the fundamentals of the physical and anthropogenic complex phenomena inherent to the integrated study of estuaries and beaches is of paramount importance for a healthy and sustainable coastal environment.

In a highly energetic wave environment such as the Portuguese coast, in-depth knowledge of processes involving long sediment transport is of crucial importance for the design and maintenance of coastal protection structures. On the other hand, these structures are especially vulnerable to climate change due to their long lifespan and their location in an aggressive marine environment.

Since the predictable consequences of climate change on coastal zones are the rise in mean sea level and the change in the wave climate regimes, with the increase in the frequency and duration of the storms, it is necessary to analyse the variability of its parameters, specifically the significant wave height, maximum wave height, direction, peak period, among others.

The quantification of the effect of climate change on the loss of reliability of maritime works requires tools that predict the behaviour of structures, their deformation and the triggering of different failure modes throughout the evolution of the structure's damage.

For this, research work is needed for improving technical solutions inspired by nature and for the understanding of structural materials with adequate compatibility with the coastal environment when applied as control measures for mitigating erosion.

The main outcome of this research work is the design and assessment of an innovative coastal protection solution based on numerical modelling and observation of natural accretion or sedimentary stable processes, applying high structural multifunctional eco-materials (tested through numerical modelling) with high durability and ductility. Following a multidisciplinary approach, the purpose is to provide coastal infrastructure designers with nature-based solutions reproducing and manipulating natural processes, such as sediment transport involving longitudinal drift and drift reversal phenomena in order to mitigate coastal erosion processes. The most relevant scientific contributions are summarized as follows.

7.1.1 Wave statistics

An extreme wave value analysis under uncertainty scenarios using comprehensive simulated wave datasets downscaled by Meteogalicia from CMIP5 models to 17 stations off the Iberian Peninsula coastal zone has been performed. From this study, it was possible to obtain results that allow determining the extreme values of waves for H_s and T_p, which are essential parameters for the maritime structural design in this coastal zone.

Those values for H_s and T_p were calculated through the Gumbel, Fréchet and Weibull distributions for the 10-, 50-, and 100-year return period, considering five wave climate scenarios using historical observed data and projected data of RCP4.5_mid, RCP4.5_end, RCP8.5_mid, and RCP8.5_end.

Statistical analysis of the obtained results demonstrated that extreme H_s values for all return periods considered have different values in different locations in the coastal zone with decreasing values from North to South, being considerably lower on the most southern stations. In each station, historical data values are similar to those calculated in the RCPs_mid, and projected values obtained from the RCPs_end have higher values when compared to historical data values. For each return period, wave peak period T_p results show constant values in all stations, independently the scenario considered.

Wave extreme value analysis for the H_s and T_p is an essential element for marine structural design. The high-quality of the database applied and the assumptions taken in this research work allowed the determination of 100-year return period of H_s and T_p values that can be used with confidence as design values for structural analyses in maritime works to be built in the western coast off Iberian Peninsula.

7.1.2 Hydro-morphodynamics

Sediment transport from the action of sea waves incoming at an angle with the coastline induces a net sediment transport alongshore. In the case of the NW Portuguese coast, this phenomenon corresponds to a predominant transport from N to S promoted by waves approaching from NW. The traditional adopted coastal engineering solutions take advantage of this N-S drift, like groins that are constructed as protection works. In these cases, the sediment transport is interrupted by these transverse structures, which favour the sediment accretion in the updrift side of such structures. However, these solutions appear to be useless where the sedimentary sources are scarce not allowing the supply of sediment, and, most importantly, they induce negative environmental impacts such as erosion of beaches, and increase of the height of surf zone waves.

A comparative numerical modelling study to assess the performance of a multifunctional artificial reef (MFAR) structure and three traditional coastal protection solutions was developed to

understand the hydro-morphodynamics on a local bathymetry (Leirosa). When the impact of the MFAR on a coastal zone was compared with a submerged and an emerged detached breakwater, the conclusion was that the emerged detached breakwater was the most efficient in reducing significant wave heights and in sediment accretion at the shoreline compared to the submerged detached breakwater and the MFAR.

When the impact of the MFAR on a coastal zone was compared with one submerged and a group of two submerged detached breakwaters the conclusion was that the most significant sediments accretion at the shoreline is noticeable for the group of detached breakwaters, while the largest overall sediments accumulation is visible for the MFAR.

The observation of the impact of existing engineering structures on the longshore drift reversing phenomenon using GIS (Google Earth Pro) served as basis for the characterization of the geometric and sedimentary conditions, in order to determine the most important drivers responsible for morpho-sedimentary changes.

Hydro- and morphodynamics numerical simulations near Iberian Peninsula shoreline under storm conditions have been developed in order to obtain optimized geometries for maritime protection structures under longitudinal drift reversal conditions. Hydrodynamics modelling with SWAN was applied to determine the effect of the wave regime in wave energy dissipation and the reversal of longitudinal drift in different bathymetric conditions when the domain was considered without implantation of structures or when structures with different geometries were considered. Morphodynamics modelling with XBeach was applied to describe sediments transport behaviour (accretion and erosion) for pre-defined protection structures with the best hydrodynamics performance related to the reversal of longitudinal drift.

The results obtained allow concluding that the selected innovative structure (with a shape similar to the MFAR) could be adequate for protecting coastal zones, since there is no interruption of the longitudinal drift, and downdrift contributing to sediments accumulation near shoreline. Overall, the sedimentary distribution of this structure is good, except for the scouring next to its extremities. Nonetheless, the structure stability is ensured, if knowing its intensity by making sure the foundation is at a deeper elevation than the erosion level. The overall results of the developed hydro-morphodynamic studies allow concluding that the tested innovative structures can be an excellent alternative technical solution to overcome problems and weaknesses presented by traditional protection structures.

7.1.3 Strength and resilience of eco-materials

In a prone retreat coastal zone under high wave energy action, without natural protection and large sediment transport deficit, many different solutions can be used to reduce or to control coastal erosion. The most common protection structures based on "hard-engineering" may locally reduce risks of exposure to wave action but do not eliminate them. A comprehensive state of the art regarding existing solutions for the design of breakwater armour units served as basis for the conceptualization of the proposed innovative concrete armour unit shapes and geometrical design.

An innovative shape for a concrete armour unit was designed applying the van der Meer formula and combines the advantages of the resilience associated to robust blocks and the interlocking abilities in order to obtain good structural and hydraulic stabilities for coastal erosion protection.

The armour unit has a cube-like shape with a cross section with round edges to avoid chipping and a convex shape at the centre parts that will allow a better interlocking with the surrounding blocks. To increase the interlocking capabilities, two different armour unit shapes that complement each other were proposed, in order to ensure good impact resistance guaranteeing that no significant damage due to the collisions of blocks (rocking) will occur. This shape, with holes on its faces, increases the wave energy dissipation and allows the easy attachment of colonies of marine organisms, and at the same time allows natural fibre rope confinement through the holes.

Since the proposed concrete armour units have large dimensions, the generation of high temperatures in the construction phase is recognized as a critical design situation. In this context, the structural behaviour of these units namely their composition, mechanical properties and the cracking had been analysed applying numerical modelling.

The application of steel fibres as concrete reinforcement has been analysed, since in recent studies results have shown that fibre-reinforced concrete can enhance the post-cracking response and impact resistance of the concrete. From a structural and environmental point of view, the application of recycled steel fibres from tyres, which is not widely applied in maritime works, is justified by the fact that they exhibit similar mechanical response than the industrial steel fibres with far lesser energy consumption in production with a positive ecological contribution.

The main objective of the proposed armour unit shapes was to overcome some of the fragilities of the existing blocks and to consider an adequate concrete mix with recycled steel fibres that could enhance the concrete mechanical properties, as well as post-cracking behaviour. In order to achieve this, thermo-mechanical numerical modelling under six different scenarios was applied to predict the

influence of types of cement and cement contents on the evolution of temperatures, stresses and strength of concrete, as well as on the crack risk.

From the obtained thermal modelling results, it can be concluded that the variation of temperature is a function of the size of the armour unit, type and content of cement used in the casting, and that higher temperatures imply the increase of cracking risk due to the evolution of stresses in the concrete.

The mechanical analysis allowed calculating the stresses and strength of concrete, as well as the evolution of the crack formation. The analysis consisted in the behaviour of stresses and strength evolution considering linear, nonlinear and nonlinear with shrinkage and creep simulations. The most critical scenario served as basis for the analysis of two different sizes for the armour unit, and for the comparative study between RSFRC and plain concrete. The linear simulation allowed assuming the RSFRC has a linear compression behaviour and that the elastic behaviour predicts unrealistic results for the tensile stresses. The nonlinear simulation demonstrated that the consideration for 2 cracks per IP is the most adequate, as it predicts a realistic stress development. The shrinkage and creep modelling allowed concluding that the evolution of stresses, crack width and crack pattern is a function of temperature, cement content, type of cement, size of the armour unit, and type of concrete.

Globally, the analytical approach followed in this work and the pre-design formulas applied give enough scientific confidence to propose an innovative technical solution for armour units in terms of shape and materials.

7.2 Suggestions for future Research

The multidisciplinary nature of the present work in the search and proposal of innovative solutions for the protection of coastal erosion makes it possible to identify several complementary thematic areas that can be the object of future research.

In the present work, an extreme wave value analysis under uncertainty scenarios was developed using comprehensive simulated wave datasets downscaled by Meteogalicia from CMIP5 models to 17 stations off the Iberian Peninsula coastal zone. Previous studies in the western coast of Portugal were based on limited time series periods and considered single locations over the region. Future research work based on long field observations time series of wave climate regimes could be of great interest to compare with the findings of this research work, complementing the description of the variability of wave parameters off the Iberian Peninsula, especially at the Portuguese coast.

In this work, an optimized geometry for maritime protection structure based on longitudinal drift reversal conditions was analysed for a generic bathymetry. A future scientific development could be

carried out to complement this study with specific fieldwork collecting historical records of bathymetry and sediment characteristics of a given coastal stretch.

The modification of the coastal seabed by the introduction of innovative permanent structures capable of inducing the local reverse of the dominant longshore drift and mitigating the installed erosive processes was the object of study in this work. More research should be explored comparing the results obtained in this thesis with the effect of artificial sediments nourishment deposition in coastal segments using a similar methodological approach.

In this research work an innovative solution for coastal protection structures was studied and proposed. This solution includes a new shape and geometrical design of armour units whose structural behaviour had been analysed applying numerical modelling. Further research based on experimental studies with physical models could be developed in order to understand the stability behaviour of the proposed armour unit complementing the numerical modelling outcomes of this work.

In the present study, the service analysis of the proposed armour unit was not considered. However, it is suggested that the analysis of the behaviour of the concrete hardened state could be developed in future research work, since this is an important aspect for its application.

The innovative shape for a concrete armour unit, with holes on its faces, is proposed to increase the wave energy dissipation and to allow the easy attachment of colonies of marine organisms. Since this shape allows rope confinement through the armour unit holes, complementary research work could be conducted to predict axial load and deformation capacity, as well as the energy absorption from rocking. Properties of widely tested RSFRC with application in current structural elements were adopted. However, as these properties are determined considering smaller granulometry than it would be expected for large blocks, it would be interesting to develop an experimental program for RSFRC with larger granulometry, more in line with the size of these blocks.

The thermo-mechanical behaviour of the proposed armour unit was developed in order to determine the evolution of stresses and strength of concrete in the course of the hydration process. Further research could be developed applying computational fluid dynamics to determine critical actions in the structure and using FEMIX software to calculate stresses and deformations of the block.

In this work, the study of the proposed armour unit integrated scientific contributions in the fields of hydraulic and structural engineering, and ecology. Complementary financial considerations on first investment and maintenance costs of this structure could be object of future research to assess its economic sustainability.